

Advances in development and utilization of underground space

Edited by

Yuwei Zhang, Zhanping Song, Liang Cui, Ping Zhang and Naifei Liu

Published in

Frontiers in Earth Science



FRONTIERS EBOOK COPYRIGHT STATEMENT

The copyright in the text of individual articles in this ebook is the property of their respective authors or their respective institutions or funders. The copyright in graphics and images within each article may be subject to copyright of other parties. In both cases this is subject to a license granted to Frontiers.

The compilation of articles constituting this ebook is the property of Frontiers.

Each article within this ebook, and the ebook itself, are published under the most recent version of the Creative Commons CC-BY licence. The version current at the date of publication of this ebook is CC-BY 4.0. If the CC-BY licence is updated, the licence granted by Frontiers is automatically updated to the new version.

When exercising any right under the CC-BY licence, Frontiers must be attributed as the original publisher of the article or ebook, as applicable.

Authors have the responsibility of ensuring that any graphics or other materials which are the property of others may be included in the CC-BY licence, but this should be checked before relying on the CC-BY licence to reproduce those materials. Any copyright notices relating to those materials must be complied with.

Copyright and source acknowledgement notices may not be removed and must be displayed in any copy, derivative work or partial copy which includes the elements in question.

All copyright, and all rights therein, are protected by national and international copyright laws. The above represents a summary only. For further information please read Frontiers' Conditions for Website Use and Copyright Statement, and the applicable CC-BY licence.

ISSN 1664-8714
ISBN 978-2-8325-3520-2
DOI 10.3389/978-2-8325-3520-2

About Frontiers

Frontiers is more than just an open access publisher of scholarly articles: it is a pioneering approach to the world of academia, radically improving the way scholarly research is managed. The grand vision of Frontiers is a world where all people have an equal opportunity to seek, share and generate knowledge. Frontiers provides immediate and permanent online open access to all its publications, but this alone is not enough to realize our grand goals.

Frontiers journal series

The Frontiers journal series is a multi-tier and interdisciplinary set of open-access, online journals, promising a paradigm shift from the current review, selection and dissemination processes in academic publishing. All Frontiers journals are driven by researchers for researchers; therefore, they constitute a service to the scholarly community. At the same time, the *Frontiers journal series* operates on a revolutionary invention, the tiered publishing system, initially addressing specific communities of scholars, and gradually climbing up to broader public understanding, thus serving the interests of the lay society, too.

Dedication to quality

Each Frontiers article is a landmark of the highest quality, thanks to genuinely collaborative interactions between authors and review editors, who include some of the world's best academicians. Research must be certified by peers before entering a stream of knowledge that may eventually reach the public - and shape society; therefore, Frontiers only applies the most rigorous and unbiased reviews. Frontiers revolutionizes research publishing by freely delivering the most outstanding research, evaluated with no bias from both the academic and social point of view. By applying the most advanced information technologies, Frontiers is catapulting scholarly publishing into a new generation.

What are Frontiers Research Topics?

Frontiers Research Topics are very popular trademarks of the *Frontiers journals series*: they are collections of at least ten articles, all centered on a particular subject. With their unique mix of varied contributions from Original Research to Review Articles, Frontiers Research Topics unify the most influential researchers, the latest key findings and historical advances in a hot research area.

Find out more on how to host your own Frontiers Research Topic or contribute to one as an author by contacting the Frontiers editorial office: frontiersin.org/about/contact

Advances in development and utilization of underground space

Topic editors

Yuwei Zhang — Xi'an University of Architecture and Technology, China

Zhanping Song — Xi'an University of Architecture and Technology, China

Liang Cui — Lakehead University, Canada

Ping Zhang — Luleå University of Technology, Sweden

Naifei Liu — Xi'an University of Architecture and Technology, China

Citation

Zhang, Y., Song, Z., Cui, L., Zhang, P., Liu, N., eds. (2023). *Advances in development and utilization of underground space*. Lausanne: Frontiers Media SA.
doi: 10.3389/978-2-8325-3520-2

Table of contents

05	Bearing capacity of driven pile and determination of inhomogeneous mudstone around the pile Yamei Zhang, Gan Sun, Xiaoyu Bai, Songkui Sang, Jianyong Han, Nan Yan, Mingyi Zhang, Xiaodong Gao and Weiqi Li
15	Three-dimensional characterization and quantitative research of Malan loess microstructure under seismic loading Tingting Wei, Zhijian Wu, Yanping Chen and Liang Luo
27	The stability evaluation of clay tunnels via the non-linear deterioration of physical and mechanical properties of surrounding rocks Jun Huang, Xingwang Liu, Zongyuan Ma, Gao Lv and Kangning Dang
38	The formation mechanism of landslides in typical fault zones and protective countermeasures: A case study of the Nanpeng River fault zone Youjun Li, Hongri Zhang, Liming Huang, Hongming Li and Xuexiao Wu
49	Mechanical behaviors of surrounding rock and supporting structure of shallow-buried unsymmetrical pressure tunnel crossing soil–rock interface Zhinan Hu, Ji Zhang, Yonggang Wang and Yunfei Wang
63	Research on the deformation control of surrounding rock about large-section tunnel in strong-medium weathered slate Zelin Niu, Yaqiong Wang and Shengyuan Fan
75	Numerical analysis of metro station pit dewatering and its influence Zongyuan Ma, Shitong Tang and Zhiguo Yang
83	A preliminary analysis of the mining-induced rock movement characteristics in the Xinli deposit of the Sanshandao gold mine Jia Liu, Fengshan Ma, Jie Guo, Guang Li, Yewei Song and Fangrui Li
96	Crater effects of shallow burial explosions in soil based on SPH-FEM analysis Ying Cui, Zhangjian Li, Jun Fang and Ben Zhao
105	Liquefaction evaluation method of coral sand: Case study on the ports in Indonesia Zezhou Ji, Xiangji Ye and Yingmin Zhang
118	Study of the disaster-causing mechanism and reinforcement measures for soft rock deformation and lining cracking J. W. Shi, P. Y. Zhou, X. Li, S. Y. Fan, Z. F. Zhou, B. Zhi and Y. Cheng
130	Influence of mud intercalation on the stability of seepage flow in tailings dams Hongru Li, Min Yang and Tong Dang

- 138 **Insight into the critical morphological characteristics of earthquake-induced sequential rock avalanches in weathered-fractured rock cliffs**
Shuangfeng Guo, Yajing Liu, Peng Zhang, Rui Zhu and Youkai Qian
- 156 **Experimental tests and theoretical analysis for mechanical behaviors of side wall opening construction in mined excavation subway station**
Zhinan Hu, Hongtao Mao, Lixin Zhang and Zhichun Liu
- 168 **Influence of filling sequence of concrete faced rockfill dam on deformation of squeezed sidewall and dam**
Li Hongru, Yang Min and Li Jiaqi
- 179 **Reaction and deformation mechanism of a slipping-stretching landslide: Example of the Liangtianao ancient landslide, Guangxi Province, China**
Li Youjun, Zhang Hongri, Huang Liming, Lan Sulian, Li Hongming and Wu Xuexiao
- 189 **Impact of subway shield tunnel construction on deformation of existing utility tunnel**
Shi Wei, Hong Zenglin, Yang Min, Li Ning and Tan Tianxiang



OPEN ACCESS

EDITED BY
Naifei Liu,
Xi'an University of Architecture and
Technology, China

REVIEWED BY
Chong Jiang,
Central South University, China
Zhen Guo,
Zhejiang University, China

*CORRESPONDENCE
Xiaoyu Bai,
✉ baixiaoyu538@163.com

SPECIALTY SECTION
This article was submitted to
Environmental Informatics and Remote
Sensing, a section of the journal
Frontiers in Earth Science

RECEIVED 18 November 2022
ACCEPTED 09 December 2022
PUBLISHED 04 January 2023

CITATION
Zhang Y, Sun G, Bai X, Sang S, Han J, Yan N,
Zhang M, Gao X and Li W (2023), Bearing
capacity of driven pile and determination
of inhomogeneous mudstone around
the pile.
Front. Earth Sci. 10:1101955.
doi: 10.3389/feart.2022.1101955

COPYRIGHT
© 2023 Zhang, Sun, Bai, Sang, Han, Yan,
Zhang, Gao and Li. This is an open-access
article distributed under the terms of the
[Creative Commons Attribution License
\(CC BY\)](https://creativecommons.org/licenses/by/4.0/). The use, distribution or
reproduction in other forums is permitted,
provided the original author(s) and the
copyright owner(s) are credited and that
the original publication in this journal is
cited, in accordance with accepted
academic practice. No use, distribution or
reproduction is permitted which does not
comply with these terms.

Bearing capacity of driven pile and determination of inhomogeneous mudstone around the pile

Yamei Zhang^{1,2}, Gan Sun^{1,2}, Xiaoyu Bai^{1,2*}, Songkui Sang^{1,2},
Jianyong Han³, Nan Yan^{1,2}, Mingyi Zhang^{1,2}, Xiaodong Gao⁴ and
Weiqi Li⁴

¹School of Civil Engineering, Qingdao University of Technology, Qingdao, Shandong, China, ²Cooperative Innovation Center of Engineering Construction and Safety in Shandong Blue Economic Zone, Qingdao University of Technology, Qingdao, China, ³College of Civil Engineering, Shandong Jianzhu University, Jinan, China, ⁴Qingdao Zhongjian United Group Co., Ltd., Qingdao, China

Whether the inhomogeneity of mudstone foundation leads to abnormal bearing capacity of the driven pile remains controversial. This study introduces the standard penetration test hammering number and needle penetration strength for quantitative analysis by macroscopic observation of the engineering field on the mudstone stratum self-structure and microscopic observation by simple and feasible electronic magnification. The analysis of typical engineering examples demonstrated that the abnormal bearing capacity of piles in the mudstone stratum was related to mudstone inhomogeneity. This study also proposes a method of evaluating mudstone uniformity using the heterogeneous index η , in which $\eta > 2$ suggests the need for engineering measures. These findings assist in determining a reasonable solution to the problem of abnormal bearing capacity at driven piles in mudstone foundations.

KEYWORDS

mudstone, inhomogeneity, penetration strength, pile-bearing capacity, driven pile

1 Introduction

Mudstone is the product of weakly consolidated clay becoming strongly consolidated clay due to extrusion and dewatering. Mudstone has properties between those of hard rock and quaternary settlement, as well as its own characteristics. Macro and micro research on the mechanical properties of mudstone have revealed engineering properties of mudstone including poor diagenesis, weak cementation, easy weathering, weak interbedding, and easy expansion, disintegration, and softening when water is encountered (Zhao et al., 2018; Hashemnejad et al., 2021; Zeng et al., 2021; Liu et al., 2022a). Due to the special engineering nature of mudstone, insufficient bearing capacity of driven piles in mudstone foundations occurs frequently (Xu and Li, 2004; Terente et al., 2017). Therefore, the study of the basic engineering properties of mudstone and their influence on the bearing capacity of pile foundations is of theoretical and engineering significance.

Water-rock interactions greatly influence the mechanical properties of rock (Liu et al., 2022b). Many studies and engineering cases have assessed the softening of mudstone under water as an important influencing factor. Jiang et al. (2014) observed the dynamic softening process of the mesostructure of mudstone by scanning electron microscopy and X-ray diffraction. They observed meso-fractures in the mudstone in diagenetic conditions and that water molecules immersed in the mudstone led to the volume expansion of clay minerals and dissolution of soluble carbonate, resulting in negative mechanical effects. Yang et al. (2016) analyzed the softening characteristics and mechanism of siltstone in

water through a series of mechanical and microstructure tests, in which changes in the microstructure of rock in water were the main factors affecting the strength of rock. Liu et al. (2020) verified that softening and swelling of rock due to water absorption can lead to structural failure. However, some studies reported that the mudstone at the pile end did not soften when exposed to water; rather, the abnormal bearing capacity of the pile foundation was caused by mudstone inhomogeneity (Zhang et al., 2016). Therefore, such inhomogeneity should also be considered an important research topic. Kiani et al. (2022) studied the intrinsic characteristics of tuff in the Meymand area and reported that these rocks have a heterogeneous texture comprising very coarse-grained clasts to fine-grained matrices. Manouchehrian and Cai (2016) used finite element software (Abaqus) to simulate the failure process of homogeneous and heterogeneous rocks and study the influence of material inhomogeneity on rock failure strength in compression tests.

The easy disintegration of mudstone makes it difficult to prepare specimens for laboratory tests of its mechanical properties. The standard penetration field test is an effective method used to determine the mechanical properties of rock and soil. Zhang and Chen (2012) predicted the bearing capacity of piles based on this test, while Nejad et al. (2009) and Erzin and Gul (2014) used this test to calculate foundation settlement. Moreover, Jha and Suzuki (2009) proposed a soil liquefaction assessment method based on the standard penetration test. Finally, Asem (2020) applied the standard penetration test to determine mudstone strength and deformation modulus. The needle penetration test is a convenient method used to test the mechanical properties of soft rock without requiring sample preparation (Ulusay et al., 2013). Kahraman et al. (2017) discussed the application of needle penetration instruments in coal rock, performed a regression analysis of the relationship between needle penetration degree and uniaxial compressive strength, and determined the conversion coefficient. Erguler and Ulusay (2009) explored the strength characteristics of clay-bearing rock through needle penetration tests, in which this test was particularly suitable for testing the uniaxial compressive strength of soft rock.

Thus, while research on mudstone softening in water has been relatively comprehensively studied, studies on mudstone inhomogeneity are generally on the level of the nature of the rock itself, without considering the influence of mudstone inhomogeneity on the pile foundation. Therefore, the present study evaluated mudstone inhomogeneity at the microscopic level by observing mudstone samples at the macroscopic level combined with electron microscopy and quantified the uniaxial compressive strength of mudstone by the needle penetration test. Combined with standard penetration number and needle penetration strength, the influence of mudstone inhomogeneity on pile bearing capacity was analyzed. Finally, this study summarized the method of judging mudstone inhomogeneity and proposed a method for judging mudstone uniformity based on the inhomogeneity index η .

2 Observations of mudstone inhomogeneity

2.1 Macroscopic observations

In this study, mudstone refers broadly to mudstone; in addition to pure mudstone, this definition also includes sandy mudstone,

argillaceous sandstone, and even some local inclusion sandstone, the properties of which are closely related to the sand content.

During rock formation, initial damage occurs due to environmental and geological forces (Wu et al., 2022). Mudstone shows primary and secondary micro-voids, micro-cracks, and other defects in the interior (Zhang et al., 2020; Lv et al., 2022) and is itself not uniform in certain dimensions; thus, it is easy to produce greater damage or even failure, which greatly influences the engineering characteristics of mudstone (Lv et al., 2022). Initial defects in mudstones can be observed at the mesoscopic level.

Compared to the usual initial defects, in a certain hardness of weathered mudstone, the joints and fissures cause a fragmentary structure. The uneven intercalation (inclusion) results in its inhomogeneity, which affects the engineering properties of mudstone and can be broadly considered as “damage”. To fully reveal the mudstone inhomogeneity, this study collected data in the author’s area, and the inhomogeneity of mudstone was revealed by excavation and drilling.

2.1.1 Macroscopic interbed

Figure 1 shows the mudstone interbedded structure revealed by the foundation pit and the natural slope of a site in the study region.

2.1.2 Jointed fissure in mudstone

Figure 2 is a schematic diagram of mudstone joints, fissures, and massive structures in the test site.

2.1.3 Uneven mudstone inclusions

Figure 3 is a schematic diagram of mudstone joints and uneven inclusions at the test site, in which some mudstones have both inclusions and fissures.

2.2 Fine microscopic observation and quantitative tests

This study performed both micro-observations and quantitative tests of drill core samples. The field test used an 8.3t hammer of the driven pile. The test pile was a PHC closed-mouth pipe pile with a diameter of 500 mm and a strength of C80. The pile ends were all located in mid-weathered mudstone. Mudstone samples were taken at .69 m around the pile before and after pile driving, and drilling fluid was used. During the test, the mudstone was below the groundwater level; therefore, the drilling fluid had little effect on the mudstone.

2.2.1 Mudstone microstructure

Scanning electron microscopy (SEM) image analysis is a common method used to study the microstructure of rock and soil and was also performed in the present study. The separation test showed that more than 60% of the sandy mudstone had a particle size >0.005 mm (5 μ m). SEM observation with 2000 \times magnification showed single particles measuring 10 mm, resulting in a large display ratio, which was not conducive to the observation of a wider range of cracks and pore structures. Pan (2014) conducted a SEM analysis of mudstone with different amplification ratios. The image comparison of the two proportions is shown in Figure 4. Figure 4A and Figure 4B show images at 500 \times and 2000 \times magnification, in which the latter does not reflect the overall structure as well as the former.

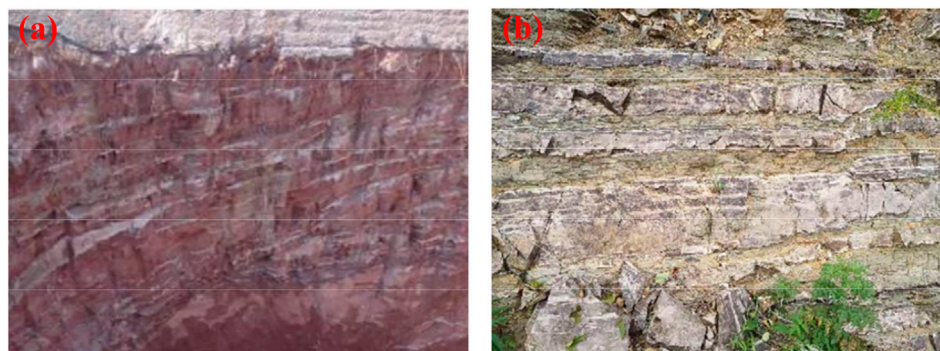


FIGURE 1
Mudstone interbedded structure of the foundation pit and slope. (A) Foundation pit. (B) Interbedded outcrops of sandstone and mudstone.



FIGURE 2
Schematic diagram of mudstone joints and fissures. (A) Mudstone core. (B) Massive mudstone.

Therefore, the SEM magnification should not be too large during the microscopic analysis of mudstone samples. This study used a more flexible method of imaging based on an electronic magnifying glass. This method can also display color, which is more conducive to the observation of mineral structure.

Ordinary SEM samples are cut with a knife, leaving residual powder particles on the surface. The gold-spraying operation during sample preparation can also block the particles, affecting microstructure observation and analysis. Moreover, the absence of color is not conducive to the analysis of mineral composition. Using the electronic magnifying glass directly on the mudstone for fracture observation, the particles and color are clearly visible. In addition, ordinary SEM samples must be dried, a process that is not suitable for mudstone, as mudstone cracks and deforms after losing water, changing its original appearance. The electronic magnifying glass is directly connected to a computer to directly observe the section of the core sample with its natural water content, thus overcoming the disadvantages mentioned previously.

After piling and static load tests, the working situation of the sample section was observed with an electronic magnifying glass (Figure 5). Images magnified at 200× are shown in Figures 6, 7. Color images can be used to analyze mudstone fissures and

damage in pile driving, identify rock mineral composition, and determine sand content.

In Figure 7, the soil at the pile end is compacted. However, the pile with static load failure has an obvious secondary fracture due to large settlement deformation.

The color image from the electronic magnifying glass showed that the sand-bearing mudstone was mainly volcanic clastic deposit, containing montmorillonite, hydromica, volcanic debris, calcite veins, quartz, feldspar, etc. Among them, feldspar, quartz, and other minerals were cemented by brick-red clay particles. The quartz grains were round or elliptic, while the feldspar particles were angular. The darker minerals appeared as small nodules containing iron and manganese, with a few mica fragments.

2.2.2 Mudstone strength

Uniaxial compressive strength is an important index reflecting the classification and characteristics of rock masses. The uniaxial compressive strength test (UCS test) has high requirements to produce rock samples, while the point load strength test (PLT) is a simple test method for strength indexes. The sample is not required to be cylindrical; thus, irregular block rock can be used. The measured point load strength index I_{s50} is multiplied by the relevant factor k to

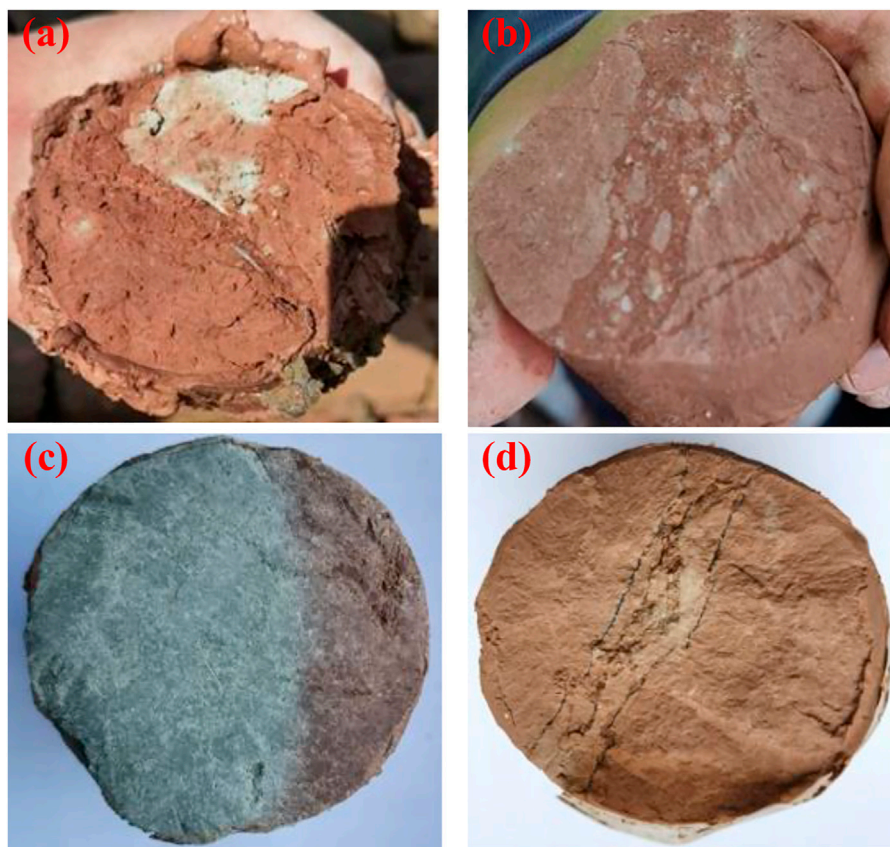
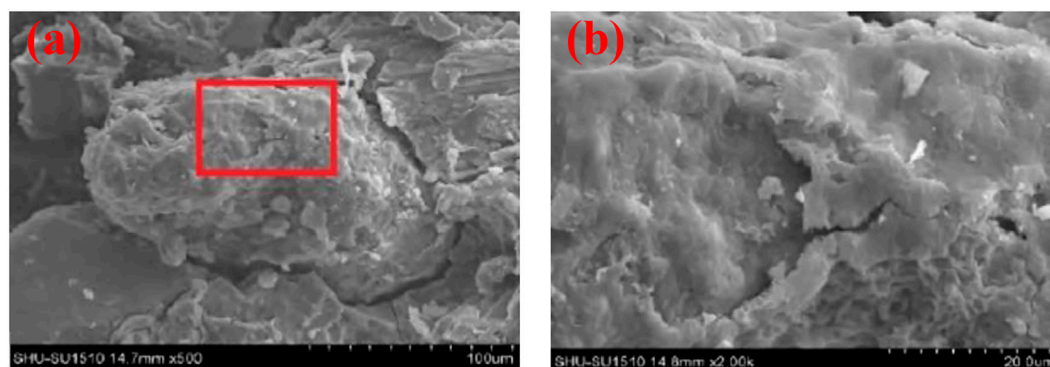
**FIGURE 3**

Diagram of mudstone joints and uneven inclusions. (A–D) Mudstone specimens 1–4, respectively.

**FIGURE 4**

Effect comparison of mudstone SEM images at different magnifications. (A) $\times 500$. (B) $\times 2000$.

obtain the uniaxial compressive strength of the rock. However, k is related to the rock type and weathering degree, so is difficult to accurately obtain and accuracy is problematic. To solve these challenges, Japanese researchers invented an instrument, the needle penetrometer, to test the strength of soft rock. Calculating uniaxial compressive strength by testing the needle penetration index of soft rock does require sample preparation. In general, soft rock can also be

assessed; thus, the test has good applicability (Yao et al., 2015; Li et al., 2016). The best test range is .5–20 MPa. This non-destructive testing can be applied both indoors and on the engineering site. Therefore, this test has become the recommended method for strength testing of soft rock mass strength by the International Society of Rock Mechanics (ISRM). This method is especially suitable for mudstone, which is difficult to assess using conventional samples.

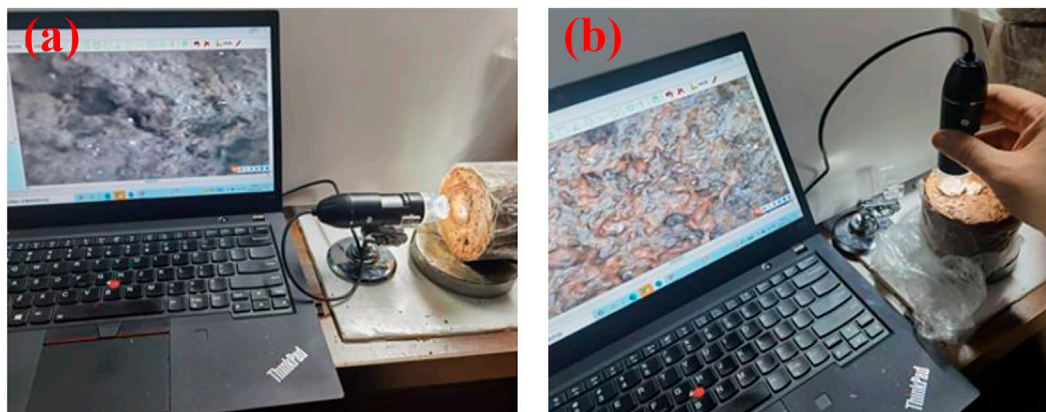


FIGURE 5
Sample observations of a mudstone section with an electronic magnifying glass. (A) Sample 1. (B) Sample 2.

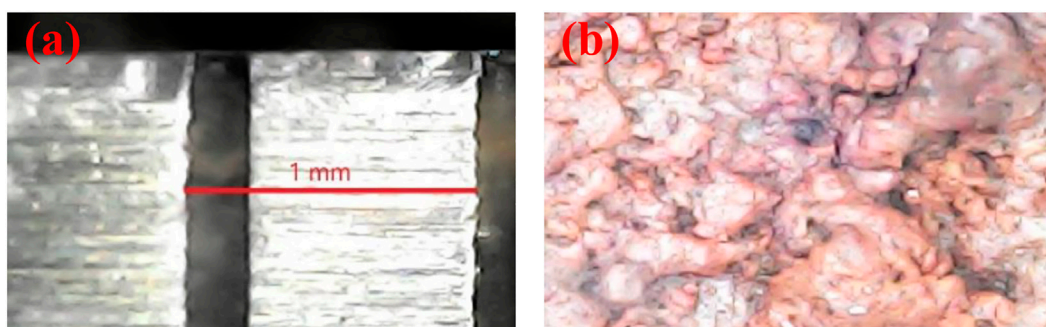


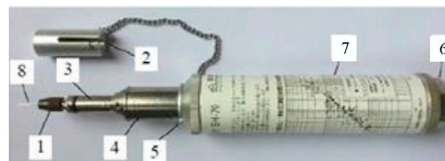
FIGURE 6
Two-hundred-fold enlargement using an electronic magnifier. (A) Graphic scale: steel plate ruler 1 mm. (B) Mudstone fractures.



FIGURE 7
Pile tip mudstone images of normal and damaged piles in static load tests. (A) Normal pile. (B) Pile with static load failure. 1, collet; 2, press; 3, penetration scale; 4, penetration force scale; 5, indicator ring; 6, rear cover; 7, diagram of the needle penetration ratio and uniaxial compressive strength; 8, penetration needle.

The penetrometer consists of a press (to measure the penetration force and protect the penetration needle), collet (a fixed penetration pin), penetration scale, penetration force scale, indicator ring (showing the size of penetration force), and rear cover and other parts (Figure 8).

The instrument parameters are as follows: penetration force test, 10–100 N; minimum scale, 10 N; end diameter of the penetration needle, .84 mm; penetration needle length, 39.5 mm; maximum penetration, 10 mm; minimum scale, 1 mm. In this test, a relatively



1- collet, 2-the press, 3- penetration scale, 4- penetration force scale, 5- indicator ring, 6- rear cover,
7- diagram of needle penetration ratio and uniaxial compressive strength, 8- Penetration needle

FIGURE 8
Needle penetrometer (Yao et al., 2015).



FIGURE 9
Needle penetration test on a mudstone core.

flat rock surface without cracks is selected for testing. The press is pushed vertically against the test point. The pressure is stopped immediately, and the needle is slowly pulled out when the penetration depth reaches 10 mm. The penetration force and penetration volume are recorded.

The statistical analysis of a large amount of test data during the instrument development resulted in an empirical formula for the conversion of the needle penetration ratio to uniaxial compressive strength. The expression for defining the pin penetration ratio N_p is $N_p = F/D$, where N_p is the needle penetration ratio (N/mm²), F is the penetration force (N), and D is the penetration depth (mm). Taking the logarithms of uniaxial compressive strength R_c and the needle penetration ratio N_p respectively is shown in Eq. 1:

$$y = \lg R_c, \quad x = \lg N_p. \quad (1)$$

After regression fitting, the formula is as follows:

$$y = 0.978x + 2.621. \quad (2)$$

According to Eq. 2, the uniaxial compressive strength R_c of mudstone around the pile can be obtained. While this relation can also be obtained from the relation diagram attached to the instrument, the calculation result obtained using Eq. 2 is more convenient and accurate.

Figure 9 shows a photograph of needle penetration of mudstone cores. The needle penetration test is simple and convenient and can be performed at multiple points, which can be used to eliminate measurement error.

3 Bearing capacity of prefabricated pile

3.1 Bearing capacity of driven pile with an abnormal mudstone foundation

The mudstone in the study area belongs to the silty mudstone of Wang group of the Cretaceous red cliffs group (KwH), which is partially intercalated with argillaceous siltstone. In this region and other parts of China, the bearing capacity of driven piles with mudstone as the pile tip bearing layer differs from that of the common pile foundation and the problems with abnormal bearing capacity occur frequently. Concrete performance in the pile bearing capacity includes lower capacity than before loading or partly higher part and partly lower. While the static load test during the pile test stage shows normal results, the final bearing capacity of the pile can be problematic. Figure 10 shows two engineering examples with problems in static load test capacity.

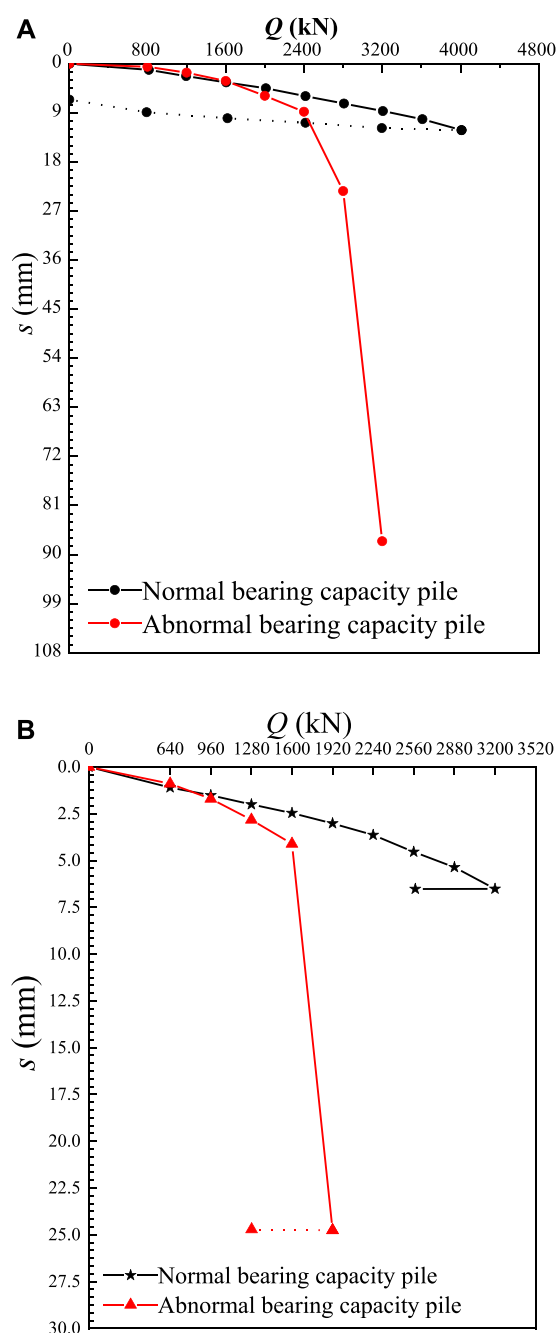


FIGURE 10
Case diagram of abnormal bearing capacity of driven piles in mudstone foundation. (A) Project Example 1. (B) Project Example 2.

The load-displacement curve of the test pile was obtained by *in situ* static load tests. As shown in Figure 10A, the bearing capacity of the normal pile was 4000 kN, while the settlement of the pile under the maximum load was only 12 mm, far from the 40 mm stipulated in the code, indicating that the bearing capacity of this pile still had a certain potential. However, a pile of the same size and the same construction method as the test pile was destroyed at a loading of 3200 kN. As shown in Figure 10B, the results of the static load test showed that the bearing capacity of the normal pile was 3200 kN, while that of the abnormal pile was <1920 kN.

Drilling holes added in the pile side to determine the causes of the bearing capacity problems showed that all of the problems were related to the inhomogeneity of the mudstone stratum. The pile-end soil drilling core of engineering example 1 was in a block with uneven fragmentation (Figure 11).

The results of the standard penetration test of the pile end-bearing layer are shown in Table 1, with one test pile for each project. The number of standard penetration strikes is denoted by N . The maximum and minimum standard penetration strike numbers of the two projects are very different, and there is obvious inhomogeneity. This engineering example illustrates the feasibility of using the standard penetration strike number index to judge mudstone inhomogeneity.

3.2 Needle penetration test

Drilling and exploration of the mudstone foundation of one of the projects showed that the foundation was argillaceous siltstone with a layer thickness of 16 m and a reddish-brown color. A sample of mudstone in the borehole was obtained, and a penetration strength test was performed. The observation of mudstone samples from the same borehole at different depths showed the mudstone of the borehole was interbedded with soft and hard layers, with greatly varying sand content. Core No. 4 belonged to the interlayer due to its high sand content. The sampling depth and penetration strength of mudstone samples are shown in Table 2. The relationships between needle penetration strength and foundation depth are shown in Figure 12.

The needle penetration intensity in Table 2 and Figure 12 varied greatly. Due to the effects of sand content and soft and hard interbedding, the minimum and maximum compressive strengths were .63 MPa and 9.15 MPa, respectively. This typical severely heterogeneous mudstone stratum was divided into the same stratum with different test indexes.



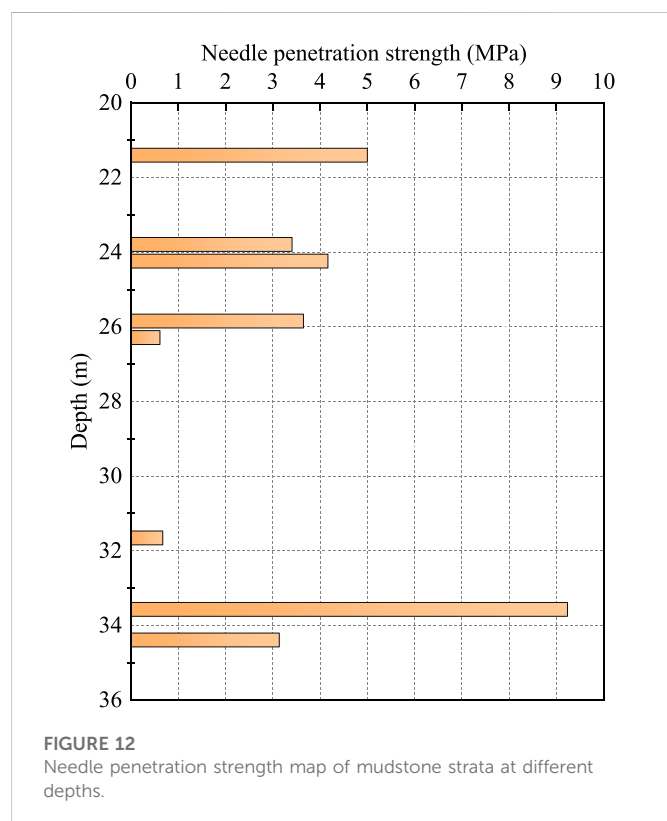
FIGURE 11
Mudstone at the pile tip in Project Example 1.

TABLE 1 Hammer strike numbers of pile end bearing layers with abnormal bearing capacities.

Name	Pile tip layer	Pile tip condition	<i>N</i>	Average of <i>N</i>	Max/min of <i>N</i>	Evaluation of non-uniformity
Project 1	Highly weathered argillaceous siltstone	Pile end into the bearing layer by 6.4–7.3 m	120	120	241/22	Soft layer beneath the hard layer
Project 2	Argillaceous siltstone strongly weathered lower subzone	Pile tip into the strong weathering subzone	232	—	300/56	Uneven, locally hard on the top and soft on the bottom

TABLE 2 Test number and needle penetration strength.

Test number	Sampling depth/m	Rock type	Cutting observation	Needle penetration test strength/MPa
1	21.3–21.5	Argillaceous siltstone		5.00
2	23.7–24.0	Argillaceous siltstone		3.39
3	24.1–24.3	Argillaceous siltstone		4.17
4	25.7–26.0	Sandstone (interlayer)	High sand content	3.61
5	26.2–26.4	Argillaceous siltstone	Color slant green	.63
6	31.6–31.8	Argillaceous siltstone		.70
7	33.5–33.7	Argillaceous siltstone		9.15
8	34.3–34.5	Argillaceous siltstone		3.14



4 Determination of the formation inhomogeneity

4.1 Conventional determination method

The non-uniformity of mudstone cannot be judged by subjective feeling but rather should have objective indexes and standards. Therefore, the application of the test index to rocks at the same depth (depth range of 2 m) at the site is recommended to measure rock inhomogeneity. The following two methods can be used to quantitatively determine mudstone inhomogeneity.

The hammer number of the standard penetration test at the same depth in the mudstone layer is used as the criterion. The data obtained from the *in situ* standard penetration test are simple, objective, and true, which can ensure the accuracy of the results. The encryption test is carried out at the test pile position to reduce the influence of accidental factors on the results. This method has high adaptability and is suitable for most mudstone foundations. Analysis of the two engineering cases in this study illustrated the large difference between the maximum and minimum standard penetration numbers of the foundation-bearing layer, in addition to the non-uniformity of the mudstone. These findings demonstrated the feasibility of determining mudstone inhomogeneity using the standard penetration number.

In addition, the compressive strength obtained by needle penetration tests at the same depth of the mudstone formation can be used as the criterion. The field penetration test is performed directly on the mudstone

TABLE 3 Suggested criteria for determining mudstone inhomogeneity.

η	Adjoint phenomenon	Heterogeneity
1.3–1.6	—	Slight heterogeneity
1.6–2.0	Hard on the top and soft on the bottom	Heterogeneous
	Irregular inhomogeneity	
>2.0	Hard on the top and soft on the bottom	Severe heterogeneity
	Irregular inhomogeneity	

drill core, which is easy to operate, and the corresponding depth is clear. The average value of the test data on more than three points was taken for each position to ensure the accuracy of the test results. The point load test of rock can also be avoided by obtaining the compressive strength of rock through the needle penetration test.

4.2 Comprehensive determination method

Mudstone inhomogeneity cannot be determined only by deriving a formula. Based on the aforementioned quantitative testing methods, this study proposes the following comprehensive determination methods.

First, the inhomogeneity index η is defined in the mudstone formation, as shown in Eq. 3:

$$\eta = \frac{R_{\max}}{R_{\min}}, \quad (3)$$

where R_{\max} and R_{\min} represent the maximum and minimum hammer blows in the standard penetration test or the maximum and minimum strength in the needle penetration test.

The inhomogeneity index η of mudstone is similar to the sensitivity of clay. The recommended standards for judging the inhomogeneity of mudstone layers are shown in Table 3.

Sufficient attention should be paid to mudstone in the bearing layers of hammer-driven piles judged to be heterogeneous. In cases of severe inhomogeneity, design and construction measures are needed to avoid abnormal bearing capacity.

5 Conclusion

- (1) Inhomogeneity and irregular interbedding between soft and hard mudstone greatly influence the bearing capacity of piles, leading to their abnormal bearing capacity. These factors are often ignored in geotechnical investigations of actual projects, with simple descriptions as homogeneous mudstone, which requires consideration.
- (2) The heterogeneous structure of mudstone is easily observed with electronic magnifying glasses, which have the advantages of simple operation, color display, and adjustable magnification, making them superior to SEM.

- (3) The method of measuring mudstone inhomogeneity by needle penetration strength is simple and accurate. This method can replace point load strength tests of mudstone and even partially replace the conventional compression test of cylindrical specimens.
- (4) The inhomogeneity of mudstone formations can be judged according to the inhomogeneity index obtained from the hammer number in standard penetration tests and the strength in needle penetration tests. The identification of seriously heterogeneous mudstone suggests the need for corresponding engineering technical measures.

Data availability statement

The original contributions presented in the study are included in the article/supplementary material. Further inquiries can be directed to the corresponding author.

Author contributions

Writing—original draft: YZ; writing—review and editing: GS and JH; formal analysis: XB; investigation: SS; methodology: NY; conceptualization: MZ; data curation: XG and WL.

Funding

This research was supported by the National Natural Science Foundation of China (grant no. 51708316), the Key Program of Natural Science Foundation of Shandong Province (grant no. ZR2020KE009), China Postdoctoral Science Foundation Funding (2018M632641), and the Shandong Provincial Post-doctoral Innovation Project (grant no. 201903043).

Conflict of interest

XG and WL were employed by Qingdao Zhongjian United Group Co., Ltd.

The remaining authors declare that the research was conducted in the absence of any commercial or financial relationships that could be construed as a potential conflict of interest.

Publisher's note

All claims expressed in this article are solely those of the authors and do not necessarily represent those of their affiliated organizations, or those of the publisher, the editors, and the reviewers. Any product that may be evaluated in this article, or claim that may be made by its manufacturer, is not guaranteed or endorsed by the publisher.

References

- Asem, P. (2020). Prediction of unconfined compressive strength and deformation modulus of weak argillaceous rocks based on the standard penetration test. *Int. J. Rock Mech. Min. Sci.* 133, 104397. doi:10.1016/j.ijrmms.2020.104397
- Erguler, Z. A., and Ulusay, R. (2009). Water-induced variations in mechanical properties of clay-bearing rocks. *Int. J. Rock Mech. Min. Sci.* 46 (2), 355–370. doi:10.1016/j.ijrmms.2008.07.002
- Erzin, Y., and Gul, T. O. (2014). The use of neural networks for the prediction of the settlement of one-way footings on cohesionless soils based on standard penetration test. *Neural Comput. Appl.* 24 (3), 891–900. doi:10.1007/s00521-012-1302-x
- Hashemnejad, A., Aghda, S. M. F., and Talkhablou, M. (2021). Introducing a new classification of soft rocks based on the main geological and engineering aspects. *Bull. Eng. Geol. Environ.* 80 (6), 4235–4254. doi:10.1007/s10064-021-02192-8
- Jha, S. K., and Suzuki, K. (2009). Reliability analysis of soil liquefaction based on standard penetration test. *Comput. Geotechnics* 36 (4), 589–596. doi:10.1016/j.compgeo.2008.10.004
- Jiang, Q., Cui, J., Feng, X., and Jiang, Y. (2014). Application of computerized tomographic scanning to the study of water-induced weakening of mudstone. *Bull. Eng. Geol. Environ.* 73 (4), 1293–1301. doi:10.1007/s10064-014-0597-5
- Kahraman, S., Aloglu, A. S., Aydin, B., and Saygin, E. (2017). The needle penetration test for predicting coal strength. *J. South. Afr. Inst. Min. Metallurgy* 117 (6), 587–591. doi:10.17159/2411-9717/2017/v117n6a9
- Kiani, M., Hashemi, M., Ajalloeian, R., and Benavente, D. (2022). Investigating the geological and geomechanical characteristics governing the weathering behavior of Meymand tuff[J]. *Environ. Earth Sci.* 81 (2), 1–18. doi:10.1007/s12665-022-10169-3
- Li, Z., Xu, G., Yuan, J., Huang, P., Zhao, X., Fu, Y., et al. (2016). Application of needle penetrometer to soft rock strength test[J]. *Rock Soil Mech.* 37, 651–658. (in chinese). doi:10.16285/j.rsm.2016.S1.086
- Liu, N., Li, N., Li, G., Song, Z., and Wang, S. (2022a). Method for evaluating the equivalent thermal conductivity of a freezing rock mass containing systematic fractures[J]. *Rock Mech. Rock Eng.* 55, 7333–7355. doi:10.1016/j.coldregions.2022.103707
- Liu, N., Li, N., Wang, S., Li, G., and Song, Z. (2022b). A fully coupled thermo-hydro-mechanical model for fractured rock masses in cold regions. *Cold Regions Sci. Technol.* 205, 103707. doi:10.1016/j.coldregions.2022.103707
- Liu, N., Li, N., Xu, C., Song, Z., and Yang, M. (2020). Mechanism of secondary lining cracking and its simulation for the dugongling tunnel. *Rock Mech. Rock Eng.* 53 (10), 4539–4558. doi:10.1007/s00603-020-02183-3
- Lv, H., Wang, D., Cheng, Z., Zhang, Y., and Zhou, T. (2022). Study on mechanical characteristics and failure modes of coal–mudstone combined body with prefabricated crack. *Mathematics* 10 (2), 177. doi:10.3390/math10020177
- Manouchehrian, A., and Cai, M. (2016). Influence of material heterogeneity on failure intensity in unstable rock failure. *Comput. Geotechnics* 71, 237–246. doi:10.1016/j.compgeo.2015.10.004
- Nejad, F. P., Jaksa, M. B., Kakhi, M., and McCabe, B. A. (2009). Prediction of pile settlement using artificial neural networks based on standard penetration test data. *Comput. geotechnics* 36 (7), 1125–1133. doi:10.1016/j.compgeo.2009.04.003
- Pan, L. (2014). Microscopic features of mudstone images from scanning electron microscopy[J]. *Subgr. Eng.* 173 (2), 119–122. doi:10.13379/j.issn.1003-8825.2014.02.28
- Terente, V., Torres, I., Irvine, J., and Jaecck, C. (2017). “Driven pile design method for weak rock[C],” in Offshore Site Investigation Geotechnics 8th International Conference, United Kingdom, London, 12-09-2017 - 14-09-2017, 652–657.
- Ulusay, R., Aydan, Ö., Erguler, Z. A., Ngan-Tillard, D. J. M., Seiki, T., Verwaal, M., et al. (2013). “ISRM suggested method for the needle penetration test[M],” in *The ISRM suggested methods for rock characterization, testing and monitoring: 2007-2014* (Cham: Springer), 143–155.
- Wu, L., Wang, Z., Ma, D., Zhang, J. W., Wu, G., Wen, S., et al. (2022). A continuous damage statistical constitutive model for sandstone and mudstone based on triaxial compression tests[J]. *Rock Mech. Rock Eng.* 55, 4963–4978. doi:10.1007/s00603-022-02924-6
- Xu, T., and Li, S. (2004). Testing study on bearing capacity of pipe piles with bearing stratum of mudstone[J]. *Chin. J. Rock Mech. Eng.* 23 (2), 329–333. (in chinese). doi:10.3321/j.issn:1000-6915.2004.02.031
- Yang, Y., Zhou, J., Xu, F., and Xing, H. (2016). An experimental study on the water-induced strength reduction in zigong argillaceous siltstone with different degree of weathering. *Adv. Mater. Sci. Eng.* 2016, 1–12. doi:10.1155/2016/4956986
- Yao, Z., Xu, G., Zhu, Z., Wang, K., and Hu, X. (2015). Application of pin-penetration test to mudstone in wuhan area[J]. *Constr. Technol.* 44 (S2), 66–68. (in chinese).
- Zeng, L., Luo, J. T., Liu, J., Gao, Q. F., and Bian, H. B. (2021). Disintegration characteristics and mechanisms of carbonaceous mudstone subjected to load and cyclic drying-wetting. *J. Mater. Civ. Eng.* 33 (8), 04021195. doi:10.1061/(asce)mt.1943-5533.0003817
- Zhang, L., and Chen, J. J. (2012). Effect of spatial correlation of standard penetration test (SPT) data on bearing capacity of driven piles in sand. *Can. Geotechnical J.* 49 (4), 394–402. doi:10.1139/t2012-005
- Zhang, X., Li, R., Zheng, Y., Zeng, Z., and Li, G. (2016). Field experimental study on prestressed concrete tube-pile bearing stratum softening in strong weathered rock formation of Shunde area[J]. *Sci. Sin. Technol.* 46 (9), 975–986. (in chinese). doi:10.1360/N092015-00328
- Zhang, X., Liu, X., Chen, C., Kong, L., and Wang, G. (2020). Engineering geology of residual soil derived from mudstone in Zimbabwe. *Eng. Geol.* 277, 105785. doi:10.1016/j.enggeo.2020.105785
- Zhao, Y., Ren, S., Jiang, D., Liu, R., Wu, J., and Jiang, X. (2018). Influence of wetting-drying cycles on the pore structure and mechanical properties of mudstone from Simian Mountain. *Constr. Build. Mater.* 191, 923–931. doi:10.1016/j.conbuildmat.2018.10.069



OPEN ACCESS

EDITED BY

Yuwei Zhang,
Xi'an University of Architecture and
Technology, China

REVIEWED BY

Guopeng Wu,
Lanzhou University of Technology,
China
Yongting Duan,
Northeastern University, China

*CORRESPONDENCE

Zhijian Wu,
✉ zhijianlz@163.com

SPECIALTY SECTION

This article was submitted to
Environmental Informatics and Remote
Sensing,
a section of the journal *Frontiers in Earth
Science*

RECEIVED 23 November 2022

ACCEPTED 09 December 2022

PUBLISHED 04 January 2023

CITATION

Wei T, Wu Z, Chen Y and Luo L (2023),
Three-dimensional characterization
and quantitative research of Malan loess
microstructure under seismic loading.
Front. Earth Sci. 10:1106168.
doi: 10.3389/feart.2022.1106168

COPYRIGHT

© 2023 Wei, Wu, Chen and Luo. This is
an open-access article distributed
under the terms of the [Creative
Commons Attribution License \(CC BY\)](#).
The use, distribution or reproduction in
other forums is permitted, provided the
original author(s) and the copyright
owner(s) are credited and that the
original publication in this journal is
cited, in accordance with accepted
academic practice. No use, distribution
or reproduction is permitted which does
not comply with these terms.

Three-dimensional characterization and quantitative research of Malan loess microstructure under seismic loading

Tingting Wei, Zhijian Wu*, Yanping Chen and Liang Luo

College of Transportation Science and Engineering, Nanjing Tech University, Nanjing, China

The deformation and failure of loess in areas of high seismic intensity are closely related to the dynamic vulnerability, which is primarily controlled by the loess microstructure. This study performed a series of dynamic triaxial tests and microstructure tests on intact loess to track and quantitatively characterize the evolution of the three-dimensional microstructure during deformation. The microstructural observations were performed using micro-CT on the samples after varying vibration times. The microstructure parameters (including pore radius, elongation, orientation, coordination number, pore throat area, and channel length) were obtained using a reconstructed pore network model. The results of this study demonstrated that the loess seismic subsidence originated from both compositional and microstructural characteristics. The intact loess had a loose structure with high porosity and limited cementation. Upon cyclic loading, cementation and contact breakdown led to the failure of the loess structure, followed by particle rearrangement. With increasing vibration times, the spaced and inter-aggregate pores became intra-aggregate pores, the pore throat size tended to decrease while the pore number tended to increase, the connectivity tended to weaken, and the shape tended to be long and flat. Pores $>28\ \mu\text{m}$ mainly provided spatial conditions for collapse deformation under seismic load. In addition, under the ultimate loading, large-volume cracks occurred inside the sample. The findings of this study provide further insights into loess seismic subsidence from the perspective of three-dimensional microstructures and a research basis for analyzing the stability of loess in relation to construction projects by combining finite and discrete elements.

KEYWORDS

Loess, microstructure, seismic subsidence, vibration time, quantitative analysis

Introduction

Loess is a Quaternary sedimentary soil widely distributed in Asia, Europe, America, and Africa (Wei et al., 2019a; Nan et al., 2021). In China, the loess covers an area of 631,000 km² (Wang et al., 2011). Moreover, the Loess Plateau, with an area >440,000 km², is the largest loess deposition area on earth (Meng et al., 2021). The engineering properties of soils are mainly controlled by their metastable microstructure, with less cement, higher porosity, and loose arrangement prone to liquefaction, subsidence, landslide, and other disasters due to earthquakes (Yuan and Wang, 2009; Juang et al., 2019; Zhang et al., 2022). Several strong earthquakes occurred in the loess region of China, all of which triggered seismic landslides, resulting in many casualties and high property damage (Sun et al., 2017; Zhuang et al., 2018). With the implementation of the “The Belt and Road Initiative”, construction activities in loess areas are increasing, and it is especially important to clarify the dynamic properties of loess. Therefore, the study of microstructural changes of loess under dynamic loading will help to solve the engineering geological problems in loess areas.

Since the middle of the last century, scholars have applied low-precision microscopic equipment to explore loess microstructure (Matalucci et al., 1970; Cremaschi et al., 1990; Ma et al., 1998). Over time, studies on the microstructure of loess have progressed to a high-precision stage. SEM is widely used in the research of loess microstructure owing to its high precision and the ability to analyze mineral composition (Xie et al., 2018; Ni et al., 2020; Xu et al., 2020a). Quantitative data on loess particles and pore structure have been analyzed through SEM images to summarize the changes in pore quantity, area, and form corresponding to different dynamic loading stages (Li et al., 2018; Lian et al., 2022). The MIP technique is widely used in the study of loess pore size and collapsibility (Mu et al., 2020; Wang et al., 2021). Based on MIP tests, scholars have explored the impacts of different cycles on soil mechanics and pore characteristics, indicating that the cycling effects play a dominant role in the deterioration of loess engineering properties (Li et al., 2019; Wang et al., 2020). Micro-CT scans have been performed on saline intact loess to investigate the relationship between loess microstructure and hydraulic conductivity under freeze-thaw cycle conditions (Xu et al., 2020b). Based on the evaluation of the 3D pore structure of loess by X-ray scanning (Chen et al., 2019; Li and Shao, 2020), two different types of pores have been extracted, providing new research ideas on loess collapse (Yu et al., 2021). With the development of micron scanning equipment, research on loess microstructure is maturing. However, most studies have focused on two-dimensional parameters such as particle area distribution and pore area ratio. Research on the three-dimensional (3D) microstructure requires further exploration.

The integration of loess dynamic properties with loess microstructure has become a critical issue, with promising findings (Nan et al., 2021; Wang et al., 2021). To simulate the earthquake process, undisturbed loess is preloaded.

Microstructure analysis has demonstrated that increasing dynamic stress amplitude aggravates soil microstructure deterioration (Li et al., 2019; Xu et al., 2021). The soil colloidal is damaged and the particle contact mode changes (Wang et al., 2011). Moreover, loading the loess leads to its transformation from a bimodal into a trimodal PSD, which defines three major pore series. However, the trimodal nature of PSD is destroyed under higher vertical stresses (Wang et al., 2020) and the loess grains are rearranged (Li et al., 2019). To quantitatively characterize the relationship between dynamic load frequency and loess microstructure, a series of dynamic triaxial tests and SEM scanning tests were conducted to establish the relationship between the dynamic characteristic and microscopic characteristic parameters of structural units (Wang et al., 2016; Kou et al., 2017; Zeng et al., 2022). The dynamic load type significantly affects the microstructure parameters of loess. Moreover, the diameter and direction probability entropy of these structural elements differ significantly under different wave loads (Chen et al., 2021). The study of loess microstructure has included the analysis of the amplitude, frequency, and waveform of the applied dynamic load. The loss of strength and deformation begins with the gradual change of microstructure. However, the continuous observation of the microstructure during cycling vibration is not enough to study the microstructure evolution.

The present study reconstructed a 3D pore network model of loess based on the analysis of 700 micro-CT images with a voxel size of 1 μm³. The primary objective of this study was to characterize and quantitatively assess the evolution process of 3D loess microstructure under cyclic loading. The pore size, throat size, shape, and connectivity variation law of loess under different vibration times were evaluated. The results are expected to provide an in-depth and comprehensive understanding of loess microstructure and seismic subsidence behavior.

Experimental materials and methods

Material

The loess samples used in the study were Q₃ Malan loess collected from the Loess Plateau in the central-eastern part of Gansu Province (Figure 1). The samples were collected at 5 m in the Late Pleistocene strata, were undisturbed by engineering activity, showed a homogeneous distribution, and demonstrated few plant roots and wormholes.

The intact loess was cut into rectangles measuring approximately 25 cm × 25 cm × 15 cm. The samples were wrapped in many layers of cling film and shockproof film immediately after collection to preserve them without interference, with markings to indicate intact orientation. Table 1 shows the basic physical parameters of the collected loess. The particle size distribution of the intact loess is shown in Figure 2.

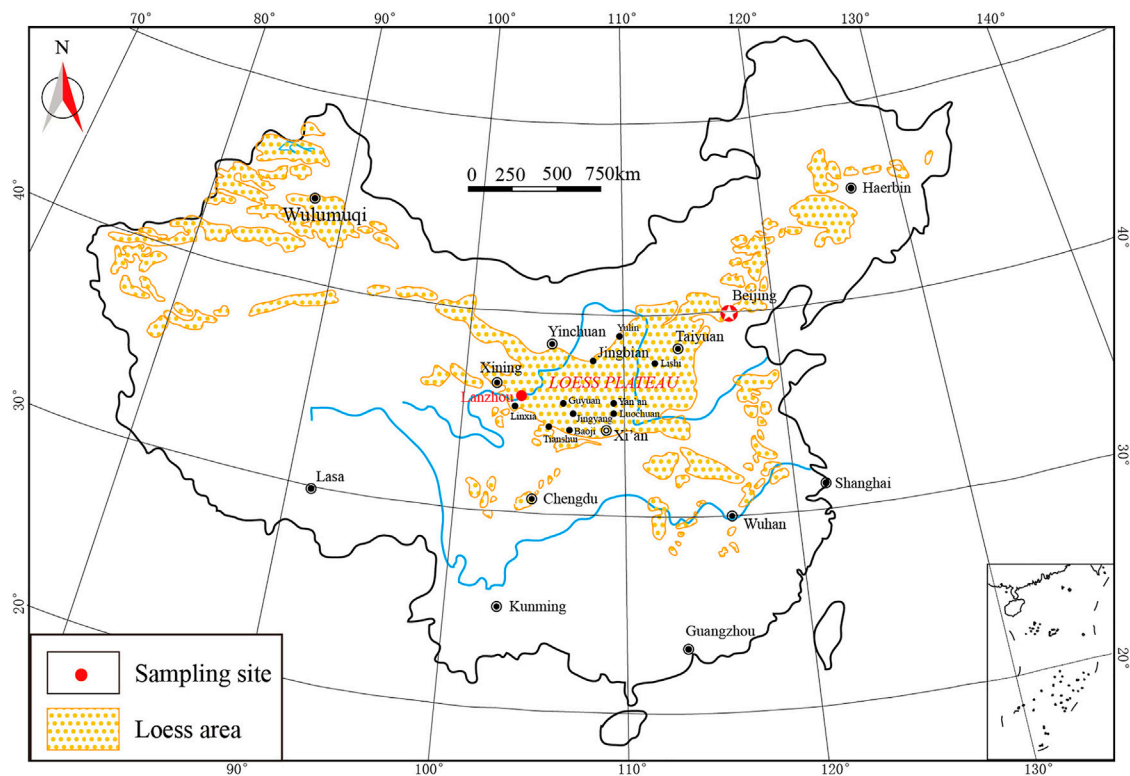


FIGURE 1
Sampling site of the studied loess.

TABLE 1 Physical property indices of the intact loess.

Dry density, ρ_d (g/cm ³)	Specific gravity, ρ (g/cm ³)	Saturation, S_r (%)	Porosity	Moisture content, ω (%)	Liquid limit, W_L (%)	Plastic limit, W_P (%)
1.33	2.71	5.73	0.51	2.2	29.59	20.73

Dynamic triaxial tests

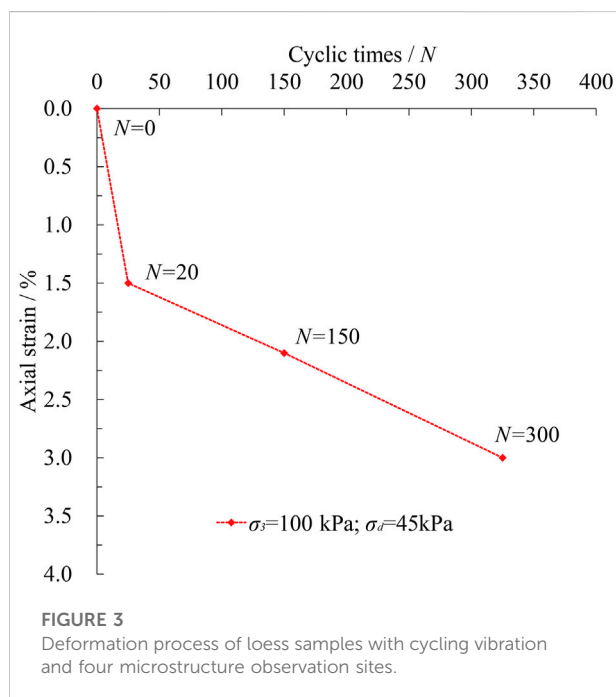
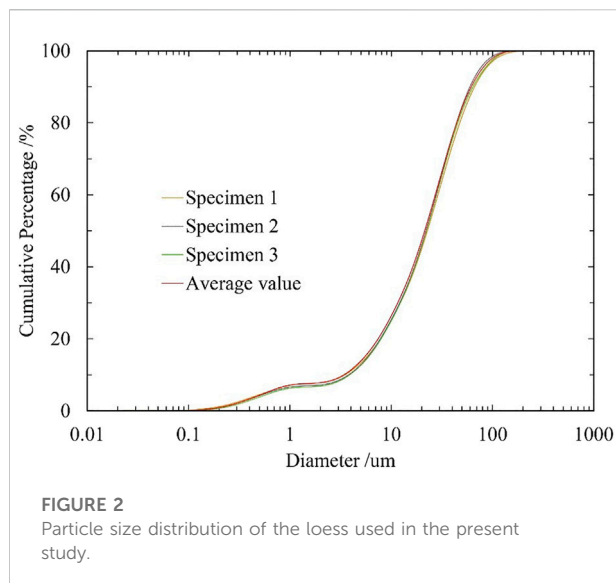
These tests were performed utilizing the British GDS dynamic triaxial system to investigate the dynamic characteristics of the intact loess. Using a soil chipper and a cutter, samples of intact loess were produced in a standard size of $\phi 50 \text{ mm} \times h 100 \text{ mm}$.

The seismic load, as a random vibratory load, was reduced to an equal-amplitude sine wave load with cyclic loading in the analysis of the dynamic stress-strain relationship characteristics of loess, the frequency of which was set to 1 Hz. Before shearing, the intact loess samples were consolidated in the triaxial chamber until the changes in sample total volume remained stable (Nan, et al., 2021). This experiment addressed the effect of different cyclic vibrations of dynamic load on the dynamic properties of

loess based on consolidation without drainage conditions. The consolidation ratio was $K_C=1.0$, the cell pressure was $\sigma_3=100 \text{ kPa}$, and the dynamic load was $\sigma_d=45 \text{ kPa}$. Considering a seismic fortification intensity in Lanzhou is 8°, the corresponding cyclic vibration times of the equivalent sine wave load were 20 times, and the cyclic vibration times of the dynamic load are set to 20, 150, and 300 times (or while the axial strain ε was $>5\%$) (Figure 3).

Microstructure observation

After dynamic triaxial tests under default cyclic times (Figure 3), samples were collected from the center of the samples and scanned using an X-ray micro-CT scanner (Xradia 520 Versa, Zeiss) at the State Key Laboratory of



Continental Dynamics (Figure 4). Five triaxial samples were cut from a single large block, and the microstructure scanning samples were collected from the center of the samples. The scanning samples were cylinders approximately 4 mm in diameter. During scanning, the voltage and current were set to 50 kV and 81 μ A, respectively. The scanning range was $2000 \times 2000 \times 2000$ voxels and the resolution was 1 μ m for each pixel in this study. After scanning, 2000 16-bit images in the XY plane for each sample were obtained at 1- μ m spacing between adjacent images.

3D microstructure reconstruction and characterization

The serial images obtained by micro-CT scanning were imported into Avizo software (FEI Company, France) to reconstruct the 3D microstructure. First, the images were preprocessed using the non-local means filter to eliminate noise and smooth the images (Wei et al., 2019a) (Figure 5A). Then, an appropriate threshold was selected to segment the pores and particles. The blue areas are pores in Figures 5B–E. Small holes in pores often lead to excessive separation during pore segmentation. Thus, the holes were filled with the appropriate values (Wei et al., 2020). Next, a watershed algorithm was used to split the pores into a set of connected and individually numbered pore bodies (Figure 5F). The watershed algorithm assumed the color value of the image as the elevation, simulated the flooding process, and segmented the region according to the watershed lines. Figure 6 shows the segmented results of four randomly selected slices from the intact loess. Finally, the pore network model (PNM) was generated based on the separated pores. The pore structure was characterized using a ball-stick model in which the balls represented pore bodies and the sticks represented the throats between two adjacent pores (Wei et al., 2019a) (Figures 5G, H).

Quantitative parameters

A cubic region of interest of $700 \times 700 \times 700$ voxels was selected to calculate the pore microstructure parameters (Wei et al., 2019a). 3D porosity (n) was defined as the total number of pore voxels within the volume of interest divided by the total number of voxels of the volume. The equivalent radius (r_n) was defined as the radius of a sphere with a volume equal to the pore volume. The equivalent pore-throat area (A_b) was the radius of the thinnest contact position between two connected pore bodies. The channel length (CL) was defined as the length of the bond between two connected node centers, indicating the distance between two pore bodies. The orientation (O) was the angle between the short axis of the pore body and the horizontal plane. Pore elongation (EL) referred to the ratio of the short axis to the long axis of a pore body, ranging from 0 to 1. The smaller the value, the more elongated the pore. The coordination number (CN) was used to describe the connectivity of the pore structure, which was defined as the number of pores surrounding and connecting to one pore.

Results

Figure 7 shows the PNM reconstructed from the X-ray micro-CT images and the 3D binarized volumes of the samples (intact, cycle vibration 20, 150, and 300 times) with separated pore 2D sections, and lists their major structural parameters including the porosity (n), average equivalent pore radius (r_n), average pore coordination number (CN), pore elongation (EL), pore short axis orientation (O),

average equivalent pore-throat area (A_b) and average pore-throat channel length (CL).

Pore size distribution

The ability of loess soil to resist deformation and damage depends on its microstructure characteristics. The pore size distribution can indicate the complex pore structure in far

more detail than porosity alone, and is one of the main factors to influence the microstructure.

The average equivalent pore radius (r_n) gradually decreased from 13 μm to 10.15 μm with increasing vibration times and decreased by 21.92% when destruction occurred. The significant variations in pore size distribution are shown in Figure 7. For intact loess ($N=0$), 75.1% of pores had radii of 4–16 μm (Figure 8A), while 87.1% had diameters of 8–44 μm (Figure 8B). These pores included spaced pores and some

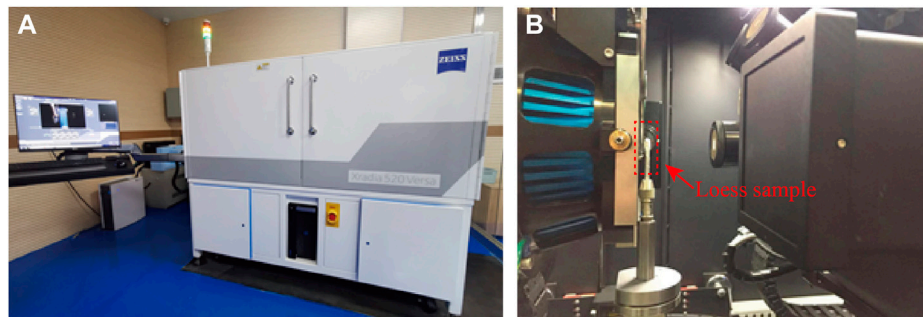


FIGURE 4
Micro-CT machine (A) and sample scanning stage (B).

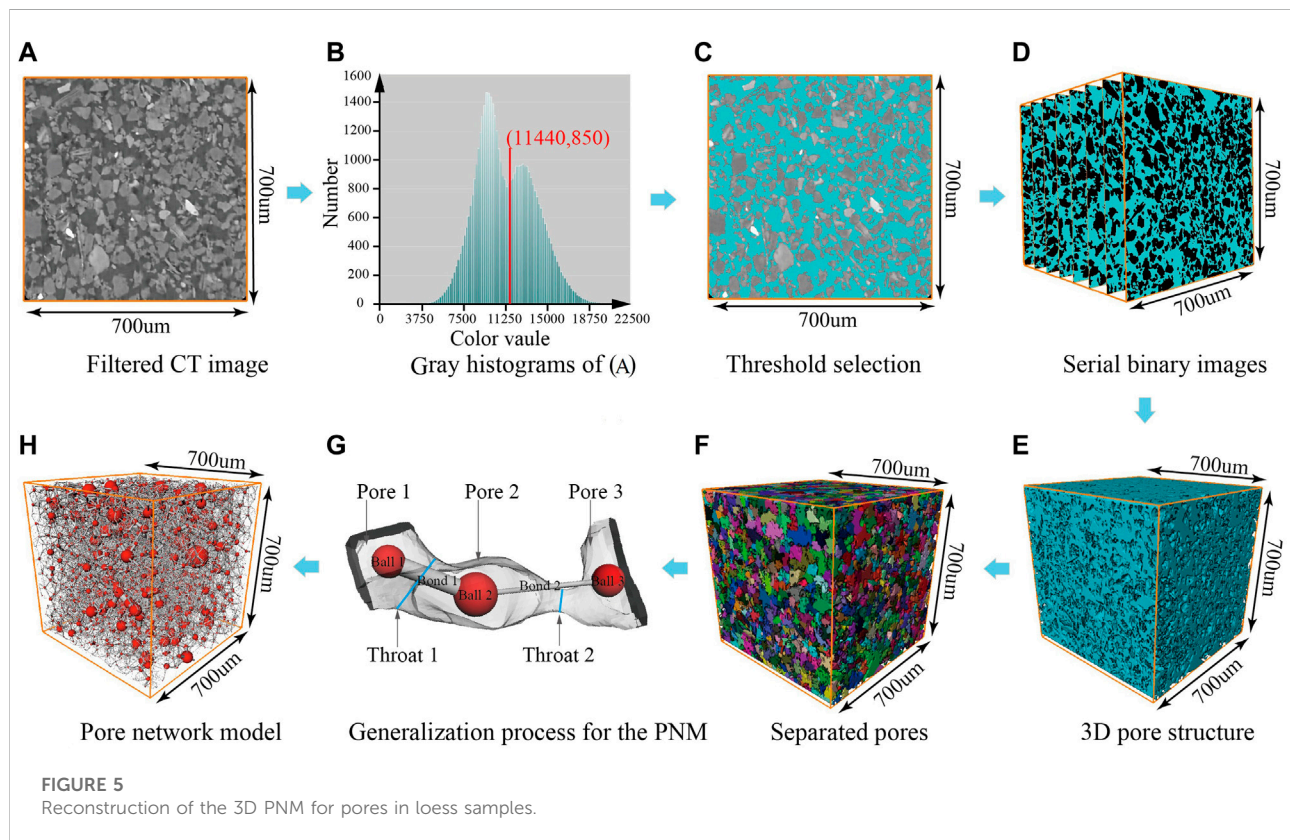


FIGURE 5
Reconstruction of the 3D PNM for pores in loess samples.

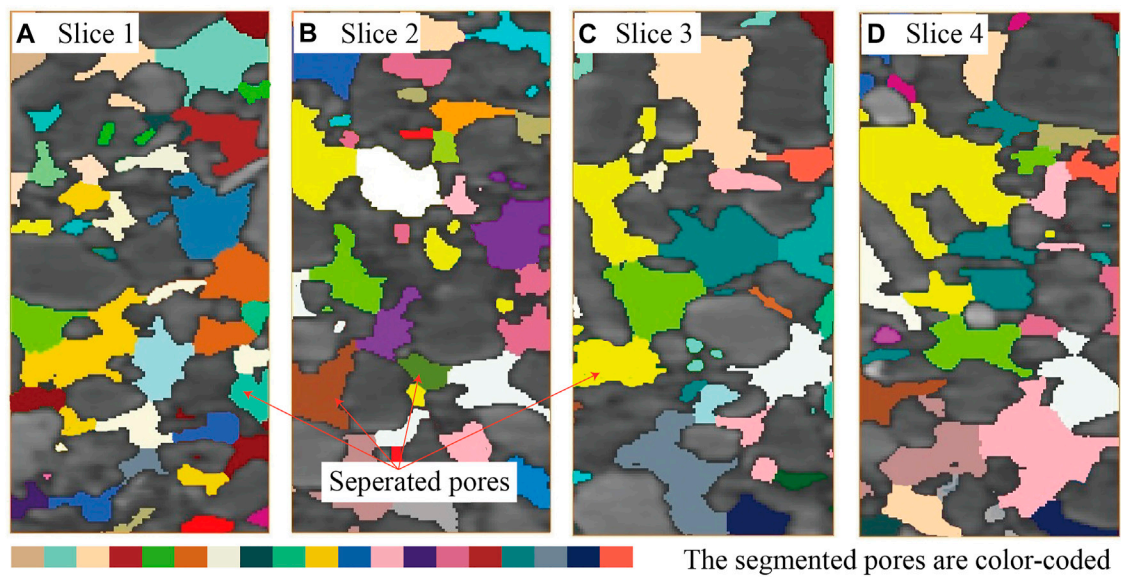


FIGURE 6
Pores segmented by the watershed algorithm.

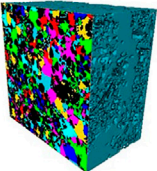
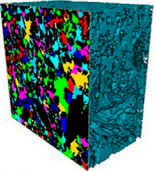
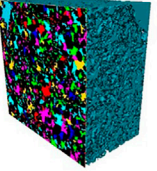
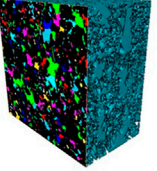
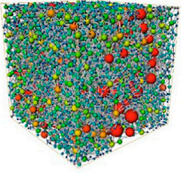
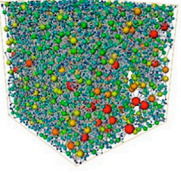
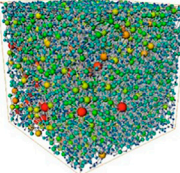
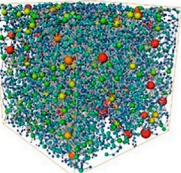
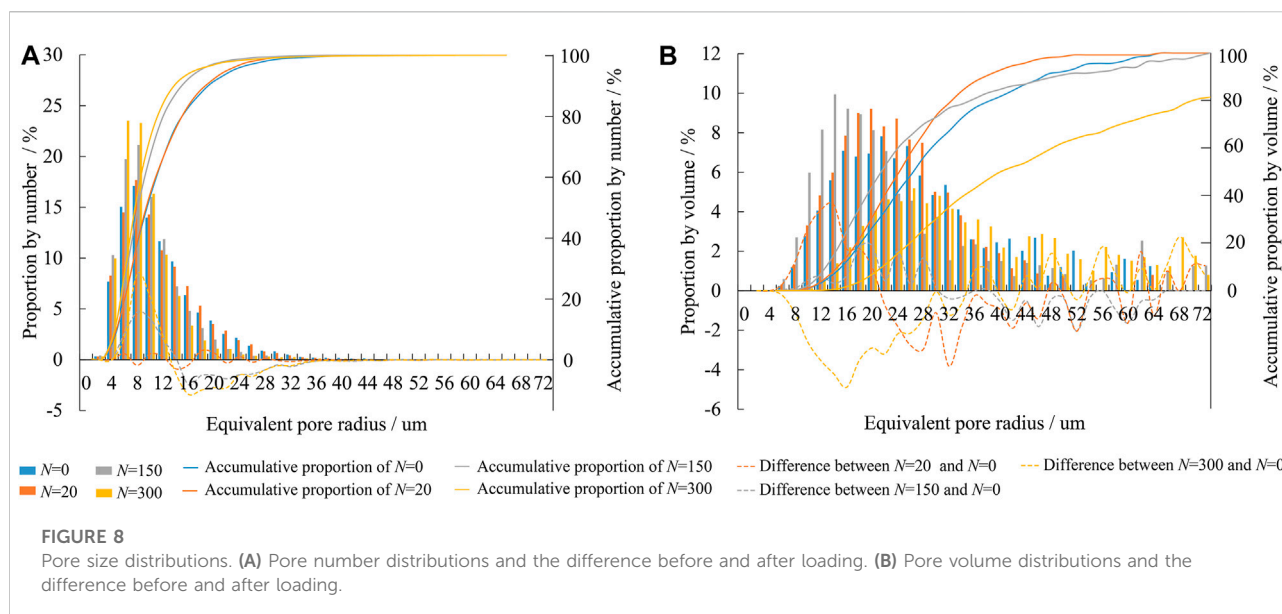
Sample	N=0	N=20	N=150	N=300
3D pore				
	Size: 700 × 700 × 700 μm; Voxel size (μm³): 1			
	Porosity n : 0.47	Porosity n : 0.40	Porosity n : 0.33	Porosity n : 0.31
PNM				
	Average CN : 8.18	Average CN : 7.06	Average CN : 5.77	Average CN : 3.66
	Average r_n (μm): 13.00	Average r_n (μm): 12.35	Average r_n (μm): 10.75	Average r_n (μm): 10.15
	Average A_b (μm²): 132.21	Average A_b (μm²): 49.06	Average A_b (μm²): 42.11	Average A_b (μm²): 39.53
	Average CL (μm): 44.28	Average CL (μm): 43.74	Average CL (μm): 39.30	Average CL (μm): 40.26
	Average EL : 0.50:	Average EL : 0.49	Average EL : 0.47	Average EL : 0.45
	Average O (°): 57.88	Average O (°): 56.92	Average O (°): 58.27	Average O (°): 58.84

FIGURE 7
3D pore volumes and extracted PNMs with their characteristics.



relatively large inter-particle pores (Wei et al., 2020). The peaks of pore number distribution for $N=0$, $N=20$, $N=150$, and $N=300$ were 17.1%, 17.7%, 21.1%, and 23.5% corresponding to pore equivalent radii of approximately 8 μm , 8 μm , 8 μm , and 6 μm , respectively. The larger the peak amplitude, the more concentrated the pore size distribution, indicating that the pore size distribution gradually concentrated with increasing vibration times (Figure 8A). The peaks of the pore volume distribution for $N=0$, $N=20$, $N=150$, and $N=300$ were 7.8%, 9.2%, 9.9%, and 5.2% corresponding to pore equivalent radii of approximately 22 μm , 18 μm , 12 μm , and 24 μm , respectively. From $N=0$ to $N=150$, the pore volume distribution gradually concentrated and shifted to smaller radii. However, $N=300$ showed the opposite trend (Figure 8B).

The differences in pore number and volume proportion among the four samples are plotted in Figures 8A, B. Overall, large pores showed decreased numbers and volumes, while small pores showed increases. The proportions of pores $<14 \mu\text{m}$ increased by 13.6% and 17.9% in the samples after 150 and 300 vibration cycles, respectively. When $N=20$, the pore number change range was not obvious. Regarding pore volume change, the proportion of pores with radii $<28 \mu\text{m}$ increased by 11.6% for $N=20$ and by 19.0% for $N=150$. However, pores with radii $<28 \mu\text{m}$ decreased in volume by 32% for 300 cyclic loads.

The pore distributions and variations under cyclic loading reflect the process of loess subsidence. Spaced pores and some of the relatively large inter-particle pores decreased in number and volume and shifted to small inter-particle pores or intra-aggregate pores. However, after destruction, although the number of small pores increased, loose fracture zones were

generated, resulting in an increased proportion of large pore volume (Figure 8B).

Pore throat

The pore throat is the thinnest part connecting two pore bodies, with the throat the channel connecting two pores. In the intact loess, the pore throat number was 8388 in the area of interest, the average pore-throat area was 132.21 μm^2 , and the average channel length was 44.28 μm . For $N=20$, $N=150$, and $N=300$, the pore throat numbers were 8738, 9875, and 11,085; the average pore-throat areas were 49.06 μm^2 , 42.11 μm^2 , and 39.53 μm^2 ; and the average channel lengths were 43.74 μm , 39.30 μm , and 40.26 μm , respectively (Figure 7). Figure 9 depicts the percentage distributions of pore throats for different throat areas and the difference among the four samples under different vibration times. For vibration times from 20 to 300, the number of pores with throat area $>50 \mu\text{m}^2$ decreased by 6%, 11%, and 13%, respectively, compared to the intact loess. Moreover, the proportion of those $<50 \mu\text{m}^2$ increased (Figure 9A). The number of pores with throat channel lengths $>50 \mu\text{m}$ decreased by 9.6% when the loess was vibrated 20 times. When the loess was subjected to 150 and 300 cyclic vibrations, the number of pores $>40 \mu\text{m}$ decreased by 13.7% and 18.0%, respectively (Figure 9B).

The results indicated that the loess structure is compressed during cyclic vibration loads and that large pores are transformed into many small pores, forming more pores and throats with smaller areas and channels. The effect was especially strong after 150 cyclic vibrations, in which the number of pores and throats was the largest, but the size was the smallest.

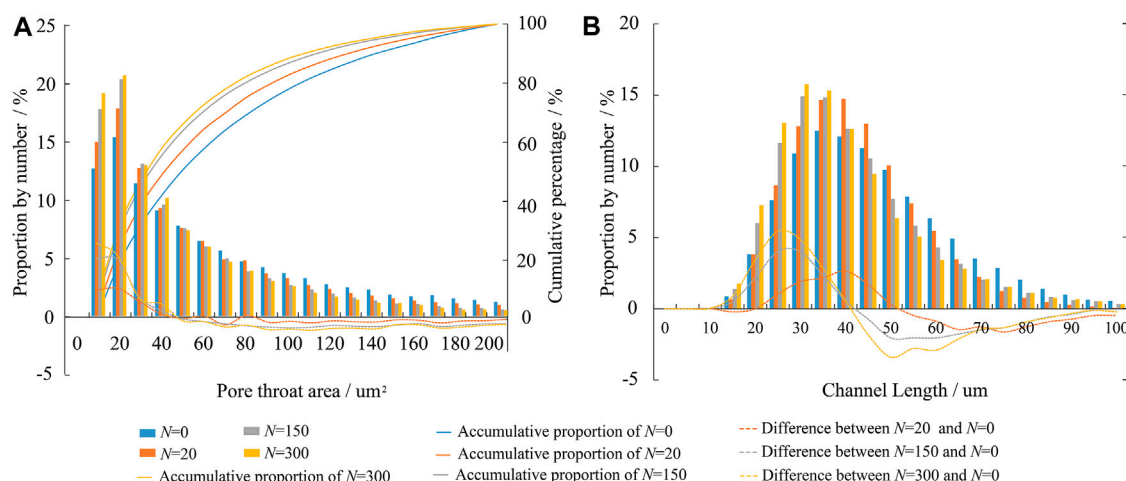


FIGURE 9

Pore-throat size distributions. (A) Pore-throat area distributions and the difference before and after loading. (B) Channel length distributions and the difference before and after loading.

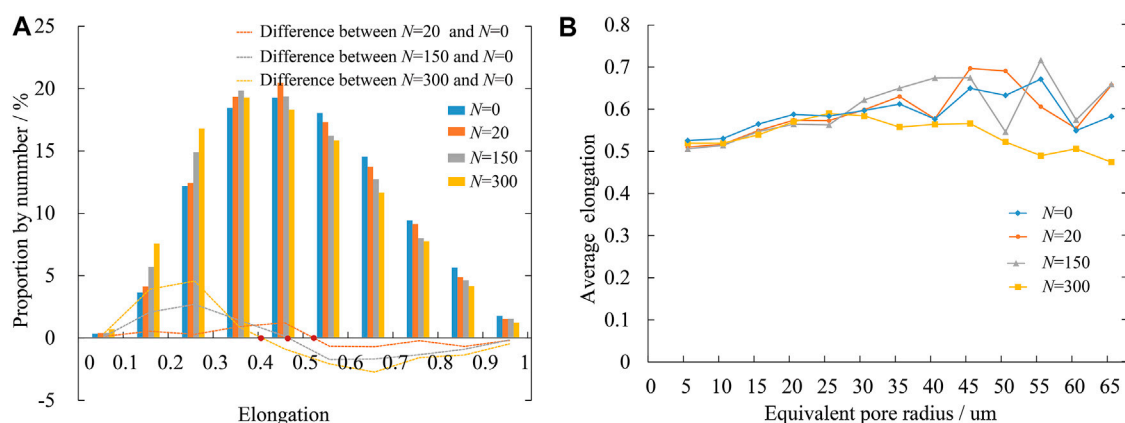


FIGURE 10

Pore elongation distribution. (A) Pore elongation distributions and the difference before and after loading. (B) Relationship between pore equivalent radius and elongation.

Pore elongation

Variation in pore elongation can reflect the microscopic deformation characteristics of the loess structure. The average pore elongation values of the four samples were 0.50, 0.49, 0.47, and 0.45, respectively (Figure 7). More than 98% of the pores showed elongation values between 0.1 and 0.9 in intact loess. The difference among the four samples is shown in Figure 10A. The turning point of elongation variation in the samples before and after loading was about 0.45. The number of pores smaller than this value increased by 3%, 6%, and 10%, respectively, while the

number of pores above this value decreased correspondingly. These results indicated that the loess structure was compressed and that the pores gradually flattened under the action of cyclic load.

Figure 10B shows the average elongation of the pores according to the radius. For pores $<28\mu\text{m}$ in the four samples, the average elongation increased gradually with increasing pore radius. For pores $>28\mu\text{m}$, the average elongation in the $N=0$, $N=20$, and $N=150$ samples showed varying elongation increases; however, the curve showed no obvious linear trend. In the $N=300$ sample, the average

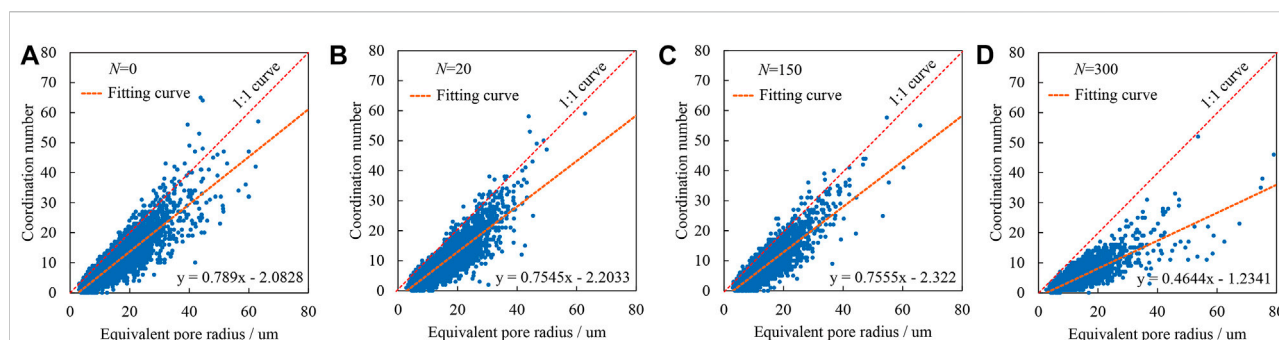


FIGURE 11

Coordination number distributions and the relationship between coordination number and equivalent radius.

elongation decreased significantly with the pore increase to $>28\ \mu\text{m}$. These results indicated that the pores with a radius $>28\ \mu\text{m}$ are seriously deformed after being loaded and are pressed into a flat elongated shape. This result is consistent with the change in pore volume.

Pore connectivity

The average CN values were 8.18, 7.06, 5.77, and 3.66 for the $N=0$, $N=20$, $N=150$, and $N=300$ samples, respectively. CN can roughly reflect the weakening of pore connectivity in loess after loading. Figures 11A–D show the relationships between CN distributions and the equivalent pore radius of the four loess samples. With increased vibration times, the number of pores with $CN > 10$ decreased significantly, especially when the vibration reached 300. Meanwhile, the fitting curve of CN distribution gradually deviated from the 1:1 curve, indicating that with increased vibration times, the CN of the same radius pore decreased. These findings demonstrated that although these pores were large, including those created after destruction, their connectivity was worse than that of pores of the same size in intact loess.

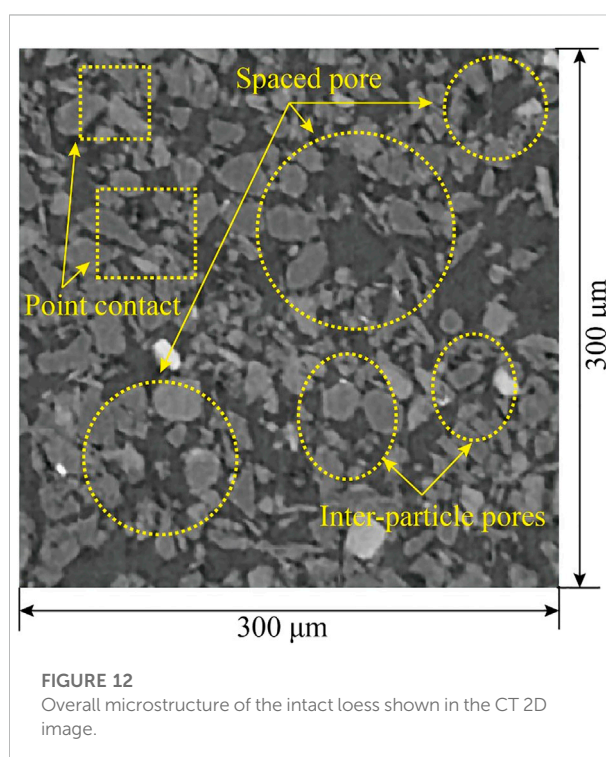


FIGURE 12

Overall microstructure of the intact loess shown in the CT 2D image.

Discussion

Occurrence of seismic subsidence

Regarding loess seismic subsidence, a critical challenge is associated with the transition from spaced and loosely packed to compacted and more stable structures. The Malan loess in the present study had a loose microstructure, with pores diameters of $8\text{--}44\ \mu\text{m}$ predominating in the total volume at a proportion of 87.1% (Figure 8). These widely distributed spaced, inter-particle, and inter-aggregate pores are the main contributors to loess structural collapse (Lei Wang, 1987; Osipov and Sokolov, 1995). The spaced pores are formed

by the stacking of particles, and their size is much larger compared to the surrounding particles (Figure 12). Clay particles $<5\ \mu\text{m}$ accounted for only 10% of the studied loess and acted as the main the cement, formed clay bridges and aggregates, and attached to the surface of the silt and sand (Wei et al., 2019b). These characteristics determined the weak cementation in the studied loess and the contact between particles was mainly point contact (Figure 12). The cohesion and internal friction under low water content supported the stability of the structural system, keeping the loess relatively stable in its intact state.

However, when subjected to cyclic loading, the weak cementation and direct point contact no longer function

effectively and consistently. When the external load exceeds the bond yield strength, the surrounding particles will break off at weak cementation points. The exfoliated particles will fall into the pore space, forming a new rearrangement structure (Nan et al., 2021). During this process, in terms of pore volume distribution, the collapse of pores $>28\ \mu\text{m}$ resulted in an increased number of small-sized pores and a decreased number of large-size pores (Figures 8–10). After the structure collapse, the loess was compressed, resulting in decreased pore-throat channel length and elongation, in addition to flat pore development (Figures 8–10). Under low confining pressure, cyclic loading disintegrated the local microstructure, resulting in structural loss and the generation of large pore cracks (Figure 8). Thus, the microstructural characteristics of loess, including pore types, contact relationship, and cementation degree, are internal factors related to its resistance to external loads.

Engineering applications and implications

Loess soil stability challenges exist in underground engineering, slope engineering, and foundations in loess regions (Liu et al., 2018; Juang et al., 2019; Liu et al., 2020). The process of loess deformation and instability is gradual, beginning with local microstructural changes that progressively produce microcracks, which then gradually expand into through-cracks, and finally, slope sliding. Alternatively, microstructure collapse may lead to a large area of uneven settlement, resulting in the instability of the foundation and surrounding tunnel rock. The results of this study showed that multiple dynamic loads can lead to significant changes in soil pore microstructure. The change in pore structure from loose to compact occurs mainly due to microstructure collapse and rearrangement. In some filling and tunnel projects, we can pre-treat the soil in advance to produce subsidence. Regarding earthquakes, the amount of seismic subsidence will be little or even none, thus reducing the amount and speed of deformation. The microstructure evolution can be applied to numerical simulations to simulate variations in local microstructure when combining finite and discrete elements. This new method more accurately simulates soil stability.

Conclusion

The seismic subsidence of loess is closely related to its microstructure. This study reconstructed the 3D microstructure based on micro-CT images with a voxel size of $1\ \mu\text{m}^3$. The PNM was also generated based on the 3D pore structure to extract quantitative pore parameters. By studying

the evolution law of microstructures during cyclic vibration, the influence of seismic duration on microstructure can be studied to explore the microscopic mechanisms of seismic deformation. The results of the analysis led to the following major conclusions:

- 1) For the intact Malan loess in Lanzhou with low water content examined in this study, the high porosity of 0.51 and the small proportion of clay led to loose particle arrangement and weak cementation, which was mainly an unstable direct point contact. The spaced and inter-aggregate pores predominated the total pore volume.
- 2) Pore size was most sensitive to the cyclic loading; in the dynamic triaxial tests, the spaced and inter-aggregate pores transformed into intra-aggregate pores, the total number of pore throats and channels increased but the connectivity decreased; and the pores were flatter, indicating pore compression. Pores $>28\ \mu\text{m}$ mainly provide spatial conditions for collapse deformation under seismic load.
- 3) Loess seismic subsidence originates from both compositional and microstructural characteristics. The former primarily involve the clay and water content, which directly affects the particle arrangement and bonding strength. The latter primarily involve the volume content of spaced and inter-aggregate pores and contact relationships.
- 4) The microstructure characterization and evolution of loess during seismic loading can be applied to the numerical simulation. The combination of finite and discrete elements to simulate slope stability can better restore the slope instability process from local structural variation gradually expanding to a large range.

Future work will focus on seismic amplitude and frequency to analyze the influence of seismic factors on the microstructure and microstructure sensitivity to seismic factors, to reveal in depth the microscopic mechanism of loess subsidence.

Data availability statement

The raw data supporting the conclusion of this article will be made available by the authors, without undue reservation.

Author contributions

TW was responsible for the study concept and manuscript writing. ZW was responsible for the study concept and resources. YC performed the

experiments. LL was responsible for editing the manuscript draft.

Funding

This work was supported by the National Natural Science Foundation of China (grant numbers 42102305 and U1939209) and the Six Talent Peaks Project of Jiangsu Province (JZ-016).

Acknowledgments

All authors thank the constructive review of the reviewer and editor for the early version of the manuscript.

References

- Chen, H. E., Shan, W. C., and Jiang, Y. L. (2021). Dynamic characteristics of xianyang loess based on microscopic analysis: A quantitative evaluation. *B. Eng. Geol. Environ.* 80 (10), 8247–8263. doi:10.1007/s10064-021-02432-x
- Chen, S. J., Ma, W., and Li, G. Y. (2019). Study on the mesostructural evolution mechanism of compacted loess subjected to various weathering actions. *Cold Reg. Sci. Technol.* 167 (1), 102846. doi:10.1016/j.coldregions.2019.102846
- Cremaschi, M., Fedoroff, N., Guerreschi, A., Huxtable, J., Colombi, N., Castelletti, L., et al. (1990). Sedimentary and pedological processes in the upper pleistocene loess of northern Italy: the bagaggera sequence. *Quatern. Int.* 5, 23–38. doi:10.1016/1040-6182(90)90022-V
- Juang, C. H., Dijkstra, T., Wasowski, J., and Meng, X. (2019). Loess geohazards research in China: Advances and challenges for mega engineering projects. *Eng. Geol.* 251, 1–10. doi:10.1016/j.enggeo.2019.01.019
- Kou, X. H., Zhang, Q., and Dong, X. Q. (2017). Study on dynamic characteristics of acid compacted loess under different vibration frequencies. *Nat. Sci. Ed.* 38 (2), 249–254. doi:10.3969/j.issn.1673-3193.2017.02.027
- Lei, X. Y., and Wang, S. F. (1987). Size of loess pores in relation to collapsibility. *Hydrogeol. Eng. Geol.* 14 (5), 15–18.
- Li, P., and Shao, S. (2020). Can X-ray computed tomography (CT) be used to determine the pore-size distribution of intact loess. *Environ. Earth Sci.* 79 (1), 29–12. doi:10.1007/s12665-019-8777-z
- Li, P., Xie, W. L., Pak, R., and Vanapalli, S. K. (2018). Microstructural evolution of loess soils from the loess plateau of China. *Catena* 173, 276–288. doi:10.1016/j.catena.2018.10.006
- Li, T. L., Fan, J. W., Xi, Y., Xie, X., and Hou, X. K. (2019). Analysis for effect of microstructure on swcc of compacted loess. *J. Eng. Geol. Chin.* 27 (5), 045. doi:10.13544/j.cnki.jeg.2019045
- Lian, B. Q., Wang, X. G., Zhan, H. B., Wang, J., Peng, J., Gu, T., et al. (2022). Creep mechanical and microstructural insights into the failure mechanism of loess landslides induced by dry-wet cycles in the Heifangtai platform, China. *Eng. Geol.* 300, 106589. doi:10.1016/j.enggeo.2022.106589
- Liu, N. F., Li, N., Li, G. F., Zhang, Z. Q., and Mu, Y. M. (2018). Deformation and collapse mechanisms of water-rich soil tunnels. *Soil Mech. Found. Eng.* 54 (6), 384–394. doi:10.1007/s11204-018-9485-5
- Liu, N. F., Li, N., Xu, C. B., Li, G. F., Song, Z. P., and Yang, M. (2020). Mechanism of secondary lining cracking and its simulation for the dugongling tunnel. *Rock Mech. Rock Eng.* 53, 4539–4558. doi:10.1007/s00603-020-02183-3
- Ma, W., Cheng, G. D., Zhu, Y. L., and Xu, X. Z. (1998). The state key laboratory of frozen soil engineering: Review and prospect. *J. Glaciol. Geocryol.* 4, 1–10.
- Matalucci, R. V., Abdel-Hady, M., and Shelton, J. W. (1970). Influence of microstructure of loess on triaxial shear strength. *Eng. Geol.* 4 (4), 341–351. doi:10.1016/0013-7952(70)90024-4
- Meng, Z. J., Ma, P. H., and Peng, J. B. (2021). Characteristics of loess landslides triggered by different factors in the Chinese loess plateau. *J. Mt. Sci-Engl.* 18 (12), 3218–3229. doi:10.1007/s11629-021-6880-6
- Mu, Q. Y., Zhou, C., and Ng, C. W. W. (2020). Compression and wetting induced volumetric behavior of loess: Macro- and micro-investigations. *Transp. Geotech.* 23, 100345. doi:10.1016/j.trgeo.2020.100345
- Nan, J. J., Peng, J. B., Zhu, F. J., Ma, P. H., Liu, R., Leng, Y. Q., et al. (2021). Shear behavior and microstructural variation in loess from the Yan'an area, China. *Eng. Geol.* 280, 105964. doi:10.1016/j.enggeo.2020.105964
- Ni, W. K., Yuan, K. Z., Lü, X. F., and Yuan, Z. H. (2020). Comparison and quantitative analysis of microstructure parameters between original loess and remoulded loess under different wetting-drying cycles. *Sci. Rep-UK* 10 (1), 5547–5612. doi:10.1038/s41598-020-62571-1
- Osipov, V. I., and Sokolov, V. N. (1995). Factors and mechanism of loess collapsibility. *Genesis Prop. collapsible soils* 6, 49–63. doi:10.1007/978-94-011-0097-7_4
- Sun, P., Li, R. J., Jiang, H., Lgwe, O., and Shi, J. S. (2017). Earthquake-triggered landslides by the 1718 tongwei earthquake in gansu province, northwest China. *B. Eng. Geol. Environ.* 76, 1281–1295. doi:10.1007/s10064-016-0949-4
- Wang, F., Li, G., Ma, W., Mu, Y., Zhou, Z. W., Zhang, J., et al. (2020). Effect of repeated wetting-drying-freezing-thawing cycles on the mechanic properties and pore characteristics of compacted loess. *Adv. Civ. Eng.* 1, 1–8. doi:10.1155/2020/8839347
- Wang, H. B., Zhou, B., Wu, S. R., Shi, J. S., and Li, B. (2011). Characteristic analysis of large-scale loess landslides: A case study in baoji city of Loess Plateau and northwest China. *Nat. Hazard Earth. Sys.* 11 (7), 1829–1837. doi:10.5194/nhess-11-1829-2011
- Wang, J. D., Li, P., Ma, Y., Vanapalli, S. K., and Wang, X. G. (2020). Change in pore-size distribution of collapsible loess due to loading and inundating. *Acta Geotech.* 15 (5), 1081–1094. doi:10.1007/s11440-019-00815-9
- Wang, N. Q., Luo, D. H., Yao, Y., Chen, X. X., and Yang, J. G. (2011). Dynamic strength and Microstructure change of Malan loess under triaxial cyclic loading. *J. Eng. Geol. Chin.* 19, 467–471. doi:10.1007/s12182-011-0118-0
- Wang, Q., Zhong, X. M., Su, Y. Q., Li, N., Che, G. F., and Wang, L. L. (2016). Study of the dynamic deformation properties of loess under a dynamic load in the Lanzhou Metro. *Mod. Tunn. Tech.* 53, 137–142. doi:10.13807/j.cnki.mtt.2016.06.019
- Wang, Y., Yang, H., and Jing, X. (2021). Structural characteristics of natural loess in northwest China and its effect on shear behavior. *Geotech. Eng. Geol.* 39 (1), 65–78. doi:10.1007/s10706-020-01420-4
- Wei, T. T., Fan, W., Yu, N. Y., and Wei, Y. N. (2019a). Three-dimensional microstructure characterization of loess based on a serial sectioning technique. *Eng. Geol.* 261, 105265. doi:10.1016/j.enggeo.2019.105265
- Wei, T. T., Fan, W., Yuan, W. N., Wei, Y. N., and Yu, B. (2019b). Three-dimensional pore network characterization of loess and paleosol stratigraphy from

Conflict of interest

The authors declare that the research was conducted in the absence of any commercial or financial relationships that could be construed as a potential conflict of interest.

Publisher's note

All claims expressed in this article are solely those of the authors and do not necessarily represent those of their affiliated organizations, or those of the publisher, the editors, and the reviewers. Any product that may be evaluated in this article, or claim that may be made by its manufacturer, is not guaranteed or endorsed by the publisher.

south Jingyang plateau, China. *Environ. Earth. Sci.* 78 (11), 333. doi:10.1007/s12665-019-8331-z

Wei, Y. N., Fan, W., Yu, B., Deng, L. S., and Wei, T. T. (2020). Characterization and evolution of three-dimensional microstructure of Malan loess. *Catena* 192, 104585. doi:10.1016/j.catena.2020.104585

Xie, W. L., Li, P., Zhang, M. S., Cheng, T. E., and Wang, Y. (2018). Collapse behavior and microstructural evolution of loess soils from the loess plateau of China. *J. Mt. Sci-Engl.* 15, 1642–1657. doi:10.1007/s11629-018-5006-2

Xu, J., Li, Y. F., Ren, C., Wang, S. H., Vanapalli, S. K., and Chen, G. (2020b). Influence of freeze-thaw cycles on microstructure and hydraulic conductivity of saline intact loess. *Cold Reg. Sci. Technol.* 181, 103183. doi:10.1016/j.coldregions.2020.103183

Xu, J., Li, Y. F., Ren, C., and Wei, L. (2020a). Damage of saline intact loess after dry-wet and its interpretation based on sem and nmr. *Soils Found.* 60 (4), 911–928. doi:10.1016/j.sandf.2020.06.006

Xu, J., Ren, C., Wang, S. H., Gao, J. Y., and Zhou, X. G. (2021). Permeability and microstructure of a saline intact loess after dry-wet cycles. *Adv. Civ. Eng.* 2021, 1–18. doi:10.1155/2021/6653697

Yu, B., Fan, W., Dijkstra, T. A., Wei, Y. N., and Deng, L. S. (2021). Heterogeneous evolution of pore structure during loess collapse: Insights from X-ray micro-computed tomography. *Catena* 201, 105206. doi:10.1016/j.catena.2021.105206

Yuan, Z. X., and Wang, L. M. (2009). Collapsibility and seismic settlement of loess. *Eng. Geol.* 105 (1-2), 119–123. doi:10.1016/j.enggeo.2008.12.002

Zeng, C. Q., Zhang, W. Y., Ma, Q., and Wen, S. J. (2022). Experimental study on the stiffness degradation of remolded loess in Haibei area under cyclic loading. *J. Earthq. Eng.* 44, 292–298. doi:10.20000/j.1000-0844.20200617004

Zhang, Y. W., Song, Z. P., and Weng, X. L. (2022). A constitutive model for loess considering the characteristics of structurality and anisotropy. *Soil Mech. Found. Eng.* 59, 32–43. doi:10.1007/s11204-022-09781-z

Zhuang, J. Q., Peng, J. B., Xu, C., Li, Z., Densmore, A., Milledge, D., et al. (2018). Distribution and characteristics of loess landslides triggered by the 1920 haiyuan earthquake, northwest of China. *Geomorphology* 314 (6), 1–12. doi:10.1016/j.geomorph.2018.04.012



OPEN ACCESS

EDITED BY
Yuwei Zhang,
Xi'an University of Architecture and
Technology, China

REVIEWED BY
Chunbo Zhou,
China University of Mining and
Technology, China
Zhenlong Song,
Southern University of Science and
Technology, China

*CORRESPONDENCE
Jun Huang,
✉ hgyyoe@xsyu.edu.cn

SPECIALTY SECTION
This article was submitted to
Environmental Informatics and Remote
Sensing,
a section of the journal
Frontiers in Earth Science

RECEIVED 30 November 2022
ACCEPTED 20 December 2022
PUBLISHED 05 January 2023

CITATION
Huang J, Liu X, Ma Z, Lv G and Dang K
(2023), The stability evaluation of clay
tunnels via the non-linear deterioration of
physical and mechanical properties of
surrounding rocks.
Front. Earth Sci. 10:1112410.
doi: 10.3389/feart.2022.1112410

COPYRIGHT
© 2023 Huang, Liu, Ma, Lv and Dang. This is
an open-access article distributed under
the terms of the [Creative Commons
Attribution License \(CC BY\)](https://creativecommons.org/licenses/by/4.0/). The use,
distribution or reproduction in other
forums is permitted, provided the original
author(s) and the copyright owner(s) are
credited and that the original publication in
this journal is cited, in accordance with
accepted academic practice. No use,
distribution or reproduction is permitted
which does not comply with these terms.

The stability evaluation of clay tunnels via the non-linear deterioration of physical and mechanical properties of surrounding rocks

Jun Huang^{1*}, Xingwang Liu², Zongyuan Ma³, Gao Lv¹ and Kangning Dang⁴

¹School of Earth Sciences and Engineering, Xi'an Shi-you University, Xi'an, China, ²Urban Construction and Transport Engineering Division, PowerChina Northwest Engineering Corporation Limited, Xi'an, China, ³Guizhou Communications Polytechnic, Guiyang, China, ⁴Hanjiang-to-Weihe River Valley Water Diversion Project Construction Co.LTD, Xi'an, China

Simple, fast, and reliable methods for the stability evaluation of tunnels can facilitate the construction and development of tunneling projects. The problems related to tunnel stability at this stage can be well analyzed via theoretical analysis method, model test method, or numerical analysis method. On the other hand, those methods are hard to be effectively analyzed these projects with higher importance, shorter decision and design period, and more urgent construction period. This paper proposed research works on the stability evaluation of clay tunnels. Firstly, a state function with the variables of stress and strain state is presented to predict the stress and strain states of surrounding rocks caused by tunnel excavation, which characterize the physical-mechanical state of surrounding rocks (also called stability state). Secondly, the non-linear deterioration of the physical and mechanical properties of surrounding rocks will be simulated, and the expressions and calculation methods of the tunnel stability reserve factor will be yielded. Finally, the results of the proposed method were compared with the strength reduction method and the limit equilibrium method with a clay tunnel example. The comparison between the three feature points of the arch crown, sidewall, and arch bottom showed that the stability reserve factor of the clay tunnel was smaller than those of the strength reduction method and the limit equilibrium method. The values of limit displacement obtained by the proposed method were closer to the field monitoring data than that of the strength reduction method. Therefore, this study could be better applied to the stability evaluation of clay tunnels.

KEYWORDS

clay tunnel, stability evaluation, properties of surrounding rocks, numerical model, limit state

1 Introduction

Research in tunnel stability evaluation is very important for the safe construction and operation of tunnel projects. Modern subway tunnels have short construction cycles and high construction and operation safety requirements. Thus, tunnel engineers need to process the project more rapidly, and more efficiently, and make stability analysis decisions accurately. Therefore, tunnel stability evaluation is facing challenges i.e., rapid response, decision-making judgment, prevention and disposal, and the need for further in-depth optimization.

At present, the research methods of tunnel stability can be summarized as the empirical, theoretical, experimental, and numerical analysis methods (Song et al., 2001; Osman et al., 2006; Son and Cording, 2008; Yang and Yang, 2009; Fraldi and Guarracino, 2010; Yang and Huang, 2013; Shiau and Al-Asadi, 2020; Song and Marshall, 2020; Tan et al., 2020; Tyagi et al., 2020; Yertutanol et al., 2020; Li L. P. et al., 2021; Pandit and Sivakumar, 2021; Liu et al., 2022a; Zhang et al., 2022a; Zhang Z. et al., 2022; Hao et al., 2022; Lu et al., 2022; Qin et al., 2022; Li et al., 2023; Xue et al., 2023). The primary purpose of these methods is to obtain more effective and accurate stability analysis results and provide a more reliable basis for the actual tunnel construction and operation decisions. Early researchers (Broms and Bennermark, 1967; Davis et al., 1979; Mair, 1979; Rowe and Kack, 1983; Assadi and Sloan, 1991a; Assadi and Sloan, 1991b; Leca and Dormieux, 1991; Sloan and Assadi, 1991; Mair et al., 1993) usually relied on the experience to evaluate the stability of tunnels due to the lack of theoretical basis. The experience of tunnel construction is accumulated with the development of geotechnical theory and technology. The researchers (Lee and Park, 2000; Lyamin et al., 2001; Wang et al., 2001; Lee et al., 2006; Fraldi and Guarracino, 2009; Wilson et al., 2011; Yang and Huang, 2011; Fan et al., 2013; Rojat et al., 2015) considering more influencing factors to evaluate the stability of tunnels and formed the corresponding stability evaluation methods and techniques. The tunnel stability evaluation methods have been developed by the emergence of more adverse factors and complex environmental conditions with the continuous development of tunnel construction. Since the researchers of tunnel stability evaluation focus on the response of surrounding rocks' stress field and deformation field caused by tunnel excavation, tunnel model tests (Marshall et al., 2012; Shiau and Al-Asadi, 2020; Song and Marshall, 2020; Yertutanol et al., 2020; Lu et al., 2022; Sun et al., 2022; Qin et al., 2023a; Qin et al., 2023b) is used to reveal the rule of the stress field and deformation field of surrounding rocks by excavation. The model's test of tunnel experimental (Franza, 2019; Huang et al., 2019; Zhang et al., 2020), *in-situ*, and centrifugal, can be well revealed the failure pattern. The stress distribution and deformation characteristics of surrounding rocks will help to understand tunnel stability research. Researchers (Liu et al., 2020; Antão et al., 2021; Fernández et al., 2021; Han et al., 2021; Nguyen and Nguyen-Son, 2022; Pelech et al., 2022; Zhuo et al., 2022; Qin et al., 2023c) established numerical models based on the numerical method, e.g., finite element method or discrete element method with the continuous improvement of computer performance and the development of computing technology. Numerical modeling is closer to the accurate geometric scale, surrounding rock materials, loading effects, boundary conditions, etc., and visualizes the process of surrounding rock loading evolution. Numerical methods can solve the construction problems faced by large tunnel projects effectively, and promote tunnel engineering development. Currently, the methods of tunnel stability are not limited to a narrow field. These methods (Sukkarak et al., 2019; Shiau and Al-Asadi, 2020; Kumar and Jain, 2021; Li T. Z. et al., 2021; Liu et al., 2022b; Zhang et al., 2022b; Man et al., 2022; Xue et al., 2022; Xue et al., 2023) are not only applied to but also inspired by other fields of research. The researchers of tunnel stability problems still have the power of sustainable development.

Researchers are still trying to find more operational, more straightforward physically meaningful, and applicable methods for tunnel stability evaluation problems. In this paper, a clay tunnel project is used as the case study, and the deterioration

characteristics of the physical and mechanical properties of surrounding rocks are taken into account. The development of surrounding rocks from the stable to the limit state until the failure. This paper introduced a strategy for the deterioration of the strength and deformation resistance of surrounding rocks for tunnel stability evaluation.

2 State function of clay tunnel surrounding rocks

The general failure of tunnel loading can be summarized into two cases. The first one is the redistribution of stresses in surrounding rocks and destabilization is yield due to the stress is exceeded the limit value (the accumulated deformation before stress failure may not exceed the limit). The second type of instability is due to the cumulative deformation caused by excavation-induced restraint relaxation exceeding the limit (the stress state may not exceed the limit at this time). The basic idea of the strength reduction method is to allow the material strength to deteriorate until the material reaches its ultimate state. In general, the failure of clay tunnels has been corresponding to both cases described. The deterioration of the strength and deformation resistance in surrounding rocks should take into account to evaluate stability reserves.

According to the basic knowledge of solid mechanics, elastic mechanics, and material mechanics, it is known that stress redistribution occurs in clay strata due to tunnel excavation, which leads to the change of stress-strain state in surrounding rocks. The stress state at a point in surrounding rocks can be characterized by the stress and strain of this point at this moment. So it assumed the existence of a state function F_s , which was a function of the stress state and strain state at a point in surrounding rocks. It was that the state function could reflect the stress state characteristics of surrounding rocks. The expression of the state function F_s was as follows.

$$F_s = f(\sigma, \varepsilon) \quad (1)$$

Where σ refers to the stress state at a point in surrounding rocks, and ε refers to the strain state at a point in surrounding rocks.

According to the definition of the state function, when the stress state or strain state of any point in surrounding rocks reaches the limit state, it can be considered that the state function at that point reaches the limit state at this time. There should be three limit states at a point in surrounding rocks.

- 1) A point of surrounding rocks stress state and strain state have reached the limit state: $F_{SL} = f(\sigma_L, \varepsilon_L)$;
- 2) Only the stress state at a point of surrounding rocks reaches the limit state: $F_{SL} = f(\sigma_L, \varepsilon)$;
- 3) Only the deformation at a point of surrounding rocks reaches the limit state: $F_{SL} = f(\sigma, \varepsilon_L)$.

F_{SL} is the limit state function. The stability of the point can be determined *via* the limit state function at a point of surrounding rocks,

- 1) if $F_s = F_{SL}$, it is in the limit state;
- 2) if $F_s < F_{SL}$, it is in a steady state;
- 3) if $F_s > F_{SL}$, it is in the failure state.

These can be used as guidelines to distinguish the stability state of tunnel surrounding rocks. Then, these guidelines can play an important role when the engineer needs to evaluate the tunnel stability quantitatively. According to strength theory, the limit state of surrounding rocks at a point can be considered as the limit stress or strain state, which depends on the strength or deformation resistance of surrounding rocks. Then, since the physical and mechanical properties of surrounding rocks deteriorate during the redistribution of stress due to excavation, the objective of quantitative evaluation of the stability of surrounding rocks can be achieved by characterizing the evolution of their deterioration.

3 Method of characterizing the deterioration of surrounding rocks

The stability state evolution of the tunnel surrounding rocks can be described as follows: stable to the limit state, and reach the failure. In the whole state of the evolution process, the physical and mechanical state of surrounding rocks is constantly changed, while the quantitative evaluation of the stability reserve of the tunnel surrounding rocks only needs to measure the “distance” between the physical and mechanical state of the surrounding rocks at the stable and the limit state. “Large distance” indicates that the surrounding rocks are more stable. According to the strength theory, the limit state of a point of surrounding rocks depends on its strength or deformation resistance, while the failure state indicates that the physical and mechanical state at that point exceeds the limit state. Therefore, the deterioration of the physical and mechanical properties of the surrounding rock can be used to bring it closer to the actual state of stress at that point. The quantitative parameters which reflect the deterioration can be used to measure the stability reserve of the tunnel surrounding rocks at that point. This method considering the deterioration of the physical and mechanical properties of surrounding rocks is called the strength-deformation parameter deterioration method.

3.1 Principle of strength-deformation parameter deterioration method

The stability reserve of a tunnel can be estimated *via* the strength-deformation parameter deterioration method, and simulating the deterioration of the physical and mechanical properties of surrounding rocks reach the limit state. The failure mechanism of the clay tunnel failure mechanism can be divided into tensile and shear failure. Tensile failure also can be regarded as a generalized shear failure. Therefore, at a point of surrounding rocks, the stress state can be determined by its shear stress, and strength parameters can characterize the shear strength. The strain state can be determined by the deformation of that point, and the strength parameters and deformation parameters can characterize the deformation resistance at that point. A function (Eq. 2) that takes the shear stress and strain state into account can represent the state of the point.

$$F_s = f(\tau, \varepsilon) \quad (2)$$

Where τ represents the shear stress state at this point of surrounding rocks; ε represents the generalized strain state at this point of surrounding rocks.

If the shear stress state or strain state of any point in surrounding rocks reaches the ultimate stress state or ultimate strain state, the state function at that point will reach the limit state. This paper established a method taking the coupled deterioration of strength and deformation resistance into account. To distinguish from the previous method, which only considers the strength deterioration of surrounding rocks, this paper assumed the limit state for the state function, as shown below.

$$F_{SL} = f(\sigma_L, \varepsilon_L) \quad (3)$$

The strength and deformation resistance deterioration process is described as a form of strength and deformation resistance reduction, such as the strength reduction method. Based on the above analysis and the core idea of the strength-deformation parameter deterioration method, the basic idea of this method was expressed as follows when exploring the stability of clay tunnels by changing the limit state of surrounding rocks at a certain point (F_{SL}) and bringing it to the actual state (F_{S0}).

$$F_{S0} = \frac{F_{SL}}{D} \quad (4)$$

Where D is the deterioration coefficient, which can measure the quantitative parameter of the deterioration of physical and mechanical properties at a point in surrounding rocks, and the value is constantly greater than zero.

Then, combining Eqs. 2, 3, the strength-deformation parameter deterioration method was expressed as that,

$$F_{S0} = \frac{F_{SL}}{D} = f\left(\frac{\tau_L}{D_s}, \frac{\varepsilon_L}{D_d}\right) \quad (5)$$

Where F_{S0} denotes the actual state function at a certain point of the tunnel surrounding rocks, and, D_s , D_d are the strength deterioration coefficient and the deformation resistance deterioration coefficient respectively, and their values are not less than zero.

The strength-deformation parameter deterioration method is applied by first reducing the shear strength and the deformation resistance simultaneously, stopping the iterative calculation once the tunnel is in the limit state. The shear strength corresponds to a strength deterioration coefficient and deformation resistance deterioration coefficient (which D_s may be different from the value of D_d). The stability reserve factor of tunnel surrounding rocks can be defined as the ratio of the maximum shear strength and the maximum deformation resistance of the tunnel surrounding rocks to the actual shear stress or deformation by the external load, without taking into account the influence of water and dynamic factors.

$$S_f = D = \frac{F_{SL}}{F_{S0}} \quad (6)$$

According to Eqs. 4, 5, the stability reserve factor of the tunnel surrounding rocks S_f is equal to the deterioration coefficient D . When considering the non-linear characteristics of the overall physical and mechanical property deterioration, the values of the strength deterioration coefficient D_s and the deformation resistance deterioration coefficient D_d may be different. According to the definition of the limit state, the stability reserve factor at a point of the tunnel surrounding rocks could be obtained according to the minimum principle.

$$S_f = \min(D_s, D_d) \quad (7)$$

The parameters affecting the shear strength of the clay are cohesion c and the internal friction angle φ according to Coulomb's law. The parameters of the deformation resistance of clay are as follows: the cohesion c and the internal friction angle φ , Young's modulus E , and Poisson's ratio ν . Eq 5 can be expressed as

$$F_{S0} = \frac{F_{SL}}{D} = f \left[\frac{(c + \sigma \tan \varphi)}{D_s}, \frac{\varepsilon(c, \varphi, E, \nu)}{D_d} \right] \quad (8)$$

Eq 8 can be expressed as

$$F_{S0} = f(\tau_0, u_0) = \frac{f(\tau_L, \varepsilon_L)}{D} = f \left(\frac{c}{D_c}, \frac{\varphi}{D_\varphi}, \frac{E}{D_E}, \frac{\nu}{D_\nu} \right) \quad (9)$$

D_c , D_φ , D_E and D_ν are the deterioration coefficients of cohesion, the internal friction angle, Young's modulus, and Poisson's ratio, respectively.

Then, according to Eqs. 6, 8, the stability reserve factor of surrounding rocks can be further calculated.

$$S_f = \min(D_c, D_\varphi, D_E, D_\nu) \quad (10)$$

3.2 Calculation of the deterioration coefficients

Coulomb's law can also be expressed by the shear strength of clay as

$$\tau_L = c_0 + \sigma \tan \varphi_0 \quad (11)$$

The strength deterioration coefficient of clay can be obtained by referring to the principle of the strength reduction method. For example, c_0 and $\tan \varphi_0$ are reduced by D_s , respectively.

$$\tau = \frac{c_0}{D_s} + \sigma \frac{\tan \varphi_0}{D_s} \quad (12)$$

Where c_0 and φ_0 are the actual cohesion and the actual internal friction angle of surrounding rocks at this moment, respectively. Previous researchers (Duncan and Chang, 1970; Lade and Duncan, 1975) proposed to fit the triaxial stress-strain relationship of clay with a hyperbolic curve, in which Young's modulus can be expressed as the tangential modulus. Then, Young's modulus of the clay can be calculated by the following equation.

$$E_i = (1 - R_f s)^2 E_0 \quad (13)$$

Where E_0 is the initial Young's modulus of clay, E_i is Young's modulus (also tangential modulus) of the clay in the i th state via the parameter reduction; the deviatoric stress ratio of the clay is expressed as $s = \frac{(\sigma_1 - \sigma_3)}{(\sigma_1 - \sigma_3)_f}$, the clay failure ratio is expressed as $R_f = \frac{(\sigma_1 - \sigma_3)_f}{(\sigma_1 - \sigma_3)_{ult}}$. $(\sigma_1 - \sigma_3)$ is the deviatoric stress; $(\sigma_1 - \sigma_3)_f$ is the yield strength. $(\sigma_1 - \sigma_3)_{ult}$ refers to the ultimate value of deviatoric stress corresponding to the horizontal asymptote of the hyperbola, and can be determined by laboratory tests.

From Eq. 13, the deterioration coefficient of Young's modulus can be calculated by the following equation.

$$D_E = \frac{E_0}{E_i} = \frac{1}{(1 - R_f s)^2} \quad (14)$$

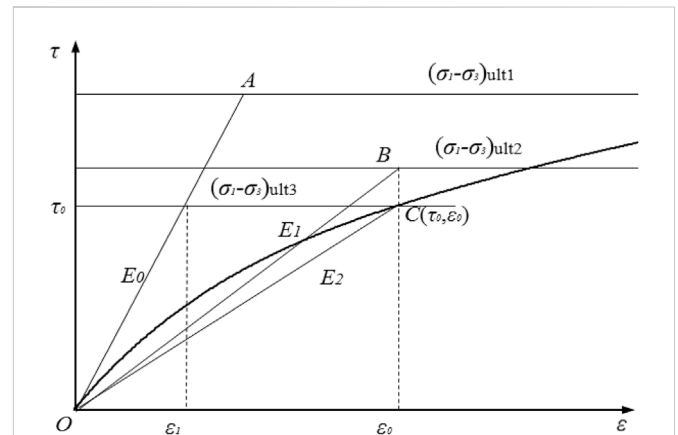


FIGURE 1
Non-linear stress-strain relationship in hardening soil.

According to Eq. 14, we will obtain the following expressions.

$$\sigma_1 - \sigma_3 = [1 - (D_E)^{-0.5}] (\sigma_1 - \sigma_3)_{ult} \quad (15)$$

If let $(\sigma_1 - \sigma_3)_{ult} = (\sigma_1 - \sigma_3)_f$

$$\sigma_1 - \sigma_3 = [1 - (D_E)^{-0.5}] (\sigma_1 - \sigma_3)_f \quad (16)$$

According to the Mohr-Coulomb theory, the yield strength can be expressed as the following equation.

$$(\sigma_1 - \sigma_3)_f = \frac{2c \cos \varphi + 2\sigma_3 \varphi}{1 - \sin \varphi} \quad (17)$$

$$\sigma_1 - \sigma_3 = [1 - (D_E)^{-0.5}] \left(\frac{2c \cos \varphi + 2\sigma_3 \varphi}{1 - \sin \varphi} \right) \quad (18)$$

Therefore, when c_0 and φ_0 are reduced by the strength deterioration coefficient D_s , the new cohesion and internal friction angle can be substituted into Eq. 18. It also indicates the effect of the deterioration coefficient of Young's modulus D_E on the stress state. It could also characterize the non-linear deterioration of the physical and mechanical properties of the clay tunnel surrounding rocks.

It was found that Poisson's ratio change on stress, strain, and displacement could be far less than the impact of other parameters, so Poisson's ratio deterioration was not considered here.

3.3 The physical meaning of the strength-deformation parameter deterioration method

The specific physical meaning of the strength-deformation parameter deterioration method was given in Figure 1. The coordinate of a point on the constitutive curve is (τ_0, ε_0) , which means the actual stress and strain state of surrounding rocks. The horizontal line in Figure 1 is the asymptote of the hyperbola, which is mainly controlled by c and φ , reflecting the strength of the clay, $(\sigma_1 - \sigma_3)_{ult}$; Reducing the value of cohesion c and internal friction angle φ , the horizontal asymptote keeps moving downward. However, this process is consistent with the strength reduction method. If only change the strength parameters of surrounding rocks are changed and the initial Young's modulus E_0 is kept constant (the line OA as shown

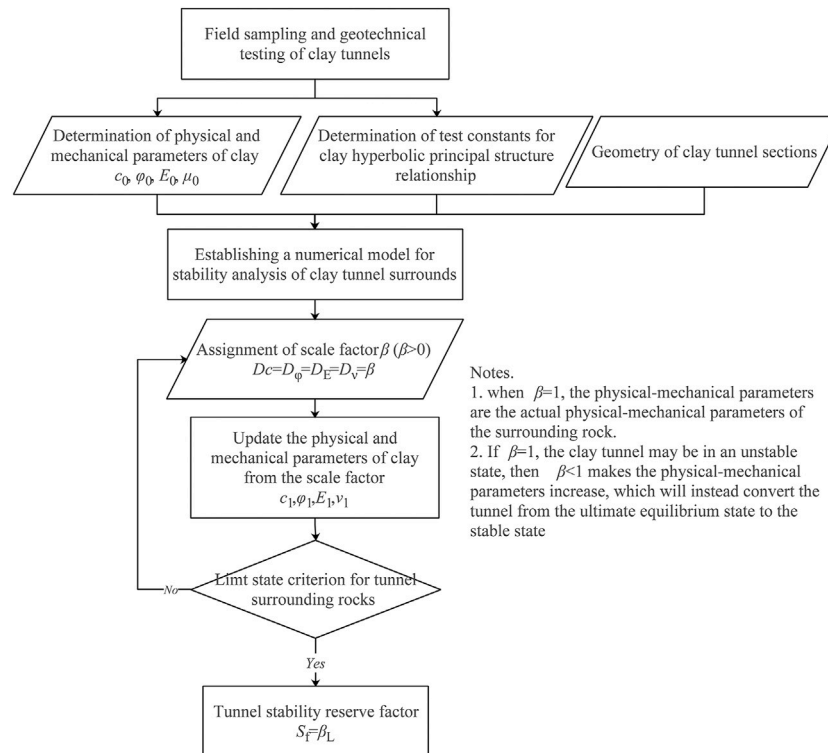


FIGURE 2
Calculation step of strength-deformation parameter deterioration method.

in Figure 1), the strength changes from $(\sigma_1 - \sigma_3)_{ult1}$ to $(\sigma_1 - \sigma_3)_{ult3}$ and close to the actual stress state τ_0 , the strain state at this time is not close to or consistent with the initial strain state. However, at the same time, Young's modulus E_0 degrades to E_2 in the process of strength deterioration, as shown in line OC, then the stress state at the yield point at this moment is closer to the stress state and strain states are closer to the actual stability states (τ_0, ε_0) .

In summary, the actual state changes of surrounding rocks deterioration during tunnel excavation and the stability evaluation of clay tunnels with non-linear behavior can be better simulated by the strength-deformation parameter deterioration method (simultaneous reducing of the cohesive force c , the internal friction angle φ , and Young's modulus E). Both the strength and deformation parameters can be reduced by the same scale factor when simulating the deterioration process of the physical and mechanical properties of surrounding rocks, and the different contributions of these parameters to the limit state can also be reflected. At the same time, when the strength and deformation resistance of surrounding rocks is weakened, the displacement of surrounding rocks at a point will increase, making the surrounding rocks more prone to instability. The cohesion, internal friction angle, Young's modulus, Poisson's ratio of the deterioration coefficients and the scale factor β satisfy the following relationship equation.

$$D_c = D_\varphi = D_E = D_\mu = \beta \quad (19)$$

Generally, if the strength and deformation parameters are all known, the stress, strain, and displacement of a point of surrounding rocks can be calculated according to the relevant

theory of geotechnics. The strength or deformation parameters are variables in these formulas and have different relationships with the dependent variables (stress, strain, displacement), which also reflects the different influences of these parameters. Therefore, in the numerical analysis of clay tunnels using the strength-deformation parameter deterioration method, the process of non-linear deterioration of the physical and mechanical properties of surrounding rocks can be better simulated, although the strength and deformation parameters are reduced by the same scale factor. If the clay's physical-mechanical properties make surrounding rocks reach the limit state at a point during the process, the tunnel stability reserve factor is equal to the scale factor.

$$S_f = \beta_L \quad (20)$$

β_L refers to the scale factor corresponding to the limit state at a point of the surrounding rock.

To sum up, the key point of the strength-deformation parameter deterioration method (referred to as "the proposed method") is that the strength and deformation parameters are continuously reduced with the scale factor until the limit state. The specific calculation step is shown in Figure 2.

3.4 Limit state conditions of tunnel numerical model

Many researchers have proposed a variety of limit state criteria for tunnel numerical model, among which the more widely used are

TABLE 1 Allowable values of relative convergence around tunnels and caverns (from GB50086-2015 in China).

Classification of surrounding rocks	Allowable values of relative convergence, $\omega(\%)$		
	$depth < 50$ m	$50 \leq depth \leq 300$ m	$300 < depth \leq 500$
III	0.10–0.30	0.20–0.50	0.40–1.20
IV	0.15–0.50	0.40–1.20	0.80–2.00
V	0.20–0.80	0.60–1.60	1.00–3.00

1) the connectivity of the plastic zone, 2) the abrupt and accelerated increase in strain or displacement at the feature points of surrounding rocks, and 3) the non-convergence of numerical calculation. This paper used a hyperbolic model to fit the stress-strain relationship of clay, there was no plastic strain and plastic zone. Then the above criterion 1) could not apply to this proposed method, but it could still be used for the strength reduction method.

The field monitoring data indicates that surrounding rocks may have great deformation before the abrupt stress, strain, or displacement change. Furthermore, adopting the hyperbolic principal model, which is closer to the actual mechanical behavior of the clay, also makes the numerical analysis of the tunnel deformation field closer to reality. Finally, the displacement (or strain) at a point of surrounding rocks is itself a comprehensive response to the physical and mechanical properties of surrounding rocks under the external load. Therefore, this paper adopted the allowable relative convergence value between two measurement points as a further criterion for identifying the tunnel stability state, which can be described as follows: when the displacement (or strain) changes abruptly and the calculation does not converge, if the relative convergence value between two feature points in surrounding rocks does not exceed the limit value, the tunnel surrounding rocks is identified to be in the limit state.

For a clay tunnel, if the defined state function is a one-point displacement function of the surrounding rock, then its limit state corresponds to the displacement limit state. Table 1 shows the allowable values of relative convergence ω of tunnels which can be calculated by linear interpolation of the tunnel burial depth. The allowable limit displacement u_L at the feature point of the tunnel can be calculated using the following equation.

$$u_L = \frac{\omega d}{2} \quad (21)$$

Where d is the diameter of the tunnel. The parameter $depth$ is the burial depth of the tunnel in Table 1.

4 Limit equilibrium method for clay tunnel stability evaluation

4.1 The wedge-shaped failure mechanism of surrounding rocks

This paper derived the analytical formula of the stability reserve factor of the tunnel surrounding rocks via the limit equilibrium analysis theory and took the more ideal clay tunnel surrounding rocks loading mechanics model into

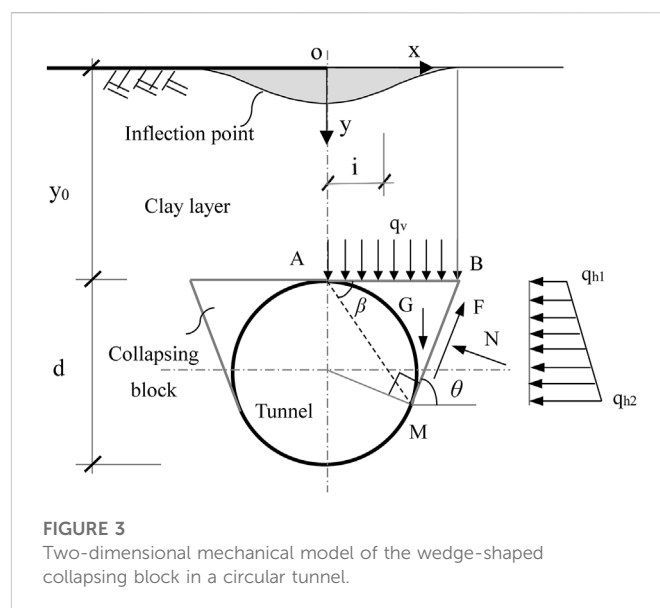


FIGURE 3 Two-dimensional mechanical model of the wedge-shaped collapsing block in a circular tunnel.

account, analogous to the slope safety factor idea. The limit equilibrium method takes the failure mechanism of the wedge-shaped block as an example according to Terzaghi's theoretical soil mechanics.

4.2 Mechanics of wedge-shaped collapsing block in clay surrounding rocks

It assumed that the collapsing block is wedge-shaped in the circular clay tunnel, and the stability reserve factor can be calculated by the limit equilibrium method. The mechanics of the wedge-shaped collapsing block (the block is rigid) is shown in Figure 3, and clay conforms to rigid plastic constitutive relation.

y_0 is the tunnel burial depth and d is the tunnel diameter. According to symmetry, the right-hand part ABM of the wedge-shaped collapsing block is chosen as the calculation object. The angles between the wedge failure lines BM and the horizontal plane are θ , and point M is the intersection point between the failure surface and the tunnel boundary.

The stability reserve factor for the collapsing block can be defined as:

$$S_f = \frac{P_R}{P_1} \quad (22)$$

S_f is the stability reserve factor of the tunnel surrounding rocks; P_R and P_1 are the anti-slip force, and the slip force, respectively.

4.3 Limit equilibrium analysis based on the mechanical model of wedge-shaped failure

The static equilibrium equation of the wedge can be listed according to Figure 3. The main loads in this model are as follows: G is the self-weight of the right-hand collapsing block ABM , q_v is the vertical loosening pressure generated by the overlying soil and P_v is the combined vertical pressure on the right-hand collapsing block ABM , q_{h1} and q_{h2} are the upper and lower pressure of the horizontal pressure trapezoid acting on the collapsing block ABM , P_h is the combined horizontal pressure force acting on the collapsing block ABM , T is the shear resistance acting on the collapsing block ABM , N is the normal force acting on the side BM .

$$P_1 = (G + P_v) \sin \theta + P_h \cos \theta \quad (23)$$

$$P_R = F \quad (24)$$

$$F = (c + q_h \tan \varphi) L_{BM} \quad (25)$$

Where,

$$N = (G + P_v) \cos \theta + P_h \sin \theta$$

$$G = \gamma \cdot S_{ABM}, \quad \theta = \frac{\pi}{4} + \frac{\varphi}{2}, \quad q_h = \frac{1}{2} (q_{h1} + q_{h2})$$

Where S_{ABM} is the area of the collapsing block ABM . γ , c and ϕ are the bulk unit weight, cohesion, and internal friction angle of the clay, respectively. According to the geometry relationship, the side length L_{BM} can be calculated via the equation as follows.

$$\frac{L_{AB}}{\sin \theta} = \frac{L_{BM}}{\sin \beta} \quad (26)$$

Where α and β are the angles between side AB and side BM and the horizontal line, respectively, and satisfy $\beta = \frac{\pi - \alpha}{2}$.

The formula for calculating the vertical soil stress acting on the collapsing block ABM is expressed as follows.

$$q_v = \frac{L_{AB} (L_{AB} \gamma - c)}{2K_0 \tan \varphi} \left(1 - e^{-2K_0 \frac{y_0}{L_{AB}} \tan \varphi} \right) \quad (27)$$

According to the Gaussian curve of ground settlement (the shadow area in Figure 3),

$$L_{AB} = 2.5i, \quad i = k(y_0 + d/2)$$

Where i is the horizontal distance from the inflection point of the ground settlement curve to the axis; k is the scale constant, generally taken as $k = 0.5$.

The combined vertical pressure can be calculated by the following equation for the collapsing block ABM .

$$P_v = \frac{L_{AB}^2 (L_{AB} \gamma - c)}{2K_0 \tan \varphi} \left(1 - e^{-2K_0 \frac{y_0}{L_{AB}} \tan \varphi} \right) \quad (28)$$

Where L_{AB} and L_{BM} are the lengths of the sides AB and BM , respectively; K_0 is the lateral pressure coefficient.

The horizontal pressure acting on the sliding surface BM of the collapsing block ABM can be calculated according to the following equation.

$$P_h = q_h L_{BM} \sin \theta = \left(\frac{1}{2} \gamma L_{BM}^2 \sin^2 \theta + \sigma_v L_{BM} \sin \theta \right) K_a \quad (29)$$

where the parameter q_{h1} satisfies $q_{h1} = q_v K_a$, and the parameter q_{h2} satisfies the relation of $q_{h2} = (q_v + \gamma L_{BM} \sin \theta) K_a$. Where K_a is the active earth pressure coefficient, a dimensionless parameter.

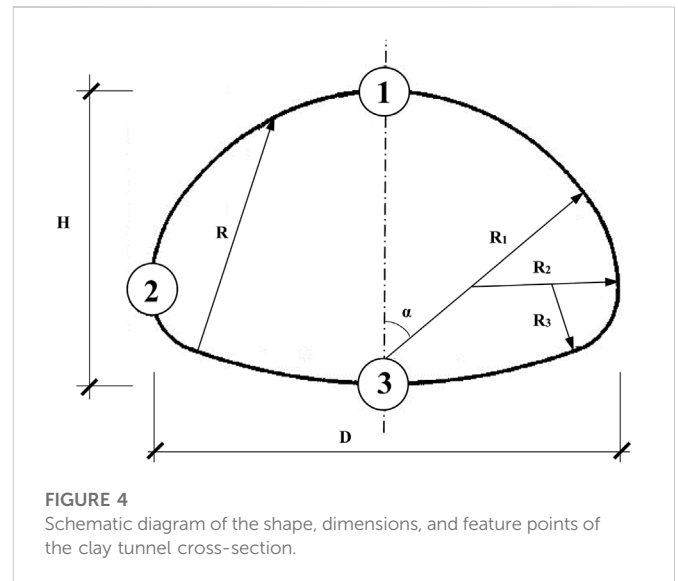


FIGURE 4
Schematic diagram of the shape, dimensions, and feature points of the clay tunnel cross-section.

$$K_a = \tan^2 \left(\frac{\pi}{4} - \frac{\varphi}{2} \right) \quad (30)$$

Finally, we can obtain the stability reserve factor for the clay tunnel surrounding rocks by substituting the anti-slip force and slip force on the sliding surface calculated from the wedge failure mechanics model into Eq. 22.

5 An example application of stability analysis of clay tunnels

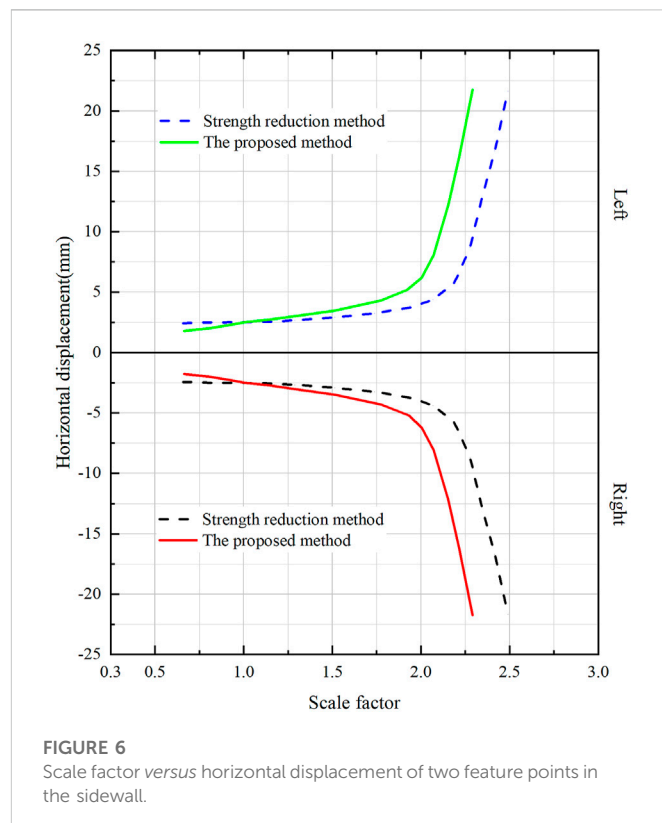
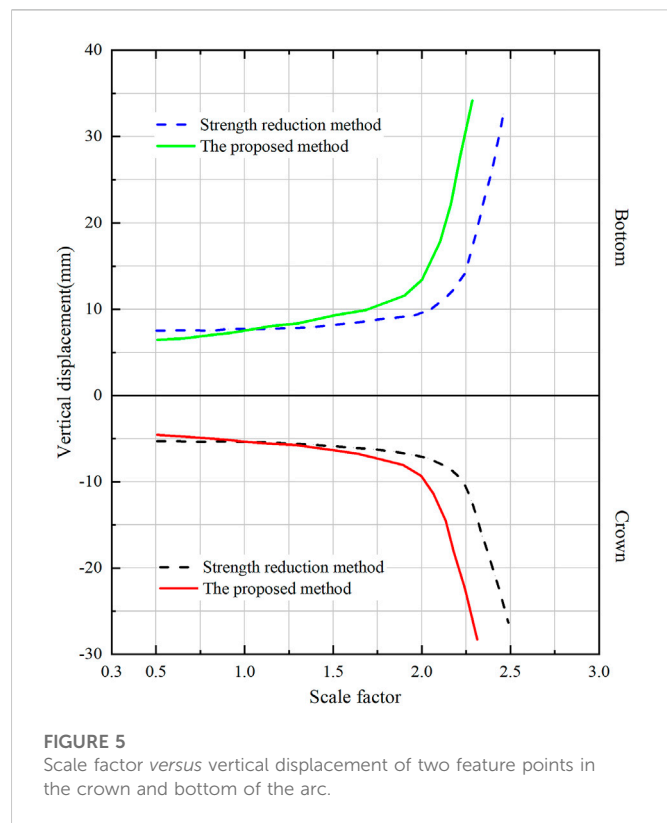
5.1 Engineering overview and cross-sectional geometry of a clay tunnel

The Yinchuan-Xi'an high-speed railway tunnel was used as a study case in this paper. The tunnel mainly traverses across the loess plateau area, and most of the strata powder clay layer. The tunnel section at DK267+457.1 was selected for the study. The burial depth of the tunnel at this location is 170.5 m, the span D is about 12.75 m, and the height H is about 11.50 m. The radii of these arcs are $R=10.50$ m, $R_1=8.78$ m, $R_2=7.10$ m, and $R_3=1.50$ m, and the angle α is 62.03° . The location of the feature points of the tunnel and the simplified model was shown in Figure 4 (the feature points at the tunnel perimeter are located at the arch crown, left and right sidewalls, and arch bottom respectively). The above-mentioned feature points were arranged with displacement monitoring devices, which mainly monitor their vertical displacements and horizontal displacements.

To facilitate the validation of the proposed method, it was assumed that the stratum is a single isotropic and homogeneous clay layer, and the physical and mechanical parameters of the clay can be given in Table 2. It was also assumed that the constitutive model of the clay is hyperbolic and satisfies the Mohr-Coulomb yield criterion of non-associated flow. To apply the strength reduction method, it assumed the clay is an ideal elastic-plastic material, while all other conditions are consistent. The length of the left and right boundaries of the numerical model of the clay tunnel is more than 3 times the span from the center axis of the tunnel. The left and right boundaries are

TABLE 2 Physical and mechanical parameters of clay.

Unit weight (kN/m ³)	Young's modulus (MPa)	Poisson's ratio	Cohesion (kPa)	Internal friction angle (deg)
19.6	20.6	0.30	43.5	27.0



respectively constrained horizontally, the bottom boundary is fixed, and the upper boundary is free. This tunnel stability evaluation could be considered a plane strain problem.

5.2 Analysis of the results of different methods

A numerical model for tunnel stability evaluation was developed based on a tunnel section of the Yinchuan-Xi'an high-speed railway. Firstly, the strength reduction method and the proposed method were used to analyze the stability of the same tunnel finite element model; secondly, based on the geometry and material parameters of this tunnel, it was assumed that a wedge-shaped failure mechanism also occurs in this tunnel, so that the limit equilibrium analysis method could be used to calculate the tunnel stability reserve factor; finally, the results of the three stability analyses were compared.

First of all, the key point of both the strength reduction method and the method is to simulate the deterioration of the physical and mechanical properties of surrounding rocks as realistically as possible, and the scale factor is a quantitative description of the deterioration mechanism of surrounding rocks so that the displacement of the feature point of surrounding rocks will change with the change of the scale factor. When the scale factor increases to a certain level, the actual rock condition is at the limit, and the scale factor can be

regarded as the stability reserve factor of the tunnel, which is given by the abrupt change of the displacement-scale factor curve at the point of the scale factor (Figures 5–6). Although the scale factors of the intensity reduction method and the proposed method are close in the range of values, the results of these two methods are not only different in value but also the physical meaning. The proposed method not only simulates the deterioration process of the strength parameters but also couples the deterioration process of the deformation parameters of surrounding rocks, which is closer to reality. Moreover, the strength reduction method only considers strength deterioration in the analysis process, and can not represent the realistic representation of the actual change in the deformation field of surrounding rocks during the deterioration process for clay. The constitutive relationship is consistent with either the elastic or elastoplastic model.

The three feature points of the tunnel correspond to three key locations, such as the arc crown, the sidewall, and the arc bottom. The displacements of each feature point are different, and the direction of displacement of the arc crown is vertical (settlement), the direction of displacements of two feature points in the left and right sidewall are horizontal, and these values are equal due to the symmetry. The direction of displacement of the arch bottom is vertical displacement (uplift). The displacement values of the feature points based on the strength reduction method are

TABLE 3 Displacement of each feature point with different scale factors (Unit: mm).

Feature points	Strength reduction method			The proposed method		
	$\beta=0.6$	$\beta=1.5$	$\beta=2.0$	$\beta=0.6$	$\beta=1.5$	$\beta=2.0$
1st	6.57	9.02	13.03	7.53	7.69	9.95
2nd	2.43	2.92	4.38	1.81	3.04	5.21
3rd	4.67	6.35	11.38	5.30	5.88	7.25

TABLE 4 Limit displacement at feature points in surrounding rocks obtained by different methods (Unit: mm)

Feature points	Strength reduction method	The proposed method	GB50086-2015 (in China)	Field monitoring
1st	9.95	10.44	6.42	12.35
2nd	5.65	6.01	7.05	8.71
3rd	8.96	11.38	6.65	16.22

TABLE 5 Stability reserve factors of the tunnel calculated by different methods.

Feature points	Strength reduction method	The proposed method	Limit equilibrium method (wedge-shaped failure form)
1	2.03	1.85	3.56
2	2.13	1.96	
3	2.17	2.01	

generally smaller than those based on this paper's method when the scale factor is less than one. However, the relationship between the two magnitudes is reversed (Figures 5, 6; Table 3) when the scale factor is greater than one. Meanwhile, the allowable limit displacement of feature points (also as the recommended limit displacement) can be calculated by Eq. 30, according to the classification of surrounding rocks, the tunnel depth, tunnel diameter, and the allowable values of relative convergence specified in Table 4. The limit displacements of feature points (the displacement value corresponding to the abrupt curve change in Figures 5, 6 calculated by the proposed method are closer compared with the recommended limit displacement values. The actual deformation field in the tunnel stability evaluation will be predicted *via* the proposed method. It also reflects the variation of the displacement with the physical and mechanical properties of the clay with a small scale factor corresponding to the abrupt change in displacement. The analysis results indicate that the actual stability reserve of the tunnel is smaller than the evaluation results of the strength-deformation method (Table 5). This paper took the strength-deformation property deterioration of surrounding rocks into account to reflect the actual stress or deformation fields and achieve the goal of better evaluation of the tunnel stability reserve.

The stability reserve factor calculated by the limit equilibrium method based on the wedge-shaped collapsing block ($\theta=\pi/4+\varphi/2$) is significantly larger than the other two results significantly. The limit equilibrium method can not reflect the actual state, because the tunnel cross section is circular instead of the one shown in Figure 4. More assumptions will be used in the calculation process of the limit equilibrium method. The

tunnel stability reserve factors obtained from the displacement-scale factor curves of the different feature points are relatively close, despite the different types and directions of displacement at the different feature points. This analysis shows that the overall tunnel stability can also be reflected by the stability reserve factor of a single point, and this method is recommended in preference.

6 Conclusion

The method suggested in this paper provides a practical and efficient way to evaluate the stability reserve of clay tunnels. The following conclusions can be drawn based on theoretical analysis and example calculation results.

- 1) The stress and deformation fields in the surrounding rock will be redistributed by tunnel excavation. The state function F_S is defined with the stress state and strain state of a point as variables, which can comprehensively characterize the stability state of the point at this moment.
- 2) The formula for calculating the tunnel stability reserve factor S_f from the actual state F_{S0} at a point of the surrounding rock and its limit state F_{SL} at a point of the surrounding rock is established with the definition of the state function. Then, taking the non-linear relationship between this limit state and the physical and mechanical properties of the surrounding rock into account, the non-linear deterioration of the physical and mechanical properties of the surrounding rock is simulated to calculate the tunnel stability reserve factor. The strength and deformation parameters that

characterize the clay properties are discounted by a scaling factor until the limit state is close to or equal to the actual state.

- 3) An analytical formula for the calculation of the tunnel stability reserve factor by the limit equilibrium method is established based on the physical model of wedge-shaped failure of the surrounding rock.
- 4) The analysis results of a clay tunnel project example show that the non-linear deterioration process of physical and mechanical properties of the surrounding rock will be better predicted by the proposed method in this paper. Compared with the strength reduction and the limit equilibrium methods, could the proposed method in this paper have more reliable quantitative evaluation results of tunnel stability.
- 5) The analysis results in this paper could provide broader and more valuable references in the study of clay tunnel stability problems and also support the engineering practice. However, tunnel stability is also closely related to construction factors for the actual tunnel construction. Therefore, construction factors such as construction methods and support forms should be introduced into tunnel stability evaluation as variables as well and guided the construction of tunnel projects.

Data availability statement

The original contributions presented in the study are included in the article/Supplementary Material, further inquiries can be directed to the corresponding author.

Author contributions

JH was in charge of conceptualization, funding acquisition, writing of the original draft, and editing. XL was in charge of data resources and analysis. ZM was in charge of the development of the mathematical model of the research and overall supervision of the whole research investigation. GL was in charge of the numerical simulations. KD was in charge of the post-processing data.

References

- Antão, A. N., Vicente da Silva, M., Monteiro, N., and Deusdado, N. (2021). Upper and lower bounds for three-dimensional undrained stability of shallow tunnels. *Transp. Geotech.* 27, 100491. doi:10.1016/j.trgeo.2020.100491
- Assadi, A., and Sloan, S. (1991b). "Stability of a shallow circular tunnel in cohesive-frictional soil," in International Conference on Finite Element Methods.
- Assadi, A., and Sloan, S. (1991a). Undrained stability of shallow square tunnel. *J. Geotechnical Eng.* 117:117 (8), 11528–21173. doi:10.1061/(asce)0733-9410(1991)117:8(1152)
- Broms, B. B., and Bennermark, H. J. (1967). Stability of clay at vertical opening. *Soil Mech. Found. Div. J.* 193 (1), 71–94. doi:10.1061/JSEFAQ.0000946
- Davis, E. H., Gunn, M. J., Mair, R. J., and Seneviratne, H. N. (1979). The stability of shallow tunnels and underground openings in cohesive material. *Géotechnique* 30, 397–416. doi:10.1680/geot.1980.30.4.397
- Duncan, J. M., and Chang, C. Y. (1970). Nonlinear analysis of stress and strain in soils. *J. Soil Mech. Found. Div. ASCE* 96 (5), 1629–1653. doi:10.1061/JSEFAQ.0001458
- Fan, W., Yu, M., Deng, L., Peng, X., and Chen, L. (2013). New strength formulae for rock surrounding a circular opening. *Can. Geotechnical J.* 50 (7), 735–743. doi:10.1139/cgj-2012-0001
- Fernández, F., Rojas, J. E. G., Vargas, E. A., Velloso, R. Q., and Dias, D. (2021). Three-dimensional face stability analysis of shallow tunnels using numerical limit analysis and material point method. *Tunn. Undergr. Space Technol.* 112, 103904. doi:10.1016/j.tust.2021.103904
- Fraldi, M., and Guarracino, F. (2010). Analytical solutions for collapse mechanisms in tunnels with arbitrary cross sections. *Int. J. Solids Struct.* 47 (2), 216–223. doi:10.1016/j.ijsolstr.2009.09.028
- Fraldi, M., and Guarracino, F. (2009). Limit analysis of collapse mechanisms in cavities and tunnels according to the Hoek–Brown failure criterion. *Int. J. Rock Mech. Min. Sci.* 46 (4), 665–673. doi:10.1016/j.ijrmms.2008.09.014
- Franza, A., Marshall, A. M., and Zhou, B. (2019). Greenfield tunnelling in sands: The effects of soil density and relative depth. *Géotechnique* 69 (4), 297–307. doi:10.1680/jgeot.17.P.091
- Han, K., Wang, L., Su, D., Hong, C., Chen, X., and Lin, X. (2021). An analytical model for face stability of tunnels traversing the fault fracture zone with high hydraulic pressure. *Comput. Geotechnics* 140, 104467. doi:10.1016/j.compgeo.2021.104467
- Hao, X., Yuan, L., Sun, Z., Zhao, Y., Ren, B., Zhao, D., et al. (2022). An integrated study of physical and numerical modelling on the stability of underground tunnel influenced by unloading rate. *Tunn. Undergr. Space Technol.* 129, 104602. doi:10.1016/j.tust.2022.104602
- Huang, M., Wang, H., Yu, J., and Tang, Z. (2019). Undrained stability analysis of a plane strain circular tunnel using streamline velocity fields. *Int. J. Geomechanics* 19 (5), 06019006. doi:10.1061/(ASCE)GM.1943-5622.0001395

Funding

This work was supported by the Science and technology innovation fund project of Hanjiang-to-Weihe river valley water diversion project construction Co. LTD. (Grant No. 2020302), Open Research Fund Program of State Key Laboratory of Eco-hydraulics in Northwest Arid Region (Grant No. 2018KFKT-16), Shaanxi Provincial Urban and Rural Construction Science and Technology Research and Development ProgramProject (2020-K41), National Natural Science Foundation of China (51806173).

Acknowledgments

The authors would like to thank Shaanxi Key Lab of Petroleum Accumulation Geology for providing high-performance computing devices.

Conflict of interest

XL was employed by PowerChina Northwest Engineering Corporation Limited; KD was employed by Hanjiang-to-Weihe River Valley Water Diversion Project Construction Co.LTD.

The authors declare that this study received funding from Hanjiang-to-Weihe river valley water diversion project construction Co. LTD. The funder had the following involvement in the study: the funder participated in the data processing.

The remaining authors declare that the research was conducted in the absence of any commercial or financial relationships that could be construed as a potential conflict of interest.

Publisher's note

All claims expressed in this article are solely those of the authors and do not necessarily represent those of their affiliated organizations, or those of the publisher, the editors and the reviewers. Any product that may be evaluated in this article, or claim that may be made by its manufacturer, is not guaranteed or endorsed by the publisher.

- Kumar, J., and Jain, H. (2021). Elasto-plastic ground settlement response and stability of single and twin circular unsupported and supported tunnels. *Transp. Geotech.* 30, 100620. doi:10.1016/j.trgeo.2021.100620
- Lade, P. V., and Duncan, J. M. (1975). Elasto-plastic stress-strain theory for cohesionless soil with curved yield surfaces. *J. Geotechnical Eng. Div.* 101 (10), 1019–1035. doi:10.1016/0020-7683(77)90073-7
- Leca, E., and Dormieux, L. (1991). Upper and lower bound solutions for the face stability of shallow circular tunnels in frictional material. *Géotechnique* 40 (4), 581–606. doi:10.1680/geot.1990.40.4.581
- Lee, C. J., Wu, B. R., Chen, H. T., and Chiang, K. H. (2006). Tunnel stability and arching effects during tunneling in soft clayey soil. *Tunn. Undergr. Space Technol.* 21 (2), 119–132. doi:10.1016/j.tust.2005.06.003
- Lee, I. M., and Park, J. K. (2000). Stability analysis of tunnel keyblock: A case study. *Tunn. Undergr. Space Technol.* 15 (4), 453–462. doi:10.1016/S0886-7798(01)00014-1
- Li, L. P., Shang, C. S., Chu, K. W., Zhou, Z. Q., Song, S. G., Liu, Z. H., et al. (2021). Large-scale geo-mechanical model tests for stability assessment of super-large cross-section tunnel. *Tunn. Undergr. Space Technol.* 109, 103756. doi:10.1016/j.tust.2020.103756
- Li, T. Z., Gong, W. P., and Tang, H. M. (2021). Three-dimensional stochastic geological modeling for probabilistic stability analysis of a circular tunnel face. *Tunn. Undergr. Space Technol.* 118, 104190. doi:10.1016/j.tust.2021.104190
- Li, Z., Lai, J., Ren, Z., Shi, Y., and Kong, X. (2023). Failure mechanical behaviors and prevention methods of shaft lining in China. *Eng. Fail. Anal.* 143, 106904. doi:10.1016/j.engfailanal.2022.106904
- Liu, N. F., Li, N., Li, G. F., Song, Z. P., and Wang, S. J. (2022a). Method for evaluating the equivalent thermal conductivity of a freezing rock mass containing systematic fractures. *Rock Mech. Rock Eng.* 55 (12), 7333–7355. doi:10.1007/s00603-022-03038-9
- Liu, N. F., Li, N., Wang, S. J., Li, G. F., and Song, Z. P. (2022b). A fully coupled thermo-hydro-mechanical model for fractured rock masses in cold regions. *Cold Regions Sci. Technol.* 205, 103707. doi:10.1016/j.coldregions.2022.103707
- Liu, N. F., Li, N., Xu, C. B., Li, G. F., Song, Z. P., and Yang, M. (2020). Mechanism of secondary lining cracking and its simulation for the dugongling tunnel. *Rock Mech. Rock Eng.* 53 (9), 4539–4558. doi:10.1007/s00603-020-02183-3
- Lu, H., Gutierrez, M., and Kim, E. (2022). Empirical approach for reliability evaluation of tunnel excavation stability using the Q rock mass classification system. *Undergr. Space* 7 (5), 862–881. doi:10.1016/j.undsp.2022.01.001
- Lyamin, A. V., Jack, D. L., and Sloan, S. W. (2001). “Collapse analysis of square tunnels in cohesive-frictional soils,” in *Computational mechanics-new Frontiers for the new millennium*. Editors S. Valliappan and N. Khalili (Elsevier), 405–414. doi:10.1016/B978-0-08-043981-5.50063-8
- Mair, R. J. (1979). *Centrifuge modelling of tunnel construction in soft clay*. PhD Thesis. Cambridge University.
- Mair, R. J., Taylor, R. N., and Bracegirdle, A. (1993). Subsurface settlement profiles above tunnels in clays. *Géotechnique* 43 (2), 315–320. doi:10.1680/geot.1993.43.2.315
- Man, J., Zhou, M., Zhang, D., Huang, H., and Chen, J. (2022). Face stability analysis of circular tunnels in layered rock masses using the upper bound theorem. *J. Rock Mech. Geotechnical Eng.* 14, 1836–1848. doi:10.1016/j.jrmge.2021.12.023
- Marshall, A. M., Farrell, R., Klar, A., and Mair, R. (2012). Tunnels in sands: The effect of size, depth and volume loss on greenfield displacements. *Géotechnique* 62 (5), 385–399. doi:10.1680/geot.10.P.047
- Nguyen, H. C., and Nguyen-Son, L. (2022). A stable CS-FEM for the static and seismic stability of a single square tunnel in the soil where the shear strength increases linearly with depth. *J. Rock Mech. Geotechnical Eng.* 14 (4), 1253–1265. doi:10.1016/j.jrmge.2022.01.006
- Osman, A. S., Mair, R. J., and Bolton, M. D. (2006). On the kinematics of 2D tunnel collapse in undrained clay. *Géotechnique* 56 (9), 585–595. doi:10.1680/geot.2006.56.9.585
- Pandit, B., and Sivakumar, B. G. (2021). Probabilistic stability assessment of tunnel-support system considering spatial variability in weak rock mass. *Comput. Geotechnics* 137, 104242. doi:10.1016/j.compgeo.2021.104242
- Pelech, T., Barnett, N., Dello-Iacovo, M., Oh, J., and Saydam, S. (2022). Analysis of the stability of micro-tunnels in lunar regolith with the Discrete Element Method. *Acta Astronaut.* 196, 1–12. doi:10.1016/j.actaastro.2022.03.037
- Qin, Y., Lai, J., Gao, G., Yang, T., Zan, W., Feng, Z., et al. (2022). Failure analysis and countermeasures of a tunnel constructed in loose granular stratum by shallow tunnelling method. *Eng. Fail. Anal.* 141, 106667. doi:10.1016/j.engfailanal.2022.106667
- Qin, Y. W., Chen, Y. H., Lai, J. X., Qiu, J. L., Yang, T., and Liu, T. (2023a). *Loess landslide-tunnel system: A systematic review of its failure characteristics, interaction mechanism and countermeasures*. Engineering Geology. inpress.
- Qin, Y. W., Lai, J. X., Cao, X. Y., Zan, W. B., and Feng, Z. H. (2023b). *Experimental study on the collapse evolution law of unlined tunnel in boulder-cobble mixed formation*. Tunnelling and Underground Space Technology. inpress.
- Qin, Y. W., Lai, J. X., Li, C., Fan, F. F., and Liu, T. (2023c). *Negative pressure testing standard for welded scar tightness of waterproofing sheet for tunnels: Experimental and Numerical Investigation*. Tunnelling and Underground Space Technology. inpress.
- Rojat, F., Labiouse, V., and Mestat, P. (2015). Improved analytical solutions for the response of underground excavations in rock masses satisfying the generalized Hoek–Brown failure criterion. *Int. J. Rock Mech. Min. Sci.* 79, 193–204. doi:10.1016/j.ijrmms.2015.08.002
- Rowe, R. K., and Kack, G. J. (1983). A theoretical examination of the settlements induced by tunnelling: Four case histories. *Can. Geotechnical J.* 20 (2), 299–314. doi:10.1139/t83-033
- Shiau, J., and Al-Asadi, F. (2020). Determination of critical tunnel heading pressures using stability factors. *Comput. Geotechnics* 119, 103345. doi:10.1016/j.compgeo.2019.103345
- Sloan, S., and Assadi, A. (1991). Undrained stability of a square tunnel in a soil whose strength increases linearly with depth. *Comput. Geotechnics* 12 (4), 321–346. doi:10.1016/0266-352X(91)90028-E
- Son, M., and Cording, E. J. (2008). Numerical model tests of building response to excavation-induced ground movements. *Can. Geotechnical J.* 45 (11), 1611–1621. doi:10.1139/t08-074
- Song, G., and Marshall, A. M. (2020). Centrifuge modelling of tunnelling induced ground displacements: Pressure and displacement control tunnels. *Tunn. Undergr. Space Technol.* 103, 103461. doi:10.1016/j.tust.2020.103461
- Song, J., Lee, C., and Seto, M. (2001). Stability analysis of rock blocks around a tunnel using a statistical joint modeling technique. *Tunn. Undergr. Space Technol.* 16 (4), 341–351. doi:10.1016/S0886-7798(01)00063-3
- Sukkarak, R., Jongpradist, P., and Pramthawee, P. (2019). A modified valley shape factor for the estimation of rockfill dam settlement. *Comput. Geotechnics* 108, 244–256. doi:10.1016/j.compgeo.2019.01.001
- Sun, M., Liang, H., Zhu, Y., Gao, X., Liu, H., and Zhu, Z. (2022). Deformation and failure mode analysis of the tunnel structure based on the tunnel-related landslides cases. *Front. Earth Sci.* 10. doi:10.3389/feart.2022.906884
- Tan, X., Chen, W., Wang, L., Tan, X., and Yang, J. (2020). Integrated approach for structural stability evaluation using real-time monitoring and statistical analysis: Underwater shield tunnel case study. *J. Perform. Constr. Facil.* 34 (2), 04019118. doi:10.1061/(ASCE)CF.1943-5509.0001391
- Tyagi, A., Liu, Y., Pan, Y.-T., and Lee, F.-H. (2020). Equivalent strength for tunnels in cement-admixed soil columns with spatial variability and positioning error. *J. geotechnical geoenvironmental Eng.* 146 (10), 04020101. doi:10.1061/(ASCE)GT.1943-5606.0002351
- Wang, W. L., Wang, T. T., Su, J. J., Lin, C. H., Seng, C. R., and Huang, T. H. (2001). Assessment of damage in mountain tunnels due to the Taiwan Chi-Chi Earthquake. *Tunn. Undergr. Space Technol.* 16 (3), 133–150. doi:10.1016/S0886-7798(01)00047-5
- Wilson, D. W., Abbo, A. J., Sloan, S. W., and Lyamin, A. V. (2011). Undrained stability of a circular tunnel where the shear strength increases linearly with depth. *Can. Geotechnical J.* 48 (9), 1328–1342. doi:10.1139/t11-041
- Xue, Y., Liu, J., Ranjith, P. G., Gao, F., Xie, H., and Wang, J. (2022). Changes in microstructure and mechanical properties of low-permeability coal induced by pulsating nitrogen fatigue fracturing tests. *Rock Mech. Rock Eng.* 55, 7469–7488. doi:10.1007/s00603-022-03031-2
- Xue, Y., Ranjith, P. G., Chen, Y., Cai, C., Gao, F., and Liu, X. (2023). Nonlinear mechanical characteristics and damage constitutive model of coal under CO₂ adsorption during geological sequestration. *Fuel* 331, 125690. doi:10.1016/j.fuel.2022.125690
- Yang, F., and Yang, J. S. (2009). “Rigid blocks failure mechanism for stability of shallow tunnel using upper bound solution,” in *Recent advancement in soil behavior, in situ test methods, pile foundations, and tunneling*, 249–255. doi:10.1061/41044(351)39
- Yang, X. L., and Huang, F. (2011). Collapse mechanism of shallow tunnel based on nonlinear Hoek–Brown failure criterion. *Tunn. Undergr. Space Technol.* 26 (6), 686–691. doi:10.1016/j.tust.2011.05.008
- Yang, X. L., and Huang, F. (2013). Three-dimensional failure mechanism of a rectangular cavity in a Hoek–Brown rock medium. *Int. J. Rock Mech. Min. Sci.* 61, 189–195. doi:10.1016/j.ijrmms.2013.02.014
- Yertutanol, K., Akgün, H., and Sopacı, E. (2020). Displacement monitoring, displacement verification and stability assessment of the critical sections of the Konak tunnel, İzmir, Turkey. *Tunn. Undergr. Space Technol.* 101, 103357. doi:10.1016/j.tust.2020.103357
- Zhang, X., Wang, M., Wang, Z., Li, J., Zhao, S., Tong, J., et al. (2020). Stability analysis model for a tunnel face reinforced with bolts and an umbrella arch in cohesive-frictional soils. *Comput. Geotechnics* 124, 103635. doi:10.1016/j.compgeo.2020.103635
- Zhang, Y., Fan, S., Yang, D., and Zhou, F. (2022a). Investigation about variation law of frost heave force of seasonal cold region tunnels: A case study. *Front. Earth Sci.* 9, 806843. doi:10.3389/feart.2021.806843
- Zhang, Y., Song, Z., and Weng, X. (2022b). A constitutive model for loess considering the characteristics of structurality and anisotropy. *Soil Mech. Found. Eng.* 59 (1), 32–43. doi:10.1007/s11204-022-09781-z
- Zhang, Z., Zhao, C., Peng, L., Zhang, X., and Lei, M. (2022). Research on the stability of shallow-buried large cross-section tunnel by construction method conversion. *Front. Earth Sci.* 10. doi:10.3389/feart.2022.831169
- Zhuo, H., Xie, D., Sun, J., and Shi, X. (2022). Mining hazards to the safety of segment lining for tunnel boring machine inclined tunnels. *Front. Earth Sci.* 9. doi:10.3389/feart.2021.814672



OPEN ACCESS

EDITED BY

Naifei Liu,
Xi'an University of Architecture and
Technology, China

REVIEWED BY

Yuliang Lin,
Central South University, China
Wu Zhiwen,
Guangxi University, China

*CORRESPONDENCE

Hongri Zhang,
✉ 253541461@qq.com

SPECIALTY SECTION

This article was submitted to
Environmental Informatics
and Remote Sensing,
a section of the journal
Frontiers in Earth Science

RECEIVED 08 November 2022

ACCEPTED 28 November 2022

PUBLISHED 05 January 2023

CITATION

Li Y, Zhang H, Huang L, Li H and Wu X
(2023), The formation mechanism of
landslides in typical fault zones and
protective countermeasures: A case
study of the Nanpeng River fault zone.
Front. Earth Sci. 10:1092662.
doi: 10.3389/feart.2022.1092662

COPYRIGHT

© 2023 Li, Zhang, Huang, Li and Wu.
This is an open-access article
distributed under the terms of the
[Creative Commons Attribution License
\(CC BY\)](https://creativecommons.org/licenses/by/4.0/). The use, distribution or
reproduction in other forums is
permitted, provided the original
author(s) and the copyright owner(s) are
credited and that the original
publication in this journal is cited, in
accordance with accepted academic
practice. No use, distribution or
reproduction is permitted which does
not comply with these terms.

The formation mechanism of landslides in typical fault zones and protective countermeasures: A case study of the Nanpeng River fault zone

Youjun Li¹, Hongri Zhang^{1,2*}, Liming Huang¹, Hongming Li¹ and
Xuexiao Wu¹

¹Guangxi Transportation Science and Technology Group Co., Ltd., Guangxi, China, ²School of Naval
Architecture, Ocean and Civil Engineering, Shanghai Jiaotong University, Shanghai, China

Landslides are frequent in the Nanpeng River fault zone in southwest Yunnan. Based on a Zhen Qing Expressway survey, the geological conditions and characteristics of landslides in this area were studied. The conclusions are as follows: 1) the geological background was the internal cause of local highly steep slopes and broken rock masses. The main landslide types in study area are fault-type and accumulation landslides. 2) The formation of fault-type landslides is related to endogenous causes, such as tectonic movements, but they are less easily triggered than accumulation landslides. Accumulation landslides are related to broken rock masses and are sensitive to external factors such as rainfall and artificial unloading. 3) The coordinated control of permanent support engineering, local deformation control, and overall support reinforcement should be considered as preventive measures.

KEYWORDS

landslide formation mechanism, disaster prevention, landslide, fault zone, accumulation landslide

Introduction

Fault zones are a common geological structure mainly formed by crustal extrusion or plate relative movement and results in the fragmentation of the rock structure and uneven stress in these areas. Then, frequent landslides (Sun, 2005; Lin and Wang, 2017; Huang et al., 2020; Deng et al., 2021) and structural damage (Liu et al., 2020) are often reported in fault zones. The origin of the geological structure has an important influence on the formation and development of landslides (Martel, 2004). The inter-laminar shear dislocation zones formed by fractures may become potential slide zones, which has been proved by field tests and mesoscopic analysis (Huang et al., 2008). Fractures of river valleys and bank slopes have had barrier and differentiation effects on the transfer of valley slope stress (Huang and Li 2008). The size of landslide distribution in a vertical fault strike was determined to be negatively correlated with the dip angle of the fault, and

landslides were more likely to occur when the slope direction is parallel to the fault strike (Chen et al., 2014). Unique original fault structures (like a natural sustaining arch) can strongly inhibit the movement of a landslide before structures are damaged to the volume-expansion point, thus avoiding the occurrence of sudden landslides (Chen et al., 2021). Meanwhile, in highly tectonically active regions, landslides and active faults have been closely related in spatial distribution (Qi et al., 2010; Qi et al., 2021). Some typical landslide movement rates have increased by more than 20% related to the fault activity (Huang et al., 2013; Jiang et al., 2015). Landslide movement rates (LMR) have indicated that more than 70% of global landslides are caused by earthquakes (Broeckx et al., 2020). Therefore, it is necessary to conduct a study on the cause and formation mechanism of landslides in fault zones and then propose appropriate treatment measures.

The faults in southwest Yunnan Province, China, occur at equal intervals and in parallel and cut across geological bodies and geomorphological units with high mountain slopes and deep canyons. Landslides are the main regional geological hazard with a high-frequency in these regions (Huang and Li et al., 2011; Yin et al., 2017). Landslide susceptibility maps prepared by different methods showed that landslides in this area are closely related to fractures, rainfall, and human activities (Lan et al., 2004; Sidle et al., 2011; Shao et al., 2020). As landslides occurred frequently during construction and have caused property damage and geological hazards in Yunnan Province, geological surveys, field experiments, numerical simulations and other methods have been used to study landslides (Sidle et al., 2014; Yang et al., 2015; Du & Chen, 2022) and more results have been obtained in areas with frequent human activities.

However, the Nanpeng River fault zone in southwest Yunnan is subject to few human activities and so inadequate geological and hydrological engineering data are available. The formation mechanisms and classification of landslides in the Nanpeng River fault zone have not been reported. The Zhenkang to Qingshuihe Expressway (hereinafter referred to as Zhen Qing Expressway) follows the Nanpeng River fault zone, which provides research data for landslides in this area. Based on the construction results of Zhen Qing Expressway, this paper examines the geological conditions in the Nanpeng River fault zone, summarizes the local landslide development, characteristics, causes, and history, explores the distribution and formation of landslides, and analyzes the typical landslide design principles and effects to provide reference information for the prevention of landslides.

Project overview

The starting point of Zhen Qing Expressway is located near Zhenkang County, Yunnan Province, and the route is generally oriented from north to south. The end point is at the Dawan

River in north Mengding Town (Figure 1). The overview is shown in Table 1.

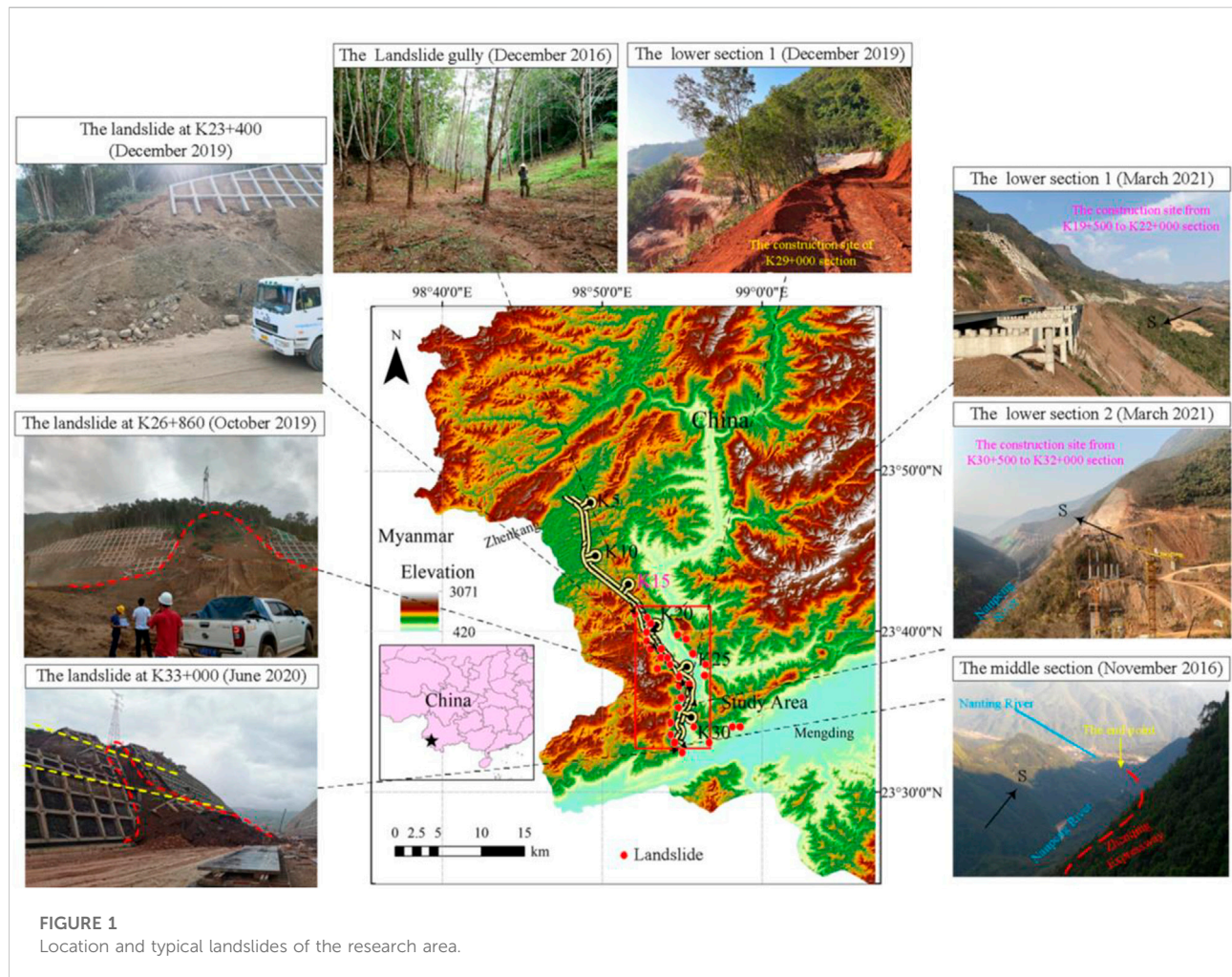
The K19 to K33 section of Zhen Qing Expressway is the main research area of this paper and it is spread along the west bank of the Nanpeng River fault zone. During the survey process, geological mapping and site surveys were conducted at a ratio of 1:2000. The researchers participated in the design of landslide treatment for the entire project, identified 50 landslides and hidden danger points, and tracked and verified possible landslides that may occur in the construction process. A total of 10 new landslides and hidden danger points, which were caused by heavy rainfall and artificial disturbances, were added during the construction process.

Analysis of factors influencing landslide development

Topographical features

This research area has a deep canyon due to long-term erosion. The mountain range is mainly north to east; the topography and landform as a whole presents a steep upper, less-steep lower, and deep stepped features. The elevation is 420 m–3,000 m and the relative height difference is 50 m–350 m; the slope topography is mostly concave with a wide upper and narrow lower arc; and the terrain is steep in the middle and flat at the bottom. The sections with different elevations in the research area have greatly different terrain as follows. 1) The upper section (elevation 900 m–3,000 m) has a gradient that varies from 60 to 80 with some parts nearly vertical. 2) The middle section (Elevation 700 m–900 m) exhibits different lithological characteristics, which were mostly formed by accumulation with a main component of from a collapse and the residue. Its gradient varies from 20–45 and has a platform width of 20 m–100 m. 3) The lower section (Elevation 500 m–700 m) with a gradient of approximately 30–60, covered by the Quaternary (Figures 2, 3), and the bottom is the Nanpeng River. The K19 to K33 section of Zhen Qing Expressway is mainly distributed along the lower section.

Along the route, the ridgelines are distributed along the both banks of the Nanpeng River, and the strong tectonic movement and erosion-solution effects lead to deep river valleys and the confrontation of peaks on both sides. Topographic and geomorphological factors, such as elevation, gradient, and undulation, exhibit the following characteristics. 1) The elevations of the bottom of the Nanpeng River, the collapsed slope platform on the west bank, and the west side are 200 m–400 m, 498 m–3,000 m, and 1,000 m–1,500 m, respectively. This huge height difference constitutes a natural air front. 2) The gradient change trend is steep-slow-steep and forms a typical stepped landform. The steeper slope controls the direction of gravity and tectonic stress on the slope and increases the possibility and danger of landslides. 3) The gradient of the upper section is greater than 45, which provides a material source to the middle section.



Stratigraphic lithology and geological formations

The research area is located at the boundary between the Myanmar and Philippine plates. The fold belts named Fugong-Zhenkang and Changning-Menglian intersect in this area. The principal stress direction is NNE-SEE (Xie et al., 2001), and the research area is subjected to compressive stress from the east and west sides. The geological strata of the Quaternary, the Upper Triassic, and the Lower Permian is exposed in the research area and excludes the Cretaceous and Jurassic. The area is dominated by a large area of sedimentary strata. Clastic and carbonate rocks are the main components. The loose clastic and carbonate rock groups with soft and weak phases are distributed in strips along the

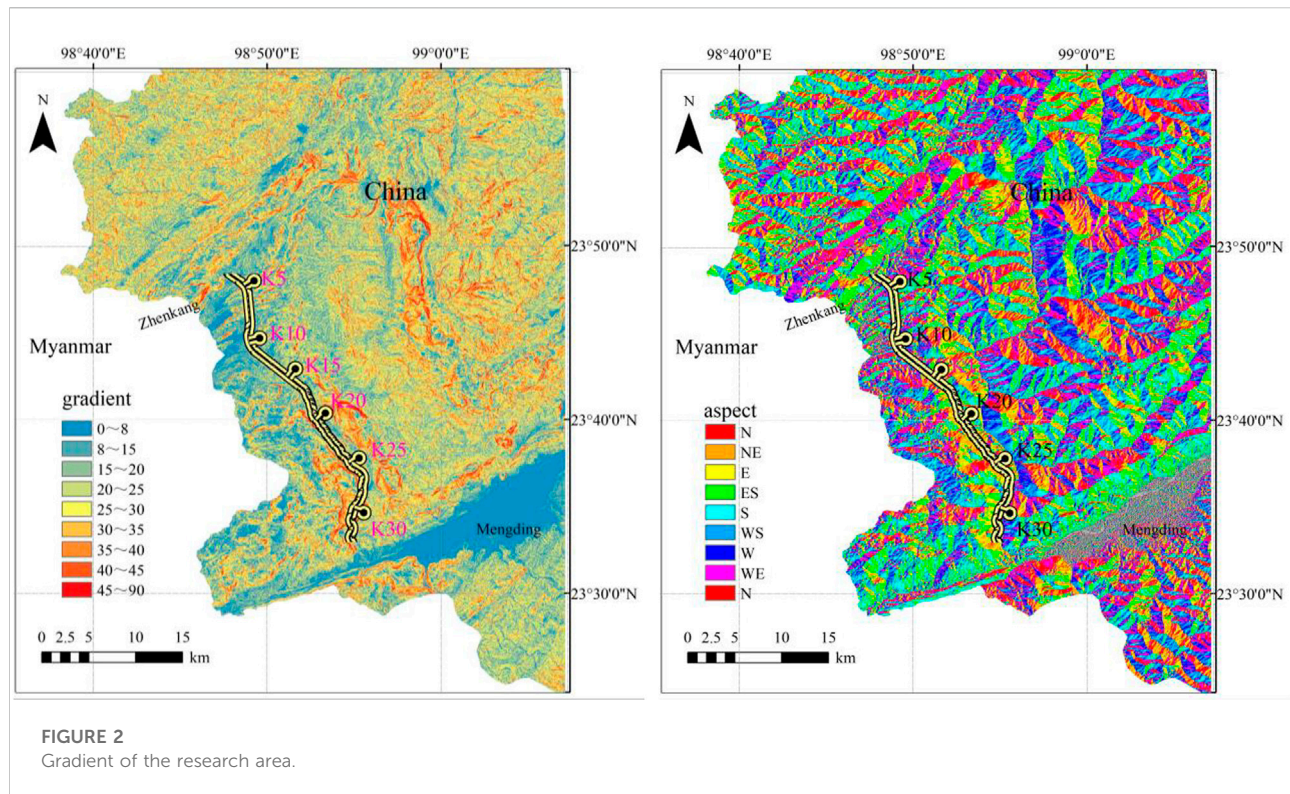
fault zone (Figure 3). The main attitude of the rock mass of the K19 to K30 section varies from $SW215^{\circ} < 30^{\circ}$ to $SW240^{\circ} < 60^{\circ}$. In the area near the Nanting River fault, a M7.6 earthquake occurred in 1988 (Zhu et al., 1994; Wang et al., 2015) and the attitude of the rock mass changed from $NE50^{\circ} < 20^{\circ}$ to $SW200^{\circ} < 30^{\circ}$. Carbonate faulting and clastic rock twisting are found in the area. Therefore, the rock mass structure in the research area is relatively broken, which indicates that the landslide has a rich source of material.

Meteorology and hydrology

The research area is in the low-latitude area of southwestern Yunnan, with an average annual rainfall of 1300 m–1,500 mm, and

TABLE 1 Overview of the Zhen Qing Expressway.

Total length (km)	Design speed (km/h)	Roadbed width (m)	Seismic parameters (GB18306-2015, China)
35.819	80	25.5	0.2g/0.45s



the rainy season is concentrated in May to October. The area lies in the subtropical monsoon climate zone. Continuous rainfall in the rainy season often exceeds 15 days. The rainfall in this area exhibits characteristics of high intensity, long time, and short interval. The types of groundwater in the research area are mainly loose rock pore water, bedrock fissure water and carbonate rock karst fissure water. All of them are recharged by rainfall and have the characteristics of seasonal variation. As shown in Figure 3, the watersheds on both sides are composed of carbonate rocks, so the pore water and bedrock fissure water are in the recharge area and runoff area of karst fissure water, and receive recharge from karst fissure water. This means karst fissure water recharges them directly.

Types of landslides and formation mechanisms of the Nanpeng River fault zone

Types of landslides in the Nanpeng River fault zone

The above analysis indicates that the research area has a typical stepped landform and large undulating terrain, which provides space for landslides. The hard carbonate rock composition controls the maximum boundary of slope deformation and failure so that the soft clastic rock in the area easily forms secondary structural planes after the action

of the structure and earthquake, which becomes the priority failure deformation portion. The softer clastic rock in the middle section is in the runoff and drainage area of carbonate fissure water. The rock mass structure of clastic rock in this area is broken, and provides abundant groundwater migration and recharge channels (Liu et al., 2022a) and favorable conditions for the development of the rainfall slip effect (Liu et al., 2022b). Earthquakes frequently occur in southwestern Yunnan. The minimum straight-line distance between the research area and the Nanpeng River fault is only 5 km, which indicates an obvious seismic distance effect. Earthquakes can damage the mechanical properties of the rock mass and provide internal power for the formation of landslides. Finally, human activities, such as road cutting, are likely to cause stress redistribution of the slope and break the original stable state. Therefore, the geological background of this area is the internal cause of landslide formation and rainfall and artificial activity are external causes. According to the above factors, the landslide type in the research area can be divided into fault-affected landslides and accumulation landslides.

Mechanism of landslide formation in the Nanpeng River fault zone

According to the results of the regional investigation and engineering exploration, the formation mechanism of landslides

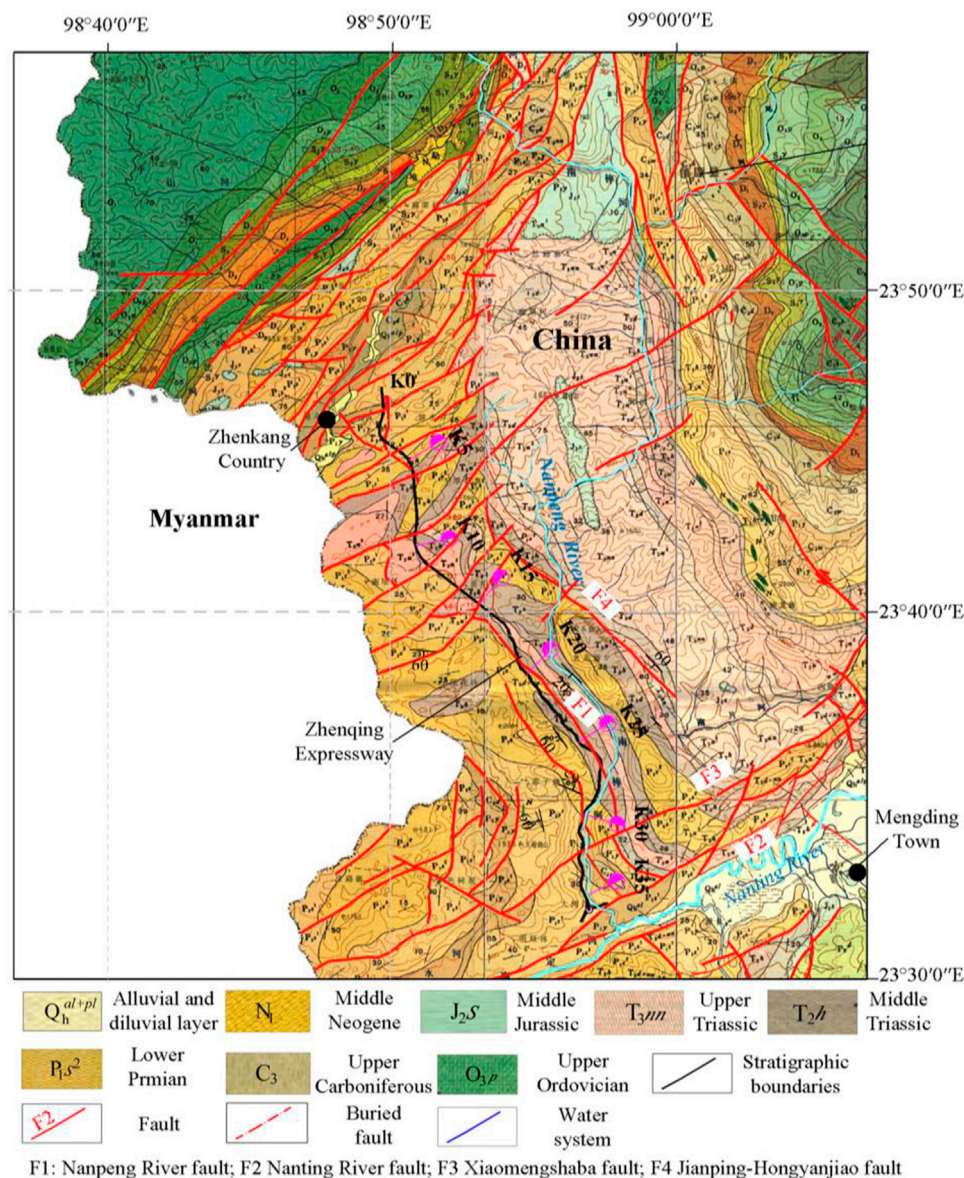
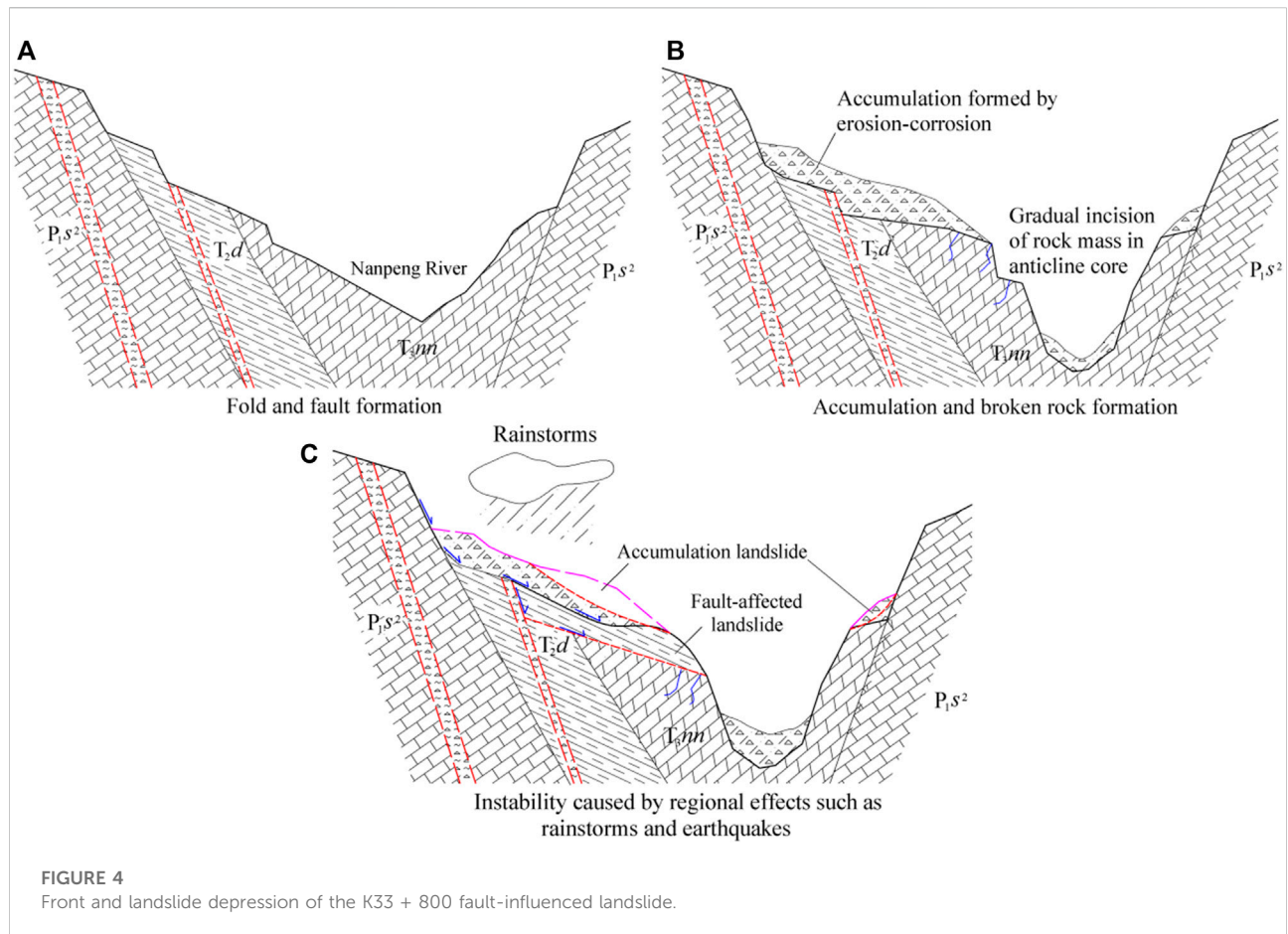


FIGURE 3
Main strata and faults in the research area.

in the Nanpeng River fault zone occurs as follows. 1) During the formation of folds and faults, the two groups of large faults in the NW and NE directions strongly squeeze the rock mass and act on the four-dimensional stress field pattern. The harder rock layers in the Daxiaodong anticline are uplifted to form an unloading effect and the softer rock layers are extruded into strips to form a wide platform. 2) During the process of mountain denudation, weathering, and river erosion, the rock mass in the core of the anticline is gradually cut down, the bottom support is gradually reduced, the front surface of the rock mass is increased, and the unloading effect is further intensified. In the process of weathering and denudation, a large amount of colluvial gravel

and gravel soil are formed in the carbonate rock formation, which are accumulated on the platform of the softer rock formation. 3) Events, such as strong earthquakes and rainstorms, cause loose blocks to become unstable and push to form landslides and further push the front edge of the collapsed slope to deform. 4) Under the action of erosion, part of the material of the steeper landslide body accumulates on the slope, and along with the lithological different zone in the long-term high-intensity rainfall season, a saturated zone is formed, which results in a lateral net water pressure and pushes the upper part of the landslide body again. Thus, the existing landslide gradually forms (Figure 4). The formation of fault-affected landslides undergoes the above



processes, whereas that of accumulation landslides mainly undergoes different processes.

Countermeasures for slope protection design in the Nanpeng River fault zone

Characteristics of fault-influenced landslides and countermeasure design

The formation of fault-influenced landslides in the research area is mainly affected by the geological background and earthquakes. Such landslides have the following characteristics in topography, distribution range, plane shape, and rock structure. 1) The topography has a typical steep-gentle-steep step-like topography. 2) The distribution area of the landslide is near the influence range of the Holocene active fault, which is called the Nanteng River fault, and the distance effect on landslide is obvious. 3) The plane of landslide is mostly tower shaped, and the sliding surface is in the weak structural plane of the rock mass. 4) The lithology of the stratum is mainly composed of

clastic and carbonate rocks, and the carbonate weathering layer of landslides is more than 50 m thick. As the main boundary of this type of landslide, carbonate rock controls the deformation range of the landslide and recharges the groundwater in the clastic rock. The harder carbonate rock boundary facilitates the amplification of seismic effects, and so landslides with huge volumes are mostly distributed nearby or above the Holocene active fault influence range.

Considering the K33+800 landslide as an example (Figure 5), the landslide is located on a slope approximately 4.5 km from the Nanteng River fault. The overall terrain slope is 25–35°. The steep-platform-gentle typical chair landform had the following shape: the width of the gentle slope platform was approximately 100 m, the main sliding direction of the landslide was approximately 94°, the trailing edge is a chair-shaped steep sill with a height difference of approximately 100 m, and landslide depressions develop under the steep sill. On both sides of the depression branch, the depression is a double-ditch homologous landform, the front edge is convex like a tongue, and the sliding body is approximately 1.8 km long and 1.2 km wide. The landslide volume is estimated at more than 18 million m³. The east side of the mountain limits the possibility of large

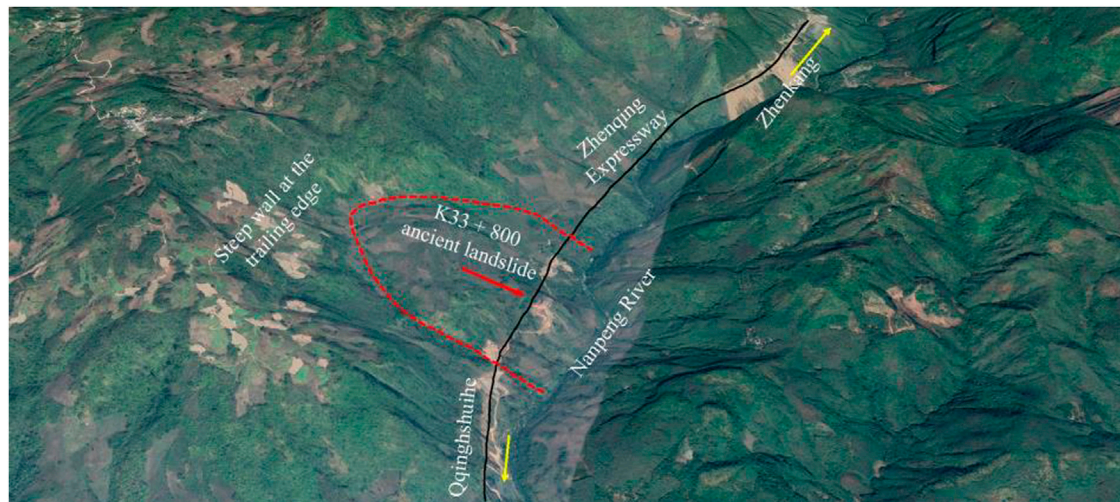


FIGURE 5
K33 + 800 fault-affected ancient landslide (from Google Earth).

deformation of the landslide. The long-term erosion and unloading of the Nanpeng River could not revive the landslide. Therefore, the occurrence of the landslide is mainly affected by the earthquake and the sensitivity to external factors is low. The Zhen Qing Expressway raises the longitudinal plane in this section to avoid cutting the toe of the slope and tries to pass as a bridge to minimize disturbance to the landslide. No signs of deformation have been observed to date (after the completion of this section of the bridge).

Characteristics of accumulation landslides and protection countermeasures

Accumulation landslides have the following characteristics and triggering factors in the distribution range. These landslides are mainly distributed in the middle section of the stepped landform, which is mainly covered by residual and slope deposits of poor sorting and high porosity. The underground water type is loose rock pore water and is recharged by rain. For common accumulation landslides, rainfall and engineering construction have a great influence on the stability of the landslides in the study area. The failure modes of accumulation landslides are mainly of the traction type, and the sliding surface is an arc or broken line type. The sliding surface is shallow and often located at the rock-soil interface, and the landslide volume is generally small.

The landslide from cutting accumulation on the right side of K26 + 860 is considered as an example. The slope was originally designed to be 40 m high (10 m-high a grade) and limited by the 220 kV electrical tower at the rear; the comprehensive slope rate was

designed as 0.75 and the whole slope was equipped with anchor cable lattice beams. The grade 3# and 4# had completed the excavation and anchor cable tensioning before the landslide occurred. Cumulative rainfall in the landslide area reached 203 mm in 24 h on 7 October 2019, and the landslide occurred 2 days later. The slope dropped rapidly in a projectile shape and accumulated at a comprehensive slope degree of 9. The structure of the non-sliding soil on the trailing edge of the landslide was extremely loose and the section was rough. The sliding surface of 15 m deep is located inside the accumulation body with an arc shape. The shear entrance is approximately 10 m behind the excavation line, and the shear exit is at the foot of grade 2# (Figures 6, 7). An overly loose soil structure may be the cause of landslides still occurring after protective structures are completed, and researchers have built a corresponding slope FEM under saturated conditions by the GEO5 to verify. A comprehensive method combining test evaluation, empirical assessment, and back calculation evaluation is used to evaluate the physical and mechanical parameters of the rock and soil. For the underlying bedrock, its parameters have little effect on the results of slope simulation analysis, which can be directly evaluated based on field investigation data. For residual soil and the sliding zone, the key parameters, such as modulus and strength, are calculated by a back analysis method according to the parameter interval provided by a laboratory test. According to the consistency requirements of slope failure characteristics and the stability coefficient in each excavation stage of landslide simulation analysis and actual working conditions, the rock and soil adopts the Mohr-Coulomb model and the parameters under saturated conditions as shown in Table 2.

The origin slope design adopted the lattice beam anchor cable with a horizontal and vertical spacing of 3 m, a length of 20 m–40 m, and a single anchor cable design pullout force of 550 kN. The

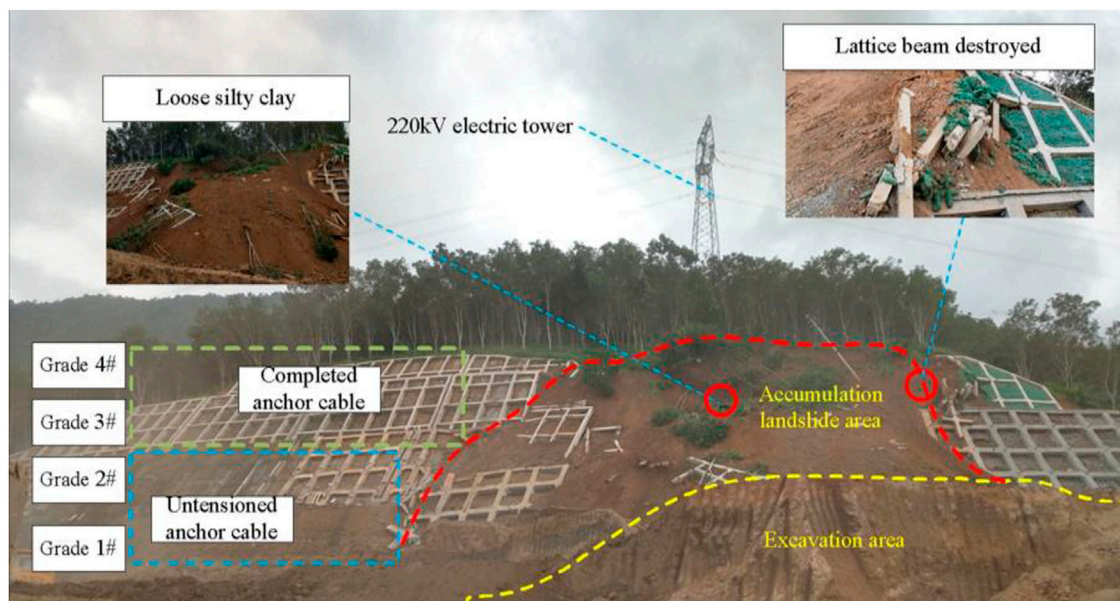


FIGURE 6
Accumulation landslide at K26 + 860 (7 October 2019).

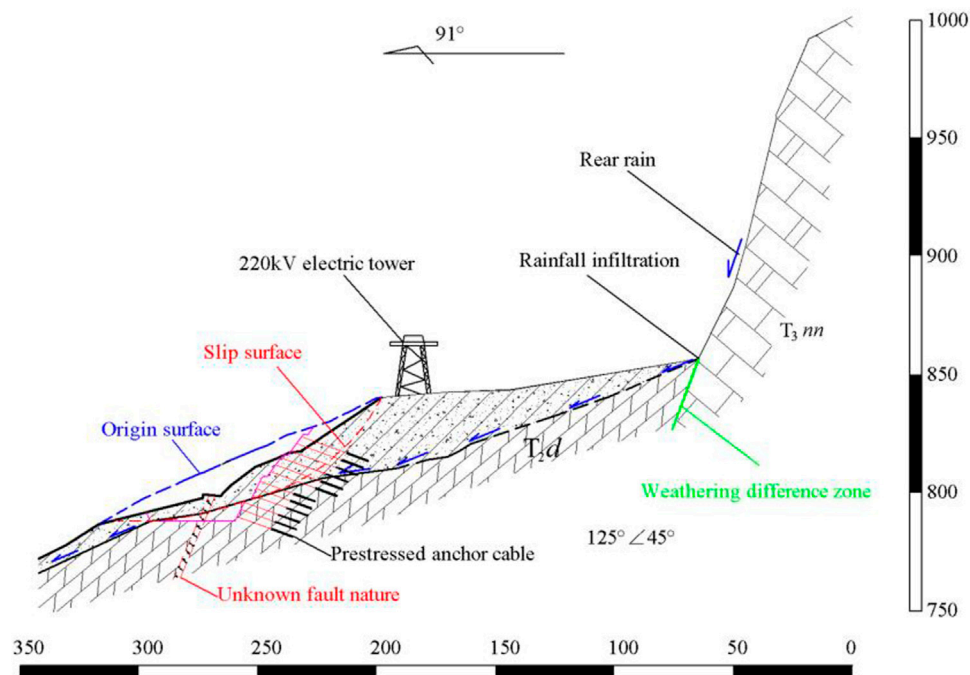


FIGURE 7
Engineering geologic profile of K26 + 860.

calculation results show that after completion of grade 4#, the approximately connected plastic zone distributed from the bottom to the top appeared. After completion of grade 2#, the plastic zone

appears and rapidly penetrates the whole slope (Figure 8). Therefore, the main reasons for the landslide are as follows. 1) The soil has a high porosity, low shear strength, and developed seepage channels. Rainfall

TABLE 2 Physical and mechanical parameters.

Material	E/MPa	ν	$\gamma/\text{kN}\cdot\text{m}^{-3}$	C/kPa	$\Phi/(^{\circ})$
Silt clay	80	0.35	18.7	15.0	20.0
Strongly weathered rock	120	0.25	23.0	45.0	28.0
Sliding surface	100	0.3	21.0	10.5	8.0

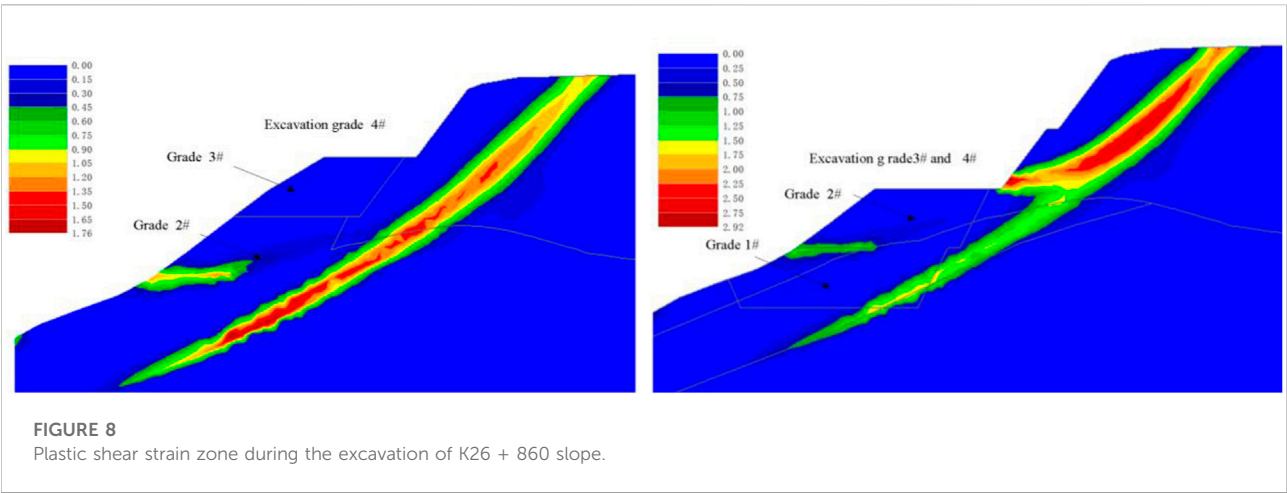


FIGURE 8 Plastic shear strain zone during the excavation of K26 + 860 slope.

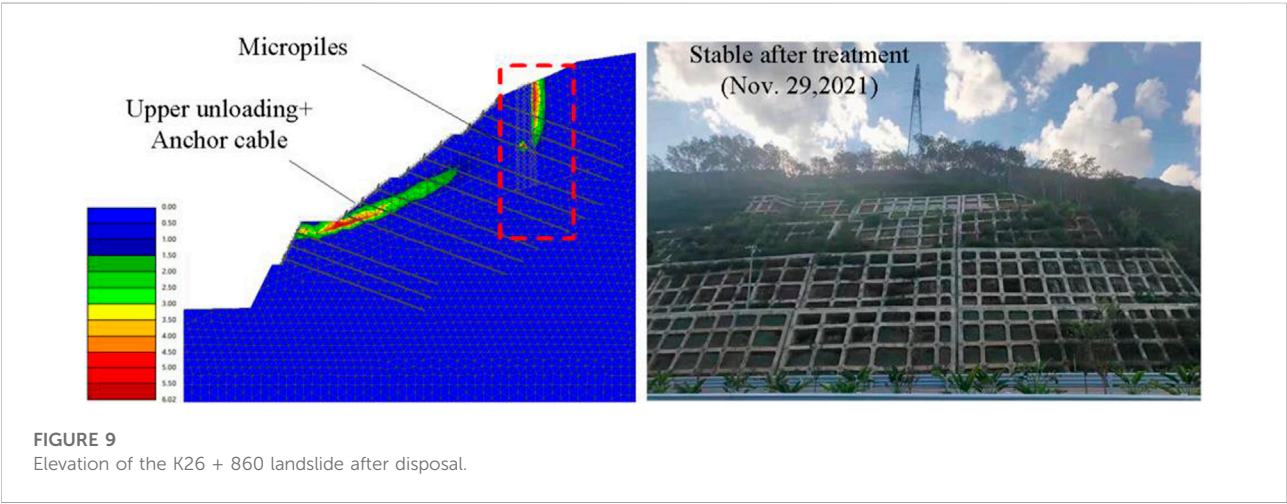


FIGURE 9 Elevation of the K26 + 860 landslide after disposal.

easily infiltrates along the surface and accumulates at the rock-soil interface, forming a potentially weak surface. 2) Through the unloading excavation at the front edge of the slope, even if the unloading height is as small as 5 m, the plastic zone is easily formed.

The basic countermeasures to deal with the landslide of the accumulation body are as follows. 1) In the design of the landslide of the accumulation body at the fault, when rainstorm conditions are considered, the influence of the average rainfall intensity and duration on the slope stability in the past 3 years should be

combined with the meteorological and hydrological conditions of the region for the temporary safety of construction. 2) Unloading at the bottom of the loose accumulation easily causes deformation cracks in the rear, and the slopes at all levels should be cut off based on the feasibility. According to the above treatment countermeasures, the K26 + 860 landslide is treated by clearing unloading, slope top micro piles, and using deep anchoring. A cut landslide generally remains stable for at least 2 years after completion (Figure 9).

Conclusions

- 1) The tectonic background of the Nanpeng River fault zone is the internal cause of landslide formation, and the stress pattern of extrusion on all sides is the main factor that constitutes high and steep slopes and broken rock bodies, which provides space for landslides; frequent seismic activities provide energy sources for landslides.
- 2) The formation process of the landslide in the Nanpeng River fault zone is mainly as follows: the fault strongly squeezes the rock mass to form steep terrain and an initial structural plane → under the action of erosion and dissolution, the mountain mass cuts into a loose deposit → and the mountain mass becomes unstable due to strong earthquakes, rainstorms, and artificial activities. Then, blocks become unstable and move to form landslides. These types of landslides are mainly fault-affected and accumulation landslides.
- 3) The fault-affected landslides in the Nanpeng River fault zone have good stability and their gentle slope platforms can be used as construction sites; accumulation landslides are more sensitive to rainfall and artificial activities. Unfavorable working conditions should be fully predicted and dynamic adjustments should be implemented to coordinate permanent support. Coordination of engineering measures and local deformation control measures should be used as preventive measures (AQSIQ, 2015).

References

- Aqsiq (2015). General administration of quality supervision, inspection, and quarantine of the people's republic of China. *Seismic Ground Motion Param. Zonation Map China*, GB18306. 30.
- Broeckx, J., Rossi, M., Lijnen, K., Campforts, B., Poesen, J., and Vanmaercke, M. (2020). Landslide mobilization rates: A global analysis and model. *Earth-Science Rev.* 201, 102972. doi:10.1016/j.earscirev.2019.102972
- Chen, H., Qin, S. Q., Xue, L. L., and Xu, C. (2021). Why the Xintan landslide was not triggered by the heaviest historical rainfall: Mechanism and review. *Eng. Geol.* 294, 106379. doi:10.1016/j.enggeo.2021.106379
- Chen, X. L., Hui, H. J., and Zhao, Y. H. (2014). The relationship between fault properties and landslide distribution: Taking the large-scale landslide in the Wenchuan earthquake as an example. *Seismol. Geol.* 36 (2), 358–367.
- Deng, J. H., Gao, Y. J., Yao, X., Dai, F. C., Ren, K. Y., Wang, F., et al. (2021). Recognition and implication of Basu giant rock avalanche. *Adv. Eng. Sci.* 53 (03), 19–28.
- Du, Y., and Chen, C. (2022). Data mining for landslide genetic mechanism analysis in the yunnan Province of China. *Geotech. Geol. Eng. (Dordr.)* 40 (11), 5631–5642. doi:10.1007/s10706-022-02237-z
- Huang, R. Q., and Li, W. (2011). Formation, distribution and risk control of landslides in China. *J. Rock Mech. Geotechnical Eng.* 3 (2), 97–116. doi:10.3724/spj.1235.2011.00097
- Huang, R. Q., and Li, W. L. (2008). Research on development and distribution rules of geohazards induced by Wenchuan earthquake on 12th may. *Yanshilixue Yu Gongcheng Xuebao/Chinese Journal of Rock Mechanics and Engineering*, 27(12), 2585–2592.
- Huang, R. Q., Pei, X., and Cui, S. A. (2016). Study on the fragmentation characteristics and formation mechanism of rock mass in the sliding zone of Daguangbao landslide. *J. Rock Mech. Eng.* 35 (1), 1–15.
- Huang, R. Q., Pei, X. J., and Li, T. B. (2008). Basic characteristics and formation mechanism of the largest scale landslide at Daguangbao occurred during the Wenchuan earthquake. *J. Eng. Geol.* 16 (6), 730–741.
- Huang, X., Yang, W. M., Zhang, C. S., Shen, J. F., and Liu, T. (2013). The genetic mechanism of the Suoertou landslide in the Pingding-Huama fault zone in southern Gansu. *Geol. Bull.* 32 (12), 1936–1942.
- Jiang, X. Z., Wen, B. P., and Jiang, S. (2015). Analysis of the main controlling factors of the luertou landslide activity in zhouqu, Gansu. *Jilin Univ. (Earth Sci. Ed.)* 45 (6), 1798–1807.
- Lan, H. X., Zhou, C. H., Wang, L. J., Zhang, H. Y., and Li, R. H. (2004). Landslide hazard spatial analysis and prediction using GIS in the Xiaojiang watershed, Yunnan, China. *Eng. Geol.* 76 (1–2), 109–128. doi:10.1016/j.enggeo.2004.06.009
- Lin, Q. G., and Wang, Y. (2018). Spatial and temporal analysis of a fatal landslide inventory in China from 1950 to 2016. *Landslides* 15 (12), 2357–2372. doi:10.1007/s10346-018-1037-6
- Liu, N. F., Li, N., Li, G. F., Song, Z. P., and Wang, S. G. (2022a). Method for evaluating the equivalent thermal conductivity of a freezing rock mass containing systematic fractures. *Rock Mech. Rock Eng.* 55, 7333–7355. doi:10.1007/s00603-022-03038-9
- Liu, N. F., Li, N., Wang, S. G., Li, G. F., and Song, Z. P. (2022b). A fully coupled thermo-hydro-mechanical model for fractured rock masses in cold regions. *Cold Regions Sci. Technol.* 205, 103707. doi:10.1016/j.coldregions.2022.103707
- Liu, N. F., Li, N., Xu, C. B., Li, G. F., Song, Z. P., and Yang, M. (2020). Mechanism of secondary lining cracking and its simulation for the Dugongling tunnel. *Rock Mech. Rock Eng.* 53 (10), 4539–4558. doi:10.1007/s00603-020-02183-3
- Martel, S. J. (2004). Mechanics of landslide initiation as a shear fracture phenomenon. *Mar. Geol.* 203 (3–4), 319–339. doi:10.1016/s0025-3227(03)00313-x
- Qi, S., Xu, Q., Lan, H., Zhang, B., and Liu, J. (2010). Spatial distribution analysis of landslides triggered by 2008.5. 12 Wenchuan Earthquake, China. *Eng. Geol.* 116 (1–2), 95–108. doi:10.1016/j.enggeo.2010.07.011
- Qi, T., Meng, X., Qing, F., Zhao, Y., Shi, W., Chen, G., et al. (2021). Distribution and characteristics of large landslides in a fault zone: A case study of the NE qinghai-tibet plateau. *Geomorphology* 379, 107592. doi:10.1016/j.geomorph.2021.107592

Data availability statement

The datasets presented in this study can be found in online repositories. The names of the repository/repositories and accession number(s) can be found in the article/Supplementary Material.

Author contributions

HZ: writing and revising the manuscript and presiding over relevant research. YL: data editing and sorting of the manuscript and manuscript writing.

Conflict of interest

YL, HZ, LH, HL, and XW were employed by Guangxi Transportation Science and Technology Group Co., Ltd.

Publisher's Note

All claims expressed in this article are solely those of the authors and do not necessarily represent those of their affiliated organizations, or those of the publisher, the editors, and the reviewers. Any product that may be evaluated in this article, or claim that may be made by its manufacturer, is not guaranteed or endorsed by the publisher.

- Shao, X., Ma, S., Xu, C., Shen, L., and Lu, Y. (2020). Inventory, distribution, and geometric characteristics of landslides in baoshan city, yunnan Province, China. *Sustainability* 12 (6), 2433. doi:10.3390/su12062433
- Sidle, R. C., Furuichi, T., and Kono, Y. (2011). Unprecedented rates of landslide and surface erosion along a newly constructed road in Yunnan, China. *Nat. Hazards (Dordr)*. 57 (2), 313–326. doi:10.1007/s11069-010-9614-6
- Sidle, R. C., Ghestem, M., and Stokes, A. (2014). Epic landslide erosion from mountain roads in yunnan, China – challenges for sustainable development. *Nat. Hazards Earth Syst. Sci.* 14, 3093–3104. doi:10.5194/nhess-14-3093-2014
- Sun, D. Y. (2005). Landslide at badu station on nankun railway and its treatment. *J. Railw. Eng. Soc.* S1, 320–326.
- Wang, S. J., Liu, B. J., Zhang, J. S., Liu, B. F., Duan, Y. L., Song, X. H., et al. (2015). Study on the velocity structure of the crust in southwest Yunnan of the north-south seismic belt—results from the menghai-gengma-lushui deep seismic sounding profile. *Sci. China Earth Sci.* 58 (12), 2175–2187. doi:10.1007/s11430-015-5189-0
- Xie, F. R., Su, G., Cui, X. F., Shu, S. B., and Zhao, J. T. (2001). Modern tectonic stress field in Southwest Yunnan, China. *Acta seimol. Sin.* 14 (1), 18–24. doi:10.1007/s11589-001-0157-5
- Yang, Y. Y., Xu, Y. S., Shen, S. L., Yuan, Y., and Yin, Z. Y. (2015). Mining-induced geo-hazards with environmental protection measures in yunnan, China: An overview. *Bull. Eng. Geol. Environ.* 74 (1), 141–150. doi:10.1007/s10064-014-0608-6
- Yin, Y., Xing, A., Wang, G., Feng, Z., Li, B., and Jiang, Y. (2017). Experimental and numerical investigations of a catastrophic long-runout landslide in Zhenxiong, Yunnan, southwestern China. *Landslides* 14 (2), 649–659. doi:10.1007/s10346-016-0729-z
- Zhu, Y. X., Li, F., and Ren, J. W. (1994). Fault activity characteristics and paleoearthquake events of Nandinghe fault zone. *China Earthq.* 04, 347–356.



OPEN ACCESS

EDITED BY
Yuwei Zhang,
Xi'an University of Architecture and
Technology, China

REVIEWED BY
Chao Kong,
Southwest University of Science and
Technology, China
Chao Yin,
Shandong University, China

*CORRESPONDENCE
Yonggang Wang,
✉ wangyonggang202211@163.com

SPECIALTY SECTION
This article was submitted to
Environmental Informatics and Remote
Sensing,
a section of the journal
Frontiers in Earth Science

RECEIVED 01 December 2022

ACCEPTED 15 December 2022

PUBLISHED 06 January 2023

CITATION
Hu Z, Zhang J, Wang Y and Wang Y (2023),
Mechanical behaviors of surrounding rock
and supporting structure of shallow-
buried unsymmetrical pressure tunnel
crossing soil–rock interface.
Front. Earth Sci. 10:1113430.
doi: 10.3389/feart.2022.1113430

COPYRIGHT
© 2023 Hu, Zhang, Wang and Wang. This is
an open-access article distributed under
the terms of the [Creative Commons
Attribution License \(CC BY\)](https://creativecommons.org/licenses/by/4.0/). The use,
distribution or reproduction in other
forums is permitted, provided the original
author(s) and the copyright owner(s) are
credited and that the original publication in
this journal is cited, in accordance with
accepted academic practice. No use,
distribution or reproduction is permitted
which does not comply with these terms.

Mechanical behaviors of surrounding rock and supporting structure of shallow-buried unsymmetrical pressure tunnel crossing soil–rock interface

Zhinan Hu¹, Ji Zhang¹, Yonggang Wang^{2*} and Yunfei Wang³

¹State Key Laboratory of Mechanical Behavior and System Safety of Traffic Engineering Structures, Shijiazhuang Tiedao University, Shijiazhuang, China, ²Shijiazhuang Traffic Investment Development Co., Ltd., Shijiazhuang, China, ³CCCC Road Bridge Inspection and Maintenance Co., Ltd., Beijing, China

Shallow bias tunnels are sensitive at the entrance section, where the existence of soil–rock interface (SRI) results in more complex deformation of surrounding rock and supporting structure. This study investigates the mechanical properties of surrounding rock and supporting structure of a shallow-buried bias tunnel crossing the soil–rock interface by a combination of model tests and numerical simulations. A shallow-buried biased tunnel with significant cracking at its entrance section is selected in southwest China. The plastic zone distribution, deformation, and pressure of surrounding rock, as well as the stress and deformation of supporting structure, are analyzed under different conditions with the tunnel vault, arch haunch, arch spring, and wall foot crossing the soil–rock interface. The test and numerical results show that the internal force of the lining structure is the largest at the left arch haunch and the right arch spring, with cracks occurring in the project. The surrounding rock and supporting structure are most prominently influenced by the arch haunch and arch spring crossing the soil–rock interface among different positions of the tunnel. The supporting structure is subjected to stress in three modes: there is mainly shearing when the tunnel vault passes through the soil–rock interface, extrusion and shearing co-exist when the tunnel arch haunch and arch spring pass through the soil–rock interface, and extrusion is dominant when the tunnel wall foot passes through the soil–rock interface. Inserting grouting steel pipes perpendicular to the soil–rock interface on the deep-buried side of the tunnel can effectively control the deformation of surrounding rock and the stress of supporting structure.

KEYWORDS

soil–rock interface, shallow-buried tunnel, unsymmetrical pressure, cracking feature, deformation analysis

Introduction

Shallow buried bias is a common phenomenon in mountain tunnels in southwest China owing to terrain conditions (Yan, 2018). For example, the shallow-buried biased section accounts for 60% of the left tube of the Nansai Tunnel of Yunnan Mangliang Expressway. Shallow-buried biased tunnels are associated with highly weathered overlying strata and weak rock mass. The weathering degree of overlying strata continues to decrease with an increase in buried depth, and a soil–rock interface (SRI) emerges between the strong weathering layer and the medium weathering layer (Kaya et al., 2017; Zhang et al., 2021). Tunnels inevitably



encounter the SRI during the tunneling process and with increasing buried depth (Zhou et al., 2014; Liu X. J. et al., 2015). Then, the rock mass around the tunnel undergo extrusion and slide along the SRI due to bias pressure, and cracking or falling of secondary lining may occur, which endangers the safety of construction and operation (Yang and Wu, 2011; Chiu et al., 2017; Li et al., 2018; Qin et al., 2022).

Numerical studies on shallow-buried biased tunnels have been conducted worldwide. The deformation and mechanical behaviors of surrounding rock were revealed by characterizations of rock mass deformation (Song et al., 2018), ground surface settlement (Wang et al., 2019), surrounding rock pressure (Liu X. R. et al., 2015; Liu et al., 2017; Zhang et al., 2022), surrounding rock stress field with different bias coefficients (Qiu et al., 2022), and sensitive factors in the surrounding rock loosening zone (Qiao et al., 2021). In addition, model tests were carried out to examine surrounding rock pressure and internal force distribution of supporting structure under different terrain conditions (Lei et al., 2015; Gao and Guo, 2016), and to evaluate the effects of water immersion (Liu and Lai, 2020; Zhang et al., 2020). Kong et al. (2016, 2022), Hu et al. (2021), Liu et al. (2021), Liu et al. (2022), and Qin et al. (2022) combined site monitoring with numerical analysis to investigate the cracking characteristics of secondary lining of shallow bias tunnels. The fast Lagrangian analysis of continua in 3 dimensions (FLAC 3D) numerical model (Yang et al., 2013; Xiao et al., 2014; Xiao et al., 2016; Yang et al., 2020) and model tests (He et al., 2015; Lei et al., 2016) were employed to explore the cracking behaviors and mechanisms of shallow bias tunnels. Furthermore, shaking table model tests were conducted to explore the dynamic responses, damage mechanisms, and failure modes of shallow-buried bias tunnels subjected to dynamic loads (Xu et al., 2016; Wang et al., 2017; Jiang et al., 2018; Wang et al., 2018; Liu et al., 2019; Li et al., 2021; Sun et al., 2021).

This study is carried out based on a shallow-buried bias tunnel with severe cracking in the secondary lining of entrance section in southwest China. Model tests and numerical simulations are conducted to investigate the pressure distribution, deformation characteristics, and plastic zone of surrounding rock, and to characterize the stress of supporting structure when different positions of the tunnel cross the SRI. The failure mechanisms of supporting structure under four conditions of crossing the SRI at different positions of the tunnel are revealed. The reinforcement effect

of inserting grouting steel pipes perpendicular to the SRI is also analyzed.

Engineering background

A left-right separated primary road tunnel in the southwest region of China is selected in this study (Figure 1). The tunnel with the design width of 10.25 m and the height of 8.55 m has a design speed of 80 km/h. The left and right tunnel tubes are 3060 and 3030 m long, respectively; their maximum burial depths are 455 and 457 m, respectively. The ground elevation of the mountain where the tunnel centerline is located ranges from 2130 to 2620 m, with a relative height of 490 m. The longitudinal slope of the right tube is 1.94%. The inlet section of the tunnel is located in the slope area in front of the mountain with a natural slope of 35°, which was basically stable before excavation.

The strata at the entrance of the tunnel from top to bottom consist of gravel-containing silty clay, gravel, and strongly weathered basalt, along with a small amount of moderately weathered basalt (Figure 2). Both gravel-containing silty clay and gravel have a limited anti-scouring ability, while joints and fissures are well developed in highly weathered basalt, resulting in broken soft rock with poor self-stabilizing capacity.

Cracks of the secondary lining appeared at the entrance section of the right tunnel tube after pouring. The maximum width and depth of the cracks were 2.18 and 245 mm, respectively. The lining cracks developed from k35+780 to k35+815. The cracks mainly extended longitudinally along the tunnel axis and paralleled each other. The cracks were primarily located at the left arch haunch and the right wall foot (Figure 3; Hu et al., 2021). The detailed cracking states and site investigation methods can be referred to the literature of Hu et al. (2021).

The entrance section of the tunnel consists of an open section (5 m) and a buried section. The buried section adopts a composite lining, and the design of composite lining supporting structure is shown in Figure 4 (Hu et al., 2021).

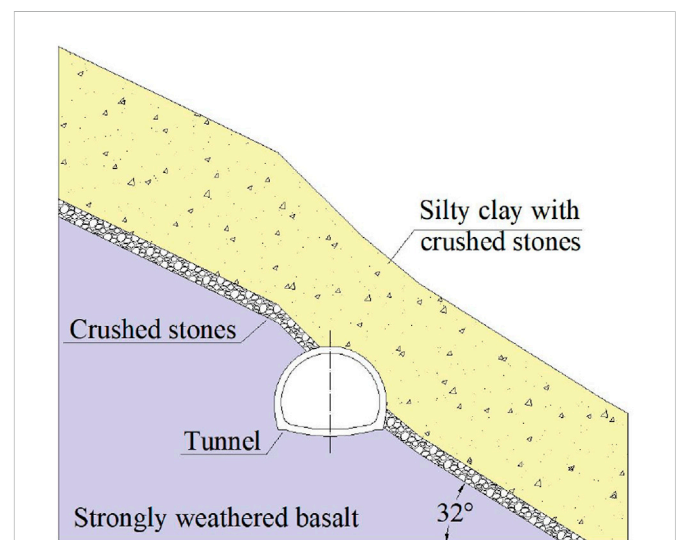
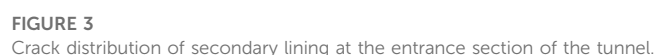


FIGURE 2
Geological cross-section profile of the tunnel entrance section.



Model materials

The ratio of mechanical parameters closest to similar materials is selected, namely, .5: .08: .42 for the upper ground layer, .65: .25: .1 for the lower rock layer, and 1 : : .9: .2 for the initial support material. The

Model tests

frontiersin.org

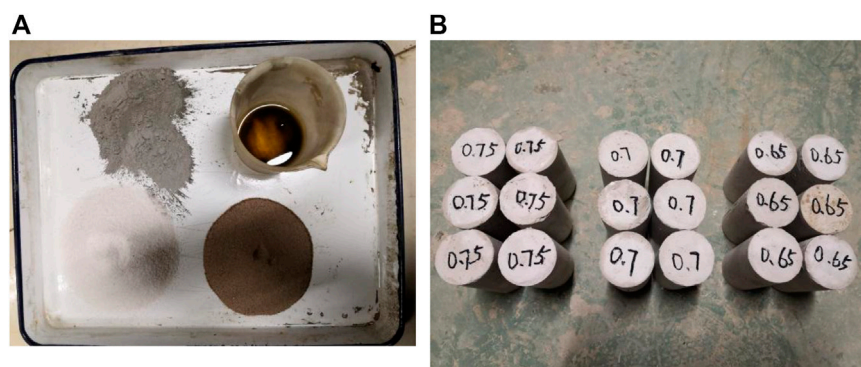


FIGURE 5
Materials used for orthogonal tests: (A) Surrounding rock material preparation and (B) Gypsum specimens.

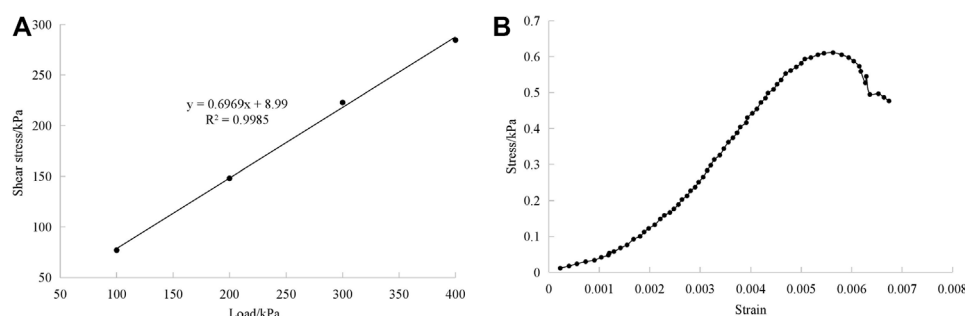


FIGURE 6
Material properties: (A) Shear strength of similar material of surrounding rock and (B) Mechanical performance of gypsum.

TABLE 1 Mechanical parameters of model materials for the surrounding rock and supporting structure.

Material	γ (kN/m ³)	E (GPa)	μ	c (kPa)	φ (°)
Upper surrounding rock	17.6	0.06	0.36	0.8	27.5
Lower surrounding rock	20.0	0.60	0.32	4	34.0
Supporting structure	—	0.56	0.2	—	—

two reserved openings based on the upper and lower bench excavation method. Excavation of the upper half section is 4 cm ahead of the lower half section, and the cyclical footage is 4 cm (Figure 7B).

Structural stress varying with excavation

The first principal stress

Strain rosettes are laid on the 12-cm section of the lining structure, and variation in the first principal stress of the lining structure monitoring part with the excavation step is calculated. The first principal stress at each monitoring point increases with the advance of tunnel excavation (Figure 8). There is a slow increase in the first principal stress on the outside of the structure, which reaches its maximum value at 16.5 kPa in the vault (Figure 8A). Specifically,

the first principal stress in the left wall foot and inverted arch increases remarkably after the first excavation step of the upper bench. It continues to increase slowly after passing the monitoring section and then levels off.

The first principal stress on the inside of the structure increases considerably with excavation and also peaks at the vault, reaching 26.6 kPa (Figure 8B). The variation in the first principal stress is smaller on the outside than on the inside. Overall, the principal stress changes rapidly when the excavation step is just initiated. After the excavation reaches the middle of the tunnel, the principal stress basically doesn't increase, and the mechanical conditions of the lining structure gradually stabilize to reach the final mechanical state. This indicates that excavation of the latter half section of the tunnel has minimal effect on the entrance section.

The third principal stress

Variation in the third principal stress of the lining structure with the excavation step is illustrated in Figure 9. In the course of tunnel excavation, the third principal stress at each monitoring point outside the structure exhibits an overall slow upward trend with minor changes (Figure 9A). The maximum compression exists near the right wall foot, with the third principal stress of −23.6 kPa. When the excavation approaches the monitoring section, the third principal stress value at the left arch-spring and the left wall foot increases suddenly.

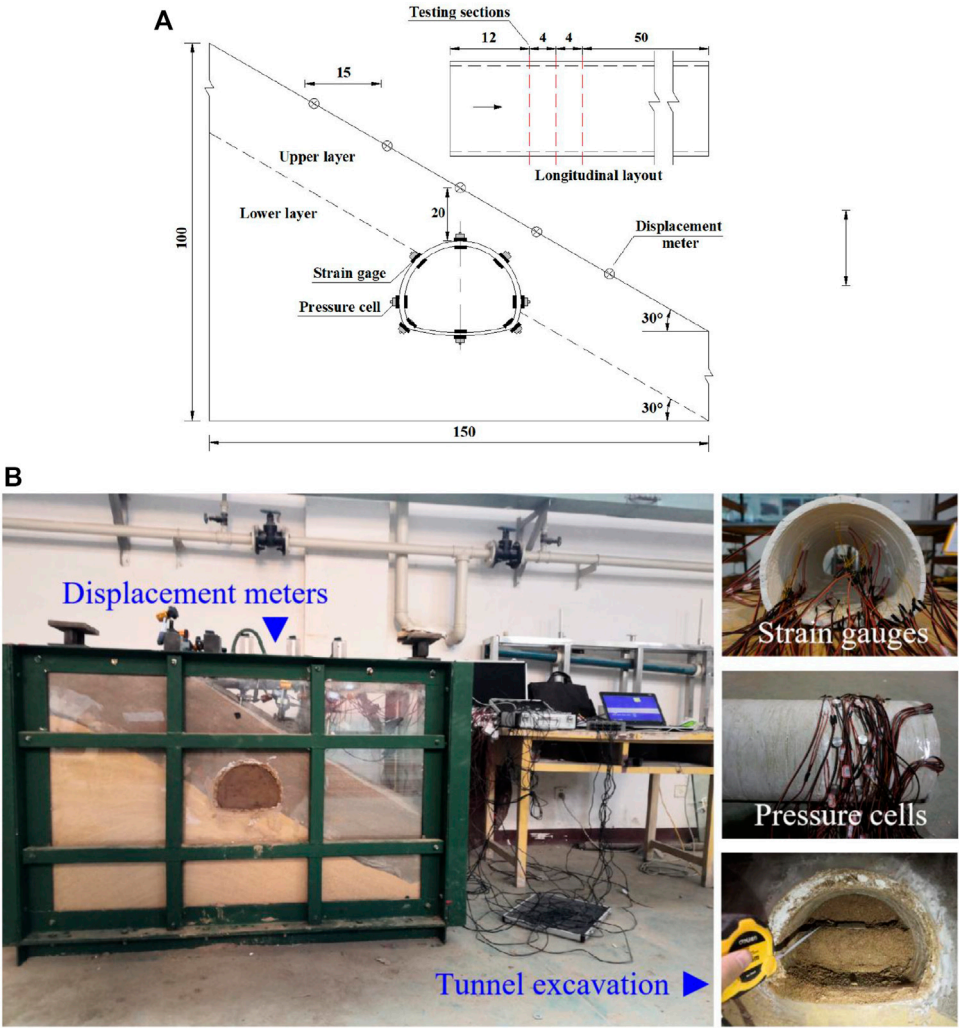


FIGURE 7 Model tests: (A) Cross-section layout of test elements and (B) Photographs of model tests.

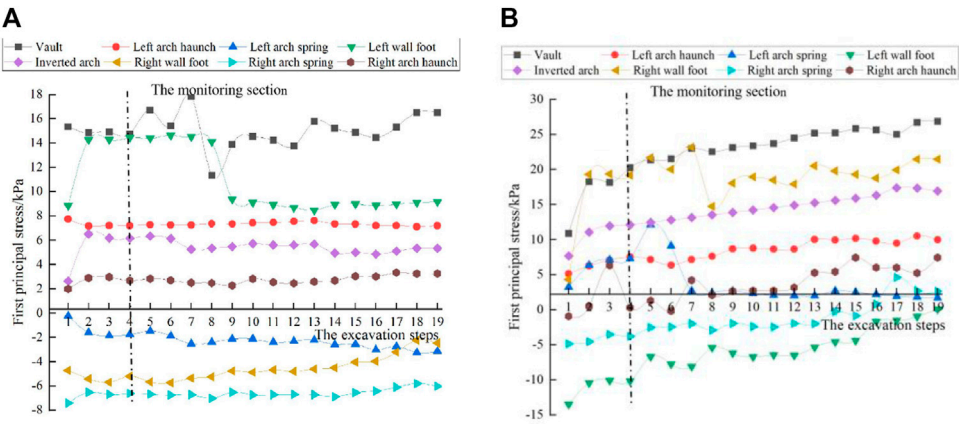


FIGURE 8 First principal stress of lining structure: (A) Stress at the 12-cm section outside of the structure and (B) Stress at the 12-cm section inside of the structure.

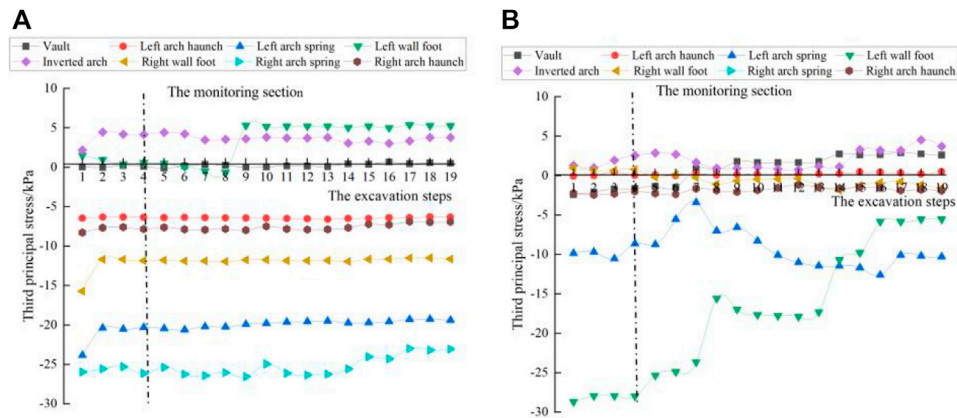


FIGURE 9

Third principal stress of lining structure: (A) Stress at the 12-cm section outside of the structure and (B) Stress at the 12-cm section inside of the structure.

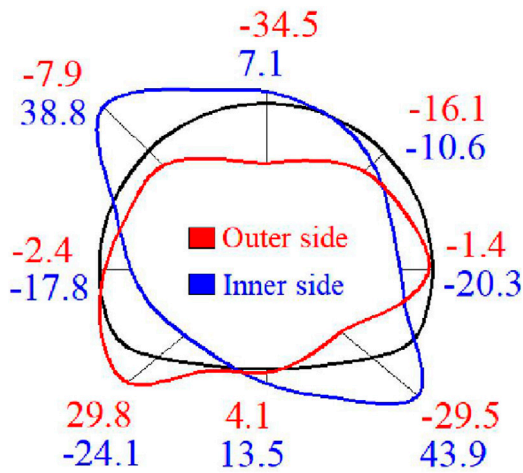


FIGURE 10

Circumferential stress of supporting structure (unit: kPa).

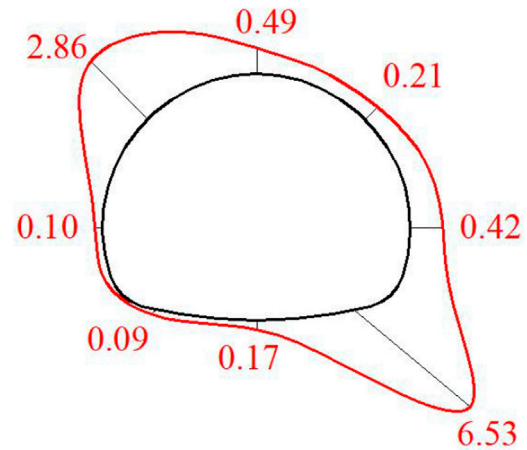


FIGURE 11

Pressure of surrounding rock (unit: kPa).

Distinct changes occur in the third principal stress on the inside of the lining structure (Figure 9B). Before the excavation, the third principal stress is located at the left wall foot, with the third principal stress of -28.3 kPa. After the excavation is completed, the largest third principal stress occurs at the left arch spring, -13.6 kPa. The third principal stress at the vault is first compressed and then tensioned during excavation, whereas at other points of the lining structure, the stress decreases minimally. With continuous advance of excavation distance, the third principal stress at each part of the lining gradually decreases and tends to be stable.

Circumferential stress of supporting structure

Data are collected from the inner and outer strain gauges at the two monitoring sections on the model. The final circumferential strain values are used to obtain the circumferential stress of the monitoring points on the monitoring section of the lining model.

On the outer side of the supporting structure, the vault is compressed most seriously at -34.5 kPa and the left wall foot is tensioned the most at 29.8 kPa. On the inner side, the left wall foot is most severely compressed at -24.1 kPa and the right wall foot is tensioned to a maximum of 43.9 kPa (Figure 10). The results show that the disturbance of surrounding rock has a strong influence on the circumferential stress of supporting structure during excavation.

Surrounding rock pressure

After the excavation is completed and the structure is stabilized, surrounding rock pressure is redistributed and dramatically changed. The trend of surrounding rock pressure (Figure 11) is consistent with that observed for the circumferential stress of the supporting structure (Figure 10). Large pressure changes also occurs at the left arch haunch (2.86 kPa) and the right wall foot (6.53 kPa),

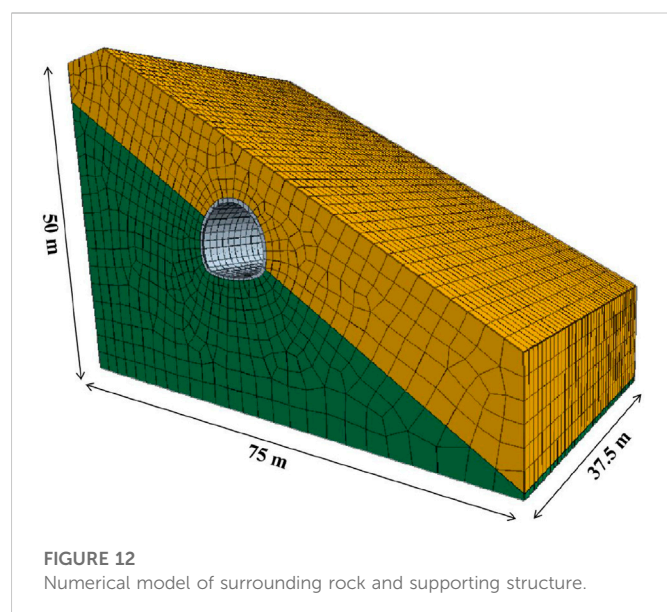


FIGURE 12
Numerical model of surrounding rock and supporting structure.

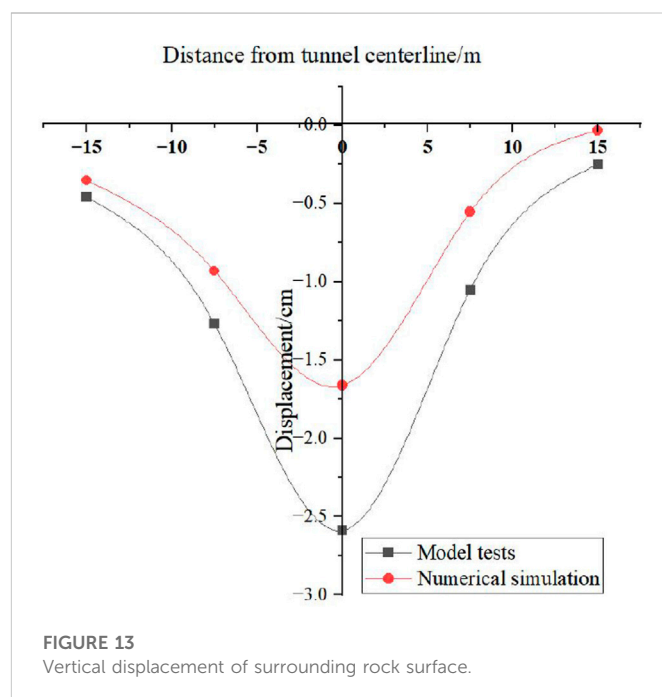


FIGURE 13
Vertical displacement of surrounding rock surface.

both of which are located at the SRI. This indicates that the maximum surrounding rock pressure occurs on the deep-buried side, with the peak value at the SRI.

Numerical model and parameters

The full-scale numerical model is constructed using the FLAC 3D finite difference software, and the test results are inverted to the engineering entity for comparative analysis. The stratum and the supporting structure are simulated by solid elements using the Mohr-Coulomb model and elastic model, respectively. The SRI is simulated using interface elements (Figure 12).

The initial supporting structure is applied after excavation. The parameters of supporting materials are calculated according to the equivalent stiffness, and the elastic modulus of steel arch and reinforcement mesh is converted to the elastic modulus of shotcrete (Yu et al., 2016; Luo et al., 2018). The conversion of elastic modulus is as follows:

$$E = E_0 + \frac{S_g E_g}{S_c}$$

The specific parameters of surrounding rock and supporting structure are listed in Table 2.

TABLE 2 Material parameters for the numerical model.

Material	ρ (kg/m ³)	E (GPa)	ν	c (MPa)	φ (°)	K_s (GPa)	K_n (GPa)
Silty clay with crushed stone layer	1,850	0.06	0.4	0.1	25	—	—
Strongly weathered basalt layer	2,000	0.3	0.31	0.4	32	—	—
Supporting structure	2,500	27.5	0.2	—	—	—	—
Soil-rock interface (Ji et al., 2016)	—	—	—	0.05	15	2.46	2.46

Comparative analysis of numerical simulations and model tests

To facilitate comparison with numerical results, model test results are inversely derived into the actual scale of the project.

Ground surface settlement

The vertical displacements of surrounding rock surface are compared between model tests and numerical calculations for monitoring points at the same position (Figure 13). Based on model tests, the vertical displacement curve of ground surface is similar to that of Peck curve. The maximum value appears on the right side of the tunnel centerline, but the left and right sides are asymmetrical. Within 0–15 m from the left and right sides of the tunnel centerline, there are remarkable changes in the vertical displacement of the surface on the deep-buried side. This indicates that surface displacement on the deep-buried side is strongly disturbed by excavation. The surface displacements based on numerical simulations and model tests show basically consistent patterns, although the model test results are greater than the numerical simulation results.

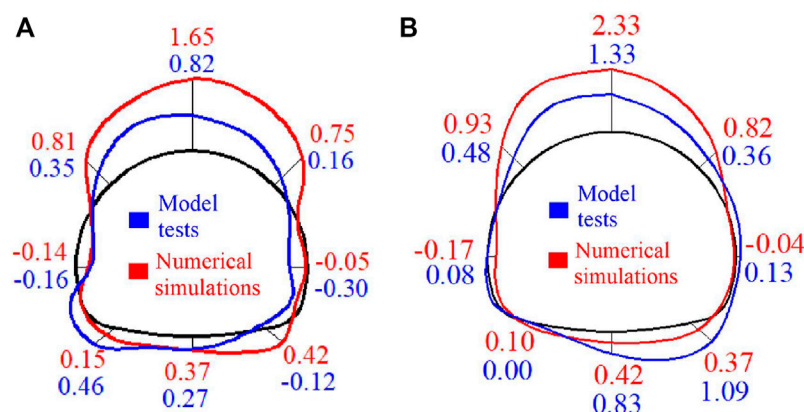


FIGURE 14

First principal stress of lining structure in numerical simulations and model tests (unit: MPa): (A) Stress outside the lining structure and (B) Stress inside the lining structure.

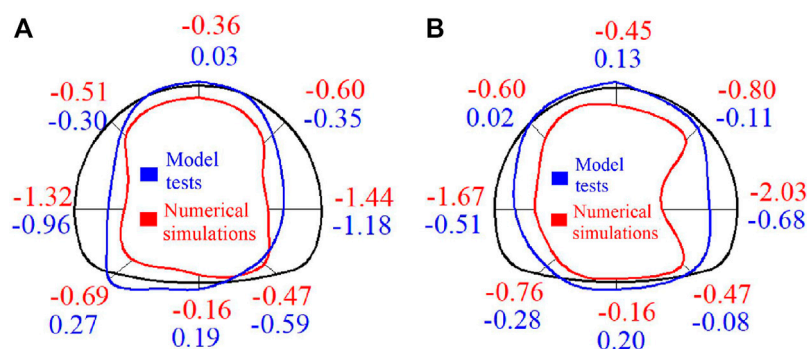


FIGURE 15

Third principal stress of lining structure in numerical simulations and model tests (unit: MPa): (A) Stress outside the lining structure and (B) Stress inside the lining structure.

Principal stress of supporting structure

The first principal stress envelope curves of the supporting structure show that the maximum value is distributed in the vault and left arch haunch of the lining structure (Figure 14). As for the third principal stress of the lining structure, large values are distributed in the left arch spring and the right arch spring (Figure 15). In these parts, evident stress concentration occurs because of the following reasons: 1) due to the effect of load on the deep-buried side, the tunnel has a tendency to slip to the lower right side; and 2) due to the constraint of surrounding rock on the shallow-buried side, the arch haunch is under considerable pressure. The stress in the arch spring and inverted arch is smaller than that in other parts. The full-scale numerical simulation results are basically consistent with the final internal force distribution of the lining structure in model tests.

Internal force of supporting structure

The internal force distribution of the supporting structure is basically consistent between full-scale numerical simulations and

model tests (Figure 16). Larger values of positive bending moment are distributed in the vault and inverted arch of the lining structure, whereas larger values of negative bending moment are distributed in the arch haunch and arch spring. There is small bending moment in other parts of the structure, and the bending moment is asymmetrically distributed due to bias (Figure 16A). The axial force values of the lining are all negative, and the lining structure is basically in a compressed state. The maximum axial force appears in the left arch spring and the right arch spring of the lining. The axial force values in the vault and the right arch haunch are relatively large, with small values in the other parts of the lining (Figure 16B). The numerical results and the test results are well-fitted.

Mechanical analysis with different SRI-crossing positions

To further reveal the relationship between the tunnel and the SRI, four relative position relationships are established, with the tunnel vault, arch haunch, arch spring, and wall foot crossing the SRI. The

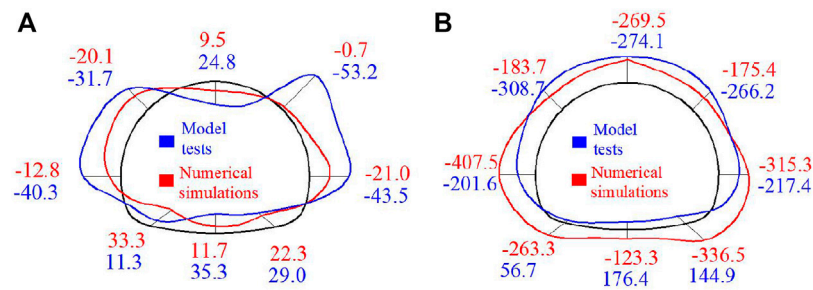


FIGURE 16 Structural internal forces in numerical simulations and model tests: **(A)** Bending moment of lining structure (unit: kNm) and **(B)** Axial force of lining structure (unit: kN).

TABLE 3 Material parameters of secondary lining.

Bulk modulus (GPa)	Ksner (MPa)	qdil	qvcl	Shear modulus (GPa)	Tensile strength (MPa)
16.8	7.4	0.25	0.255	12.5	2.2

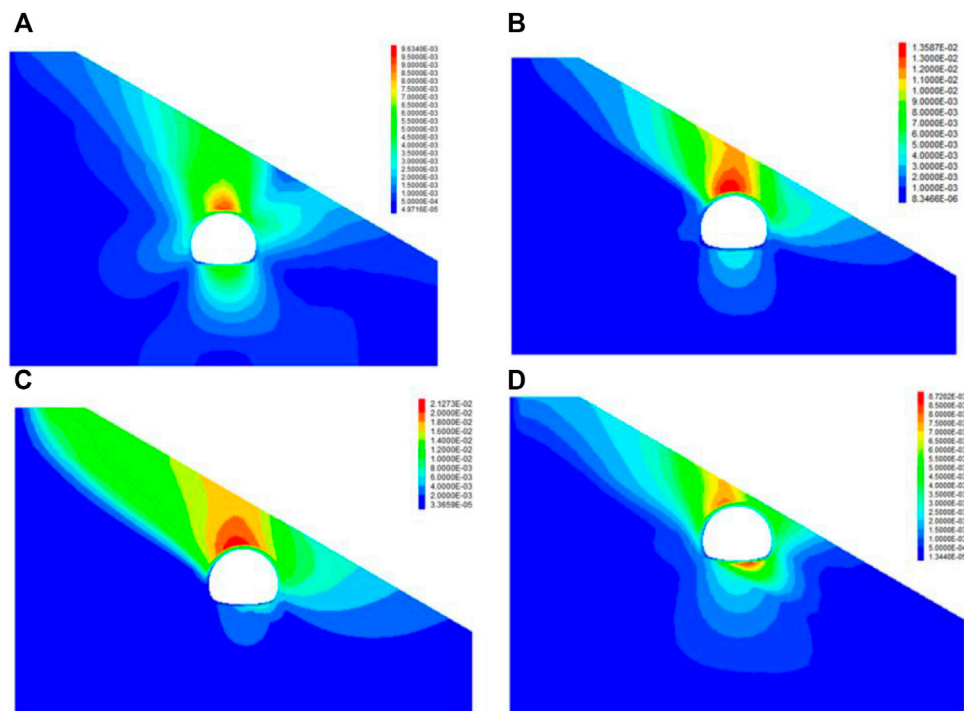


FIGURE 17 Surrounding rock displacement under four different conditions: **(A)** Tunnel vault crossing the soil–rock interface; **(B)** Arch haunch crossing the soil–rock interface; **(C)** Arch spring crossing the soil–rock interface; and **(D)** Wall foot crossing the soil–rock interface.

influence of relative position change on surrounding rock deformation and lining structure stress is analyzed. The model size is 75 m × 50 m × 37.5 m. The stratum and supporting structure are consistent with the earlier description in Section 4. The secondary lining is added to the supporting structure and simulated by solid elements using the Drucker-Prager material model. The material parameters of the secondary lining are provided in Table 3.

Deformation of surrounding rock

The deformation of surrounding rock at different positions of the supporting structure crossing the SRI is shown in Figure 17. The largest displacement of surrounding rock occurs with the arch spring crossing the SRI (2.12 cm), followed by that with the arch haunch crossing the SRI (1.36 cm). The displacement of surrounding rock

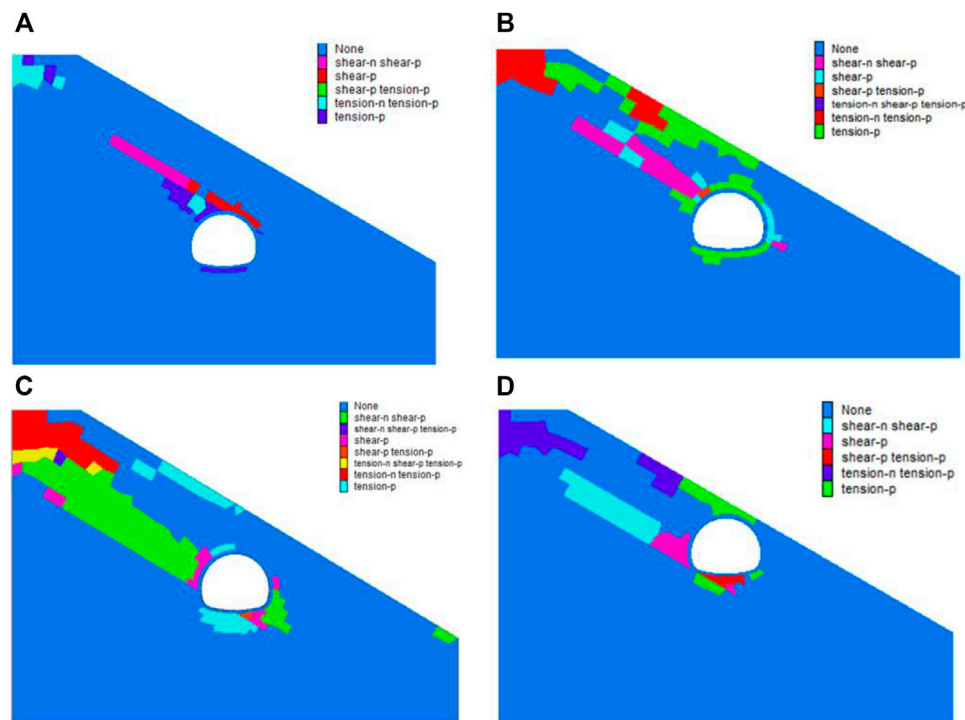


FIGURE 18

Plastic zone of surrounding rock under four different conditions: (A) Tunnel vault crossing the soil–rock interface; (B) Arch haunch crossing the soil–rock interface; (C) Arch spring crossing the soil–rock interface; and (D) Wall foot crossing the soil–rock interface.

with the vault and wall foot crossing the SRI is .96 and .87 cm, respectively. The maximum displacement always occurs near the vault, with a bias toward the deep-buried side. Further analysis reveals that as the SRI moves down relative to the supporting structure, surrounding rock displacement is influenced by the supporting structure more prominently.

Plastic zone of surrounding rock

The plastic zone of surrounding rock at different positions of the supporting structure crossing the SRI is shown in Figure 18. The plastic zone of surrounding rock displays a distinct asymmetric distribution after tunnel excavation. It is mainly distributed in the ground layer above the SRI and shows a remarkable shear slip surface. The distribution pattern of the plastic zone is similar to that of surrounding rock deformation. When crossing the SRI, the tunnel arch haunch and arch spring impose a strong influence on the plastic zone of surrounding rock. Shear failure mainly occurs along the SRI, with tensile failure primarily on the surface and inverted arch.

First principal stress of secondary lining

The secondary lining stress at different positions of the supporting structure crossing the SRI is shown in Figure 19. The first principal stress is located near the vault and the left arch haunch. The first principal stress of the secondary lining reaches its maximum value at

2.3 MPa when the arch spring passes through the SRI, followed by that with the arch haunch crossing the SRI. The first principal stress at the wall foot is the lowest, only 1.02 MPa. These results indicate that above the arch spring, the first principal stress gradually decreases with the upward movement of the SRI. The largest tensile stress of the structure appears near the vault of the deep-buried side, where cracking occurs first. The structure is compressed near the arch spring and the wall foot, but within a safe range.

Deformation and load-bearing patterns of secondary lining

The deformation results of the secondary lining are uniformly enlarged by 100 times (Figure 20). When the tunnel arch spring passes through the SRI, the secondary lining deformation reaches its maximum value at 2.13 cm. In other cases, the secondary lining deformation ranks in descending order with the tunnel arch haunch, vault, and wall foot crossing the SRI. When the tunnel passes through the SRI, the upper rock and soil mass loses support because of excavation, and consequently slides along the SRI. The supporting structure is then subjected to extrusion and shearing in the following three modes.

- 1) With the tunnel vault crossing the SRI, the supporting structure is mainly subjected to shearing, and shear failure may occur at the vault position.
- 2) With the tunnel arch haunch and arch spring crossing the SRI, the supporting structure is subjected to both extrusion and shearing. Shear failure may occur at the intersection

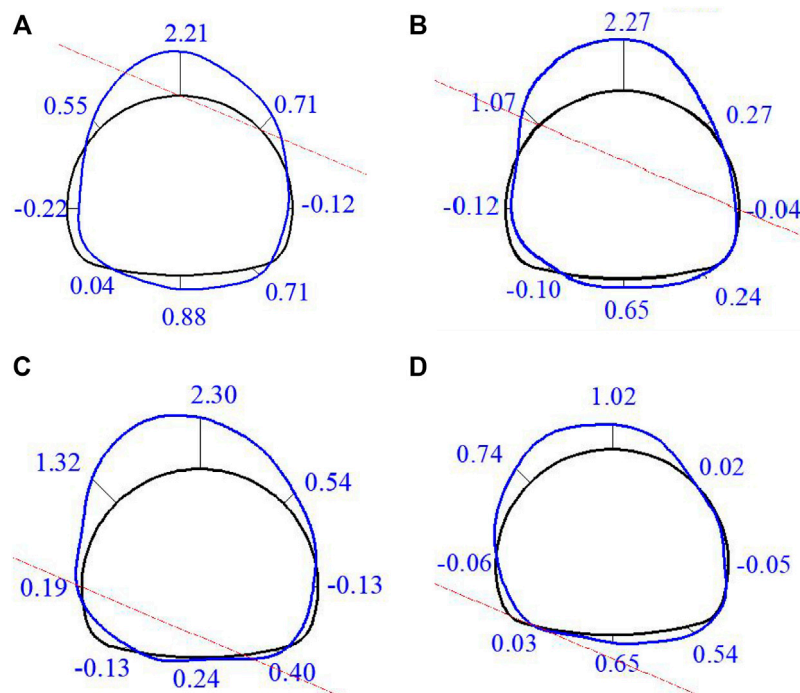


FIGURE 19

First principal stress of secondary lining under four different conditions (unit: MPa): (A) Tunnel vault crossing the soil–rock interface; (B) Arch haunch crossing the soil–rock interface; (C) Arch spring crossing the soil–rock interface; and (D) Wall foot crossing the soil–rock interface.

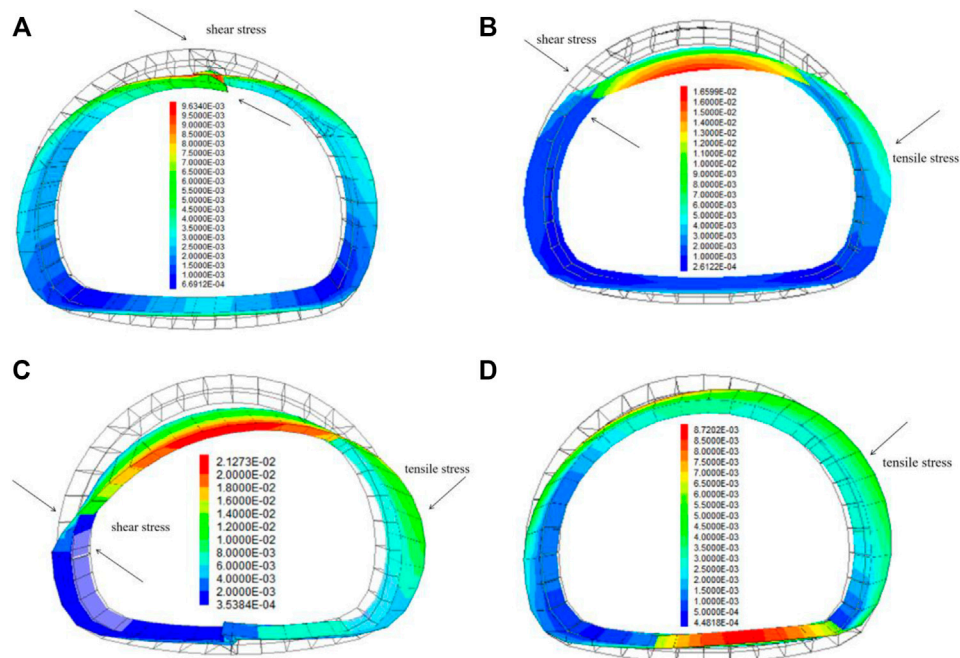


FIGURE 20

Structural displacement of secondary lining under four different conditions (unit: m): (A) Tunnel vault crossing the soil–rock interface; (B) Arch haunch crossing the soil–rock interface; (C) Arch spring crossing the soil–rock interface; and (D) Wall foot crossing the soil–rock interface.

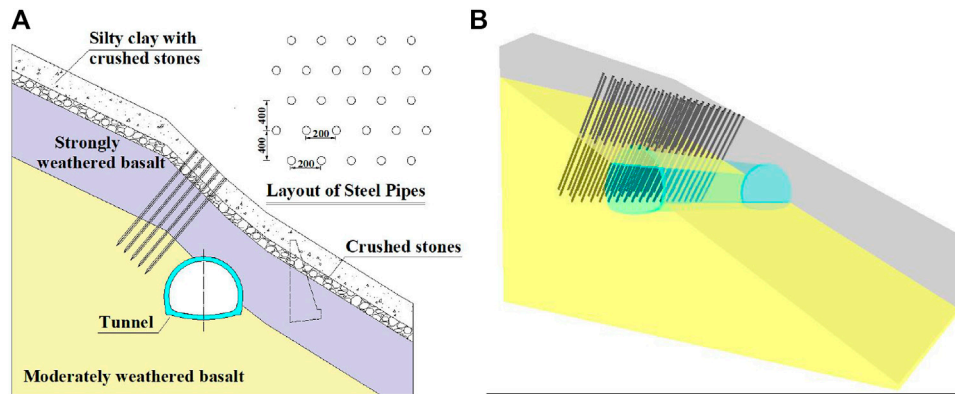


FIGURE 21

Ground reinforcement of grouting steel pipes: (A) Detailed design of grouting steel pipe and (B) Numerical simulation of ground reinforcement.

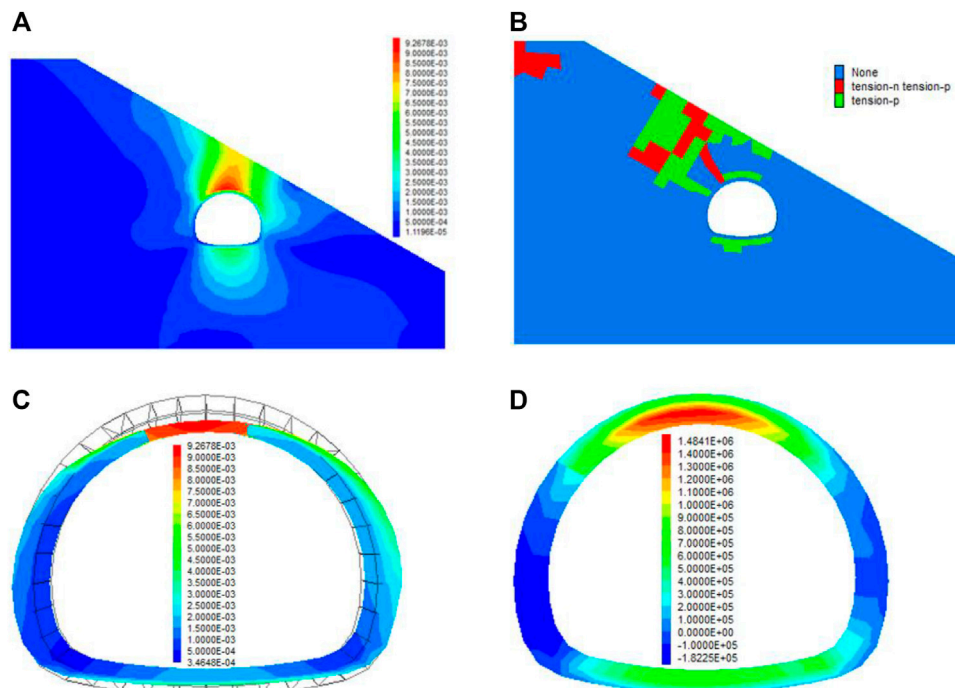


FIGURE 22

Controlling effects of grouting steel pipes: (A) Deformation of surrounding rock (unit: m); (B) Plastic zone of surrounding rock; (C) Deformation of secondary lining (unit: m); and (D) First principal stress of secondary lining (unit: Pa).

of the SRI and the tunnel, whereas tensile cracking caused by extrusion may occur on the deep-buried side of the supporting structure, and the extrusion is stronger when the tunnel arch spring passes through the SRI. 3) With the tunnel wall foot crossing the SRI, the supporting structure shows the least deformation, and the stress of the supporting structure is dominated by squeezing. On the deep-buried side of the supporting structure, the positions of the arch haunch, the vault, and the inverted arch can produce large extrusion deformation and tensile stress. On the shallow-buried

side of the supporting structure, the arch haunch to the wall foot can produce outward extrusion deformation.

Control effect of grouting steel pipes

According to the deformation characteristics of surrounding rock and supporting structure with different SRI-crossing positions, the cracking of the secondary lining is mainly attributed to the shear and

extrusion of the rock mass caused by the sliding of the upper rock and soil mass after tunnel excavation. In such tunnels, the sliding of the upper rock and soil should be controlled. It is recommended to insert grouting steel pipes or anti-slide piles perpendicular to the SRI on the upper part of the deep-buried side of the tunnel. Taking the tunnel arch haunch crossing the SRI as an example, the effect of grouting steel pipes on controlling rock mass deformation and supporting structure stress is analyzed by the numerical simulation, and the specific design of grouting steel pipes is shown in Figure 21. Grouting steel pipes are simulated by anchor cable elements with the elastic modulus of 210 GPa and slurry bonding force of 15 kN.

The numerical results (Figure 22) show that after inserting grouting steel pipes, the deformation of surrounding rock is reduced by 32% compared with that before inserting grouting steel pipes. In particular, the deformation is markedly reduced near the grouting steel pipes. The plastic zone of surrounding rock is also changed distinctively, the shear slip surface disappears, and the surrounding rock is only subjected to tension. In addition, the first principal stress of the secondary lining is reduced by 34% and the secondary lining is mainly squeezed after inserting grouting steel pipes. The reinforcement area of the grouting bolts is mainly subjected to unsymmetrical pressure, and the unsymmetrical pressure state of the structure disappears. Furthermore, the deformation of the secondary lining is reduced by 43.9% after inserting grouting steel pipes. In summary, both the stress and deformation of the secondary lining are effectively controlled by inserting grouting steel pipes.

Conclusion

In this paper, a combination of model tests and numerical simulations is used to characterize the deformation of surrounding rock and the stress of supporting structure in a shallow-buried biased tunnel crossing the soil-rock interface (SRI). A highway tunnel in southwest China with severe cracking of the secondary lining at the entrance section is taken as an example. The major findings are as follows:

- 1) The surface displacement is the largest along the tunnel centerline and decreases toward both sides, with the deep-buried side being influenced more than the shallow-buried side. When the arch spring of the tunnel passes through the SRI, it has the greatest influence on the displacement of surrounding rock. The deformation of surrounding rock is smaller for the tunnel arch haunch crossing SRI than that for the tunnel arch spring crossing the SRI. When the tunnel vault and inverted arch cross the SRI, the deformation of surrounding rock is relatively small.
- 2) The plastic zone of surrounding rock exhibits a remarkable asymmetric distribution after tunnel excavation. It is mainly located in the stratum above the SRI on the deep-buried side of the tunnel, showing a distinct shear slip surface. The plastic zone is changed most prominently when the tunnel arch haunch or arch spring passes through the SRI, and it is least influenced when the tunnel vault passes through the SRI. The surrounding rock slides along the SRI, resulting in the first failure of the left arch haunch and the left arch spring. The plastic zone tends to continuously expand upward from the left arch haunch and has emerged in the surface soil over a large range.
- 3) The surrounding rock pressure peaks at the crossing positions of SRI and tunnel, when the tunnel arch haunch or arch spring passes through the SRI. The law of surrounding rock pressure is consistent with the outer circumferential stress of the supporting structure.
- 4) When the tunnel arch spring passes through the SRI, the first principal stress is concentrated at the left arch haunch (2.3 MPa). As the SRI moves upward relative to the tunnel position, the first principal stress at the left arch haunch decreases with the tunnel arch haunch and vault crossing the SRI, in contrast to the slow increase at the inverted arch. When the tunnel wall foot passes through the SRI, the stress is relatively low at the left arch haunch.
- 5) When the tunnel crosses the SRI, the supporting structure is subjected to extrusion and shearing in three different modes: mainly shearing (tunnel vault crossing the SRI), simultaneous extrusion and shearing (arch haunch and arch spring crossing the SRI), and mainly extrusion (wall foot crossing the SRI).
- 6) Inserting grouting steel pipes perpendicular to the SRI on the deep-buried side of the tunnel can effectively control the deformation of surrounding rock. Compared with that before inserting grouting steel pipes, the deformation of surrounding rock is reduced by 32%, and its shear slip surface disappears. In addition, the unsymmetrical pressure effect of the secondary lining is markedly alleviated, and its first principal stress is reduced by 34%.

Data availability statement

The original contributions presented in the study are included in the article/supplementary material, further inquiries can be directed to the corresponding author.

Author contributions

ZH and JZ wrote the manuscript. YoW revised the manuscript, conceived the experiments, and contributed to the data interpretation. The fieldwork and preliminary study of samples were carried out by YuW. All authors have read and agreed to the published version of the manuscript.

Funding

The authors acknowledge the financial support provided by the Young Talent Program of the Hebei Provincial Education Department (BJ2019009), the National Natural Science Foundation of China (52178392), the Central Leading Local Science and Technology Development Fund Program (226Z5403G), and the Excellent Youth Program of the Hebei Provincial Natural Science Foundation (E2021210025), China.

Conflict of interest

YoW was employed by Shijiazhuang Traffic Investment Development Co., Ltd. YuW was employed by CCCC Road Bridge Inspection and Maintenance Co., Ltd.

The remaining authors declare that the research was conducted in the absence of any commercial or financial relationships that could be construed as a potential conflict of interest.

Publisher's note

All claims expressed in this article are solely those of the authors and do not necessarily represent those of their affiliated

References

- Chiu, Y. C., Lee, C. H., and Wang, T. T. (2017). Lining crack evolution of an operational tunnel influenced by slope instability. *Tunn. Undergr. Sp. Technol.* 65, 167–178. doi:10.1016/j.tust.2017.03.004
- Gao, F. Q., and Guo, J. J. (2016). Stress mechanism and deformation monitoring of bias tunnel. *Int. J. Simul. Syst. Sci. Technol.* 17 (43), 14.1–14.4. doi:10.5013/IJSSST.a.17.43.14
- He, M., Peng, Y., Zhao, S., Shi, H. Y., Wang, N., and Gong, W. L. (2015). Fracture mechanism of inverted trapezoidal shaped tunnel excavated in 45° inclined rock strata. *Int. J. Min. Sci. Technol.* 25, 531–535. doi:10.1016/j.ijmst.2015.05.003
- Hu, Z. N., Shen, J., Wang, Y. F., Guo, T. Z., Liu, Z. C., and Gao, X. Q. (2021). Cracking characteristics and mechanism of entrance section in asymmetrically-load tunnel with bedded rock mass: A case study of a highway tunnel in southwest China. *Eng. Fail. Anal.* 122, 105221. doi:10.1016/j.engfailanal.2021.105221
- Ji, T. Y., Zhang, D., Li, C. S., Shi, B., and Chen, X. X. (2016). Sensitivity analysis on gravel-soil interface parameters of the soil-rock mixture. *J. Eng. Geol.* 24, 1203–1208. (in China). doi:10.13544/j.cnki.jeg.2016.s1.175
- Jiang, X. L., Wang, F. F., Yang, H., Sun, G. C., and Niu, J. Y. (2018). Dynamic response of shallow-buried small spacing tunnel with asymmetrical pressure: Shaking table testing and numerical simulation. *Geotech. Geol. Eng.* 36 (4), 2037–2055. doi:10.1007/s10706-017-0444-0
- Kaya, A., Karaman, K., and Bulut, F. (2017). Geotechnical investigations and remediation design for failure of tunnel portal section: A case study in northern Turkey. *J. Mt. Sci.* 14, 1140–1160. doi:10.1007/s11629-016-4267-x
- Kong, C., Gao, X. Q., Cao, L., and Liu, K. (2016). Analysis of the failure of primary support of a deep-buried railway tunnel in silty clay. *Eng. Fail. Anal.* 66, 259–273. doi:10.1016/j.engfailanal.2016.04.008
- Kong, C., Wang, H. Y., Zhao, K., and Gao, X. Q. (2022). Numerical simulation of long-term deterioration of rock mass supported by shotcrete lining. *Front. Earth. Sci.* 10, 891084. doi:10.3389/FEART.2022.891084
- Lei, M. F., Lin, D. Y., Yang, W. C., Shi, C. H., Peng, L. M., and Huang, J. (2016). Model test to investigate failure mechanism and loading characteristics of shallow-bias tunnels with small clear distance. *J. Cent. S. Univ.* 23, 3312–3321. doi:10.1007/s11771-016-3397-1
- Lei, M. F., Peng, L. M., and Shi, C. H. (2015). Model test to investigate the failure mechanisms and lining stress characteristics of shallow buried tunnels under unsymmetrical loading. *Tunn. Undergr. Sp. Technol.* 46, 64–75. doi:10.1016/j.tust.2014.11.003
- Li, A., Xu, N. W., Dai, F., Gu, G. K., Hu, Z. H., and Liu, Y. (2018). Stability analysis and failure mechanism of the steeply inclined bedded rock masses surrounding a large underground opening. *Tunn. Undergr. Sp. Technol.* 77, 45–58. doi:10.1016/j.tust.2018.03.023
- Li, L., Guo, X. D., Zou, Z. Y., Zhu, Z. Y., Guo, Z. H., Xiao, W. M., et al. (2021). Study on dynamic response characteristics and damage mechanism of tunnel lining at entrance of shallow bias tunnel. *Shock. Vibr.* 2021, 8930560. doi:10.1155/2021/8930560
- Liu, C., Yang, H., Jiang, X. L., and Shi, H. T. (2019). Shaking table test and numerical simulation for acceleration response laws of shallow-buried biased double-arch tunnel. *J. Vibro. Eng.* 21 (4), 1188–1200. doi:10.21595/jve.2019.20623
- Liu, D. J., Li, M., Zuo, J. P., Gao, Y., Zhong, F., Zhang, Y., et al. (2021). Experimental and numerical investigation on cracking mechanism of tunnel lining under bias pressure. *Thin-Walled. Struct.* 163, 107693. doi:10.1016/j.tws.2021.107693
- Liu, D. J., Shang, Q., Li, M., Zuo, J. P., Gao, Y., and Xu, F. (2022). Cracking behaviour of tunnel lining under bias pressure strengthened using FRP Grid-PCM method. *Tunn. Undergr. Sp. Technol.* 123, 104436. doi:10.1016/j.tust.2022.104436
- Liu, X. J., Yang, C., and Yu, J. (2015). The influence of moisture content on the time-dependent characteristics of rock material and its application to the construction of a tunnel portal. *Adv. Mater. Sci. Eng.* 3, 1–13. doi:10.1155/2015/725162
- Liu, X. R., Chen, H. J., Liu, K., and He, C. M. (2017). Model test and stress distribution law of unsymmetrical loading tunnel in bedding rock mass. *Arab. J. Geosci.* 10, 184–195. doi:10.1007/s12517-017-2949-5
- Liu, X. R., Li, D. L., Wang, J. B., and Wang, Z. (2015). Surrounding rock pressure of shallow-buried bilateral bias tunnels under earthquake. *Geomech. Eng.* 9 (4), 427–445. doi:10.12989/gae.2015.9.4.427
- Liu, Y. Y., and Lai, H. P. (2020). Experimental study on lining cracking of shallow buried loess tunnel under the simulation of effect of slide surface immersion. *Appl. Sci.* 10 (17), 6080. doi:10.3390/app10176080
- Luo, Y. B., Chen, J. X., Chen, Y., Diao, P. S., and Qiao, X. (2018). Longitudinal deformation profile of a tunnel in weak rock mass by using the back analysis method. *Tunn. Undergr. Sp. Technol.* 71, 478–493. doi:10.1016/j.tust.2017.10.003
- Qiao, S. F., Cai, Z. Y., Xu, P., Tan, J. K., and Zhang, Y. G. (2021). Investigation on the scope and influence factors of surrounding rock loose circle of shallow tunnel under bias pressure: A case study. *Arab. J. Geo Sci.* 14 (15), 1428. doi:10.1007/s12517-021-07869-8
- Qin, Y. W., Lai, J. X., Yang, T., Zan, W. B., Feng, Z. H., Liu, T., et al. (2022). Failure analysis and countermeasures of a tunnel constructed in loose granular stratum by shallow tunnelling method. *Eng. Fail. Anal.* 141, 106667. doi:10.1016/j.engfailanal.2022.106667
- Qiu, H. S., Qiu, R. H., Luo, G., Ayasrah, M., and Wang, Z. (2022). Study on the mechanical behavior of fluid-solid coupling in shallow buried tunnels under different biased terrain. *Symmetry* 14 (7), 1339. doi:10.3390/sym14071339
- Song, D. Q., Chen, J. D., and Cai, J. H. (2018). Deformation monitoring of rock slope with weak bedding structural plane subject to tunnel excavation. *Arab. J. Geosci.* 11, 251–261. doi:10.1007/s12517-018-3602-7
- Sun, W. Y., Yan, S. H., Ma, Q. G., Liang, Q. G., Ou, E., Cao, X. P., et al. (2021). Dynamic response characteristics and failure mode of a bias loess tunnel using a shaking table model test. *Transp. Geotech.* 31, 100659. doi:10.1016/j.tge.2021.100659
- Wang, F. F., Jiang, X. L., and Niu, J. Y. (2017). The large-scale shaking table model test of the shallow-bias tunnel with a small clear distance. *Geotech. Geol. Eng.* 35, 1093–1110. doi:10.1007/s10706-017-0166-3
- Wang, F. F., Jiang, X. L., Niu, J. Y., and Yang, H. (2018). Experimental study on seismic dynamic characteristics of shallow-bias tunnel with a small space. *Shock. Vibr.* 2018, 6412841–6412849. doi:10.1155/2018/6412841
- Wang, Z., Yao, W. J., Cai, Y. Q., Xu, B., Fu, Y., and Wei, G. (2019). Analysis of ground surface settlement induced by the construction of a large-diameter shallow-buried twin-tunnel in soft ground. *Tunn. Undergr. Sp. Technol.* 83, 520–532. doi:10.1016/j.tust.2018.09.021
- Xiao, J. Z., Dai, F. C., Wei, Y. Q., Min, H., Xu, C., Tu, X. B., et al. (2014). Cracking mechanism of secondary lining for a shallow and asymmetrically-loaded tunnel in loose deposits. *Tunn. Undergr. Sp. Technol.* 43, 232–240. doi:10.1016/j.tust.2014.05.013
- Xiao, J. Z., Dai, F. C., Wei, Y. Q., Xing, Y. C., Cai, H., and Xu, C. (2016). Analysis of mechanical behavior in a pipe roof during excavation of a shallow bias tunnel in loose deposits. *Environ. Earth. Sci.* 75, 293–311. doi:10.1007/s12665-015-5176-y
- Xu, H., Li, T. B., Xia, L., Zhao, J., and Wang, D. (2016). Shaking table tests on seismic measures of a model mountain tunnel. *Tunn. Undergr. Sp. Technol.* 60, 197–209. doi:10.1016/j.tust.2016.09.004
- Xu, Z. L., Luo, Y. B., Chen, J. X., Su, Z. M., Zhu, T. T., and Yuan, J. P. (2021). Mechanical properties and reasonable proportioning of similar materials in physical model test of tunnel lining cracking. *Constr. Build. Mater.* 300, 123960. doi:10.1016/j.conbuildmat.2021.123960
- Yan, S. C. (2018). *Deformation control of weak surrounding rock unsymmetrical loading tunnel entrance section of Yibin-Bijie expressway*. dissertation/master's thesis (Beijing: Beijing Jiaotong University).
- Yang, C., Hu, Z. X., Huang, D., and Guo, F. (2020). Failure mechanism of primary support for a shallow and asymmetrically loaded tunnel portal and treatment measures. *J. Perform. Constr. Facil.* 34 (1), 19435509. doi:10.1061/(asce)cf.1943-5509.0001385
- Yang, C., Zhang, Y. X., Huang, D., and Zhu, Q. (2013). Deformation behavior of topographic unsymmetrical loaded tunnels and their pre-reinforcements after excavation. *Highw. Transp. Res. Dev. Engl. Ed.* 7, 69–75. doi:10.1061/jhtrcq.0000334
- Yang, X. L., and Wu, B. (2011). Optimization analysis of rockbolts supporting for double-arch shallow tunnels subjected to unsymmetrical loads. *Geotech. Spec. Pub.* 221, 88–95. doi:10.1061/47632(411)12
- Yu, H. T., Chen, J. T., Bobet, A., and Yuan, Y. (2016). Damage observation and assessment of the Longxi tunnel during the Wenchuan earthquake. *Tunn. Undergr. Sp. Technol.* 54, 102–116. doi:10.1016/j.tust.2016.02.008
- Zhang, J., Kuang, M. X., Zhang, Y. H., and Feng, T. G. (2021). Evaluation and analysis of the causes of a landslide and treatment measures during the excavation of a tunnel through a soil-rock interface. *Eng. Fail. Anal.* 130, 105784. doi:10.1016/j.engfailanal.2021.105784
- Zhang, Y. T., Ding, X. L., Huang, S. L., Wu, Y. J., and He, J. (2020). Strength degradation of a natural thin-bedded rock mass subjected to water immersion and its impact on tunnel stability. *Geomech. Eng.* 21 (1), 63–71. doi:10.12989/gae.2020.21.1.063
- Zhang, Y. W., Fan, S. Y., Yang, D. H., and Zhou, F. (2022). Investigation about variation law of frost heave force of seasonal cold region tunnels: A case study. *Front. Earth Sci.* 9, 806843. doi:10.3389/feart.2021.806843
- Zhou, X. J., Wang, J. H., and Lin, B. T. (2014). Study on calculation of rock pressure for ultra-shallow tunnel in poor surrounding rock and its tunneling procedure. *J. Mod. Transp.* 22, 1–11. doi:10.1007/s40534-013-0025-8



OPEN ACCESS

EDITED BY
Ping Zhang,
Luleå University of Technology, Sweden

REVIEWED BY
Y. Bentian,
Lanzhou Jiaotong University, China
Wang Yajun,
Lanzhou University, China

*CORRESPONDENCE
Zelin Niu,
✉ niuzldq@xauat.edu.cn
Yaqiong Wang,
✉ ys08@gl.chd.edu.cn

SPECIALTY SECTION
This article was submitted to
Environmental Informatics and Remote
Sensing,
a section of the journal
Frontiers in Earth Science

RECEIVED 10 November 2022
ACCEPTED 20 December 2022
PUBLISHED 09 January 2023

CITATION
Niu Z, Wang Y and Fan S (2023), Research
on the deformation control of surrounding
rock about large-section tunnel in strong-
medium weathered slate.
Front. Earth Sci. 10:1094325.
doi: 10.3389/feart.2022.1094325

COPYRIGHT
© 2023 Niu, Wang and Fan. This is an
open-access article distributed under the
terms of the [Creative Commons
Attribution License \(CC BY\)](#). The use,
distribution or reproduction in other
forums is permitted, provided the original
author(s) and the copyright owner(s) are
credited and that the original publication in
this journal is cited, in accordance with
accepted academic practice. No use,
distribution or reproduction is permitted
which does not comply with these terms.

Research on the deformation control of surrounding rock about large-section tunnel in strong-medium weathered slate

Zelin Niu^{1,2,3,4*}, Yaqiong Wang^{4,5*} and Shengyuan Fan^{1,2}

¹School of Civil Engineering, Xi'an University of Architecture and Technology, Xi'an, China, ²Shaanxi Key Lab of Geotechnical and Underground Space Engineering, Xi'an, China, ³XAUAT Engineering Technology Co., Ltd., Xi'an, China, ⁴Shaanxi Provincial Major Laboratory for Highway Bridge and Tunnel, Xi'an, China, ⁵School of Highway, Chang'an University, Xi'an, China

Affected by dip angle and thickness of strata and the tunneling method, soft rock tunnel has obvious characteristics of large deformation, long deformation time and difficult support. Based on a case study of Gelong the deformation and failure mechanism of surrounding rock, stress characteristics of supporting structural and control method of large section highway tunnel passing through strong-medium weathered carbonaceous slate stratum are studied. This paper proposed construction method based on strengthening the longitudinal stiffness of supporting structure and increasing the integrity of surrounding rock, The results showed that the deformation of surrounding rock and the stress of supporting structure increased rapidly in the early stage of construction. The cumulative deformation of vault settlement and horizontal convergence reached 116.9 mm and 97.9 mm, respectively, accounting for 73.53% and 76.62% of the total deformation. The proportion of surrounding rock pressure shared by the primary support and the secondary lining was about 8.9:1.1. This shows that the initial support after comprehensive reinforcement has a strong supporting capacity, and effectively reduces the secondary lining pressure of the tunnel, which plays a vital role in the long-term service of the secondary lining.

KEYWORDS

large-section highway tunnel, highly-weakly weathered slate, comprehensive reinforcement CD method with integrated reinforcement, deformation control, surrounding rock pressure

1 Introduction

With the rapid development of infrastructure construction, tunnel and underground engineering construction was faced with more complex geological and construction problems, such as large deformation of surrounding rock, water seepage and mud inrush, high geostress and approaching excavation (Xie ZZ. et al., 2019; Fan et al., 2020; Niu et al., 2020; Dutta and Bhattacharya 2022; Hu et al., 2022). Mountain tunnel has the geological characteristics of large burial depth and high tectonic stress. In the development area of metamorphic rocks and soft rocks, the surrounding rock is more prone to large deformation under the action of high geostress (Niu et al., 2021; Zhang H. et al., 2019; Zhang Q. et al., 2019; Bian et al., 2019; Song et al., 2020; Yao et al., 2021; Lei et al., 2022). Scholars have done a lot of research on the deformation mechanism of soft rock. Chen et al. (2019b) investigated the anisotropic mechanical properties of deep-buried carbonaceous phyllite and its influence on the asymmetrical mechanical behavior of supporting structures in practical engineering. And it can

be concluded that the asymmetrical deformations of surrounding rock and the cracking of secondary lining were results of the coupling effect of layered soft rock and shearing action along the foliation based on the field data and numerical simulation results. To further study the mechanical mechanism of large deformation, Yu et al. (2020) based on the repair engineering of the chambers of Pingdingshan No.6 mine in China, the field investigation, laboratory test, numerical simulation, and theoretical analysis were studied to reveal the main factors affecting the stability of the surrounding rock of the chambers. Li et al. (2021) established a microseismic (MS) monitoring system and performed numerical simulation based the discrete element method (DEM) to investigate the stability of rock mass in high geostress underground powerhouse caverns subjected to excavation. Liu et al. (2020) taken the Badaling Great Wall station in Beijing as the engineering background, a typical monitoring section was selected in the super-span transition section of the tunnel and the deformation and forces of both the surrounding rock and the support structures were systematically monitored. The results showed that the deformation and the forces acting on both the surrounding rock and the tunnel's lining are directly related to the construction procedures, the geological conditions and the locations in the super-span tunnel.

The deformation and stability of the surrounding rock are closely related to the excavation and support methods. A reasonable excavation and support method is of great significance to the stability of the surrounding rock and engineering safety (Guo et al., 2018; Song et al., 2019; Tian et al., 2019; Zhao et al., 2019; Li et al., 2022; Jia et al., 2022). In particular, tunnels in weak strata should be supported timely and reasonably after excavation, otherwise they are vulnerable to surrounding rock rupture and structural damage. To control the large deformation of surrounding rock in soft rock tunnels under deep burial and high geostress, the support and reinforcement methods commonly adopted are empirical design method, theoretical analysis method and on-site monitoring method (Chen et al., 2019a; Froech et al., 2019; Guo et al., 2021). Parisio et al. (2018) conducted a numerical study of the excavation of the FE tunnel in a coupled hydro-mechanical finite element framework, employing an anisotropic plasticity coupled with damage constitutive model. The approach was validated by comparing numerical predictions and *in situ* observations during and after tunnel excavation in terms of displacements, pore water pressure evolution and degradation of elasticity. To investigate the effect of alternating soft and hard strata on the stability of rock surrounding tunnels Lv et al. (2019) analyzed the shield construction project of two tunnels with a small clearance of 2.6 m. Comparing the simulation results with the on-site monitoring data, finding that with the reinforcement, the tunnel lining deformation and the ground settlement can be reduced significantly and the effect of subway shield construction on the construction of the first subway tunnel will significantly reduce. The results revealed that the single primary support method cannot ensure the long-term safety of the tunnel, while the double primary support method can be able to control the large deformation and rheological effects of broken phyllite under high geo-stress effectively.

With the increasingly complex geological conditions, the deformation and failure of soft rock tunnels under high geostress and bedding structure strata have become increasingly serious. Based on the Gelong tunnel of Weiyuan-Wudu

Expressway, this paper studied the reinforcement method for excavation and large deformation of large-section tunnel in slate through numerical simulation and field test. According to the numerical calculation results, the CD method was determined for tunnel excavation. Through theoretical analysis and field test, this paper studies the support failure mechanism, surrounding rock deformation law, and structural stress characteristics and control of large-section highway tunnels passing through highly-weakly weathered carbonaceous slate strata. The results show that the CD method excavation can effectively control the large deformation of surrounding rock and ensure the safe excavation of tunnel. The research conclusions can provide theoretical reference for the structural design and safe construction of similar projects.

2 Project overview

2.1 Basic information of tunnel

The Gelong Tunnel of the Weiyuan-Wudu Expressway is located in Dingxi City, Gansu Province. It is a two-hole four-lane tunnel with a total length of 2485 m, a clear width of 10.86 m and a clear height of 7.19 m. The maximum buried depth of the left-line tunnel is 187.8 m, and that of the right-line tunnel is 192.4 m. In the tunnel, there are 6 pedestrian crossing passages, 2 vehicle crossing passages and 4 emergency parking sections with a clear width of 13 m. The basic information of the tunnel is shown in Figure 1.

2.2 Geological condition

The geological structure of the tunnel site is complex. The surrounding rock is mostly highly-weakly weathered slate, with V-grade surrounding rocks accounting for more than 91.3%, which are relatively fragmented and not suitable for excavation. The surface soil layer is mainly deposited silty clay containing 20%–30% of gravels. The lower layer is highly-weathered slate with layered structure, poorly cemented and partially embedded with weakly weathered rocks. Moreover, the tunnel bottom bedrock is also weakly weathered slate with layered structure, developed fissures and poor stability. Local sections of the tunnel have a large burial depth and belong to high-stress surrounding rock areas. The groundwater is mostly pore-water and bedrock fissure water with a groundwater level ranges from 2.9 m to 27.5 m, which is mainly supplied by vertical infiltration of atmospheric precipitation. During construction, the cavern wall has some dripping water and local seepage. The geological profile is shown in Figure 2 and the soil layer parameters are listed in Table 1.

2.3 Engineering problems

The geological conditions of Gelong Tunnel are complex due to the influence of geological structures. The surrounding rock is mainly composed of deposited silty clay containing gravels and Triassic highly-weakly weathered slate. The silty clay and strongly weathered slate have a loose rubbly structure, and the rock mass is fragmented, which results in poor stability during excavation. The on-

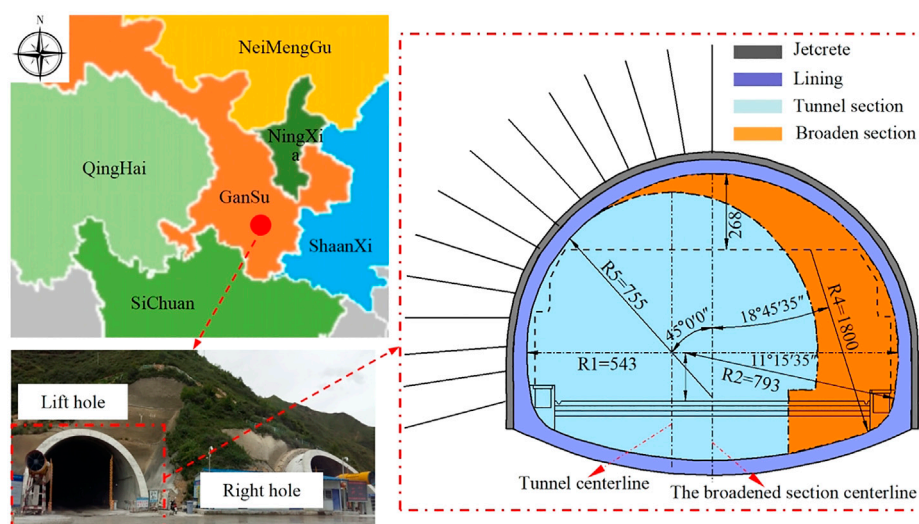


FIGURE 1
Basic information of Gelong Tunnel.

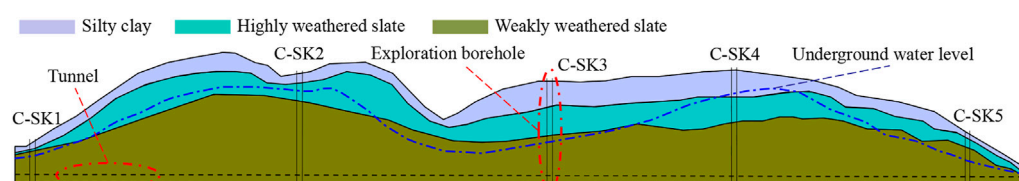


FIGURE 2
Geological profile.

TABLE 1 Soil layer parameters.

Soil layer	E /(GPa)	γ /(kN/m ³)	μ	c /(kPa)	ϕ /(°)
Silty clay	0.015	19	0.45	30	30
Highly weathered slate	0.2	21	0.4	50	40
Weakly weathered slate	5	23	0.26	100	50

site construction monitoring and measurement showed that the tunnel is subjected to deformation, cracking during construction. The large deformation mainly concentrated in the arch shoulder and the left arch waist (seeing Figure 3), and the maximum deformation within 80–100 cm.

3 Research method

3.1 Reinforcement plan

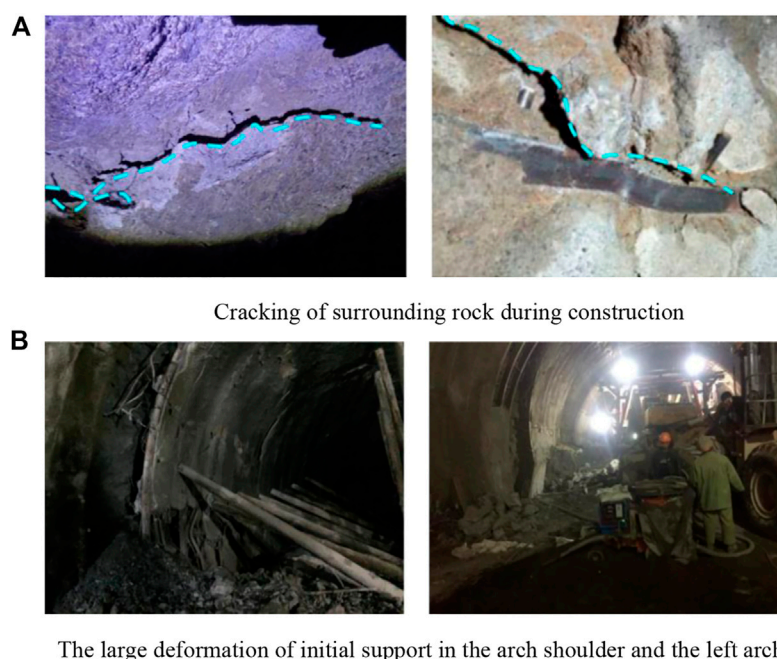
Aiming at the problems existing in the project, this paper proposed a CD excavation method based on integrated

reinforcement system. The specific reinforcement steps are as follows: 1) Grouting the surrounding rock radially to improve the integrity of surrounding rock; 2) Selecting high-strength steel arches and reducing the spacing between each steel arch; 3) Connecting 3–5 trusses of steel arch frames longitudinally to improve the overall longitudinal stiffness of initial support; 4) Adding additional grouting anchor pipes to each steel arch and temporary support inverted to further control the deformation of surrounding rock; 5) Adjusting the excavation method in time, and adopting the CD method that can quickly and effectively control the deformation of the surrounding rock.

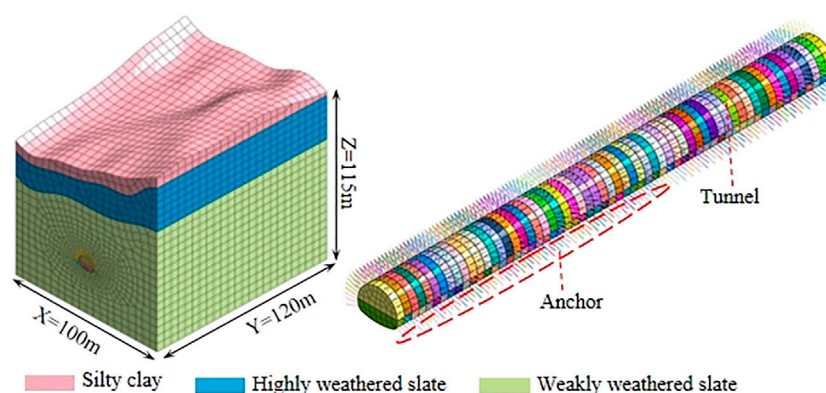
3.2 Numerical simulation

3.2.1 Model

The finite element software MIDAS GTS/NX is adopted to analyze the deformation and stress characteristics of surrounding rock under different working conditions. In order to ensure the reliability of the calculation results, the influence range of tunnel excavation is fully considered. Thus the specific dimensions of the model are $X=100$ m, $Y=120$ m and $Z=115$ m, as shown in Figure 4.

**FIGURE 3**

Large deformation and cracking of surrounding rock and initial support. (A) Cracking of surrounding rock during construction. (B) The large deformation of initial support in the arch shoulder and the left arch waist.

**FIGURE 4**

3D finite element model.

3.2.2 Model parameters

The soil and material parameters are obtained according to geological exploration data and laboratory tests, as shown in Table 2.

3.3 Field monitoring of stress and strain

The stress and deformation of surrounding rock and support structure shall be strictly monitored during tunnel excavation and support construction. The feasibility of the integrated reinforcement method proposed in this paper is further

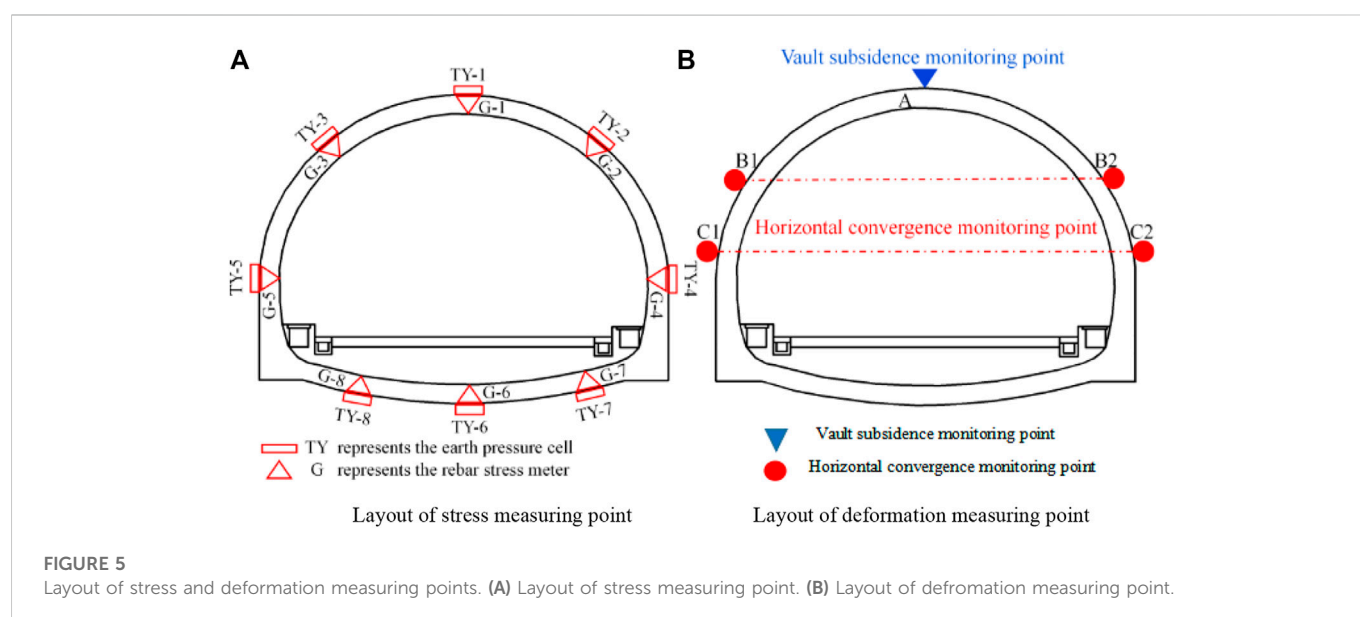
verified, which ensured the safety and rapid construction of the tunnel.

3.3.1 Measuring point arrangement

To keep track of the stress and deformation of the surrounding rock and support structure during tunnel excavation and ensure construction safety, the Earth pressure cells were arranged between the surrounding rock and the initial support, between the initial support and the secondary lining, and the bar stress meters were arranged at the web of the steel arch. The schematic diagram of measuring point layout was shown in Figure 5A, At the same time, the horizontal convergence and vault

TABLE 2 Calculation parameters used in the model.

Material	E/GPa	$\gamma/(\text{kN/m}^3)$	μ	c/kPa	$\phi/^\circ$
Silty clay	0.015	19	0.45	30	30
Highly weathered slate	5	21	0.4	50	40
Weakly weathered slate	0.2	23	0.26	100	50
Anchor	210	78.5	0.3	—	—
Shotcrete	30	24	0.2	—	—
Secondary lining	29.5	25	0.3	—	—
Temporary support and longitudinal connection steel bar	200	78.5	0.3	—	—



subsidence monitoring point were placed according to the surrounding rock conditions, as shown in Figure 5B.

3.3.2 Measuring element installation and data acquisition

Figure 6 shows the arrangement of bar stress meters and Earth pressure cells on-site.

4 Result analysis

4.1 Analysis of numerical simulation results

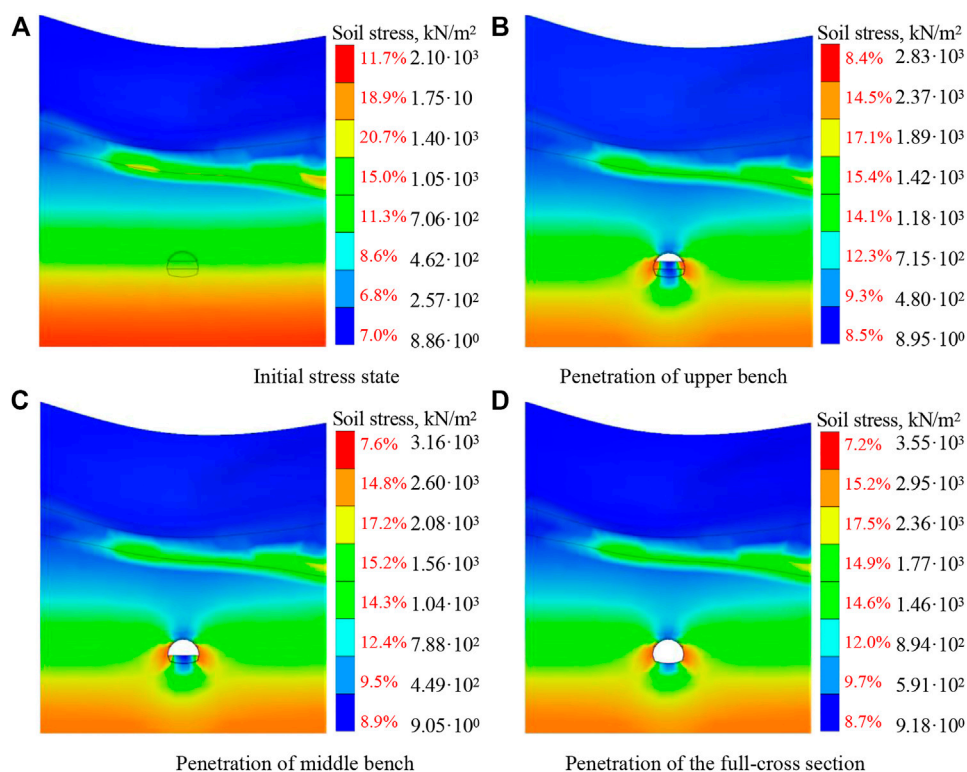
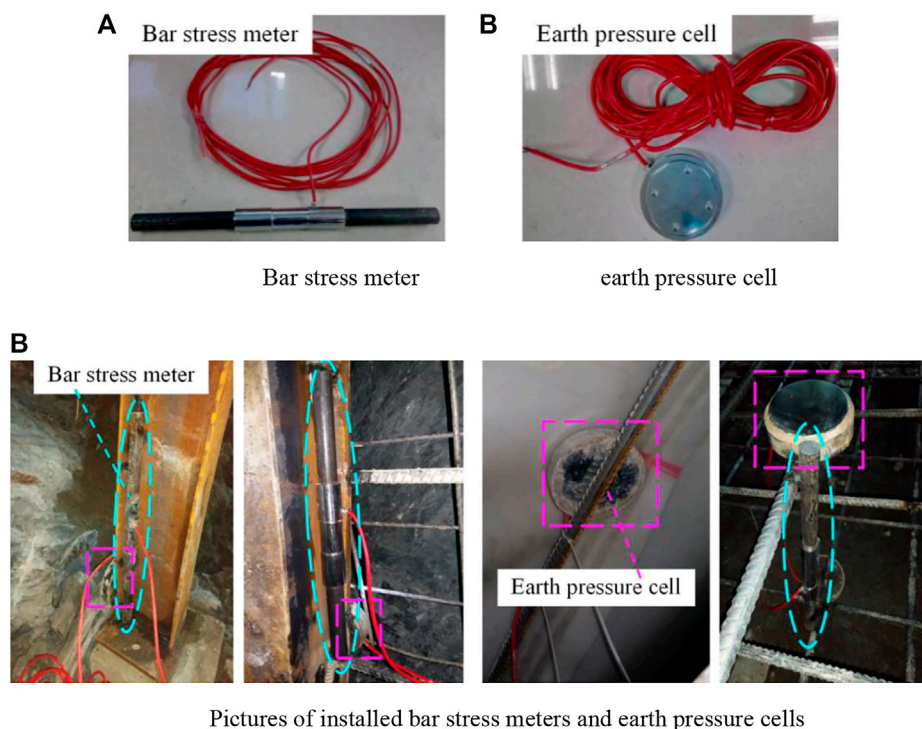
This paper compared and analyzed the stress and deformation of tunnel surrounding rock and structure under three-step method and comprehensive reinforcement CD method.

4.2 Stress analysis

The stress cloud image of surrounding rock under the above two working conditions are shown in Figures 7, 8.

Figure 7B showed that the stress concentrated at the left and right arches after upper bench excavation, and the maximum stress was 2.83 MPa. After the middle bench is excavated, the stress was mainly distributed in the arch waist, arch foot and side wall. And the stress was roughly symmetrical on both sides, with the maximum stress appeared in the left wall, about 3.16 MPa, as shown in Figure 7C. After the excavation of lower bench and the addition of secondary lining, the stress of the structure was still mostly concentrated in the arch waist, arch foot and side wall, with the stress release ratios were about 80% 10% and 10%, and the maximum stress was 3.55 MPa, as shown in Figure 7D.

It can be seen from Figure 8 that during soil excavation at the left upper bench, the stress gradually concentrated at the left arch foot, with a maximum of 2.75 MPa. After the excavation of the left lower bench, the large stress was mainly concentrated in the arch waist, arch foot and side wall on the left side. In addition, a large stress appeared at the temporary support arch foot for the right upper bench, with the value of 2.86 MPa. With the removal of the temporary support and the construction of secondary lining, the response range of surrounding rock stress dwindled and eventually stabilize. This indicated that the stress was basically released and the maximum stress was 3.12 MPa, as



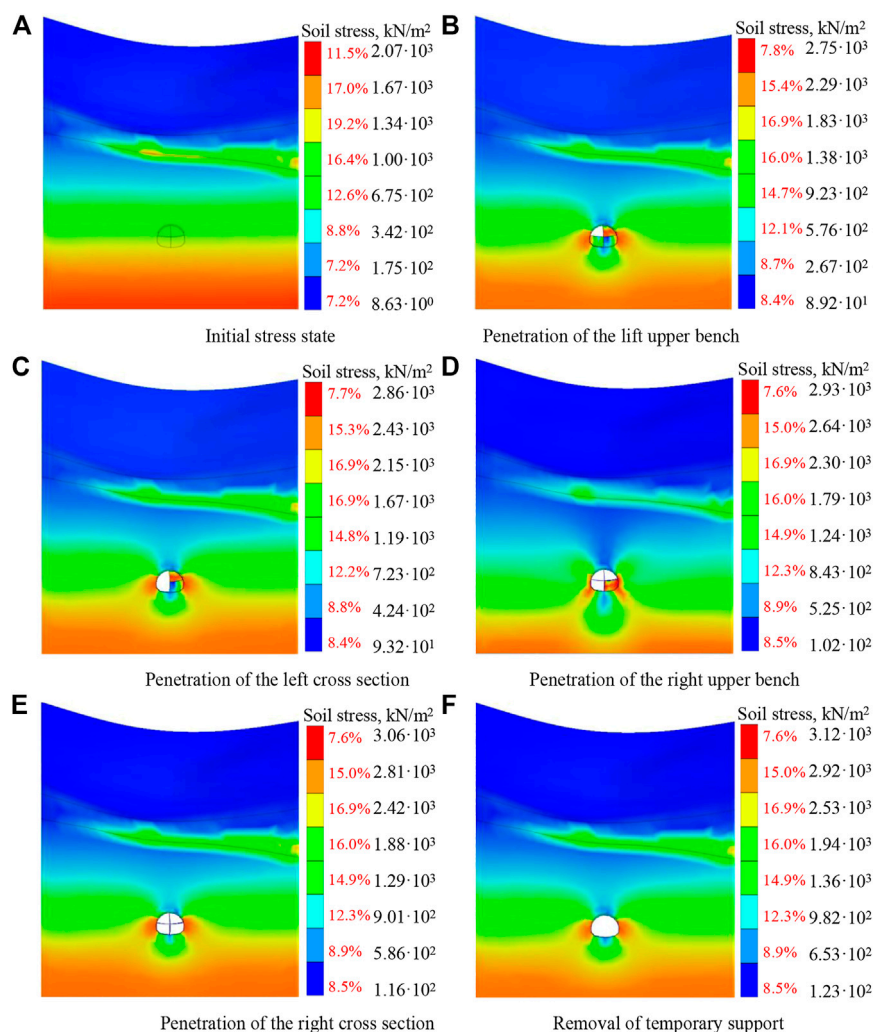


FIGURE 8

Stress of tunnel surrounding rock under CD method construction. (A) Initial stress state (B) Penetration of the lift upper bench. (C) Penetration of the left cross section (D) Penetration of the right upper bench. (E) Penetration of the right cross section (F) Removal of temporary support.

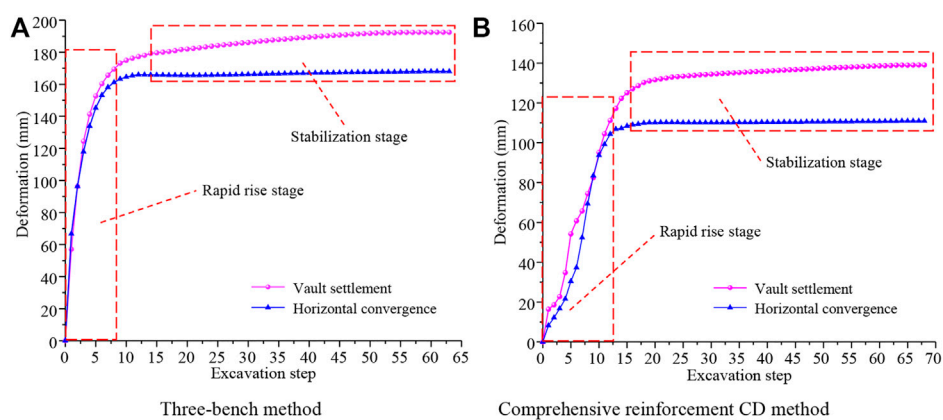
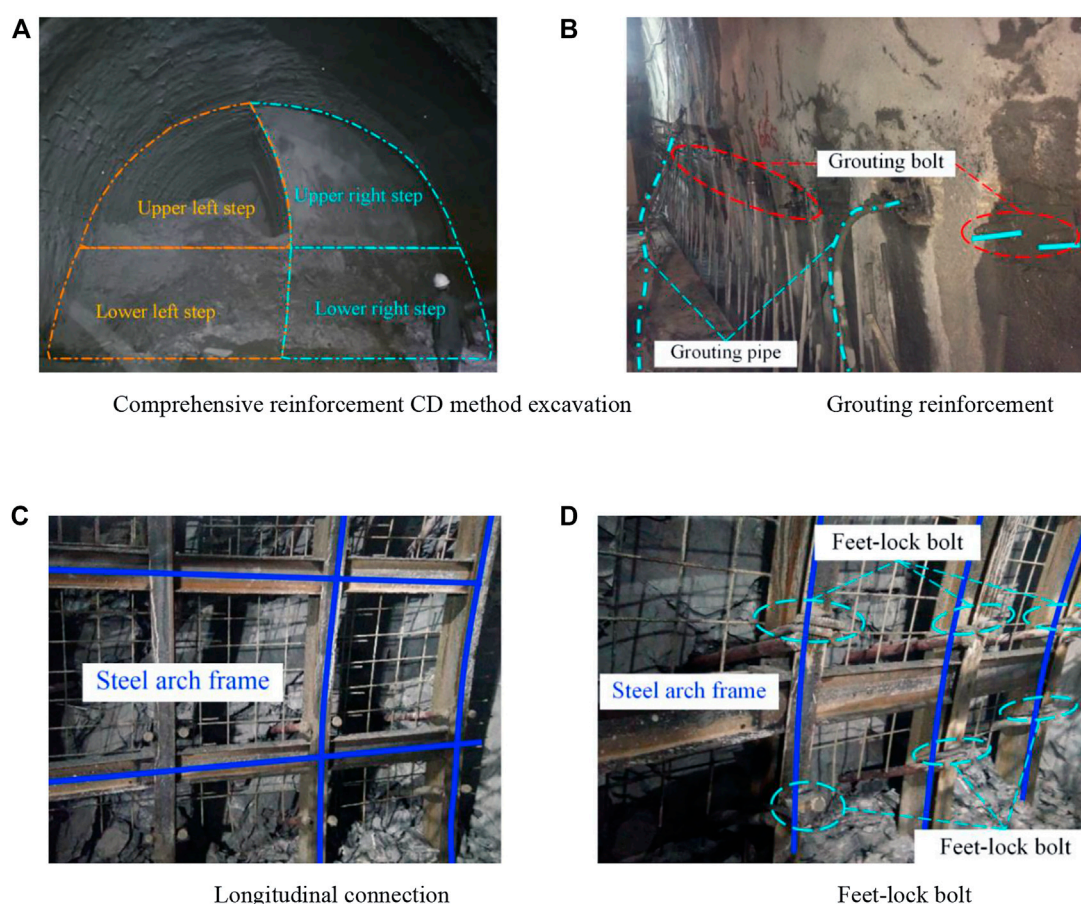


FIGURE 9

Deformation curves of surrounding rock under two working conditions. (A) Three-bench method (B) CD method.

TABLE 3 Comparison of surrounding rock stress and deformation.

Excavation method	Stress (kPa)		Displacement (mm)	
	Maximum value	Minimum value	Vault settlement	Horizontal convergence
Three Bench Method	3550	9	192.5	168.1
CD Method with integrated reinforcement	3120	12.3	148.6	110.9

**FIGURE 10**

Comprehensive reinforcement CD method construction and supporting structure. (A) CD method excavation. (B) Grouting reinforcement. (C) Longitudinal connection (D) Feet-lock bolt.

shown in Figure 8D. The comparative analysis of Figures 7, 8 showed that the stress distribution range of surrounding rock under the two working conditions was about 1.5 D (20 m), and the stress levels were roughly the same. After the tunnel penetrated, the maximum stress in the three-bench method was 3.55 MPa, which was 0.43 MPa higher than that in the CD method.

4.3 Deformation analysis

To better understand the control effect of different construction methods (three-bench method and CD method) on the large deformation of surrounding rock, the variation curves of vault

settlement and horizontal convergence of surrounding rock during the construction are drawn, as shown in Figure 9.

It is obvious from Figure 9 that the surrounding rock deformation can be well controlled by reasonable selection of construction method. As shown in Figure 9A, in the first 10 excavation steps, the vault settlement and horizontal convergence deformation increased rapidly to 172.5 mm and 161.3 mm owing to excavation of the soil, accounting for 89.6% and 95.9% of the total deformation, respectively. This indicated that the release of soil constraint had a significant effect on the stability of surrounding rock. With the construction of inverted arch frame and lining structure, the vault settlement and horizontal convergence gradually increased after the 15th excavation step (the whole tunnel section was excavated), which tended to stabilize around

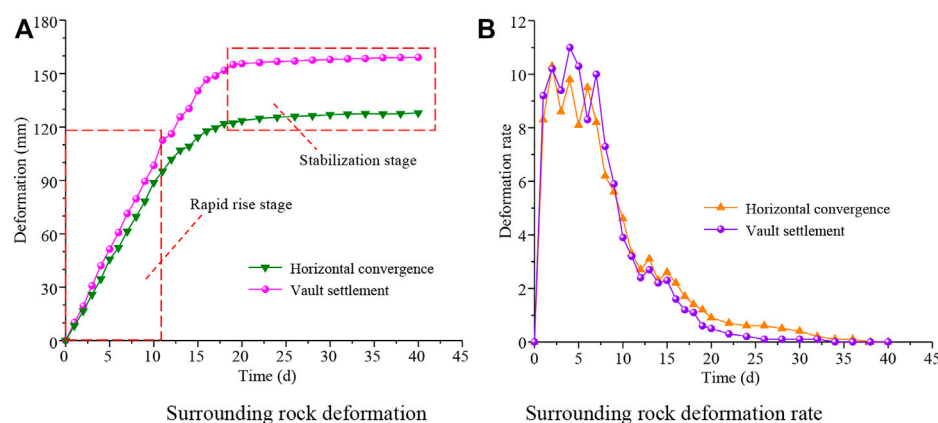


FIGURE 11
Surrounding rock deformation. (A) Surrounding rock deformation (B) Surrounding rock deformation rate.

the 30th step with the stayed value of 192.5 and 168.1 mm respectively. As shown in Figure 9B, the deformation rate of surrounding rock in the first 10 excavation steps was obviously lower than that in the three-bench method. However, the deformation was still developing rapidly, and the vault settlement and horizontal convergence surged to 99.4 mm and 98.1 mm, accounting for 66.9% and 88.5% of the total deformation, respectively. Due to the construction of temporary support and inverted arch, there were several deformation fluctuations. Subsequently, with the construction of the integrated reinforcement system and the lining structure, the deformation of the surrounding rock in the 10th to 15th excavation steps showed an obvious inflection point. After the 20th excavation step, the deformation tended to be stabilize. The vault settlement and horizontal convergence finally stabilized at 148.6 and 110.9 mm, respectively. This demonstrated the excellent effect of the integrated reinforcement CD method on controlling the deformation of surrounding rock. The specific results of the two methods are presented in Table 3.

It can be seen from Table 3 that the CD method outperformed greatly the three bench method in controlling the deformation of surrounding rock. It reduced the vault settlement and horizontal convergence deformation by 27.8% and 34.0%, respectively, and the surrounding rock deformation tended to be stable faster. For the structural stress, the stress on the second lining structure in the case of CD method was small, and the maximum stress was 13.8 lower than that of the three-bench method. In conclusion, the CD method can better control the large deformation of surrounding rock during the construction of large-section soft rock tunnel.

5 Analysis of measured results

5.1 Field application of reinforcement measures

On the basis of the CD method, measures such as reducing spacing and strengthening the longitudinal connection of steel arch frame, adding a feet-lock anchor pipe and a temporary inverted arch were adopted to constrain the surrounding rock deformation and ensure the construction safety. The site implementation of the reinforcement measures is shown in Figure 10.

5.2 Monitoring data analysis

Based on the measured data of ZK253+860 section (V-grade surrounding rock) at the Gelong Tunnel entrance, the deformation characteristics of surrounding rock and the stress variation of supporting structures were analyzed to verify the effectiveness of the proposed method.

5.2.1 Analysis of surrounding rock deformation

Figure 11 showed the time-history curves of the accumulated deformation and deformation rate of surrounding rock.

It can be seen from Figure 11 that the deformation rate of the surrounding rock was relatively large in the first 11 days of excavation. The vault settlement and horizontal convergence were 116.9 and 97.9 mm respectively, accounting for 73.53% and 76.62% of the

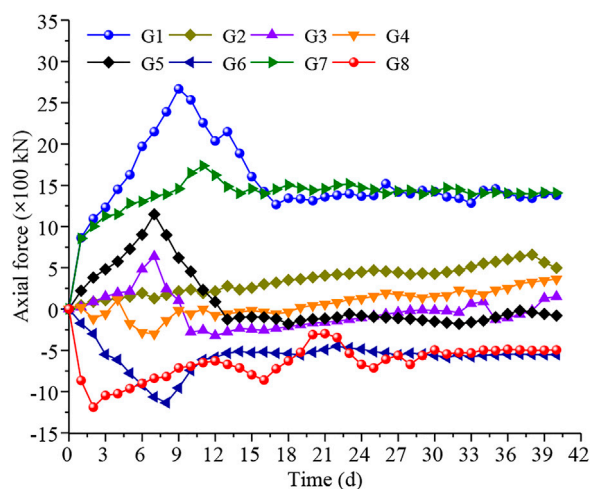


FIGURE 12
Time-history curve of axial force of steel arch frame at section ZK253+860.

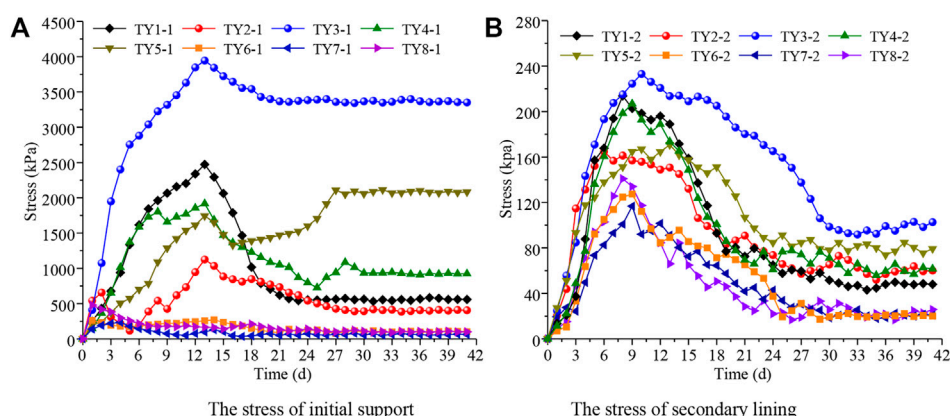


FIGURE 13

Time-history characteristic curves of surrounding rock stress on supporting structures. (A) The stress of initial support (B) The stress of secondary lining.

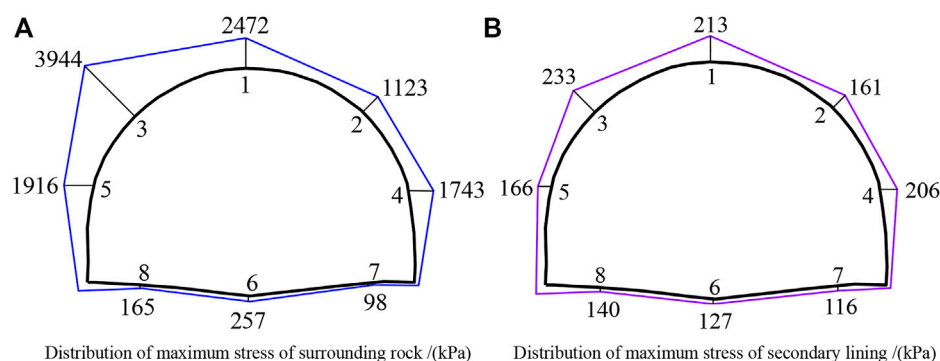


FIGURE 14

Distribution of maximum stress of surrounding rock and secondary lining. (A) Distribution of maximum stress of surrounding rock/(kPa) (B) Distribution of maximum stress of secondary lining/(kPa).

total deformation. In the following 12–18 days, the deformation rate declined significantly due to the construction of the integrated reinforcement system. After the 20th day, the deformation tended to be stable and the vault settlement and horizontal convergence finally stabilized at 159.1 and 127.9 mm respectively. The measured results were slightly larger than the numerical results (as shown in Figure 9B) due to uncertainties in the construction, while, the difference between them was quite small. The surrounding rock deformation in both results tended to stabilize in roughly the same time, indicating that the CD method proposed in this paper was feasible and very effective.

5.2.2 Axial force analysis of steel arch frame

The real-time axial force of the steel arch frame at the ZK253+860 section were collected, based on which the time-history variation curve was drawn (positive for tension and negative for compression), as shown in Figure 12.

It can be seen from Figure 12 that the steel arch frame was subjected to tension in the whole process at the vault (G1), the right spandrel (G2) and the right side of inverted arch (G7). At the initial stage, the tensile stress rose in a roughly straight line.

Among them, the vault bore the largest tensile stress of 2775 kN, which stabilized at about 1500 kN after 16d. The steel arch frame was subjected to compressive stress at the left (G8) and middle (G6) of the inverted arch throughout the whole process, and the peak values of the two were relatively close. The maximum was 1250 kN, which basically stabilized at about 1500 kN after 27d. In the initial stage, the other parts of the steel arch were mainly subjected to tension. After the deformation of the surrounding rock lasted for about 12d, the steel arch began to bear a small compressive stress. From the stress distribution, the steel arch frame at the left half of the tunnel arch was subjected to larger stress, which was completely consistent with the deformation of the surrounding rock. At the same time, under the strong support of the integrated reinforcement system, the axial force of the steel arch frame was rapidly stabilized.

5.2.3 Stress analysis of surrounding rock and secondary lining

To investigate the stress characteristics of the supporting structure under the action of the integrated reinforcement system, the stress of initial support and secondary lining at section (ZK253+860) were

collected. And the time-history characteristic curves of the stress variation were drawn, as shown in Figure 13.

As can be seen from Figure 13, the surrounding rock stress on the supporting structures was generally large, which gradually stabilized after 25d of tunnel excavation. The proportion of initial support and secondary lining to bear the surrounding rock stress was about 8.9:1.1. It can be observed from Figure 13A that the initial support was subjected to uneven stress. Specifically, the pressure at the vault, left shoulder and right wall was large and the growth rate was fast. And they all reached the extreme values about 12 days after excavation, which were 2472 kPa, 39544 kPa, and 1916 kPa respectively. The left wall suddenly surged to a maximum on the 24th day and basically remained at 1743 kPa. With the continuous release of surrounding rock stress and the construction of comprehensive reinforcement system, the surrounding rock stress gradually tended to be stable. As can be seen from Figure 13B, the stress on the second lining also showed a trend of first increasing and then decreasing. However, the overall stress was far less than that on the initial support, and its maximum appeared at the left spandrel, which was only 233 kPa. Due to the strong bearing capacity of initial support, the surrounding rock stress born by the secondary lining was very small and evenly distributed. This proved that the initial support was of great significance to the safety of secondary lining structure, and that the proposed CD method could significantly reduce large deformation of soft rock tunnel.

Figure 14 shows the distribution of maximum stress of surrounding rock and secondary lining. It can be observed that the surrounding rock stress on the initial support was unevenly distributed, large on the left and small on the right. In particular, the vault, left spandrel, and left side wall bore larger stress and were prone to deformation and collapse, which was completely consistent with the field disaster situation.

6 Conclusion

In view of the large deformation of surrounding rock during the construction of large-section tunnel in soft rock strata, this paper conducted a case study based on Gelong Tunnel passing through carbonaceous slate. Through theoretical analysis and numerical simulation, this paper proposed the CD method with integrated reinforcement to control the large deformation of surrounding rock, and verified by on-site monitoring results. The main conclusions were as follows:

- (1) The CD excavation method supplemented by strengthening the longitudinal stiffness of the supporting structure and the integrity of the surrounding rock can well control the large deformation of soft rock tunnel. The vault settlement and convergence deformation of surrounding rock under CD method reduced by 27.8% and 34.0% respectively than three-bench method, and the value of stress on second lining structure was 13.8%, which could provide reference for the design and construction of similar projects.
- (2) The surrounding rock deformation was large in the early stage, and the vault settlement and horizontal convergence were 116.9 and 97.9 mm respectively, accounting for 73.53% and 76.62% of the total deformation. The deformation rate declined

significantly due to the construction of the integrated reinforcement system. The vault settlement and horizontal convergence finally stabilized at 159.1 mm and 127.9 mm respectively, indicating that the proposed method was feasible and effective in controlling the large deformation of surrounding rock.

- (3) The steel arch frame was subjected to tension in the whole process at the vault, the right spandrel and the right side of the inverted arch, and the vault bore the largest tensile stress of 2775 kN. By contrast, the steel arch frame was subjected to compressive stress at the left and middle of the inverted arch throughout the whole process, and the maximum was 1250 kN. For the stress distribution, the steel arch frame at the left half of the tunnel arch was subjected to larger stress, which was completely consistent with the deformation of the surrounding rock.
- (4) The surrounding rock stress on the supporting structures was generally large, and the proportion of initial support and secondary lining to bear the surrounding rock stress was about 8.9:1.1. The surrounding rock stress acting on the initial support was large on the left and small on the right. The stress on the second lining was evenly distributed and much smaller than that on the initial support, with the maximum of 120 kPa. This demonstrated that the initial support was of great significance to the safety of secondary lining structure, and the proposed CD method could significantly control the large deformation of soft rock tunnel.

Data availability statement

The original contributions presented in the study are included in the article/Supplementary Material, further inquiries can be directed to the corresponding authors.

Author contributions

ZN, overall control of the article research methods, indoor and outdoor tests and theoretical calculations. YW, theoretical calculation guide. SF, outdoor test data acquisition.

Funding

The present work was subsidized and supported by the National Natural Science Foundation of China (No. 52178393; No. 51578447), the Science and Technology Innovation Team of Shaanxi Innovation Capability Support Plan (No. 2020TD005), the Science and Technology Development Program of Shaanxi Provincial Department of Housing and Urban-rural Construction (No. 2019-K39), and the Special Project of Shaanxi Provincial Education Department (No. 20JK0709).

Acknowledgments

The financial supports are gratefully acknowledged and the data is available for the journal.

Conflict of interest

ZN was employed by XAUAT Engineering Technology Co., Ltd.

The remaining authors declare that the research was conducted in the absence of any commercial or financial relationships that could be construed as a potential conflict of interest.

References

- Bian, K., Liu, J., Liu, Z. P., Liu, S. G., Ai, F., Zheng, X. Q., et al. (2019). Mechanisms of large deformation in soft rock tunnels: A case study of huangjiazhai tunnel. *B Eng. Geol. Environ.* 78 (1), 431–444. doi:10.1007/s10064-017-1155-8
- Chen, F., Tang, C. A., Sun, X. M., Ma, T. H., and Du, Y. H. (2019a). Supporting characteristics analysis of constant resistance bolts under coupled static-dynamic loading. *J. Mt. Sci.-Engl* 16 (5), 1160–1169. doi:10.1007/s11629-018-5044-9
- Chen, Z. Q., He, C., Xu, G. W., Ma, G. Y., and Wu, D. (2019b). A case study on the asymmetric deformation characteristics and mechanical behavior of deep-buried tunnel in phyllite. *Rock Mech. Rock Eng.* 52 (11), 4527–4545. doi:10.1007/s00603-019-01836-2
- Dutta, P., and Bhattacharya, P. (2022). Stability of rectangular tunnels in weathered rock subjected to seepage forces. *Arab. J. Geosci.* 15 (1), 61. doi:10.1007/s12517-021-08817-2
- Fan, S. Y., Song, Z. P., Zhang, Y. W., and Liu, N. F. (2020). Case study of the effect of rainfall infiltration on a tunnel underlying the roadbed slope with weak inter-layer. *KSCE J. Civ. Eng.* 24 (5), 1607–1619. doi:10.1007/s12205-020-1165-0
- Froeh, G., Flora, M., Gaechter, W., Harpf, F., and Tautschnig, A. (2019). Application possibilities of a digital ground model in tunnel construction. *Bautechnik* 96 (12), 885–895. doi:10.1002/bate.201900080
- Guo, K., Xu, Y. P., and Li, J. F. (2018). Thrust force allocation method for shield tunneling machines under complex load conditions. *Autom. Constr.* 96, 141–147. doi:10.1016/j.autcon.2018.08.016
- Guo, X. L., Zhu, Y. Q., Tan, Z. S., Li, L., Li, A., and Yan, Y. T. (2021). Research on support method in soft rock tunnel considering the rheological characteristics of rock. *Arab. J. Geosci.* 14 (3), 2703. doi:10.1007/s12517-021-08635-6
- Hu, Z. P., An, X. X., Li, F. T., and Zhang, Y. H. (2022). The shape characteristics of circular tunnel surrounding rock plastic zone in the complex stress field. *Arab. J. Geosci.* 15 (2), 150. doi:10.1007/s12517-021-08567-1
- Jia, J. Q., Tenorio, V. O., Zhang, B. X., Li, M. Z., and Xin, C. P. (2022). Stability and reliability of a shallow tunnel in soft surrounding rock: Construction technology and prediction. *Arab. J. Geosci.* 15 (3), 289. doi:10.1007/s12517-022-09428-1
- Lei, D. X., Xie, L. L., and Wu, L. (2022). Three-dimensional collapse mechanism and failure probability analysis of deep-buried tunnel based on the upper bound theorem of limit analysis and Hoek-Brown failure criterion. *Arab. J. Geosci.* 15 (2), 139. doi:10.1007/s12517-021-09392-2
- Li, B., Ding, Q. F., Xu, N. W., Lei, Y. F., Xu, Y., Zhu, Z. P., et al. (2021). Erratum to: Mechanical response and stability analysis of rock mass in high geostress underground powerhouse caverns subjected to excavation. *J. Cent. South Univ.* 28 (3), 982. doi:10.1007/s11771-021-4659-0
- Li, Y. H., Wang, H. L., Zhao, Y., and Dong, J. (2022). Prediction of the vibration waveform of surface particles under the action of tunnel cutting blast. *Arab. J. Geosci.* 15 (1), 38. doi:10.1007/s12517-021-09311-5
- Liu, D. P., Zhang, D. L., Fang, Q., Sun, Z. Y., Luo, J. W., and Li, A. (2020). Field monitoring of the deformation and internal forces of the surrounding rock and support structures in the construction of a super-span high-speed railway tunnel-A case study. *Appl. Sci-Basel* 10 (15), 5182. doi:10.3390/app10155182
- Liu, N. F., Li, N., Li, G. F., Song, Z. P., and Wang, S. J. (2022). Method for evaluating the equivalent thermal conductivity of a freezing rock mass containing systematic fractures. *Rock Mechanics and Rock Engineering* 55 (12), 7333–7355. doi:10.1007/s00603-022-03038-9
- Lv, J. B., Li, X. L., Li, Z. R., and Fu, H. L. (2019). Numerical simulations of construction of shield tunnel with small clearance to adjacent tunnel without and with isolation pile reinforcement. *KSCE J. Civ. Eng.* 24 (1), 295–309. doi:10.1007/s12205-020-1167-y
- Niu, Z. L., Cheng, Y., Zhang, Y. W., Song, Z. P., Yang, G. Y., and Li, H. (2020). A new method for predicting ground settlement induced by pipe jacking construction. *Math. Probl. Eng.* 2020, 1–11. doi:10.1155/2020/1681347
- Niu, Z. L., Xu, J., Li, Y. F., Wang, Z. F., and Wang, B. (2021). Strength deterioration mechanism of bentonite modified loess after wetting-drying cycles. *Scientific Reports*, 1–17. doi:10.1038/s41598-022-06962-6
- Parisio, F., Vilarrasa, V., and Laloui, L. (2018). Hydro-mechanical modeling of tunnel excavation in anisotropic shale with coupled damage-plasticity and micro-dilatant regularization. *Rock Mech. Rock Eng.* 51 (12), 3819–3833. doi:10.1007/s00603-018-1569-z
- Qin, Y. W., Lai, J. X., Yang, T., Zan, W. B., Feng, Z. H., and Liu, T. (2022). Failure analysis and countermeasures of a tunnel constructed in loose granular stratum by shallow tunnelling method. *Engineering Failure Analysis* 141, 106667. doi:10.1016/j.engfailanal.2022.106667
- Song, Z. P., Cheng, Y., Tian, X. X., Wang, J. B., and Yang, T. T. (2020). Mechanical properties of limestone from Maixi tunnel under hydro-mechanical coupling. *Arab. J. Geosci.* 13 (11), 402. doi:10.1007/s12517-020-05373-z
- Song, Z. P., Shi, G. L., Zhao, B. Y., Zhao, K. M., and Wang, J. B. (2019). Study of the stability of tunnel construction based on double-heading advance: Construction method. *Adv. Mech. Eng.* 12 (1), 168781401989696. doi:10.1177/1687814019896964
- Tian, X. X., Song, Z. P., and Wang, J. B. (2019). Study on the propagation law of tunnel blasting vibration in stratum and blasting vibration reduction technology. *Soil Dyn. Earthq. Eng.* 126, 105813. doi:10.1016/j.soildyn.2019.105813
- Xie, Z. Z., Zhang, N., Feng, X. W., Liang, D. X., Wei, Q., and Weng, M. Y. (2019a). Investigation on the evolution and control of surrounding rock fracture under different supporting conditions in deep roadway during excavation period. *Int. J. Rock Mech. Min.* 123, 104122. doi:10.1016/j.ijrmms.2019.104122
- Yao, Y., Lai, H. P., Zhang, Q., and Liu, Y. Y. (2021). Prediction of plastic and fractured zone extent around deep circular tunnel subjected to spatial constraint effect. *Arab. J. Geosci.* 14 (20), 2098. doi:10.1007/s12517-021-08428-x
- Yu, W. J., and Li, K. (2020). Deformation mechanism and control technology of surrounding rock in the deep-buried large-span chamber. *Geofluids* 2020, 1–22. doi:10.1155/2020/8881319
- Zhang, H., Chen, L., Zhu, Y. M., Zhou, Z. L., and Chen, S. G. (2019). Stress field distribution and deformation law of large deformation tunnel excavation in soft rock mass. *Appl. Sci-Basel* 9 (5), 865. doi:10.3390/app9050865
- Zhang, Q., Song, Z. P., Li, X. L., Wang, J. B., and Liu, L. J. (2019). Deformation behaviors and meso-structure characteristics variation of the weathered soil of Pisha sandstone caused by freezing-thawing effect. *Cold Reg. Sci. Technol.* 167, 102864. doi:10.1016/j.coldregions.2019.102864
- Zhang, Y. W., Fan, S. Y., Yang, D. L., and Zhou, F. (2022a). Investigation about variation law of frost heave force of seasonal cold region tunnels: A Case Study. *Front. Earth Sci* 9, 806843. doi:10.3389/feart.2021.806843
- Zhang, Y. W., Song, Z. P., and Weng, X. L. (2022b). A constitutive model for loess considering the characteristics of structurality and anisotropy. *Soil Mechanics and Foundation Engineering* 59 (1), 32–43. doi:10.1007/s11204-022-09781-z
- Zhao, Z. H., Ma, Q., Tan, Y. L., and Gao, X. J. (2019). Load transfer mechanism and reinforcement effect of segmentally yieldable anchorage in weakly consolidated soft rock. *Simul-T Soc. Mod. Sin.* 95 (1), 83–96. doi:10.1177/0037549718770284

Publisher's note

All claims expressed in this article are solely those of the authors and do not necessarily represent those of their affiliated organizations, or those of the publisher, the editors and the reviewers. Any product that may be evaluated in this article, or claim that may be made by its manufacturer, is not guaranteed or endorsed by the publisher.



OPEN ACCESS

EDITED BY

Naifei Liu,
Xi'an University of Architecture and
Technology, China

REVIEWED BY

Jinting Huang,
Xi'an University of Science and
Technology, China
Zizhao Zhang,
Xinjiang University, China

*CORRESPONDENCE

Zongyuan Ma,
✉ mzy_gogo@hotmail.com

SPECIALTY SECTION

This article was submitted to
Environmental Informatics and Remote
Sensing,
a section of the journal
Frontiers in Earth Science

RECEIVED 10 December 2022

ACCEPTED 28 December 2022

PUBLISHED 10 January 2023

CITATION

Ma Z, Tang S and Yang Z (2023), Numerical
analysis of metro station pit dewatering
and its influence.
Front. Earth Sci. 10:1120772.
doi: 10.3389/feart.2022.1120772

COPYRIGHT

© 2023 Ma, Tang and Yang. This is an
open-access article distributed under the
terms of the [Creative Commons
Attribution License \(CC BY\)](#). The use,
distribution or reproduction in other
forums is permitted, provided the original
author(s) and the copyright owner(s) are
credited and that the original publication in
this journal is cited, in accordance with
accepted academic practice. No use,
distribution or reproduction is permitted
which does not comply with these terms.

Numerical analysis of metro station pit dewatering and its influence

Zongyuan Ma^{1,2*}, Shitong Tang² and Zhiguo Yang³

¹Guizhou Communications Polytechnic, Guiyang, Guizhou, China, ²Xi'an University of Technology, Xi'an, Shaanxi, China, ³China Railway First Survey and Design Institute Group Co., Ltd., Xi'an, Shaanxi, China

The underground water level in Xi'an city is generally shallow, and the excavation of the deep foundation pit mainly needs underground water dewatering. The ground deformation due to the dewatering and its influences should be fully analyzed. The empirical formula estimates the water inflow of the foundation pit, and the process of dewatering and metro station construction is simulated via the finite element method and the theory of soil consolidation according to the field investigation and survey data of the natural geological and hydrological environment. The time of water level falling and recovery, ground settlement, and strata deformation caused by pit dewatering and excavation are predicted. The analysis results of the ground settlement are within reasonable limits and close to the previous metro projects. Finally, the influence of groundwater dewatering on Xi'an Metro Line 14 is discussed. The settlement induced by dewatering for constructing a metro station in the sandy stratum is relatively small, and the loess stratum has the most significant dewatering settlement. The proportion of settlement due to dewatering of the station construction in the loess stratum is nearly 1/3 versus the total land subsidence.

KEYWORDS

metro station, foundation pit, groundwater dewatering, hydraulic discharge prediction, consolidation deformation

1 Introduction

The construction of urban rail traffic is the megacity's critical development target of public transport engineering, and it plays an important role in alleviating urban traffic congestion (Sun et al., 2015). Subway or metro is an emerging urban rail transit mode with the characteristics of being fast and comfortable, less occupation of land resources, large passenger volume, less pollution, and high safety performance. Xi'an metro has entered a new period of vigorous development in recent years, and most of the main lines are built in the downtown area. However, a deep foundation pit must be excavated before the construction of the metro station. The groundwater should be dewatered before the excavation of the foundation pit if the groundwater level exceeds the bottom of the pit. The groundwater extraction should be carried out during the foundation pit construction to reduce the shallow underground water levels (referred to as dewatering) (Shaqour and Hasan, 2008; Pujades et al., 2014; Attard et al., 2016). The seepage of the foundation pit slope and basement will be prevented effectively by dewatering the groundwater level below the bottom of the foundation pit (Attard et al., 2016). Otherwise, the soil strength and the stability of the foundation pit can also be enhanced by decreasing the soil water content. Thus, studying the influence of foundation pit dewatering on the project site and surrounding environment is necessary. Currently, empirical formulas and numerical simulation methods are often used to analyze the influence of the deformation of strata and the land subsidence caused by dewatering on the surrounding buildings and underground pipelines (Zhou et al., 2010; Wang et al., 2013; Pujades et al., 2017; Wang et al., 2022). The deep foundation pit dewatering and ground settlement are efficiently analyzed via the water-soil coupling consolidation

theory and three-dimensional finite element method. Numerical simulation is an essential method for researching the problems of foundation pit dewatering. This paper uses the finite element method to analyze the consolidation deformation of the foundation after groundwater extraction of a deep foundation pit excavation before the construction of the metro station.

2 Engineering background and geological conditions

Line 14 is an east-west subway line in the north of Xi'an city and an express line in the Xi'an subway network. The geological environment conditions along line 14 are relatively simple, with no geological disasters appearing, such as collapse, landslide, debris flow, ground collapse, or ground cracks. The depth of the groundwater level is about 10–20 m. The thickness of the submersible aquifer is about 50–80 m, and the annual variation of the groundwater level is about 1–3 m. The groundwater recharge mainly includes lateral runoff and atmospheric dewatering, and the discharge methods are runoff discharge, artificial extraction, and

evaporation. The underground water level should be declined before the pit excavation to ensure the safety of metro station construction. However, groundwater dewatering will affect the groundwater level along the subway for a certain period and may cause local land subsidence and deformation (Roy and Robinson, 2009; Wang et al., 2012; Zeng et al., 2022).

2.1 Stratum characteristics

The landform along Metro Line 14 and the Cross section the Wei River terraces are shown in Figures 1, 2, respectively. The geomorphic units along Line 14 are as follows: the floodplain of the Wei River, the terrace of the Wei River, the floodplain of the Ba River, and the first and second terraces of the Ba River. The detailed characteristics of the strata along the Line 14 are described respectively from the surface as follows. Wei River's floodplain: mixed fill, Quaternary alluvial silty clay, Quaternary alluvial silt, and interbedded sand. The stratum of the first terraces of the Wei River are as follows: mixed fill soil, Quaternary alluvial loess-like soil, Quaternary alluvial soil, and fine sand. Ba River's floodplain: mixed fill soil, Quaternary alluvial loessial soil,

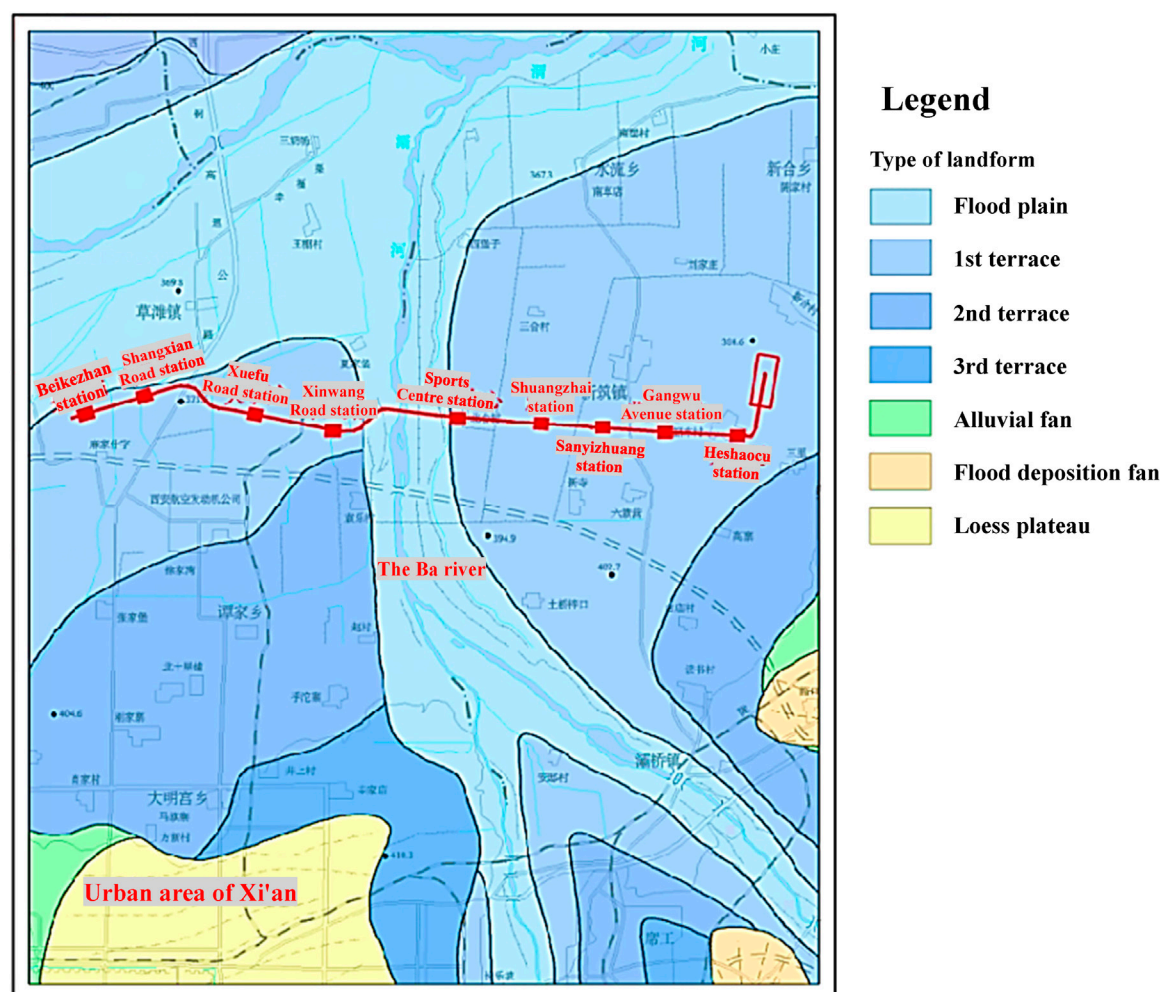


FIGURE 1
Topography along metro Line 14 of Xi'an.

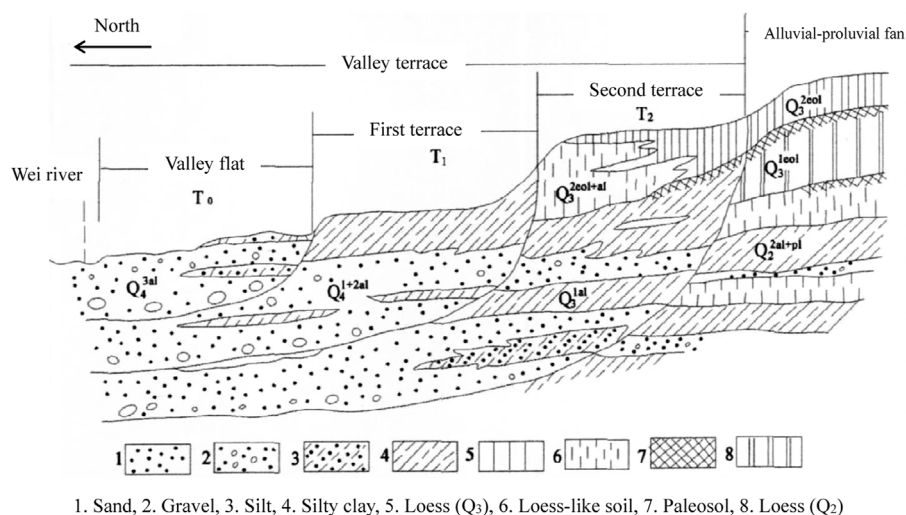


FIGURE 2

Cross section of Wei River terraces. 1. Sand, 2. Gravel, 3. Silt, 4. Silty clay, 5. Loess (Q₃), 6. Loess-like soil, 7. Paleosol, 8. Loess (Q₂).

TABLE 1 Summary table of underground water depth and permeability coefficient of metro stations on Line 14.

Station	Buried depth of groundwater (m)	Elevation of groundwater level (m)	Suggested value of permeability coefficient (m/d)
Shangxian Road station	12.00–13.50	358.06–359.06	25.0
Xuefu Road station	10.80–12.90	360.78–362.87	27.0
Xinwang Road station	13.60–14.30	361.96–362.78	22.0
Sports Centre station	11.70–13.30	363.30–364.60	27.0
Shuangzhai station	13.00–18.30	362.31–362.84	27.0
Sanyizhuang station	15.00–18.40	362.04–363.47	27.0
Gangwu Avenue station	19.10–21.00	361.23–361.81	23.0
Heshaoou station	22.00–25.50	359.34–361.34	25.0

Quaternary alluvial soil, and gravel. The first and second terraces of the Ba river: mixed fill soil, Quaternary alluvial loessial soil, Quaternary alluvial soil, and gravel.

2.2 Hydrogeological characteristics

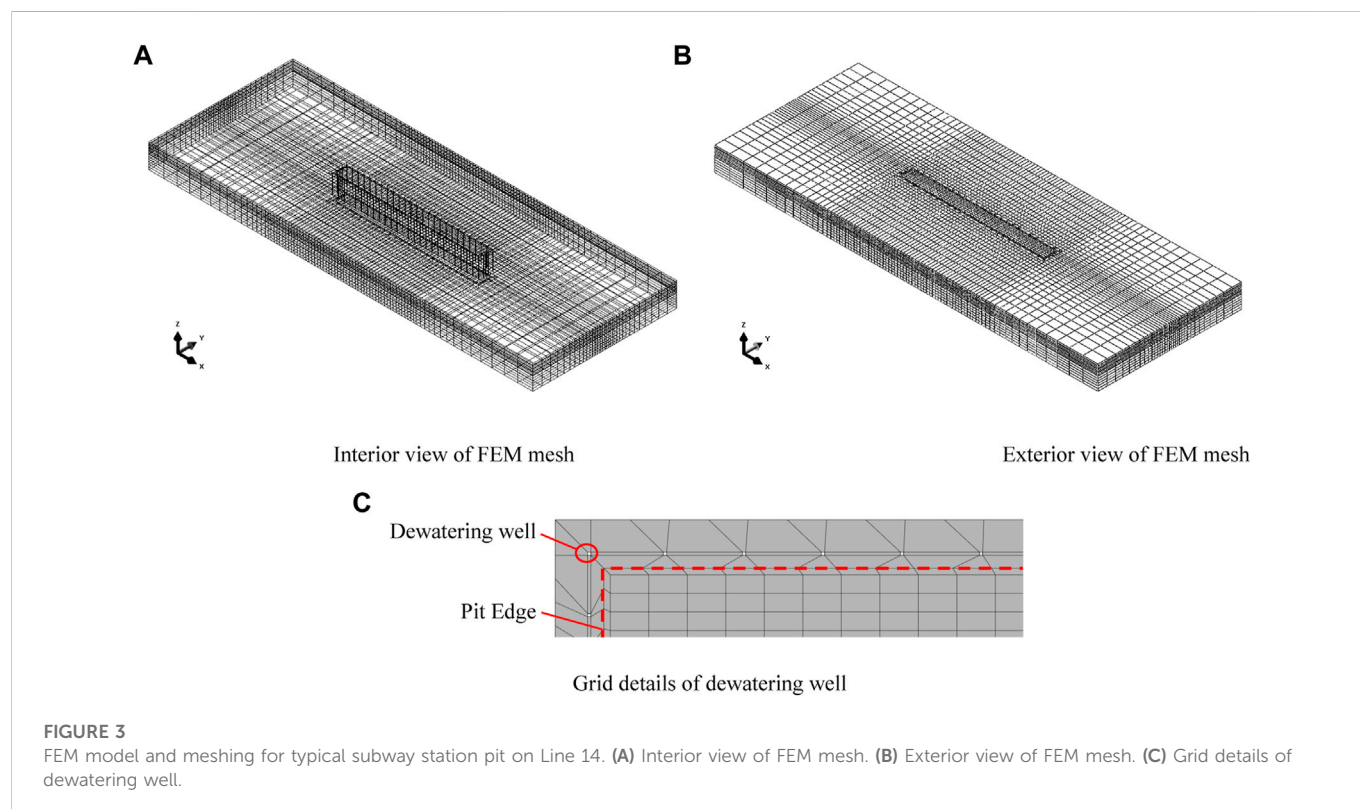
The aquifers along metro Line 14 are mainly submersibles. The alluvial and diluvial strata are composed of sand and gravel, partially interspersed with clay interlayer. The groundwater depth along Line 14 is generally shallow, and the average permeability coefficient of the strata ranges from 15 to 60 m/d. The first terrace of Wei River: the buried depth of the groundwater level is 10.0–14.5 m. The primary aquifer is medium coarse gravel sand with strong water permeability. Ba River Valley and floodplain: the buried depth of the groundwater level is about 5.0–10.0 m, and the aquifer is the sand and gravel layer

with high permeability. Wei River terrace: the groundwater depth is 12.5–26.0 m (gradually deepening from west to east). The primary aquifer is a medium coarse gravel layer with high permeability. The underground water depth and permeability coefficient of metro stations on Line 14 are listed in Table 1.

The atmospheric dewatering and irrigation infiltration mainly recharge the groundwater along Line 14, and the Ba River and groundwater are complementary in the wet season. The whole region of Line 14 is recharged by atmospheric dewatering, and the dynamic water level is consistent with the dewatering curve. The water level is shallow buried, and the infiltration volume is significant in rainy years or seasons. Generally, the lithologic grain size becomes finer with the increase of groundwater depth, and the permeability coefficient values will decrease. The lateral recharge of the Ba River will influence Line 14, which crosses the Ba River in the section between Xinwang Road and Sports Center.

TABLE 2 Estimation of water inflow of metro stations pit on Line 14.

Station	Geomorphic unit	Dewatering well	Drop of water level (m)	Prediction of water inflow (m ³ /d)
Shangxian Road station	Valley flat of Wei river	55	6.0	6,500
Xuefu Road station	First terrace of Wei river	34	6.5	4,253
Xinwang Road station	First terrace of Wei river	35	5.5	3,170
Sports Centre station	First terrace of Ba river	20	13.0	3,537
Shuangzhai station	First terrace of Ba river	52	5.0	5,980

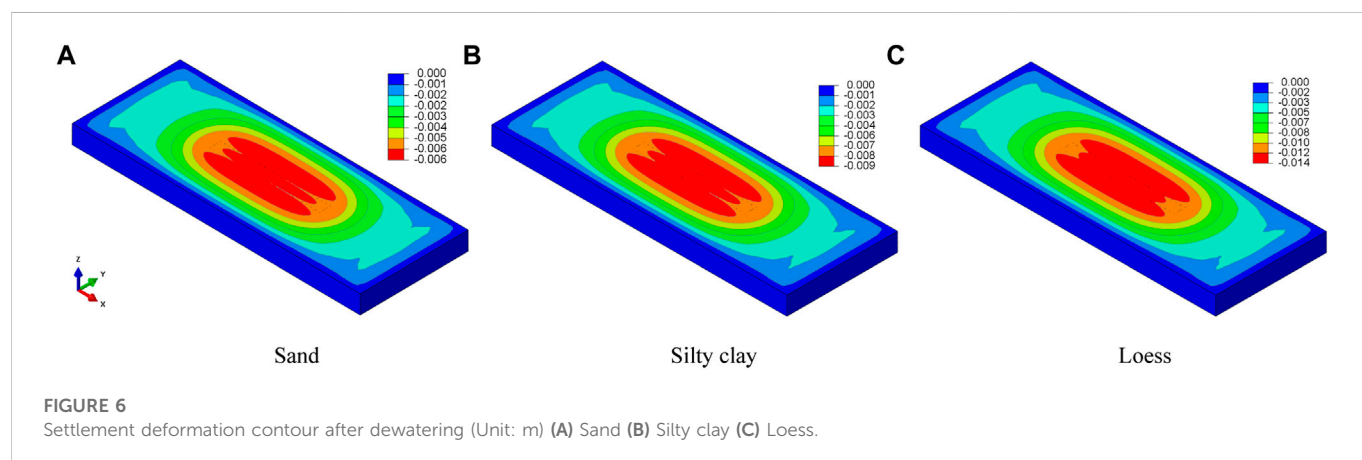
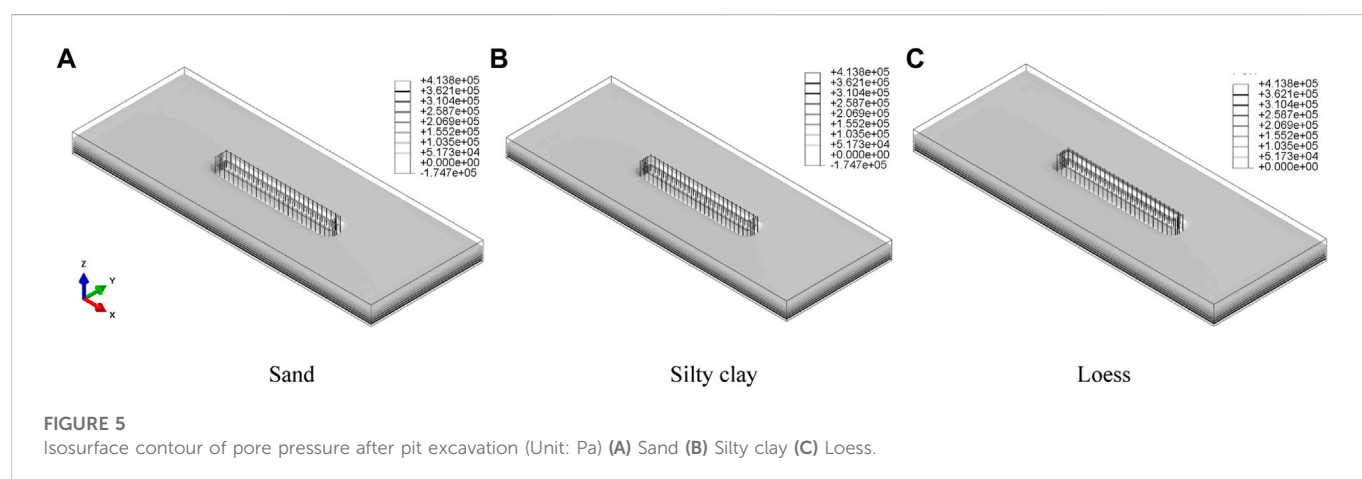
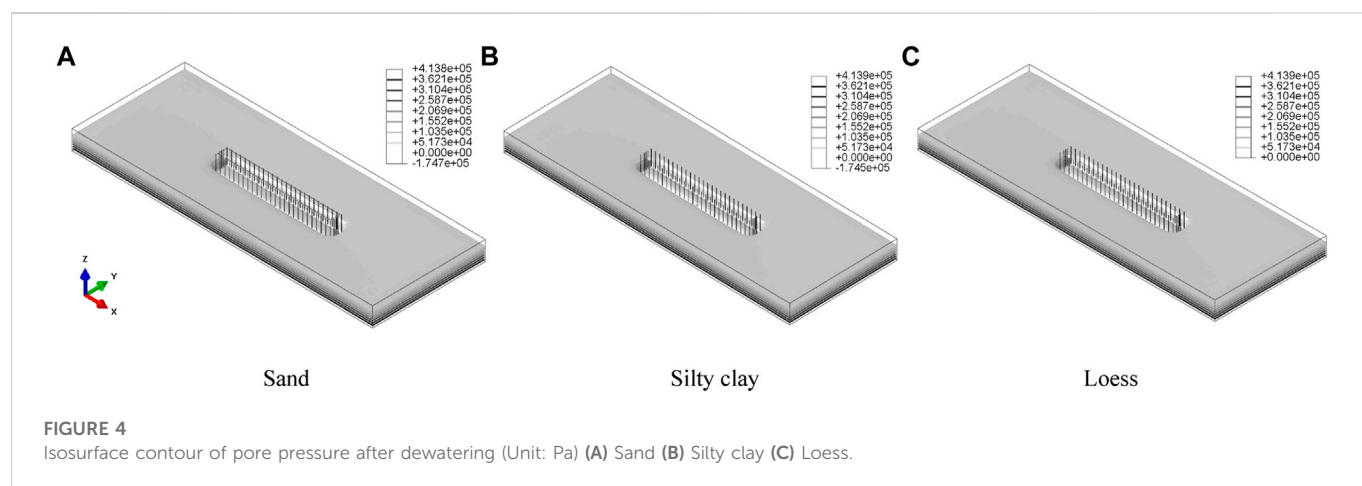
**TABLE 3** Parameter value of soil for dewatering and consolidation analysis.

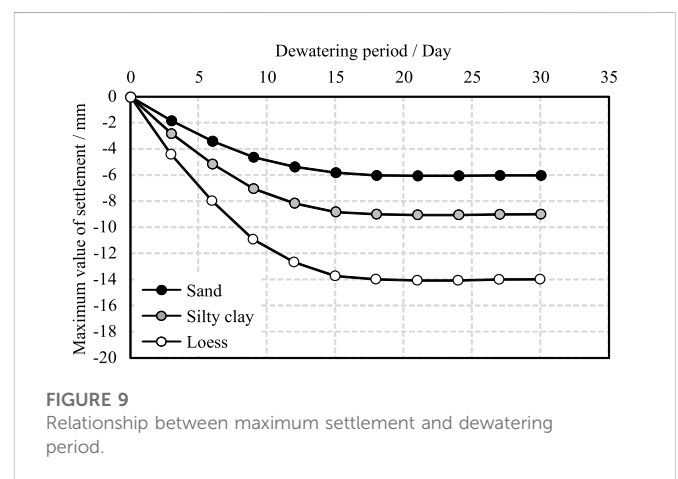
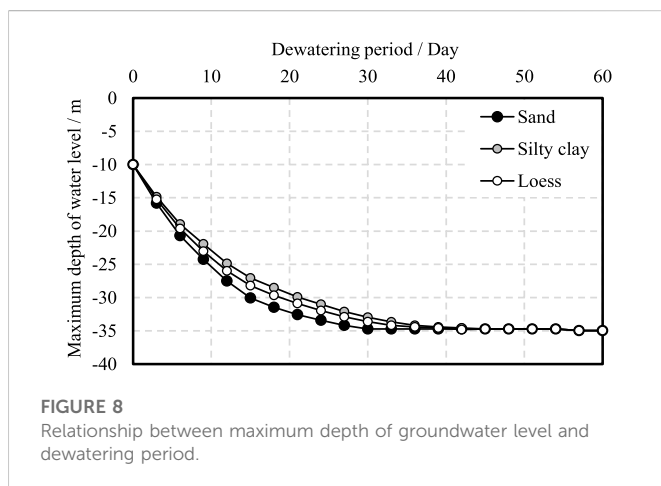
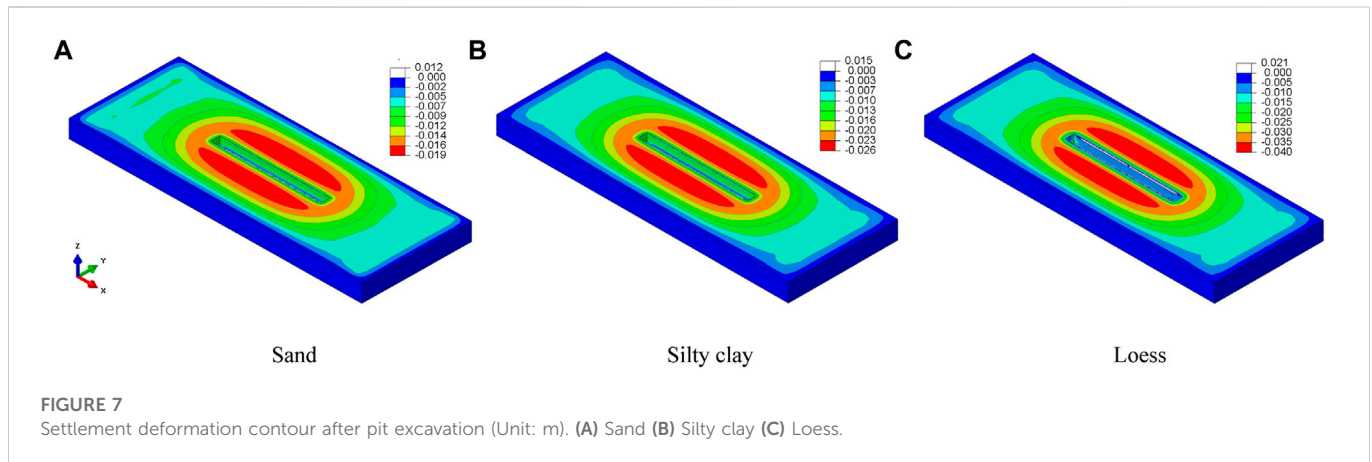
Soil layer	Density (g/cm ³)	Liquid limit w_L (%)	Void ratio e	η (g/s-cm)	s (cm ⁻¹)	Modulus of compression E_s (MPa)	Cohesion C (kPa)	Friction angle φ (°)	Permeability coefficient k (cm/s)
Medium sand	1.85	10.8	0.606	1.01	3,000	10.8	0	32.5	3.34E-05
Silty clay	1.93	26.9	0.748	1.175	60,000	8.3	28	21.0	6.64E-08
Loess	1.90	22.7	0.709	1.088	40,000	8.1	29	20.0	1.63E-07

3 Hydraulic discharge prediction of metro line 14 dewatering

Xi'an metro Line 14 project has a total length of 14.4 km, and all station construction needs well dewatering. The hydraulic discharge of stations is estimated via the formula suggested in

the standard of JGJ 120-2012. The stations of metro Line 14 are generally elongated, with a length of 164–527 m and a width of 19.7–24.7 m. The spacing of dewatering wells is generally 15–20 m, and the wells are arranged around the foundation pit. The water inflow of the foundation pit is close to a fixed value when the groundwater level is controlled to a certain depth via





foundation pit pumping, i.e., the pumped and the replenishment water reach a dynamic balance. The total water inflow of the metro station foundation pit is estimated using the calculation formula of the foundation pit water inflow of the non-integral well (see appendix E of the literature (Ministry of housing and urban-rural development of the People's Republic of China, 2012)). The group wells are simplified according to a whole large well for this formula. The calculation formula is as follows:

$$Q = \pi k \frac{H^2 - h^2}{\ln\left(1 + \frac{R}{r_0}\right) + \frac{h_m - l}{l} \ln\left(1 + 0.2 \frac{h_m}{r_0}\right)} \quad (1)$$

Where Q is the total water inflow of foundation pit dewatering (m^3/d); k is the permeability coefficient of foundation (m/d); H is the submersible aquifer thickness (m); R is the influence radius (m); r_0 is the equivalent radius of foundation pit (m), $r_0 = \sqrt{A/\pi}$, where A is the pit area (m^2); h is the height of water level in the foundation pit after dewatering (m); l is the length (m) of the inlet water part of the filter, $h_m = (H + h)/2$. The water inflow estimation for the foundation pit of Line 14 station is shown in Table 2.

4 Numerical simulation of dewatering of metro station's pit

The Cartesian coordinate system is used to analyze this problem. The vertical direction is the z -axis, and the vertical direction is positive. The length, width, and depth of a typical metro station of Line 14 are 300 m, 25 m, and 20 m, respectively. The spacing and depth of the dewatering well are 20 m and 40 m, respectively. The horizontal distance between the well and the foundation pit boundary is 2 m, the thickness of the overlying layer on the metro station is 3 m, the rest is silty clay, and the depth of the groundwater level is 10 m. The model of the metro station foundation pit is divided into more than 60,000 eight-node hexahedral elements. The implicit consolidation calculation module of finite element software ABAQUS is used to analyze the problem of metro station pit dewatering (Simulia, 2017). The calculation model and element division of numerical simulation of foundation pit dewatering and station construction are shown in Figure 3.

In this paper, the permeability coefficient values for foundation soil are estimated by the modified Corson-Karman empirical formula (Singh and Wallender, 2008; Dang et al., 2015). The calculation formula is as follows:

TABLE 4 Summary of settlement deformation triggered by dewatering and pit excavation of metro station pit on Line 14.

Dewatering period (Day)	Groundwater level recovery period (Day)	Maximum settlement due to dewatering (mm)	Maximum settlement due to dewatering and pit excavation (mm)	Proportion of settlement due to dewatering
35	31	6/4 (Numerical analysis/Empirical formula)	19 (Numerical analysis)	31.6% (Numerical analysis)
49	48	9/5 (Numerical analysis/Empirical formula)	26 (Numerical analysis)	34.6% (Numerical analysis)
45	40	14/8 (Numerical analysis/Empirical formula)	39 (Numerical analysis)	35.0% (Numerical analysis)

$$k = \frac{c_2 \rho_{wz} (e - e_0)^3}{s^2 \eta (1 + e - e_0)} \quad (2)$$

Where c_2 is the shape coefficient of soil particles (about .125), s is the specific surface area of soil particles, η is the viscosity coefficient of pore water, ρ_{wz} is the density of free pore water (about 1.0 g/cm³), e is the pore ratio of the soil, e_0 is the ineffective pore ratio of the soil (depend on the liquid limit of the soil).

Three types of foundation soil (medium sand, silty clay, and loess) are used to analyze the influence of dewatering and consolidation deformation. The parameter value of soil for dewatering and consolidation analysis is shown in Table 3. The boundary conditions of the numerical model are set as follows: normal constraint boundary conditions are applied around the model, and three directions constraints are applied on the bottom surface of the model. A flow boundary is applied to the pumping well, and a zero pore pressure boundary is applied to the groundwater level (infiltration surface) (Wang et al., 2017; Wang et al., 2018; Zeng et al., 2021). The finite element method is used to calculate and analyze the dewatering and construction process of the typical station of Line 14. The numerical simulation predicts the time of groundwater level drop and the ground settlement (triggered by dewatering and pit excavation). The linear elastic constitutive model is used to calculate and analyze the concrete structure of the station. The density is 2.5 g/cm³, the elastic modulus is 43 GPa, and the Poisson's ratio is .188.

5 Influence analysis of dewatering for loess metro station pit

The contour of pore water pressure and settlement deformation of the strata after dewatering and foundation pit excavation with sandy soil, silty clay, and loess stratum is shown in Figures 4–7. Where the pore water pressure of the stratum below the groundwater level before pit excavation is shown in the three-dimensional isosurface contour, the pore pressure unit is Pa, and the settlement unit is m.

The drop in water level mainly triggers the strata settlement due to the process of dewatering, and the settlement after station construction is mainly triggered by the pit excavation and supporting structure deformation. According to the theoretical calculation results, the settlement caused by the dewatering of each line project generally accounts for 10–40% of the total settlement. The finite element method is used to simulate the dewatering and construction of the typical metro station of Line 14. The analysis results show that the ground settlement is generally about 10–30 mm after the dewatering. The settlement value shows a trend of low in the west and high in the east along the metro line. The land subsidence of the metro station on the

second terrace of the Ba River (loess stratum) due to dewatering is more significant than the first terrace of the Ba River (silty clay stratum). The flood plain and the first terrace of the Wei River (sandy soil stratum) have the lowest ground settlement after the dewatering. These results are mainly related to the soil properties of the stratum in this region. The loess stratum is prone to deformation after water loss due to the distribution of large pores. In contrast, the sand stratum will be compacted after dehydration, and the deformation of the stratum will be reduced. The finite element calculation results show that the silty clay stratum has the longest groundwater dewatering and recovery time, and the sandy soil stratum is the shortest. The relationships between the settlement deformation and underground water level of the typical metro station with sandy soil, silty clay, and loess stratum are shown in Figures 8, 9.

Based on the previous data, the finite element method is used to simulate the dewatering and construction of a typical station of Xi'an metro Line 14. According to the theoretical calculation results, the settlement caused by the dewatering before the metro station construction generally accounts for 10–40% of the total settlement. The predicted analysis shows that the ground settlement of Line 14 after the dewatering is generally about 10–30 mm. Most of the settlements for the metro construction are due to the deformation caused by underground excavation. A small part of the settlements is related to the influence of pipelines and basement deformation. According to the previous experience of the Xi'an metro, the settlement deformation due to the metro construction is within the controllable range. The formula suggested in the literature (Ministry of housing and urban-rural development of the People's Republic of China, 2012) is adopted to calculate the settlement deformation caused by foundation pit dewatering of a pumping well in a homogeneous aquifer (Xu et al., 2019; De Caro et al., 2020), and the estimation formula is as follows:

$$S = \psi_w \sum_{i=1}^n \frac{\Delta \sigma'_{zi} \Delta h_i}{E_{si}} \quad (3)$$

where s is the amount of formation deformation caused by dewatering (m), the empirical settlement coefficient ψ_w should be calculated according to local engineering experience, and it is better to obtain $\psi_w=1$ in general. $\Delta \sigma'_{zi}$ is the additional effective stress (kPa) at the middle point of the first layer of the ground caused by dewatering. For cohesive soil, the additional effective stress should be taken under the consolidation degree of soil at the end of dewatering. The thickness of Δh_i the i th layer soil (m); E_{si} is the compression modulus (kPa) of the i th layer soil, and n indicates the number of strata (In this paper, $n = 2$). Table 4 shows the summary results of ground settlement deformation caused by dewatering and construction of a typical station (loess strata) of metro Line 14, which is predicted by using the finite element method and empirical calculation formula. The

ground settlement induced by pit dewatering also can be further analyzed via numerical methods taking the coupled thermo-hydro-mechanical influence into account (Liu et al., 2022a; Liu et al., 2022b; Zhang et al., 2022).

6 Conclusion

Based on the dewatering problem of the foundation pit of Xi'an Metro Line 14, the finite element method is used to analyze the influence of the foundation pit dewatering on land subsidence and ground deformation. The results show that the ground settlement induced by dewatering obtained by the numerical simulation are close to the results yield by the empirical formula suggested by the standard. The groundwater level in the sandy stratum has the fastest drops and recovers rate during dewatering compared with the clay (silty clay and loess) stratum. The sandy stratum's settlement induced by dewatering is relatively small, and the loess stratum has the most significant settlement induced by dewatering among the three kinds of strata. The proportion of settlement due to dewatering of the station construction in loess stratum is nearly 1/3 versus the total land subsidence.

Data availability statement

The original contributions presented in the study are included in the article/Supplementary Material, further inquiries can be directed to the corresponding author.

References

- Attard, G., Winiarski, T., Rossier, Y., and Eisenlohr, L. (2016). Review: Impact of underground structures on the flow of urban groundwater. *Hydrogeology J.* 24 (1), 5–19. doi:10.1007/s10040-015-1317-3
- Dang, F. N., Liu, H. W., Wang, X. W., Xue, H. B., and Ma, Z. Y. (2015). Empirical formulas of permeability of clay based on effective pore ratio. *Chin. J. Rock Mech. Eng.* 34 (9), 1909–1917. (In Chinese).
- De Caro, M., Crosta, G. B., and Prevati, A. (2020). Modelling the interference of underground structures with groundwater flow and remedial solutions in Milan. *Eng. Geol.* 2020 (105652), 105652. doi:10.1016/j.enggeo.2020.105652
- Liu, N. F., Li, N., Li, G. F., Song, Z. P., and Wang, S. J. (2022). Method for evaluating the equivalent thermal conductivity of a freezing rock mass containing systematic fractures. *Rock Mechanics and Rock Engineering*. doi:10.1007/s00603-022-03038-9
- Liu, N. F., Li, N., Wang, S. J., Li, G., and Song, Z. (2022). A fully coupled thermo-hydro-mechanical model for fractured rock masses in cold regions. *Cold Regions Sci. Technol.* 205 (2023), 103707. doi:10.1016/j.coldregions.2022.103707
- Ministry of housing and urban-rural development of the People's Republic of China (2012). *Technical specification for retaining and protection of building foundation excavations*. JGJ 120-2012).
- Pujades, E., De Simone, S., Carrera, J., Vazquez-Sune, E., and Jurado, A. (2017). Settlements around pumping wells: Analysis of influential factors and a simple calculation procedure. *J. Hydrology* 548, 225–236. doi:10.1016/j.jhydrol.2017.02.040
- Pujades, E., Vazquez-Sune, E., Carrera, J., and Jurado, A. (2014). Dewatering of a deep excavation undertaken in a layered soil. *Eng. Geol.* 178, 15–27. doi:10.1016/j.enggeo.2014.06.007
- Roy, D., and Robinson, K. E. (2009). Surface settlements at a soft soil site due to bedrock dewatering. *Eng. Geol.* 107 (3–4), 109–117. doi:10.1016/j.enggeo.2009.05.006
- Shaour, F. M., and Hasan, S. E. (2008). Groundwater control for construction purposes: A case study from Kuwait. *Environ. Geol.* 53 (8), 1603–1612. doi:10.1007/s00254-007-0768-9
- Simulia, D. S. (2017). *Abaqus 6.17 help documentation*. Paris, France: Dassault Systems Corp.
- Singh, P. N., and Wallender, W. W. (2008). Effects of adsorbed water layer in predicting saturated hydraulic conductivity for clays with Kozeny-Carman equation. *J. Geotechnical Geoenvironmental Eng.* 134 (6), 829–836. doi:10.1061/(asce)1090-0241(2008)134:6(829)
- Sun, D., Zhao, Y. H., and Lu, Q. C. (2015). Vulnerability analysis of urban rail transit networks: A case study of Shanghai, China. *Sustainability* 7 (6), 6919–6936. doi:10.3390/su7066919
- Wang, J. X., Deng, Y. S., Wang, X. B., Liu, X. T., and Zhou, N. Q. (2022). Numerical evaluation of a 70-m deep hydropower station foundation pit dewatering. *Environ. Earth Sci.* 81 (14), 364–368. doi:10.1007/s12665-022-10493-8
- Wang, J. X., Deng, Y. S., Ma, R. Q., Liu, X., Guo, Q., Liu, S., et al. (2018). Model test on partial expansion in stratified subsidence during foundation pit dewatering. *J. Hydrology* 557, 489–508. doi:10.1016/j.jhydrol.2017.12.046
- Wang, J. X., Feng, B., Liu, Y., Wu, L., Zhu, Y., Zhang, X., et al. (2012). Controlling subsidence caused by dewatering in a deep foundation pit. *Bull. Eng. Geol. Environ.* 71 (3), 545–555. doi:10.1007/s10064-012-0420-0
- Wang, J. X., Feng, B., Yu, H. P., Guo, T., Yang, G., and Tang, J. (2013). Numerical study of dewatering in a large deep foundation pit. *Environ. Earth Sci.* 69 (3), 863–872. doi:10.1007/s12665-012-1972-9
- Wang, J. X., Liu, X. T., Wu, Y. B., Liu, S., Wu, L., Lou, R., et al. (2017). Field experiment and numerical simulation of coupling non-Darcy flow caused by curtain and pumping well in foundation pit dewatering. *J. Hydrology* 549, 277–293. doi:10.1016/j.jhydrol.2017.03.070
- Xu, Y. S., Yan, X. X., Shen, S. L., and Zhou, A. N. (2019). Experimental investigation on the blocking of groundwater seepage from a waterproof curtain during pumped dewatering in an excavation. *Hydrogeology J.* 27 (7), 2659–2672. doi:10.1007/s10040-019-01992-3
- Zeng, C. F., Liao, H., Xue, X. L., Long, S. C., Luo, G. J., Diao, Y., et al. (2022). Responses of groundwater and soil to dewatering considering the barrier effect of adjacent metro station on multi-aquifers. *J. Hydrology* 612, 128117. doi:10.1016/j.jhydrol.2022.128117
- Zeng, C. F., Song, W. W., Xue, X. L., Li, M. K., Bai, N., and Mei, G. X. (2021). Construction dewatering in a metro station incorporating buttress retaining wall to limit ground settlement: Insights from experimental modelling. *Tunn. Undergr. Space Technol.* 116, 104124. doi:10.1016/j.tust.2021.104124
- Zhang, Y. W., Fan, S. Y., Yang, D. H., and Zhou, F. (2022). Investigation about variation law of frost heave force of seasonal cold region tunnels: A case study. *Front. Earth Sci.* 9, 806843. doi:10.3389/feart.2021.806843
- Zhou, N. Q., Vermeer, P. A., Lou, R. X., Tang, Y., and Jiang, S. (2010). Numerical simulation of deep foundation pit dewatering and optimization of controlling land subsidence. *Eng. Geol.* 114 (3–4), 251–260. doi:10.1016/j.enggeo.2010.05.002

Author contributions

All authors listed have made a substantial, direct, and intellectual contribution to the work and approved it for publication.

Funding

The research described in this paper was funded by the National Natural Science Foundation of China (No. 51979225).

Conflict of interest

Author ZY was employed by China Railway First Survey and Design Institute Group Co., Ltd.

The remaining authors declare that the research was conducted in the absence of any commercial or financial relationships that could be construed as a potential conflict of interest.

Publisher's note

All claims expressed in this article are solely those of the authors and do not necessarily represent those of their affiliated organizations, or those of the publisher, the editors and the reviewers. Any product that may be evaluated in this article, or claim that may be made by its manufacturer, is not guaranteed or endorsed by the publisher.



OPEN ACCESS

EDITED BY
Naifei Liu,
Xi'an University of Architecture and
Technology, China

REVIEWED BY
Jiuyang Huan,
Yangzhou Polytechnic Institute, China
Shuangfeng Guo,
Nanjing Tech University, China

*CORRESPONDENCE
Fengshan Ma,
✉ fisma@mail.iggcas.ac.cn

SPECIALTY SECTION
This article was submitted to
Environmental Informatics and Remote
Sensing, a section of the journal
Frontiers in Earth Science

RECEIVED 18 November 2022
ACCEPTED 28 December 2022
PUBLISHED 11 January 2023

CITATION
Liu J, Ma F, Guo J, Li G, Song Y and Li F
(2023), A preliminary analysis of the
mining-induced rock movement
characteristics in the Xinli deposit of the
Sanshandao gold mine.
Front. Earth Sci. 10:1101807.
doi: 10.3389/feart.2022.1101807

COPYRIGHT
© 2023 Liu, Ma, Guo, Li, Song and Li. This is
an open-access article distributed under
the terms of the [Creative Commons
Attribution License \(CC BY\)](https://creativecommons.org/licenses/by/4.0/). The use,
distribution or reproduction in other
forums is permitted, provided the original
author(s) and the copyright owner(s) are
credited and that the original publication in
this journal is cited, in accordance with
accepted academic practice. No use,
distribution or reproduction is permitted
which does not comply with these terms.

A preliminary analysis of the mining-induced rock movement characteristics in the Xinli deposit of the Sanshandao gold mine

Jia Liu^{1,2,3}, Fengshan Ma^{1,2*}, Jie Guo^{1,2}, Guang Li^{1,2,3}, Yewei Song^{1,2,3} and Fangrui Li^{1,2,3}

¹Key Laboratory of Shale Gas and Geoengineering, Institute of Geology and Geophysics, Chinese Academy of Sciences, Beijing, China, ²Innovation Academy for Earth Science, Chinese Academy of Sciences, Beijing, China, ³College of Earth and Planetary Sciences, University of Chinese Academy of Sciences, Beijing, China

Commensurate with economic globalization, the demand for mineral resources is increasing. With increased mining activity, problems related to ground subsidence and rock movement are becoming increasingly prominent, even affecting mining production activities. However, the physical mechanisms behind the ground subsidence phenomenon have been poorly studied, especially for metal mines with a steep dip. This paper applies the Interferometric Synthetic Aperture Radar (InSAR) technique and the numerical simulation method to deduce the characteristics of rock movement in the Xinli deposit of the steeply inclined Sanshandao gold mine. The InSAR results indicate that more subsidence has occurred in the southern part of the Xinli Village coastline area than in the northern part. This is also supported by the numerical simulation results obtained by the fast Lagrangian analysis of continua in three dimensions (FLAC3D). Notably, the range of ground subsidence obtained by numerical simulation shows an obvious asymmetry. The monitoring data of the No. 55 prospecting profile offer a plausible explanation for this, as the surrounding rock of the fault's hanging wall has a wider range of rock movements. Furthermore, the sublevels of the No. 55 prospecting profile at different depths show different rock movement characteristics, and a logistic function can be well applied to the right part of the settlement curve; the parameter "a" in the function formula is very close to the maximum subsidence value for each sublevel. We defined the ratio "r" to measure the difference between the maximum subsidence value and the corresponding parameter "a" and found this value to be positively correlated with the fractal dimension value of deeper sublevels (–320 m, –400 m, –480 m, and –600 m) and negatively correlated with the fractal dimension value of lower sublevels (–200 m and –240 m).

KEYWORDS

ground subsidence, InSAR, asymmetry, logistic function, fractal dimension value

1 Introduction

The rapid development of the global economy has led to an increase in the demand for ore resources, which has forced the surging exploitation and deeper exploitation of minerals (Wagner, 2019; Li et al., 2020a; Xu et al., 2021). This means that problems caused by mining also arise, such as ground subsidence, water inrush accidents, and rock burst phenomena (Meng et al., 2012; Sepehri et al., 2020; Li et al., 2022). Numerous researchers have investigated rock movement characteristics and failure mechanisms of relatively gentle coal (Cui et al., 2001; Ren et al., 2014; Adhikary and Guo,

2015; Ghabraie et al., 2015; Adhikary et al., 2016; Cheng et al., 2017; Tuncay et al., 2021). Since the 19th century, relevant theoretical research has gradually developed due to the needs of increased mining production activities (Whittaker and Reddish, 1989). Later, mature theoretical methods were gradually applied to study ground subsidence. For instance, the influence function method has been popular since the 1950s and serves as the foundational principle behind Knothe's theory (Kwinta and Gradka, 2020); and the random medium theory, introduced by the Polish scholar Litviniszyn, is a theoretical study of ground subsidence based on the random walk model (Litwiniszyn, 1954; Jiang et al., 2019). At the end of the 20th century, numerous empirical and theoretical methods were gradually developed. In China, the probability integration model created by Liu and Liao is the most frequently applied prediction method in mining-induced subsidence (Liu and Liao, 1965; Liu and Dai, 2016; Hu et al., 2022). The empirical method mostly combines actual monitoring data with suitable mathematical functions, such as varied profile function methods and typical curve methods (Diez and Alvarez, 2000; Xu and Li, 2005; Chen et al., 2016; Meng et al., 2021). Numerical models also played an important role in studying ground subsidence induced by mining (Xie et al., 1999; Sheorey et al., 2000; Park et al., 2005; Svartsjaern et al., 2016).

Although horizontal coal seams are common in mining production activities, there are also numerous steeply inclined coal seams worldwide; however, the study of steeply inclined coal is far from adequate (Alejano et al., 1999; Dai et al., 2002; Asadi et al., 2005; Tu et al., 2015), let alone steeply dipped metal orebodies (Diez and Alvarez, 2000; Ma and Ding, 2009; Zhao et al., 2013a; Li et al., 2022). Metal mining differs from coal mining in many aspects and cannot be treated the same (Cao, 2019). First, the formation conditions and environment of geological occurrence for metal orebodies are more complex and specialized than those of coal mines (Gastaldo et al., 1993; Bai et al., 2002; Villegas et al., 2011; Jiráseka et al., 2018). Second, the two differ in terms of their associated mining methods and techniques. Longwall mining is particularly prevalent in

coalfields (Ren et al., 2014), while the filling mining method is popular in metal mines (Holla and Buizen, 1991; Li et al., 2004; Li et al., 2020b). Regardless, it is important and meaningful to study the ground subsidence and rock movement phenomenon caused by the mining of inclined metal orebodies.

With the rapid development of the Interferometric Synthetic Aperture Radar (InSAR) technique, high-resolution SAR imagery has become beneficial to understanding ground deformation influenced by natural hazards or human activities (Yerro et al., 2014; Valkaniotis et al., 2018; Murgia et al., 2019). For instance, the advanced time-series InSAR technology (the small baseline subset technique and the Persistent Scatterer Interferometry technique) has been well developed in the past few decades (Berardino, Fornaro, Lanari, Sansosti; Ferretti et al., 2001; Aly et al., 2012; Foroughnia et al., 2018), especially in applications related to ground subsidence (Sócrates et al., 2020; Tarighat et al., 2021; Bao et al., 2022). In addition, numerical simulation and theoretical research on rock movements are also important. For instance, the fractal theory has been applied in rock mechanics (Xie and Pariseau, 1993; Shen, 2002; Biancolini et al., 2006). In fact, the fractal phenomenon reflects the self-organized criticality (SOC) characteristic of a complex system (Bak et al., 1987; Qin, 2000); that is, the system tends to reach a new equilibrium after being disturbed.

In this paper, we applied InSAR techniques to monitor the ground subsidence induced by mining a steeply inclined metal orebody. We used FLAC3D software to build a realistic depiction of the Xinli deposit in a Sanshandao gold mine model and simulated the excavation process. The essence of ground subsidence in the mining area is related to the movement of the deep rock mass. We took the No. 55 prospecting profile of the Xinli deposit of the Sanshandao gold mine as the study subject, formulated the subsidence curves by a logistic function, and analyzed the subsidence velocity of each sublevel by the fractal theory. We found that the fractal dimension is related to one parameter in the logistic function formula and is also relevant to the mining activities of each sublevel, especially sublevels characterized by a “funnel”-type

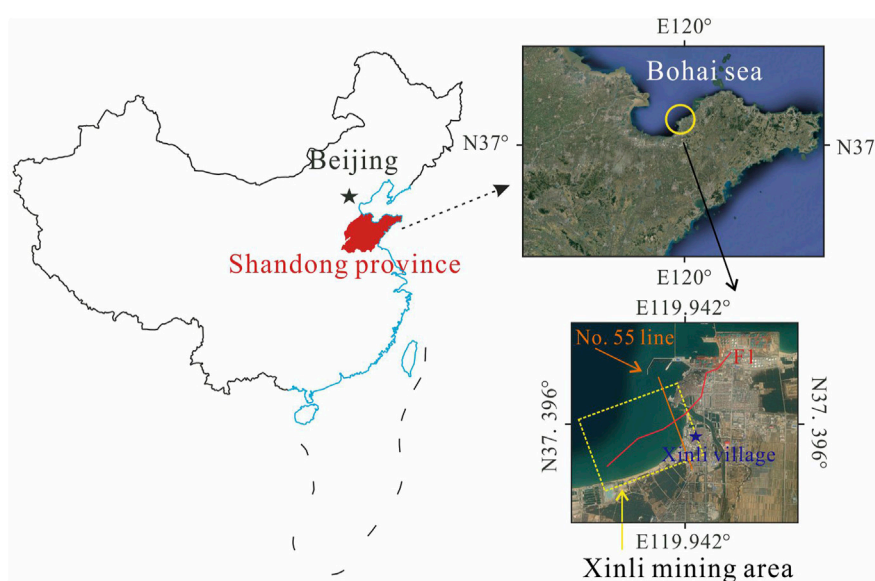


FIGURE 1
Location of the study area.



FIGURE 2
Overview of the Xinli mining area by the sea.

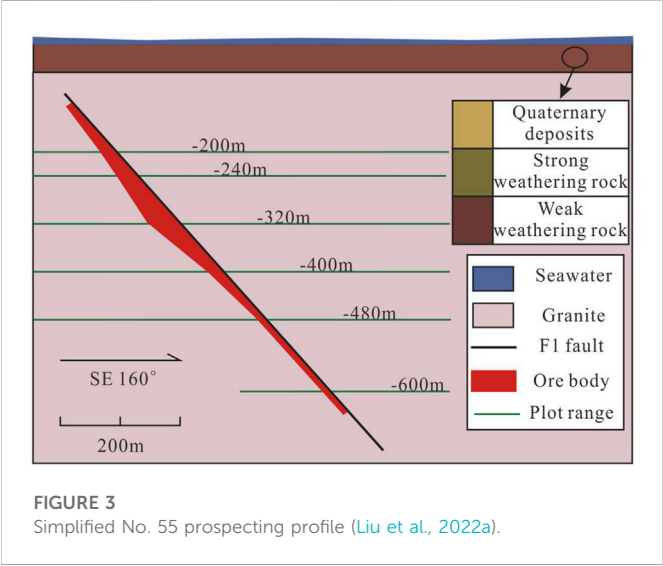


FIGURE 3
Simplified No. 55 prospecting profile (Liu et al., 2022a).

subsidence curve. In general, we provide a comprehensive understanding of ground subsidence and rock movement caused by a steeply inclined metal mine after analyzing the monitoring data of the ground and surrounding rock. This may offer a reference for other mines with similar geological conditions. Hereafter, we will focus more on the deformation characteristic of the jointed rock mass to better study the rock movement mechanism of a steeply inclined metal mine.

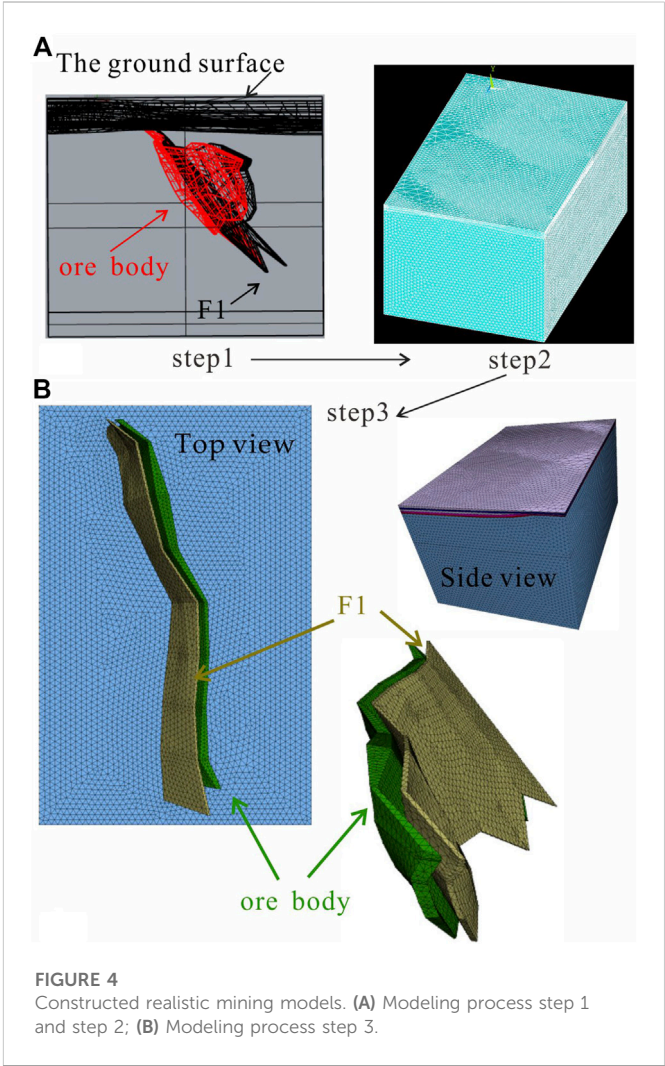


FIGURE 4
Constructed realistic mining models. (A) Modeling process step 1 and step 2; (B) Modeling process step 3.

2 Background

2.1 Geological setting

The study area is located in Xinli Village, Laizhou City, Shandong Province. As shown in Figure 1, Xinli Village is remotely situated on the west coast of the Shandong Peninsula, bordering the Bohai Sea. The Xinli deposit of the Sanshandao gold mine is the only coastal metal orebody in China, which has a large dip angle. The study area is situated in the eastern area of the Tan–Lu

TABLE 1 Main parameters of the hanging wall, footwall, and orebody.

	Bulk modulus K (MPa)	Shear modulus G (MPa)	Cohesion (MPa)	Tensile strength (MPa)	Poisson's ratio	Friction angle peak (degrees)
Hanging wall	2.24	1.79	5.72	3.18	0.2	30.6
Footwall	3.29	2.07	10.7	4.31	0.24	37.0
Orebody	2.42	1.89	6.43	3.72	0.19	32.6

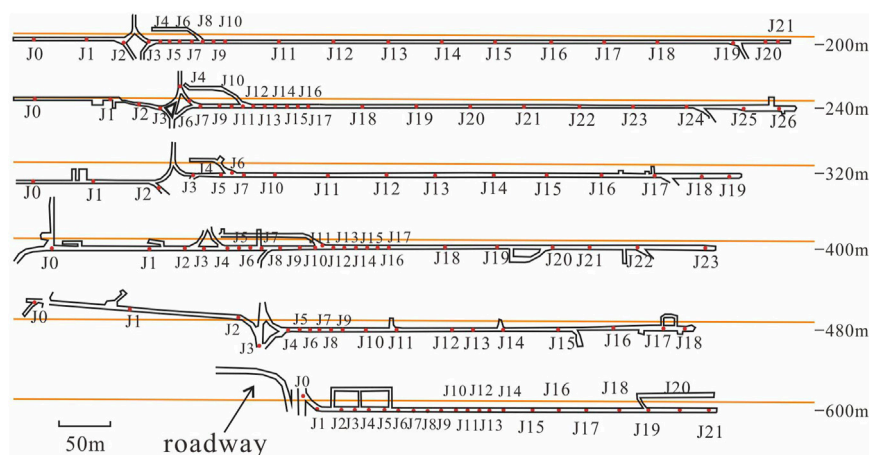


FIGURE 5

Monitoring network system of the No. 55 prospecting profile of the Xinli mining area (Liu et al., 2022a).

fault, the northeastern area of the Sanshandao–Cangshang fault zone, and the north limb of the Qixia anticlinorium. The exposed strata in the mining area are the Lugezhuang Formation of the Paleoproterozoic Jingshan Group, found in the Lujia unit of the Qixia super unit (Zhao et al., 2013b). The fault F1 is the ore-controlling fault with an extended depth of about 1000 m, with a strike of 62° , and an average dip angle of 46° in the study area. The altered rocks are zoned along the F1 fault, whose lithology mainly includes different types of granite and cataclasite. The upper surface,

corresponding to the main part of the mining area, is comprised of a silt layer and seawater. In Figure 1, the area encircled by the dotted yellow line is the Xinli deposit of the Sanshandao gold mine. According to the available reports, the horizontal tectonic stress in the mining area is significant; the maximum horizontal principal stress lies in a nearly horizontal direction (NNW direction). The maximum horizontal principal stress, the minimum horizontal principal stress, and the vertical principal stress increase with the increasing depth, and they share a nearly linear relationship.

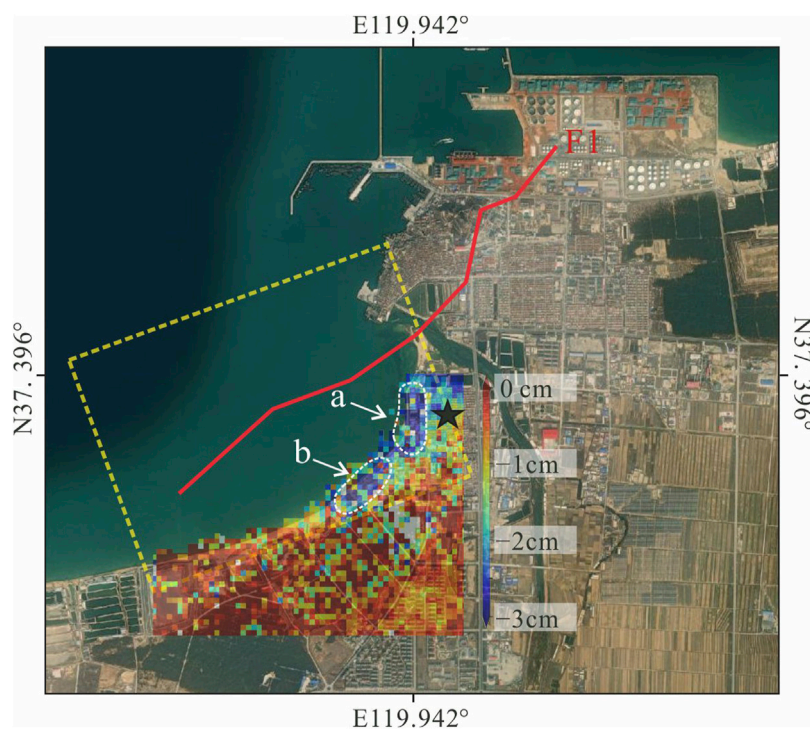


FIGURE 6

Spatial characteristics of the LOS displacement field (SBAS result).

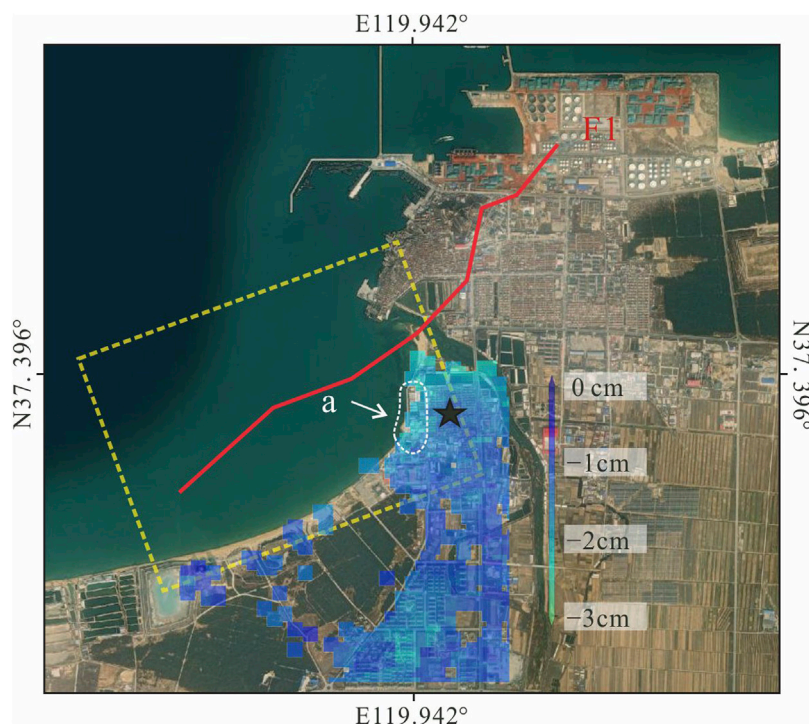


FIGURE 7
Spatial characteristics of the LOS displacement field (PSI result).

$$\begin{aligned}\sigma_{hmax} &= 0.11 + 0.0539H, \\ \sigma_{hmin} &= 0.13 + 0.0181H, \\ \sigma_z &= 0.08 + 0.0315H.\end{aligned}\quad \begin{matrix} (1) \\ (2) \\ (3) \end{matrix}$$

Here, σ_{hmax} , σ_{hmin} , σ_z , and H represent the maximum horizontal principal stress, the minimum horizontal principal stress, the vertical stress (MPa), and the depth (m), respectively.

The climate in the study area is pleasant, and the tourism industry is well developed. As displayed in Figure 2, the mining facilities of the

Xinli mining area are near the sea with hills in the distance. Thus, more attention should be paid to the healthy development of the mining industry in the Xinli mining area.

2.2 Mining setting

It has been nearly 20 years since the Xinli mining area was built in 2005. The mechanical upward horizontal slice stopping-filling

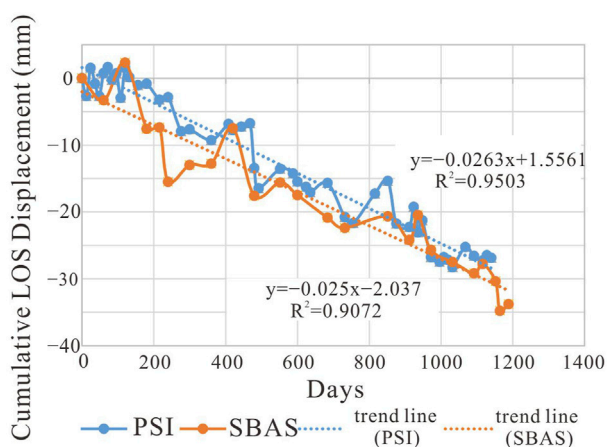


FIGURE 8
Cumulative LOS displacement of zone "a" (PSI and SBAS results).

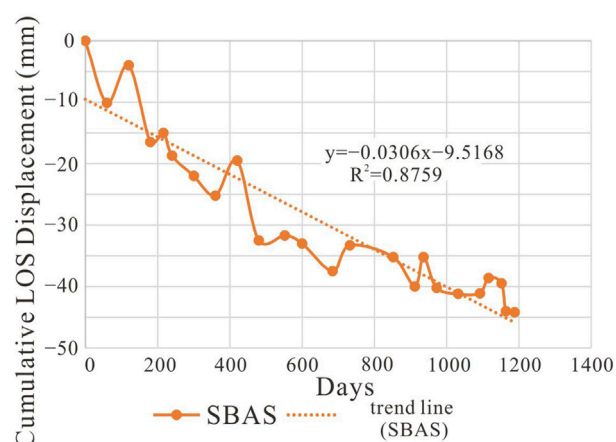


FIGURE 9
Cumulative LOS displacement of zone "b" (SBAS result).

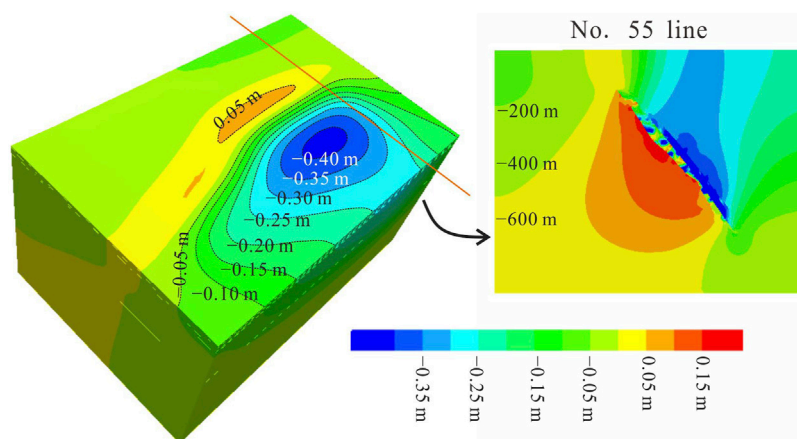


FIGURE 10
Vertical displacement result of the study area.

method was used in the mining process, and the method of simultaneous upward mining in several sublevels was adopted for the mitigation of rock deformation and higher production efficiency (Liu et al., 2022a). To facilitate survey and design work, prospecting profile lines were designed and aligned almost perpendicular to the orebody. As shown in Figure 1, the orange line represents the location of the No. 55 prospecting profile line. Figure 3 also offers the simplified geological condition of the No. 55 prospecting profile (Liu et al., 2022a). After the excavation, the mined-out volume was immediately filled with backfill slurry paste.

3 Materials and methods

3.1 InSAR monitoring and numerical simulation

In this paper, we collected 57 SAR images for data processing, which were acquired using Sentinel-1A between 11 April 2018 and 12 July 2021. In addition, we conducted data processing by two time-series InSAR techniques, an SBAS technique, and a PSI technique. Detailed information about SAR images and data processing is available (Liu

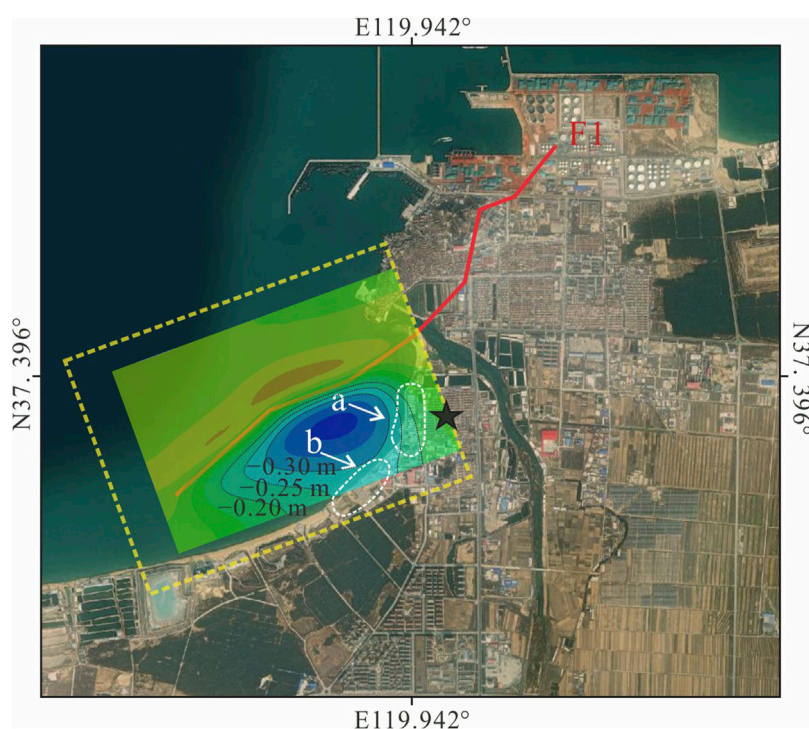


FIGURE 11
Result of superimposing the subsidence contour plot onto the map.

et al., 2022b). Because the Xinli mining area is mainly located below the sea level, the range of ground subsidence caused by mining is small. To more comprehensively present the characteristics of ground subsidence, we adopted a numerical simulation method. First, we used Rhinoceros and ANSYS software to establish a realistic mining model (Figure 4A); second, we exported the node information and element information of the meshes; finally, we imported the obtained information of the existing real model into FLAC3D software (Figure 4B). According to the rock mechanics test results of the rock mass at different positions in the mine, as conducted by the mining company, we attributed different properties for different groups. The main parameters of the key groups are listed in Table 1. Furthermore, we used FLAC3D software to simulate the excavation and backfilling of the orebody.

3.2 Displacement monitoring of the roadway

Ground subsidence is usually the external manifestation of the movement, deformation, and failure of the deep rock mass; namely, the deformation of the rock mass is an essential cause of ground subsidence. Thus, it is significant and necessary to study the rock movement phenomenon. In the Xinli mining area, the subsidence monitoring system has been established in several sublevels of the No. 55 prospecting profile (−200 m, −240 m, −320 m, −400 m, −480 m, and −600 m) since August 2015. The fourth-level leveling method was adopted, and the time interval for the monitoring work is usually 1 or 2 months. The monitoring network system of the No. 55 prospecting profile is shown in Figure 5 (Liu et al., 2022a). In this paper, we collected monitoring data from August 2015 to November 2021 with a monitoring interval of 1 to 2 months. Notably, there were two special situations: the workers ended the monitoring work of the −200 m sublevel earlier in April 2019 due to some unexplainable reasons, and the −600 m sublevel was more recently excavated, delaying the start time of the monitoring work there.

4 Results

4.1 The spatial characteristics of line-of-sight (LOS) displacement fields of Xinli Village

As shown in Figures 6, 7, we obtained the LOS displacement fields for Xinli Village using SBAS and PSI techniques. The two monitoring results of the cumulative LOS displacement indicate values of more than 3 cm during the monitoring period. The flat area to the west of Xinli Village has a large subsidence value, while the ground subsidence phenomenon of other areas of Xinli Village is not obvious. Notably, there is a very obvious phenomenon within the monitoring results: the image obtained by the PSI technique is missing a portion of the domain. This is related to the inherent property of the PSI technique, that is, areas with dense vegetation have fewer permanent scatterers. Additionally, due to atmospheric influences, the propagation path of the radar beam will be delayed in the process of passing through the atmosphere, which is the so-called atmospheric effect (Massonnet et al., 1994). The atmospheric effect is especially pronounced in coastal areas. Although we applied the Generic Atmospheric Correction Online Service (GACOS) data processed by the Toolbox for Reducing Atmospheric Phase Screen Estimation (TRAIN) to eliminate atmospheric errors during data processing (Yu et al., 2017; Yu et al., 2018a; Yu et al., 2018b), the outcome is imperfect. However, the

results provide some meaningful subsidence data and the overall ground subsidence pattern of Xinli Village.

To obtain the cumulative LOS displacement of Xinli Village over time, we isolated zones (represented by the letters “a” and “b” in Figures 6, 7) for analysis. As shown in Figure 8, the values of the cumulative LOS displacements of zone “a” at different time periods are nearly equal (3 cm). Both results show stochastic fluctuations of the ground subsidence (Hui et al., 2019). Namely, the subsidence value does not continually increase in the subsidence area, and the subsidence events and uplift events can occur at any time in the ground subsidence area. The curves were linearly fitted, allowing us to obtain the corresponding formulas, as given in Figure 8. The LOS velocities are −0.0263 mm/day and −0.025 mm/day for PSI and SBAS methods, respectively. The linear fitting effect is satisfactory, and the corresponding “R²” values are 0.95 (PSI) and 0.91 (SBAS). After calculation and comparison, we found that the LOS subsidence velocity of zone “a” is nearly 9 mm/year. In a similar manner, we obtained the cumulative LOS displacement of zone “b”, with a SBAS-derived LOS subsidence velocity of 0.0306 mm/day, which translates to a subsidence velocity that is nearly 11.2 mm/year (Figure 9). Apparently, zone “b” has a bigger LOS subsidence velocity.

4.2 The simulated result of vertical displacement

We conducted the excavation and backfilling on the existing FLAC3D numerical model. According to the actual production plan of the Xinli deposit of the Sanshandao gold mine, the general direction of mining is from the northeast to the southwest (that is, along the orebody), from shallow to deep. Thus, we first excavated the upper northeast orebody, then the lower northeast orebody and the upper southwest orebody, and finally, the lower southwest orebody. In this way, we obtained the vertical displacement result of the study area and the vertical displacement of the No. 55 profile (Figure 10). We obtained an oval-shaped basin of subsidence, with the long axis of the ellipse aligned with the strike of the orebody.

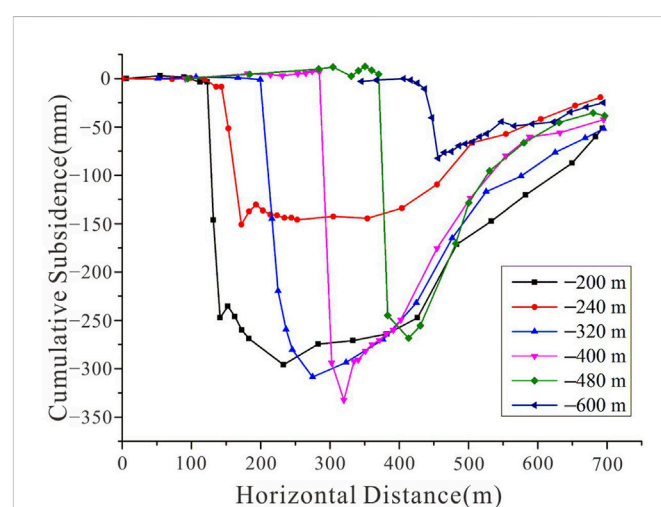


FIGURE 12
Cumulative subsidence of various sublevels of the No. 55 prospecting profile.

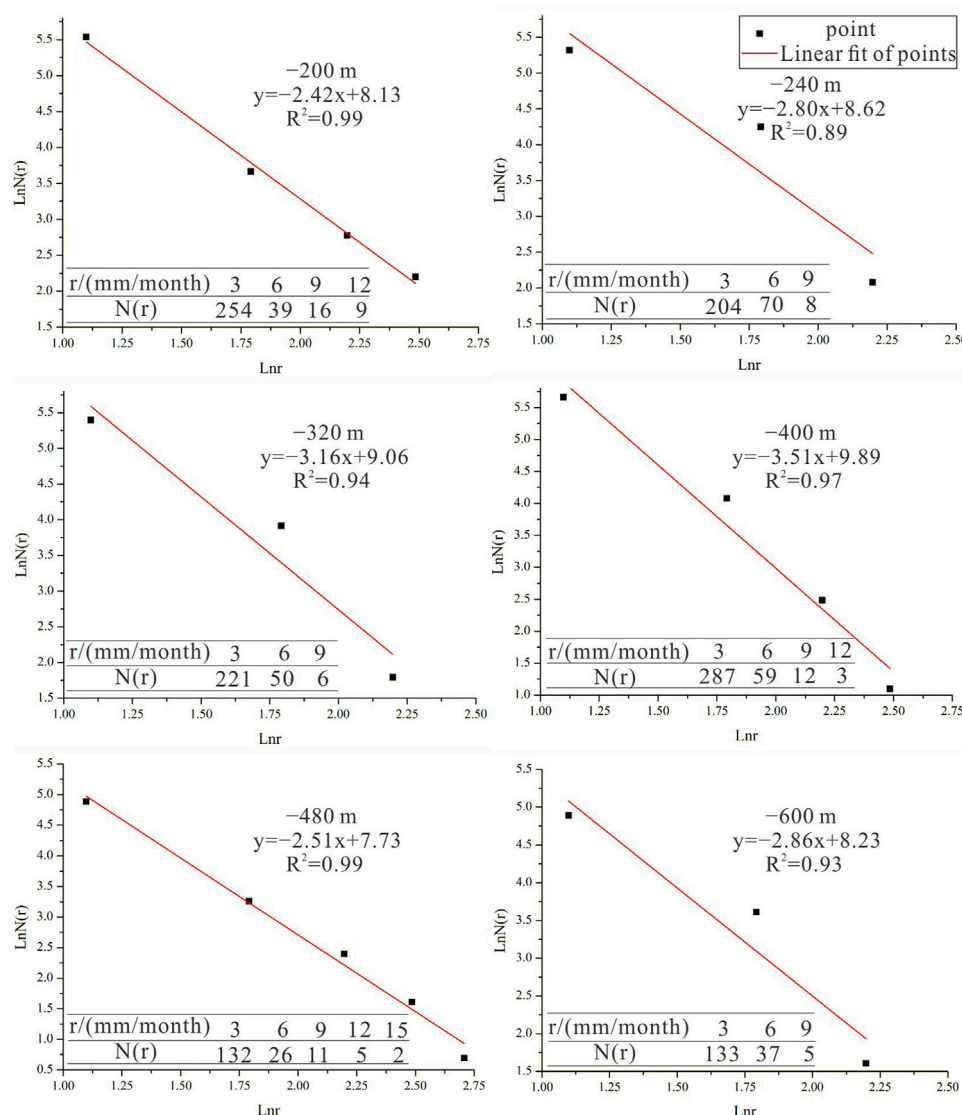


FIGURE 13

Fractal dimensions of various sublevels of the No. 55 prospecting profile.

The subsidence isolines are the densest on the side nearest to the orebody and sparse on the side near the coast. In addition, a long and narrow uplift zone existed in the mining area. In the study area, the cumulative maximum ground subsidence value is about 0.42 m, and the cumulative maximum ground uplift value is about 0.066 m. Additionally, we projected the numerical simulation contour plot onto the map and concluded that zone “b” has a larger subsidence value than zone “a”, which is due to the special shape of the subsidence basin (Figure 11).

4.3 The cumulative subsidence of various sublevels

We plotted the cumulative subsidence of various sublevels of the No. 55 prospecting profile in Figure 12. The ordinate

represents the cumulative subsidence value, and the abscissa represents the horizontal distance for each monitoring point of each sublevel from the starting point of the -240 m sublevel. According to the shapes of the cumulative subsidence curves, we divided them into two categories: the “pan” type (-200 m and -240 m) and the “funnel” type (-320 m, -400 m, -480 m, and -600 m) (Liu et al., 2022a). In addition, we counted the monitoring data of each sublevel of the No. 55 prospecting profile for many years. We obtained subsidence velocity values of 254 (-200 m), 204 (-240 m), 221 (-320 m), 287 (-400 m), 132 (-480 m), and 133 (-600 m), all of which were less than 3 cm/month. We used the fractal theory to analyze the monitoring data, and the function model is expressed as $N(r) = C r^{-D}$. In this equation, “r” represents a characteristic scale, “C” represents the proportionality factor, “D” represents the fractal dimension, and “N(r)” represents the number of scales greater than “r.” Finally, we

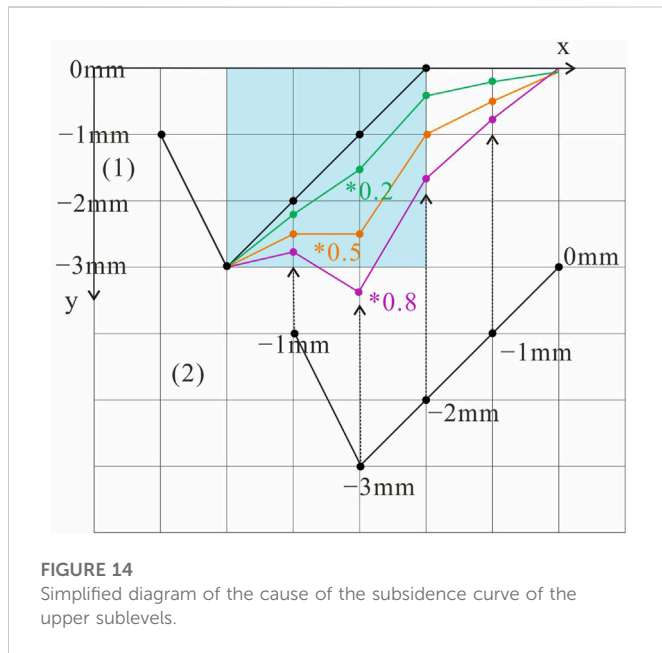


FIGURE 14
Simplified diagram of the cause of the subsidence curve of the upper sublevels.

obtained “N(r)” values for each sublevel (Figure 13, tables). We projected the results onto a logarithmic coordinate graph and fitted them by the least square method specific to a log–log plot. In fact, the absolute value of the slope of the line is the fractal dimension “D.” Figure 13 displays the linear fitting formula of each sublevel and the determination coefficient “R².”

5 Discussion

5.1 The characteristics of cumulative subsidence curves

As mentioned previously, we divided the cumulative subsidence curves into two categories: the “pan” type (–200 m and –240 m) and the “funnel” type (–320 m, –400 m, –480 m, and –600 m). Apparently, “pan”-type subsidence curves of the upper sublevels have more numerous large cumulative subsidence values; that is, the bottom of the curves are wider and softer. We infer that this phenomenon is related to the amount of the excavated orebody. From 2016 to 2021, the mining activities are mainly conducted in deep sublevels of the No. 55 prospecting profile, whereas there is little mining activity conducted in the upper sublevels of the No. 55 prospecting profile. It is well known that as a body moves under a force, it acquires inertia and that gravity is the root cause of subsidence. In other words, the upper rock mass will be affected by the mining activities in the lower rock mass, just as underground mining causing the upper ground surface to subside. This is illustrated in the simplified diagram in Figure 14, where “(1)” is the upper subsidence curve (we assume its presence) and “(2)” is the newly formed subsidence curve. We also assumed that the newly formed subsidence curve will transfer a certain degree of subsidence to the upper subsidence curve. The green line represents the sum of the subsidence values of the original “(1)” curve and the corresponding lower subsidence

value of the “(2)” curve multiplied by the coefficient (0.2). The other cases remain the same. According to the superimposed results in three cases, we found that the slope of the curve becomes smaller in the light blue area. In general, the scope of subsidence of the “(1)” curve becomes greater than that in the original situation. Since the subsidence curves of the upper sublevels are affected by the lower mining activities, the numerical simulation result is deemed reasonable.

5.2 The logistic fit of cumulative subsidence

As shown in Figure 12, the cumulative subsidence value will drop abruptly at a certain stage and then change steadily. Combined with Figure 5, the right part of the cumulative subsidence curves, which change steadily, mainly reflects the cumulative subsidence of the fault’s hanging wall rock mass. According to the previous content, this part of the curve is S-shaped. To further study the characteristics of the curves, we used the profile function method [66] to fit the curves. We applied a logistic function and the simplex method, both of which are the built-in functions in Origin software, to fit the subsidence values of this part, and obtained good fitting results, as evidenced by a determination coefficient (R²) mostly in the range of 0.95–1. The curve-fitting formula is shown as follows:

$$y = \frac{a - b}{1 + \left(\frac{x}{c}\right)^d} + b. \quad (4)$$

Figure 15 shows the fitting results and the relevant parameters in the formula. We found that parameter “a” is close to the value of the maximum subsidence. We defined a ratio “r” to measure the difference (“δ”) between the maximum subsidence value and the corresponding parameter “a.” Here, “r” is equal to the difference (“δ”) divided by the maximum subsidence value. Interestingly, there was a negative correlation between the value of “r” and fractal dimensions “D” of each sublevel for the “pan”-type curves (–200 m and –240 m); in contrast, these parameters are positively correlated for “funnel”-type curves. The relevant parameters are listed in Table 2. As for the deep sublevels of the No. 55 prospecting profile (–480 m and –600 m), “a” is approximately equal to the maximum subsidence value. This implies that we only need information on the maximum subsidence value and the three other values to obtain the right part of the subsidence curve of the entire sublevel. In addition, the “–480 m” sublevel had the highest total amount of rock excavated compared with other deep sublevels. For example, the amount of rock excavated from the “–400 m” sublevel, “–480 m” sublevel, and “–600 m” sublevel accounts for 0.23, 0.47, and 0.3 of the total amount of rock excavated from all three sublevels, respectively. The deep part of the mine has been exploited much more than the shallow part, which has hardly been exploited in recent years. Therefore, we believe mining activities are the root reason for rock movement. In fact, the fractal phenomenon reflects the self-organized criticality (SOC) characteristic of a complex mining system. In other words, while the equilibrium state of the underground rock mass is disturbed by mining activities, the rock mass itself will still tend to develop toward a stable equilibrium critical state. We found a common characteristic among those sublevels which have a “funnel”-type subsidence curve; that is, the more severely disturbed the rock

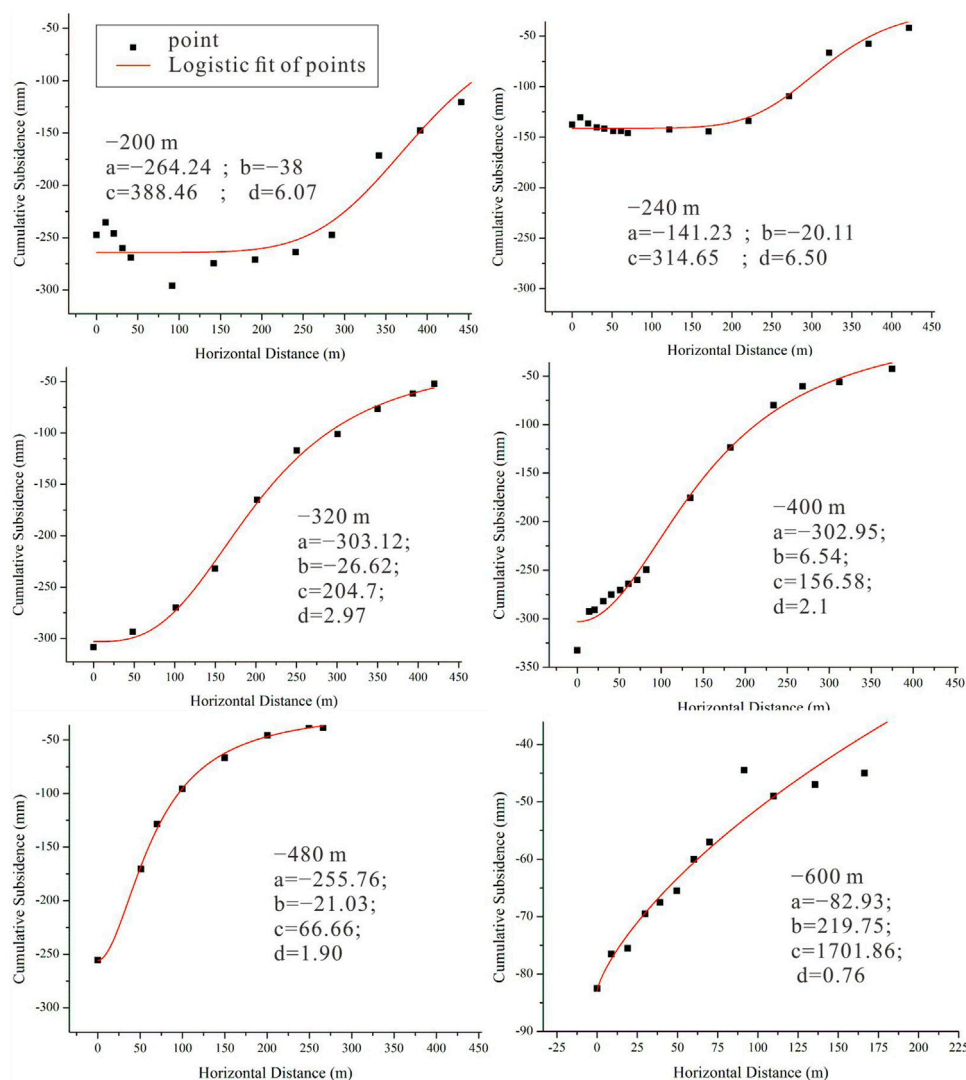


FIGURE 15
Logistic fitting results and relevant parameters in the formula.

mass is, the smaller the fractal value is. As for sublevels with a “pan”-type subsidence curve, the small fractal dimension values are due to the influence of the lower sublevels. Thus, we believe that the logistic

function can be used to fit subsidence curves, and the fractal dimension value reflects the degree to which the excavated sublevel is disturbed.

TABLE 2 Relevant parameters.

Sublevel	D	r	δ	A	Maximum subsidence value
-200 m	2.42	0.0676	-16.74	-264.24	-247.5
-240 m	2.80	0.0271	-3.73	-141.23	-137.5
-320 m	3.16	0.0174	5.38	-303.12	-308.5
-400 m	3.51	0.0889	29.55	-302.95	-332.5
-480 m	2.51	0.0010	-0.26	-255.76	-255.5
-600 m	2.86	0.0052	-0.43	-82.93	-82.5

6 Conclusion

As a coastal, steeply inclined gold mine, the rock movement caused by mining in the Xinli deposit of the Sanshandao gold mine is of great research value as seawater may flood into the roadway along the damaged rock mass, and the movement and deformation of the surrounding rock may threaten the safety of workers and damage surface buildings. In this paper, we conducted a preliminary analysis of the mining-induced rock movement characteristics in the Xinli deposit of the Sanshandao gold mine; the key conclusions are presented in the following paragraphs.

First, the InSAR results indicated that the southern part of the coastline within the Xinli Village area is experiencing greater subsidence than the northern part.

Second, the numerical simulation results obtained using FLAC3D are consistent with the InSAR results. In addition, the range of ground subsidence obtained by numerical simulation shows an obvious asymmetry. Specifically, the subsidence value on the southeast side of the subsidence basin changes more gently.

Third, the monitoring data of the No. 55 prospecting profile can provide a plausible explanation for the subsidence results: the slope of the right part of the maximum subsidence point of the subsidence curve is smaller than that on the left part; namely, the surrounding rock of the fault's hanging wall has a wider range of rock movements. Furthermore, although the sublevels of the No. 55 prospecting profile at different depths have different rock movement characteristics, the upper sublevels (−200 m and −240 m) of the No. 55 prospecting profile tend to show “pan”-type curves, while the lower sublevels (−320 m, −400 m, −480 m, and −600 m) tend to show “funnel”-type curves.

Finally, a logistic function can well fit the right part of the subsidence curve, and the value of parameter “a” in its function formula is very close to the maximum subsidence value of each sublevel, especially the newly excavated sublevels. We found that the value of “r” is positively correlated with the fractal dimension value in deeper sublevels (−320 m, −400 m, −480 m, and −600 m) and is negatively correlated with the fractal dimension value in more shallow sublevels (−240 m and −200 m), and the fractal dimension value reflects the degree of disturbance of the excavated sublevel.

Data availability statement

The original contributions presented in the study are included in the article/Supplementary Material; further inquiries can be directed to the corresponding author.

References

- Adhikary, D., and Guo, H. (2015). Modelling of longwall mining-induced strata permeability change. *Rock Mech. Rock Eng.* 48, 345–359. doi:10.1007/s00603-014-0551-7
- Adhikary, D., Khanal, M., Jayasundara, C., and Balusu, R. (2016). Deficiencies in 2D simulation: A comparative study of 2D versus 3D simulation of multi-seam longwall mining. *Rock Mech. Rock Eng.* 49, 2181–2185. doi:10.1007/s00603-015-0842-7
- Alejano, L. R., Ramôáñez-Oyanguren, P., and Taboada, J. (1999). FDM predictive methodology for subsidence due to flat and inclined coal seam mining. *Int. J. Rock Mech. Min. Sci.* 36 (4), 475–491. doi:10.1016/s0148-9062(99)00022-4
- Aly, M. H., Klein, A. G., and Zebker, H. A. (2012). Land subsidence in the Nile Delta of Egypt observed by persistent scatterer interferometry. *Int. J. Remote Sens.* 33, 2068–2096.
- Asadi, A., Shahriar, K., Goshtasbi, K., and Najm, K. (2005). Development of a new mathematical model for prediction of surface subsidence due to inclined coal-seam mining. *J. S Afr. I Min. Metall.* 105 (1), 15–20.
- Bai, Y. R., Gu, Z. M., and Bai, S. W. (2002). Preliminary study on surface subsidence and strata movement caused by underground mining in eastern Chengchao Iron Mine. *Chin. J. Rock Mech. Eng.* 21, 340–342.
- Bak, P., Tang, C., and Wiesenfeld, K. (1987). Self-organized criticality an explanation of the 1/f noise. *Phys. Rev. Lett.* 59, 381–384. doi:10.1103/physrevlett.59.381
- Bao, X., Zhang, R., Shama, A., Li, S., Xie, L. X., Lv, J. C., et al. (2022). Ground deformation pattern analysis and evolution prediction of shanghai pudong international airport based on PSI long time series observations. *Remote Sens.* 14 (3), 610. doi:10.3390/rs14030610

Author contributions

Conceptualization, JL and FM; methodology, JL and JG; formal analysis, JL and FM; investigation, JG and GL; resources, FL; data curation, YS; writing—original draft preparation, JL; writing—review and editing, FM; supervision, JG; project administration, GL and FL; funding acquisition, FM. All authors have read and agreed to the published version of the manuscript.

Funding

This research was funded by the National Natural Science Foundation of China (Grant numbers 41831293 and 42072305). The authors express grateful appreciation for the support.

Acknowledgments

The authors would like to thank the Copernicus program of the European Space Agency (ESA) for providing Sentinel-1A data and NASA for arranging the SRTM DEM data. The data for eliminating atmospheric errors were provided by Generic Atmospheric Correction Online Service (GACOS). The authors also thank Lv for professional instructions. The authors also thank the editor and reviewers for their valuable advice, which improved the paper.

Conflict of interest

The authors declare that the research was conducted in the absence of any commercial or financial relationships that could be construed as a potential conflict of interest.

Publisher's note

All claims expressed in this article are solely those of the authors and do not necessarily represent those of their affiliated organizations, or those of the publisher, the editors, and the reviewers. Any product that may be evaluated in this article, or claim that may be made by its manufacturer, is not guaranteed or endorsed by the publisher.

- Berardino, P., Fornaro, G., Lanari, R., and Sansosti, E. A new algorithm for surface deformation monitoring based on small baseline, *IEEE Transactions on Geoscience and Remote Sensing*, 40, 2002.
- Biancolini, M. E., Brutti, C., Paparo, G., and Zanini, A. (2006). Fatigue cracks nucleation on steel, acoustic emission and fractal analysis. *Int. J. Fatigue* 28, 1820–1825. doi:10.1016/j.jfatigue.2005.12.003
- Cao, J. Y. (2019). Study on deformation law of rock mass caused by mining of seabed inclined ore body. Ph.D. Thesis. Beijing, China: University of Chinese Academy of Sciences.
- Chen, S. J., Wang, H. L., Wang, H. Y., Guo, W. J., and Li, X. S. (2016). Strip coal pillar design based on estimated surface subsidence in eastern China. *Rock Mech. Rock Eng.* 49, 3829–3838. doi:10.1007/s00603-016-0988-y
- Cheng, G. W., Chen, C. X., Ma, T. H., Liu, H. Y., and Tang, C. A. (2017). A case study on the strata movement mechanism and surface deformation regulation in chengchao underground iron mine. *Rock Mech. Rock Eng.* 50, 1011–1032. doi:10.1007/s00603-016-1132-8
- Cui, X. M., Wang, J. C., and Liu, Y. S. (2001). Prediction of progressive surface subsidence above longwall coal mining using a time function. *Int. J. Rock Mech. Min. Sci.* 38, 1057–1063. doi:10.1016/s1365-1609(01)00061-2
- Dai, H. Y., Wang, J. Z., Cai, M. F., Wu, L. X., and Guo, Z. Z. (2002). Seam dip angle based mining subsidence model and its application. *Int. J. Rock Mech. Min. Sci.* 39, 115–123. doi:10.1016/s1365-1609(02)00008-4
- Diez, R. R., and Alvarez, J. T. (2000). Hypothesis of the multiple subsidence trough related to very steep and vertical coal seams and its prediction through profile functions. *Geotechnical Eng. Eng.* 18, 289–311. doi:10.1023/a:1016650120053
- Ferretti, A. C., Prati, C., and Rocca, F. (2001). Permanent scatterers in SAR interferometry. *Trans. Geosci. Remote Sens.* 39, 8–20. doi:10.1109/36.898661
- Foroughnia, F., Nemati, S., Maghsoudi, Y., and Perissin, D. (2018). An iterative PS-InSAR method for the analysis of large spatio-temporal baseline data stacks for land subsidence estimation. *Int. J. Appl. Earth Obs. Geoinf.* 74, 248–258. doi:10.1016/j.jag.2018.09.018
- Gastaldo, R. A., Demko, T. M., and Liu, Y. J. (1993). Application of sequence and genetic stratigraphic concepts to carboniferous coal-bearing strata – An example from the black warrior basin. *USA. Geol. Rundsch.* 82, 212–226.
- Ghabraie, B., Ren, G., Zhang, X., and Smith, J. (2015). Physical modelling of subsidence from sequential extraction of partially overlapping longwall panels and study of substrata movement characteristics. *Int. J. Coal Geol.* 140, 71–83. doi:10.1016/j.coal.2015.01.004
- Holla, L., and Buizen, M. (1991). The ground movement, strata fracturing and changes in permeability due to deep longwall mining. *Int. J. Rock Mech. Min. Sci. Geomech. Abstr.* 28 (2/3), 207–217. doi:10.1016/0148-9062(91)92168-x
- Hu, Q. F., Cui, X. M., Liu, W. K., Feng, R. M., Ma, T. J., and Li, C. Y. (2022). Quantitative and dynamic predictive model for mining-induced movement and deformation of overlying strata. *Eng. Geol.* 311, 106876. doi:10.1016/j.enggeo.2022.106876
- Hui, X., Ma, F., Zhao, H. J., and Xu, J. M. (2019). Monitoring and statistical analysis of mine subsidence at three metal mines in China. *Bull. Eng. Geol. Environ.* 78, 3983–4001. doi:10.1007/s10064-018-1367-6
- Jiang, Y., Misa, R., Li, P. Y., Yuan, X., Sroka, A., and Jiang, Y. (2019). A review of the development process of mine subsidence theory. *Metal. Mine* 10, 1–7.
- Jiráseka, J., Opluštil, S., Sivek, M., Schmitz, M. D., and Abels, H. A. (2018). Astronomical forcing of Carboniferous paralic sedimentary cycles in the Upper Silesian Basin, Czech Republic (Serpukhovian, latest Mississippian): New radiometric ages afford an astronomical age model for European biozonations and substages. *Earth-Science Rev.* 177, 715–741. doi:10.1016/j.earscirev.2017.12.005
- Kwinta, A., and Gradka, R. (2020). Analysis of the damage influence range generated by underground mining. *Int. J. Rock Mech. Min. Sci.* 128, 104263. doi:10.1016/j.ijrmms.2020.104263
- Li, G., Hui, X., Ma, F. S., and Guo, J. (2022). Temporal analysis of ground movement at a metal mine in China. *Remote Sens.* 14 (19), 4993. doi:10.3390/rs14194993
- Li, G., Ma, F. S., Guo, J., and Zhao, H. J. (2020). Deformation characteristics and control method of kilometer-depth roadways in a nickel mine: A case study. *Appl. Sci.* 10, 3937. doi:10.3390/app10113937
- Li, G., Ma, F. S., Guo, J., Zhao, H. J., and Liu, G. (2020). Study on deformation failure mechanism and support technology of deep soft rock roadway. *Eng. Geol.* 264, 105262. doi:10.1016/j.enggeo.2019.105262
- Li, X., Wang, S. J., Liu, T. Y., and Ma, F. S. (2004). Engineering geology, ground surface movement and fissures induced by underground mining in the Jinchuan Nickel Mine. *Eng. Geol.* 76, 93–107. doi:10.1016/j.enggeo.2004.06.008
- Litwiniszyn, J. (1954). Displacements of a rock mass in the light of the theory of probability Tom II. *Arch. Górn i Hut. Z.* 2.
- Liu, B. C., and Dai, H. Y. (2016). Research development and Origin of probability integral method. *J. Min. Strata Control Eng.* 21 (02), 1–3.
- Liu, B. C., and Liao, G. H. (1965). *The Basic Law of the Movement of the Surface of the Coal Mine*. Beijing, China: China Industry Press.
- Liu, J., Ma, F. S., Guo, J., Li, G., Song, Y. W., and Wan, Y. (2022). A field study on the law of spatiotemporal development of rock movement of under-sea mining, Shandong, China. *Sustainability* 14, 5864. doi:10.3390/su14105864
- Liu, J., Ma, F. S., Li, G., Guo, J., Wan, Y., and Song, Y. W. (2022). Evolution assessment of mining subsidence characteristics using SBAS and PS interferometry in Sanshandao gold mine, China. *Remote Sens.* 14, 290. doi:10.3390/rs14020290
- Ma, F. H., and Ding, Y. (2009). Numerical simulation of ground movement behavior inclined multiple seams mining with deep dip angle. *Chin. Min. Mag.* 18 (06), 71–73.
- Massonnet, D., Feigl, K., Rossi, M., and Adragna, F. (1994). Radar interferometric mapping of deformation in the year after the Landers earthquake. *Nature* 369 (6477), 227–230. doi:10.1038/369227a0
- Meng, F. F., Piao, C. D., Shi, B., Sasaoka, T., and Shimada, H. (2021). Calculation model of overburden subsidence in mined-out area based on Brillouin optical time-domain reflectometer technology. *Int. J. Rock Mech. Min. Sci.* 138, 104620. doi:10.1016/j.ijrmms.2021.104620
- Meng, Z. P., Li, G. Q., and Xie, X. T. (2012). A geological assessment method of floor water inrush risk and its application. *Eng. Geol.* 143, 51–60. doi:10.1016/j.enggeo.2012.06.004
- Murgia, F., Bignami, C., Brunori, C. A., Tolomei, C., and Pizzimenti, L. (2019). Ground deformations controlled by hidden faults: MultiFrequency and multitemporal InSAR techniques for urban hazard monitoring. *Remote Sens.* 11, 2246. doi:10.3390/rs11192246
- Park, E. S., Choi, S. O., and Shin, H. S. (2005). Simulation of the ground subsidence mechanism using a PFC2D. *The 40th U.S. Symposium on Rock Mechanics, Anchorage, Alaska*, 29, 05–735.
- Qin, S. Q. (2000). Catastrophe model and chaos mechanism of ramp instability. *Chin. J. Rock Mech. Eng.* 19, 486–492.
- Ren, G., Li, G., and Kullessa, M. (2014). Application of a generalised influence function method for subsidence prediction in multi-seam longwall extraction. *Geotech. Geol. Eng.* 32 (4), 1123–1131. doi:10.1007/s10706-014-9787-y
- Sepehri, M., Apel, B. D., Adeeb, S., Leveille, P., and Hall, A. R. (2020). Evaluation of mining-induced energy and rockburst prediction at a diamond mine in Canada using a full 3D elastoplastic finite element model. *Eng. Geol.* 266, 105457. doi:10.1016/j.enggeo.2019.105457
- Shen, G. Q. (2002). Fractal dimension and fractal growth of urbanized areas. *Int. J. Geogr. Inf. Sci.* 16, 419–437. doi:10.1080/13658810210137013
- Sheorey, P. R., Loui, J. P., Singh, K. B., and Singh, S. K. (2000). Ground subsidence observations and a modified influence function method for complete subsidence prediction. *Int. J. Rock Mech. Min. Sci.* 37, 801–818. doi:10.1016/s1365-1609(00)00023-x
- Sócrates, F. M., Víctor, M. H. M., José, T. V., and Cecilia, I. V. R. (2020). Evolution assessment of structurally-controlled subsidence using SBAS and PS interferometry in an emblematic case in Central Mexico. *Eng. Geol.* 279, 105860. doi:10.1016/j.enggeo.2020.105860
- Svartsjaern, M., Saiang, D., Nordlund, E., and Eitzenberger, A. (2016). Conceptual numerical modeling of large-scale footwall subsidence at the kiirunavaara mine, and implications for deformation monitoring. *Rock Mech. Min. Sci.* 49, 943–960. doi:10.1007/s00603-015-0750-x
- Tarighat, F., Foroughnia, F., and Perissin, D. (2021). Monitoring of power towers' movement using persistent scatterer SAR interferometry in south west of tehran. *Remote Sens.* 13 (3), 407. doi:10.3390/rs13030407
- Tu, S. H., Yuan, Y., Wang, F. T., and Bai, Q. S. (2015). Present situation of fully mechanized mining technology for steeply inclined coal seams in China. *Arab. J. Geosci.* 8, 4485–4494. doi:10.1007/s12517-014-1546-0
- Tuncay, D., Tulu, B. I., and Klemetti, T. (2021). Re-Analysis of abutment angle method for moderate and deep cover retreat room and pillar mines and investigation of loading mechanics using finite volume modeling. *Rock Mech. Rock Eng.* 54, 3447–3468. doi:10.1007/s00603-020-02336-4
- Valkaniotis, S., Papathanassiou, G., and Ganas, A. (2018). Mapping an earthquake-induced landslide based on UAV imagery; case study of the 2015 Okeanos landslide, Lefkada, Greece. *Eng. Geol.* 245, 141–152. doi:10.1016/j.enggeo.2018.08.010
- Villegas, T., Nordlund, E., and Dahnér-Lindqvist, C. (2011). Hangingwall surface subsidence at the kiirunavaara mine, Sweden. *Eng. Geol.* 121, 18–27. doi:10.1016/j.enggeo.2011.04.010
- Wagner, H. (2019). Deep mining: A rock engineering challenge. *Rock Mech. Rock Eng.* 52, 1417–1446. doi:10.1007/s00603-019-01799-4
- Whittaker, B. N., and Reddish, D. J. (1989). *Subsidence: Occurrence, Prediction and control*. Amsterdam, Netherlands: Elsevier Amsterdam.
- Xie, H. P., and Pariseau, W. G. (1993). Fractal character and mechanism of rock bursts. *Chin. J. Rock Mech. Eng.* 30, 343–350. doi:10.1016/0148-9062(93)91718-x
- Xie, H. P., Zhou, H. W., Wang, J. A., Li, L. Z., and Kwasniewski, M. A. (1999). Application and comparative analysis of FLAC in coal mining subsidence prediction. *Chin. J. Rock Mech. Eng.* 4, 397–401.

- Xu, H. Z., and Li, X. H. (2005). Time function of surface subsidence based on Logistic growth model. *Rock Soil Mech.* (S1), 151–153.
- Xu, J. M., Zhu, W. B., Xu, J. L., Wu, J. Y., and Li, Y. C. (2021). High-intensity longwall mining-induced ground subsidence in Shendong coalfield, China. *Int. J. Rock Mech. Min. Sci.* 141, 104730. doi:10.1016/j.ijrmms.2021.104730
- Yerro, A., Corominas, J., Monells, D., and Mallorquí, J. J. (2014). Analysis of the evolution of ground movements in a low densely urban area by means of DInSAR technique. *Eng. Geol.* 170, 52–65. doi:10.1016/j.enggeo.2013.12.002
- Yu, C., Li, Z., Penna, N. T., and Crippa, P. (2018). Generic atmospheric correction model for interferometric synthetic aperture radar observations. *J. Geophys. Res. Solid Earth.* 123, 9202–9222. doi:10.1029/2017jb015305
- Yu, C., Li, Z., and Penna, N. T. (2018). Interferometric synthetic aperture radar atmospheric correction using a GPS-based iterative tropospheric decomposition model. *Remote Sens. Environ.* 204, 109–121. doi:10.1016/j.rse.2017.10.038
- Yu, C., Penna, N. T., and Li, Z. (2017). Generation of real-time mode high-resolution water vapor fields from GPS observations. *J. Geophys. Res. Atmos.* 122, 2008–2025. doi:10.1002/2016jd025753
- Zhao, D. D., Jin, G., Li, H. S., and Huang, J. Y. (2013). Geological characteristics of Sanshandao island gold deposit in Laizhou, Shandong province and the genetic discussion. *Contributions Geol. Mineral Resour. Res.* 28 (04), 546–551.
- Zhao, H. J., Ma, F. S., Zhang, Y. M., and Guo, J. (2013). Monitoring and mechanisms of ground deformation and ground fissures induced by cut-and-fill mining in the Jinchuan Mine 2, China. *Environ. Earth Sci.* 68, 1903–1911. doi:10.1007/s12665-012-1877-7



OPEN ACCESS

EDITED BY
Naifei Liu,
Xi'an University of Architecture and
Technology, China

REVIEWED BY
Chunhui Ma,
Xi'an University of Technology, China
Sai Wu,
Chang'an University, China

*CORRESPONDENCE
Ying Cui,
✉ cuiying126@163.com

SPECIALTY SECTION
This article was submitted to
Environmental Informatics and Remote
Sensing,
a section of the journal
Frontiers in Earth Science

RECEIVED 02 December 2022
ACCEPTED 28 December 2022
PUBLISHED 12 January 2023

CITATION
Cui Y, Li Z, Fang J and Zhao B (2023), Crater
effects of shallow burial explosions in soil
based on SPH-FEM analysis.
Front. Earth Sci. 10:1114178.
doi: 10.3389/feart.2022.1114178

COPYRIGHT
© 2023 Cui, Li, Fang and Zhao. This is an
open-access article distributed under the
terms of the [Creative Commons
Attribution License \(CC BY\)](#). The use,
distribution or reproduction in other
forums is permitted, provided the original
author(s) and the copyright owner(s) are
credited and that the original publication in
this journal is cited, in accordance with
accepted academic practice. No use,
distribution or reproduction is permitted
which does not comply with these terms.

Crater effects of shallow burial explosions in soil based on SPH-FEM analysis

Ying Cui^{1,2*}, Zhangjian Li³, Jun Fang³ and Ben Zhao³

¹Civil Engineering College, Xi'an Shiyong University, Xi'an, China, ²The Key Laboratory of Well Stability and Fluid and Rock Mechanics in Oil and Gas Reservoir of Shaanxi Province, Xi'an, China, ³Mechanical Engineering College, Xi'an Shiyong University, Xi'an, China

This study analyzed the effects and influencing factors of shallowly-buried explosions in soil based on the design and implementation of static explosion experiments and numerical simulations. Based on the static explosion test data, a numerical analysis model of SPH-FEM was established and the explosion process and pit parameters in explosions shallowly buried in soil were analyzed. The results of numerical calculations and comparisons verified the effectiveness of the SPH-FEM method in simulating shallowly-buried explosions in soil. Furthermore, the similarities and differences between the SPH-FEM and ALE methods in the numerical simulation of the same explosion in the soil were assessed. The relationships between the blasting pit radius and explosive depth, and between the explosives weight and pit volume were analyzed. The empirical curve formula of the explosive depth and the crater radius with 9.35 kg of TNT explosive were obtained by mathematical fitting. The results showed that the SPH-FEM method was more refined and more computationally efficient than the ALE method to simulate shallow burial explosions in soil. The established empirical curve formula, which expressed the relationship between the explosive burial depth and the pit radius, effectively predicted the pit radius of the shallow burial explosion. With increasing explosive burial depth, the pit radius increased to the peak value and then decreased rapidly.

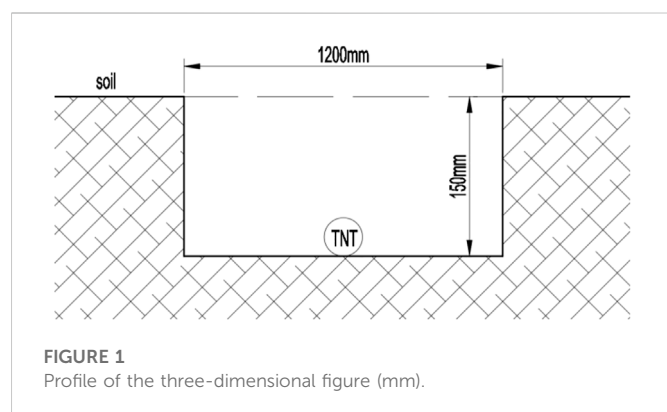
KEYWORDS

shallow burial explosion, static explosion test, SPH-FEM method, numerical simulation, crater parameter

1 Introduction

With the rapid development of China's infrastructure, shallowly-buried explosions in soil are increasingly widely used in various types of engineering construction (Xie, 2007). Under blast loading, the initial natural density and moisture content of the soil changes, and various geological factors of the soil have a greater impact on the transmission of impulse in shallowly buried explosions. In addition, the process of shallowly-buried explosions in soil is more complex, both in terms of soil breakage and the propagation of blast products and blast shock waves (Qian, 2009; Wang et al., 2016; Liu et al., 2022a; Zhang et al., 2022a; Zhao et al., 2022; Liu et al., 2023; Zhang et al., 2022b). Therefore, establishing an effective method to describe the effects of shallowly buried explosions in soil is a scientific challenge that requires the study of the dynamic response and soil parameters of soils during blast loading (Du and Lu, 2011).

The blast crater formation of shallowly buried explosions is related to factors including soil type and explosive type. Liu et al. (2022b) used ANSYS/AUTODYN for modeling and simulation analysis to study the ground impact effect of the explosion in soil. They showed that the distribution of the blast stress wave changed with increasing burial depth of the charge



ratio, with the central zone increasing rapidly, the surface zone decreasing rapidly, and the near-surface increasing gradually. Feng et al. (2020) summarized research on the effect of explosive near-surface explosion into pits and analyzed the formula for calculating the size of the blast crater formed by the explosion and the applicable conditions. Mu et al. (2010) studied explosive explosion cratering in soil and the accompanying stress wave propagation law at variable burial depths and established the stress wave propagation law in soil, the semi-empirical formula for explosion cratering, and the prediction formula for crater radius in a semi-closed explosion stage. Jia et al. (2017) conducted a series of field experiments in low moisture and saturated sandy soil to analyze the effect of explosive charge, explosive burial depth, and soil moisture content on the crater, and classified the crater pattern according to moisture content and burial depth. Yue et al. (2012) determined the relationship between charge volume and burial depth, as well as the volume of thrown funnel pits.

These previous studies in the experimental and numerical simulation of explosions in soil have provided many valid conclusions. However, when using the traditional ALE (Arbitrary Lagrange-Euler) finite element method to simulate explosions in soil, although the rapid propagation of shock waves in the soil medium is

well simulated, it is difficult to accurately address large deformation aspects such as splash and crushing phenomenon after the explosion. Meanwhile, SPH (Smooth Particle Hydrodynamics), a meshless numerical method, deals relatively accurately with difficult problems such as large deformation and fluid flow; however, its disadvantages include long computational time, poor stability, and low accuracy. The coupled SPH-FEM method can consider the advantages of both and improve the computational efficiency while ensuring accuracy (Hu et al., 2015; Liang et al., 2017). The present study designed and conducted shallowly buried static explosion tests in soil to obtain the parameters of shallowly buried explosion craters. We also established a numerical model of shallowly buried explosion in soil based on the SPH-FEM and ALE methods, respectively. We then compared the numerical simulation and test results to verify the effectiveness of the SPH-FEM coupling algorithm for the numerical simulation of explosions in soil. Furthermore, by comparing the simulation results of SPH-FEM and ALE simultaneously with the error of the test results, we confirmed the superiority of the SPH-FEM method in simulating shallowly buried explosions in soil. Based on the numerical simulation results and through mathematical fitting, we established a shallowly buried explosion formula that expressed the explosive burial depth and the burst pit radius (a proportional burial depth of not more than $.8 \text{ m/kg}^{1/3}$).

2 Methods

2.1 Shallowly buried static explosion test in soil

2.1.1 Test preparation

The test bury pit site measuring 1,200 mm (length) \times 900 mm (width) \times 150 mm (height) was excavated. The profile is shown in Figure 1. The explosive used for the test was 9.35 kg of columnar TNT. The soil in the test site excavation area was clay due to the explosive's proportional burial depth of $.07 \text{ m/kg}^{1/3}$ and not more than $.8 \text{ m/kg}^{1/3}$,

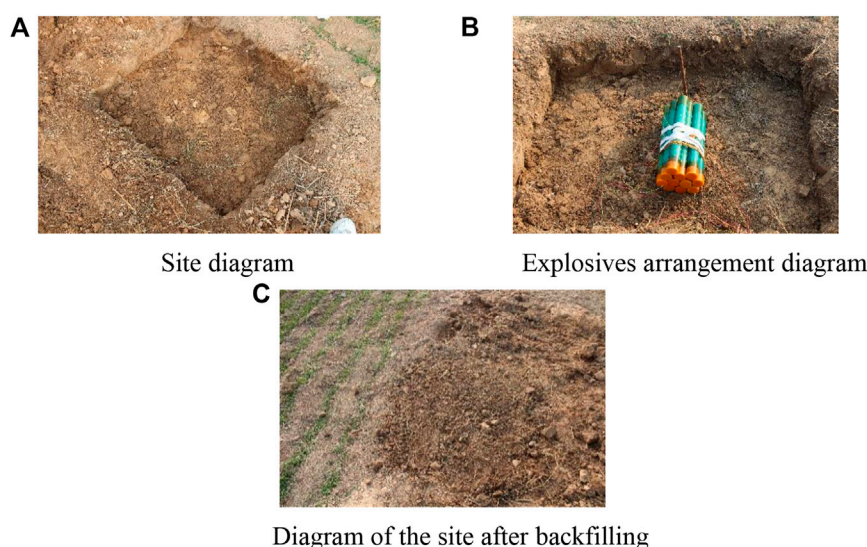


FIGURE 2
Schematic diagram of the explosive arrangement and backfill site. (A) Site diagram. (B) Explosive arrangement. (C) Site after backfilling.



FIGURE 3
Soil deformation.

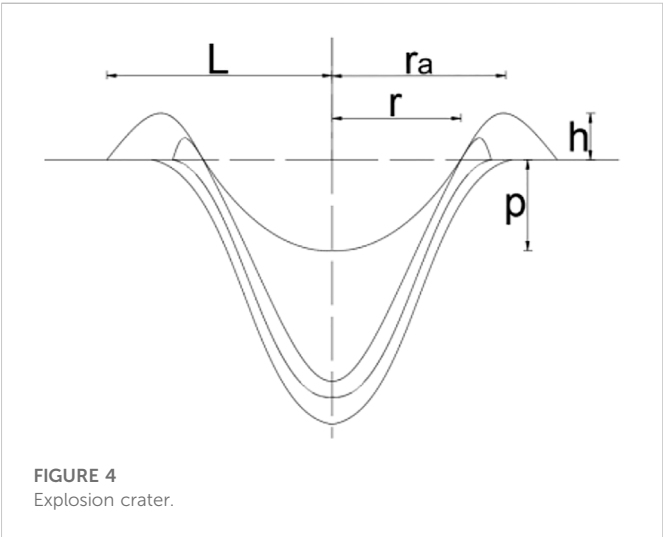


FIGURE 4
Explosion crater.



FIGURE 5
Schematic diagram of the field measurements of the main parameters.

which was defined as a shallowly buried explosion (Ambrosini and Luccioni, 2019). The site explosive arrangement and backfill are shown in Figure 2.

TABLE 1 Crater parameters.

Physical quantities	Measured value (mm)
r	1,100
p	660

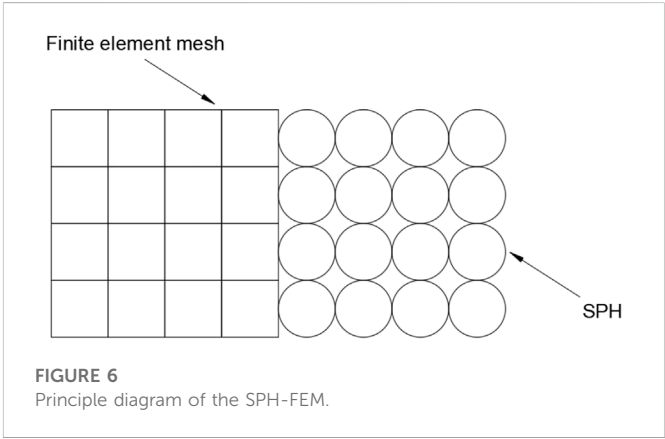


FIGURE 6
Principle diagram of the SPH-FEM.

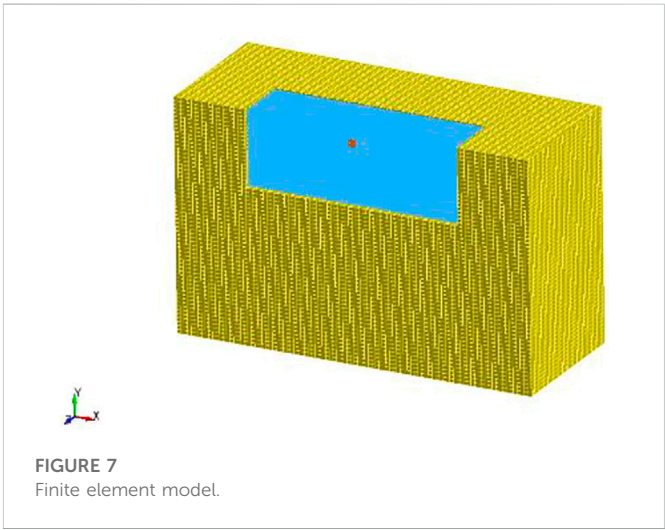


FIGURE 7
Finite element model.

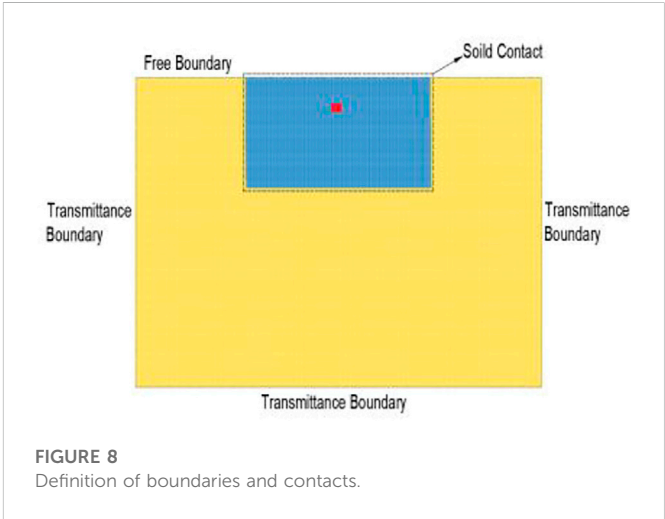


FIGURE 8
Definition of boundaries and contacts.

TABLE 2 Soil parameters.

Parameters	RO	G	BULK	a_0	a_1	a_2	PC
Takes values	1.73×10^{-3}	63.85	3×10^4	1.73×10^{-3}	7.033×10^{-2}	0.3	-6.9×10^{-3}
Parameters	VCR			REF			
Takes values	0			0			
Parameters	EPS ₁	EPS ₂	EPS ₃	EPS ₄	EPS ₅	EPS ₆	EPS ₇
Takes values	0	.05	.09	.11	.15	.19	.21
Parameters	EPS ₈	EPS ₉	EPS ₁₀				
Takes values	.22	.25	0.3				

TABLE 3 Explosive material parameters

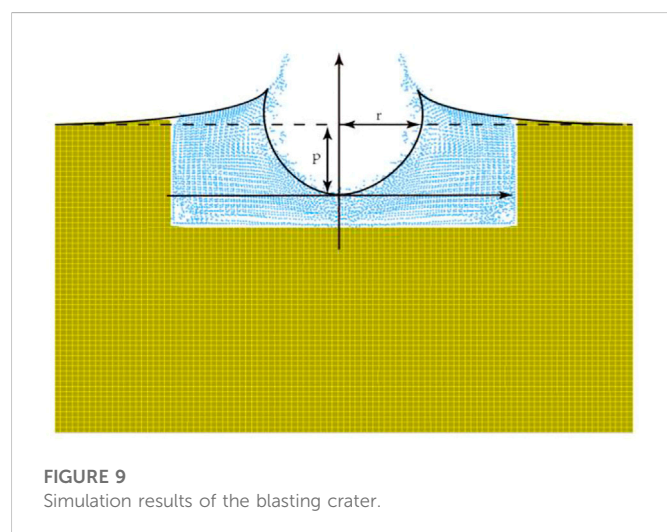
Parameters	RO	D	PCJ	BETA	K	G	SIGY
Takes values	1.64×10^{-3}	6.93×10^3	2.1×10^4	0	0	0	0

TABLE 4 Equations for the state parameters of the explosive.

Parameters	A	B	R ₁	R ₂	OMEG	E ₀	V ₀
Takes values	3.74×10^5	3.23×10^3	4.15	.95	0.3	7,000	1.0

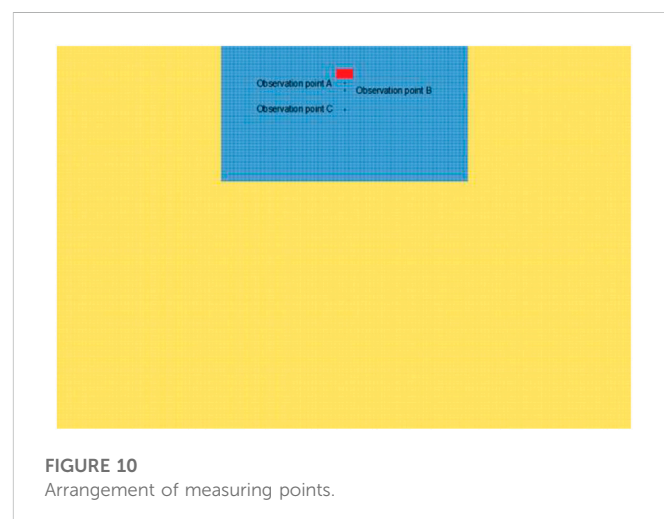
TABLE 5 Comparisons of numerical simulation and experimental results.

Comparative content	r/mm	p/mm
Test results	1,100	660
Numerical simulation results	964	618
Relative Error	12.4%	6.36%



2.1.2 Analysis of the experimental results

The soil deformation after the explosion is shown in Figure 3. After absorbing the energy released by the explosion of explosives, the soil body showed a large deformation. Due to the shallow burial depth, after the energy absorbed by the elastic deformation of the soil body reached saturation, the soil body quickly expanded and emitted failed soil particles and clods to form a blast funnel. Based on the description of the blast funnel in blast mechanics, the parameters that mainly reflect the energy of the shallow burial blast are the funnel radius r , the visible depth p , the lip radius r_a , the lip stacking height h , and the maximum stacking distance L (Zhou, 2014), as shown in Figure 4. Compared to other parameters, the funnel radius r and the visible depth p are easy to measure and the error was lower in the real test. This experiment measured the



funnel radius r and the visible depth p . The field measurements and results of these two main parameters are shown in Figure 5 and Table 1.

2.2 Numerical simulation of soil damage and destruction based on the SPH-FEM method under a shallowly buried blast load

2.2.1 Principle of the SPH method

The basic idea of the SPH method is to describe a continuous fluid (or solid) by a group of interacting masses, with each material point carrying various physical quantities, including mass, velocity, etc. By solving the kinetic equations of the mass group and tracking the motion trajectory of each mass, the mechanical behavior of the whole system can be described. By using an interpolation function for the

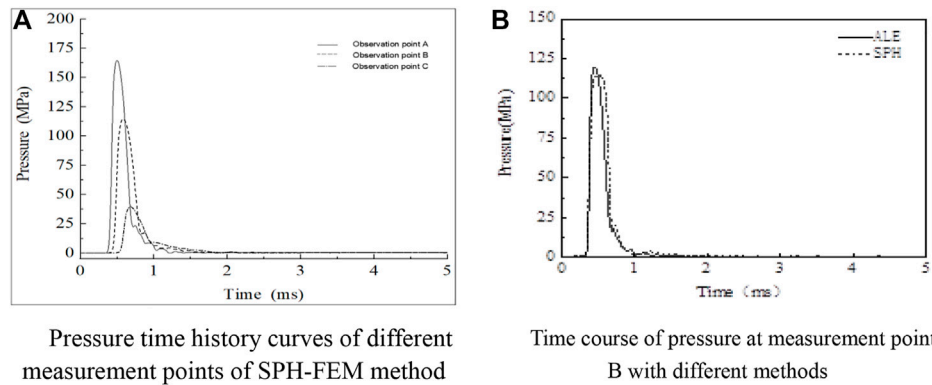


FIGURE 11

Pressure time course curve. (A) Pressure time history curves of different measurement points using the SPH-FEM method. (B) Pressure time course at measurement point B for different methods.

action between each variable mass point in the SPH, the expression can be formulated (Zhang and Fedoroff, 1996), which can be approximated as follows.

$$f(x) = \int_{\Omega} f(x')W(x-x',h)dx' \quad (1)$$

where $f(x)$ is a function of the three-dimensional coordinates x , $x-x'$ is the spacing between particles, and h is the smooth length of the particle

Eq. 1 can be transformed into the spatial derivative of the kernel function using the scattering theorem.

$$\nabla f(x_i) = \int_{\Omega} f(x')\nabla_i W(x-x',h)dx' \quad (2)$$

Using the particle approximation, Eq. 2 can be summarized by discretization as follows.

$$\nabla f(x_i) = \sum_j \frac{m_j}{\rho_j} f(x_j)\nabla_i W_{ij} \quad (3)$$

where m_j is the mass of SPH particle j , ρ_j is the density of SPH particle j , and N is the number of particles in the smooth length range.

2.2.2 Implementation of the coupling algorithm

In modeling with the SPH-FEM method, the soil in the near blast zone is discretized based on the SPH method, while the remaining soil is meshed by FEM. The SPH particles and FEM mesh are coupled through the contact algorithm, in which the stress-strain and other information transferred from the SPH particles is passed to the FEM mesh to ensure displacement coordination as a point-plane connection, the principle of which is shown in Figure 6.

2.3 Model building

By analyzing the test parameters and considering the symmetry, ANSYS ADPL was used to define the cell properties and material type and perform the meshing to build a half model. LS-Prepost was used to

convert the explosive and the soil in the near area of the explosion into SPH particles and modify the keywords. Since the SPH-FEM method does not need to consider the coupling between air and soil, the air part was not established in the model. To ensure concordance with the test site, the location of the explosives in the model was maintained to be consistent with the real position. ANSYS ADPL was used to define the NODES group, add contact and boundary conditions, ensure the accuracy of the calculation results, and improve the calculation efficiency by setting the appropriate SPH particle density and FEM mesh. The established finite element model is shown in Figure 7.

Based on the actual constraint conditions, the transmittance boundary was selected on both sides and the bottom of the soil cell, and the free boundary is selected on the top. A solid contact was selected between the FEM cell and SPH particles; contact pairs were established using CONTACT_TIED_TO_SURFACE_OFFSET; the symmetry surface was set to the SPH and FEM symmetry boundaries respectively; and DEFINE_BOX was used to control the particle range, boundary, and contact, as defined in Figure 8 in mm-ms-MPa.

2.4 Material ontology model

1) Soil material

The dynamic mechanical response of soils under shallowly buried blast loading was simulated numerically using LS-DYNA software. Using the SOIL_AND_FOAM material model, the ideal plastic yield function is:

$$\Phi = \frac{\sigma_{ij}\sigma_{ij}}{2} - (a_0 + a_1\sigma + a_2\sigma^2) \quad (4)$$

where σ_{ij} is the partial stress component; σ is the average stress; and a_0 , a_1 , and a_2 are constant terms of the dimensionless $J_{2-\sigma}$ quadratic fitting curve. The specific calculation parameters of the soil body are shown in Table 2.

2) Explosives

The *MAT_HIGH_EXPLOSIVE_BURN high-energy explosive combustion model and the JWJ equation of state were used to

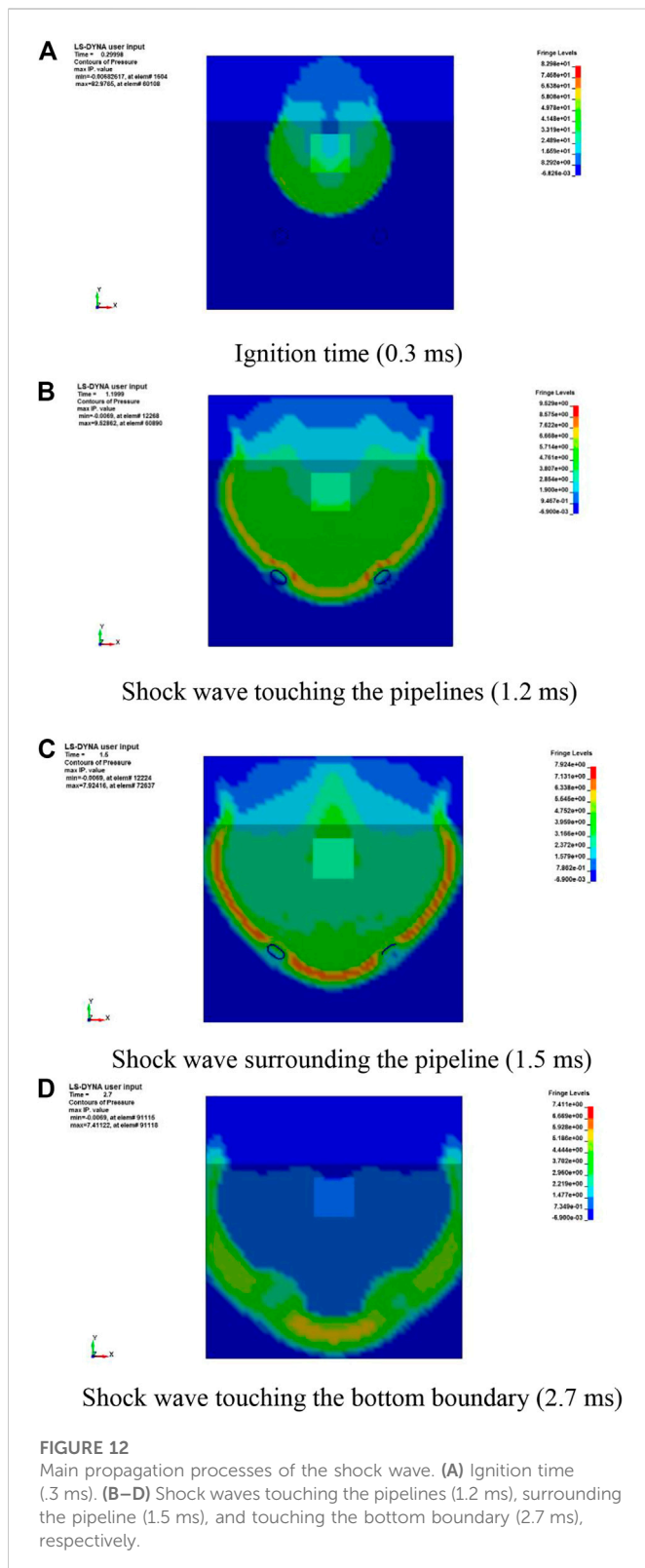


FIGURE 12
Main propagation processes of the shock wave. (A) Ignition time (0.3 ms). (B–D) Shock waves touching the pipelines (1.2 ms), surrounding the pipeline (1.5 ms), and touching the bottom boundary (2.7 ms), respectively.

simulate the explosive. The JWL equation of state can be expressed as follows:

$$P = A \left(1 - \frac{w}{R_1 V} \right) e^{-R_1 V} + B \left(1 - \frac{w}{R_2 V} \right) e^{-R_2 V} + \frac{wE}{V} \quad (5)$$

where P is the explosion pressure; V is the relative volume of the explosive; E is the initial energy per unit volume of the explosive; and w , A , B , R_1 , and R_2 are material constants. The explosive parameters are shown in Tables 3, 4.

3 Results and discussion

3.1 Comparison of SPH-FEM and experimental results

To verify the effectiveness of the SPH-FEM method, the experimentally obtained burst crater radius r and visible depth p were calibrated to the simulation results, as shown in Figure 9. The results of the comparison of the numerical simulation and experimental results of these two main parameters are shown in Table 5. Table 5 shows that the relative error of the radius of the burst hole r was 12.4%, the relative error of the visible depth p was 6.36%, and the results did not vary by more than $\pm 15\%$. The measured size deviation was about 10%. The comparative analysis of the experimental results showed that the numerical simulations of shallowly buried explosions in soil using the SPH-FEM scheme were reasonable and acceptable.

3.2 Analysis of the propagation law of explosion shock waves in soil

To further verify the effectiveness of the SPH-FEM method, as shown in Figure 10 selected along the depth and distance from the location of the burst core proportional distances of .17, .21, and .31 $\text{m/kg}^{1/3}$ of the three measurement points to extract the time course of the blast shock wave pressure curve in the soil (Figure 11). The test data showed that the propagation of the spherical shock wave and compressional wave generated by the explosion in the soil also obeyed the “explosion similarity law”. Therefore, the maximum pressure P_m of the blast wave at d from the center of the explosion can be obtained according to the volume analysis (Luo et al., 2016). The maximum pressure P_m equation can be expressed as follows:

$$P_m = k \left(\frac{\sqrt[3]{\omega}}{d} \right)^\alpha \quad (6)$$

where P_m is the maximum pressure, ω is the explosives quality, d is the distance to the explosion center and k and α are test constants.

As shown in Figure 11A, with increasing time, the peak pressure of the blast shock wave of each measurement point decayed sharply, finally tending to zero. The blast shock wave pressure of different measurement points also varied. The peak pressure of the blast shock wave decayed sharply with increasing depth and distance. Further comparison of the results from different numerical simulation methods revealed that the peak pressure detected by the SPH-FEM method was 4.6% smaller than that detected by the ALE method for the same measurement point, as shown in Figure 11B. Since the density and looseness of the backfill were also close to the original soil layer

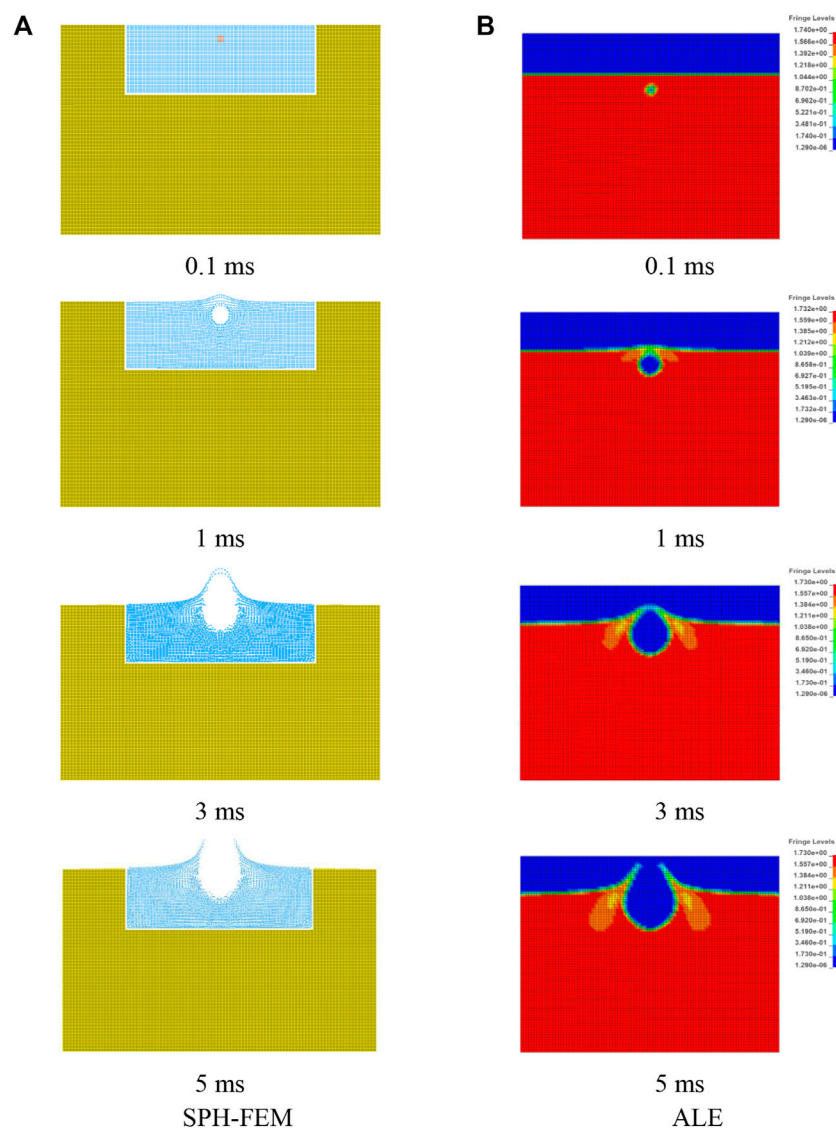


FIGURE 13

Comparisons of the crater formation process between SPH-FEM and ALE. (A) SPH-FEM. (B) ALE.

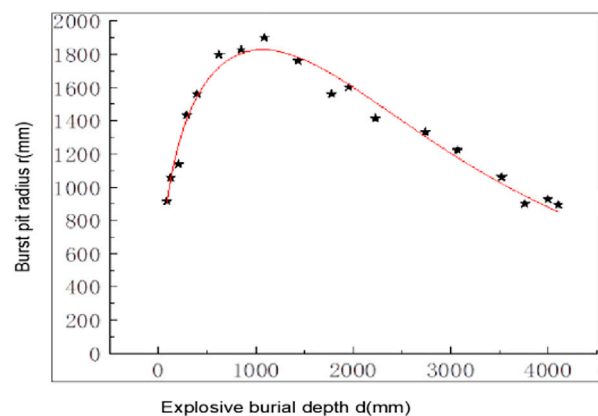


FIGURE 14

Relationship between explosive buried depth and crater radius.

after backfilling, the SPH-FEM method was fit for the simulation of explosions in soil. Comprehensive analysis showed that the SPH-FEM method effectively simulated the effect of soil cratering under shallowly buried blast loading.

3.3 Comparison of numerical simulation results between the SPH-FEM and ALE methods

The pressure of the shock wave from an explosion is another key factor affecting the damage to a target. The shallowly buried explosion caused shock wave propagation in both the air and the soil. The main propagation processes of a shock wave in the soil and air were determined, as shown in Figure 12.

Figures 12A–D show that the pressure values of the shock wave declined rapidly from 82.98 to 7.41 MPa in 2.7 ms. Additionally, the

pressure values declined significantly by 88.5% from .3 to 1.2 ms. This meant that the shallowly buried explosion released energy quickly; thus, we focused on the early response of the object. To visualize the shock wave transmission, two pipelines were added to the simulation, as shown in Figures 12B,C. Deformation of the two pipelines was evident, as shown in Figures 12B,C. Furthermore, because the propagation velocity of the shock wave differed between the air and the soil, the shapes of the shock waves also differed, and the projectile effect on the boundary between the air and soil was consistent with the experimental results. Diffraction occurred in the two specimens being surrounded by the shock wave, as shown in Figures 12C,D. All the analysis results showed that the shallowly buried explosion would result in damage to the buried object and the object near the boundary between the air and soil.

The burst crater formation processes simulated by the two methods at different moments are shown in Figure 13. Although both the SPH-FEM and ALE methods simulated the formation process of the burst crater, the same moment based on the SPH-FEM method simulation to obtain the soil deformation was slightly larger than that in the ALE method, while the SPH-FEM method to simulate the height of the soil throw differed from that of the ALE method, likely due to the influence of air and SPH particle mass. Since the SPH is a Lagrangian particle method, in which the calculation of the physical quantities is based on the sum of particles in the cell search domain, and some SPH particles quit working after the explosion, the implementation of boundary conditions in the SPH-FEM method is completely different from the boundary conditions. Although both algorithms can describe the movement and throwing phenomena of the soil after the explosion, the SPH-FEM method clearly represented the peeling phenomenon of the upper soil, while the ALE method was relatively vague. Moreover, the SPH-FEM method effectively avoided problems such as mesh entanglement and distortion and meshed the small deformation region to reduce the computational stress. Therefore, the SPH-FEM method showed more advantages over the ALE method in the simulation of shallowly buried explosions in soil.

3.4 Establishment of the relationship between explosive depth and burst pit radius in shallowly buried explosives in soil

The cratering effect of shallowly buried explosions in soil was mainly affected by the explosive burial depth and explosive quantity, which are also important parameters for determining the crater size and shape (Ambrosini et al., 2002). Using the SPH-FEM method, the radii of 9.35 kg of TNT explosives at different depths to produce craters were further extracted (Figure 14). Figure 14 demonstrates the trend of increasing crater radius with increasing explosive burial depth in the early stage, which decreased with increasing burial depth after reaching the peak in shallowly buried explosions in the soil. To effectively determine the number of explosives in the correspondence of the crater radius and explosives burial depth, a mathematical fitting method was used to establish the corresponding empirical curve Eq. 7. This empirical curve expressed the relationship between the explosive burial depth d and the radius of the crater r (Figure 14) and determined the relationship between the explosive burial depth and the burst pit radius for 9.35 kg of TNT explosive.

$$r = \frac{3699.1}{\left(1 + \left(\frac{696.8}{d}\right)^{0.54}\right) \left(1 + \left(\frac{d}{2853.8}\right)^{2.09}\right)} \quad (7)$$

where r is the radius of the burst pit and d is the depth of burial of explosives.

4 Conclusion

This study designed and implemented a shallow burial static explosion test in soil to determine the parameters of the burst crater. Based on the SPH-FEM and ALE methods, the test data were used to compare the effects of explosive explosion cratering. The conclusions were as follows.

- 1) Shallowly buried explosions in the soil make a blast funnel and have a particle splash effect. The SPH-FEM method effectively simulated the soil deformation and dispersion effect in this process with a small actual error.
- 2) The SPH-FEM and ALE methods effectively simulated shallowly buried explosions in soil. Compared to the ALE method, the SPH-FEM method more effectively simulated the shock wave formation of overpressure caused by the deformation of the surrounding soil until the process of breaking.
- 3) Both SPH-FEM and ALE methods effectively simulated the process of soil explosion cratering. The SPH-FEM method provided a more detailed view of the soil by the explosion load after the peeling phenomenon, with a more efficient calculation.
- 4) The combination of test data and numerical simulation results with mathematical fitting effectively established a relationship between the explosive burial depth and blast crater radius. The empirical formula established in this study can effectively determine the relationship between the burst crater radius and explosive burial depth of the soil with 9.35 kg of TNT.

Data availability statement

The original contributions presented in the study are included in the article/Supplementary Material. Further inquiries can be directed to the corresponding author.

Author contributions

YC, ZL, and JF designed the experiments, defined the intellectual content, performed the literature search, acquired the data, performed data analysis, and prepared the manuscript. JF, ZL, and BZ assisted in the data acquisition, data analysis, and statistical analysis. YC, JF, and ZL performed the literature search, data acquisition, and manuscript editing. YC and ZL performed the manuscript review. All authors have read and approved the content of the manuscript.

Funding

This study received funding from the Natural Science Foundation of China (51974255 and 51878056), Natural Science Basic Research Program of Shaanxi Province (2023-JC-YB-296), Key Scientific Research Projects of Shaanxi Provincial Department of Education

(22JT035) Postgraduate Innovation, and Practical Ability Cultivation Program of Xi'an Shiyou University (YCS22213121).

Conflict of interest

The authors declare that the research was conducted in the absence of any commercial or financial relationships that could be construed as a potential conflict of interest.

References

- Ambrosini, R. D., Luccioni, B. M., Danesi, R. F., Riera, J. D., and Rocha, M. M. (2002). Size of craters produced by explosive charges on or above the ground surface. *Shock Waves* 12, 69–78. doi:10.1007/s00193-002-0136-3
- Ambrosini, R. D., and Luccioni, B. M. (2019). Effects of underground explosions on soil and structures. *Undergr. Space* 5, 324–338. doi:10.1016/j.undsp.2019.09.002
- Du, X. L., and Lu, D. C. (2011). Advances in soil dynamics and geotechnical earthquake engineering. *Rock Soil Mech.* 32, 10–20. doi:10.16285/j.rsm.2011.s2.008
- Feng, W. T., Xu, C. P., and Li, X. (2020). Calculation and experimental study of pit size. *Eng. Blasting* 26, 68–72+81. doi:10.3969/j.issn.1006-7051.2020.05.010
- Hu, Y. G., Lu, W. B., Chen, M., Yan, P., and Liu, L. (2015). Implementation and verification of SPH-FEM coupling blasting damage analytical method. *Chin. J. Rock Mech. Eng.* 34, 2740–2748. doi:10.13722/j.cnki.jrme.2014.0104
- Jia, Y. S., Wang, W. G., Xie, X. Q., Yang, G., and Yao, Y. K. (2017). Characterization of blast-induced craters in low-moisture and saturated sand from field experiments. *Explos. Shock Waves* 37, 799–806. doi:10.11883/1001-1455(2017)05-0799-08
- Liang, B., Jiang, H. Y., Xu, T. L., Yao, A. L., and Wen, X. (2017). Impact dynamic response of near-field explosion in buried gas pipeline based on SPH-FEM coupling algorithm. *Acta Pet. Sin.* 38, 1326–1334. doi:10.7623/syxb201711012
- Liu, N. F., Li, N., Li, G. F., Song, Z. L., and Wang, S. J. (2022a). Method for evaluating the equivalent thermal conductivity of a freezing rock mass containing systematic fractures. *Rock Mech. Rock Eng.* 55, 7333–7355. doi:10.1007/s00603-022-03038-9
- Liu, Q., Zhai, C. C., Zhang, Y. F., Qu, J. B., and Wu, X. Y. (2022b). Numerical simulation and experimental study of ground impact partitioning in ground and buried explosive soils. *Explos. Impact* 42, 3–21. doi:10.11883/bzycj-2021-0326
- Liu, N. F., Li, N., Wang, S. J., Li, G. F., and Song, Z. P. (2023). A fully coupled thermo-hydro-mechanical model for fractured rock masses in cold regions. *Cold Regions Sci. Technol.* 205, 103707. doi:10.1016/j.coldregions.2022.103707
- Luo, X. B., Zhang, Y. L., and Ding, Y. K. (2016). *Explosive mechanics theory course*. Arlington Virginia: National Defense Industry Press.
- Mu, C. M., Ren, H. Q., Xin, K., and Shi, P. (2010). The effect of explosion in soil under the condition of variable burial depth. *J. PLA Univ. Sci. Technol. Nat. Sci. Ed.* 11, 112–116. doi:10.7666/j.issn.1009-3443.20100203
- Qian, Q. H. (2009). Some advances in rock explosion dynamics. *Chin. J. Rock Mech. Eng.* 28, 1945–1968. doi:10.3969/j.issn.1000-0844.2007.01.019
- Wang, Z. P., Li, H. C., Zhou, S. T., and Li, B. J. (2016). Numerical simulation of cavity volume rule of explosion in loess. *Blasting* 33, 73–77. doi:10.3963/j.issn.1001-487X.2016.04.013
- Xie, D. Y. (2007). Developing situation and problems of soil dynamics in China. *Northwest. Seismol. J.* 29, 94–95. doi:10.3321/j.issn:1000-6915.2009.10.001
- Yue, S. L., Wang, D. R., Fan, P. X., and Wang, M. Y. (2012). “A review of the crater effect of explosions of different scales in rock and soil,” in the conference proceeding of the 3rd national conference on engineering safety and protection, Wuhan, Hubei, 184–190.
- Zhang, S. C., and Fedoroff, S. (1996). Neuron microglia interactions *in vitro*. *Chin. J. Comput. Phys.* 13, 385–395. doi:10.1007/s004010050440
- Zhang, Y. W., Fan, S. Y., Yang, D. H., and Zhou, F. (2022a). Investigation about variation law of frost heave force of seasonal cold region tunnels: A case study. *Front. Earth Sci.* 9, 806843. doi:10.3389/feart.2021.806843
- Zhang, Y. W., Song, Z. P., and Weng, X. L. (2022b). A constitutive model for loess considering the characteristics of structurality and anisotropy. *Soil Mech. Found. Eng.* 59, 32–43. doi:10.1007/s11204-022-09781-z
- Zhao, Z. Y., Zhou, Y. L., Ren, J. W., and Lu, T. J. (2022). Explosion morphology and impact effect of shallow buried explosives. *Explos. Impact* 42, 52–64. doi:10.11883/bzycj-2021-0376
- Zhou, X. (2014). *Missile damage effectiveness test and evaluation*. Arlington Virginia: National Defense Industry Press.

Publisher's note

All claims expressed in this article are solely those of the authors and do not necessarily represent those of their affiliated organizations, or those of the publisher, the editors, and the reviewers. Any product that may be evaluated in this article, or claim that may be made by its manufacturer, is not guaranteed or endorsed by the publisher.



OPEN ACCESS

EDITED BY

Naifei Liu,
Xi'an University of Architecture and
Technology, China

REVIEWED BY

Jiawei Jiang,
Nanjing Tech University, China
Wujian Yan,
Lanzhou Earthquake Research Institute,
China Earthquake Administration, China

*CORRESPONDENCE

Zezhou Ji,
✉ jizezhou@fdine.net
Yingmin Zhang,
✉ zhangym16@outlook.com

SPECIALTY SECTION

This article was submitted to
Environmental Informatics and Remote
Sensing,
a section of the journal
Frontiers in Earth Science

RECEIVED 01 November 2022

ACCEPTED 05 December 2022

PUBLISHED 16 January 2023

CITATION

Ji Z, Ye X and Zhang Y (2023),
Liquefaction evaluation method of coral
sand: Case study on the ports
in Indonesia.
Front. Earth Sci. 10:1086250.
doi: 10.3389/feart.2022.1086250

COPYRIGHT

© 2023 Ji, Ye and Zhang. This is an
open-access article distributed under
the terms of the [Creative Commons
Attribution License \(CC BY\)](https://creativecommons.org/licenses/by/4.0/). The use,
distribution or reproduction in other
forums is permitted, provided the
original author(s) and the copyright
owner(s) are credited and that the
original publication in this journal is
cited, in accordance with accepted
academic practice. No use, distribution
or reproduction is permitted which does
not comply with these terms.

Liquefaction evaluation method of coral sand: Case study on the ports in Indonesia

Zezhou Ji*, Xiangji Ye and Yingmin Zhang*

CCCC First Harbor Consultants Co., Ltd., Tianjin, China

While the liquefaction evaluation methods of siliceous sand have undergone extensive studies, few research efforts were conducted to establish standard for the liquefaction susceptibility of coral sand. The current study develops an innovative method to evaluate the liquefaction potential of coral sand. Specifically, the method integrates the grain-size distribution of coral sand, effective overburden stress and equivalent seismic acceleration. Scanning electron microscopy image of coral sand was processed to reveal the microstructural characteristics of coral sand. The correction equation for standard penetration resistance of coral sand in Indonesian ports was given based on geotechnical investigations, and the recommended values of correction factors were proposed for the regions lacking relevant data in the previous period. The process for liquefaction evaluation method of coral sand was described and applied to evaluate the liquefaction potential of coral sand in Indonesian port projects. This study demonstrates the feasibility of integrating standard penetration test and grain-size distribution for liquefaction evaluation of coral sand.

KEYWORDS

coral sand, microstructure, standard penetration resistance, grain-size distribution, liquefaction evaluation method

1 Introduction

With the continuous expansion of scientific research and engineering projects, coral sand and other special soils have brought a series of new difficulties and challenges to the construction of coastal ports along the 21st-Century Maritime Silk Road. Unlike siliceous sands formed by physical or chemical origin, coral sands are mostly calcareous sands formed by various marine organisms such as corals and shells through long-term geological effects (Wu et al., 2022) (Figure 1). Coral sand is a special geotechnical material that is widely distributed in tropical oceans between N30° and S30°, and it has been found in the Caribbean Sea, Hawaii, Polynesia, Indonesia, the north coast of Australia, the Indian Ocean, the Persian Gulf, the Red Sea, the South China Sea (Lv et al., 2019; Yang et al., 2022).

Changes in microstructure and microfracture will affect mechanical properties (Liu et al., 2006; Shih et al., 2010; Liu et al., 2022). There is a correlation between concrete pore size and UCS (Liu X. et al., 2020b). Microstructure can be employed to observe

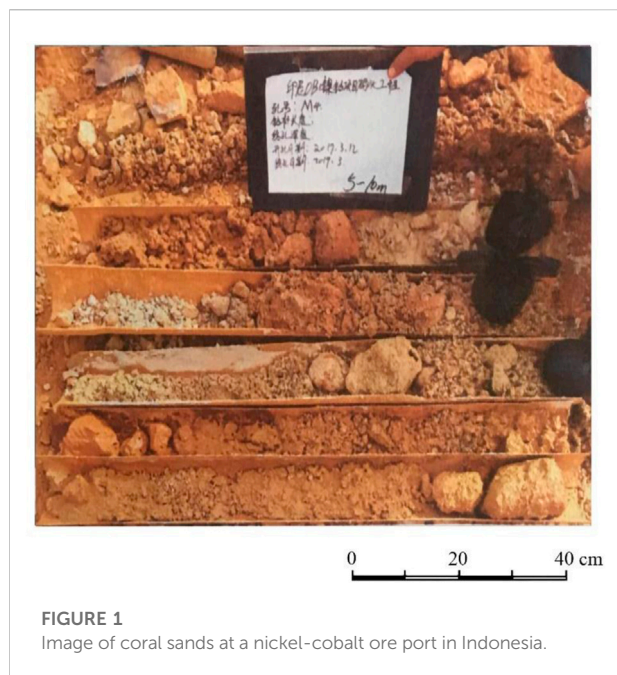


FIGURE 1
Image of coral sands at a nickel-cobalt ore port in Indonesia.

deformation and failure of materials (Wang et al., 2015; Zhao et al., 2015; Liu N. et al., 2020a). Previous studies have shown that coral sand has many characteristics that are different from siliceous sand, such as irregular particle shapes (Wang et al., 2019), high particle angularity (Hyodd et al., 1998; Brandes, 2010; Morsy et al., 2019), large porosity (Wang et al., 2014), low mechanical strength (Arumugam and Ramamurthy, 1996; Coop et al., 2004; Wu et al., 2018), high compressibility (Wang et al., 2011), and high carbonate content (Xiao et al., 2018), owing to its special marine biological origin. Hassanlourad et al. (2014) reported quartz sand was greatly affected by the initial relative density, while coral sand was significantly influenced by the inherent filler. When calcareous sand and siliceous sand are tested under similar conditions, calcareous sand is more malleable and contractile and has a larger peak friction angle than siliceous sand with similar grain-size distribution, while siliceous sand has higher shear modulus (Carraro and Bortolotto, 2015; Giang et al., 2015) and damping (Brandes, 2010; Catano and Pando, 2010). Coral sand is less susceptible to liquefaction than siliceous sand with the same relative density under similar conditions (LaVielle, 2008; Pando et al., 2012).

Terzaghi and Peck (1967) used the term soil liquefaction to describe the sudden loss of strength of sandy soils that lead to flow slides by a slight disturbance. Numerous strong earthquakes, such as the Guam earthquake of 1993, the Hawaii earthquake of 2006, the Haiti earthquake of 2010, and many others, exhibited the extensive damage caused by intense shaking of calcareous sands, and the liquefaction of calcareous sands was observed in these cases, leading to severe damage to coastal port facilities (Brandes, 2010). Soil

liquefaction also caused severe damage to the port facilities in the earthquake of Kobe in 1995 (Robertson and Wride, 1998). Attempts thus far have been carried out to explore the liquefaction susceptibility of siliceous sand. The cyclic stress ratio is commonly employed to evaluate the liquefaction potential of siliceous sand. The dynamic properties of coral sand vary significantly from those of siliceous sand. The strength of coral sand is low, and the particle breakage is easy to occur under the seismic action, leading to changes in compactness. The relative density, depth reduction coefficient and confining pressure have a great influence on the cyclic stress ratio. Therefore, the variability of liquefaction evaluation results by using conventional cyclic stress ratio is large according to the above-mentioned arguments. Besides, the standard penetration test-based procedure (Seed and Idriss, 1971), cone penetration test-based procedure (Robertson and Wride, 1998), and shear wave velocity-based procedure (Andrus and Stokoe II, 2000) are also employed to assess the liquefaction potential of sandy soils. At present, liquefaction resistance evaluation results of coral sands are not accurate. There are obvious shortcomings in using the liquefaction evaluation standards of siliceous sand to assess the liquefaction potential of coral sand. Hawaii seismic data in 2006 showed that the *in-situ* modified shear wave velocity of the coral sand liquefaction layer was 314 m/s, which was 43% higher than the upper limit of modified shear wave velocity for siliceous sand to reach liquefaction. Applying the liquefaction evaluation method of siliceous sand to coral sand will cause obvious misjudgment, thus leading to unnecessary investment in projects (Shahnazari et al., 2016). Tang et al. (2013) compared various liquefaction evaluation methods, such as the standard penetration test method, and shear wave velocity method. However, the applicability of these methods to the assessment of liquefaction potential of coral sands requires further study. Research efforts on liquefaction evaluation methods of coral sand are not sufficient; hence it is of great practical significance to investigate the liquefaction evaluation method of coral sand.

This research aims to explore a method to study the liquefaction susceptibility of coral sand based on the liquefaction evaluation method of siliceous sand. The method has been successfully applied in the design of relevant port projects in Indonesia. This paper demonstrates the feasibility of integrating the grain-size distribution and standard penetration resistance for liquefaction potential analysis, and confirms the broad application prospects of this method.

2 Test procedure and theoretical study of liquefaction evaluation method

2.1 Sample preparation and treatment

Coral sands were sampled within a nickel-cobalt ore port in Indonesia. 23 coral sand samples were drilled for geotechnical

tests within the depth range of 4.15–14.45 m in the pontoon berthing area. Geotechnical tests were conducted as per GB 50021-2009 (Ministry of Housing and Urban-Rural Development of the People's Republic of China, 2009). The average value of the experimental results was taken as the characteristics of coral sand to reduce experimental deviations.

2.2 Image processing of coral sands

Since the microstructural characteristics of coral sand particles and pores are closely related to the engineering properties of coral sand, it is necessary to analyze the microstructure of coral sand for exploring the liquefactions susceptibility of coral sand. The microstructure of coral sand can be obtained by scanning electron microscope images (Seneviratne et al., 2020; Zhang et al., 2022a).

Although the large magnification image shows the shape and size of particles and voids in detail, it is difficult to accurately represent the real microstructure of coral sand due to the small number of particles and voids. It can only characterize the local microstructure of coral sand. The image with small magnification presents a large number of particles and voids; however, too small a magnification can make coral sand particles and voids indistinguishable. In the microstructural characterization analysis of coral sands, the microscopic image should cover as many particles as possible while ensuring the clear representation of particles and voids. The magnification of coral sand image of coral sand used in this paper was 100 times after fully considering the above arguments. Scanning electron microscope images of coral sand were collected at a 15 kV voltage.

The image was processed by the spatial domain method to remove or attenuate image noise and highlight the edge contours of the objects for easy target recognition. Soil is a three-phase system consisting of solid gas water (Bi et al., 2018; Bi et al., 2020). Dry coral sand is considered as a two-phase system composed of solids and gases. The threshold segmentation method was employed to divide the processed image into two regions, namely, coral sand particles and voids (Matsushima et al., 2009; Zhao et al., 2015; Zhang et al., 2022b). The binary image of coral sand was thus obtained, and microstructural parameters of voids were then extracted.

The binary images of coral sands allow the quantification and analysis of microstructural parameters such as surface porosity, void equivalent diameter and void area. The void equivalent diameter in two-dimensional space refers to the diameter of an equal-area circle, as shown in Eq. 1.

$$D = \sqrt{4S/\pi} \quad (1)$$

where D is the equivalent diameter of void; and S is the area of void.

2.3 Liquefaction potential of siliceous sand by standard penetration test (SPT)

According to the Chinese Code for Seismic Design of Buildings (Ministry of Housing and Urban-Rural Development of the People's Republic of China, 2016), the liquefaction index for each borehole can be calculated by

$$I_{LE} = \sum_{i=1}^n \left(1 - \frac{N_i}{N_{cri}} \right) d_i W_i \quad (2)$$

where I_{LE} is the liquefaction index; n is the total number of standard penetration tests per borehole in the depth of the investigation; N_i and N_{cri} are the measured and critical values of the standard penetration resistance at position i , respectively, and the critical value is taken if the measured value is greater than the critical value; d_i is the thickness of the i -layer soils, which can be half of the difference in depth between the upper and lower standard penetration test positions adjacent to position i , but the upper boundary is not higher than the groundwater table, and the lower boundary is not lower than the liquefaction depth (m); W_i is the weight function value of the layer influence of the unit thickness of the i -layer soils (m^{-1}).

As for the liquefaction index, when $0 < I_{LE} \leq 6$, the liquefaction grade is slight; when $6 < I_{LE} \leq 18$, the liquefaction grade is medium; when $I_{LE} > 18$, the liquefaction grade is severe. When the midpoint depth of the layer is not greater than 5 m, $W_i = 10$; when the midpoint depth of the layer is 20 m, $W_i = 0$; when the midpoint depth of the layer is greater than 5 m and less than 20 m, W_i should be taken by linear interpolation.

2.4 Liquefaction susceptibility of coral sand

The susceptibility and hazard degree of coral-sand liquefaction should be investigated based on the properties of the sand and seismic intensity at the site. The grain-size distribution and standard penetration test (SPT) are firstly conducted for liquefaction evaluation. If the results are near the dividing line between occurrence and non-occurrence of liquefaction, the cyclic triaxial test should be employed for further determination.

2.4.1 Liquefaction susceptibility of coral sand by grain-size distribution

As shown in Figure 2, if the grain-size distribution curve of sand is outside the range of the possible liquefaction boundary, the sand may liquefy. The influence of the uniformity coefficient U_c ($U_c = D_{60}/D_{10}$) should be considered in selecting the boundary curves, and its critical value is 3.5. Soil with $U_c < 3.5$ classifies as a low uniformity coefficient soil, while soil with $U_c > 3.5$ classifies as a high uniformity coefficient soil

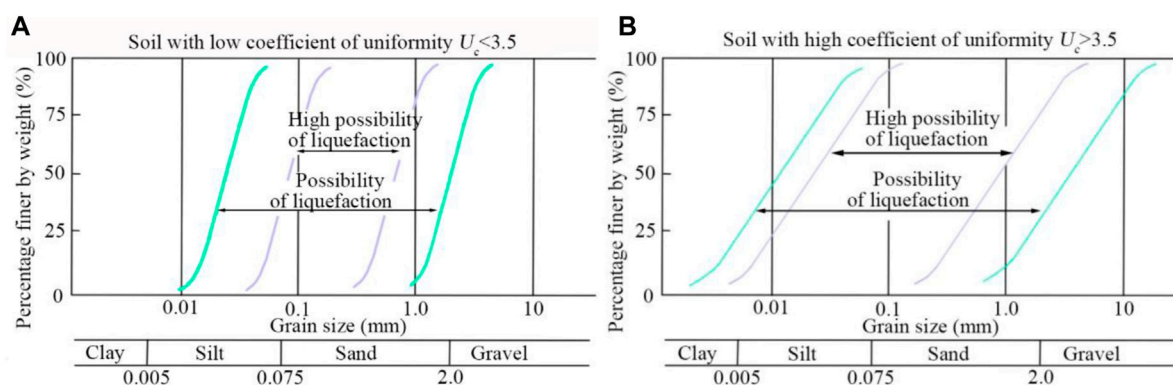


FIGURE 2
Grand-size distribution curves of possible liquefied soils: (A) $U_c < 3.5$; (B) $U_c > 3.5$.

according to the Unified Soil Classification System (Osamu 2020). If the grain-size distribution curve of sand falls into the possible liquefaction zone, further judgment is required to determine whether liquefaction occurs in the sand. For soils with a high fine-grained content, cyclic triaxial test is needed. For soils with a high coarse-grained content, liquefaction susceptibility depends on the permeability coefficient, and if the permeability coefficient is greater than 3 cm/s, liquefaction will not occur. However, if the underlying soil layer is a soil with poor permeability such as clay or silt, the method corresponding to the possible liquefaction zone should be strictly followed for liquefaction evaluation.

2.4.2 Liquefaction susceptibility of coral sand by equivalent SPT blow count and equivalent acceleration

The equivalent SPT blow count $(N)_{65}$ can be determined according to the following formula:

$$(N)_{65} = \frac{N - 0.019(\sigma'_v - 65)}{0.0041(\sigma'_v - 65) + 1.0} \quad (3)$$

where $(N)_{65}$ is the equivalent SPT blow count; σ'_v is the effective overburden pressure at the bottom of the soil layer (kN/m^2), and the volumetric weight of the overlying soil is 18.5 kN/m^3 , thus the effective volumetric weight is 8.5 kN/m^3 ; N is the actual SPT blow count at the bottom of the soil layer.

As for the N value of coral sand, many scholars have suggested the relationship between the cone head resistance of siliceous sand and calcareous sand by referring to the static penetration test. Almeida et al. (1991) believed that the cone head resistance of siliceous sand was about 1.8–2.2 times that of calcareous sand, while Cudmani (2000) found that the ratio was between 1.4 and 3.5, and the specific value was related to the relative density. In the static penetration test, the end resistance

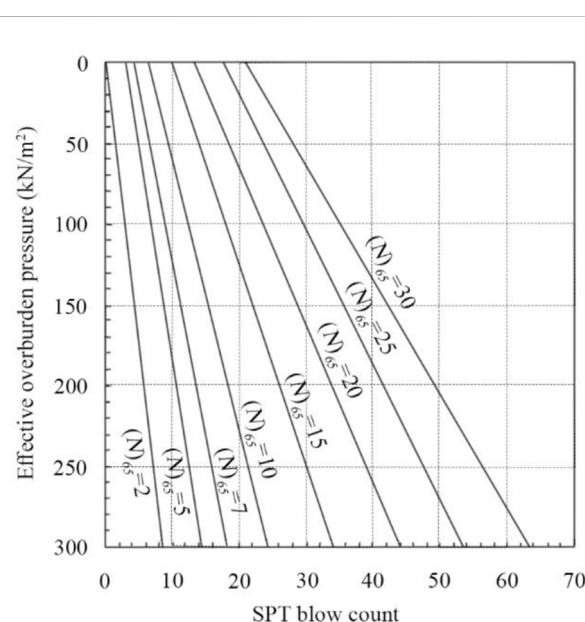
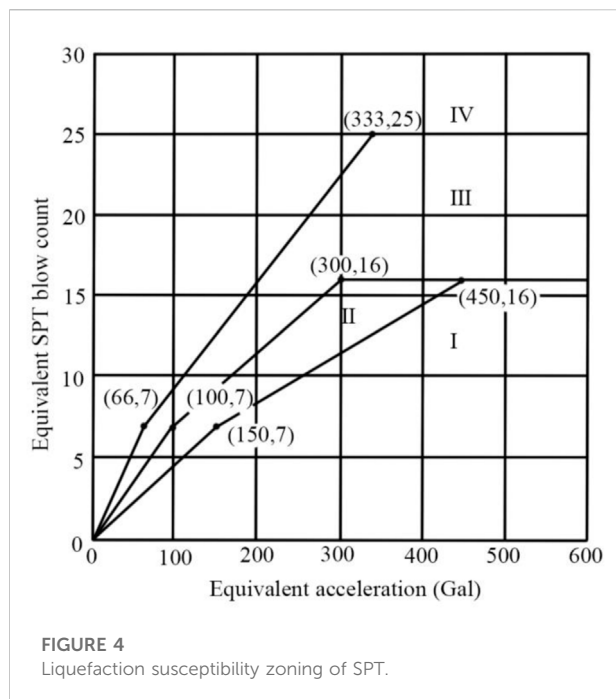


FIGURE 3
Modified SPT fitting curves.

and side resistance of quartz sand were about 1.3–2.2 times that of coral sand. Foray et al. (1999) compared the ultimate pressure of siliceous sand and calcareous sand, and demonstrated that the ultimate bearing capacity of siliceous sand was 2–3 times that of calcareous sand, and the ultimate bearing capacity was related to the initial confining pressure. According to the above-mentioned literature study, siliceous sand is about twice the SPT blow count of calcareous sand under the same confining pressure and compactness. Therefore, in the liquefaction evaluation analysis of coral sand, the measured SPT blow count can be scaled and then combined with the traditional liquefaction evaluation



method of siliceous sand. Eq. 3 can also be represented by Figure 3.

Equivalent acceleration can be calculated by

$$\alpha_{eq} = 0.7 \frac{\tau_{max}}{\sigma'_v} g \quad (4)$$

where α_{eq} is equivalent acceleration (Gal); τ_{max} is maximum shear stress (kN/m^2); g is gravitational acceleration (Gal).

According to the equivalent SPT blow count and equivalent acceleration, the liquefaction potential of coral sand can be determined according to Figure 4.

Liquefaction potential in each zone is as follows:

If the equivalent acceleration and equivalent SPT blow count of coral sand fall in zone I, then liquefaction will certainly occur.

If the equivalent acceleration and equivalent SPT blow count of coral sand fall in zone II, then coral sand has a high probability of liquefaction, and further evaluation should be conducted by combining the results of cyclic triaxial test.

If the equivalent acceleration and equivalent penetration of coral sand fall in zone III, then the liquefaction potential of coral sand is small, and the cyclic triaxial test should be employed for further determination.

If the equivalent acceleration and equivalent penetration of coral sand fall in zone IV, then coral sand will certainly not liquefy.

When the fine soil content is more than 5%, the SPT blow count should be corrected. The fine soil content of the site is 3%; hence there is no need to correct the SPT blow count.

2.4.3 Steps for liquefaction evaluation of coral sand

The shear strength of coral sand density is 1.8–2.2 times that of siliceous sand with the same relative density under similar conditions. The SPT blow count should be multiplied by the correction coefficient. The experimental results of Indonesian coral sand with the effective overburden stress of 0 kPa–100 kPa were regressed, and the formula of correction coefficient F_{ca} of SPT blow count was derived:

$$F_{ca} = 0.72 * D_r + 1.62 \quad (5)$$

where D_r is relative density.

For Indonesian coral sand, the SPT blow count was corrected according to Eq. 5. Thereafter, the combination of grain-size distribution and SPT can assess the liquefaction susceptibility of coral sand. The specific steps are as follows:

- (1) The SPT blow count of coral sands at different depths is determined by field SPT;
- (2) Acid drop test is performed using disturbed samples to obtain the content of calcium ions to determine the type of sand;
- (3) The grain-size distribution and uniformity coefficient are investigated by sampling and sieving test;
- (4) The measured grain-size distribution curve of coral sands is compared with the possible liquefaction zone corresponding to the uniformity coefficient in accordance with Figure 2. If the curve is outside the liquefiable area, the liquefaction will not occur. Otherwise, the liquefaction evaluation needs to go to the next step.
- (5) The equivalent SPT blow count can be obtained according to Eq. 3 or Figure 3;
- (6) The theoretical range of relative density of coral sand is $0 < D_r \leq 1$, hence the correction coefficient of the SPT blow count is $1.69 < F_{ca} \leq 2.34$ according to Eq. 5. Considering that coral sand is one kind of biomass sand, the dynamic characteristics of coral sand in different regions are relatively consistent, hence the correction coefficient F_{ca} can be taken as two to correct the SPT blow count for other regions lacking relevant data in the previous period.
- (7) The equivalent acceleration is calculated according to Eq. 4;
- (8) The liquefaction of coral sand can be identified by combining the corrected SPT blow count and equivalent acceleration according to Figure 4.

2.5 Engineering projects

2.5.1 A nickel-iron ore port project in Indonesia

The nickel-iron ore port, located in Sulawesi Island, Indonesia, is mainly used for receiving and unloading sulfuric acid, containers, and other regular cargoes. The port measures

15 m by 120 m. The pontoon is moored in front of the port, and they have their own loading and unloading equipment. The bulk carrier, with a displacement of 57,000 tons, is anchored outside the pontoon. Four exploration positions were taken in the pontoon berthing area, labeled M1 to M4. The geological conditions within the depth range of 39.0 m were investigated and the basic acceleration of ground motion was calculated. Subsequently, the liquefaction potential of the site was evaluated by the SPT and the new evaluation method proposed in this paper, respectively.

2.5.2 A nickel-cobalt ore port project in Indonesia

The nickel-cobalt ore port, located in Sulawesi Island, Indonesia, is mainly used for receiving and unloading laterite nickel ore, and other heavy cargoes. The port measures 18 m by 150 m. Five exploration positions were taken in the port, labeled M5 to M9. Five exploration sites were selected in the revetment, labeled H1 to H5, and two exploration sites were selected in the land, labeled BH1 and BH2. Similar to the last project, the geological conditions within the depth range of 20.0 m were investigated and the basic acceleration of ground motion was calculated. Subsequently, the liquefaction potential of the site was evaluated by the SPT and the new evaluation method proposed in this paper, respectively.

3 Engineering application and validation study

This paper aims to develop an innovative method to evaluate the liquefaction potential of coral sand. Specifically, standard penetration test and grain-size distribution are considered in the liquefaction evaluation method of coral sand. This method has been applied to assess liquefaction susceptibility of a nickel-iron ore port site and a nickel-cobalt ore port site in Indonesia.

3.1 Properties of coral sands

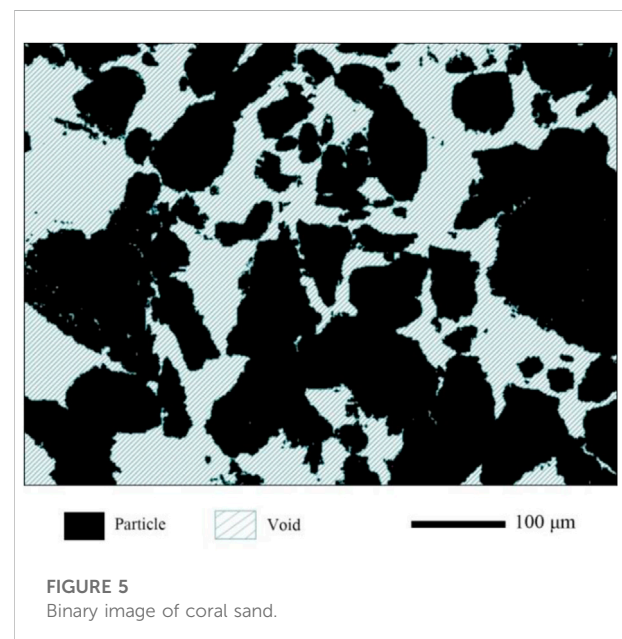
It is necessary to obtain the basic parameters of soil to deeply understand the hydro and dynamic properties of soil (Liu et al., 2023). The basic parameters of the coral sands are provided in Table 1.

3.2 Microstructural characterization of coral sands

The binary image of coral sand is shown in Figure 5. Morphologies of the coral sand particles are diverse, and there are four common shapes, namely, flaky particles, dendritic

TABLE 1 Properties of the coral sands.

Property	Value
Gravity density (kN/m^3)	19.5
Maximum void ratio	3.0
Minimum void ratio	0.8
Uniformity coefficient	45.5
Coefficient of gradation	5.9
Internal friction angle ($^\circ$)	40.0
Cohesion (kPa)	0
SPT blow count (N/30 cm)	8.8
Correction SPT blow count (N/30 cm)	7.6
Bearing capacity (kPa)	110
Modulus of compressibility (MPa)	6.3



particles, spindle-like particles and block-like particles. Spindle-like particles and block-like particles account for most of them. Dendritic particles, spindle-like particles and block-like particles are rich in the native internal voids of organisms. Flaky particles and spindle-like particles are prone to breakage when they are subjected to stress.

As observed in Figure 6, the equivalent diameters of voids range from 1.90 μm to 121.15 μm . The average equivalent diameter of voids is 22.41 μm , and the median equivalent diameter of voids is 14.61 μm . The equivalent diameter distribution of voids is concentrated. The voids with

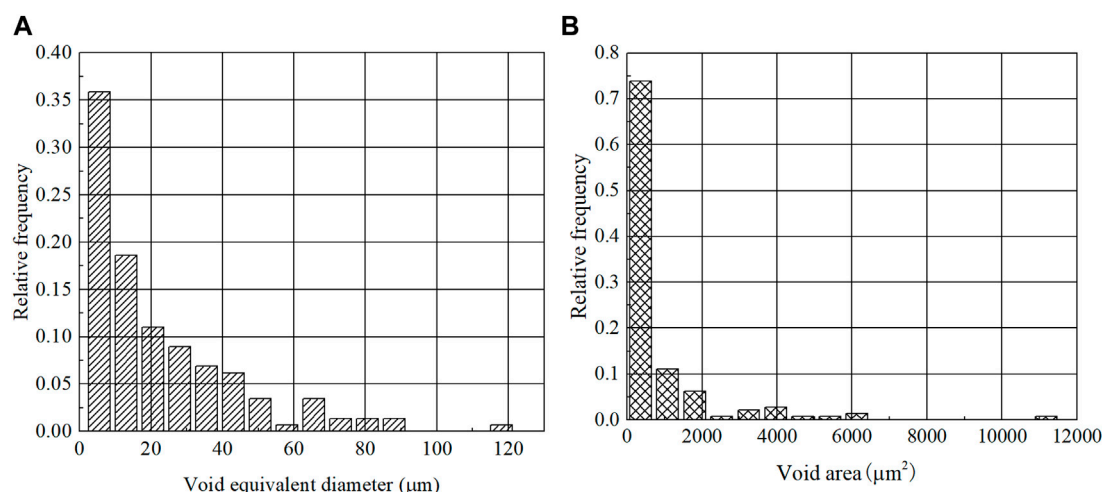


FIGURE 6
Microstructural parameters of voids: (A) equivalent diameter; (B) area.

equivalent diameters between 1.8 μm and 9.3 μm account for about 1/3 of the total number of voids, and the number of large voids is small. The variance of void equivalent diameter distribution is very small, about 0.005. The areas of voids range from 2.83 μm^2 to 11527.67 μm^2 , with an average void area of 762.92 μm^2 and a median void area of 170.36 μm^2 . The void area distribution is concentrated, and the number of small void areas is huge, accounting for more than 2/3 of the total number of voids, and the variance of the void area distribution is minimal, only 2.204 e-06.

3.3 Liquefaction evaluation of a nickel-iron ore port site in Indonesia

3.3.1 Geological conditions of the nickel-iron ore port site

The strata within the depth of 39.0 m revealed by the borehole are Quaternary talus accumulation. According to their burial conditions, distribution, lithological characteristics, and physical and mechanical properties, they can be divided into the following four engineering geological layers, which are briefly described as follows:

I Plain fill (Q_4^{ml}): variegated, loose, slightly wet, mainly clay and gravel, and locally block stone.

II Coral sand (Q_4^{dl}): grayish-white, dense, saturated, and cores with short columnar or blocky shapes.

III Fine sand (Q_4^{dl}): grayish-yellow, slightly dense, saturated, moderately rounded, poorly graded, impure sand, and mainly feldspar and quartz.

Silty clay (Q_4^{dl}): grayish-brown, plastic, smooth cut surface, slightly shiny, medium dry strength, medium toughness, rust spots, and no shaking and vibration reaction.

IV Strongly weathered peridotite (pTum): grey-green, strongly weathered, mostly damaged tissue structure, broken or relatively broken core with fragmented or short columnar shape, crack development, and local water leakage.

According to the Indonesian Seismic Resistant Design Standard for Building Structures (Wangsadinata, 2002) and the Chinese Code for Seismic Design of Buildings (Ministry of Housing and Urban-Rural Development of the People's Republic of China, 2016), the seismic precautionary intensity of the site is 8 degree. The basic ground-motion acceleration of a site with a design service life of 50 years and an exceedance probability of 10% is 0.3 g as per the Indonesia Seismic Zoning Map (2010 edition). The design seismic group of the site is Group 2. The foundation soil type of the site is medium soft soil, and the construction site category is class II, hence the site is an unfavorable earthquake-resistant area. Since the design service life of the port is 20 years, the corresponding seismic regression period is 190.3 years under the premise of 10% exceedance probability. In accordance with the earthquake regression period, it can be concluded that the 50-year exceedance probability is 23.16%. The intensity probability of the 50-year design reference period conforms to the extreme value type III distribution. Based on the known basic seismic precautionary intensity (8 degree) and exceedance probability, the corresponding seismic intensity can be deduced to be 7.45 degree. Therefore, the basic acceleration of ground motion is 0.203 g for a site with a 20-year design life and a 10% exceedance probability.

3.3.2 Liquefaction susceptibility of the nickel-iron ore port site by SPT

The liquefaction susceptibility of coral sand assessed using the evaluation method for siliceous sand is listed in Table 2.

TABLE 2 Liquefaction susceptibility of port by SPT.

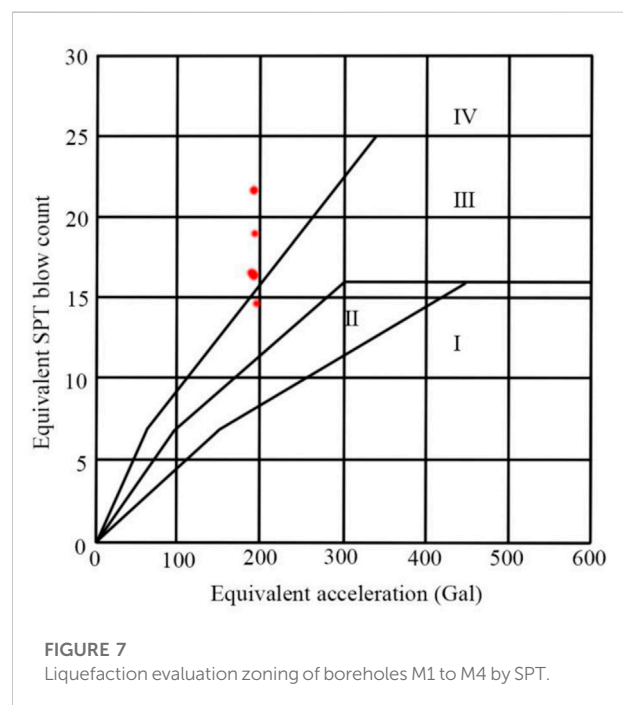
Borehole	Midpoint depth of soil layer (m)	Thickness of soil layer (m)	Critical SPT blow count	Measured SPT blow count	Weight function value	Liquefaction index	Liquefaction grade
M1	4.20	1.20	20.64	7.00	10.00	41.93	Severe
	7.30	1.00	26.19	8.00	8.47		
M2	3.85	1.90	20.76	7.00	10.00	57.42	Severe
	7.30	1.00	26.31	8.00	8.47		
	14.00	1.40	34.50	12.00	4.00		
M3	4.20	1.20	19.78	7.00	10.00	50.95	Severe
	7.30	1.00	25.33	8.00	8.47		
	12.75	1.90	31.60	9.00	4.83		
M4	5.15	2.30	23.26	10.00	9.90	12.98	Medium

When the seismic acceleration of the site is 0.3 g, most of the boreholes in the site may liquefy according to the liquefaction evaluation method of siliceous sand. Therefore, the site is a severely liquefied area and requires avoidance or foundation treatment to eliminate liquefaction, which will greatly increase the project cost. Vibroflotation rubble piles should be used underneath the port to eliminate liquefaction. The treatment area is from 15 m from the seaside of the port front to 40 m from the land side of the port front, and the treatment depth is up to the rock surface line. The vibroflot positions are arranged in a triangular shape with a spacing of 2 m, the treatment area measures 70 m by 200 m, and the average treatment depth is 15 m. An additional investment of about 20 million yuan is needed as per the preliminary estimate.

3.3.3 Liquefaction susceptibility of the nickel-iron ore port site by grain-size distribution and SPT

The drilling results of the port show that the stratum within 20 m of the surface layer is coral sand. Since no grain-size distribution data are available for boreholes M1 to M4, the gradation curve is considered to have fallen into the range of possible liquefaction according to the most unfavorable case, and then the liquefaction susceptibility is evaluated as per steps 5, 6, 7 and 8 described in Section 2.4.3. The relevant results are shown in Figure 7.

The SPT data of the boreholes M1 to M4 are mostly located in zone IV, that is, liquefaction will not occur. Only the data of individual depths of borehole M3 fall into zone III, which has a low possibility of liquefaction. This liquefaction risk should be considered in the design. No foundation treatment is required for the port area, thus saving 20 million yuan in engineering cost. It has been 3 years since the project was put into operation in 2019. During this period, several earthquakes



have occurred, and no liquefaction has been observed at the site.

3.4 Liquefaction evaluation of a nickel-cobalt ore port site in Indonesia

3.4.1 Geological conditions of the nickel-cobalt ore port site

The investigation reveals that the site strata are marine sedimentary layers and bedrock within the depth reached by

TABLE 3 Basic properties of the site strata.

Number	Stratum	Thickness of layer (m)	Bottom depth (m)	Description of stratum
I	Plain fill	2.4–4.0	2.4–4.0	Variegated, slightly wet, loose, mainly clay and gravel, and local block stone
II	Coral sand	2.3–12.6	6.3–15.0	Grayish-white, saturated, slightly dense, mainly coral debris and shell debris, locally cementation with blocky or short columnar shape
III	Fully weathered peridotite	2.5	17.2	Grayish-green, fully weathered, original rock with fully destroyed structure, earthy, the stratum can be dug by a shovel pick and drilled by dry drilling, partial containing fragments of incomplete weathering
IV	Strongly weathered peridotite	—	—	Grayish-green, strongly weathered, the basic destruction of the original rock structure, significant changes in mineral composition, weathering fracture development, broken rock mass, the stratum can be dug by a shovel pick, dry drilling is not easy to enter

TABLE 4 Liquefaction susceptibility of the nickel-cobalt ore port site by SPT.

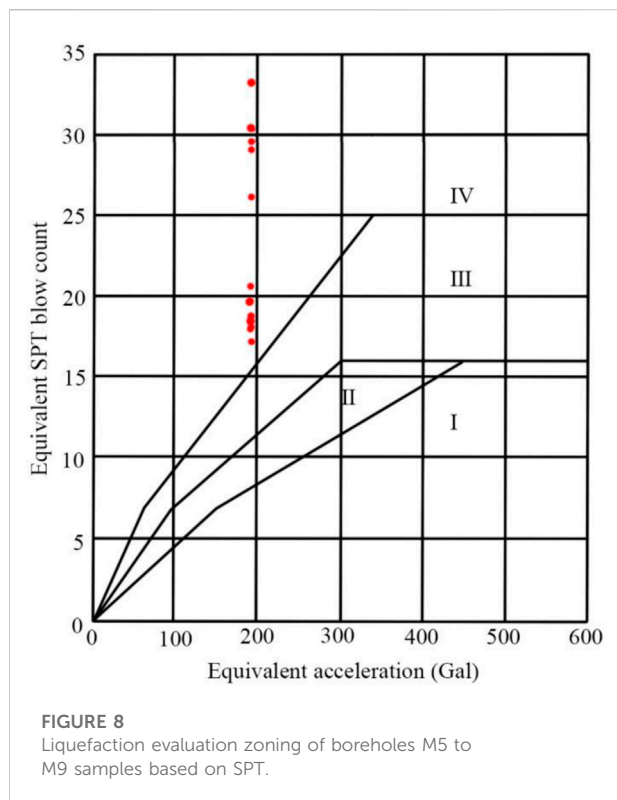
Borehole	Midpoint dactepth of soil layer (m)	Thickness of soil layer (m)	Critical SPT blow count	Measured SPT blow count	Weight function value	Liquefaction index	Liquefaction grade
M5	3.42	1.25	15.99	14.00	10.00	34.60	Severe
	6.68	2.25	19.89	9.00	8.32		
	12.75	1.90	27.69	12.00	2.25		
M6	2.92	1.25	15.34	13.00	10.00	32.40	Severe
	6.95	2.90	20.41	9.00	8.05		
	14.25	1.50	30.81	12.00	0.75		
M7	3.42	1.25	15.99	12.00	10.00	31.0	Severe
	7.72	1.35	21.84	8.00	7.28		
	12.93	1.25	28.34	13.00	2.08		
M8	3.92	2.25	15.22	11.00	10.00	25.30	Severe
	8.13	1.85	20.42	9.00	6.88		
	11.43	1.75	24.32	12.00	3.58		
M9	1.52	3.05	14.69	11.00	10.00	36.40	Severe
	7.15	1.70	21.19	9.00	7.85		
	14.49	1.20	30.29	12.00	0.60		

the drilling, except for the plain fill. According to the burial conditions, lithologic characteristics, and physical and mechanical properties of the strata, the foundation soil of the site is divided into four engineering geological layers. The basic properties of each layer are presented in Table 3. Similar to the last engineering case, the design life of the port in this project is 20 years, and the basic acceleration of ground motion with an exceedance probability of 10% is 0.203 g. The foundation soil type of the site is medium soft soil, and the construction site

category is class II, hence the site is an unfavorable earthquake-resistant area.

3.4.2 Liquefaction susceptibility of the nickel-cobalt ore port site by SPT

The drilling results of the site show that the surface layer of 20 m is coral sand, the depth of liquefaction potential evaluation is 15 m, and the buried depth of the site foundation is 3 m. The liquefaction susceptibility assessment of the port area is carried



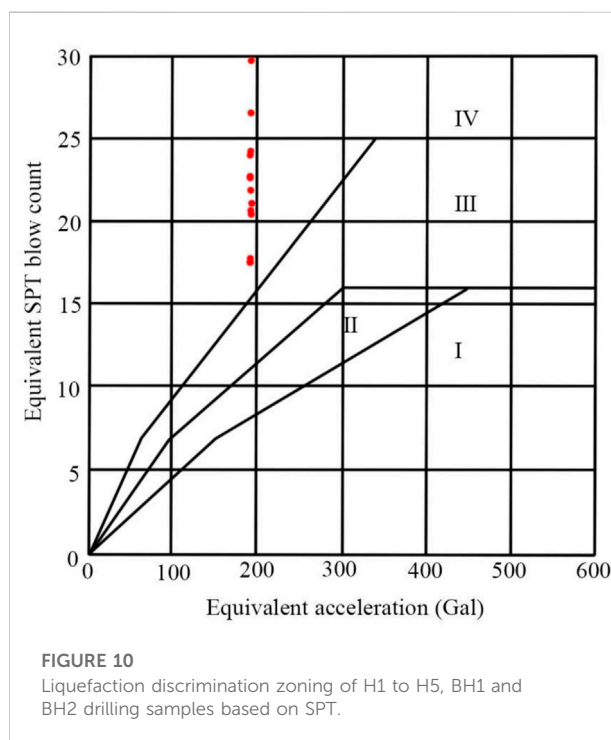
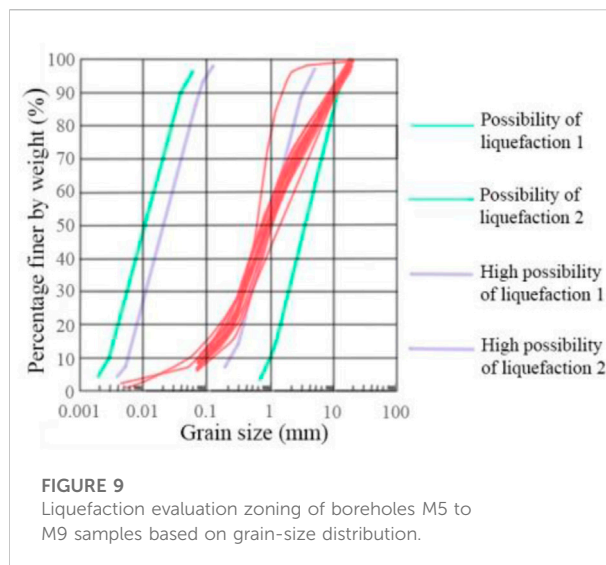
out based on the method described in Section 2.3, and the results are demonstrated in Table 4.

Severe liquefaction will occur in all boreholes in the site in accordance with the evaluation method for siliceous sand. The site needs to be avoided or ground treated to eliminate liquefaction, which will significantly increase the project cost. Vibroflotation rubble piles are required underneath the port to eliminate liquefaction. The treatment area is from 15 m from seaside to 40 m from land side along the port front, and the depth of treatment is up to the rock surface line. The vibroflot positions are arranged in a triangle shape with a spacing of 2 m. The treatment area measures 60 m by 180 m, and the average treatment depth is 13 m. It is estimated that an additional investment of about 22 million yuan is needed.

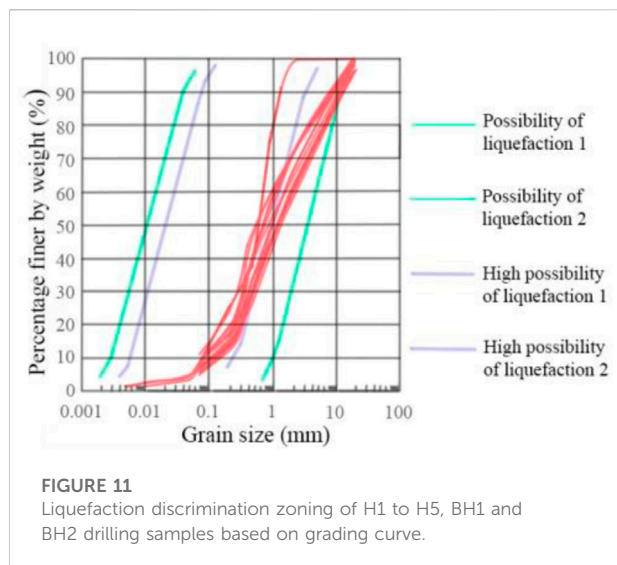
3.4.3 Liquefaction susceptibility of coral sand by grain-size distribution and SPT

The liquefaction susceptibility assessment of drilling samples M5 to M9 in the port area is carried out based on the method described in Section 2.4, and the results are demonstrated in Figures 8, 9.

Boreholes H1 to H5 are located in the revetment area, and boreholes BH1 and BH2 are located in the land area. The liquefaction potential evaluation is performed based on the method described in Section 2.4, and the results are demonstrated in Figures 10, 11.



For the revealed boreholes near the port, revetment and land area, the SPT data are all in zone IV, thus the site will not liquefy. The grain-size distribution curves are almost not in the high liquefaction possibility range, or have a little overlap with it; hence the possibility of liquefaction in these strata is low. In general, liquefaction will not occur in port, revetment and land area, and the effect of liquefaction on these areas does not need to be considered. Therefore, there is no need to carry out foundation treatment, which saves a large amount of the engineering cost. It



has been 3 years since the project was put into operation in 2019. During this period, several earthquakes have occurred at the project site, and no liquefaction has been observed at the site.

4 Discussion

The current regulations on the liquefaction evaluation are commonly for the silica sand. Previous studies on the liquefaction evaluation of coral sand are limited. Coral sand has the following characteristics compared with siliceous sand with the same relative density and tested under similar conditions:

- The SPT blow count of coral sand is smaller than that of siliceous sand;
- Coral sand has a higher compressibility than siliceous sand;
- The internal friction angle of coral sand is larger than that of siliceous sand;
- Coral sand is less susceptible liquefaction than siliceous sand.

In the liquefaction potential assessment of the sites in the above-mentioned projects, coral sand have severe or moderate liquefaction potential according to the evaluation methods of siliceous sand, and these locations need to be avoided or ground treated to eliminate liquefaction, however, this process is time-consuming, energy-intensive, and financially costly, thus enhancing the engineering cost significantly. The new method proposed in this paper is employed to investigate the liquefaction susceptibility of coral sand in these two projects. The results show that the coral sands in most of the boreholes in the nickel-iron ore port will not liquefy. Only a borehole sample at a certain depth has a low probability of liquefaction, hence the liquefaction risk

of this position should be considered in the design of port. There is no possibility of liquefaction in the nickel-cobalt ore port, revetment and land area, and there is no need to consider the influence of liquefaction on these areas. The liquefaction evaluation method of coral sand has been successfully applied to these two projects in Indonesia, the acceptance and review of them has been completed. The two projects do not need to carry out foundation treatment, which saves a large amount of engineering costs.

This research supports the construction of port projects among countries along the Silk Road Economic Belt, and fills the gaps in the current design standards and specifications for port engineering. The study provides a reference for the design of other port projects with similar conditions, and creates significant economic and social benefits.

5 Conclusion

The microstructures of the coral sands were studied through a series of image-processing and analysis procedures. The geological conditions were investigated by boreholes. A new method was proposed to evaluate the liquefaction susceptibility of coral sands and was applied to two port projects in Indonesia to verify its feasibility. The main following conclusions can be drawn based upon the presented results:

- (1) The liquefaction evaluation methods of siliceous sands are not applicable to coral sands.
- (2) The correction formula for the SPT blow count of coral sand is developed, and the recommended value of correction coefficient is proposed for the first time for the regions lacking relevant data in the previous period.
- (3) An innovative liquefaction evaluation method for coral sand is proposed by combining the standard penetration test and grain-size distribution curve, i.e., the grain-size distribution, effective overburden stress, equivalent standard penetration test blow count and equivalent seismic acceleration are comprehensively considered to evaluate the liquefaction potential of coral sand.
- (4) The liquefaction evaluation method of coral sand has been successfully applied to a nickel-iron ore port project and a nickel-cobalt ore port project in Indonesia. These two projects save a lot of engineering investment compared with the traditional liquefaction evaluation method.

Data availability statement

The original contributions presented in the study are included in the article/Supplementary Material; further inquiries can be directed to the corresponding authors.

Author contributions

ZJ: Conceptualization, Methodology, Validation, Data curation, Writing—original draft preparation, Writing—review and editing, Supervision, Project administration, Funding acquisition. XY: Conceptualization, Validation, Investigation, Resources, Writing—original draft preparation. YZ: Software, Formal analysis, Writing—review and editing. All authors agree to be accountable for the content of the work.

Funding

This research was supported by the National Natural Science Foundation of China (Project No. U1906231).

References

- Almeida, M. S., Jamiolkowski, M., and Peterson, R. (1991). Preliminary results of CPT tests in calcareous Quaternary soils. *Proceedings of the International Symposium on Calibration Chamber Testing*, 28–29, 41–53. Potsdam, U. S. A. June 1991.
- Andrus, R. D., and Stokoe, K. H., II (2000). Liquefaction resistance of soils from shear-wave velocity. *J. Geotech. Geoenviron. Eng.* 126 (11), 1015–1025. doi:10.1061/(asce)1090-0241(2000)126:11(1015)
- Arumugam, R. A., and Ramamurthy, K. (1996). Study of compressive strength characteristics of coral aggregate concrete. *Mag. Concr. Res.* 48 (176), 141–148. doi:10.1680/mac.1996.48.176.141
- Bi, J., Zhang, M., Chen, W., Lai, Y., and Lu, J. (2018). A new model to determine the thermal conductivity of fine-grained soils. *Int. J. Heat. Mass Transf.* 123 (123), 407–417. doi:10.1016/j.ijheatmasstransfer.2018.02.035
- Bi, J., Zhang, M., Lai, Y., Pei, W., Lu, J., You, Z., et al. (2020). A generalized model for calculating the thermal conductivity of freezing soils based on soil components and frost heave. *Int. J. Heat. Mass Transf.* 150, 119166. doi:10.1016/j.ijheatmasstransfer.2019.119166
- Brandes, H. G. (2010). Simple shear behavior of calcareous and quartz sands. *Geotech. Geol. Eng.* 29 (1), 113–126. doi:10.1007/s10706-010-9357-x
- Carraro, J. A. H., and Bortolotto, M. S. (2015). Stiffness degradation and damping of carbonate and silica sands. *Proceedings of the Frontiers in offshore geotechnics III*. Oslo, Norway, 1179–1183.
- Catano, J., and Pando, M. A. (2010). *Static and dynamic properties of a calcareous sand from southwest Puerto Rico*. *Proc. Adv. Analysis*, Orlando, USA: Modeling & Design, 842–851.
- Coop, M. R., Sorensen, K. K., Bodas Freitas, T., and Georgoutsos, G. (2004). Particle breakage during shearing of a carbonate sand. *Geotechnique* 54 (3), 157–163. doi:10.1680/geot.2004.54.3.157
- Cudmani, R. (2000). *Statische, Alternierende und Dynamische Penetration in Nichtbindigen Böden*. Doctor. Karlsruhe: Universität Fridzu Karlsruhe TH.
- Foray, P. Y., Nauroy, J. F., and Colliat, J. L. (1999). Mechanisms governing the behaviour of carbonate sands and influence on the design of deep foundation. *Proceedings of the Engineering for calcareous sediments. Bahrain, Febr.* 21–24, 55–68.
- Giang, P. H. H., Impe, P. V., Impe, W. F. V., Menge, P., and Haegeman, W. (2015). Effects of grain size distribution on the initial small strain shear modulus of calcareous sand. *Proc. XVI ECSMGE Geotechnical Eng. Infrastructure Dev. Edinburgh, U. K. Sept.* 13–17, 3177–3182.
- Hassanlourad, M., Rasouli, M. R., and Salehzadeh, H. (2014). A comparison between the undrained shear behavior of carbonate and quartz sands. *Int. J. Civ. Eng.* 12 (4), 338–350.
- Hyod, M., Hyde, A. F. L., and Aramaki, N. (1998). Liquefaction of crushable soils. *Geotechnique* 48 (4), 527–543. doi:10.1680/geot.1998.48.4.527
- LaVielle, T. H. (2008). *Liquefaction susceptibility of uncemented calcareous sands from Puerto Rico by cyclic triaxial testing*. Master. Blacksburg: Virginia Polytechnic Institute and State University.
- Liu, H. T., Sun, L. Z., and Ju, J. W. (2006). Elastoplastic modeling of progressive interfacial debonding for particle-reinforced metal-matrix composites. *Acta Mech.* 181 (1–2), 1–17. doi:10.1007/s00707-005-0279-2
- Liu, N., Li, N., Li, G., Song, Z., Wang, S., and Wang, S. (2022). Method for evaluating the equivalent thermal conductivity of a freezing rock mass containing systematic fractures. *Rock Mech. Rock Eng.* 55, 7333–7355. doi:10.1007/s00603-022-03038-9
- Liu, N., Li, N., Wang, S., Li, G., and Song, Z. (2023). A fully coupled thermo-hydro-mechanical model for fractured rock masses in cold regions. *Cold Reg. Sci. Technol.* 205, 103707. doi:10.1016/j.coldregions.2022.103707
- Liu, N., Li, N., Xu, C., Li, G., Song, Z., and Yang, F. (2020a). Mechanism of secondary lining cracking and its simulation for the Dugongling tunnel. *Rock Mech. Rock Eng.* 53 (9), 4539–4558. doi:10.1007/s00603-020-02183-3
- Liu, X., Ni, C., Meng, K., Zhang, L., Liu, D., and Sun, L. (2020b). Strengthening mechanism of lightweight cellular concrete filled with fly ash. *Constr. Build. Mat.* 251, 118954. doi:10.1016/j.conbuildmat.2020.118954
- Lv, Y., Wang, Y., and Zuo, D. (2019). Effects of particle size on dynamic constitutive relation and energy absorption of calcareous sand. *Powder Technol.* 356, 21–30. doi:10.1016/j.powtec.2019.07.088
- Matsushima, T., Katagiri, J., Uesugi, K., Tsuchiyama, A., and Nakano, T. (2009). 3D shape characterization and image-based DEM simulation of the lunar soil simulant FJS-1. *J. Aerosp. Eng.* 22 (1), 15–23. doi:10.1061/(asce)0893-1321/2009/22:1/15
- Ministry of Housing and Urban-Rural Development of the People's Republic of China (2009). *Code for Investigation of geotechnical engineering*, GB 50021-2009. Beijing, China: China Construction Industry Press.
- Ministry of Housing and Urban-Rural Development of the People's Republic of China (2016). *Code for seismic design of Buildings*, GB 50011-2010. Beijing, China: China Construction Industry Press, 23–25.
- Morsy, A. M., Salem, M. A., and Elmaghlouk, H. H. (2019). Evaluation of dynamic properties of calcareous sands in Egypt at small and medium shear strain ranges. *Soil Dyn. Earthq. Eng.* 116, 692–708. doi:10.1016/j.soildyn.2018.09.030
- Osamu, K. (2020). *Technical standards and commentaries for port and harbour facilities in Japan*. Tokyo, Japan: The Overseas Coastal Area Development Institute of Japan, 322–326.
- Pando, M. A., Sandoval, E. A., and Catano, J. (2012). *Proceedings of the 15 world conference on earthquake engineering*. Lisbon, Portugal–28. 24. Liquefaction susceptibility and dynamic properties of calcareous sands from Cabo Rojo, Puerto Rico September.
- Robertson, P. K., and Wride, C. E. (1998). Evaluating cyclic liquefaction potential using the cone penetration test. *Can. Geotech. J.* 35, 442–459. doi:10.1139/t98-017
- Seed, H. B., and Idriss, I. M. (1971). Simplified procedure for evaluating soil liquefaction potential. *J. Soil Mech. Found. Div.* 97 (9), 1249–1273. doi:10.1061/jsefaq.0001662
- Seneviratne, C., Gunasekara, C., Law, D. W., Setunge, S., and Robert, D. (2020). Creep, shrinkage and permeation characteristics of geopolymer aggregate concrete:

Conflict of interest

All authors are employed by CCCC First Harbor Consultants Co., Ltd.

Publisher's note

All claims expressed in this article are solely those of the authors and do not necessarily represent those of their affiliated organizations, or those of the publisher, the editors and the reviewers. Any product that may be evaluated in this article, or claim that may be made by its manufacturer, is not guaranteed or endorsed by the publisher.

Long-term performance. *Arch. Civ. Mech. Eng.* 20 (4), 140. doi:10.1007/s43452-020-00119-w

Shahnazari, H., Jafarian, Y., Tutunchian, M. A., and Rezvani, R. (2016). Probabilistic assessment of liquefaction occurrence in calcareous fill materials of kawaihae harbor, Hawaii. *Int. J. Geomech.* 16 (6), 05016001. doi:10.1061/(asce)gm.1943-5622.0000621

Shih, T. C., Chen, J. H., Liu, D., Nie, K., Sun, L., Lin, M., et al. (2010). Computational simulation of breast compression based on segmented breast and fibroglandular tissues on magnetic resonance images. *Phys. Med. Biol.* 55 (14), 4153–4168. doi:10.1088/0031-9155/55/14/013

Tang, G., Xia, Y., and Liu, Z. (2013). Engineering behavior of coral sands in Dili, Timor-Leste. *Chin. Geotech. Eng. Tech.* 27 (5), 248–251.

Terzaghi, K., and Peck, R. B. (1967). *Soil mechanics in engineering practice*. 2nd ed. USA, New York: John Wiley & Sons.

Wang, L. L., Bornert, M., Héripré, E., Chanchole, S., Pouya, A., and Halphen, B. (2015). The mechanisms of deformation and damage of mudstones: A micro-scale study combining esem and dic. *Rock Mech. Rock Eng.* 48, 1913–1926. doi:10.1007/s00603-014-0670-1

Wang, X., Jiao, Y., Wang, R., Hu, M., Meng, Q., and Tan, F. (2011). Engineering characteristics of the calcareous sand in nansha Islands, South China Sea. *Eng. Geol.* 120 (1–4), 40–47. doi:10.1016/j.enggeo.2011.03.011

Wang, X., Tan, F., Jiao, Y., and Wang, R. (2014). A new apparatus for testing the bearing capacity of calcareous sand in laboratory. *Mar. Georesources Geotechnol.* 32 (4), 379–386. doi:10.1080/1064119x.2012.728683

Wang, X., Weng, Y., Wei, H., Meng, Q., and Hu, M. (2019). Particle obstruction and crushing of dredged calcareous soil in the Nansha Islands, South China Sea. *Eng. Geol.* 261, 105274. doi:10.1016/j.enggeo.2019.105274

Wangsadinata, W. (2002). *Seismic Resistant Design Standard for Building Structures Ministry of Housing and Regional Infrastructure in Cooperation with Japan*, SNI-1726-2002. Indonesia: International Cooperation Agency: Jakarta-Bandung-Bali, 2–5.

Wu, Q., Ding, X., and Zhang, Y. (2022). Microfabric evolution of coral sand foundations during seismic liquefaction using 3D images. *Soil Dyn. Earthq. Eng.* 162, 107445. doi:10.1016/j.soildyn.2022.107445

Wu, W., Wang, R., Zhu, C., and Meng, Q. (2018). The effect of fly ash and silica fume on mechanical properties and durability of coral aggregate concrete. *Constr. Build. Mat.* 185, 69–78. doi:10.1016/j.conbuildmat.2018.06.097

Xiao, P., Liu, H., Xiao, Y., Stuedlein, A. W., and Evans, T. M. (2018). Liquefaction resistance of bio-cemented calcareous sand. *Soil Dyn. Earthq. Eng.* 107, 9–19. doi:10.1016/j.soildyn.2018.01.008

Yang, J., Xu, D., Shen, J., Wei, H., Wang, R., and Xiao, X. (2022). Effect of coral sand powders and seawater salinity on the impact mechanical properties of cemented coral sand. *Soils Found.* 62 (5), 101206. doi:10.1016/j.sandf.2022.101206

Zhang, Y., Liu, D., Chen, W., and Sun, L. (2022a). Microstructural analysis and multiscale modeling for stiffening and strengthening of consolidated earthen-site soils. *J. Cult. Herit.* 55, 143–148. doi:10.1016/j.culher.2022.03.005

Zhang, Y., Yang, G., Chen, W., and Sun, L. (2022b). Relation between microstructures and macroscopic mechanical properties of earthen-site soils. *Materials* 15 (17), 6124. doi:10.3390/ma15176124

Zhao, B., Wang, J. F., Coop, M. R., Viggiani, G., and Jiang, M. (2015). An investigation of single sand particle fracture using X-ray micro-tomography. *Geotechnique* 65 (8), 625–641. doi:10.1680/geot.4.P.157



OPEN ACCESS

EDITED BY
Liang Cui,
Lakehead University, Canada

REVIEWED BY
Zhanguo Xiu,
Northeastern University, China
Feili Wang,
Qingdao University of Technology, China

*CORRESPONDENCE
S. Y. Fan,
✉ fanshengyuan88@163.com

SPECIALTY SECTION
This article was submitted to
Environmental Informatics and Remote
Sensing,
a section of the journal
Frontiers in Earth Science

RECEIVED 12 November 2022
ACCEPTED 28 December 2022
PUBLISHED 17 January 2023

CITATION
Shi JW, Zhou PY, Li X, Fan SY, Zhou ZF,
Zhi B and Cheng Y (2023), Study of the
disaster-causing mechanism and
reinforcement measures for soft rock
deformation and lining cracking.
Front. Earth Sci. 10:1096635.
doi: 10.3389/feart.2022.1096635

COPYRIGHT
© 2023 Shi, Zhou, Li, Fan, Zhou, Zhi and
Cheng. This is an open-access article
distributed under the terms of the [Creative
Commons Attribution License \(CC BY\)](#).
The use, distribution or reproduction in
other forums is permitted, provided the
original author(s) and the copyright
owner(s) are credited and that the original
publication in this journal is cited, in
accordance with accepted academic
practice. No use, distribution or
reproduction is permitted which does not
comply with these terms.

Study of the disaster-causing mechanism and reinforcement measures for soft rock deformation and lining cracking

J. W. Shi^{1,2}, P. Y. Zhou^{1,3}, X. Li^{1,3}, S. Y. Fan^{1,3*}, Z. F. Zhou⁴, B. Zhi⁵ and Y. Cheng^{3,6}

¹Shaanxi Key Laboratory of Geotechnical and Underground Space Engineering, Xi'an University of Architecture and Technology, Xi'an, China, ²Gongke Industrial Group Co. Ltd., Xi'an, China, ³School of Civil Engineering, Xi'an University of Architecture and Technology, Xi'an, China, ⁴CCCC Bui I ding Group Co. Ltd., Beijing, China, ⁵China Road and Bridge Engineering Co. Ltd., Beijing, China, ⁶School of Civil Engineering, Yancheng Institute of Technology, Yancheng, China

Underground engineering construction is facing increasingly complex geological conditions and engineering challenges, such as surrounding rock deformation and lining cracking, that seriously threaten the safety of tunnel construction and operation. Aiming at these problems, a pipeline tunnel crossing jointed expansive mudstone strata was taken as an example, and the disaster characteristics of surrounding rock and lining were analyzed through field investigation. The disaster-causing mechanism and corresponding control measures were studied through laboratory tests and numerical simulations, which were then applied to actual construction. Meanwhile, the deformation and stress response of the surrounding rock and tunnel structure were analyzed and investigated through monitoring and numerical data. The results showed that the vault settlement and horizontal convergence deformation of surrounding rock were reduced by 64.69 mm and 54.74 mm, respectively, under the improved construction scheme. The maximum surrounding rock stress was 430.26 kPa under the improved construction scheme, which was 18.15% lower than the original stress. The maximum axial force of the steel arch frame was 33.02 kN, ensuring the stability of the supporting structure and tunnel construction safety. Finally, the rationality and effectiveness of the reinforcement measures adopted were assessed.

KEYWORDS

tunnel, deformation, lining cracking, reinforcement, monitoring

1 Introduction

With the rapid development of infrastructure, tunnels and underground structures construction are facing more complex geological and construction problems, such as surrounding rock large deformation, seepage and mud bursts, high geostress, and adjacent construction (Lin et al., 2019; Fan et al., 2021; Fan et al., 2022; Tian et al., 2021; Tian et al., 2022; Guo et al., 2022; Zhou et al., 2022; Zhu et al., 2022; Liu et al., 2023). More and more tunnels are facing the problems of large buried depth and surrounding rock deformation and cracking, especially in areas with developed joint structures that are under the action of geological eccentric compression (Cao et al., 2018; Winn et al., 2019; Feng et al., 2021; Zhang et al., 2022a; Zhang et al., 2022b; Wang et al., 2022). Selen et al. (2020) performed extensive testing to determine the slaking and disintegration behavior of these rocks and assessed the mineralogical composition of flysch and serpentinite from the headrace tunnel of the Moglice Hydropower

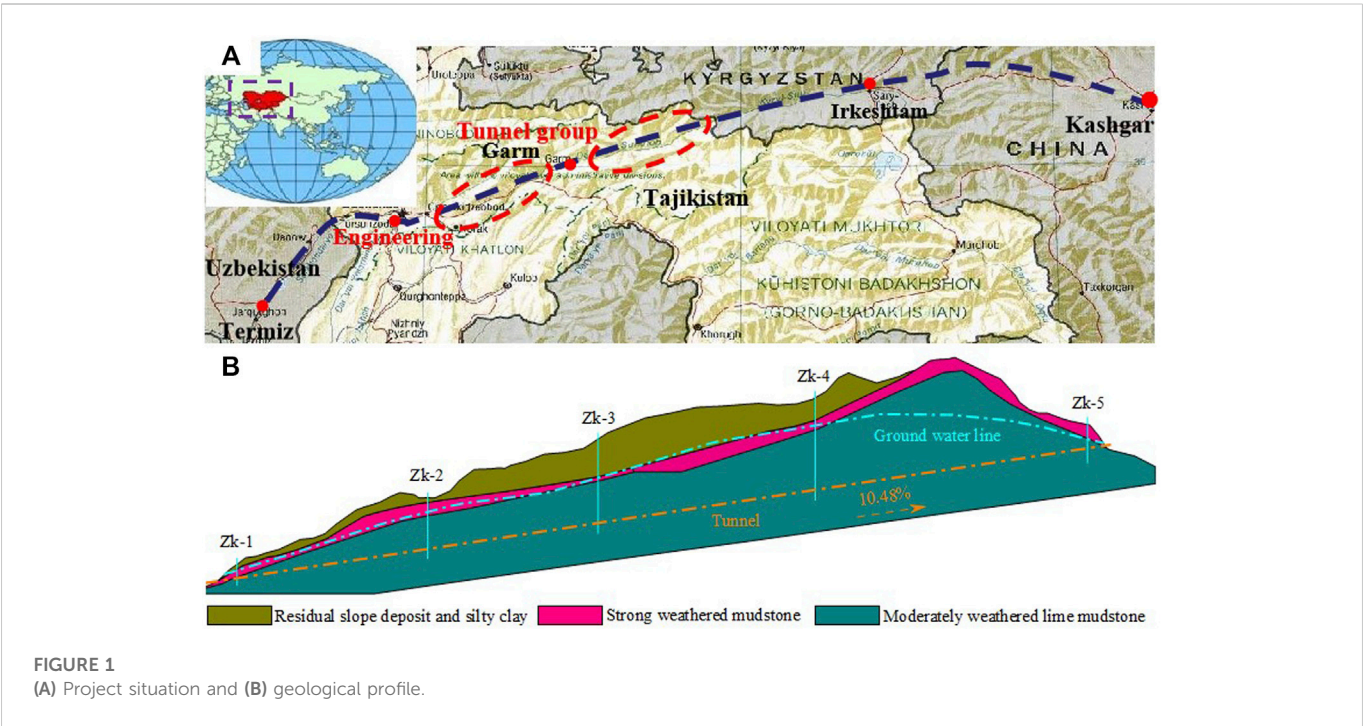


FIGURE 1
(A) Project situation and (B) geological profile.

TABLE 1 Geotechnical parameters.

Soil layer	E /(MPa)	γ /(kN/m ³)	μ	c /(kPa)	ϕ (°)
Residual slope deposit	2.52	17.5	.18	12	20
Silty clay	3.21	19	.35	18	22
Mudstone	485.96	23	.26	112	25

Note: E is the elastic modulus; γ is the unit weight; μ is Poisson's ratio; c is the cohesion; ϕ is the friction angle.

Project in Albania. The clay minerals in swelling rocks will cause volume expansion and disintegration of rocks after water softening. That study is a good reference for the cognition and control of the mechanical properties of expansive rock materials. [Tai et al. \(2020\)](#) examined the electromechanical chamber in the Tashan Coal Mine, adopting numerical simulation to analyze the surrounding rock deformation and failure characteristics during the tunneling process. Through analyzing the deformation and failure, Tai et al. (2020) suggested grouting integrated with high-strength bolts and anchor cables as a supporting measure that could effectively control the deformation. [Liu et al. \(2021\)](#) carried out a swelling test, scanning electron microscope tests, and a laboratory loading test on the swelling mudstone to further study the water effect on the swelling and mechanical properties of swelling mudstone samples. It was found that the internal friction angle did not change with the water content, while the cohesion decreased with the increasing water content. That study explained the reasons for the decrease in cohesive force of expansive mudstone and provided a strong explanation for the weakening mechanism about its mechanical properties. [Luo et al. \(2022\)](#) performed a series of true triaxial tests to investigate the influence of water on stress-induced failure in D-shaped hard rock tunnels. Softened by water, the energy storage capacity of surrounding rock decreases, the dissipation energy increases during deformation and failure, and the spalling failure of rock is induced by stress. That

study has guiding significance for the understanding of rock failure mechanism under water-rock weakening and the formulation of corresponding control measures.

The construction methods are of great significance to surrounding rock stability and construction safety. In particular, timely and reasonable supporting structures should be constructed after tunneling in the soft stratum to avoid surrounding rock deformation and structural damage ([Mikaeil et al., 2019](#); [Li et al., 2020](#); [Leng et al., 2021](#); [Li et al., 2021](#); [Pandit and Babu 2021](#); [Liu et al., 2022a](#); [Zhang et al., 2022c](#); [Zhang et al., 2022d](#); [Guan et al., 2022](#)). [Rooh et al. \(2018\)](#) established a comprehensive simulation program to study the relationship between rock mass quality and longitudinal displacement profile (LDP). They analyzed the results of the numerical modelling and showed that the LDP curves of surrounding rock with high quality ($GSI > 60$) matched well. Based on intact rock strength, joint shear strength, and joint persistence, [Renani et al. \(2019\)](#) developed linear and non-linear failure criteria utilizing an analytical model of rock mass with non-persistent joints. The model was verified through comprehensive tests on undisturbed Panguna andesite and thermally granulated Carrara marble with natural joints. Reasonable excavation and support can ensure the safety and progress of tunnel construction. [Feng et al. \(2019\)](#) studied the deformation of surrounding rock and strata of large-section tunnels under different supporting and continuous blasting schemes. Results showed that the installation of initial ground support after two rounds

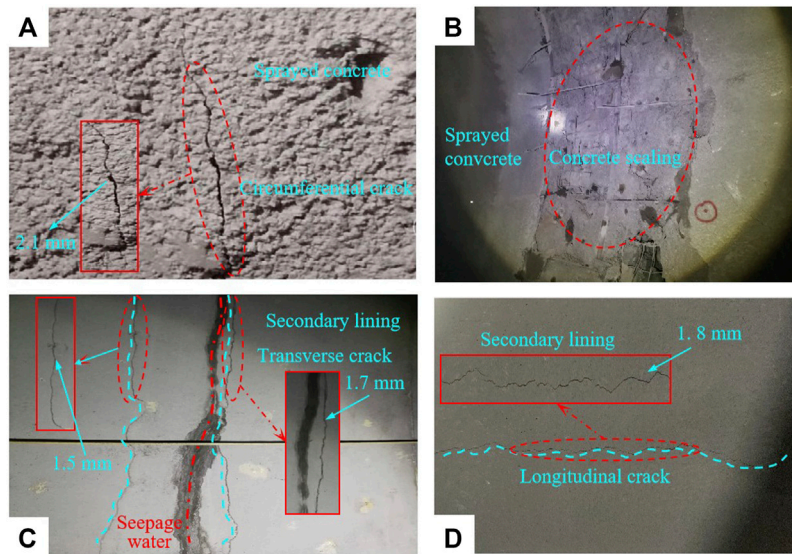


FIGURE 2
Cracking on-site of (A,B) primary supports and (C,D) secondary lining.

of blasting produced the most regular and minimum tunnel internal forces, and this installation sequence significantly accelerated tunnel construction. The conclusions of that study are of great significance to ensure the safe and rapid construction of a tunnel and to reduce the time and economic cost of tunnel construction.

As an economical and effective active support method, bolt support has been widely used in engineering support for tunnels and underground mining. Liu et al. (2020a) independently developed an anchoring synergistic component (ASC) and mainly investigated the optimization of the bolt anchoring structure and the enhancement of the bolts' ability to control the surrounding rock deformation by combining the numerical simulation and laboratory testing. The result indicated that the anchoring force and bearing capacity of the anchoring structure were noticeably improved with the ASC installed between the resin cartridges. Qin et al. (2022) analyzed the evolution of different failure modes using a shallow tunneling method in a loose granular stratum through DEM calculation, and the prevention mechanism was discussed. Comprehensive construction measures were suggested from the aspects of pre-support, excavation, bolt driving, and collapse prevention that could provide valuable references for tunnel construction control in similar projects. The aforementioned studies have laid the foundation for studying the soft rock deformation, and the deformation of surrounding rock and lining cracking in soft rock strata needs further study.

The adverse effect of broken soft rock on the stress and deformation of tunnel structure and the effective control measures were studied in this paper based on the tunnel of a natural gas pipeline crossing soft rock strata. This study first analyzed the disaster characteristics of surrounding rock deformation and lining cracking. Then, the corresponding control measures were proposed and applied to actual construction. The deformation and stress evolution law of surrounding rock and supporting structure after adopting the improved construction scheme were analyzed based on the field monitoring data to ensure the stability of supporting structure and construction safety. Finally, combined with the measured data and numerical simulation, the rationality and effectiveness of the

reinforcement measures adopted were assessed through comparative analysis of the deformation and stress response characteristics of the surrounding rock and supporting structure. The research conclusions provide theoretical guidance for design and construction.

2 Engineering situations and geological conditions

The natural gas pipeline starts in Turkmenistan, passes through Turkish-Ukish, Uzbekistan, Tajikistan, and Kyrgyzstan from west to east, and ends in Kashgar, China. The general situation of the background project is shown in Figure 1A. The tunnel is 1860 m in length with a maximum buried depth of 163 m, and the width \times height of the tunnel section is 4.5 m \times 4.5 m.

The overlying soil layer of the tunnel area was mainly quaternary residual slope soil and silty clay with a thickness of 1–20 m. The lower soil was mainly weathered mudstone (Pg1 + 2), with a developed layered joint structure and poor stability. The tunnel entrance is located at the slope foot, and the slope was gradual with loess-type silty clay. The exit was located at the mountainside slope, and the slope soil was mainly silty clay with a small amount of gravel. The groundwater in the tunnel site area mainly includes pore water and bedrock fissure water, which was mainly replenished by precipitation and ice meltwater. In addition, the groundwater had weak corrosion on the concrete structures and steel bars. The geological profile is shown in Figure 1B, and the geotechnical parameters are shown in Table 1.

3 Disaster characteristics and cause analysis

3.1 Cracking condition on site

During K1 + 663 ~ K1 + 683, longitudinal cracks with a length of roughly 1.5 m and a width of 2–4 mm appeared on primary supports

TABLE 2 Test results of mudstone composition and dilatibility.

Core no.	Clay mineral (%)				Content	Detrital mineral content (%)				Dilatibility
	Montmorillonite	Illite	Chlorite	Kaolinite		Quartz	Dolomite	Calcite	Zeolite	
1	6	33	7	10	59	21	7	4	2	9.03%
2	7	35	11	8	62	25	6	8	2	7.26%
3	6	30	6	7	46	30	6	13	3	5.34%

at the right hance, accompanied by concrete scaling. During K1 + 690 ~ K1 + 700, longitudinal and transverse cracks with a width of 1–3 mm appeared on the secondary lining at the left side wall, accompanied by local shedding and water seepage. Affected by geological eccentric compression, some deeper cracks appeared on the vault, with a width of more than 2 mm. The field cracking situation is shown in [Figure 2](#).

3.2 Disaster cause analysis

3.2.1 Layered joint structure

Combined with geological survey data, it is known that the tunnel site's surrounding structure had developed layers. The developed layered structure will intensify the inhomogeneity of the surrounding rock stress on both sides, resulting in the asymmetric distribution of deformation and cracking on both sides. In addition, the layered structure of the surrounding rock had a sliding and separating trend along the joint surface under the force of high geostress, which aggravated the risk of surrounding rock deformation and lining cracking ([Liu et al., 2020b](#); [Zhang et al., 2022a](#); [Li et al., 2022](#)).

3.2.2 Swelling property of mudstone

The groundwater runoff modulus was 2.28–7.32 L/skm² in the dry season and 4.85–9.58 L/skm² in the rainy season. The field investigation showed that the layered structure and fissures in the tunnel site were relatively developed, which facilitated the seepage of groundwater. The water–rock physicochemical reaction intensified, resulting in the strength degradation of the surrounding rock ([Yang et al., 2022](#)) and inducing uncoordinated surrounding rock deformation and cracking of the lining. Three cores were drilled in the collapsed tunnel section for laboratory tests to obtain the mineral composition and expansion ([Ahn et al., 2021](#); [Wang et al., 2022](#)). The results are shown in [Table 2](#).

[Table 2](#) shows that the mineral composition of mudstone was similar in each core. The clay minerals were mainly illite, followed by kaolinite, chlorite, and montmorillonite, which can easily cause mudstone expansion. The laboratory test results showed that the expansion rates of the three cores were 9.03%, 7.26%, and 5.34%, respectively, which was not conducive to surrounding rock stability. Moreover, the groundwater could aggravate the dilatibility and strength damage of the mudstone, threatening tunnel safety and the stability of the surrounding rock.

3.2.3 High geostress

Surrounding rock strength is an important design parameter in tunnel engineering that directly affects the load borne by the supporting structure and the overall stability of the tunnel. The maximum buried depth of the No. 1 tunnel was 260 m, and the surrounding rock comprised grade V and VI weathered mudstone. Based on laboratory tests and field surveys, the uniaxial saturated compressive strength of the surrounding rock was 11.8–24.2 MPa, and the maximum horizontal principal stress and vertical stress were about 2.8–3.6 MPa and 4.2–5.1 MPa, respectively. The strength–stress ratio was 4.2–5.7; therefore, the surrounding rock stress was not uniform, and some areas were affected by high geostress ([Yang et al., 2017](#); [Liu et al., 2022b](#); [Xu et al., 2022](#)).

3.2.4 Unqualified supporting structure and lining

It was found that the steel arch frame spacing of the primary supports in the collapsed section of the tunnel was too large, resulting in uneven stiffness and deformation along the tunnel. In addition, the

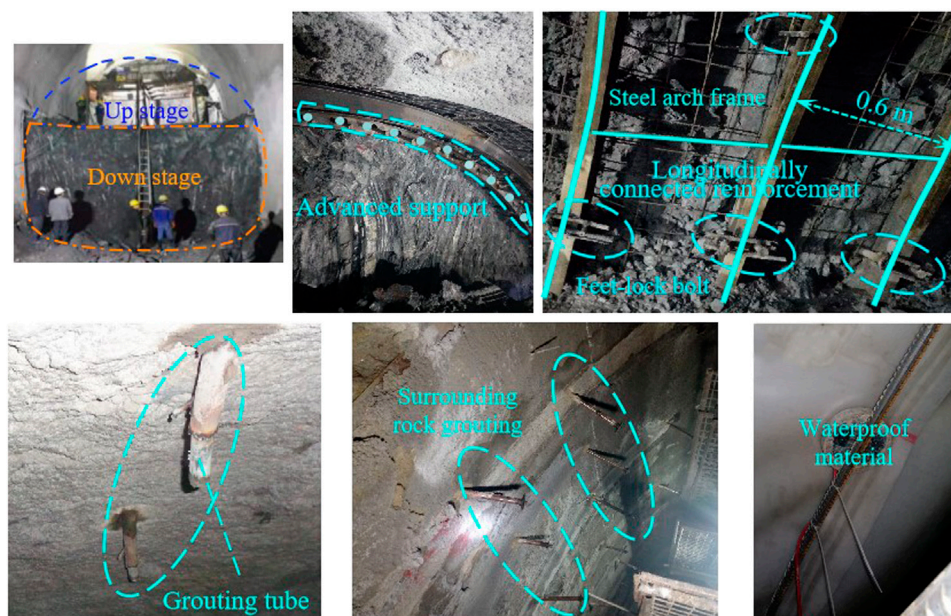


FIGURE 3
Field application of improved construction measures.

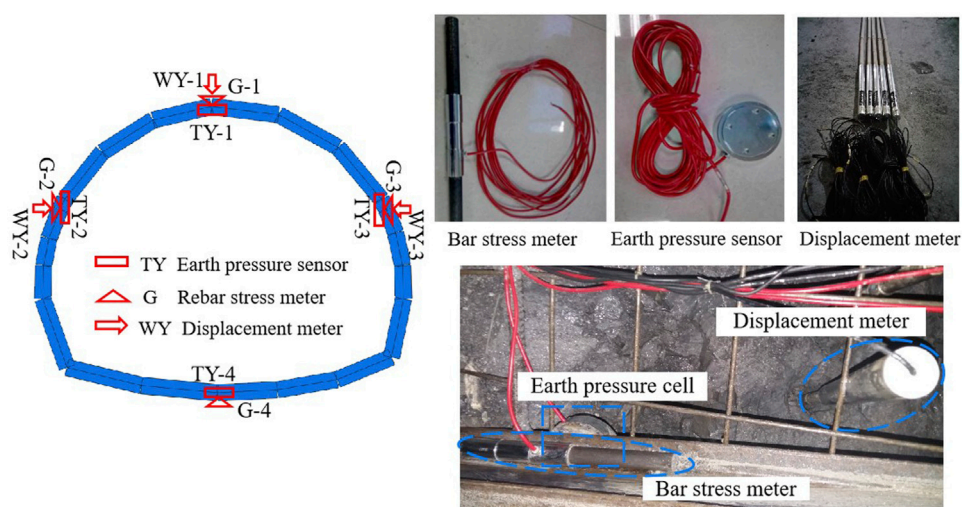


FIGURE 4
Layout of measuring points and installation of measuring components.

concrete thickness in the disaster range was about 0.06 m thinner than the design value, leading to insufficient strength, uneven stress, and cracking of the lining structure.

4 Improved measures and engineering application

4.1 Solution measures

Combined with the disaster-causing mechanism analysis of the layered jointed mudstone stratum in background engineering, the

following targeted control measures were proposed: (a) according to the existing engineering experience (Huang et al., 2021; Liu et al., 2022c), the two-step excavation method with the excavation footage $F=1.2$ m was used. (b) Pre-support measures of grouting pipe sheds were adopted. (c) The steel arch frame was densely arranged, and the locking bolt and longitudinal connection reinforcement were added to improve the overall stiffness of the supporting structure. (d) To improve the integrity of the surrounding rock, grouting bolts were used and arranged vertically to the layered joint surface instead of the original. (e) The surrounding rock was grouted by controlling the grouting pressure of 2 MPa to enhance the bonding between the joint surface and the integral rock mass. (f) Waterproof material was laid

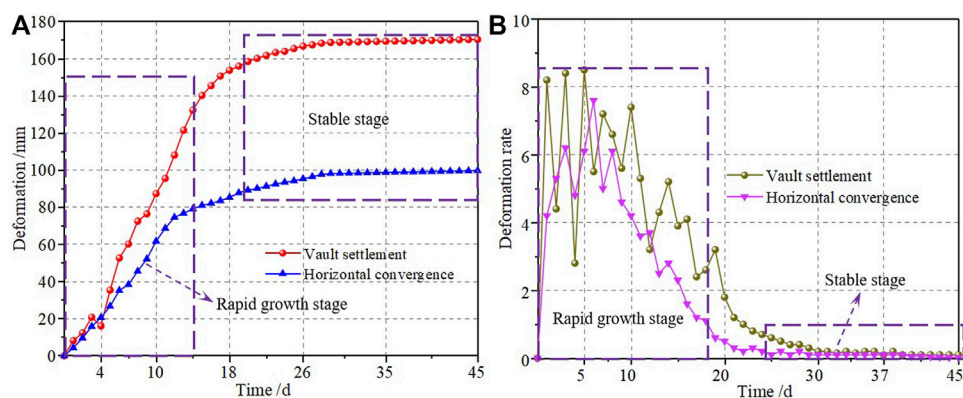


FIGURE 5
Result of surrounding rock deformation: (A) cumulative deformation curve and (B) deformation rate curve.

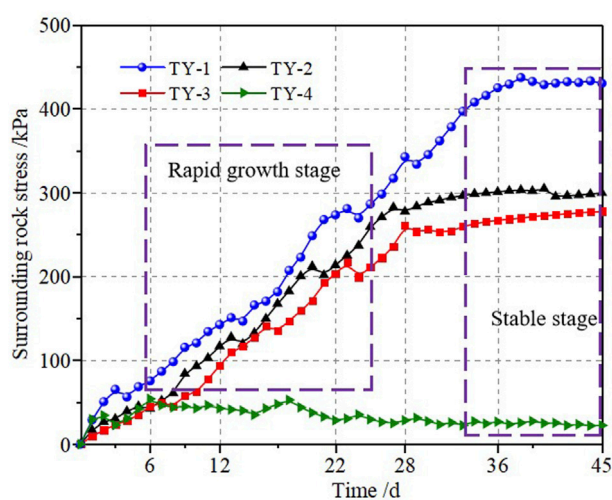


FIGURE 6
Stress of surrounding rock.

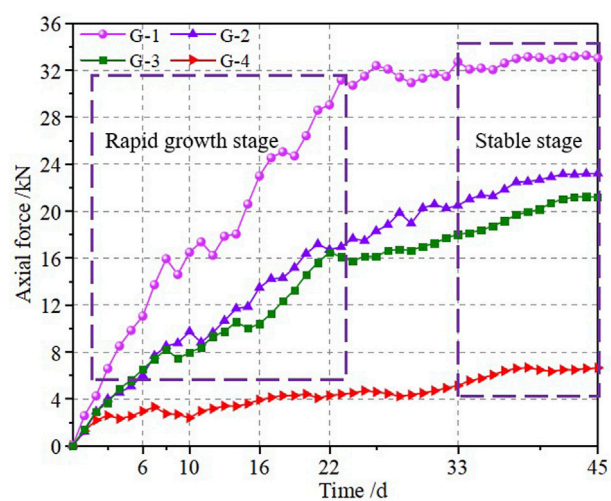


FIGURE 7
Axial force of the steel arch frame.

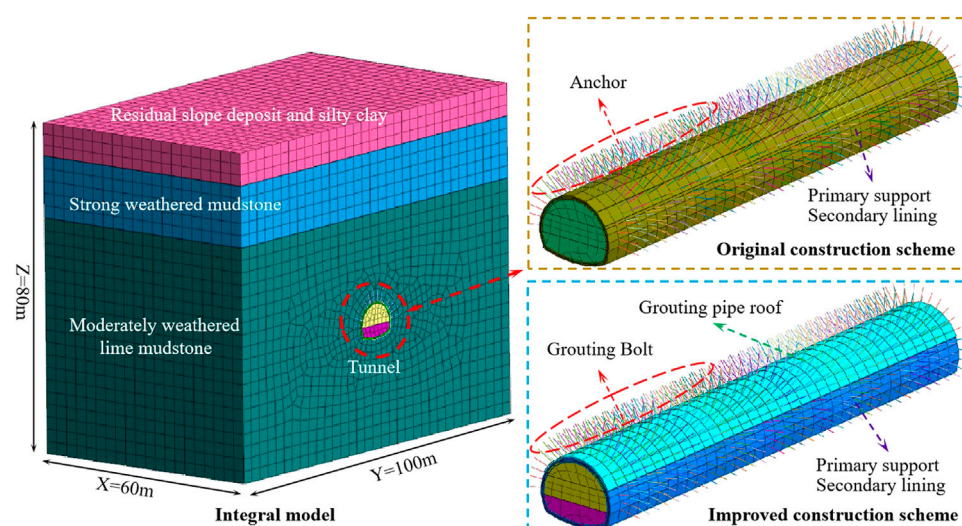


FIGURE 8
Three-dimensional finite element model.

TABLE 3 Material parameters of the supporting structure.

Material	E (GPa)	γ (kN/m ³)	μ	Thickness or length (mm)	Diameter (mm)
Anchor	210	78.5	.3	4,000	28
Grouting steel pipe	200	78.5	.3	6,000	50
Steel arch frame	200	78.5	.3	10	\
Secondary liner	30	25	.3	550	\
Concrete and grout	29.5	23	0.2	\	\

down before pouring the secondary lining concrete to prevent pore water from penetrating into the secondary lining structure. At the same time, the secondary lining concrete should be poured in strict accordance with the design, and subsequent maintenance should be carried out well. The implementation of improved control measures during actual construction is shown in Figure 3.

4.2 Engineering application and measured data analysis

The control measures proposed were applied during the subsequent tunnel construction. The earth pressure sensor and displacement meter were embedded to monitor the stress and deformation of the surrounding rock. Meanwhile, the rebar stress meter was welded onto the steel arch web to test the force of the steel arch frame. The layout of monitoring points and measuring component installation on-site is shown in Figure 4. The stress and deformation of the surrounding rock and supporting structure were monitored strictly during construction. When surrounding rock deformation or supporting structure stresses were too large, the construction was suspended, and the reasons were analyzed to ensure construction safety.

4.3 Analysis of measured results

4.3.1 Deformation of surrounding rock

Figure 5 shows the cumulative deformation and deformation rate of the surrounding rock.

Figure 5 shows that surrounding rock deformation mainly occurred in the early stage; the amount of vault settlement and horizontal convergence in the first 10 days accounted for 44.86% and 52.29% of the total deformation, respectively. The deformation rate decreased after primary supporting construction, while the cumulative deformation continued to increase. The cumulative settlement and convergence deformation increased by 43 mm and 20.6 mm, respectively, during the 11–20-day period after inverted arch construction and forming a closed ring with primary supports, which enhanced the stability of the supporting structure and controlled the surrounding rock deformation. Finally, the vault settlement and horizontal convergence stabilized at 170.52 and 99.81 mm, respectively. Meanwhile, there was no cracking on the primary supports and secondary lining during subsequent construction, indicating that the improved measures worked well. Comparing the settlement and convergence values revealed that the overall deformation of the surrounding rock was dominated by settlement. However, the horizontal convergence was also large, so the

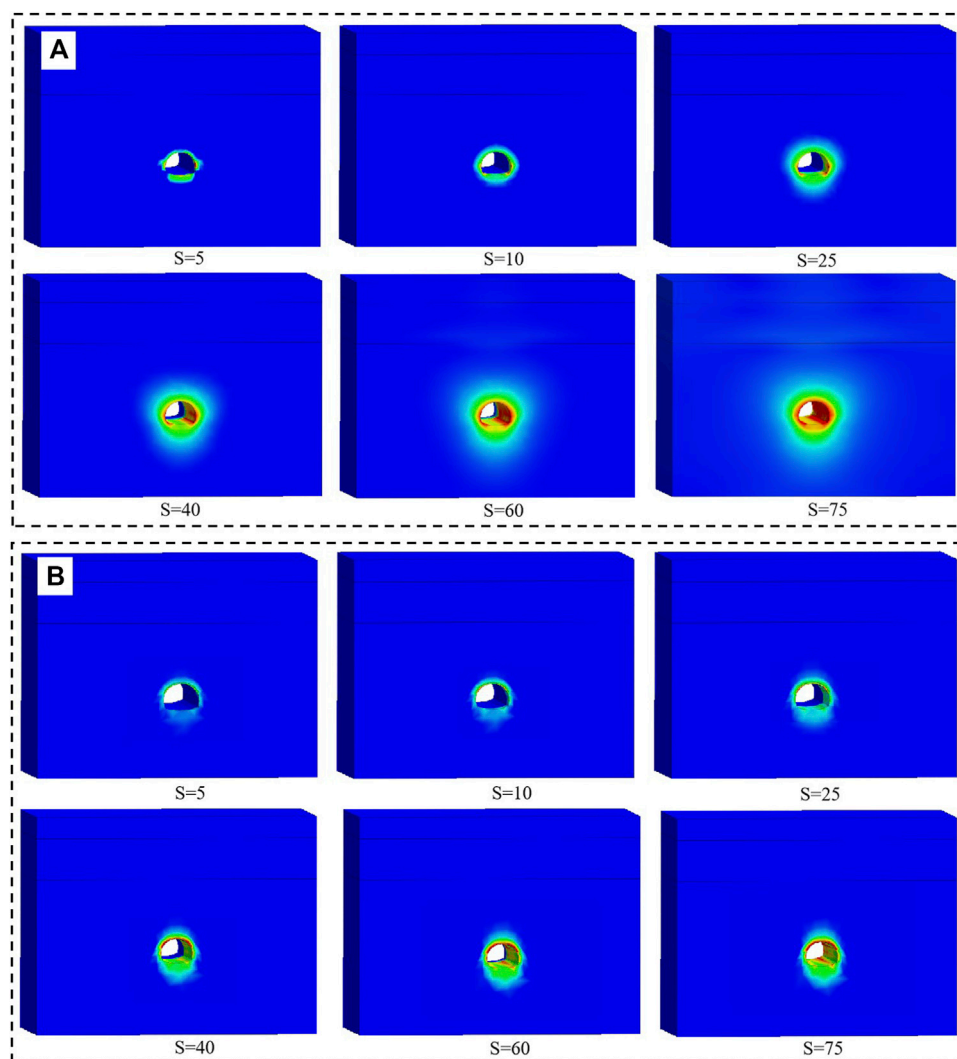


FIGURE 9

Development process of plastic zones under two construction schemes: (A) original construction scheme and (B) improved construction scheme.

surrounding rock deformation should be strictly monitored to ensure construction safety.

4.3.2 Stress of surrounding rock

Data from the earth pressure sensor were analyzed to obtain the stress variation of the surrounding rock, as shown in Figure 6.

Figure 6 shows that the stress was distributed unevenly and increased in fluctuation during construction. In the first 6 days, the surrounding rock stress at measuring points #1–4 reached 75.48, 38.45, 45.35, and 54.05 kPa, respectively. The surrounding rock stress at the vault and hance continued to increase, while the value at the arch bottom changed slightly. After 28 days, the stress at the vault and two hances reached 79.69%, 92.56%, and 94.13% of the total stress, respectively. After inverted arch construction and forming a closed ring with initial support, the surrounding rock stress at the hance and arch bottom gradually stabilized, while the value of the vault increased continuously. After 40 days, the stress at the vault gradually stabilized with the highest value of 430.26 kPa. Affected by geological eccentric compression, the stress at the two hances was larger,

reaching 292.36 and 275.29 kPa, respectively. The stress at the arch bottom was small and remained stable, ensuring safe tunnel construction.

4.3.3 Force of steel arch frame

The axial force variation of the steel arch frame is shown in Figure 7.

Figure 7 shows that the force variation of the steel arch frame was similar to surrounding rock stress, and the force increased rapidly in the early stage of construction, indicating that the steel arch frame bore loading immediately and restricted the surrounding rock deformation. In the first 8 days, the axial forces of the steel arch frame at measuring points #1–4 were 15.91, 7.37, 8.18, and 2.71 kN, respectively. The force value at the vault and hance increased with continuous excavation, while the value at the arch bottom remained stable. After 28 days, the axial forces at the vault and two hances reached 95.03%, 85.61%, and 78.97% of the largest value, respectively. After inverted arch construction and forming a closed ring with primary supports, the axial force of the steel arch frame gradually stabilized. Finally, the axial

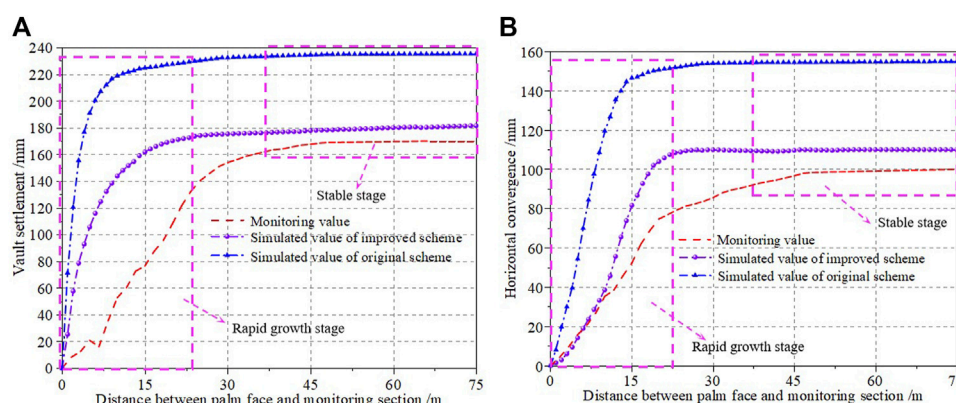


FIGURE 10

Variation of surrounding rock deformation: (A) vault settlement and (B) horizontal convergence.

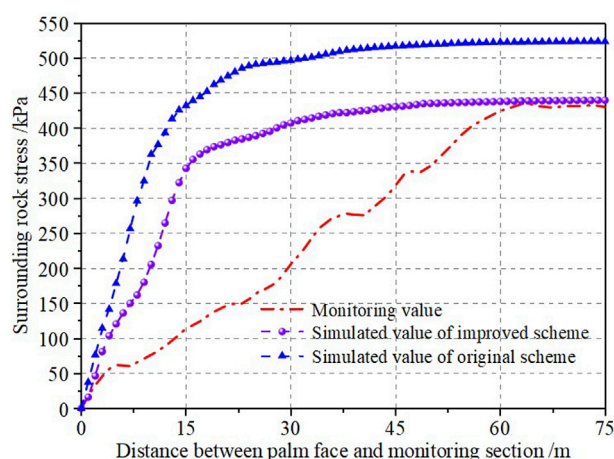


FIGURE 11

Variation of surrounding rock stress.

forces at measuring points #1–4 were 33.02, 20.15, 21.16, and 6.62 kN, respectively, ensuring construction safety.

5 Analysis and discussion

Aiming at the problems of background engineering and the disaster-causing mechanism analysis mentioned in the previous content, this study analyzed the deformation and stress characteristics of surrounding rock with a developed layered structure and supporting structure. The effectiveness of the improved measures proposed in this study was evaluated by comparing results under the original and improved construction scheme.

5.1 Model and parameters

The deformation and stress of the surrounding rock and supporting structure before and after reinforcement treatment were simulated and

analyzed using Midas GTS/NX, numerical calculation software designed for geotechnical engineering (Komu et al., 2020). The model fully considers the influence range of construction disturbance to ensure the reliability and effectiveness of calculation results. According to the “Code for design of gas transmission pipeline engineering,” considering the maximum construction disturbance range required a model of size 60 m × 100 m × 80 m (length × width × height), as shown in Figure 8. The upper surface of the model was a free surface. The horizontal displacement was constrained on the surrounding boundary, and the horizontal and vertical displacements were constrained on the bottom boundary.

The geotechnical parameters were obtained from the geological exploration report and laboratory test data (see Table 1), and the reinforcement materials parameters are shown in Table 3.

5.2 Result analysis

5.2.1 Plastic zone

According to the Mohr–Coulomb yield criterion, when the shear stress reaches the shear strength of the rock mass, the rock mass will enter the plastic stage. Thus, the plastic zone was the area where the shear stress exceeded the rock shear strength. The development process of plastic zones with construction steps (S) increasing under two construction schemes is shown in Figure 9.

Figure 9 shows that the plastic zone under two construction schemes expanded with tunnel excavation. The plastic zone of the surrounding rock developed rapidly, and the response range was large under the original construction scheme. The plastic zone showed an asymmetric development trend in the early stage, which increased sharply later. In particular, the plastic response characteristic of the surrounding rock became more obvious closer to the cave wall, which contributed to the large deformation of the surrounding rock and the actual disaster. Under the improved construction scheme, the integrity of the surrounding rock was improved by using grouting bolts and surrounding rock grouting measures, and the development of the surrounding rock plastic zone was controlled well. In addition, the plastic deformation response of the side wall under the original construction scheme was obvious when $S = 40$. Under the improved scheme, the plastic deformation response of the vault

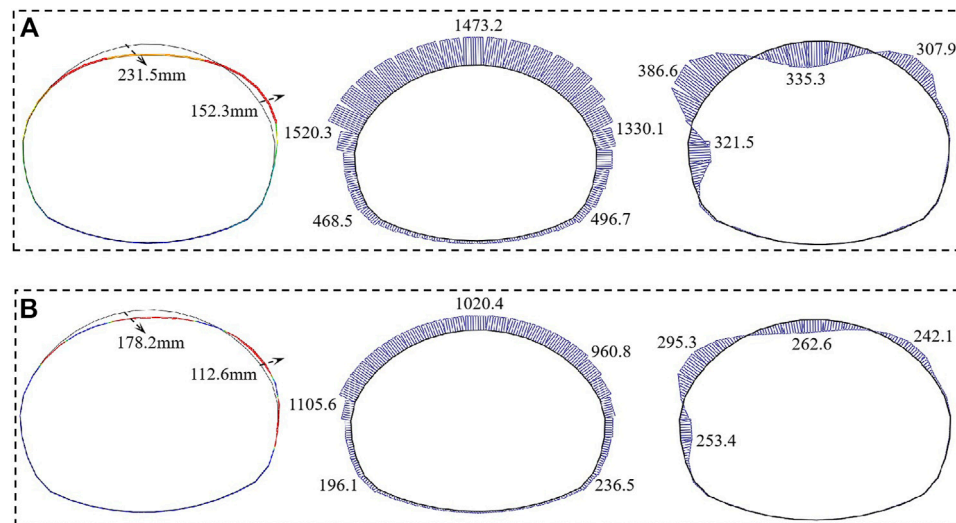


FIGURE 12
Deformation and internal force of primary supports: (A) original construction scheme and (B) improved construction scheme.

area was larger, indicating that the advanced support measures had played a role and effectively bore the load of the surrounding rock. After tunnel excavation, the plastic zone range was reduced, and the distribution was more uniform, indicating that the construction measures adopted can effectively improve the stress state of the surrounding rock and ensure the stability of the surrounding rock.

5.2.2 Deformation of surrounding rock

The variation of surrounding rock deformation at the measured section under two construction schemes is shown in Figure 10.

Figure 10 shows that the simulated development process results were similar to the measured results, and the vault settlement and horizontal convergence deformation increased rapidly early. When the palm surface pulled 30 m ahead of the monitoring section, the surrounding rock deformation slowed and gradually became stable. The simulation values of vault settlement under the two construction schemes were 235.21 and 181.45 mm, respectively, and the horizontal convergence values were 154.55 and 109.85 mm, respectively. Two deformations under the improved construction scheme were reduced by 34.29% and 39.46% compared to the original construction scheme, indicating that the improvement measures can effectively control the deformation of surrounding rock and ensure construction safety. Moreover, the measured values were closer to the simulation values under the improved construction scheme, and the differences between the two deformations were 9.45 and 10.59 mm, respectively. Considering the difference between the actual construction and numerical simulation, it is necessary to strictly monitor the deformation of surrounding rock during the actual construction process.

5.2.3 Stress of surrounding rock

The variation of maximum surrounding rock stress at the measured section under two construction schemes is shown in Figure 11.

Figure 11 shows that the surrounding rock stress increased sharply in the early stage of excavation. When the palm surface was pushed 15 m ahead of the monitoring section, the maximum stress under the two construction schemes accounted for 81.29% and 73.26% of the cumulative value, respectively. Compared with the simulation value, the measured stress of the surrounding rock increased slowly, accounting for 26.82% of the cumulative value. During the subsequent construction process, the simulated value gradually stabilized. The measured results showed that the surrounding rock stress was gradually released, which was conducive to surrounding rock stability. Finally, the measured results were closer to the simulation results of the improved construction scheme, with a difference of 9.86 kPa. Both sets of results met the requirements of surrounding rock stability, indicating that adopting the improved measures can effectively ensure construction safety.

Deformations and internal force of primary supporting: The deformations and internal forces of the primary supports at the measured section under two construction schemes are shown in Figure 12.

Figure 12 shows that the deformation trend and internal force distribution of the primary supports under the two construction schemes were similar. After tunneling excavation, the left spandrel and vault were squeezed into the tunnel, and the right side wall tended to be squeezed out of the tunnel. The vertical deformation and horizontal deformation of the primary supports were reduced by 53.3 and 39.7 mm, respectively, under the improved construction scheme. It indicated that adopting the improved measures according to the previous mechanism analysis can effectively control the deformation of the surrounding rock and the supporting structure, which is beneficial to tunnel stability. In addition, the maximum internal force was reduced, and the distribution was more uniform after improving construction. Compared with the original construction scheme, the maximum axial force and bending moment were reduced by 414.7 kN and 91.3 kN m, respectively. These results show that the measures to

enhance the stiffness and integrity of the primary supports can effectively improve the overall bearing capacity of the supporting structure, which is beneficial to construction safety.

6 Conclusion

The disaster-causing mechanism of surrounding rock deformation and secondary lining cracking of the construction of the No. 1 tunnel of the China–Tajikistan natural gas pipeline was studied. The effectiveness of the reinforcement measures was evaluated. Through analysis and discussion, the following conclusions can be drawn.

- 1) Combined with the analysis of the disaster-causing mechanism, it was found that the developed layered structure, high geostress, and the expansibility of mudstone will cause large deformation of the surrounding rock and lining cracking. The slip deformation of the layered rock mass along the structural plane was the particular reason for uneven tunnel deformation.
- 2) The deformation and stress of the tunnel structure were controlled and gradually stabilized after the integrity and stiffness of the rock mass and supporting structure were enhanced. The maximum values of vault settlement and horizontal convergence were 170.52 and 99.81 mm, respectively. The maximum stress of the surrounding rock and steel arch frame occurred at the vault, reached 430.26 kPa and 33.02 kN, and ensured construction safety and the stability of the surrounding rock.
- 3) The deformation of the surrounding rock and primary supporting were well controlled under comprehensive control measures. The vault settlement and horizontal convergence of the primary supports were reduced by 23.02% and 26.07%, respectively, compared to the original construction scheme. Moreover, the measured results of surrounding rock deformation were only 3.5% higher than the simulated values of the improved scheme, verifying the feasibility of the improvement measures.
- 4) The force distribution of the primary supports was improved, and the maximum axial force and bending moment were reduced by 27.28% and 23.62%, respectively, under the improved construction scheme. Meanwhile, the tensile region was transformed into a compressive state, giving full play to the bearing role of the supporting structure and ensuring the stability and safety of the tunnel structure.

References

- Ahn, H. S., Lim, J., and Kim, S. W. (2021). Magnetic properties of a holocene sediment core from the yeongsan estuary, southwest korea: Implications for diagenetic effects and availability as paleoenvironmental proxies. *Front. Earth Sc-switz.* 9, 593332. doi:10.3389/feart.2021.593332
- Cao, R. H., Cao, P., Lin, H., Ma, G. W., Zhang, C., and Jiang, C. (2018). Failure characteristics of jointed rock-like material containing multi-joints under a compressive-shear test: Experimental and numerical analyses. *Arch. Civ. Mech. Eng.* 18, 784–798. doi:10.1016/j.acme.2017.12.003
- Fan, S. Y., Song, Z. P., Xu, T., Wang, K. M., and Zhang, Y. W. (2021). Tunnel deformation and stress response under the bilateral foundation pit construction-a case study. *Arch. Civ. Mech. Eng.* 21 (3), 109. doi:10.1007/s43452-021-00259-7
- Fan, S. Y., Song, Z. P., Xu, T., and Zhang, Y. W. (2022). Investigation of the microstructure damage and mechanical properties evolution of limestone subjected to high-pressure water. *Constr. Build. Mater.* 316, 125871. doi:10.1016/j.conbuildmat.2021.125871
- Feng, F., Li, X. B., Luo, L., Zhao, X. D., Chen, S. J., Jiang, N., et al. (2021). Rockburst response in hard rock owing to excavation unloading of twin tunnels at great depth. *B. Eng. Geol. Environ.* 80 (10), 7613–7631. doi:10.1007/s10064-021-02377-1
- Feng, J. M., Yan, C. W., Ye, L., Ding, X. Q., Zhang, J. R., and Li, Z. L. (2019). Evaluation of installation timing of initial ground support for large-span tunnel in hard rock. *Tuun Uudergr Sp. Tech.* 93, 103087. doi:10.1016/j.tust.2019.103087

Data availability statement

The original contributions presented in the study are included in the article/Supplementary Material; further inquiries can be directed to the corresponding author.

Author contributions

JS conceived and designed the methods, provided a guide to the monitoring and theoretical research for the study, and economically supported the project. PZ, XL, and SF completed the numerical model, data analysis, and writing of the manuscript. ZZ, BZ, and YC provided the monitoring materials and completed the data collection.

Funding

The authors are grateful for the support of the National Natural Science Foundation of China (No. 51578447), the Science and Technology Innovation Team of Shaanxi Innovation Capability Support Plan (No. 2020TD005), the Science and Technology Development Program of Shaanxi Provincial Department of Housing and Urban-Rural Construction (No. 2019-K39), and the Special Project of Shaanxi Provincial Education Department (No. 20JK0709). The financial supports are gratefully acknowledged, and the data are available for the journal.

Conflict of interest

JS was employed by Gongke Industrial Group Co. Ltd. ZZ was employed by CCCC Building Group Co. Ltd. BZ was employed by China Road and Bridge Engineering Co. Ltd.

The remaining authors declare that the research was conducted in the absence of any commercial or financial relationships that could be construed as a potential conflict of interest.

Publisher's note

All claims expressed in this article are solely those of the authors and do not necessarily represent those of their affiliated organizations, or those of the publisher, the editors, and the reviewers. Any product that may be evaluated in this article, or claim that may be made by its manufacturer, is not guaranteed or endorsed by the publisher.

- Guan, K., Zhang, Q. Y., Liu, H. L., and Zhu, W. C. (2022). A new numerical procedure for the excavation response in Mohr-Coulomb rock mass exhibiting strain-softening behavior. *Front. Earth Sc-switz* 10, 872792. doi:10.3389/feart.2022.872792
- Guo, H. S., Tong, J. Q., Sun, Q. C., Yang, X., Luo, W. J., and Yu, Y. (2022). Determination method of excavation damage zone based on surrounding rock damage-fracture ratio in underground engineering. *Front. Earth Sc-switz* 10, 836313. doi:10.3389/feart.2022.836313
- Huang, X., Li, L. F., Zhang, C. F., Liu, B., Li, K. J., Shi, H. B., et al. (2021). Multi-step combined control technology for karst and fissure water inrush disaster during shield tunneling in spring areas. *Front. Earth Sc-switz* 9, 795457. doi:10.3389/feart.2021.795457
- Komu, M. P., Guney, U., Kilickaya, T. E., and Gokceoglu, C. (2020). Using 3d numerical analysis for the assessment of tunnel-landslide relationship: Bahce-nurdag tunnel (south of Turkey). *Geotech. Geol. Eng.* 38 (4), 1237–1254. doi:10.1007/s10706-019-01084-9
- Leng, X. L., Wang, C., Sheng, Q., Chen, J., and Li, H. L. (2021). An enhanced ubiquitous-joint model for a rock mass with conjugate joints and its application on excavation simulation of large underground caverns. *Front. Earth Sc-switz* 9, 744900. doi:10.3389/feart.2021.744900
- Li, G., Hu, Y., Tian, S. M., Wein, M., and Huang, H. L. (2021). Analysis of deformation control mechanism of prestressed anchor on jointed soft rock in large cross-section tunnel. *B Eng. Geol. Environ.* 80 (12), 9089–9103. doi:10.1007/s10064-021-02470-5
- Li, G., Ma, F. S., Guo, J., Zhao, H. J., and Liu, G. (2020). Study on deformation failure mechanism and support technology of deep soft rock roadway. *Eng. Geol.* 264, 105262. doi:10.1016/j.enggeo.2019.105262
- Li, Z. C., Wang, S. R., Li, L. C., and Zhang, J. Y. (2022). Numerical Investigation on interference of multiple hydraulic fractures in layered formation. *Front. Earth Sc-switz* 10, 865155. doi:10.3389/feart.2022.865155
- Lin, X. T., Chen, R. P., Wu, H. N., and Cheng, H. Z. (2019). Deformation behaviors of existing tunnels caused by shield tunneling undercrossing with oblique angle. *Tunn. Undergr. Sp. Tech.* 89, 78–90. doi:10.1016/j.tust.2019.03.021
- Liu, C. D., Cheng, Y., Jiao, Y. Y., Zhang, G. H., Zhang, W. S., Ou, G. Z., et al. (2021). Experimental study on the effect of water on mechanical properties of swelling mudstone. *Eng. Geol.* 295, 106448. doi:10.1016/j.enggeo.2021.106448
- Liu, D. M., Zhao, Z., Jin, X. M., Yang, C., Chen, W., Cai, Y. D., et al. (2022b)., 2022. Hydrodynamic and 420 geostress controls on CBM enrichment in the anze block, Southern Qinshui basin, North China. *Geofluids*, 9199715. doi:10.1155/2022/9199715
- Liu, N. F., Li, N., Li, G. F., Song, Z. P., and Wang, S. J. (2022a). Method for evaluating the equivalent thermal conductivity of a freezing rock mass containing systematic fractures. *Rock Mech. Rock Eng.* 55 (12), 7333–7355. doi:10.1007/s00603-022-03038-9
- Liu, N. F., Li, N., Wang, S. J., Li, G. F., and Song, Z. P. (2023). A fully coupled thermo-hydro-mechanical model for fractured rock masses in cold regions. *Cold Reg. Sci. Technol.* 2022 (205), 103707. doi:10.1016/j.coldregions.2022.103707
- Liu, N. F., Li, N., Xu, C. B., Li, G. F., Song, Z. P., and Yang, M. (2020a). Mechanism of secondary lining cracking and its simulation for the Dugongling tunnel. *Rock Mech. Rock Eng.* 53 (10), 4539–4558. doi:10.1007/s00603-020-02183-3
- Liu, S. W., He, D. Y., and Fu, M. X. (2020b). Experimental investigation of surrounding-rock anchoring synergistic component for bolt support in tunnels. *Tunn. Undergr. Sp. Tech.* 104, 103531. doi:10.1016/j.tust.2020.103531
- Liu, Y. X., Zhang, Y. Q., Su, P. D., Zhang, G. Z., Qiu, P., and Tang, L. (2022c). Risk prediction of rock bursts and large deformations in YL tunnel of the Chongqing-Kunming high-speed railway. *Front. Earth Sc-switz* 10, 892606. doi:10.3389/feart.2022.892606
- Luo, Y., Gong, F. Q., and Zhu, C. Q. (2022). Experimental investigation on stress-induced failure in D-shaped hard rock tunnel under water-bearing and true triaxial compression conditions. *B Eng. Geol. Environ.* 81 (2), 76. doi:10.1007/s10064-021-02564-0
- Mikaeli, R., Haghsheenas, S. S., and Sedaghati, Z. (2019). Geotechnical risk evaluation of tunneling projects using optimization techniques (case study: The second part of emamzade hashem tunnel). *Nat. Hazards* 97 (3), 1099–1113. doi:10.1007/s11069-019-03688-z
- Pandit, B., and Babu, G. L. S. (2021). Probabilistic stability assessment of tunnel-support system considering spatial variability in weak rock mass. *Comput. Geotech.* 137, 104242. doi:10.1016/j.compgeo.2021.104242
- Qin, Y. W., Lai, J. X., Yang, T., Zan, W. B., Feng, Z. H., Liu, T., et al. (2022). Failure analysis and countermeasures of a tunnel constructed in loose granular stratum by shallow tunnelling method. *Eng. Fail Anal.* 141, 106667. doi:10.1016/j.engfailanal.2022.106667
- Renani, H. R., Martin, C. D., and Cai, M. (2019). An analytical model for strength of jointed rock masses. *Tunn. Undergr. Sp. Tech.* 94, 103159. doi:10.1016/j.tust.2019.103159
- Rooh, A., Nejati, H. R., and Goshtasbi, K. (2018). A new formulation for calculation of longitudinal displacement profile (LDP) on the basis of rock mass quality. *Geomech. Eng.* 16 (5), 539–545. doi:10.12989/gae.2018.16.5.539
- Selen, L., Panthi, K. K., and Vistnes, G. (2020). An analysis on the slaking and disintegration extent of weak rock mass of the water tunnels for hydropower project using modified slake durability test. *B Eng. Geol. Environ.* 79 (4), 1919–1937. doi:10.1007/s10064-019-01656-2
- Tai, Y., Xia, H. C., and Kuang, T. J. (2020). Failure characteristics and control technology for large-section chamber in compound coal seams—a case study in Tashan coal mine. *Energy Sci. Eng.* 8 (4), 1353–1369. doi:10.1002/ese3.598
- Tian, X. X., Song, Z. P., Wang, H. Z., Zhang, Y. W., and Wang, J. B. (2022). Evolution characteristics of the surrounding rock pressure and construction techniques: A case study from taoshuping tunnel. *Tunn. Undergr. Sp. Tech.* 125, 104522. doi:10.1016/j.tust.2022.104522
- Tian, X. X., Song, Z. P., and Zhang, Y. W. (2021). Monitoring and reinforcement of landslide induced by tunnel excavation: A case study from xiaomaixi tunnel. *Tunn. Undergr. Sp. Tech.* 110, 103796. doi:10.1016/j.tust.2020.103796
- Wang, J. B., Zhou, P. Y., Song, Z. P., Li, S. H., and Zhang, Q. (2022). A new calculation method for tunneling-caused stratum settlement. *KSCE J. Civ. Eng.* 26 (6), 2624–2640. doi:10.1007/s12205-022-1258-z
- Wang, Z. Y., Nie, X., Zhang, C., Wang, M. R., Zhao, J. W., and Jin, L. D. (2022). Lithology classification and porosity estimation of tight gas reservoirs with well logs based on an equivalent multi-component model. *Front. Earth Sc-switz* 10, 850023. doi:10.3389/feart.2022.850023
- Winn, K., Wong, L. N. Y., and Alejano, L. R. (2019). Multi-approach stability analyses of large caverns excavated in low-angled bedded sedimentary rock masses in Singapore. *Eng. Geol.* 259, 105164. doi:10.1016/j.enggeo.2019.105164
- Xu, C., Xia, C. C., and Han, C. L. (2022). Elastoplastic solutions for deep tunnel excavation in weak rocks with high geostress considering different stress release measures. *Int. J. Appl. Mech. Early access* 14. doi:10.1142/S1758825122500776
- Yang, J. P., Chen, W. Z., Zhao, W. S., Tan, X. J., Tian, H. M., Yang, D. S., et al. (2017). Geohazards of tunnel excavation in interbedded layers under high *in situ* stress. *Eng. Geol.* 230, 11–22. doi:10.1016/j.enggeo.2017.09.007
- Yang, M., Liu, N. F., Li, N., Xu, C. B., Li, G. F., and Cao, M. M. (2022). Failure characteristics and treatment measures of tunnels in expansive rock stratum. *Front. Earth Sc-switz* 9, 805378. doi:10.3389/feart.2021.805378
- Zhang, L., Niu, F. J., Liu, M. H., Ju, X., Wang, Z. W., Wang, J. C., et al. (2022e). Fracture characteristics and anisotropic strength criterion of bedded sandstone. *Front. Earth Sc-switz* 10, 879332. doi:10.3389/feart.2022.879332
- Zhang, Y. J., Wang, J. Y., and Xia, H. S. (2022a). Mechanism and sensitivity analysis of collapse in large section mountain neighborhood tunnels. *Front. Earth Sc-switz* 10, 904655. doi:10.3389/feart.2022.904655
- Zhang, Y. W., Fan, S. Y., Yang, D. H., and Zhou, Fei (2022b). Investigation about variation law of frost heave force of seasonal cold region tunnels: A case study. *Front. Earth Sc-switz* 9, 806843. doi:10.3389/feart.2021.806843
- Zhang, Y. W., Song, Z. P., and Weng, X. L. (2022c). A constitutive model for loess considering the characteristics of structurality and anisotropy. *Soil Mech. Found. Eng.* 59 (1), 32–43. doi:10.1007/s11204-022-09781-z
- Zhang, Z. Y., Zhao, C. Y., Peng, L., Zhang, X. H., and Lei, M. F. (2022d). Research on the stability of shallow-buried large cross-section tunnel by construction method conversion. *Front. Earth Sc-switz* 10, 831169. doi:10.3389/feart.2022.831169
- Zhou, P. Y., Wang, J. B., Song, Z. P., Cao, Z. L., and Pei, Z. M. (2022). Construction method optimization for transfer section between cross passage and main tunnel of metro station. *Front. Earth Sc-switz* 10, 770888. doi:10.3389/feart.2022.770888
- Zhu, Q. L., and Ding, Y. P. (2022). Impact of new undercrossing tunnel excavation on the stability of the existing tunnel. *Front. Earth Sc-switz* 10, 915882. doi:10.3389/feart.2022.915882



OPEN ACCESS

EDITED BY
Zhanping Song,
Xi'an University of Architecture and
Technology, China

REVIEWED BY
Junping Yuan,
Hohai University, China
Haijun Hu,
Northwest A&F University, China

*CORRESPONDENCE
Min Yang,
✉ yangmin0069@126.com

SPECIALTY SECTION
This article was submitted to
Environmental Informatics
and Remote Sensing,
a section of the journal
Frontiers in Earth Science

RECEIVED 03 December 2022
ACCEPTED 02 January 2023
PUBLISHED 19 January 2023

CITATION
Li H, Yang M and Dang T (2023), Influence
of mud intercalation on the stability of
seepage flow in tailings dams.
Front. Earth Sci. 11:1115003.
doi: 10.3389/feart.2023.1115003

COPYRIGHT
© 2023 Li, Yang and Dang. This is an open-
access article distributed under the terms
of the [Creative Commons Attribution
License \(CC BY\)](#). The use, distribution or
reproduction in other forums is permitted,
provided the original author(s) and the
copyright owner(s) are credited and that
the original publication in this journal is
cited, in accordance with accepted
academic practice. No use, distribution or
reproduction is permitted which does not
comply with these terms.

Influence of mud intercalation on the stability of seepage flow in tailings dams

Hongru Li^{1,2}, Min Yang^{1,2*} and Tong Dang^{1,2}

¹Institute of Geotechnical Engineering, Xi'an University of Technology, Xi'an, China, ²Loess Soil Mechanics and Engineering Key Laboratory of Shaanxi Province, Xi'an, China

Layers with low permeability are an important factor affecting the stability of tailings dams. In order to analyze the influence of the weak permeability interlayer on the seepage stability of the dam, this paper establishes a numerical analysis model of the tailings dam with the weak permeability interlayer. The seepage stability of the dam slope is calculated and analyzed for the location, thickness, number, and intervals of mud intercalation on the seepage stability of the dam slope. The weakly permeable interlayers at different locations form different saturation lines in the dam. When the weak permeability interlayer is located in the middle of the dam, the height of the saturation line is the highest, and the corresponding stability safety factor is the smallest. When the weak permeability interlayer moves up or down, the buried depth of the saturation line increases, and the safety factor increases. However, when the weak permeability interlayer is located above the drainage prism, the overall slip along the weak permeability interlayer is incidental to the increase in dam height. When the thickness of the weak permeability interlayer changes, the safety factor of the dam has a positively high significance related to the leakage. When the location of the weak permeability interlayer changes, the safety factor of the dam has no obvious correlation with the leakage. With the increase of the thickness and number of weak permeability interlayer and the decrease of the intervals of mud intercalation, the height of the saturation line gradually increases, and the safety factor of the dam gradually decreases. Through the location of the sliding surface, it is found that the sliding surface eventually destabilizes through the lowest low-permeability interlayer.

KEYWORDS

tailings reservoir, weakly permeable interlayer, safety factor, saturation line, sliding surface, stability analysis

1 Introduction

“Tailings reservoir” mostly refers to the facilities that are dammed at a valley mouth to accumulate tailings slag produced in the process of mining and tunneling, beneficiation, and waste or other industrial waste generated in the smelting process. The wet discharge method is often used in the construction of tailings reservoirs in China. Due to the different ore characteristics and fabric components at different time periods, vertical deposition occurs while the slurry flows horizontally in the process of ore drawing into the dam. The flow and sedimentary process of slurry are affected by factors such as slag concentration, flow rate, particle size, and ore drawing mode (Azam et al., 2007; Duan et al., 2022). The dam structure formed by slag deposition has significant spatiotemporal variability, which leads to great mechanical properties and permeability coefficient of tailings, forming many low-permeability interlayers (Tynybekov and Aliev, 2007; Southard et al., 2010; Chen et al., 2019; Liu et al., 2022a; Zhang et al., 2022a). This dam does not have the characteristics of

artificial structures such as earth-rock dam obvious material partition. The seepage field of the dam body is affected by this low-permeability interlayer, which leads to the serration of the saturated surface becoming zigzagged and violently lifted. This low-permeability interlayer also has the characteristics of low strength, which will also affect the stability of the dam body (Yin et al., 2011; Yu et al., 2014; Chen 2016; Yang et al., 2021; Liu et al., 2022b; Zhang et al., 2022b).

The saturation line is the lifeline of the tailings reservoir (Xie et al., 2009; Yin et al., 2010; Yu et al., 2011; Lin et al., 2014). The elevation of the saturation line is extremely unfavorable to the stability of the tailings dam, which is the key factor affecting the stability of the tailings reservoir (Gens and Alonso, 2006; Azam and Li, 2010; Xie et al., 2014; Qiao et al., 2015). Many factors can cause the infiltration line to rise. Among them, there are many factors that lead to the rise of the location of the saturation line. Among them, the external factors include rainfall (Duan and Yuan, 2008), reservoir elevation (Liang et al., 2010), topography (Lu and Cui, 2006), and ore drawing mode (Zhang et al., 2016; Liang et al., 2017). The fine-grained interlayer structure is usually called lenticle in the dam (Yuan et al., 2013) and the drainage blocking caused by chemical reactions (Wu, 2008), which are caused by the differences in physical and chemical properties of minerals mined and the emission mode at different time periods. The model test and numerical simulation are generally used to study the influence of the change of infiltration surface on the stability of tailings dams. Jing et al. (2011) simulated the coupling characteristics of saturation line and stress and the development process of dam failure by indoor model test, so as to reveal the collapse mechanism and burst mode of tailings dams affected by flooding. Through the indoor dam model test, Deng et al. (2011) analyzed the characteristics of the stress field and pore-pressure field in the dam body by a numerical test based on the distribution characteristics of tailings particles and the variation law of saturation line in the process of dam accumulation. Through numerical simulation, Yin et al. (2003) analyzed the relationship between the variation of infiltration surface and the stability of dam slope under different rainfall patterns. Li Q. et al. (2017) studied the correlation between the distribution characteristics of the seepage field and the failure mode of the dam body based on typical tailing reservoir engineering. Li Z. P. et al. (2017) took the depth of saturation line as the safety index of dam and analyzed the influence of a lenticle on the dam through an orthogonal test. These researches have improved the understanding of the evolution law of the infiltration surface and the sensitivity of stability factors of the tailings dam, and these results are mostly limited to a specific tailings dam, which provides ideas for further systematic research of the influence characteristics of a certain factor.

The existing research on the factors affecting the saturation surface of tailings reservoir and the influence of saturation surface on the

stability of dam body has made the rich achievement, which improves understanding of the infiltration surface and stability of tailings dam and changes from passive disaster relief to active disaster prevention. At present, for the evaluation of the dam slope stability, tailing slag of different natures within the dam is mostly studied in the form of equivalent division or directly regarded as lenses. However, the difference in physical and chemical properties of mining ores in different periods leads to the weakly permeable layer formed by slag deposited in the reservoir. It is rare to study the influence of the weak permeable layer on the seepage stability of the tailings dam. In this paper, the influence of the low-permeability interlayer—which is completely different from lenticle formed in the process of damming—on the distribution of the saturation line is studied by numerical simulation method based on the engineering example of a tailings reservoir. The relationship among low permeability interlayer, saturation line, and the stability of the tailings dam is analyzed to provide a reference for the construction and stability evaluation of tailings reservoirs.

2 Numerical model establishment

The tailings pond is a valley-type tailings pond, which is composed of an initial dam and a tailings accumulation dam and is filled by the upstream accumulation method. The present situation of the dam is the initial dam with dam bottom elevation of 2,153 m, dam axis length of 118 m, dam height of 40.6 m, dam crest width of 3.0 m, and dam crest elevation of 2,193.6 m. The initial dam slope ratio is 1:2.5. A horseway is set on the top of the initial dam with a width of 4.0 m. The slope ratio of the tailings accumulation dam is 1:4. The sub-dams are formed by the tailings' coarse sand deposited on the sedimentary beach. The height of each sub-dam is 4.375 m, the width of the sub-dam top is 3 m, and the stack height of the final tailings accumulation dam is 74.4 m. The total height of the tailings accumulation dam is 115.0 m, and the crest elevation of the tailings accumulation dam is 2,268 m, which belongs to the grade II tailings dam.

According to the engineering geological investigation report of the tailings dam and the tailings samples obtained in the field, there are four main types of tailings dam materials, including tailings fine sand, tailings coarse sand, tailing silty sand, and tailing medium sand. The accumulation dam is formed by the accumulation of tailings coarse sand, and there are weak permeable interlayers with different locations and uneven thickness in its interior. According to the sedimentary characteristics and engineering survey data of the tailings dam, the tailings dam material is divided into four layers. The material regions diagram and calculation parameters are shown in Figure 1 and Table 1 respectively.

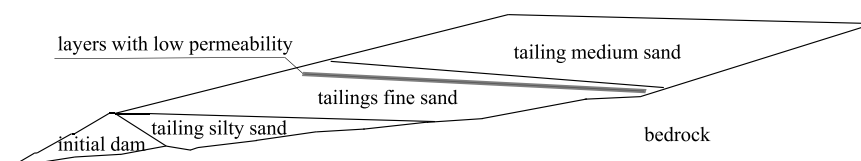


FIGURE 1
Material regions of the section.

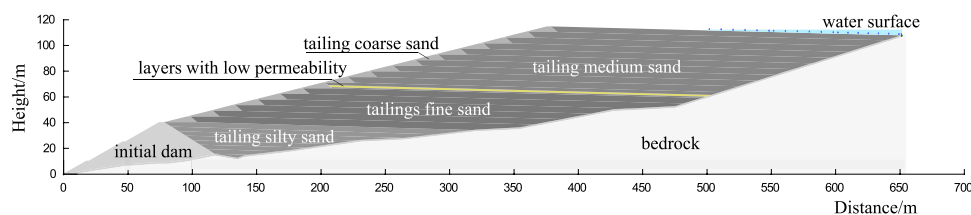


FIGURE 2
Calculation model diagram.

TABLE 1 Physical and mechanical parameters of tailing soil.

Material name	Bulk density γ (kN/m ³)	Internal friction angle φ (°)	Cohesion c (kPa)	Permeability coefficient (m/s)
tailings fine sand	20.5	28.8	2.3	2.27×10^{-3}
tailing silty sand	20	28	5	1.37×10^{-3}
tailing medium sand	21	21	1.2	3.89×10^{-3}
mudstone interlayer	14	10	4	7.50×10^{-6}
tailing coarse sand	19.1	3.2	0	4.25×10^{-3}
initial dam	17.5	19.1	0	1.00×10^{-2}

The proposed tailings dam is a second-class reservoir with a dry beach length of 125 m and an upstream water level elevation of 2,265 m. Since the initial dam is a permeable rock-fill dam, the downstream head boundary is a free permeable surface at the toe of the initial dam. The bottom of the numerical model is set as an impervious boundary. The maximum height is 115 m, the dam length is 655 m, and the average size of the unit side length is 1 m of the calculation model. The model is divided into 55,358 units and 55,924 nodes. The calculation model is shown in Figure 2.

3 Stability analysis of seepage of tailings dam by weak permeability interlayer under different working conditions

Due to the different quality of minerals mined in different periods, there are spatial differences in the discharge and storage of tailings reservoirs. Multiple low-permeability interlayers with different locations, thicknesses, numbers, and intervals are formed in the dam, which will affect the seepage field and stability of the dam.

3.1 Analysis of weak permeability interlayer location

The influence of the location of a single weak permeability interlayer with a certain thickness on the seepage stability of the tailings dam is analyzed, which reveals the influence of low-permeability interlayers at different locations on the saturation line and the safety factor of the tailings dam.

The variation of the saturation line with the location of the weakly permeable interlayer is shown in Figure 3, in which L is the distance from the weakly permeable interlayer to the dam top. Figure 3 shows

that the distribution characteristics of the saturation line are significantly changed by the low-permeability interlayer. In the upper part of the low-permeability interlayer, the saturation line is significantly higher than that of the non-weak permeability interlayer, while in the lower part of the non-low-permeability interlayer, it is mutational retreat. The infiltration line located in the lower part of the weak permeability sandwich decreases, and these lowering points are basically in the same position. The saturation line at the lower part of the weakly permeable interlayer decreases and is basically in the same location. It shows that the influence law of a single weakly permeable interlayer on the saturation line is the same. Due to the sudden change in permeability coefficient, only the upper and lower saturation line locations are staggered at the front and back, the original trend does not change. The size of the sudden change of the saturation line in the weak permeability interlayer changes with the location of the interlayer. The closer to the dam top, the greater the sudden change. The back withdrawal characteristics are shown on the dam top. In the middle of the dam, the saturation line is mainly characterized by forward uplift. The closer to the drainage prism, the smaller the sudden change, and the back withdrawal of the saturation line is not obvious. Due to the effect of a weak permeable interlayer on the uplift of the saturation surface, the depth of the saturation surface is the shallowest in the middle of the dam slope, which affects the stability of the dam. Therefore, it is necessary to pay attention to the weak permeable interlayer here.

When the single weak permeability interlayer in the horizontal direction is at different locations of the dam body, the influence on the safety factor of the dam slope is shown in Figure 4. Figure 4 shows that the influence of different locations of low permeability interlayers on the safety factor of the dam can be divided into two stages. When the distance between the weak permeability interlayer and the top of the dam increases from 10 m to 50 m, the safety factor of the dam decreases from 1.658 to 1.219. At this stage, the weak permeability

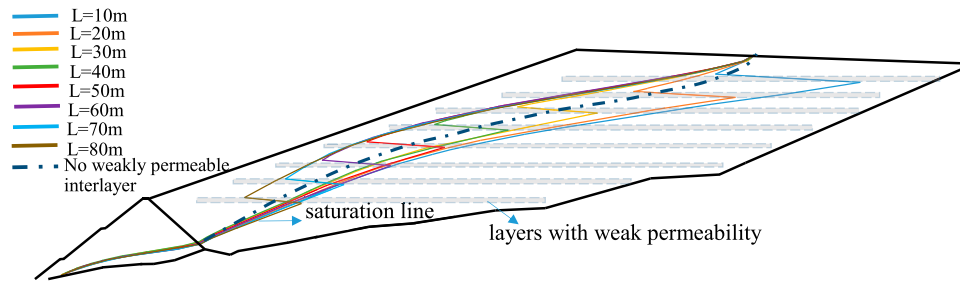


FIGURE 3
Diagram of infiltration line with the position of weakly permeable interlayer.

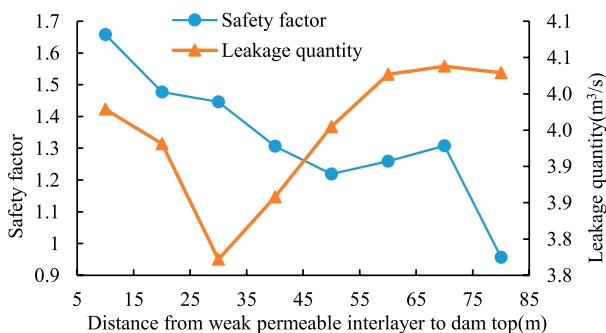


FIGURE 4
The curve between weak permeability interlayer position and leakage with the safety factor.

interlayer is located near the middle of the dam. When the distance increases from 50 m to 80 m, the safety factor increases from 1.219 to 1.356. At this stage, the stability of the dam slope is improved. The results show that there is a critical height of the weak permeable interlayer in the dam body. When the location of the single weak permeable layer formed by the ore drawing is at the critical height with the increase of the dam body, the safety factor of the dam slope is the smallest, which should be avoided in practical engineering.

By analyzing the relationship between the leakage of the dam and the location of the weak permeable interlayer, the safety factor, the leakage, and the location of the weak permeable interlayer first show a decrease then an increase. The development rule of the leakage and the height of the weak permeable interlayer is not consistent with the development of the safety factor with the height of the weak permeable interlayer. When the leakage is the smallest, the low-permeability interlayer is located at two-thirds of the dam height, which conforms to the impermeability characteristics of the low-permeability interlayer. This location is not the most dangerous to the dam. As the height of the low-permeability interlayer decreases, the leakage increases. When the low-permeability interlayer is located above half the height of the dam, the safety factor decreases, and the leakage still increases. The results show that the leakage quantity of the tailings dam is not consistent with the evolution characteristics of the safety factor of the dam slope. When the tailings dam has a permeable interlayer, the leakage cannot be used as an index to judge the stability of the dam. Attention should be paid to the selection of factors in the early warning of tailings dam safety and stability.

As the location of the weak permeability interlayer gradually moves down along the dam crest, the safety factor presents the rule of decreasing first, then increasing and decreasing again. When the weak permeability interlayer is located in the middle of the dam body, it has a great influence on the stability and safety of the dam body. The corresponding safety factor is small, and the dam slope is prone to instability. When the weak permeability interlayer is located in the upper part of the dam, the weak permeability interlayer has little effect on the stability and safety of the dam. In this case, the safety factor of the dam slope is large, which is only calculated by the arc search method. When the weak permeability interlayer is located in the lower part of the dam, which is 80 m away from the top of the dam, the whole dam slips along the weak permeability interlayer with lower strength. In this case, the failure is not the circle sliding of the dam slope, but the overall slip failure. Therefore, it is necessary to pay particular attention to the damage caused by the weak permeability interlayer located in the lower part of the dam.

3.2 Analysis of thickness of a weak permeable interlayer

In practical engineering, the thickness of weak permeability interlayer of tailings ranges from tens of centimeters to several meters, which is determined by the sedimentary characteristics of tailings. According to the above study, when the weak permeability interlayer is located in the middle of the dam, the stability safety factor is the smallest, resulting in tailings dam slope instability. Therefore, it is very important to study the influence of the thickness of the weak permeability interlayer at a certain location on the stability of the dam. When the location of a low-permeability interlayer is fixed, the influence of the low-permeability interlayer on the saturation line and stability of the tailings dam is analyzed by changing the thickness of the low-permeability interlayer, which reveals the influence of low-permeability interlayers with different thicknesses on the saturation line and safety factor of a tailings dam.

The variation of the saturation line with the thickness of the weakly permeable interlayer is shown in Figure 5, in which d is the thickness of the weakly permeable interlayer. Figure 5 shows that the height of the saturation line in the upper part of the weakly permeable interlayer gradually increases with the increase of the interlayer thickness. This is because the saturation line in the upper

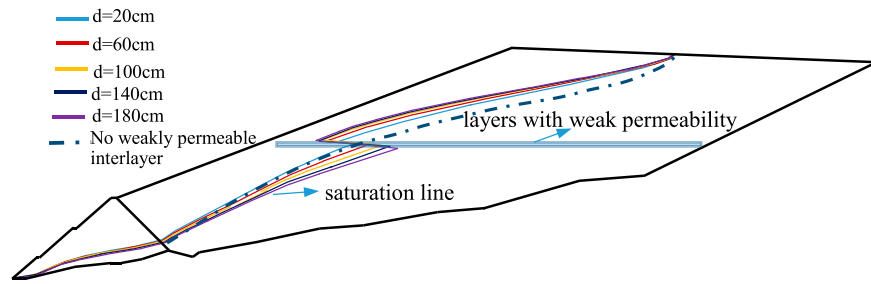


FIGURE 5
Diagram of infiltration line with the position of weakly permeable interlayer thickness.

part of the weak permeability interlayer will be raised. The thicker the interlayer is, the more obvious the saturation line is raised. The saturation line in the lower part of the weak permeability interlayer gradually decreases with the increase of the interlayer thickness, forming the characteristics of the upper extension and the lower retreat, which affects the stability of the dam. The thicker the low-permeability interlayer is, the more violent the infiltration surface abrupt change, which leads to the rapid extension of the upper part of the low-permeability interlayer to the dam slope and the retreat of the lower part to the inside of the dam body. This can easily cause the infiltration surface to seep out from the slope, which makes the local slope prone to slip, affecting the stability of the dam slope.

The influence of different thicknesses of a single weakly permeable interlayer in a horizontal direction on the safety factor of a dam is shown in Figure 6. Figure 6 shows that it is reflected that the safety factor of the dam decreases gradually with the increase of the interlayer thickness. When the thickness of a low-permeability interlayer is 140 cm, the safety factor of the tailings reservoir is 1.272. When the thickness of a low-permeability interlayer is greater than 140 cm, the safety factor decreases sharply. This is because the weak permeability interlayer generally belongs to the saturated muddy interlayer. Compared with coarse-grained tailings outside the interlayer, the mechanical strength and deformation modulus are lower. In particular, the thicker weak permeability interlayer is easy to soften and muddy in water, which reduces the shear strength and is not adverse to the anti-sliding stability of the dam. Therefore, the thickness of the low-permeability interlayer has a very important influence on the stability of the dam. In the process of tailings drawing, it should be avoided to form a thicker weak permeability interlayer in the middle of the dam, so as to ensure the safety of the tailings dam.

The results show that the safety factor and leakage decrease linearly with the increase of the thickness of the weak permeability interlayer in the case of a single horizontal weak permeability interlayer, and the slope of decreasing is close. There is a high correlation between the safety factor and the thickness of the weakly permeable interlayer, and the leakage is also highly correlated with the thickness of the weakly permeable interlayer. It provides a key index for the safety warning of tailings dam filling with a low-permeability interlayer. It is known that the dam filling material is a low-permeability material, and the leakage of the tailings dam decreases during

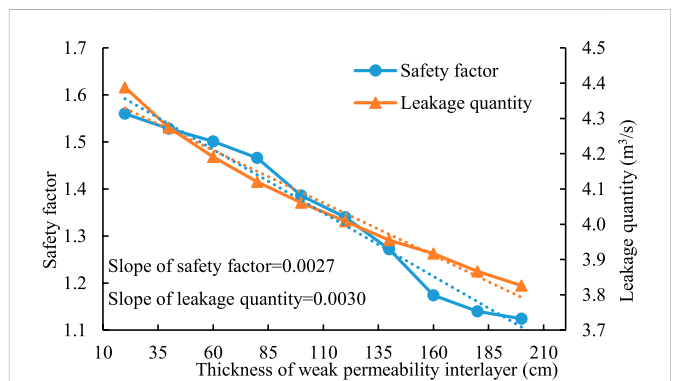


FIGURE 6
The curve between low-permeability interlayer thickness and leakage with the safety factor.

the filling process, which may indicate that the thickness of the low-permeability layer formed by the filling material needs to be paid attention to.

3.3 Analysis of the number of low-permeability interlayers

Due to the complexity of tailings engineering, it is also very difficult to determine the sedimentary characteristics of tailings. In the process of tailings ore drawing, the tailings material in the mineral pulp is deposited in turn according to the coarse, medium, and fine particles of its mud. The sedimentary process is very complicated, and multiple low-permeability interlayers are generally formed in the process of accumulating tailings material. Therefore, it is particularly important to analyze the influence of the number of low-permeability interlayers on the stability of the tailings dam. In this paper, two and three weak permeability interlayers with a spacing of 5 m and a thickness of 1 m are set at a distance of 50 m from the top of the dam to study the influence of the number of interlayers on the stability of the tailings dam. The results of the number of weakly permeable interlayers on the saturation line and the safety factor of the dam are shown in Figure 7.

Figure 7 shows that as the number of low-permeability interlayers increases, the safety factor of the dam slope

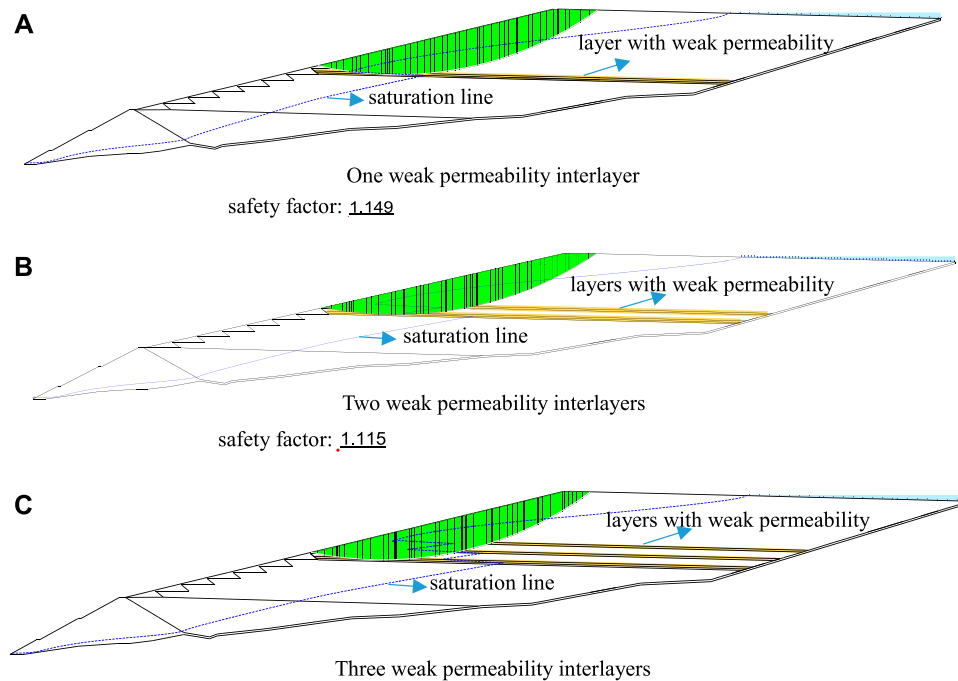


FIGURE 7

The curve of the number of low-permeability layers and safety factor. (A) One weak permeability interlayer. (B) Two weak permeability interlayers. (C) Three weak permeability interlayers.

decreases. The number of low-permeability interlayers increases from 1 to 3, and the safety factor decreases from 1.220 to 1.115. With the increase in the number of weak permeability interlayers, the saturation line has undergone multiple turns in the low-permeability interlayer, which significantly causes the saturation line to be raised. The more the number of low-permeability interlayers, the more obvious the uplift of the saturation line. The excessive number of interlayers may cause the infiltrate line to overflow on the dam slope. The low-permeability interlayer has poor permeability and low strength, resulting in the decrease of the safety factor, the landslide of the slope, and affecting the safe operation of the dam. In order to ensure the stability of the dam, vertical drainage facilities should be added to make the water stored between multiple weak permeability interlayers run through and lower saturation line of the dam.

3.4 Analysis of interlayer spacing of weakly permeable interlayer

When there are several low-permeability interlayers in a tailings reservoir, the interlayer spacing of weak permeability interlayers varies greatly. In this study, three low-permeability interlayers that are 50 m away from the top of the dam with an interlayer thickness of 1 m were used as models to analyze the influence of the interlayer spacing of multiple low-permeability interlayers on the stability of the dam slope, which reveal the influence law of the safety factor and the saturation line of the

dam with different spacing of low-permeability interlayers in Figure 8.

Figure 8 shows that the safety factor of the dam slope decreases gradually with the decrease of interlayer spacing of weak permeability interlayer. When the interlayer spacing of the weak permeability interlayer is 5 m, the safety factor of the dam slope is 1.255. When the interlayer spacing is 3 m, the safety factor is 1.080. In this situation, the tailings dam slope is close to instability, and the height of the saturation line gradually increases with the decrease of the interlayer spacing of the low-permeability interlayers. The reason is that the interlayer spacing continues to decrease, resulting in multiple low-permeability interlayers and intermediate dams forming a low-permeability belt. The saturation line through the interlayer is severely blocked, resulting in the saturation line is continuously raised. In addition, the low-permeability interlayer is easy to soften, prone to mudding, and has low shear strength, which ultimately leads to slope instability.

The above comprehensive analysis of the location, thickness, number, and spacing of the low-permeability interlayers on the safety factor of the dam slope and the shape of the landslide found that when there is a low-permeability interlayer in the dam, sliding arc exit general shear along the weak permeability interlayer.

When there are several weak permeability interlayers, the sliding zone often passes through the upper interlayer, and shear failure occurs along the bottom weak permeability interlayer, which indicates that low-permeability interlayers are the key factor to controlling the instability of the dam slope.

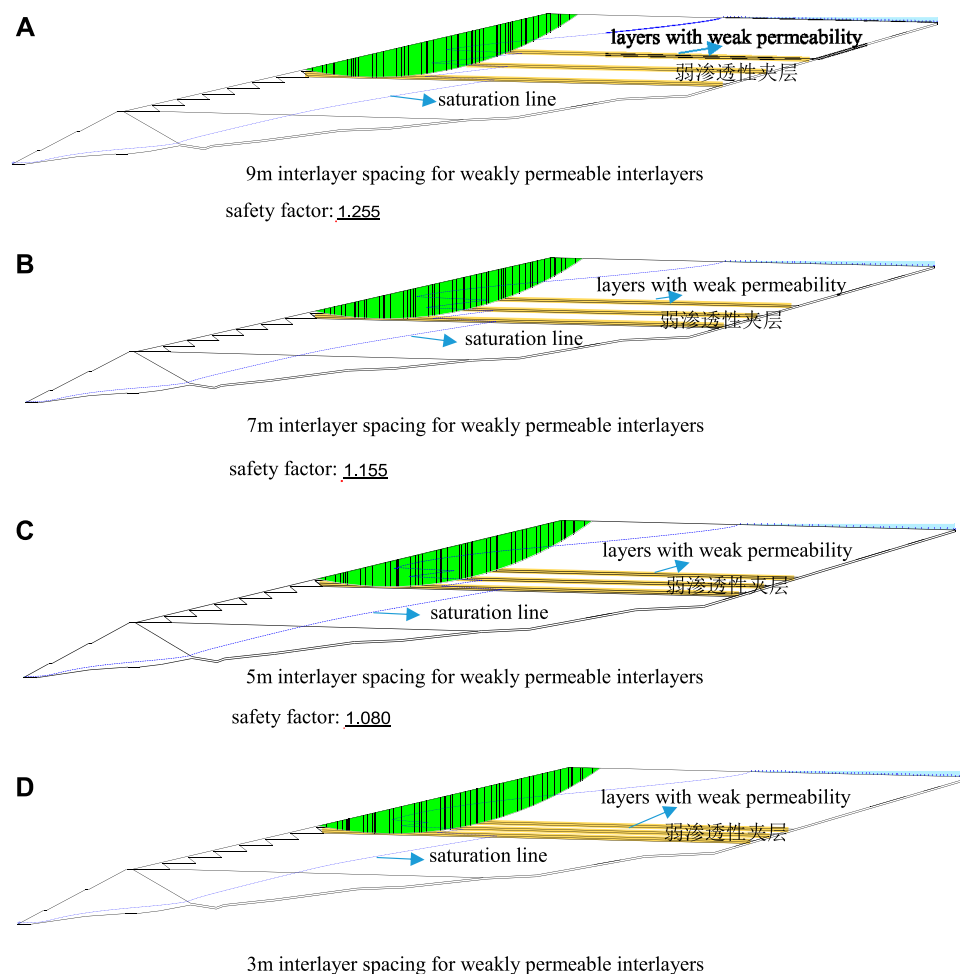


FIGURE 8

The curve of the interlayer spacing of low-permeability layer and safety factor. (A) 9 m interlayer spacing for weakly permeable interlayers. (B) 7 m interlayer spacing for weakly permeable interlayers. (C) 5 m interlayer spacing for weakly permeable interlayers. (D) 3 m interlayer spacing for weakly permeable interlayers.

4 Conclusion

The influence of low-permeability interlayers on seepage fields and safety factor is studied by establishing a two-dimensional finite element model of a tailings dam. This paper analyzes the relationship between the location, thickness, and spacing of weakly permeable interlayers and the saturation line and the stability of dam slope, and reveals the evolution mechanism of coupling influence between saturation line, seepage flow, and safety factor of the dam slope. The conclusions are as follows.

(1) The location of the low-permeability interlayer in the dam body has a significant influence on the saturation line. When a low-permeability interlayer is located in the middle of the dam, the saturation line rises significantly and is closest to the dam slope, which affects the instability of the dam. When the low-permeability interlayer is located at the top of the dam, the saturation line is far from the dam slope, which has little effect on the stability and safety of the dam, and the corresponding

safety factor is large. When the low-permeability interlayer is located at the upper part of the drainage prism, the tailings dam is the most dangerous. The overall slip failure along the weak permeability interlayer may occur, which needs special attention.

- (2) The safety factor of the dam slope continues to decrease with the increase of the thickness of the weak permeability interlayer. The saturation line on the upper part of the weak permeability interlayer will be raised. The thicker the interlayer, the more obvious the uplift of the saturation line. A low-permeability interlayer can easily cause slope instability and affects the stability of the dam.
- (3) The safety factor of the tailings dam slope continues to decline with the increase of the number of interlayers. Multiple low-permeability interlayers will cause the saturation line to undergo multiple turns in the interlayer, causing the saturation line to be raised. The greater the number of low-permeability interlayers, the more obvious the uplift of the saturation line, which seriously affects the stability of the dam.

- (4) When the interlayer spacing is large, it has little influence on the stability of the tailings dam, and the lift height of the saturation line is relatively low. However, if the spacing between low-permeability interlayers is small, the upper and lower weak permeability interlayers may form a whole, and the saturation line will rise, which will rapidly reduce the safety of the tailings dam and easily lead to the sliding failure of the dam slope.
- (5) Through the stability calculation under different working conditions, it is found that the slip surface of the dam slope is cut out along the lowermost weak permeability interlayer, which is independent of the number and spacing of the low-permeability interlayer.

Data availability statement

The raw data supporting the conclusion of this article will be made available by the authors, without undue reservation.

Author contributions

HL provided overall guidance on the article as well as wrote this paper. MY and TD modified the article language.

References

- Azam, S., and Li, Q. R. (2010). Tailing dam failures: A review of the last one hundred years. *Geotech. News* 28 (4), 50–54.
- Azam, S., Chalaturmyk, R. J., and Scott, J. D. (2005). Geotechnical characterization and sedimentation behaviour of laterite slurries. *Geotechnical Test. J.* 28 (6), 1–11. doi:10.1520/GTJ12511
- Chen, Q. L., Zhang, C., Yang, C. H., Chang, K. M., Zhen, K. P., and Daemen, J. (2019). Strength and deformation of tailings with fine-grained interlayers. *Eng. Geol.* 256, 110–120. doi:10.1016/j.enggeo.2019.04.007
- Chen, S. S. (2016). Problems and countermeasures of safety evaluation of tailing pond. *Chin. J. Geotechnical Eng.* 38 (10), 1869–1873. doi:10.11779/CJGE201610016
- Deng, T., Wan, L., and Wei, Z. A. (2011). Stacking model test of Wenzhuang tailings reservoir and its stability analysis. *Rock Soil Mech.* 32 (12), 3647–3652. doi:10.16285/j.rsm.2011.12.035
- Duan, Z. J., Li, Q. M., Zhao, X. Y., Yu, Y. Z., and Shi, H. (2022). Experimental study on optimization of ore-drawing parameters for fine grained tailings dams constructed by upstream method. *Chin. J. Geotechnical Eng.* 44 (08), 1474–1482. doi:10.11779/CJGE202208012
- Duan, Z. Y., and Yuan, B. (2008). Collapse analysis and comprehensive treatment of a mine tailings dam due to rain storm and flood impounding. *Mech. Pract.* 30 (2), 40–44+34.
- Gens, A., and Alonso, E. E. (2006). Aznalcollar dam failure. Part 2: Stability conditions and failure mechanism. *Geotechnique* 56 (3), 185–201. doi:10.1680/geot.2006.56.3.185
- Jing, X. F., Yin, G. Z., Wei, Z. A., Li, X. S., and Wang, M. L. (2011). Model experimental study of collapse mechanism and broken mode of tailings dam. *Rock Soil Mech.* 32 (5), 1377–1384+1404. doi:10.16285/j.rsm.2011.05.039
- Li, Q., Zhang, L. T., and Qi, Q. L. (2017). Three-dimensional instability characteristics and stability analysis of a tailing dam based on fluid-solid coupling theory. *J. Basic Sci. Eng.* 25 (3), 558–567. doi:10.16058/j.issn.1005-0930.2017.03.012
- Li, Z. P., Peng, Z. B., He, Z. M., and Yuan, W. (2017). Simplification method of lenticles and its impact on safety of tailings dam. *J. Central South Univ. Sci. Technol.* 48 (5), 1326–1334. doi:10.11817/j.issn.1672-7207.2017.05.027
- Liang, B., Bai, Y. P., and Jin, J. X. (2010). Influence of the water level rising on tailings dam stability. *J. Water Resour. Water Eng.* 21 (4), 11–14.
- Liang, B., Lv, Z. Q., Jin, J. X., and Wu, P. F. (2017). Model experimental study of effect of slurry draining speed on tailings delocation. *J. Exp. Mech.* 32 (6), 880–887.
- Lin, X. S., Chen, D. Q., and He, F. (2014). Calculation of monitoring warning value of tailing dam's saturation line and dry beach. *J. Water Resour. Water Eng.* 25 (4), 65–68. doi:10.11705/j.issn.1672-643X.2014.04.014
- Liu, N., Li, N., Li, G., Song, Z., and Wang, S. (2022a). Method for evaluating the equivalent thermal conductivity of a freezing rock mass containing systematic fractures. *Rock Mech. Rock Eng.* 55, 7333–7355. doi:10.1007/s00603-022-03038-9
- Liu, N., Li, N., Wang, S., Li, G., and Song, Z. (2022b). A fully coupled thermo-hydro-mechanical model for fractured rock masses in cold regions. *Cold Regions Sci. Technol.* 205, 103707. doi:10.1016/j.coldregions.2022.103707
- Lu, M. L., and Cui, L. (2006). Three-dimensional seepage analysis for complex topographical tailings dam. *Rock Soil Mech.* 27 (7), 1176–1180. doi:10.16285/j.rsm.2006.07.032
- Qiao, L., Qu, C. L., and Cui, M. (2015). Effect of fines content on engineering characteristics of tailings. *Rock Soil Mech.* 36 (4), 923–927+945. doi:10.16285/j.rsm.2015.04.002
- Southard, J. B., Boguchwal, L. A., and Romea, R. D. (2010). Test of scale modelling of sediment transport in steady unidirectional flow. *Earth Surf. Process. Landforms* 5 (1), 17–23. doi:10.1002/esp.3760050103
- Tynybekov, A. K., and Aliev, M. S. (2007). The ecological condition of Kadji-Sai uranium tailings. *Environ-mental Secur. Public Saf.* 47, 187–195. doi:10.1007/978-1-4020-5644-4_16
- Wu, J. (2008). *Mechanism and process simulation for chemical clogging of the tailings dam*. Shanghai: Shanghai Jiao Tong University for the Degree of Doctor of Philosophy.
- Xie, X. Y., Tian, W. Q., and Wang, Y. H. (2009). The safety analysis of current situation and management countermeasure on tailing reservoir in China. *J. Saf. Sci. Technol.* 5 (2), 5–9. doi:10.16031/j.cnki.issn.1003-8035.2014.03.038
- Xie, Y. D., Wu, G. L., Jin, X. G., Chen, S. Q., and Wang, L. (2014). Analysis on stability of the fill dam in Wujiagou tailing pond. *Chin. J. Geol. Hazard Control* 25 (3), 49–55.
- Yang, C. H., Zhang, C., Li, Q. M., Yu, Y. Z., Ma, C. K., and Duan, Z. J. (2021). Disaster mechanism and prevention methods of large-scale high tailings dam. *Rock Soil Mech.* 42 (1), 1–17. doi:10.16285/j.rsm.2020.1653
- Yin, G. Z., Li, G. Z., Wei, Z. A., Wan, L., Shui, G., and Jing, X. (2011). Stability analysis of a copper tailings dam via laboratory model tests: A Chinese case study. *Miner. Eng.* 24 (2), 122–130. doi:10.1016/j.mineng.2010.10.014
- Yin, G. Z., Li, Y., Wei, Z. A., Jing, X. F., and Zhang, Q. K. (2010). Regularity of the saturation lines' change and stability analysis of tailings dam in the condition of flood. *J. Chongqing Univ.* 33 (3), 72–75+86.
- Yin, G. Z., Wei, Z. A., and Wan, L. (2003). Numerical simulation analysis about seepage field of Longdu tail bay. *Chin. Rock Soil Mech.* 24 (2), 25–28. doi:10.16285/j.rsm.2003.s2.006
- Yu, G. M., Song, C. W., Pan, Y. Z., Li, L., Li, R., and Lu, S. B. (2014). Review of new progress in tailing dam safety in foreign research and current state with development trend in China. *Chin. J. Rock Mech. Eng.* 33 (1), 3238–3248. doi:10.13722/j.cnki.jrme.2014.s1.091
- Yu, G. M., Song, C. W., Wu, Y. X., Pan, Y. Z., and Li, R. (2011). Engineering characteristics and key problems of security monitoring informatization for tailings dams. *Chin. J. Geotechnical Eng.* 33 (1), 49–53.
- Yuan, W., Li, X. C., Bai, B., Li, X. C., and Wang, H. B. (2013). Parameter sensitivity analysis of lenticle impacting on tailing dam safety. *Chin. J. Central South Univ. Sci. Technol.* 44 (3), 1174–1182.
- Zhang, D. M., Zheng, B. B., Yin, G. Z., Dai, J. X., and Tang, F. J. (2016). Model tests on upstream dam-building method using concentrated and classified tailings. *Chin. Rock Soil Mech.* 37 (7), 1832–1838+1867. doi:10.16285/j.rsm.2016.07.002
- Zhang, Y., Fan, S., Yang, D., and Zhou, F. (2022b). Investigation about variation law of frost heave force of seasonal cold region tunnels: A case study. *Front. Earth Sci.* 9, 806843. doi:10.3389/feart.2021.806843
- Zhang, Y., Song, Z., and Weng, X. (2022a). A constitutive model for loess considering the characteristics of structurality and anisotropy. *Soil Mech. Found. Eng.* 59 (1), 32–43. doi:10.1007/s11204-022-09781-z

Funding

This work was supported by the Loess Soil Mechanics and Engineering Key Laboratory of Shaanxi Province Foundation (13JS073), and the Natural Science Foundation of Shaanxi Province (2017JM5059).

Conflict of interest

The authors declare that the research was conducted in the absence of any commercial or financial relationships that could be construed as a potential conflict of interest.

Publisher's note

All claims expressed in this article are solely those of the authors and do not necessarily represent those of their affiliated organizations, or those of the publisher, the editors and the reviewers. Any product that may be evaluated in this article, or claim that may be made by its manufacturer, is not guaranteed or endorsed by the publisher.



OPEN ACCESS

EDITED BY

Yuwei Zhang,
Xi'an University of Architecture and
Technology, China

REVIEWED BY

Jingmin Xu,
Southeast University, China
Nan Zhang,
Shandong University, China

*CORRESPONDENCE

Peng Zhang,
✉ zhangpeng-mail@njtech.edu.cn

SPECIALTY SECTION

This article was submitted to
Environmental Informatics and Remote
Sensing,
a section of the journal
Frontiers in Earth Science

RECEIVED 17 November 2022

ACCEPTED 06 December 2022

PUBLISHED 25 January 2023

CITATION

Guo S, Liu Y, Zhang P, Zhu R and Qian Y
(2023), Insight into the critical
morphological characteristics of
earthquake-induced sequential rock
avalanches in weathered-fractured
rock cliffs.
Front. Earth Sci. 10:1101246.
doi: 10.3389/feart.2022.1101246

COPYRIGHT

© 2023 Guo, Liu, Zhang, Zhu and Qian.
This is an open-access article
distributed under the terms of the
[Creative Commons Attribution License
\(CC BY\)](https://creativecommons.org/licenses/by/4.0/). The use, distribution or
reproduction in other forums is
permitted, provided the original
author(s) and the copyright owner(s) are
credited and that the original
publication in this journal is cited, in
accordance with accepted academic
practice. No use, distribution or
reproduction is permitted which does
not comply with these terms.

Insight into the critical morphological characteristics of earthquake-induced sequential rock avalanches in weathered-fractured rock cliffs

Shuangfeng Guo, Yajing Liu, Peng Zhang*, Rui Zhu and
Youkai Qian

College of Transportation Engineering, Nanjing Tech University, Nanjing, China

Rock avalanches are a significant threat to transportation or hydraulic infrastructure, as they can also cause catastrophic secondary destruction in large practical engineering or to nearby residents. Earthquake-induced rock avalanches have been the most common and prominent natural hazard phenomena among geological hazards in recent years. Earthquake-induced rock avalanche events usually begin when a massive rock mass or multiple rock masses separate from a rock slope, progressively fragmenting and transforming into fast-moving, cohesionless rock falls. Earthquake-induced sequential collapse often occurs on weathered and fractured rock cliffs in horizontal strata, and its kinematic dynamics and destabilization mechanism are significantly different from those of isolated collapse due to weathering. In this study, the failure characteristics of the initiation and movement process of the avalanche are revealed in detail, through physical model experiments and analytical solutions, thereby obtaining an earthquake-controlled mechanical model equation. Our methods use the inflection points of the displacement time curve at the top of the rock wall and the digital images acquired by the shaking test bench to quantify the critical damage time point and to characterize the critical morphology of continuous collapse. A mathematical model of analytical solution is proposed, which aims to address the kinematic mechanics mechanism of sequential collapse under translational and rotational motion models. The comparative analysis results of the experiment and analytical solutions reveal that the transformed motion pattern is controlled by the ratio between the model stacking height, the rock block size, and the seismic acceleration. Whereas the rotational motion pattern is mainly influenced by the nodal dip angle, model stacking height, and seismic acceleration. The results of the study are of great scientific importance to elucidate the destruction mechanism of the earthquake-induced sequential collapse of rock avalanches and to determine the evolution characteristic of subsequent rockfalls motion of dangerous rocks. The proposed framework for the analysis of rock avalanches can be applied to understand the critical topographic features and mechanical mechanism behavior of analogous geological hazards.

KEYWORDS

earthquake-induced landslide, rock avalanches, critical morphological features, sequential collapse, rockfall, translation motion, rotation motion

1 Introduction

Rock avalanches are usually triggered by strong earthquakes and cause large rock falls or long-distance debris flows that threaten the safety of inhabitants, highways, and other constructions (Erismann et al., 2001; Gong et al., 2022; Gong et al., 2020; Zhang et al., 2022). In the 60,104 landslides triggered by the 2008 Wenchuan earthquake ($M_s=8.0$) in China (Gorum et al., 2011; Fan et al., 2018; Fan et al., 2019), the major failure mode of rock avalanche along the highways is sequential collapse induced by earthquakes that occurred at weathered and fractured rock cliffs with horizontal strata. This is different from previous phenomena regarding the weather-induced collapse of individual blocks or continuous collapse caused by groundwater effects. Investigating the critical morphological characteristics of sequential collapse key issues to clarify the failure mechanisms of earthquake-induced sequential collapse and to determine the initial state of the movement dynamic in the subsequent rockfall.

Most research interest in earthquake-induced rock avalanches has focused on the trigger mechanisms, the initiation failure characteristics, the movement dynamics, and the material properties of rock avalanches (Yin et al., 2021; Guo et al., 2020a; Liu et al., 2020; Liu et al., 2022). In particular, larger geological hazards derived from the process of rockfall occurrence or dynamic propagation, such as rock falls or debris flows, have attracted the attention of many researchers (Matasci et al., 2018; Zhang et al., 2018; Singeisen et al., 2020; Mitchell et al., 2022). However, both the analysis of dynamic propagation (Chen et al., 2006; Baggio et al., 2021; Liu et al., 2022; Zhao et al., 2022) and the assessment of the rockfall movement distance (Chen et al., 2010; Zhu et al., 2020; Donati et al., 2021; Ma et al., 2021) were closely related to the influence of initiating damage factors on the triggering mechanism in rockfalls. There are some other studies on earthquake-induced rock avalanches focus on other damage modes, such as spatial slip mode, compression shear-slip mode, tensile-tipping mode, and rarely on earthquake-induced sequential collapse damage mode (Togo et al., 2014; Zeng et al., 2019; Guo et al., 2020b; Guo et al., 2020c; Do et al., 2020; Yang et al., 2022). Sequential collapse is an initial damage situation of earthquake-induced rock avalanche, which often occurs on weathered and fractured rock cliffs near the horizontal strata, where the triggering mechanism is different from the isolated rock fall mode caused by differential weathering or improper excavation (Singeisen et al., 2020; Aaron et al., 2016; Aaron et al., 2019; Dufresne et al., 2016; Hilger et al., 2019).

Weathered and fractured rock cliffs with horizontal stratigraphic levels are highly common topographic features along mountainous highway areas and roadways in the earthquake-stricken areas of Wenchuan, Sichuan Province,

China. High-intensity earthquakes usually lead to the collapse of dangerous rocks on steeper cliffs and simultaneously trigger a chain of rock collapse damage in the near-horizontal strata and adjacent dangerous rock masses along the roadside, followed by sequential rock falling disasters (Sanders et al., 2021; Zhao et al., 2022). As shown in Figure 1, the dangerous rock mass consists of multiple groups of irregular rock layers, steeply inclined rock joints, and blocks cut by vertical tensile fractures. Those dangerous rocks that have separated from the stable rock mass have the distinctive characteristics of being upright, cascading, overhanging, and pillar-shaped. These dangerous rocks are more upright and have relatively weak horizontal stability, so weathering, earthquakes, rainfall, and freezing are most likely to trigger chain collapse damage of the critical rocks (Gorum et al., 2011; Marc, Hovius, & Meunier, 2016; Fan, et al., 2018).

The previous studies were published in which failure mechanisms and modes of the rock avalanche include bulging-slip failure, bulging-toppling, overall slip shear, seismic cracking-slip collapse, block avalanche-slip failure, overall shear dislocation failure, compression-drawing-slip failure (Zhang et al., 2013; Moretti et al., 2015; Zhang et al., 2020b; Moretti et al., 2020; An et al., 2021; Guo et al., 2021; Zhang Y. W. et al., 2022). Regarding the scale of the rock avalanche, researchers suggested that the scale can be divided into individual block collapse or sequential collapse (Paguican et al., 2014; Ouyang et al., 2019). The individual block collapse occurs in a whole rock mass, and the falling rock undergoes consistent motion during the rock avalanche processing. Sequential collapse, however, consists of a cascade of multiple rock blocks, therefore, the rock collapse of multiple dangerous rock blocks and its associated mechanical mechanism is similar to retrogressive effect failure. The key to the sequential rockfalls feature is the variation in the spatial topological relationship among multiple dangerous rock masses.

In this paper, geologic analysis, model tests, and analytical solutions are employed to investigate the critical morphological characteristics of rockfall cascading collapse at cliffs induced by earthquakes. Based on the spatial topological relationships among multiple rockfalls, especially displacement velocity, critical failure time, and damage morphology, the damage characteristics of group occurrence of collapse are identified. In addition, a theoretical analytical solution is proposed to calculate the critical failure state of cascading collapse according to the analyses of the morphological characteristic of the rock avalanche. These analyses allow explaining the propagation process of sequential rock avalanches, providing additional insights into the rock avalanche problem.

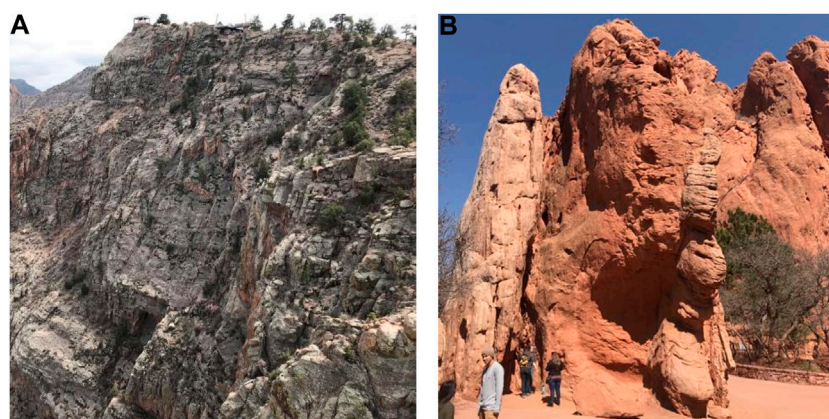


FIGURE 1
Examples of dangerous rock mass on rock cliffs. (A) Potential unstable rock mass. (B) Dangerous rock mass.

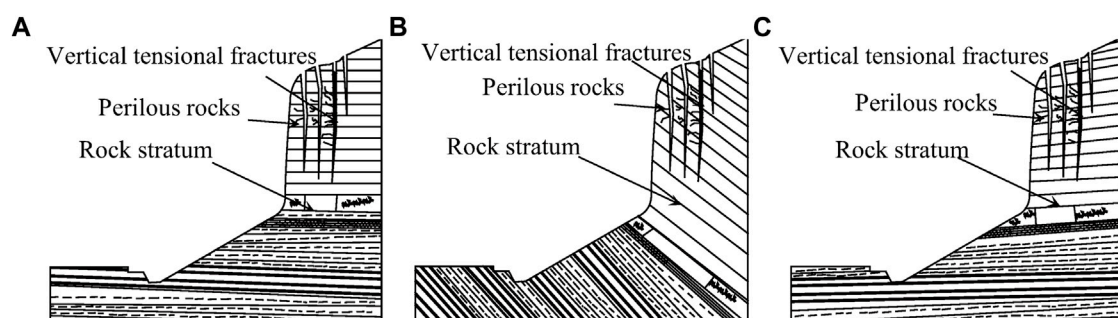


FIGURE 2
Geologic environment of dangerous rocks on cliffs. (A) Level layer. (B) Inverse layer. (C) Bedding layer.

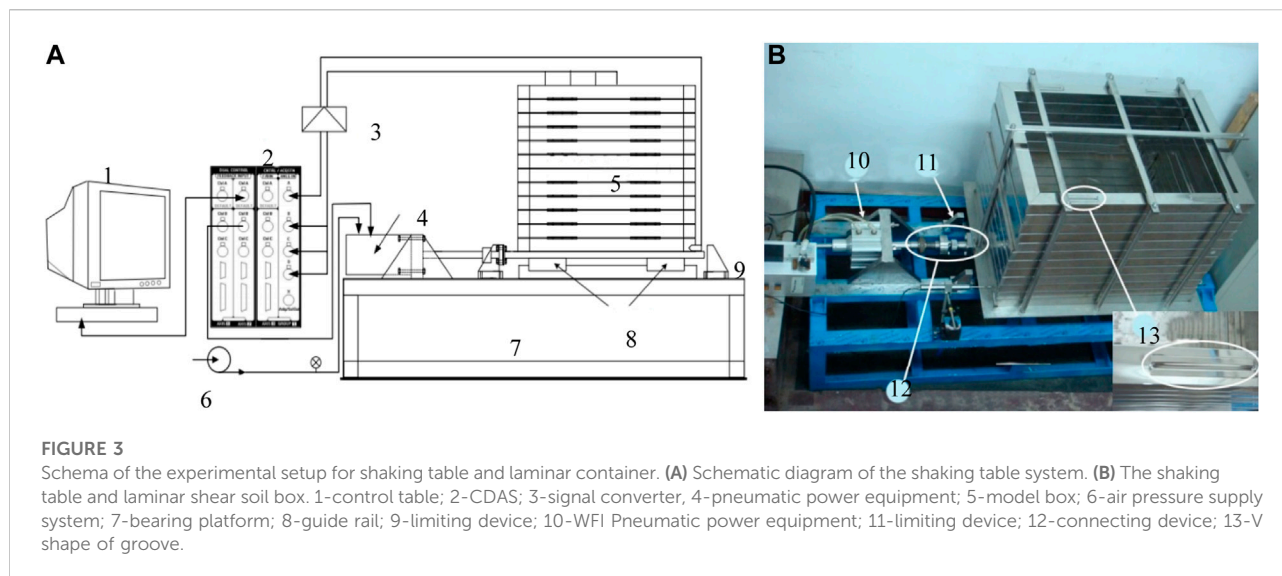
2 Rock avalanches susceptibility assessment

The governing factors of earthquake-induced rock avalanches mainly include the lithology, geological structures, and topographic and geomorphic characteristics of the rock cliffs. The representative topographic and geomorphic characteristics of the dangerous rocks are shown in Figure 2. Although the rock orientation of the three mountain belts strongly differs, the topographic characteristics of the rockfall for the three terrane zones are almost consistent, such as, the gradient of the rock cliff is greater than 70° or nearly upright. However, the undersurface of the rock cliff is a gentle incline where residual sediment damage has accumulated. The geomorphic characteristics of dangerous rocks are usually cliffs formed by almost horizontal or low-angle sedimentary strata. The release of high-ground stress leads to several vertical tension fractures or steeply dipping joints cutting into

some dangerous block of cascading rock at the top of the rock cliff.

Based on the field geologic survey of rock avalanches, the heights of the rock cliffs are generally between 50 m and 140 m, with an average height of 86 m (Bergillos et al., 2022; Flor-Blanco et al., 2022; Zhang Y. et al., 2022). The gradient of the rock cliff is in the range of about 70° to 90° . The investigation of unstable and dangerous rock masses revealed that representative rock formations weathered into many layers, with tension fractures and fracture joints at the top of the rock cliffs. According to the size of the rock block, the dangerous rocks are classified into boulders ($>1,000 \text{ m}^3$), large ($100\text{--}1,000 \text{ m}^3$), medium ($10\text{--}100 \text{ m}^3$), small ($1\text{--}10 \text{ m}^3$), and fallen rocks ($<1 \text{ m}^3$) (Yin et al., 2021; Qin et al., 2023).

It is important to determine the causes of the formation of such topography and the factors that lead to earthquake-induced rock avalanches to assess the risk of rock falls, develop measures to prevent and control dangerous rocks, in addition, to determine



the mechanism of rock avalanches in plateau areas. Numerous lateral spreading phenomena have been observed in the topography of earthquake-induced rock avalanches. The vertical and overhanging top of the rock cliff is very likely to promote lateral spreading, which could trigger another rock fall of the former rock pillar.

The vertical tensile fractures or steeply inclined joints on the cliff are re-expanded and developed downward under high-ground stress, whereby the gently inclined sedimentary layers are subject to shear breakdown at the base of the cliff due to the pressure of the dangerous rock at the top of the rock cliff. The creep deformation of soft and weak rock layers in the fracture-hazardous rock mass or due to differential weathering of soft and hard rocks will lead to the formation of cavities in soft rocks, and subsequently, stress weathering accelerates the development of cavities. With the expansion of the cave, the dangerous rock lost the support of the rock stratum at the base of the rock cliff, and then a chain reaction occurred. To assess the risk of dangerous rockfalls, develop measures to prevent rockfalls, and determine the mechanical mechanisms of earthquake-induced rockfalls in the southwestern plateau region, it is important to determine the causes of the formation of such topographic characteristics and the critical factors leading to rock avalanches.

3 Physical model experiments

3.1 Apparatus of model experiments

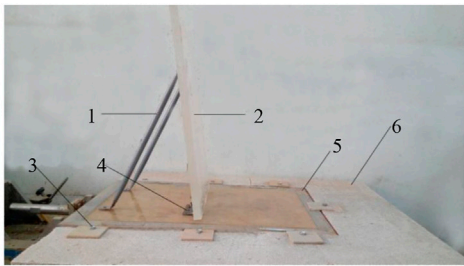
In this paper, the experimental apparatus includes a unidirectional and horizontal shaking table system. The dangerous rock accumulation test shaking test table and high-speed camera device are shown in Figure 3. The unidirectional and horizontal shaking table system is

manufactured by Nanjing Tech University and is composed of a power system, control system, and support and guidance systems (Chen et al., 2016; Hushmand et al., 2016; Xu et al., 2021; Yang et al., 2021). The power system is equipped with a pneumatic pressure source. The control system is refitted from an IPO controller in WFI and CDAS. The support and guidance systems are composed of a shaking table-board, connecting device, a guide rail, and inhibiting device.

In the operation of the shaking table system, the maximum displacement of the table is ± 13 mm, the maximum acceleration is 1 g, the frequency of shaking is between 4 and 50 Hz, the maximum load capacity is 240 kg, and the maximum overturning moment is 800 Nm. The model framework is shown in Figure 4. The size of the shaking table-board is enlarged to 1 m \times 1 m. The seismic force transferred from the bedrock to the rock at risk is applied by the support plate, which is made of a Plexiglas plate with dimensions of 300 x 600 mm and a thickness of 20 mm. The support plate is fixed to the shaker plate by two hinges and two support members. The angle between the support plate and the shaker plate is changed by moving the position of the two support members. The operation process of the shaker in this paper is referred to as the reference (Srilatha et al., 2013; Yang et al., 2017; Yang et al., 2020; Panah et al., 2021; Dong et al., 2022; Kuo et al., 2015; Yin et al., 2021).

3.2 Shaking table test design and modification

The seismic waves for these model experiments were imposed by sinusoidal waves with accelerations of 0.05 g, 0.1 g, and 0.2 g, corresponding to seismic intensities of 6, 7,



1-support rod; 2-perspex sheet; 3-set screws; 4-hinge connection; 5-shaking table; 6- expanding platform;

FIGURE 4
Model frame of the shaking table.

TABLE 1 Frequency and amplitude of the sine wave.

Intensity (degrees)	Acceleration (g)	Frequency/Hz	Amplitude/mm
8	0.2	3	5.5
		3.5	4
7	0.1	3	2.76
		2	6.2
6	0.05	2	3.1
		1.5	5.5

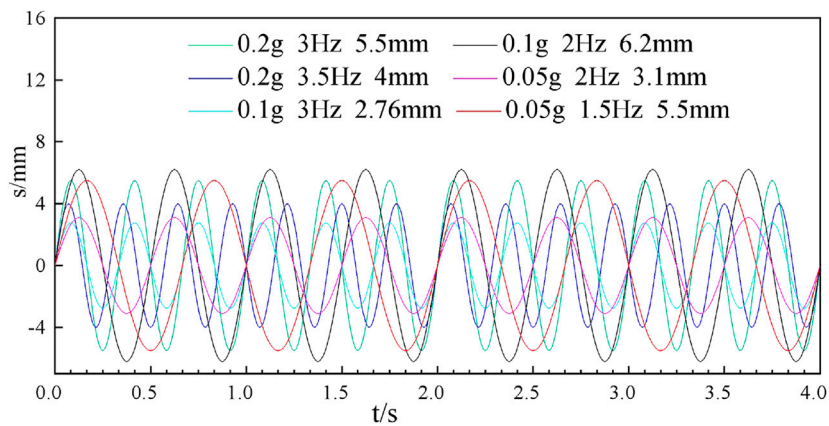


FIGURE 5
Sine form and time-history curve of the seismic wave.

and 8°, respectively. The relationship between modulation frequency, modulation amplitude, and acceleration in a shaker system is as follows:

$$a = 4A f^2 \pi^2$$

(1)

where A is the modulation amplitude, f is the modulation frequency, and a is the seismic acceleration. The detailed values and waveforms of the relationships among earthquake intensity, seismic acceleration, wave frequency, and wave amplitude are shown in [Table 1](#) and [Figure 5](#).

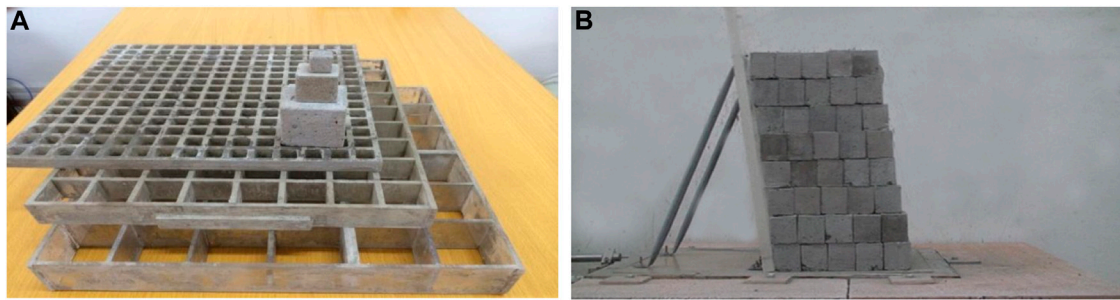


FIGURE 6
Physical model design of the shaking experiments facility. (A) Mold of block stone. (B) Stacking pattern.

TABLE 2 Experimental conditions and scheme of the model experiments.

Number	Block size (cm)	Stack height (cm)	Joint dip (°)	Acceleration(g)
1	1.5	30	90	0.1
2	3	30	90	0.1
3	5	30	90	0.1
4	3	27	90	0.1
5	3	33	90	0.1
6	3	36	90	0.1
7	3	30	80	0.1
8	3	30	70	0.1
9	3	30	60	0.1
10	3	30	90	0.05
11	3	30	90	0.2

3.3 Model materials

According to the similarity ratio of geometry, different sizes of molds were used to produce simulated critical rocks, as shown in Figure 6. The simulated rock blocks consisted of three cubic bricks with dimensions of 1.5×1.5×1.5 cm, 3×3×3 cm, and 5×5×5 cm which were made by mixing cement, sand, water, barite powder, and liquid laundry detergent in a similar ratio rule. The mixing ratio is adopted as:

barite: sand: cement: water: detergent = 12: 4: 2: 0.92: 0.35
(2)

Three sizes of simulated rock blocks represent different degrees of fragmentation. Four joint dips (60°, 70°, 80°, and 90°) and four heights (27 cm, 30 cm, 33 cm, and 36 cm) are used for the stacking of rock blocks. The stacking pattern of the blocks is shown in Figure 6B.

3.4 scheme of physical model experiments

In this study, eleven model experiments are performed to investigate the failure patterns and the critical failure state of sequential collapse of the dangerous rocks at a cliff under varying conditions, including block sizes, stacking heights, joint dips, and seismic accelerations, as shown in Table 2.

3.5 Seismic response of rock blocks

The model experiments aim to describe the damage mode and critical damage state of sequential collapse by observing the relative displacement and relative rotation between rock blocks. Since conventional strain sensors and deformation sensors cannot measure relative displacement and relative rotation,

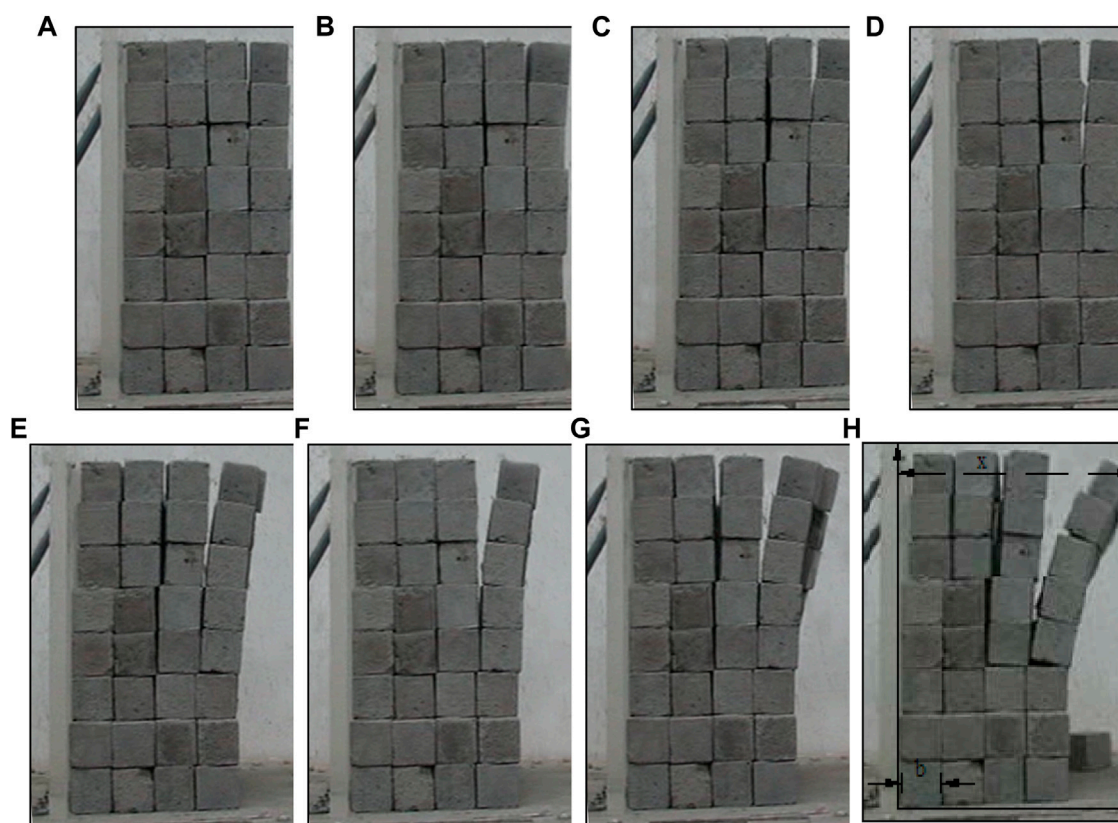


FIGURE 7

Failure forms at different times of the dangerous rock block. (A) $t = 0.2$ s. (B) $t = 0.4$ s. (C) $t = 0.8$ s. (D) $t = 1.2$ s. (E) $t = 1.6$ s. (F) $t = 1.8$ s. (G) $t = 2.0$ s. (H) $t = 2.2$ s.

image, and video digital measurements have been proposed as the primary method for measuring rock mass displacement in model experiments. The detailed sequence of operations is as follows.

- 1) The shaking process and displacement of stacked blocks over time are recorded by the high-speed camera.
- 2) A digital image time series recording the rock displacement is extracted from the digital video using Adobe Premiere and Windows Media Player software packages, as presented in Figure 7.
- 3) The displacements of rock blocks on the digital image are measured by the inquiry distance tools with AutoCAD. The connection point between the shaker plate and the Plexiglas plate is considered the origin of the workplace coordinate system.
- 4) The size of the rock masses on the digital image is also measured by the above method and compared to the known size of the rock masses. Therefore, the actual displacement of the rock block can be calculated according to the dimensional scale of the rock block size. The measurement precision of this method is controlled by the

pixel size of the image and satisfies the requirement of the model experiments.

4 Results of model experiments

4.1 Failure modes of rock blocks

Under different experimental conditions, the destabilization damage modes of rock masses induced by various factors including block size, stacking height, joint dip and dynamic load acceleration, and dynamic load intensity are displayed in Figure 8. It can be seen that there are two main failure modes of the rock blocks, including sequential collapse and sequence rolling rockfall. There are three alternative modes of continuous collapse: rotational motion, translational motion, and a combination of rotational and translational motion. Figure 8A shows that the rotational motion of sequential collapse occurred under conditions that the joint dips are greater than 70° or 80° and the dynamic load acceleration is 0.2. It can be seen that the translational motion of sequential collapse occurred under the conditions that the joint dips are

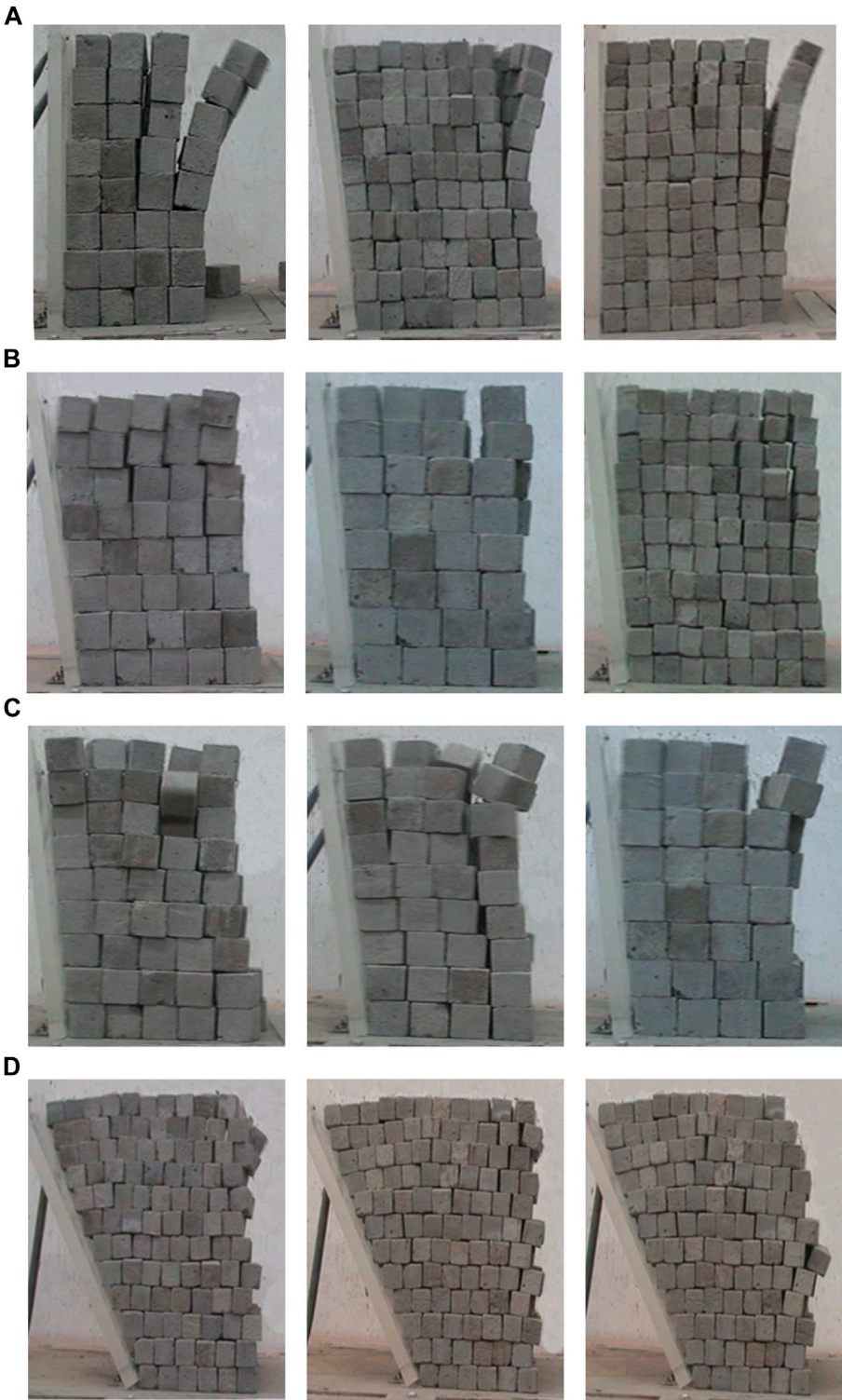


FIGURE 8
Failure motion patterns of dangerous rock block during shaking table experiments. **(A)** Rotational motion pattern of sequential collapse. **(B)** Translational motion pattern of sequential collapse. **(C)** Hybrid motion pattern of sequential collapse. **(D)** Sliding and exfoliation failure pattern.

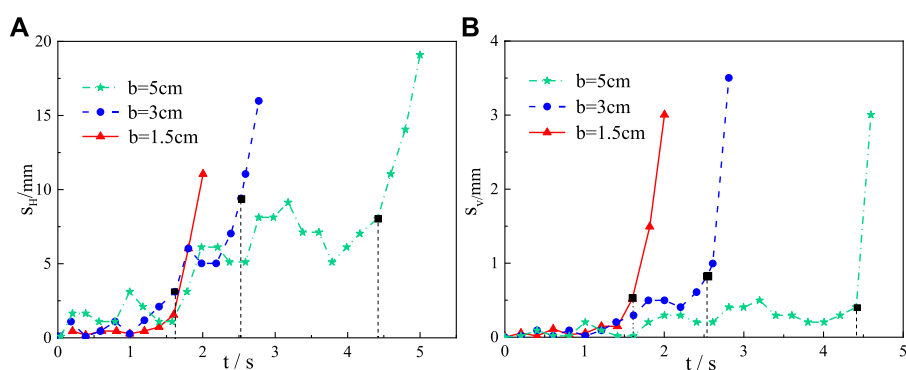


FIGURE 9
Displacement time-history curves under different rock block sizes. (A) Horizontal displacement. (B) Vertical displacement.

greater than 70° or 80° and the acceleration of dynamic load is 0.05, as shown in Figure 8B. For the combination of rotational and translational motion mode, the dynamic load acceleration is 0.1 (Figure 8C), and the precondition of the above three modes is that the joint dips are greater than 70° . Otherwise, the failure mode transitions from sequential collapse to sliding or exfoliation failure as shown in Figure 8D. When the joint dips are greater than 70° , the sensitivity of the sequential collapse stability increases with the increased vertical tensile crack inclination. Different seismic wave accelerations affect not only the damage time but also the displacement in the critical damage state. The conversion conditions among the three failure modes are based on the acceleration of the dynamic load (frequency and amplitude of the seismic wave) and the ratio between the stack height and the mass size. When the ratio is large (i.e., greater than 6–8) and the seismic wave frequency is low and the amplitude is large, the damage mode of sequential collapse is mainly rotational motion mode. Alternatively, it is the translational motion mode. The hybrid mode is the transition between the rotational motion mode and the translational motion mode.

4.2 Displacement time-history analysis

The displacement time-history curve of the top blocks of the outermost stack is represented as the failure process of sequential collapse. The displacement-time curves in the model experiments of different schemes, including block size, stack height, joint dip, and seismic wave acceleration, are plotted in Figures 9–12. From these plots, it can be found that the horizontal displacement of the rock mass is greater than the vertical displacement and the failure characteristics indicate collapse damage rather than sliding damage. Meanwhile, the trend of displacement varies with the experimental conditions. Here, the moment of accelerated displacement is defined as the critical failure state

of the sequential collapse. The black-filled points in these plots are defined as the moments of critical failure states, as the trend of displacement changes into a linear acceleration period after passing through these points.

Figure 9 shows the displacement time-history curves of the top rock blocks of the outermost stack for the block size (b) of 1.5, 3, or 5 cm, respectively, a stacking height of 30 cm, the joint dips of 90° , and seismic wave acceleration of 0.1 g. In the critical failure state, the unstable time of the block of size 5.0 cm is relatively longer than that of the block of 1.5 cm. However, the time when the block of size 3 cm reaches the critical instability state is between 5.0 cm and 1.5 cm. The vertical displacements at critical failure state are essentially the same for different block sizes. The horizontal displacement at the critical failure state increases with the increase of the block size. The ratios between height and block size for the model tests were 6, 10, and 20, respectively. When the ratio of stack height to block size increased, the test results indicated that the overall stability of the model was lower.

Figure 10 displays the displacement time-history curves of the rock masses at the top outermost edge of the model at the 90° , with joint inclinations of 80° , 70° , and 60° , when the block size is 3 cm, while the model stacking height is 30 cm with a seismic wave acceleration of 0.1 g. In the critical failure state, the time to approach the critical failure state is shorter as the joints are inclined at larger angles. For the experiments with different joint angles, the changing pattern of vertical displacements in the critical failure state is similar. The calculation results demonstrate that when the joint inclination is 90° , the dangerous rock mass is in an upright state, and the stability of the test model is the worst, in which the rock blocks at the top of the stacked layer are extremely susceptible to rockfall. When the joint dip angle is greater than 80° , the sensitivity of the stacked layer stability is higher, which is easily influenced by external induced factors.

Figure 11 presents the displacement time-history curves of rock blocks of the outermost top of the stack with heights of 27 cm, 30 cm, 33 cm, and 36 cm when the block size is 3 cm, the

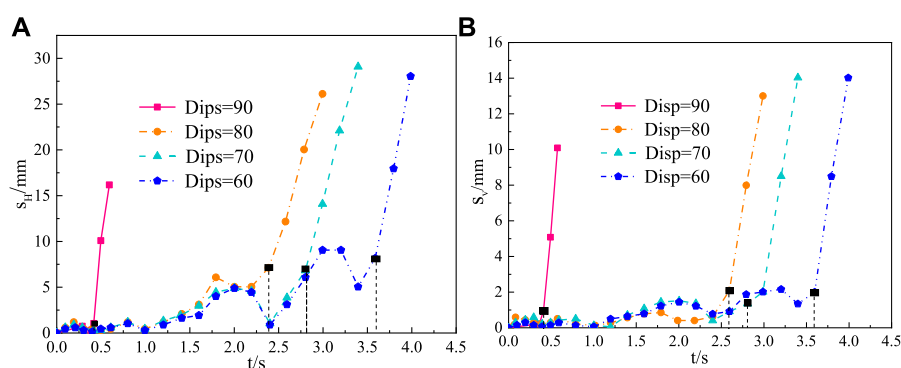


FIGURE 10

Displacement time-history curves for different joint dips. (A) Horizontal displacement. (B) Vertical displacement.

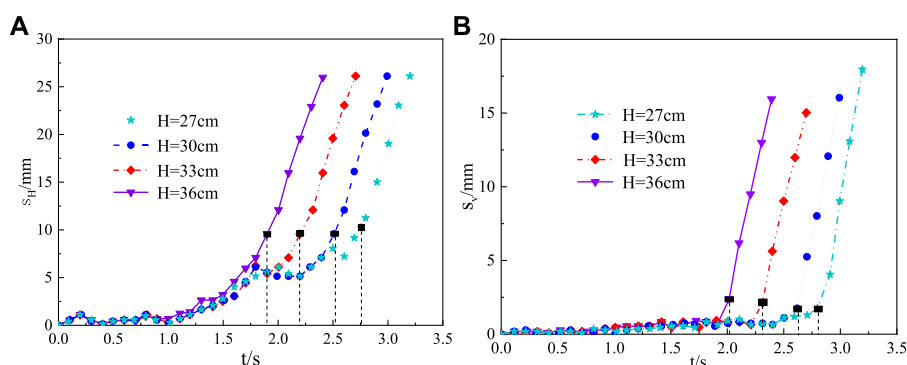


FIGURE 11

Displacement time-history curves under different stacking heights. (A) Horizontal displacement. (B) Vertical displacement.

joint inclination is 90° , and the seismic wave acceleration is 0.1 g. The critical instability time at different model stacking heights decreases with increasing stacking height, and it can also be noticed that the trends of horizontal and vertical displacements in the critical failure state are also basically the same. Therefore, the failure time is significantly affected by the model stacking height, but not by the displacement values. Based on the calculated results in Figure 11, the ratios between model stack height and rock block size are 9, 10, 11, and 12, respectively. In comparison with the results for the effect of rock block size, that is, comparing the differences between Figures 9A, 11A, it is clear that the stability of the model stack is relatively less affected by the ratio between height and rock block size.

The seismic accelerations are set to 0.05 g, 0.1 g, and 0.2 g, respectively, and the rock block size is given as 3 cm, the joint inclination as 90° , and the stack height as 30 cm. At this time, the displacement-time variation curve of the outermost top block of the model stack is plotted in Figure 12. At the critical failure state, the failure time decreases with increasing seismic wave

acceleration. The horizontal and vertical displacements are essentially similar change patterns for experiments with different seismic accelerations. It is indicated that varying seismic accelerations affect not only the critical failure time but also the displacement value at the critical failure state.

4.3 Displacement and failure form analysis

According to the failure time corresponding to the critical failure state, the horizontal displacements as a function of the outermost model stacking height represent the failure form at the critical failure state (Figure 13). In Figure 13A, the failure form varies gradually with increasing stacking height, and the ratio of model stacking height to rock block size affects the maximum displacement of the topmost rock block of the stacking. Given the model stack height, seismic acceleration, and steepest joint inclination, the rockfall of the dangerous rock mass at the top of the model became more and more obvious as the rock block

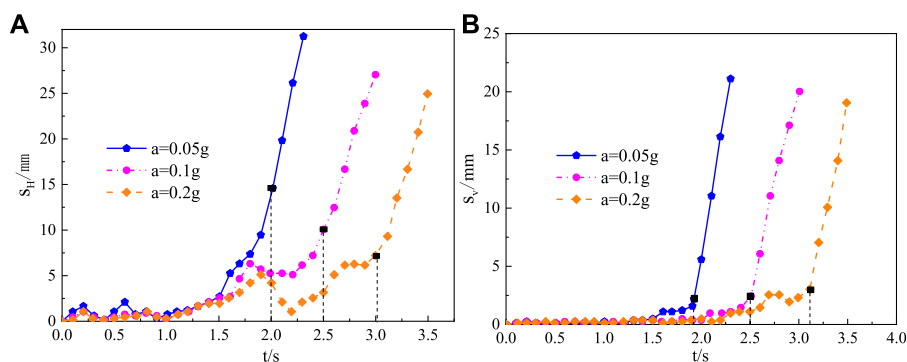


FIGURE 12

Displacement time-history curves under different seismic accelerations. (A) Horizontal displacement. (B) Vertical displacement.

size increased. When the value of b is 5 cm, the horizontal deformation reaches up to 65 mm, and the rock avalanches phenomenon occurs, as indicated in Figure 13B. It can be seen from Figure 13C, the difference of different seismic accelerations on the form of failure is relatively small, but the influence of earthquakes on the horizontal displacement of rock blocks and falling rocks is comparatively large, which is a highly sensitive influence factor in rock avalanche damage. Due to the gradual increase of the joint inclination, the failure mode of the model changes from cascading collapse to sliding or exfoliation failure, which can be seen in Figure 13D, when the joint inclination increases to 90° , the experimental model is about to have rock avalanche and falling block phenomenon.

5 Analytical solutions of the sequential collapse

Growth in the undercutting of the cliff toe eventually causes rock avalanche failure, which is caused by earthquake load, and the secondary failure modes may be the cascading collapses and sliding or exfoliation failure. The motion patterns observed in these destabilization damages are mainly translational motion and rotational motion and the translational and rotational motion destabilization patterns. Therefore, based on the limit equilibrium state, the mechanical mechanisms of the maximum translational and rotational motion patterns of the test model are established, as presented in Figure 14.

5.1 The translational motion pattern

From Figure 14A, the mechanical equations for the translational motion mode are deduced from the translational motion limit equilibrium state and its corresponding mechanical motion relations. It is assumed that the distance between the slope

surface and the joint is a , the thickness of rock strata are $b_1, b_2, b_3, \dots, b_n$, where, 1, 2, 3, \dots, n indicate the numbering of rock blocks from top to bottom, and $\Delta_1, \Delta_2, \Delta_3, \dots, \Delta_{n-1}$ are relative displacements between i -th and $i-1$ -th rock block, $g_1, g_2, g_3, \dots, g_{n-1}$ are the gravitational forces corresponding to rock blocks numbering from top to bottom, and $G_1, G_2, G_3, \dots, G_{n-1}$ are the resultant force of the corresponding rock blocks.

The limit equilibrium state of translational motion between the first and second blocks is that the center of gravity of the first block is not beyond the edge of the second block. Then, the limit of motion equilibrium relationship between the second and third blocks is that the direction of gravity of the first two blocks will not exceed the edge of the third block. By that analogy, the limit equilibrium relationship of translational motion between the $(n-1)$ -th and the n th block is that the final direction of gravity from the first block to the $(n-1)$ -th block extends no further than the outermost side of the n th block. This implies that the resultant force of the experimental model is consistently located at the edge of the next block. Consequently, the expression of Δ_{n-1} is as follows.

$$g_{n-1} \left(\frac{a}{2} - \Delta_{n-1} \right) = G_{n-2} \Delta_{n-1} \quad (3)$$

$$g_{n-1} \left(\frac{a}{2} - \Delta_{n-1} \right) = \Delta_{n-1} \sum_{j=1}^{n-2} g_j \quad (4)$$

$$\Delta_{n-1} = \frac{a g_{n-1}}{2 \sum_{j=1}^{n-1} g_j} \quad (5)$$

Therefore,

$$\Delta_i = \frac{a g_i}{2 \sum_{j=1}^i g_j} \quad (6)$$

It is supposed that S_{mH} and S_{mV} are the horizontal and vertical displacements of the first block on the top of the rock cliff in the translation motion pattern. n is the number of rock blocks from the top to the bottom of the rock cliffs. The formulas of S_{mH} and S_{mV} can be derived as follows.

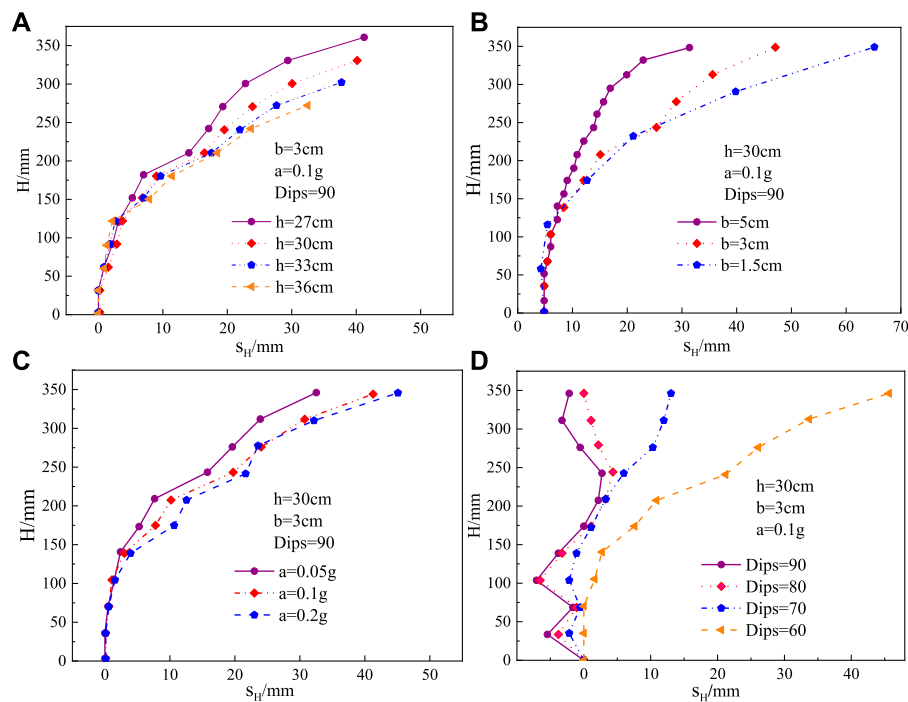


FIGURE 13

Displacement forms at critical failure state. (A) Different stacking heights. (B) Different block sizes. (C) Different seismic accelerations. (D) Different joint dips.

$$S_{mH} = \sum_{i=1}^{n-1} \Delta_i = \sum_{i=1}^{n-1} \frac{ag_i}{2\sum_{j=1}^i g_j}, (i = 1, 2, 3 \cdots n) \quad (7)$$

$$S_{mV} = 0 \quad (8)$$

When unit weights of the rock blocks are identical, and $g_i = \rho ab_i$, Eqs 6, 7 can be deduced as below.

$$\Delta_i = \frac{ab_i}{2\sum_{j=1}^i b_j} \quad (9)$$

$$S_{mH} = \sum_{i=1}^{n-1} \frac{ab_i}{2\sum_{j=1}^i b_j}, (i = 1, 2, 3 \cdots n) \quad (10)$$

5.2 The rotational motion pattern

From Figure 14B, the mechanical equations for the rotation motion mode are deduced from the translational motion limit equilibrium state and its corresponding mechanical motion relations. Assuming that the physical definitions of (a) , $(b_1, b_2, b_3, \cdots, b_n)$, $(1, 2, 3, \cdots, n)$, $(g_1, g_2, g_3, \cdots, g_{n-1})$ and $(G_1, G_2, G_3, \cdots, G_{n-1})$ have the same meaning as those of the translational motion pattern in Figure 14A. Where $\alpha_1, \alpha_2, \alpha_3, \cdots, \alpha_{n-1}$ are the relative rotation angles between the i th and $i-1$ -th blocks.

The limit equilibrium relationship of rotational motion between the first and second block is that the extension of the direction of gravity of the first rock block must cross the upper right corner of the second one. The limit equilibrium relationship of rotational motion between the second and third blocks is that the extension line of the direction of the resultant force of the first two rock blocks should pass through the upper right corner of the third one. Concurrently, the limit equilibrium relationship of rotational motion between the $(n-1)$ -th and n th rock blocks is that the extension of the direction of the resultant force from the first block to the $(n-1)$ -th block would have to pass through the upper right corner of the n th rock block. This indicates that the extension of the direction of the resultant force of gravity must cross the upper right corner of the next adjacent rock block. From the law of conservation of energy, the equation of α_{n-1} is typically

$$\begin{cases} \frac{\pi}{2} - \alpha_{n-1} + \beta_{n-1} + \gamma = \pi \\ \tan \gamma = \frac{a}{b_{n-1}} \\ \frac{g_{n-1} \sqrt{a^2 + b_{n-1}^2}}{2} \cos \beta_{n-1} = \sin \alpha_{n-1} b_{n-1} \sum_{j=1}^{n-2} g_j \end{cases} \quad (11)$$

$$\alpha_{n-1} = \tan^{-1} \left(\frac{a}{b_{n-1}} \frac{g_{n-1}}{g_{n-1} + 2\sum_{j=1}^{n-2} g_j} \right) \quad (12)$$

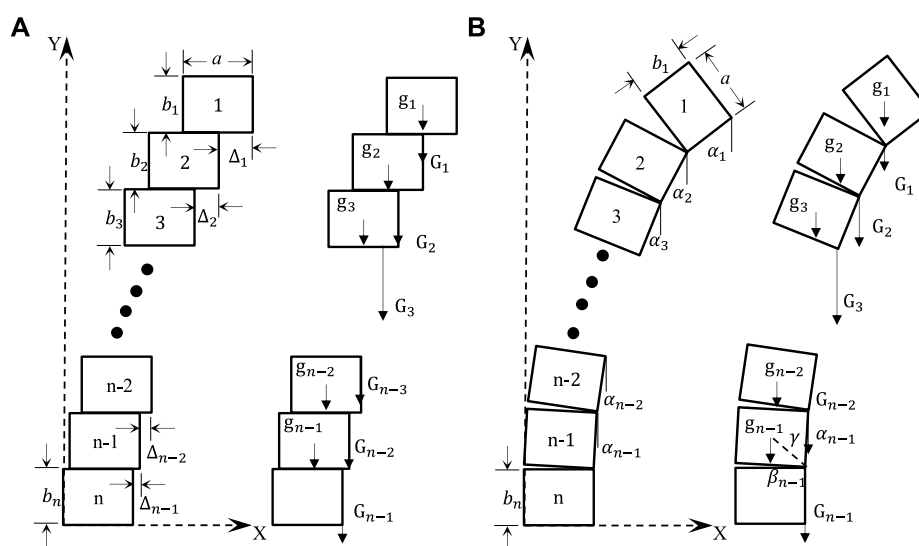


FIGURE 14

Translational and rotational motion patterns of the mechanical mechanisms. (A) Translational motion pattern. (B) Rotational motion pattern.

Then,

$$\alpha_i = \tan^{-1} \left(\frac{a}{b_i} \frac{g_i}{g_i + 2 \sum_{j=1}^{i-1} g_j} \right) \quad (13)$$

The horizontal and vertical displacements (S_{rH} and S_{rV}) of the first rock block at the top of the cliff relative to the n th block at the cliff bottom in the rotational motion mode can be attained by averaging the relative rotation angles surrounding the selected n th rock blocks in the selected experimental model. n is the number of blocks from the block on the top of the cliff to the bottom of the cliff. The formula of S_{rH} and S_{rV} are expressed as follows:

$$\begin{aligned} S_{rH} &= \sum_{i=1}^{n-1} b_i \sin \alpha_i \\ &= \sum_{i=1}^{n-1} b_i \sin \left(\tan^{-1} \left(\frac{a}{b_i} \frac{g_i}{g_i + 2 \sum_{j=1}^{i-1} g_j} \right) \right), \quad (i = 1, 2, 3 \dots n) \quad (14) \\ S_{rV} &= \sum_{i=1}^{n-1} b_i \left(1 - \cos \left(\tan^{-1} \left(\frac{a}{b_i} \frac{g_i}{g_i + 2 \sum_{j=1}^{i-1} g_j} \right) \right) \right), \quad (i = 1, 2, 3 \dots n) \quad (15) \end{aligned}$$

Hence, when the rock avalanche develops with the combined effect of gravity and seismic forces, and $g_i = \rho a b_i$, accordingly, Eqs 13–15 can be summarized as follow:

$$\alpha_i = \tan^{-1} \left(\frac{a}{b_i + 2 \sum_{j=1}^{i-1} b_j} \right) \quad (16)$$

$$S_{rH} = \sum_{i=1}^{n-1} b_i \sin \left(\tan^{-1} \left(\frac{a}{b_i + 2 \sum_{j=1}^{i-1} b_j} \right) \right), \quad (i = 1, 2, 3 \dots n) \quad (17)$$

$$S_{rV} = \sum_{i=1}^{n-1} b_i \left(1 - \cos \left(\tan^{-1} \left(\frac{a}{b_i + 2 \sum_{j=1}^{i-1} b_j} \right) \right) \right), \quad (i = 1, 2, 3 \dots n) \quad (18)$$

In conclusion, the distance between the joints and the slope surface, the thickness of the rock stratum and the number of rock blocks are the three influencing factors that have the greatest impact on horizontal and vertical displacements in rock avalanche damage.

6 Validation of analytical solutions using seismic-induced rockfall experiments

Physical experiments play a significant role in gaining a better understanding of the propagation mechanisms and factors influencing the topography and failure characteristics of rock avalanches. The results of these physical experiments and analytical solutions have revealed the failure mechanisms of rock avalanches. Assuming that all the thicknesses of rock strata are identical, and the distance between the joint and slope surfaces equals the stratum thickness. Therefore, $b_1 = b_2 = b_3 \dots = b_n = b = a$. When $b_1 = b_2 = b_3 \dots = b_n = b$, Eqs 9, 16 read as follow:

$$\Delta_i = \frac{a}{2i} \quad (19)$$

$$\alpha_i = \tan^{-1} \left(\frac{a}{(2i-1)b} \right) \quad (20)$$

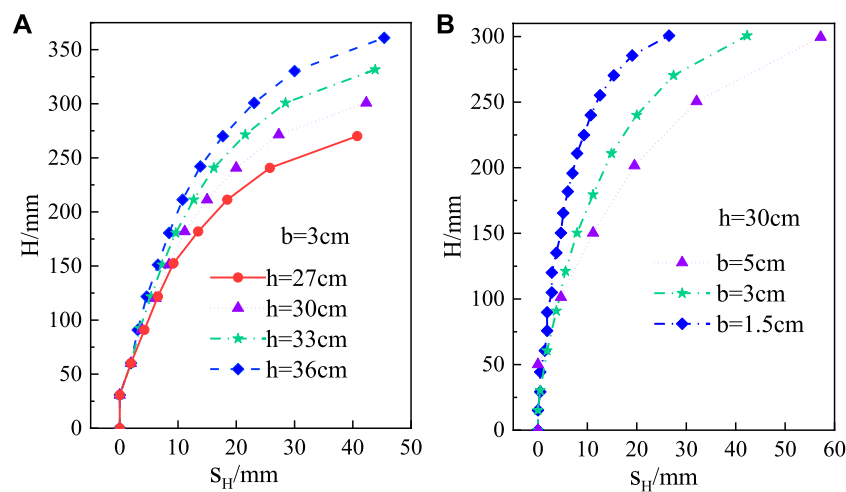


FIGURE 15

Displacement variation of rock blocks of the translational motion in the limit equilibrium state. (A) Different stacking heights of rock blocks. (B) Different rock block sizes.

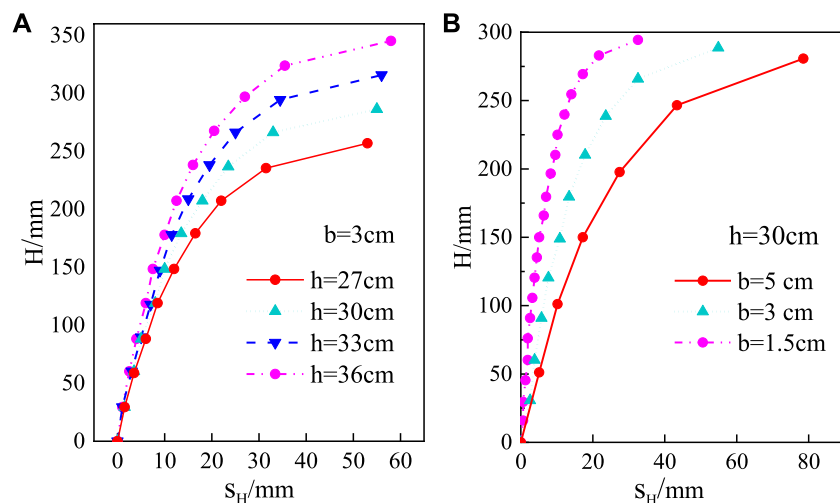


FIGURE 16

Displacement variation of rock blocks of the rotation motion in the limit equilibrium state. (A) Different stacking heights of rock blocks. (B) Different sizes of blocks.

Eqs 19, 20 are substituted into Eqs 10, 17, 18, the expressions for S_{mH} , S_{rH} and S_{rV} then can be summarized:

$$S_{mH} = \sum_{i=1}^{n-1} \frac{a}{2i}, \quad (i = 1, 2, 3 \cdots n) \quad (21)$$

$$S_{rH} = \sum_{i=1}^{n-1} b \sin \left(\tan^{-1} \left(\frac{a}{(2i-1)b} \right) \right), \quad (i = 1, 2, 3 \cdots n) \quad (22)$$

$$S_{rV} = \sum_{i=1}^{n-1} b_i \left(1 - \cos \left(\tan^{-1} \left(\frac{a}{(2i-1)b} \right) \right) \right), \quad (i = 1, 2, 3 \cdots n) \quad (23)$$

When $a = b$, Eqs 21–23 read as follow:

$$\alpha_i = \tan^{-1} \left(\frac{1}{(2i-1)} \right) \quad (24)$$

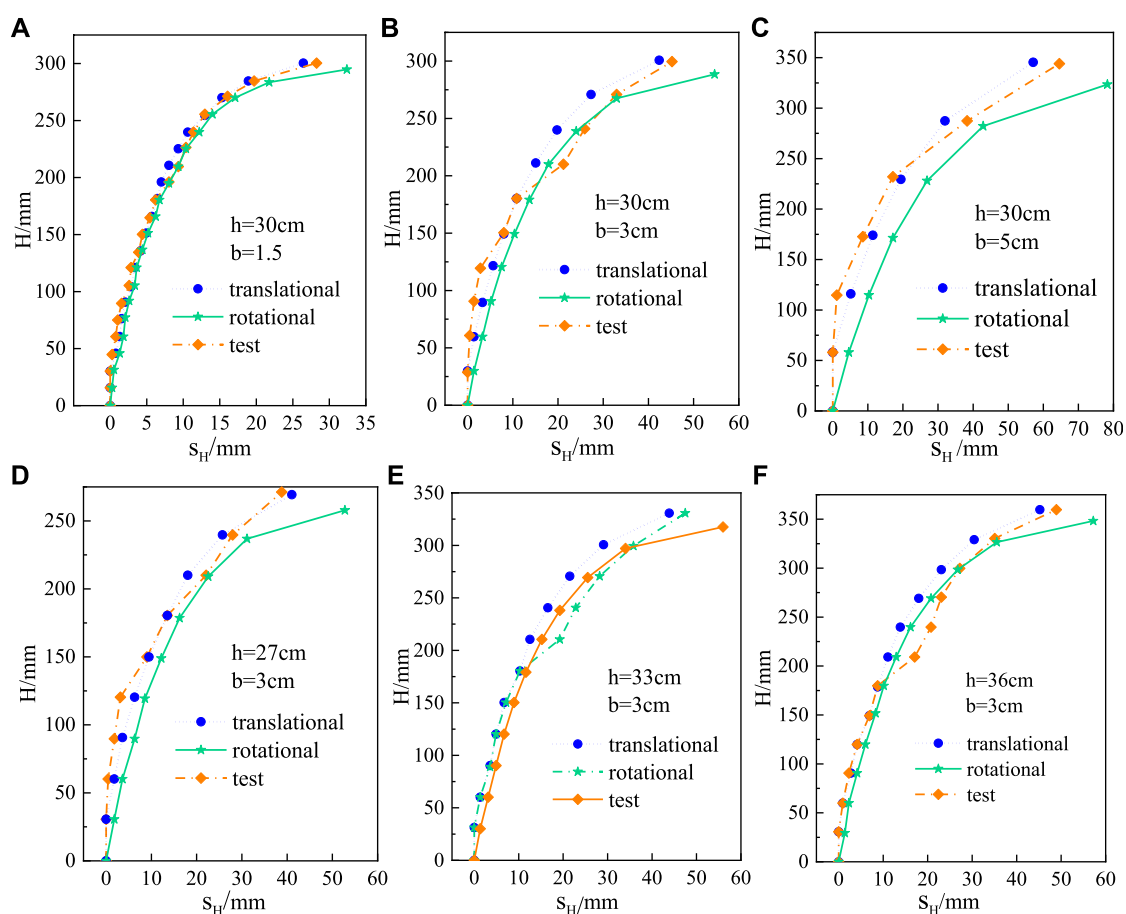


FIGURE 17

Comparison results of between model experimental and analytical solutions. (A) $h = 30\text{ cm}$; $b = 1.5\text{ cm}$. (B) $h = 30\text{ cm}$; $b = 3\text{ cm}$. (C) $h = 30\text{ cm}$; $b = 5\text{ cm}$. (D) $h = 27\text{ cm}$; $b = 3\text{ cm}$. (E) $h = 33\text{ cm}$; $b = 3\text{ cm}$. (F) $h = 36\text{ cm}$; $b = 3\text{ cm}$.

$$S_{mH} = \sum_{i=1}^{n-1} \frac{b}{2i}, (i = 1, 2, 3 \cdots n) \quad (25)$$

$$S_{rH} = \sum_{i=1}^{n-1} b_i \sin \left(\tan^{-1} \left(\frac{1}{(2i-1)} \right) \right), (i = 1, 2, 3 \cdots n) \quad (26)$$

$$S_{rV} = \sum_{i=1}^{n-1} b_i \left(1 - \cos \left(\tan^{-1} \left(\frac{1}{(2i-1)} \right) \right) \right), (i = 1, 2, 3 \cdots n) \quad (27)$$

Equations 25–27 represent the horizontal and vertical displacements of the rock block in the limit equilibrium state of translational and rotational motions. In the comparative verification, when there are translation and rotation motion modes in rock avalanche failure, the size of the rock mass and the stacking height of the model are selected as the verification objects for analysis in the physical experimental model. Based on the parameters of the corresponding experiments and given $b=3\text{cm}$, the displacements of the rock blocks for the translational and rotational motion patterns under the limit

equilibrium state are deduced from the analytical solutions as illustrated in Figures 15, 16.

It can be seen that the horizontal displacement value of the rock blocks in the horizontal motion pattern is about 40 mm, whereas the horizontal displacement of the rock blocks in the rotational motion pattern is significantly larger than the horizontal motion, and the variation range of its value is about 28 mm–58 mm, and the maximum value is not more than 60 mm. For different rock block stacking heights, the displacements of the rock block at the top of the rock cliff increase slightly with increasing block stacking height, while the displacement for the same block stacking height decreases significantly with increasing block height. In both horizontal and rotational motion modes, the displacement of the cliff top block increases significantly with increasing block size, as shown in Figures 15, 16.

Figure 17 shows the comparison results between the measured displacements of the model experiments and the predicted

displacements of the analytical solutions in translational and rotational motion patterns. The results of the comparison between the analytical solution and the model experiments include simultaneously the translational motion pattern, the rotational motion pattern, or the mixed pattern of rotation and translation and rotation for the cascade collapse. At the same given scale and test conditions, the rock block displacements for rotational motion are usually larger than those for translational motion. The differences in displacement between translational and rotational motion become progressively smaller as the size of the rock blocks decreases. When $h = 30$ cm and $b = 1.5$ cm, the trend curves of the translational and rotational motion patterns begin to gradually overlap. From Figure 17, all experimental displacement curves in the critical damage state exist near or between the displacement curves in the limit equilibrium state of translational and rotational motions. This result implies that the analytical solution can effectively solve the critical failure state of the critical rock cascade reaction at the rock cliff. There are several rock blocks in the experiment whose displacements exceed the corresponding displacements in the analytical solutions, indicating partial damage to the corresponding rock blocks.

7 Conclusion

The physical model experiment and analytical solutions are conducted to investigate the critical failure characteristics of the earthquake-induced sequential rock avalanche of the dangerous rocks at cliffs, and in particular the failure motion mechanisms of the cascading collapse. Several conclusions have been drawn as follows:

- 1) This paper conducts a laboratory analog experiment illustrating the characteristic processes of sequential collapse for the rock avalanche with the seismic load in the laboratory, which indicated that the variable seismic accelerations affect not only the critical failure time but also the sequential displacement behaviors at the critical failure state.
- 2) The earthquake-induced rock avalanche had several topographical features and structural damages, with significant variation in spatial distribution: cascading collapses, sliding, or exfoliation failure.
- 3) The physical experiments and analytical solution analyses show that from the kinematic perspective, the main rock blocks that fail during the cascading collapses are characterized by translational and rotational motion patterns or mixed motion of translational and rotational.
- 4) The significant influence factors of an earthquake-induced rock avalanche on the failure mechanism and movement mode are highlighted. The most important influencing factor that elucidate the different motion patterns leading to avalanche development are presented. The transformed motion pattern is controlled by the ratio between the model

stacking height and the rock block size and the seismic acceleration. Whereas the rotational motion pattern is mainly influenced by the nodal dip angle, model stacking height, and seismic acceleration.

- 5) In this paper, the limit equilibrium mechanical states of translational and rotational motion are proposed, and the limit equilibrium formulas for these two motion patterns in the destabilization damage process are derived. Comparing the analytical solution with the results of physical experiments, it is demonstrated that the proposed analytical solution can accurately solve the critical failure state of sequential collapse of dangerous rocks at cliffs in a rock avalanche.

Data availability statement

The original contributions presented in the study are included in the article/Supplementary Material, further inquiries can be directed to the corresponding author.

Author contributions

SG: Methodology, software, writing-original draft, visualization. YL: Investigation, data curation, software, writing-original draft. PZ: Supervision, conceptualization, methodology, funding acquisition. RZ: Visualization, Writing-review and editing. YQ: Formal analysis, data curation.

Funding

The authors gratefully acknowledge the support of the National Nature Science Foundation of China (NSFC NO. 41372295 and NO. 41102178); the Fellowship of China Postdoctoral Science Foundation (NO. 2021M701688); outstanding Postdoctoral Fellowship of Jiangsu Foundation (NO. 283762); Science and Technology Planning Project of Jiangsu Province (Grant No. BE2022605).

Conflict of interest

The authors declare that the research was conducted in the absence of any commercial or financial relationships that could be construed as a potential conflict of interest.

Publisher's note

All claims expressed in this article are solely those of the authors and do not necessarily represent those of their affiliated

organizations, or those of the publisher, the editors and the reviewers. Any product that may be evaluated in this article, or

claim that may be made by its manufacturer, is not guaranteed or endorsed by the publisher.

References

- Aaron, J., and Hungr, O. (2016). Dynamic analysis of an extraordinarily mobile rock avalanche in the Northwest Territories, Canada. *Can. Geotech. J.* 53, 899–908. doi:10.1139/cgj-2015-0371
- Aaron, J., and McDougall, S. (2019). Rock avalanche mobility: The role of path material. *Eng. Geol.* 257 (6), 105126. doi:10.1016/j.enggeo.2019.05.003
- An, H. C., Ouyang, C. J., and Zhou, S. (2021). Dynamic process analysis of the Baige landslide by the combination of DEM and long-period seismic waves. *Landslides* 18 (5), 1625–1639. doi:10.1007/s10346-020-01595-0
- Baggio, T., Mergili, M., and D'Agostino, V. (2021). Advances in the simulation of debris flow erosion: The case study of the Rio Gere (Italy) event of the 4th August 2017. *Geomorphology* 381, 107664. doi:10.1016/j.geomorph.2021.107664
- Bergillos, R. J., Rodriguez-Delgado, C., Medina, L., Fernandez-Ruiz, J., Rodriguez-Ortiz, J. M., and Iglesias, D. (2022). A combined approach to cliff characterization: Cliff Stability index. *Mar. Geol.* 444, 106706. doi:10.1016/j.margeo.2021.106706
- Chen, G., Zen, K., Zheng, L., and Jiang, Z. (2010). A new model for long-distance movement of earthquake induced landslide. The 44th U.S. Symposium on Rock Mechanics, Salt Lake City, UT, USA. June 27, 2010
- Chen, H., Crosta, G. B., and Lee, C. F. (2006). Erosional effects on runoff of fast landslides, debris flows and avalanches: A numerical investigation. *Geotechnique* 56 (5), 305–322. doi:10.1680/geot.2006.56.5.305
- Chen, Z. Y., Chen, W., Li, Y. Y., and Yuan, Y. (2016). Shaking table test of a multi-story subway station under pulse-like ground motions. *Soil Dyn. Earthq. Eng.* 82, 111–122. doi:10.1016/j.soildyn.2015.12.002
- Do, T. N., and Wu, J. (2020). Simulating a mining-triggered rock avalanche using dda: A case study in nattai north, Australia. *Eng. Geol.* 264, 105386. doi:10.1016/j.enggeo.2019.105386
- Donati, D., Stead, D., Brideau, M. A., and Ghirotti, M. (2021). Using pre-failure and post-failure remote sensing data to constrain the three-dimensional numerical model of a large rock slope failure. *Landslides* 18, 827–847. doi:10.1007/s10346-020-01552-x
- Dong, J. Y., Wang, C., Huang, Z. Q., Yang, J. H., and Xue, L. (2022). Shaking table model test to determine dynamic response characteristics and failure modes of steep bedding rock slope. *Rock Mech. Rock Eng.* 55, 3645–3658. doi:10.1007/s00603-022-02822-x
- Dufresne, A., Prager, C., and Bösmeier, A. (2016). Insights into rock avalanche emplacement processes from detailed morpho-lithological studies of the Tschirgant deposit (Tyrol, Austria). *Earth Surf. Process. Landf.* 41, 587–602. doi:10.1002/esp.3847
- Eismann, T. H., Abele, G., and Glade, T. (2001). Dynamics of rock slides and rockfalls. *Z. Geomorphol.* 54 (2), 268–269. doi:10.1007/978-3-662-04639-5
- Fan, X. M., Domènech, G., Scaringi, G., Huang, R. Q., Xu, Q., Hales, T. C., et al. (2018). Spatio-temporal evolution of mass wasting after the 2008 M_w 7.9 Wenchuan earthquake revealed by a detailed multi-temporal inventory. *Landslides* 15 (12), 2325–2341. doi:10.1007/s10346-018-1054-5
- Fan, X. M., Scaringi, G., Korup, O., West, A. J., van Westen, C. J., Tanyas, H., et al. (2019). Earthquake-induced chains of geologic hazards: Patterns, mechanisms, and impacts. *Rev. Geophys.* 57 (2), 421–503. doi:10.1029/2018RG000626
- Fan, X. M., Scaringi, G., Xu, Q., Zhan, W. W., Dai, L. X., Li, Y. S., et al. (2018). Coseismic landslides triggered by the 8th August 2017 M_s 7.0 Jiuzhaigou earthquake (Sichuan, China): Factors controlling their spatial distribution and implications for the seismogenic blind fault identification. *Landslides* 15, 967–983. doi:10.1007/s10346-018-0960-x
- Flor-Blanco, G., Bruschi, V., Adrados, L., Domínguez-Cuesta, M. J., Gracia-Prieto, F. J., Llana-Fúnez, S., et al. (2022). Geomorphological evolution of the calcareous coastal cliffs in North Iberia (Asturias and Cantabria regions). *Estuar. Coast. Shelf Sci.* 273, 107913. doi:10.1016/j.ecss.2022.107913
- Gao, G., Meguid, M. A., Chouinard, L. E., and Xu, C. (2020). Insights into the transport and fragmentation characteristics of earthquake-induced rock avalanche: Numerical study. *Int. J. Geomech.* 20 (9), 04020157. doi:10.1061/(ASCE)GM.1943-5622.0001800
- Gong, Y. F., Yao, A. J., Li, Y. L., and Tian, T. (2022). Classification and distribution of large-scale high-position landslides in southeastern edge of the Qinghai-Tibet Plateau, China. *Environ. Earth Sci.* 81, 311. doi:10.1007/s12665-022-10433-6
- Gorum, T., Fan, X. M., van Western, C. J., Huang, R. Q., Xu, Q., Tang, C., et al. (2011). Distribution pattern of earthquake-induced landslides triggered by the 12 May 2008 Wenchuan earthquake. *Geomorphology* 133, 152–167. doi:10.1016/j.geomorph.2010.12.030
- Gorum, T., Fan, X., van Westen, C. J., Huang, R., Xu, Q., Tang, C., et al. (2011). Distribution pattern of earthquake-induced landslides triggered by the 12 May 2008 Wenchuan earthquake. *Geomorphology* 133 (3–4), 152–167. doi:10.1016/j.geomorph.2010.12.030
- Guo, S. F., and Griffiths, D. V. (2020a). Failure mechanisms in two-layer undrained slopes. *Can. Geotech. J.* 57 (10), 1617–1621. doi:10.1139/cgj-2019-0642
- Guo, S. F., Li, N., Liu, C., Liu, N. F., and Liu, W. P. (2020b). Unraveling the progressive failure behaviors and mechanisms of the slope with a local dynamic method based on the double strength reduction. *Int. J. Geomech.* 20 (6), 04020069–04020111. doi:10.1061/(ASCE)GM.1943-5622.0001693
- Guo, S. F., Li, N., Liu, W. P., Ma, Z. Y., and Lv, G. (2020c). Influence of both soil properties and geometric parameters on failure mechanisms and stability of two-layer undrained slopes. *Adv. Mater. Sci. Eng.* 2020 (3), 1–13. doi:10.1155/2020/4253026
- Guo, S. F., Xu, P. W., Zhang, P., and Wang, S. N. (2021). Numerical investigation of the anti-infiltration and anti-erosion performance of composite layers mixed with polyacrylamide and basalt fibre for the protection of silt subgrade slopes. *Front. Earth Sci. (Lausanne)*. 10, 815602. doi:10.3389/feart.2022.815602
- Hilger, P., Gosse, J. C., and Hermanns, R. L. (2019). How significant is inheritance when dating rockslide boulders with terrestrial cosmogenic nuclide dating?—A case study of an historic event. *Landslides* 16, 729–738. doi:10.1007/s10346-018-01132-0
- Hushmand, A., Dashti, S., Davis, C., McCartney, J. S., and Hushmand, B. (2016). A centrifuge study of the influence of site response, relative stiffness, and kinematic constraints on the seismic performance of buried reservoir structures. *Soil Dyn. Earthq. Eng.* 88, 427–438. doi:10.1016/j.soildyn.2016.06.011
- Kuo, C., Chang, K., Tsai, P., Wei, S., Chen, R., Dong, J., et al. (2015). Identification of co-seismic ground motion due to fracturing and impact of the Tsaoiling landslide, Taiwan. *Eng. Geol.* 196, 268–279. doi:10.1016/j.enggeo.2015.07.013
- Liu, N. F., Li, N., Li, G. F., Song, Z. P., and Wang, S. J. (2022). Method for evaluating the equivalent thermal conductivity of a freezing rock mass containing systematic fractures. *Rock Mech. Rock Eng.* 55, 7333–7355. doi:10.1007/s00603-022-03038-9
- Liu, N. F., Li, N., Wang, S. J., Li, G. F., and Song, Z. P. (2022). A fully coupled thermo-hydro-mechanical model for fractured rock masses in cold regions. *Cold Reg. Sci. Technol.* 205 (7), 103707–103713. doi:10.1016/j.coldregions.2022.103707
- Liu, N. F., Li, N., Xu, C. B., Li, G. F., Song, Z. P., and Yang, M. (2020). Mechanism of secondary lining cracking and its simulation for the dugongling tunnel. *Rock Mech. Rock Eng.* 53, 4539–4558. doi:10.1007/s00603-020-02183-3
- Ma, K., Liu, G., Xu, N., Zhang, Z., and Feng, B. (2021). Motion characteristics of rockfall by combining field experiments and 3D discontinuous deformation analysis. *Int. J. Rock Mech. Min. Sci.* (1997). 138, 104591. doi:10.1016/j.ijrmm.2020.104591
- Marc, O., Hovius, N., and Meunier, P. (2016). The mass balance of earthquakes and earthquake sequences. *Geophys. Res. Lett.* 43, 3708–3716. doi:10.1002/2016GL068333
- Matasci, B., Stock, G. M., Jaboyedoff, M., Carrea, D., Collions, B. D., Guérin, A., et al. (2018). Assessing rockfall susceptibility in steep and overhanging slopes using three-dimensional analysis of failure mechanisms. *Landslides* 15, 859–878. doi:10.1007/s10346-017-0911-y
- Mitchell, A., Allstadt, K. E., George, D., Aaron, J., McDougall, S., Moore, J., et al. (2022). Insights on multistage rock avalanche behavior from runoff modeling constrained by seismic inversions. *JGR. Solid Earth* 127 (10). doi:10.1029/2021JB023444
- Moretti, L., Allstadt, K., Mangeney, A., Capdeville, Y., Stutzmann, E., and Bouchut, F. (2015). Numerical modeling of the Mount Meager landslide constrained by its force history derived from seismic data. *J. Geophys. Res. Solid Earth* 120 (4), 2579–2599. doi:10.1002/2014JB011426
- Moretti, L., Mangeney, A., Walter, F., Capdeville, Y., Bodin, T., Stutzmann, E., et al. (2020). Constraining landslide characteristics with Bayesian inversion of field and seismic data. *Geophys. J. Int.* 221 (2), 1341–1348. doi:10.1093/gji/ggaa056

- Ouyang, C. J., An, H. C., Zhou, S., Wang, Z. W., Su, P. C., Wang, D. P., et al. (2019). Insights from the failure and dynamic characteristics of two sequential landslides at Baige village along the Jinsha River, China. *Landslides* 16, 1397–1414. doi:10.1007/s10346-019-01177-9
- Paguican, E. M. R., Vries, W., and Lagmay, A. M. F. (2014). Hummocks: How they form and how they evolve in rockslide-debris avalanches. *Landslides* 11, 67–80. doi:10.1007/s10346-012-0368-y
- Panah, A. K., and Eftekhari, Z. (2021). Shaking table tests on polymeric-strip reinforced-soil walls adjacent to a rock slope. *Geotext. Geomembranes* 49 (3), 737–756. doi:10.1016/j.geotextmem.2020.12.005
- Qin, Y. W., Chen, Y. H., Lai, J. X., Qiu, J. L., Yang, T., and Liu, T. (2023). Loess landslide-tunnel system: A systematic review of its failure characteristics, interaction mechanism and countermeasures. *Eng. Geol.*
- Sanders, D., Wallner, M., and Pomella, H. (2021). Medieval age determined for the hitherto undescribed/undated rock avalanche of Münster (Inn valley, Eastern Alps). *Geomorphology* 389, 107802. doi:10.1016/j.geomorph.2021.107802
- Singeisen, C., Ivy-Ochs, S., Wolter, A., Steinemann, O., Akcar, N., Yesilyurt, S., et al. (2020). The kandersteg rock avalanche (Switzerland): Integrated analysis of a late holocene catastrophic event. *Landslides* 17, 1297–1317. doi:10.1007/s10346-020-01365-y
- Srilatha, N., Latha, G. M., and Puttappa, C. G. (2013). Effect of frequency on seismic response of reinforced soil slopes in shaking table tests. *Geotext. Geomembranes* 36, 27–32. doi:10.1016/j.geotextmem.2012.10.004
- Togo, T., Shimamoto, T., Dong, J. J., Lee, C. T., and Yang, C. M. (2014). Triggering and runaway processes of catastrophic Tsaoiling landslide induced by the 1999 Taiwan Chi-Chi earthquake, as revealed by high-velocity friction experiments. *Geophys. Res. Lett.* 41, 1907–1915. doi:10.1002/2013GL059169
- Xu, C. S., Jiang, Z. W., Du, X. L., Shen, Y. Y., and Chen, S. (2021). 1-g shaking table tests of precast horseshoe segmental tunnel: Experimental design, dynamic properties, deformation mode and damage pattern. *Tunn. Undergr. Space Technol.* 113 (7), 103976. doi:10.1016/j.tust.2021.103976
- Yang, G. X., Qi, S. W., Wu, F. Q., and Zhan, Z. F. (2017). Seismic amplification of the anti-dip rock slope and deformation characteristics: A large-scale shaking table test. *Soil Dyn. Earthq. Eng.* 115 (3), 907–916. doi:10.1016/j.soildyn.2017.09.010
- Yang, H. F., Xing, B. K., He, J. K., Jiang, H., and Cheng, Q. (2022). The formation mechanism and failure mode of a talus slope induced by rockfalls in Nayong County, Southwest China. *Front. Earth Sci. (Lausanne)*. 25. doi:10.3389/feart.2022.973528
- Yang, Y. S., Yu, H. T., Yuan, Y., and Sun, J. (2021). 1 g Shaking table test of segmental tunnel in sand under near-fault motions. *Tunn. Undergr. Space Technol.* 115 (9), 104080. doi:10.1016/j.tust.2021.104080
- Yang, Z. P., Tian, X., Jiang, Y. W., Liu, X. R., Hu, Y. X., and Lai, Y. L. (2020). Experimental study on dynamic characteristics and dynamic responses of accumulation slopes under frequent microseisms. *Arab. J. Geosci.* 13, 770. doi:10.1007/s12517-020-05781-1
- Yin, X. M., Zhang, A. M., Wang, L. A., and Chen, L. (2021). Instability modes and stability analysis of perilous rock groups with control fissures under the conditions of excavation and rainfall. *Geotech. Eng. (Dordr)*. 39, 2799–2821. doi:10.1007/s10706-020-01657-z
- Yin, X. M., Zhang, X., Lei, Y. J., and Wang, L. N. (2021). Effect of loading direction on the critical characteristic strength and energy evolution of quartz mica schist and microscale mechanisms. *Bull. Eng. Geol. Environ.* 80, 8693–8710. doi:10.1007/s10064-021-02455-4
- Zhao, K., Wang, Q. Z., Zhuang, H. Y., Li, Z. Y., and Chen, G. X. (2022). A fully coupled flow deformation model for seismic site response analyses of liquefiable marine sediments. *Ocean. Eng.* 251 (4), 111144. doi:10.1016/j.oceaneng.2022.111144
- Zeng, Q., Zhang, L., Davies, T., Yuan, G., Xue, X., Wei, R., et al. (2019). Morphology and inner structure of Luanshibao rock avalanche in Litang, China and its implications for long-runout mechanisms. *Eng. Geol.* 260, 105216. doi:10.1016/j.enggeo.2019.105216
- Zhang, D. F., Wang, J. D., Qi, L. R., Zhang, Y. S., Ma, J. F., and Lu, G. Y. (2022). Initiation and movement of a rock avalanche in the Tibetan plateau, China: Insights from field observations and numerical simulations. *Landslides* 19, 2569–2591. doi:10.1007/s10346-022-01917-4
- Zhang, M., McSaveney, M., Shao, H., and Zhang, C. (2018). The 2009 Jiweishan rock avalanche, Wulong, China: Precursor conditions and factors leading to failure. *Eng. Geol.* 233, 225–230. doi:10.1016/j.enggeo.2017.12.010
- Zhang, M., and Yin, Y. P. (2013). Dynamics, mobility-controlling factors and transport mechanisms of rapid long-runout rock avalanches in China. *Eng. Geol.* 167, 37–58. doi:10.1016/j.enggeo.2013.10.010
- Zhang, Y. W., Song, Z. P., and Weng, X. L. (2022b). A constitutive model for loess considering the characteristics of structurality and anisotropy. *Soil Mech. Found. Eng.* 59, 32–43. doi:10.1007/s11204-022-09781-z
- Zhang, Y. B., Xing, A. G., Jin, K. P., Zhuang, Y., Bilal, M., Xu, S., et al. (2020b). Investigation and dynamic analyses of rockslide-induced debris avalanche in Shuicheng, Guizhou, China. *Landslides* 17 (9), 2189–2203. doi:10.1007/s10346-020-01436-0
- Zhang, Y. W., Fan, S. Y., Yang, D. H., and Zhou, F. (2022a). Investigation about variation law of frost heave force of seasonal cold region tunnels: A case study. *Front. Earth Sci.* 9, 806843. doi:10.3389/feart.2021.806843
- Zhao, T., Crosta, G. B., and Liu, Y. (2022). Analysis of slope fracturing under transient earthquake loading by random discrete element method. *Int. J. Rock Mech. Min. Sci.* (1997). 157, 105171. doi:10.1016/j.ijrmms.2022.105171
- Zhu, C., Huang, Y., and Sun, J. (2020). Solid-like and liquid-like granular flows on inclined surfaces under vibration-Implications for earthquake-induced landslides. *Comput. Geotech.* 123, 103598. doi:10.1016/j.compgeo.2020.103598



OPEN ACCESS

EDITED BY

Yuwei Zhang,
Xi'an University of Architecture and
Technology, China

REVIEWED BY

Peng Xu,
Ningxia University, China
Ang Li,
Chang'an University, China
Xin Zhao,
Inner Mongolia Research Institute of
Transportation Science Development,
China

*CORRESPONDENCE

Lixin Zhang,
✉ zhanglixin616@sina.com
Zhichun Liu,
✉ liuzhch01@163.com

SPECIALTY SECTION

This article was submitted to
Environmental Informatics
and Remote Sensing,
a section of the journal
Frontiers in Earth Science

RECEIVED 19 December 2022

ACCEPTED 17 January 2023

PUBLISHED 01 February 2023

CITATION

Hu Z, Mao H, Zhang L and Liu Z (2023),
Experimental tests and theoretical analysis
for mechanical behaviors of side wall
opening construction in mined excavation
subway station.
Front. Earth Sci. 11:1127078.
doi: 10.3389/feart.2023.1127078

COPYRIGHT

© 2023 Hu, Mao, Zhang and Liu. This is an
open-access article distributed under the
terms of the [Creative Commons
Attribution License \(CC BY\)](https://creativecommons.org/licenses/by/4.0/). The use,
distribution or reproduction in other
forums is permitted, provided the original
author(s) and the copyright owner(s) are
credited and that the original publication in
this journal is cited, in accordance with
accepted academic practice. No use,
distribution or reproduction is permitted
which does not comply with these terms.

Experimental tests and theoretical analysis for mechanical behaviors of side wall opening construction in mined excavation subway station

Zhinan Hu¹, Hongtao Mao¹, Lixin Zhang^{2*} and Zhichun Liu^{1*}

¹State Key Laboratory of Mechanical Behavior and System Safety of Traffic Engineering Structures, Shijiazhuang Tiedao University, Shijiazhuang, China, ²Shijiazhuang State-owned Capital Investment and Operation Group Co, Ltd., Shijiazhuang, China

The connection of subway stations to surrounding underground spaces inevitably involves opening construction in the existing underground structure. The opening construction can strongly impact the existing underground structure when there is no reserved condition. In this study, three-dimensional numerical simulation, model test, and theoretical analysis are used to analyze the mechanical behaviors of side wall opening construction in a mined excavation subway station-Xuanwumen Station of Beijing Subway Line 4. Based on the deformation and stress characteristics of the existing side wall structure, two different reinforcement measures are compared. It is found that the vertical and horizontal deformations of the existing structure caused by opening construction is -1.58 and -1.79 mm, respectively, which are lower than the subway deformation control requirements (3 mm). However, the first and third principal stress increments are 2.14 and -4.62 MPa, respectively, which are markedly higher than the control requirement (10%). A "two-step opening" method is proposed for side wall opening construction in underground structures based on the solution of complex function to the orifice problem. This theoretical method is validated by numerical simulations and model tests, achieving highly consistent results. The allowable ultimate span of side wall opening is 5.75 m without reinforcement. Findings of the present study provide a reference for the design and construction of side wall openings in similar underground spaces.

KEYWORDS

side wall opening, structure demolition, mechanical behaviors, theoretical analysis, ultimate opening span

Introduction

Connections are an essential way for the development of urban underground space from isolated points to an interconnected underground space network (Wallace and Ng, 2016; Zhao and Künzli, 2016). When a subway station is connected to the surrounding underground space, it often involves the demolition of existing structural openings. The construction of opening in existing subway stations leads to stress redistribution in the station structure. In particular, when there are no reserved openings, improper construction can affect the function and structural safety of the station (Yin and Zhang, 2018; Yin et al., 2020).

Extensive research has been conducted on the opening in aboveground building structures and excavation of underground caverns. With respect to the opening in aboveground buildings, model tests and theoretical analyses (Zhang et al., 2019) were conducted to explore opening-induced changes in the mechanical properties of existing building walls (Moon et al., 2020),

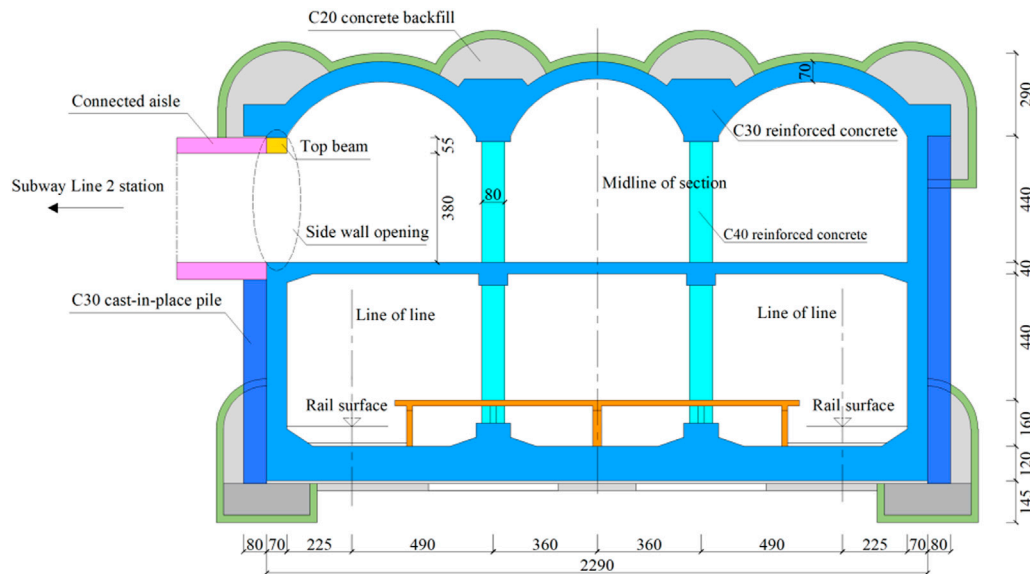


FIGURE 1
Elevation of side wall opening in Xuanwumen Station (cm).

deep beams (Ahmed et al., 2020), rigid plates (Saad-Eldeen et al., 2018), and arched steel beams (Zaher et al., 2018). In addition, studies of mine roadways or tunnel mechanics investigated the deformation (Jia et al., 2014; Li et al., 2020), plastic zone distribution (Abdellah, 2017; Kong et al., 2022), and dynamic characteristics (Aydan, 2019) of surrounding rock caused by deep underground cavern excavation.

As for the openings in the subway station structure, the construction technology of subway station side wall openings, interface waterproofing, and deformation monitoring were reported. Sun et al. (2014) analyzed the stress characteristics of existing structure during opening construction of side wall and propounded corresponding countermeasures for the new and existing structure interfaces. Wu and Yan. (2017) introduced the key points of opening construction in subway station connecting aisle and discussed the waterproof treatments of interface. Liu et al. (2018) obtained the maximum vertical displacement generated by opening construction based on site monitoring. In terms of mechanical properties, some studies mainly involved the stress characteristics, seismic responses, and theoretical model analysis of shear wall with reserved opening. Nassernia and Showkati. (2017) examined the mechanical behaviors of tensile-braced mid-span steel plate shear walls with circular openings based on theoretical and experimental methods. Zhai et al. (2019) fabricated and tested six double-short-limb reinforced concrete shear walls with different reserved openings and studied the seismic performance under cyclic horizontal loads and constant vertical loads. Zabihi et al. (2021) investigated the behavior of a panel between two openings in shear walls subjected to monotonic loads. However, there have been few studies on the construction mechanical behaviors of side wall opening in mined excavation subway stations.

In this study, finite element numerical simulation, model test, and theoretical analysis are used to analyze the construction mechanical behaviors of side wall opening in an existing subway station, the Xuanwumen Station of Beijing Subway Line 4, which is a new transfer

project in China. The force-sensitive area of opening construction is clearly defined, and the ultimate opening span under different reinforcement measures is determined.

Engineering background

The Xuanwumen Station on Beijing Subway Line four is a mined excavation station with double layers and three spans. It has a buried depth of 8 m and is constructed by the pile-beam-arch method. The opening of the station is rectangular ($6\text{ m} \times 4.35\text{ m}$) and is located in the second-floor side wall (Figure 1).

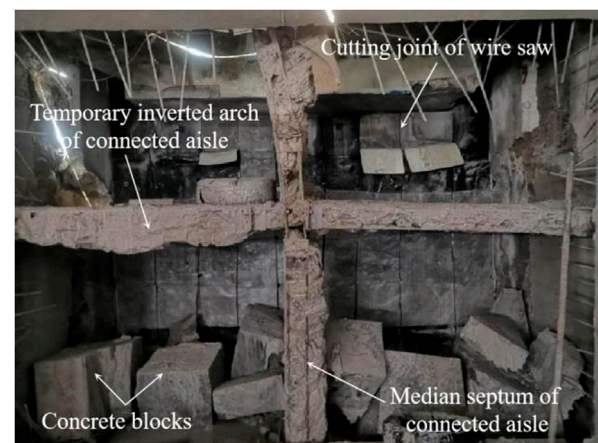


FIGURE 2
The construction site of opening demolition.

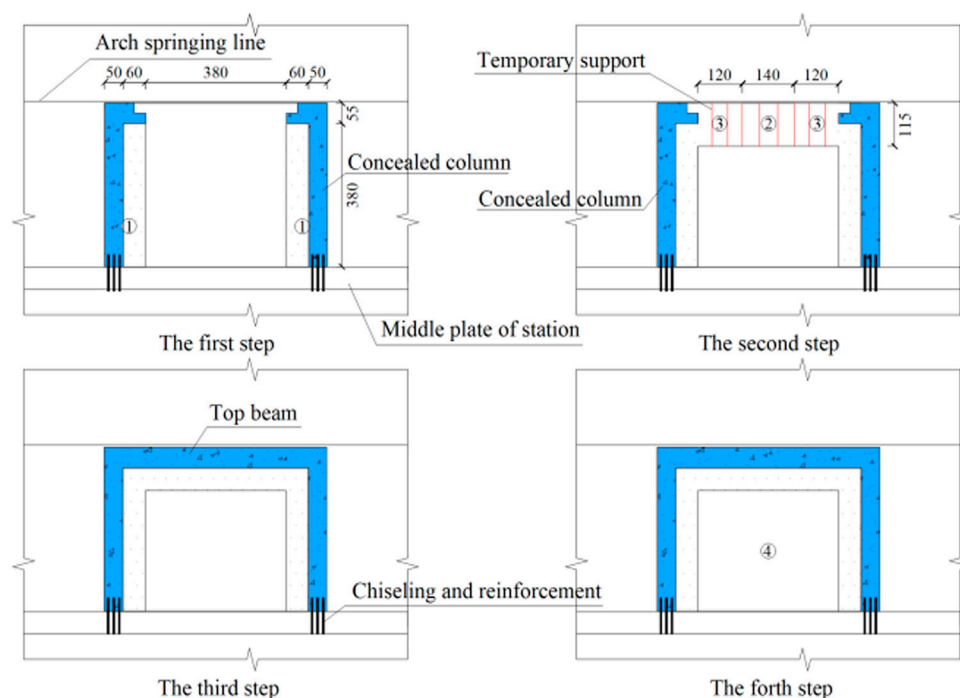


FIGURE 3
The processes of opening construction (cm).

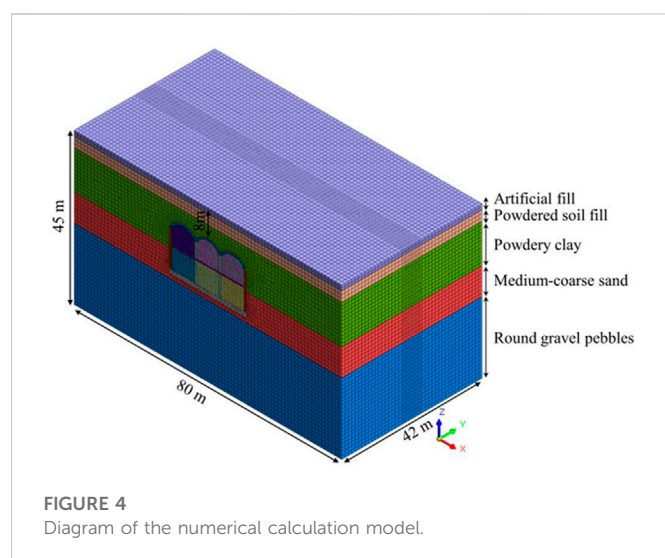


FIGURE 4
Diagram of the numerical calculation model.

The side wall opening can be demolished by a water drill and wire saw (Figure 2), with local parts demolished manually. During demolition, the reinforcement steel bars of existing structures at the side column and the top beam should be retained as much as possible. The interface between the new and old concrete should be chiseled and cleaned. In the construction process of the side wall opening (Figure 3), firstly, both sides ① are demolished, and concealed columns on both sides are poured. Secondly, areas ②

and ③ are demolished, and temporary supports are applied. Thirdly, after structure stabilization, the temporary supports are removed, and the top beam is poured. Finally, area ④ is demolished into blocks.

Numerical simulation of side wall opening

The finite element software MIDAS GTS (version 2018R1; MIDAS Information Technology Co., Ltd., Beijing, China) is used to build a three-dimensional numerical model (Figure 4). The strata are simulated using the Mohr-Coulomb model, and the station structure is simulated using the Drucker-Prager model, both with three-dimensional solid units. The concealed column and the top beam are simulated using the Drucker-Prager model, both with three-dimensional solid units. According to a previous geotechnical investigation report (Li, 2020), the mechanical parameters of the strata and station structure are obtained (Table 1).

The numerical model only considers the gravity field and does not consider the tectonic stress field. The top surface of the model is a free surface, and its front, rear, left, right, and bottom surfaces are all constrained to the displacement. Horizontal displacement constraints are imposed on the strata at the opening. The construction process of the model is shown in Figure 3. In the numerical simulation, passivating of wall elements in the existing structure, and activating of beam and column elements are used to simulate the opening construction.

TABLE 1 Mechanical parameters of the strata and station structure.

Stratum or structure	Volumetric weight γ (kN/m ³)	Elastic modulus E (MPa)	Poisson's ratio μ	Cohesive force c (kPa)	Internal friction angle φ (°)
Artificial fill (1.50 m)	17.50	7.00	0.35	10.00	12.00
Powdered soil fill (3.00 m)	20.00	20.00	0.30	30.00	12.00
Powdery clay (11.50 m)	20.00	20.00	0.30	35.00	15.00
Medium-coarse sand (8.00 m)	22.00	35.00	0.25	0.00	40.00
Round gravel pebbles (21.00 m)	25.00	45.00	0.22	0.00	45.00
Station top slab, bottom slab, medium slab, and side wall (C40 reinforced concrete)	24.00	32500.00	0.25	16700.00	51.00
Station column, concealed column, and top beam (C50 reinforced concrete)	26.00	34500.00	0.22	18900.00	51.00
Temporary support (I15 steel)	78.50	206000.00	0.30	–	–

TABLE 2 Model similarity relation and similarity ratio.

Physical quantity	Similarity relation and similarity ratio
Model scale l	$C_l = 40$
Displacement u	$C_u = C_l = 40$
Stress σ	$C_\sigma = C_l C_\gamma = 40$
Strain ϵ	$C_\epsilon = 1$
Volumetric weight γ	$C_\gamma = 1$
Elastic modulus E	$C_E = C_l C_\gamma = 40$
Poisson's ratio μ	$C_\mu = 1$
Cohesive forces c	$C_c = C_l C_\gamma = 40$
Internal friction angle φ	$C_\varphi = 1$

The station model section (75 cm × 57 cm × 37 cm) is made of organic glass (a polymer of methyl methacrylate). Its modulus of elasticity is 0.69 GPa (determined by uniaxial tensile test) and Poisson's ratio is 0.32. The width and height of the top, middle and bottom slabs and the side wall are designed using the geometric similarity ratio C_L . Its thickness is designed using the equivalent flexural stiffness [Eq. 1]:

$$E_m I_m = C_E E_P C_L^3 I_P \quad (1)$$

where E_m and I_m are the modulus of elasticity and cross-sectional moment of inertia of the prototype material, respectively; E_P and I_P are the modulus of elasticity and cross-sectional moment of inertia of the test material, respectively; and C_E and C_L are the similarity ratios of the modulus of elasticity and geometry, respectively. The thicknesses of the top, middle, bottom slabs and the side wall of the station are calculated to be 54.3, 23.4, 121.5, and 54.3 mm, respectively, with a column diameter of 8.1 mm.

Model test of side wall opening

Similarity ratio design

Based on the model chamber size and the relevant parameters of the test instrument, the geometric similarity ratio ($C_L = 40$) and the bulk density similarity ratio ($C_\gamma = 1$) are determined for the model tests (Liu et al., 2022). Using two these basic similarity ratios, the similarities of other parameters are derived through the similarity relations (Table 2).

Test material

The test stratum sample is proportioned with quartz sand and fine sand in a ratio of 1:3 (w/w). The mechanical parameters of the test stratum sample are determined by direct shear tests and converted to the corresponding mechanical parameters of the actual stratum through the similarity relations. The mechanical parameters of the test stratum sample are found to be close to those of the actual stratum (Table 3), which can meet the model test requirements (Xu et al., 2020; Qin et al., 2022; Zhang et al., 2022).

Test procedures and protocols

1) Uniaxial tensile test of organic glass specimens

Uniaxial tensile tests are carried out on organic glass specimens to verify whether the strength of organic glass after joining by hot melt adhesive (ethylene-vinyl acetate copolymer) is similar to that before it is cut. The specimens are designed according to the specification of the ASTM Committee on Standards (2003), with five specimens manufactured for each group. Specimens of group 1 is an organic glass whole specimen, and Specimens of group 2 is an organic glass specimen connected by hot melt adhesive. The width of hot melt adhesive in the specimens of group 2 is 2 mm. After sufficient cooling, the specimens are subjected to uniaxial tensile test. The stress-strain relationship of between the two groups of specimens is obtained by taking the mean values.

A universal testing machine is used as the loading device, which has a loading rate of 10 mm/min. The extensometer is fixed to the specimen at both ends of the gauge length (50 mm) to measure deformation. A 2-mm-thick polyvinyl chloride slab is applied to both ends of the specimen to prevent the breaking of its clamped

TABLE 3 Mechanical parameters of the test stratum sample.

	Volumetric weight (1:1)	Cohesive force (1:40)	Internal friction angle (1:1)
Actual stratum	17.5	35.0	15.0
Test stratum	17.5	44.0	14.9

end before the gauge length section. The device of uniaxial tensile test is shown in Figure 5. When comparing the stress–strain relationship curves of specimens in the two groups, similar trends are found (Figure 6). In both groups, the specimens show a linear increase in stress with increasing strain in the gauge length section, with a maximum error of 4.7%. This shows that the strength of organic glass specimens after joining by hot melt adhesive is relatively similar to that of uncut specimens.

2) Model test of side wall opening

The model tests are carried out in a visual model test chamber with pre-defined openings. The model chamber is made of steel and organic glass. It measures 1.5 m × 0.8 m × 1.2 m with a reserved opening of 21 cm × 17 cm. The station structure measures 75 cm × 57 mm × 37 cm and is made of organic glass, with a reserved opening in the side wall of 15 cm × 11 cm. Pre-cut organic glass blocks are used to seal the openings, leaving a 5 mm gap between the blocks. The strength of the organic glass specimen after connection by hot melt adhesive connection is relatively similar to that of the uncut specimen, and the hot melt adhesive softens quickly when exposed to heat. Therefore, the gaps between the blocks are filled with hot melt adhesive to facilitate the subsequent tests. The model test device of side wall opening is shown in Figure 7.

The model tests are conducted to measure the vertical displacement at the top of the side wall opening and the variation in the principal stresses around the opening. Specifically, strain

rosettes are placed around the opening. When the model chamber is filled with the stratum sample to the design position, the station model is placed into the chamber, with its side wall opening aligned to the model chamber opening. Settlement bars are placed at the top slab above the side wall opening and connected to a displacement meter. Subsequently, the model chamber is filled with the remaining stratum sample. The locations of the measurement points for displacement and strain are shown in Figure 8.

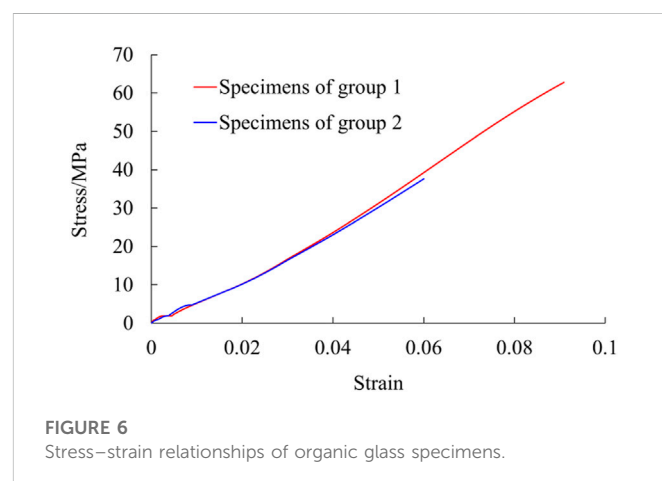
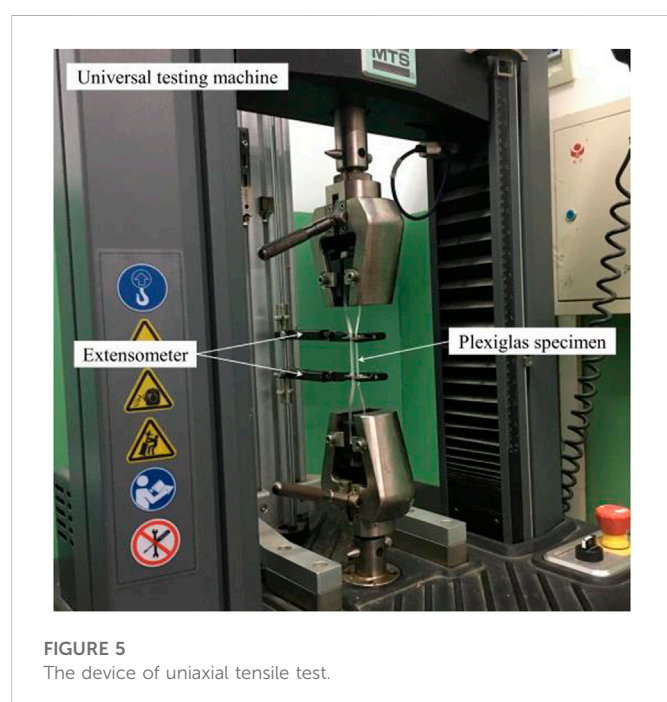
The test procedure involves cutting the hot melt adhesive between organic glass blocks in the side wall opening using an electric heating cutter (Figure 9). The cutter has a 3-mm-thick blade and can reach a temperature of 500°C. The hot melt adhesive is melted at a high temperature and then slowly cut. The overall cutting speed is maintained at 1 mm/s to minimize disturbance to the existing structure. After cutting, the unloaded glass is removed and let stand for a while. Subsequent cutting operations can be carried out when the readings in the data acquisition system are less variable. In this way, the procedure of block demolition in the opening construction of the actual project is realized.

Results and analysis

The model test results are converted into actual displacement and principal stress values through the similarity relations. The test results are then compared with the displacement and stress patterns with construction steps in numerical simulations.

1) Deformation characteristics of the existing structures in opening construction

The stress state after the completion of station construction by the pile-beam-arch method is used as the initial stress state for side wall



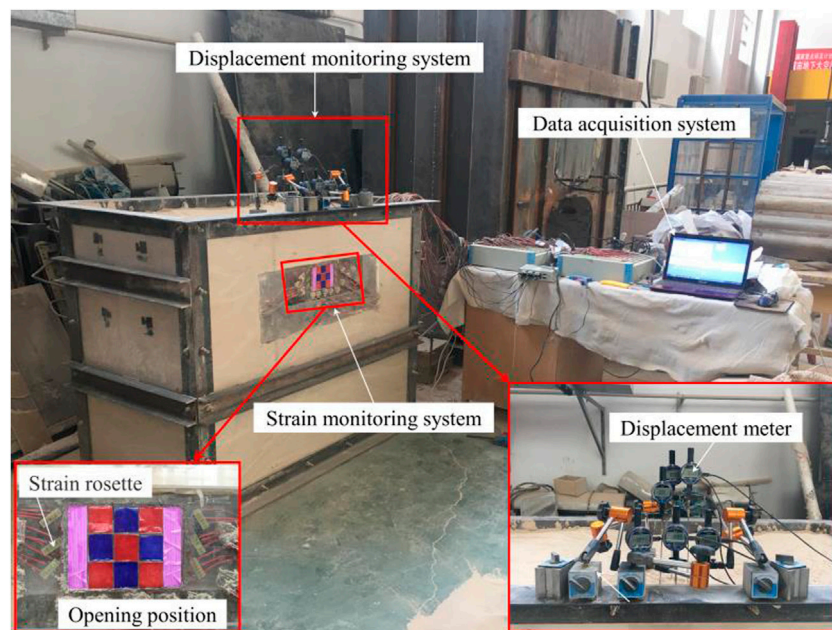


FIGURE 7
The model test device of side wall opening.

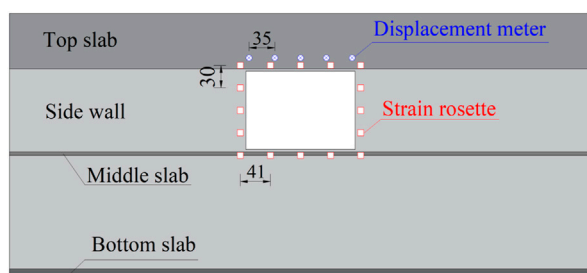


FIGURE 8
Layout of displacement and strain measurement points (mm).

opening construction. Figure 10 shows the vertical and horizontal deformations of the existing station structure. Subsidence occurs at the top of the opening, with the largest value at the mid-span of the top beam (1.58 mm). The subsidence gradually expands to the upper side of the vault, while its influence is diminished. There is a certain uplift at the bottom of the opening (0.97 mm), and the impact extends to the negative second floor.

After the side wall opening is demolished, the station shows an inward transverse deformation at the top of the top beam (−1.79 mm), along with an outward transverse deformation at the side wall (0.10 mm). According to the relevant regulations and evaluation opinions of Beijing Subway Operation Co., Ltd. On train safety operation, when the side wall structure is demolished, the vertical and transverse allowable deformations of the existing main structure and track are 3 mm (Yuan, 2019). Therefore, the deformations of the station caused by side wall

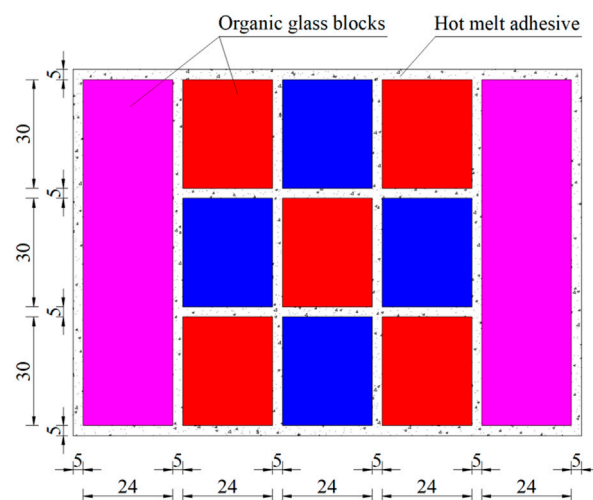


FIGURE 9
Relative position relation between organic glass blocks and hot melt adhesive (mm).

opening demolition are relatively small, and the deformations of the station and the track are in a safe state.

During opening construction, the subsidence at the top of the opening is characterized by three stages (Figure 11). In the first stage, when the two sides are demolished and the concealed columns are poured, the deformation increment is minimal (−0.17 mm). In the second stage, when the top areas are demolished and the top beam is poured, the deformation increment reaches the highest level

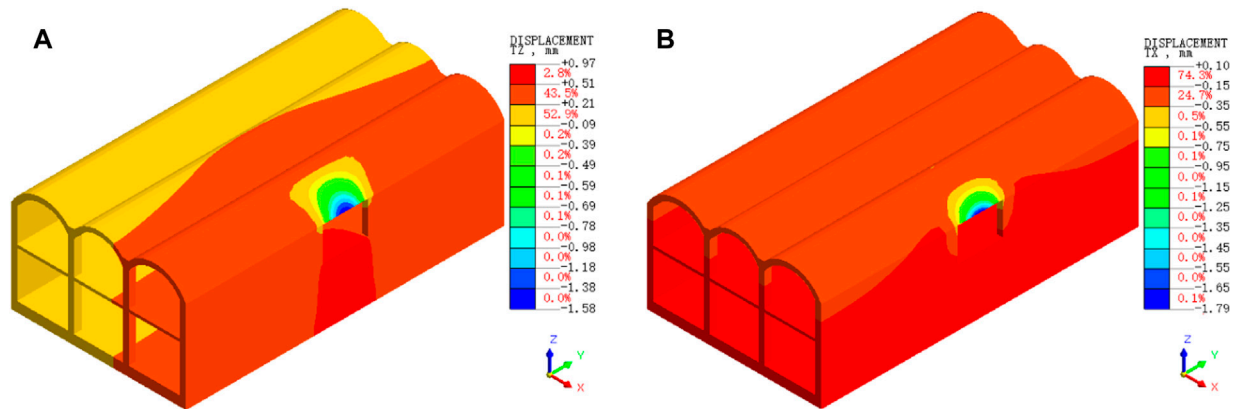


FIGURE 10
Vertical and horizontal deformations of existing station structure (mm): (A) Vertical deformation and (B) Horizontal deformation.

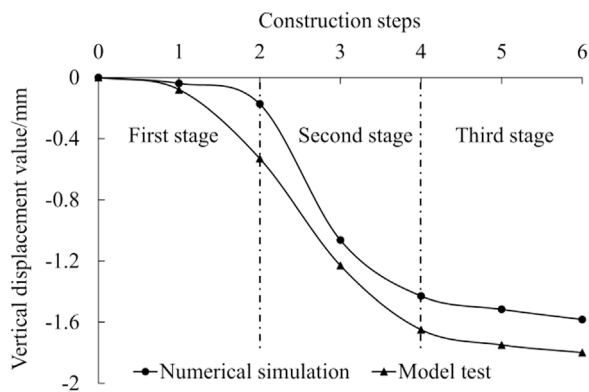


FIGURE 11
The maximum vertical displacement of existing side wall structure during opening construction.

(−1.26 mm). In the third stage, when the remaining rectangular areas are demolished, the deformation value is unchanged (−0.15 mm).

2) Stress characteristics of the existing structures in opening construction

The stress distribution of the side wall after demolition is shown in Figure 12. The first principal stress is largest at the mid-span of the top beam (1.82 MPa), and the stress increment caused by opening construction is 2.14 MPa, which indicates that the side wall below the opening should be strengthened. The third principal stress (−6.19 MPa) is concentrated at the top corner of the opening, and the stress increment caused by opening construction is −4.62 MPa. Despite the large value, it is still in the safe range. However, according to the regulations and evaluation opinions of the Beijing Subway Operation Co., Ltd., the stress change of the existing main structure should be less than 10% when demolishing the side wall structure (Yuan, 2019). Collectively, the results indicate that the stress increment caused by opening demolition has exceeded the allowable

range, and can cause cracking of the concrete structure. Before demolition, the surrounding area of the opening should be strengthened, or the structural stiffness of the concealed columns and the top beams should be improved.

The model test results are consistent with the stress patterns based on the numerical simulations, and the principal stress around the side wall openings is characterized by three stages (Figure 13). In the first stage, when the two sides are demolished and the concealed columns are poured, the stress increment is relatively small (0.43 and −1.60 MPa). In the second stage, when the rectangular areas are demolished and the top beams are poured, the stress increment is highest (1.51 and −2.85 MPa). In the third stage, when the remaining rectangular areas are demolished, the stress value is unchanged (0.02 and −0.06 MPa).

After the opening construction, the envelope curves of the principal stresses are shown in Figure 14. Although the model test results are slightly higher than the numerical simulation results, the distribution patterns of the principal stresses are consistent.

Comparing the numerical simulation and model test results reveal consistent variation in the distribution patterns of displacement and stress around the side wall opening. The first principal stress is concentrated at the mid-span of the top and the bottom, with higher values at the top (1.82 MPa) than at the bottom (0.48 MPa). The third principal stress is concentrated at the corners of the top and bottom, with higher values at the top (−6.19 MPa) than at the bottom (−3.75 MPa). The top mid-span and corners of the opening are force-sensitive positions during construction.

Theoretical analysis of side wall opening

The above-mentioned opening construction problem can be approximated as an excavation problem for the strata. Strata excavation can be considered as the first “opening construction”. The vertical and horizontal stresses around the station structure are used to calculate the load, i.e., the surrounding rock pressure exerted on the station structure. Side wall excavation can be considered as the second “opening construction”. The total vertical stress and the total horizontal stress are used to calculate the state of stress distribution around

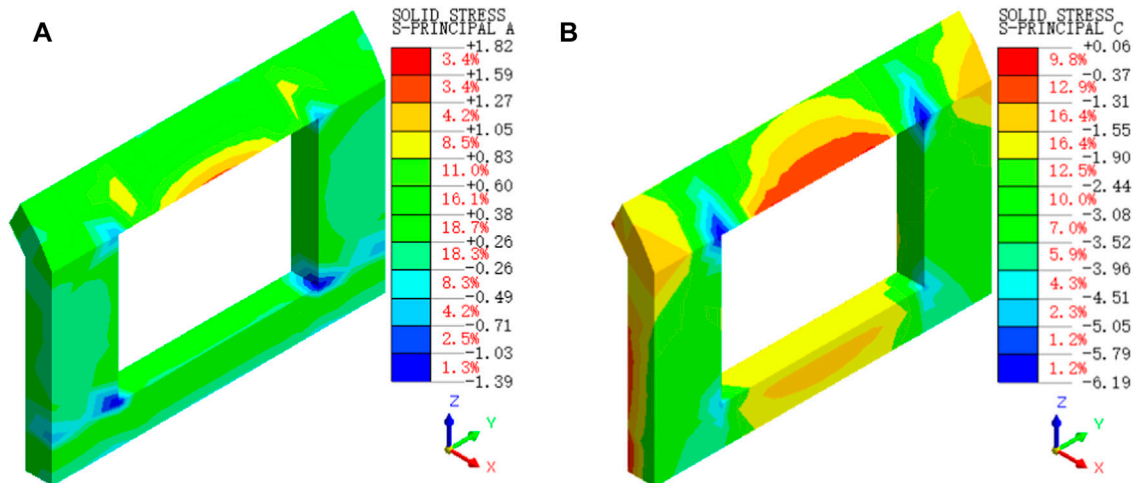


FIGURE 12
Principal stress distribution around the side wall opening (MPa): (A) First principal stress and (B) Third principal stress.

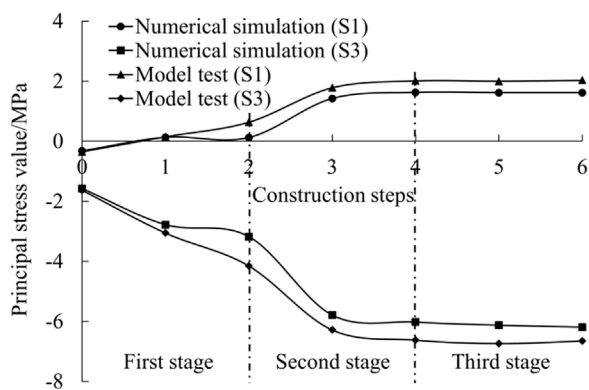


FIGURE 13
Variation in the principal stresses of existing side wall structure during opening construction.

the opening. The theoretical analysis process is illustrated in Figure 15.

Basic assumptions

- 1) The station excavated in the strata is a rectangular structure.
- 2) The side wall of the station structure is considered infinite body.
- 3) The materials of strata and station structure are continuous, uniform, and isotropic.

First-step opening

The excavated station structure is subjected to vertical and horizontal stresses exerted by the strata (Figure 16). The vertical stress ($P_z = -156.25$ kPa) is obtained by Eq. 2, and the horizontal stress ($P_x = -67.19$ kPa) is obtained by Eq. 3.

$$P_z = \sum_{i=1}^n \gamma_i h_i \quad (2)$$

$$P_x = \sum_{i=1}^n \{[\mu_i / (1 - \mu_i)] \gamma_i h_i\} \quad (3)$$

where γ_i is the volumetric weight of each stratum above the top slab of the station structure, h_i is the corresponding stratum thickness, μ_i is the corresponding Poisson's ratio, and n is 3. The relevant parameters are given in Table 1.

Based on a complex function solution to the orifice problem (Sa, 1958), the stress equations for the rectangular orifice perimeter is shown in Eq. 4, Eq. 5, Eq. 6.

$$\sigma_\theta = \frac{4(AC + BD)}{C^2 + D^2} p_x + \frac{4(A'C' + B'D')}{C'^2 + D'^2} p_z \quad (4)$$

$$\sigma_\rho = 0 \quad (5)$$

$$\tau_{\rho\theta} = 0 \quad (6)$$

where θ is the angle around the opening relative to the midline of the section ($\theta = 0^\circ - 360^\circ$);

$$A = 14 - 24 \cos 2\theta - 7 \cos 4\theta,$$

$$A' = 14 + 24 \cos 2\theta - 7 \cos 4\theta;$$

$$B = -24 \cos 2\theta - 7 \sin 4\theta,$$

$$B' = 24 \cos 2\theta - 7 \sin 4\theta;$$

$$C = 56 + 28 \cos 4\theta,$$

$$C' = 56 + 28 \cos 4\theta; \text{ and}$$

$$D = 28 \sin 4\theta,$$

$$D' = 28 \sin 4\theta.$$

The stress on the station structure is obtained by taking the corresponding values θ . The stress at a 45° angle to the midline of the section ($\theta = 45^\circ$) is chosen as the surrounding rock pressure on the side wall of the station structure ($\sigma_{45^\circ} = -652.53$ kPa; Figure 17).

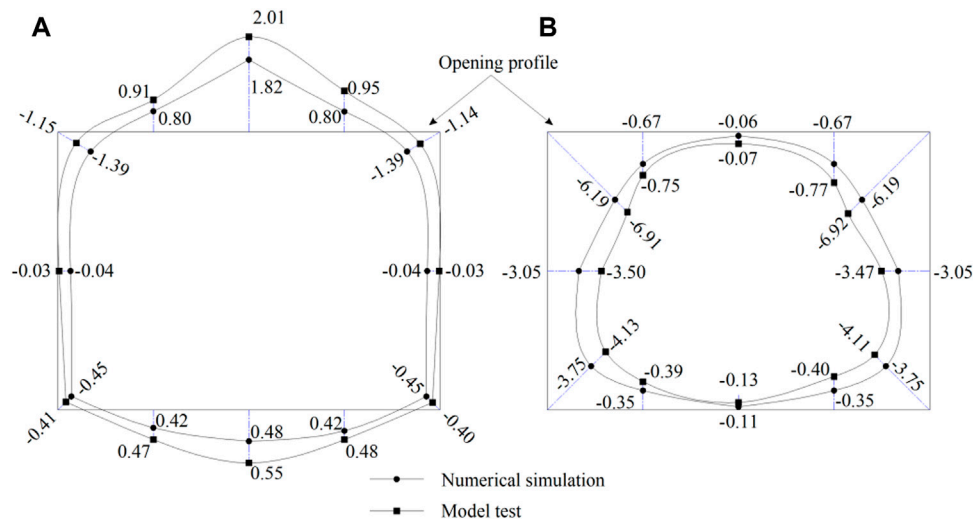


FIGURE 14
Envelope diagrams of the principal stresses around the side wall opening (MPa): (A) First principal stress and (B) Third principal stress.

Second-step opening

The side wall opening in the station structure is subjected to the surrounding rock pressure exerted by the strata and the self-weight stress of the side wall (Figure 18). The surrounding rock pressure has been calculated for the first-step opening ($\sigma_{45^\circ} = -652.53$ kPa). The self-weight stress ($\sigma_{cz} = -360$ kPa) is obtained by Eq. 2, where $\gamma = 24$ kN/m³, $h = 15$ m, and $n = 1$. The sum of the surrounding rock pressure and the self-weight stress ($\sigma_{45^\circ} + \sigma_{cz} = -1052.53$ kPa) is taken as the total vertical stress (P_z') of the second “opening construction”. The total horizontal stress (P_x') is obtained by Eq. 3, where $\mu = 0.25$ and $n = 1$.

The stress around the opening (σ_θ) is obtained by Eq. 4, Eq. 5, Eq. 6. Then, the stress distribution around the opening obtained by the theoretical analysis is compared with that obtained by the numerical simulation (Figure 19). Both methods reveal similar stress distribution patterns, but the stress values obtained from the theoretical analysis are lower. This is mainly because the equations used for the theoretical analysis are applicable to the “opening construction” in the strata, whereas

the second “opening construction” is carried out in the station structure. In addition, it is possible that the first “opening construction” has resulted in a rectangular structure, whereas the actual structure is vaulted.

Ultimate opening span

Without reinforcement

The concealed columns and top beams contribute to the reinforcement of the existing structure around the side wall opening. However, it is easy to find that, at a certain span, the displacement and stress are within the safe range, even without reinforcement. The construction period and cost can be considerably reduced if the concealed columns and top beams are not poured. A comparative analysis of five opening spans (4.35, 5.00, 5.50, 6.00, and 8.00 m) is carried out with the opening height being kept constant (4.35 m). Using the

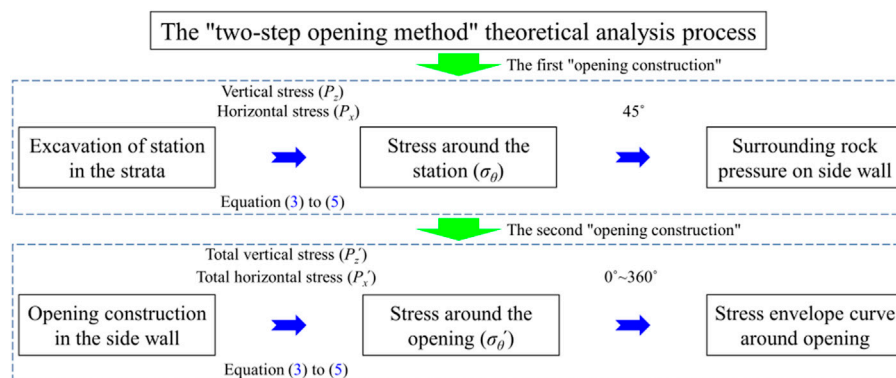


FIGURE 15
Theoretical analysis process of the “two-step opening” method.

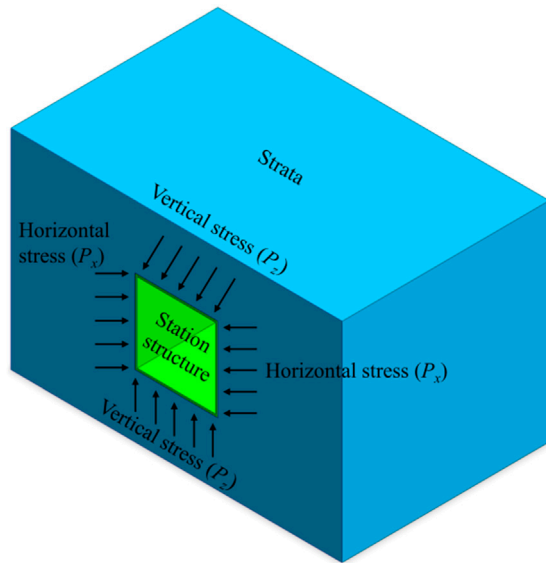


FIGURE 16
Stress distribution in the first "opening construction".

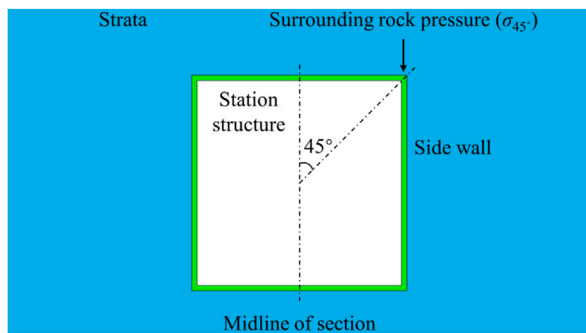


FIGURE 17
Schematic diagram of surrounding rock pressure on the side wall.

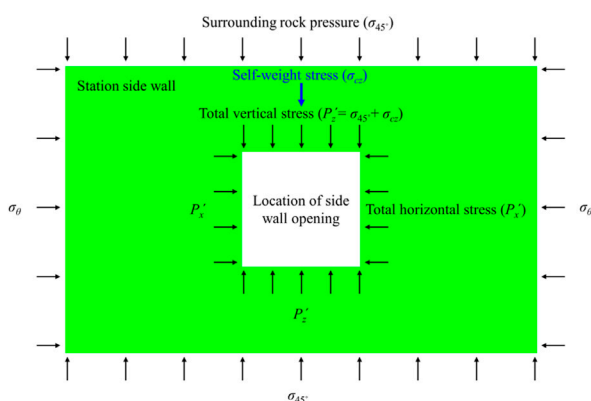


FIGURE 18
Stress distribution in the second "opening construction".

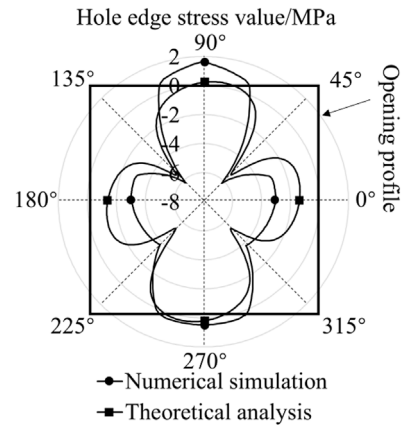


FIGURE 19
Stress distribution around the side wall opening.

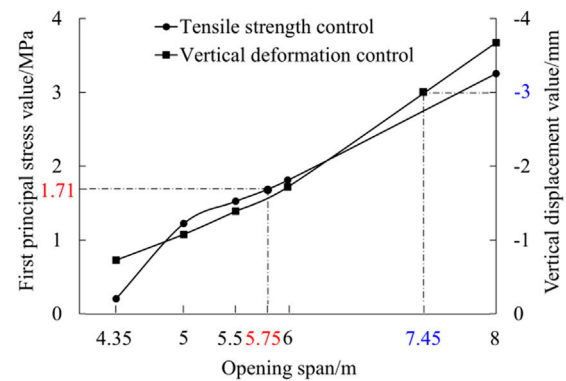


FIGURE 20
Ultimate opening span under allowable conditions.

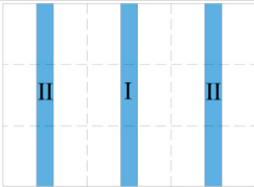
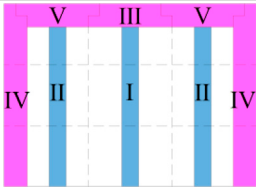
allowable vertical deformation (-3 mm) and the design tensile strength of C40 concrete (1.71 MPa), the maximum opening spans that the structure can withstand without strengthening measures are 7.45 and 5.75 m, respectively (Figure 20). The minimum value of 5.75 m is taken as the ultimate opening span.

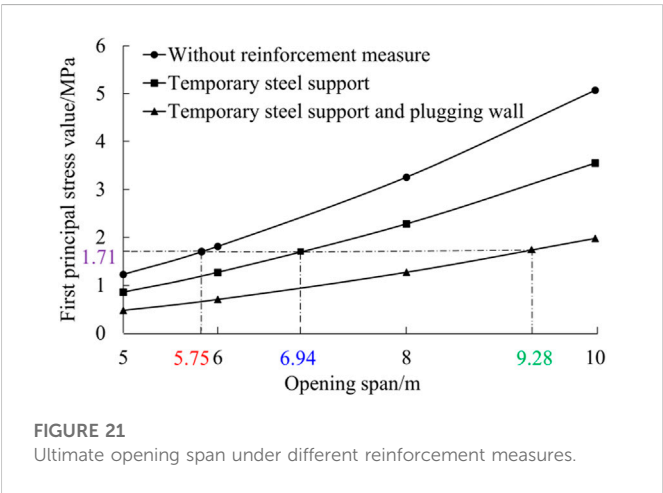
Under reinforcement

When the opening span is greater than 5.75 m, two construction control measures are proposed: temporary steel supports alone and combined with a plugging wall (Table 4). With the opening height being kept constant (4.35 m), four opening spans (5 , 6 , 8 , and 10 m) are adopted to analyze the corresponding ultimate opening spans under different reinforcement measures.

The first principal stress as a major influencing factor is taken as the control condition. The ultimate opening span under reinforcement with temporary steel supports is 6.94 m, and that under reinforcement with a combination of temporary steel supports and a plugging wall is 9.28 m (Figure 21).

TABLE 4 Description of opening construction control measures.

Control measure	Temporary steel supports	Temporary steel supports with a plugging wall
Schematic		
Description of demolition procedure and control measures	1 Demolish the areas on both sides in blocks and apply temporary steel support II	1 Demolish the areas on both sides in blocks, apply temporary steel support II, and pour column IV and beam V
	2 Demolished the middle area in blocks and apply temporary steel support I; and	2 Demolish the middle area in blocks, apply temporary steel support I, and pour beam III; and
	3 Removed temporary steel supports after stabilization of the structure	3 Remove temporary steel supports after stabilization of the structure



Conclusion

In this study, the mechanical properties of existing subway station structure are derived from the construction of side wall opening. The following conclusions are reached based on numerical simulations, model tests, and theoretical analysis.

- 1) During the opening construction, the variation in displacements and stresses is characterized by three stages: slow growth, rapid growth, and almost stable. Tensile stresses are concentrated at the mid-span and compressive stresses are concentrated at the corners. In practical engineering, attentions should be paid to the rapid growth stage and the stress concentration in the top mid-span and the corners of opening.
- 2) There is rapid growth of displacements and stresses when the uppermost layer of the structure is demolished. The opening should be strengthened at this location and even at the top beam before construction.
- 3) During the opening construction, the displacement of the existing structure is less than 3 mm and under the safe criteria, but the stress increment of the structure exceeds the control criteria, indicating that the stress variation should receive attention during construction.

- 4) According to the variation characteristics of displacement and stress during the opening construction, it is seen that the sensitive areas of the structure are the top mid-span (maximum vertical displacement and first principal stress) and the corners (maximum third principal stress).
- 5) The “two-step opening” method can be used for opening analysis of side walls in underground space structures according to the study of this paper.
- 6) An increase in the opening span can result in a sharp increase in the tensile stresses at the mid-span. The ultimate opening span without reinforcement measures is 5.75 m; temporary steel support reinforcement measures are suggested to be conducted, when the opening span is between 5.75 m–6.94 m; reinforcement measures containing temporary steel supports and plugging walls are suggested to be implemented, when the opening span is between 6.94 m–9.28 m.

Data availability statement

The original contributions presented in the study are included in the article/supplementary material, further inquiries can be directed to the corresponding authors.

Author contributions

ZH and HM wrote the manuscript. ZL revised the manuscript. LZ conceived the experiments, and contributed to the data interpretation. All authors have read and agreed to the published version of the manuscript.

Funding

The Young Talent Program of the Hebei Provincial Education Department (BJ2019009), the National Natural Science Foundation of China (52178392), the Central Leading Local Science and Technology Development Fund Program (226Z5403G), and the Excellent Youth Program of the Hebei Provincial Natural Science Foundation (E2021210025), China.

Conflict of interest

Author LZ was employed by the company Shijiazhuang State-owned Capital Investment and Operation Group Co., Ltd, China.

The remaining authors declare that the research was conducted in the absence of any commercial or financial relationships that could be construed as a potential conflict of interest.

References

- Abdellah, W. R. (2017). Serviceability analysis of deep underground openings driven in jointed-rock. *Int. J. Min. Sci. Technol.* 27 (6), 1019–1024. doi:10.1016/j.ijmst.2017.06.024
- Ahmed, I. E., Hassan, M. H., and Mohammed, A. E. S. A. (2020). Effect of longitudinal opening on the structural behavior of reinforced high-strength self-compacted concrete deep beams. *Case Stud. Constr. Mat.* 12, e00348. doi:10.1016/j.cscm.2020.e00348
- ASTM Committee on Standards (2003). *ASTM standard D638 standard test method for tensile properties of plastics*. West Conshohocken, PA, USA: ASTM International. doi:10.1520/D0638-10.1
- Aydan, O. (2019). Dynamic response of support systems during excavation of underground openings. *J. Rock Mech. Geotech. Eng.* 11, 954–964. doi:10.1016/j.jrmge.2019.06.002
- Jia, P., Zhu, W. C., and Zhang, S. C. (2014). Effect of heterogeneity on occurrence of zonal disintegration around deep underground openings. *Int. J. Min. Sci. Technol.* 24 (6), 859–864. doi:10.1016/j.ijmst.2014.10.020
- Kong, C., Wang, H. Y., Zhao, K., and Gao, X. Q. (2022). Numerical simulation of long-term deterioration of rock mass supported by shotcrete lining. *Front. Earth Sci.* 10, 891084. doi:10.3389/feart.2022.891084
- Li, A., Liu, Y., Dai, F., Liu, K., and Wei, M. D. (2020). Continuum analysis of the structurally controlled displacements for large-scale underground caverns in bedded rock masses. *Tunn. Undergr. Sp. Technol.* 97, 103288. doi:10.1016/j.tust.2020.103288
- Li, R. Z. (2020). Three-dimensional seismic response analysis of arched subway station structure with side wall opening. *Def. Transp. Eng. Technol.* 18 (2), 26–29. (in Chinese). doi:10.13219/j.ggyat.2020.02.007
- Liu, N. F., Li, N., Li, G. F., Song, Z. P., and Wang, S. J. (2022). Method for evaluating the equivalent thermal conductivity of a freezing rock mass containing systematic fractures. *Rock Mech. Rock Eng.* 55 (12), 7333–7355. doi:10.1007/s00603-022-03038-9
- Liu, S. H., Liu, J. W., and Zhang, D. X. (2018). Field measurement and analysis of the influence of break construction on the structure of existing subway stations. *Munic. Technol.* 36 (5), 105–108 [in Chinese].
- Moon, W. C., Lau, T. L., and Puay, H. T. (2020). Experimental investigations of tsunami loading on internal wall of a building with various openings and wall configurations. *Coast. Eng.* 158, 103691. doi:10.1016/j.coastaleng.2020.103691
- Nassernia, S., and Showkati, H. (2017). Experimental study of opening effects on mid-span steel plate shear walls. *J. Constr. Steel Res.* 137, 8–18. doi:10.1016/j.jcsr.2017.05.021
- Qin, Y. W., Lai, J. X., Gao, G. Q., Yang, T., Zan, W. B., Feng, Z. H., et al. (2022). Failure analysis and countermeasures of a tunnel constructed in loose granular stratum by shallow tunnelling method. *Eng. Fail. Anal.* 141, 106667. doi:10.1016/j.engfailanal.2022.106667
- Sa, V. (1958). *Stress concentration near the hole*. Beijing: Sci. Press. (in Chinese).
- Saad-Eldeen, S., Garbatov, Y., and Soares, C. G. (2018). Structural capacity of plates and stiffened panels of different materials with opening. *Ocean. Eng.* 1671, 45–54. doi:10.1016/j.oceaneng.2018.08.013
- Sun, L. Z., Chen, H., Luan, W. W., Xing, W., and Zhao, W. (2014). Study of structure linking technology between new and old subway stations. *J. Undergr. Sp. Eng.* 10 (S1), 1673–1678 [in Chinese].
- Wallace, M. I., and Ng, K. C. (2016). Development and application of underground space use in Hong Kong. *Tunn. Undergr. Sp. Technol.* 55, 257–279. doi:10.1016/j.tust.2015.11.024
- Wu, S. P., and Yan, A. (2017). Construction technology for connecting subway entrances and new projects. *Constr. Technol.* 46 (12), 53–56. (in Chinese). doi:10.7672/sjgs2017120053
- Xu, P., Wu, Y. M., Wang, Z. J., and Huang, L. (2020). Distribution laws of freeze-thaw cycles and unsaturated concrete experiments in cold-region tunnels. *Cold Reg. Sci. Technol.* 172, 102985. doi:10.1016/j.coldregions.2019.102985
- Yin, C., Li, H. R., Che, F., Li, Y., Hu, Z. N., and Liu, D. (2020). Susceptibility mapping and zoning of highway landslide disasters in China. *Plos One* 15 (9), 0235780. doi:10.1371/journal.pone.0235780
- Yin, C., and Zhang, J. L. (2018). Hazard regionalization of debris-flow disasters along highways in China. *Nat. Hazards* 91 (1), 129–147. doi:10.1007/s11069-018-3229-8
- Yuan, C. Y. (2019). Safety analysis of side wall opening at existing subway station. *Munic. Eng. Technol.* 37 (2), 106–109 [in Chinese].
- Zabihi, S., Mamazizi, A., and Ghanbari-Ghazijahani, T. (2021). A study on mid-panel of steel shear-walls with dual openings. *J. Constr. Steel Res.* 186, 106869. doi:10.1016/j.jcsr.2021.106869
- Zaher, O. F., Yossef, N. M., El-Boghdadi, M. H., and Dabaon, M. A. (2018). Structural behaviour of arched steel beams with cellular openings. *J. Constr. Steel Res.* 148, 756–767. doi:10.1016/j.jcsr.2018.06.029
- Zhai, X. M., Zhang, X. S., Cao, C., and Hu, W. B. (2019). Study on seismic performance of precast fabricated RC shear wall with opening filling. *Constr. Build. Mat.* 214, 539–556. doi:10.1016/j.conbuildmat.2019.04.070
- Zhang, Y. W., Fan, S. Y., Yang, D. H., and Zhou, F. (2022). Investigation about variation law of frost heave force of seasonal cold region tunnels: A case study. *Front. Earth Sci.* 9, 806843. doi:10.3389/feart.2021.806843
- Zhang, Y. W., Song, Z. P., Weng, X. L., and Xie, Y. L. (2019). A new soil-water characteristic curve model for unsaturated loess based on wetting-induced pore deformation. *Geofluids* 2019, 1–14. doi:10.1155/2019/1672418
- Zhao, J., and Künzli, O. (2016). An introduction to connectivity concept and an example of physical connectivity evaluation for underground space. *Tunn. Undergr. Sp. Technol.* 55, 205–213. doi:10.1016/j.tust.2015.12.017

Publisher's note

All claims expressed in this article are solely those of the authors and do not necessarily represent those of their affiliated organizations, or those of the publisher, the editors and the reviewers. Any product that may be evaluated in this article, or claim that may be made by its manufacturer, is not guaranteed or endorsed by the publisher.



OPEN ACCESS

EDITED BY

Zhanping Song,
Xi'an University of Architecture and
Technology, China

REVIEWED BY

Zhihua Yao,
Air Force Engineering University, China
Tugen Feng,
Hohai University, China

*CORRESPONDENCE

Yang Min,
✉ yangmin0069@126.com

SPECIALTY SECTION

This article was submitted to
Environmental Informatics and Remote
Sensing,
a section of the journal
Frontiers in Earth Science

RECEIVED 12 December 2022

ACCEPTED 16 January 2023

PUBLISHED 01 February 2023

CITATION

Hongru L, Min Y and Jiaqi L (2023),
Influence of filling sequence of concrete
faced rockfill dam on deformation of
squeezed sidewall and dam.
Front. Earth Sci. 11:1122153.
doi: 10.3389/feart.2023.1122153

COPYRIGHT

© 2023 Hongru, Min and Jiaqi. This is an
open-access article distributed under the
terms of the [Creative Commons
Attribution License \(CC BY\)](https://creativecommons.org/licenses/by/4.0/). The use,
distribution or reproduction in other
forums is permitted, provided the original
author(s) and the copyright owner(s) are
credited and that the original publication in
this journal is cited, in accordance with
accepted academic practice. No use,
distribution or reproduction is permitted
which does not comply with these terms.

Influence of filling sequence of concrete faced rockfill dam on deformation of squeezed sidewall and dam

Li Hongru^{1,2}, Yang Min^{1,2*} and Li Jiaqi^{1,2}

¹Institute of Geotechnical Engineering, Xi'an University of Technology, Xi'an, China, ²Loess Soil Mechanics and Engineering Key Laboratory of Shaanxi Province, Xi'an, China

During construction of concrete faced rockfill dam (CFRD), the extrusion-sidewall will be protruding or deficiency under normal. Before panel construction, local slope cutting should be taken for the squeezed side wall or supplementary filling measures should be taken after excavating the squeezed side wall, which will affect the mechanical deformation of the panel. According to the monitoring data of concrete-faced rockfill dams of some hydro-electric station in Hubei Province, the three-dimensional finite element analysis method is used to simulate the original filling sequence process of the concrete face rockfill dam. By comparing the difference between the monitoring data and the calculation results, the deformation law of the extrusion side wall and the dam is obtained, which verifies the rationality of the three-dimensional simulation analysis of the dam. The characteristic values of settlement and horizontal displacement obtained from dam monitoring and numerical calculation are compared with those of other high concrete faced rockfill dams. The characteristic values of this dam are close to those of general concrete faced rockfill dams. The deformation law of extrusion side wall and dam under two optimization schemes with different filling sequence is studied. It is found that if conditions permit, the upstream should be filled first and then the downstream to reduce the deformation of extrusion side wall to the upstream.

KEYWORDS

extruded wall, monitoring data, numerical simulation, deformation law, filling sequence

1 Introduction

The construction technology of extruding side wall (abbreviated as extruded-sidewall) is a new construction method of concrete faced rockfill dam (CFRD), which especially reduces the over-filling repair process of cushion material, reduces labor intensity and saves labor. No need for traditional construction techniques in slope leveling, slope rolling, sand blasting slurry to stabilize slope. Because of the advantages of improving the rolling quality of cushion materials, speeding up the construction progress, and protecting the surface of cushion materials from rain erosion during construction, this technology has been adopted in high face rockfill dam projects such as Shuibuya, Gongbo Gorge, Jishi Gorge, and Bakun, Malaysia (Jiang 1997; Galvao et al., 1999; Li 2011). Although the construction of the extrusion-sidewall has many advantages and has been widely used (Luo et al., 2005), the application of the extrusion-sidewall in the panel dam is still very short, and people are not very clear about many aspects of its problems. For example, because the elastic modulus of the side wall material is much larger than that of the rockfill material, a certain degree of stress concentration may occur on the extrusion-sidewall.

The sidewall concrete is different from the conventional concrete and rockfill. It is a special structural material with rapid setting, low elastic modulus, and plastic damage. As a semi-elastic layer sandwiched between the concrete panel and the rockfill, how about its stress and strain, which is not clear at present. At the same time, since the extrusion-sidewall is constructed layer by layer along the dam axis, there will be more or less staggered layers. From the perspective of contact friction, the staggered layers of the upper and lower extrusion-sidewalls will increase the deformation of the extrusion-sidewall towards the upstream, and also increase the constraint effect on the panel (Peng et al., 2008; Zhou et al., 2008). In the past, the first thing people pay attention to is the stress deformation and stability of the CFRD (Sun et al., 2006; Deng et al., 2008; Liu et al., 2010; Li and Yang, 2012; Liu and Liu, 2013; Yang et al., 2014; Zhang et al., 2022), followed by the contact between the face slab and the extrusion-sidewall (Zhang et al., 2005; Hou et al., 2008; Zou et al., 2009) and the stress and strain of the concrete face slab (Cheng et al., 2011; Deng et al., 2015; Zhou et al., 2015; Liu et al., 2022), and little attention is paid to the factors affecting the extrusion-sidewall and the deformation law (Pan et al., 2014; Hu et al., 2016).

The extrusion-sidewall is constructed at the same time with the dam. Due to the influence of dam deformation and the discontinuity between layers caused by the layered construction of the extrusion-sidewall, many concrete faced rockfill dams have to cut and fill the extrusion-sidewall before the construction of the dam is completed and the panel is not constructed, resulting in a large difference between the actual size of the extrusion-sidewall and the design size, which affects the stress and deformation of the panel. In order to reduce the cutting and filling of the extrusion-sidewall, it is generally necessary to reserve a certain amount of space for extruding sidewall to deform upstream during dam construction to meet the design requirements of the extrusion-sidewall. In the case of the dam type and filler are determined, it is worth paying attention to the study of the influence of the construction sequence on the deformation of the layered discontinuous extrusion-sidewall.

This paper strictly simulates the actual construction process through the FEM calculation method based on the actual construction of the CFRD of a hydropower station in Hubei Province. It compares the horizontal displacement and settlement deformation monitored during the actual filling process of the dam with the numerical simulation results, which verifies the scientific nature of the numerical simulation method, the rationality of material parameter selection, and the correctness of the results. On this basis, the deformation law of the extrusion side wall of the CFRD of the hydropower station under different construction schemes is studied, which provides a reference for the construction scheme design of the same type of dam.

2 Project overview

The dam of a hydropower station in Hubei is a reinforced the CFRD. The length of the dam crest axis is 465.00 m, the width of the dam crest is 10 m, the elevation of the dam crest is 524.30 m, the foundation surface elevation of the riverbed toe slab is 366.00 m, and the maximum dam height is 158.3 m. The upstream slope ratio of the dam is 1:1.4, and the downstream comprehensive slope ratio is 1:1.44. The thickness of the upper part of the reinforced concrete panel is 30 cm, and the thickness of the bottom is 84 cm. The dam is divided



FIGURE 1
The construction of concrete face rockfill dam.

into primary and secondary rockfill areas, and the downstream dam toe is equipped with a filter rockfill prism. The dam under construction is shown in Figure 1, and the material partition is shown in Figure 2.

The total filling amount of the dam is about 7 million m³, of which more than 600,000 m³ is weakly weathered sand shale excavated from the spillway, and 400,000 m³ is natural gravel of riverbed sand field. The rock material for constructing dam in the main rockfill area is mainly gray thick strip limestone and gray thick dolomite.

3 Deformation monitoring of dam and extrusion-sidewall during construction

In order to evaluate the construction quality, the deformation of the concrete face rockfill dam during the construction period is monitored to prevent accidents such as uncompacted rolling or excessive deformation of the dam. According to the characteristics of concrete face rockfill dam, a comprehensive safety monitoring system is set up to carry out real-time monitoring according to the requirements of relevant regulations and specifications during construction. Figure 3 shows that the sequence and time of dam filling.

3.1 Monitoring instrument layout scheme

In order to obtain the deformation of the dam and the extrusion-sidewall during the construction period, deformation measuring instruments are specially set at the section of the riverbed centerline perpendicular to the dam and the extrusion side wall. The vertical displacement is measured by water tube type settlement meter in Figure 4. The horizontal displacement is measured by tension wire type horizontal displacement meter in Figure 5.

3.2 Arrangement and analysis of monitoring data

When the dam was completed in March 2014, the maximum upstream deformation at the dam elevation of 412.00 was 33.0 cm, and the deformation at the downstream measuring point was 32.5 cm. At the dam elevations of 437.00 and 462.00, the upstream horizontal displacement decreases slightly and the downstream horizontal

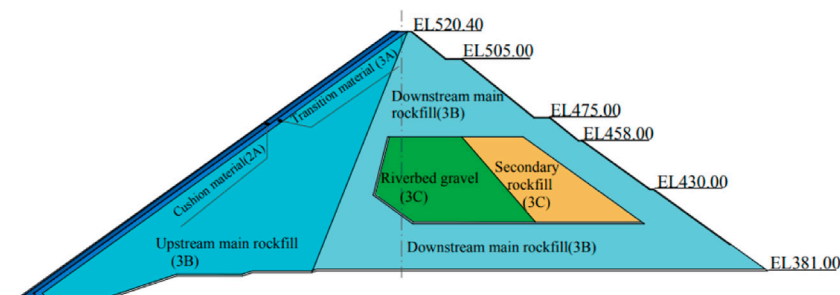


FIGURE 2
Dam material partition drawing.

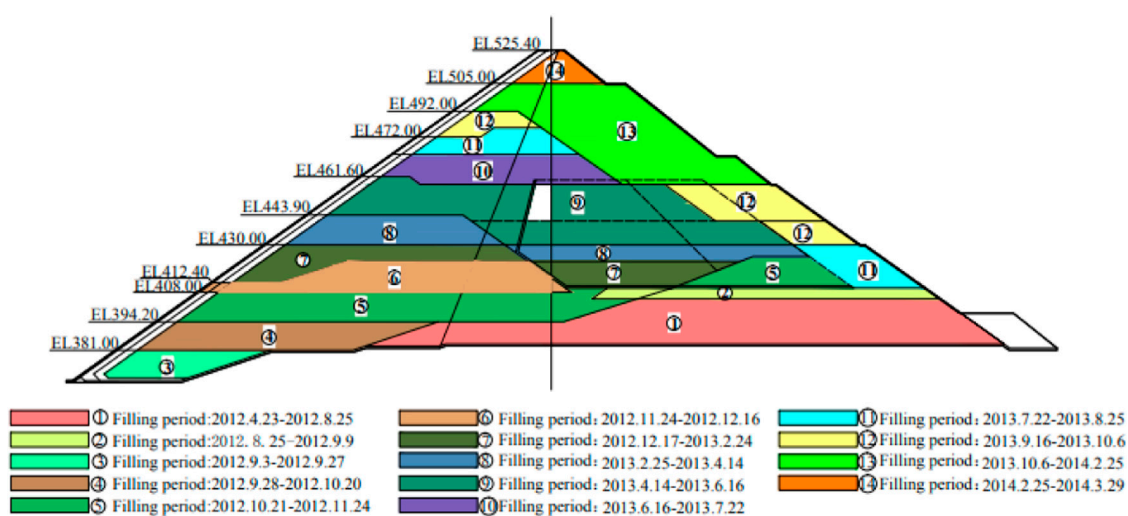


FIGURE 3
Dam filling sequence diagram.

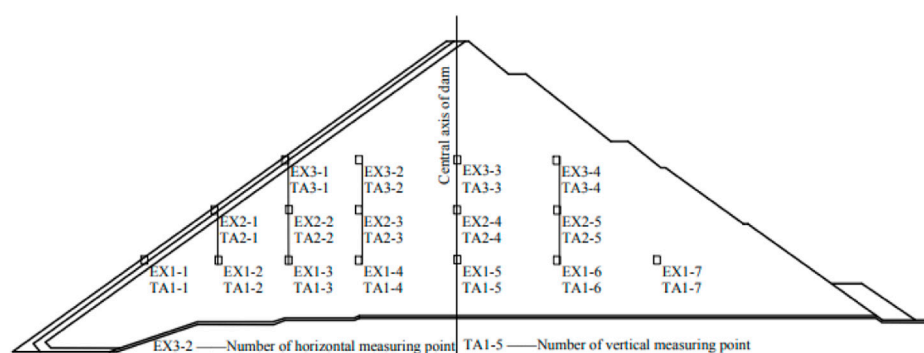


FIGURE 4
Layout of deformation monitoring instrument at riverbed cross section.

displacement increases slightly, as shown in Figure 6. The vertical displacement occurs at the elevation of 437.00, with the maximum value of 134.1 cm. It is located near the upper of one-third of the dam height, and the settlement decreases gradually along the dam towards

the upstream and downstream areas, as shown in Figure 7. The maximum position of horizontal and vertical deformation is not at the same height, but it conforms to the general deformation law of dam.

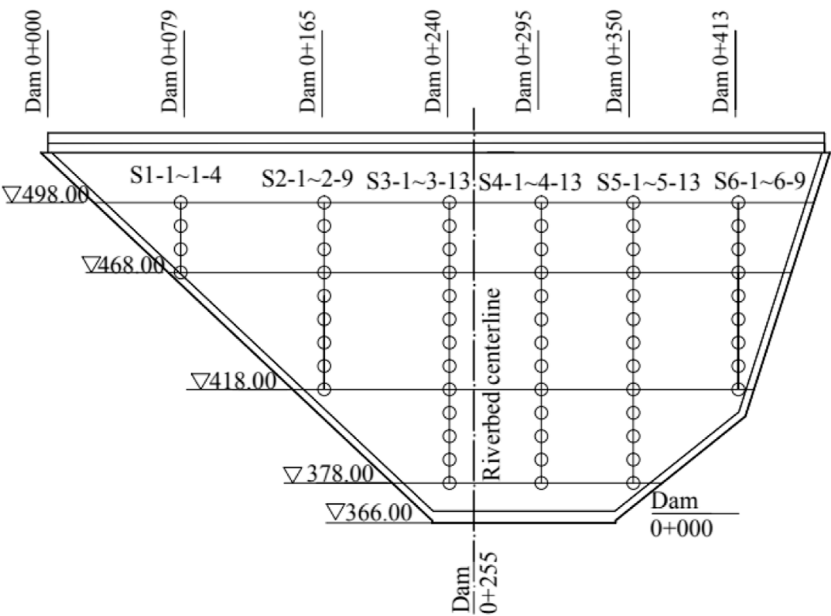


FIGURE 5
Layout of squeezed sidewall deformation monitoring instrument.

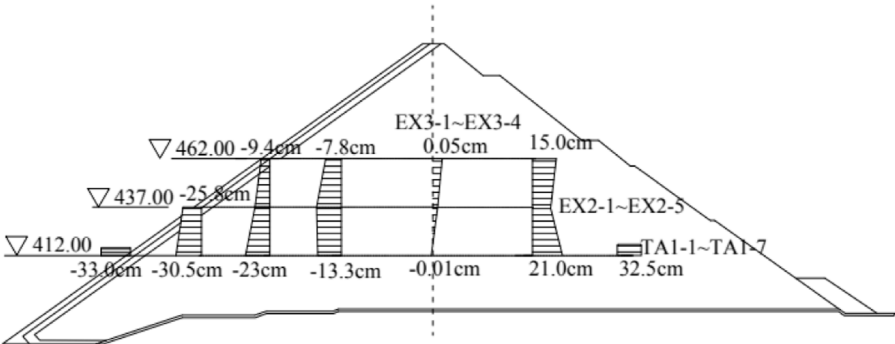


FIGURE 6
Horizontal deformation of dam in March 2014.

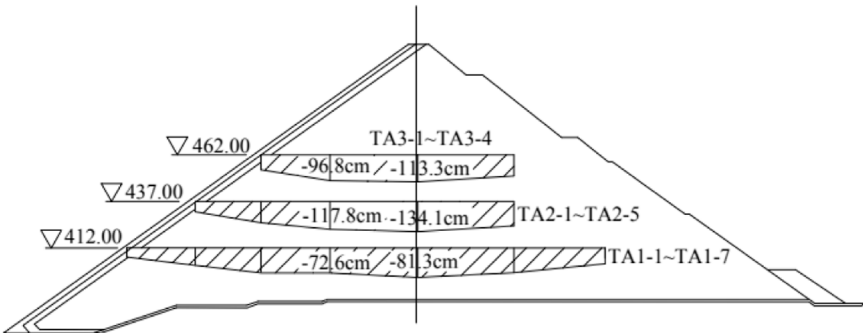


FIGURE 7
Vertical deformation of dam in March 2014.

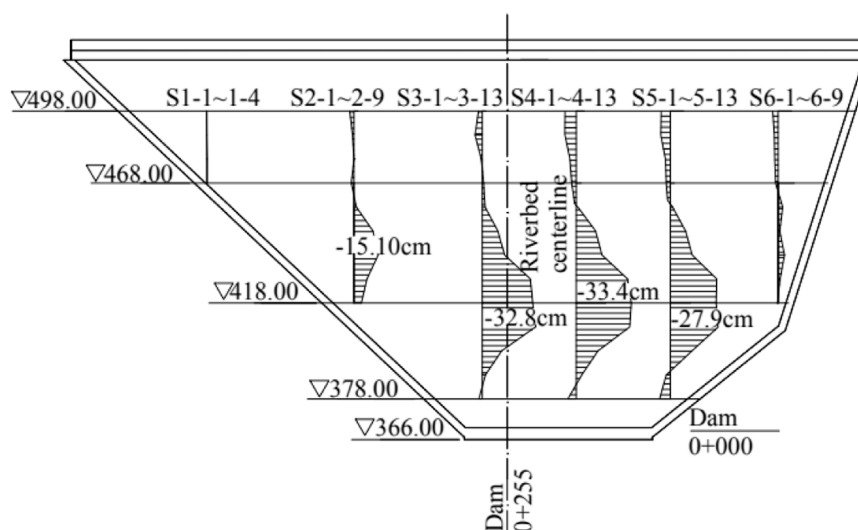


FIGURE 8
Displacement of wall extrusion along the river in March 2014.

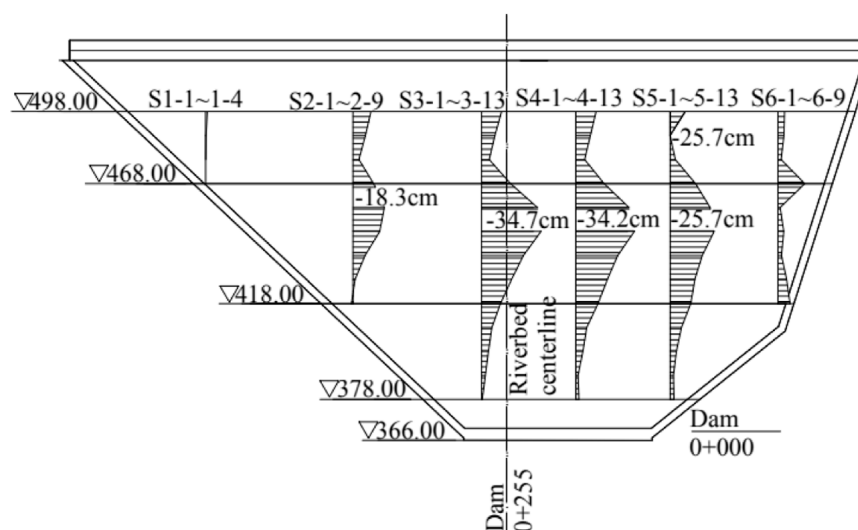


FIGURE 9
Vertical displacement of extrusion-sidewall in March 2014.

The deformation of the extruded side wall along the river occurs at the dam height of 418 m, and the maximum deformation upstream is 33.4 cm, which occurs on the left side of the dam, 40 m from the centerline of the riverbed, and is one-third of the dam height. As the right side of dam abutment is steeper than the left side, the upstream displacement along the river on the left side of the dam is smaller than the right side, and the displacement near the dam abutment on both sides is reduced, which is mainly restricted by the dam abutment on both sides, as shown in Figure 8. The maximum vertical displacement of the extrusion-sidewall is 34.7 cm, which occurs at the dam height of 450 m, and is near two-thirds of the dam height. It occurs on the left side of the dam and is 40 m away from the riverbed centerline in Figure 9. Although the maximum horizontal displacement and vertical

displacement do not occur at the same dam height, they are consistent with the laws of horizontal and vertical deformation of the dam.

4 Numerical simulation method

4.1 Calculation principle

The midpoint increment method is used in this calculation. For the first load increment $\{\Delta P\}_1$, the midpoint increment method establishes the stiffness matrix $[K]_0$ with the initial tangential modulus E_i and calculates the displacement $\{\Delta \delta\}_1$, strain $\{\Delta \varepsilon\}_1$ and stress $\{\Delta \sigma\}_1$. Starting with the second stage load increment, apply half

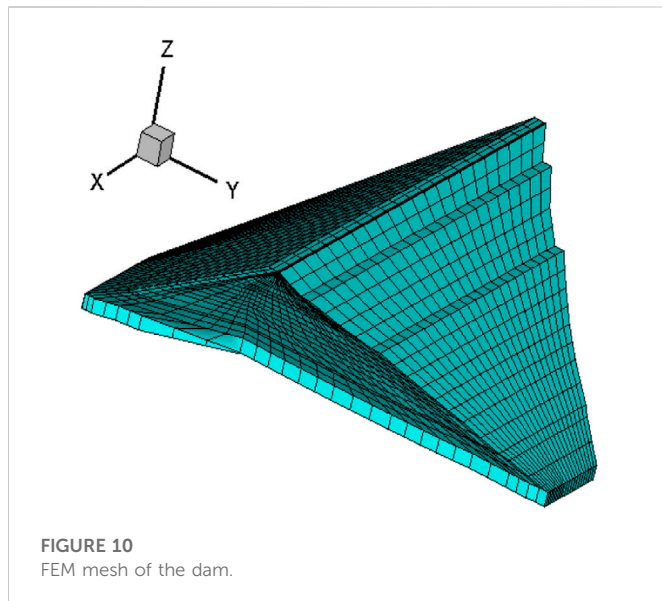


FIGURE 10
FEM mesh of the dam.

of the load increment $\{\Delta P\}_i/2$ first, and establish the stiffness matrix by using the stress level at the end of the previous increment to obtain the incremental midpoint displacement $\{\Delta\delta\}_{i-1/2}$ and the corresponding stress state $\{\Delta\sigma\}_{i-1/2}$. Based on this stress state, the corresponding modulus E_i is obtained, and then the mid-point stiffness matrix of increment i is established. Then a linear analysis is performed with the secondary full load $\{\Delta P\}_i$ to obtain the displacement $\{\Delta\delta\}_i$ and stress $\{\Delta\sigma\}_i$ under this load, which is repeated until the final increment. The experience of water conservancy design department in China shows that the calculation results obtained by midpoint increment method are closer to the actual situation than the general incremental analysis.

4.2 Computational model

Three-dimensional solid modeling and finite element meshing are carried out according to dam material partition and filling scheme, as shown in Figure 10. The rockfill, dam and foundation are modeled mainly by three-dimensional eight-node hexahedron element. It is proposed that four-node quadrilateral element are used in the local areas. The number of elements is 18,920 and the number of nodes is 21,241. The boundary is constrained by displacement, and the left and right sides and bottom of the dam are fully constrained. For the treatment of extrusion-sidewall, refer to the method in reference (Zhang et al., 2005), and the extrusion-sidewall is equivalent to a whole concrete continuous thin plate, with the thickness of the side wall equivalent to 24 cm. A thin layer unit is set between the extrusion-sidewall and the cushion material as the equivalent contact surface (Popp et al., 2010). The thickness of the thin layer unit is 10 cm, and its modulus is the modulus of the cushion.

4.3 Material constitutive model and parameters

Linear elastic constitutive model is adopted for extrusion-sidewall in this calculation. The elastoplastic “Nanshui” constitutive model is adopted for rockfill, because the elastic-plastic model can well reflect

the shear shrinkage of rockfill (Luo and Xiu-run, 2008). Calculation model parameters are shown in Table 1.

4.4 Load and application method

During the construction period of the dam, the load is the weight of the rockfill, and there is no water in the upstream and downstream of the dam. The simulated construction process is to calculate the stress-strain process of the squeezed side wall from the foundation to the dam crest elevation during construction. The load is applied to a total of 14 levels. The extrusion side wall is constructed from the third level of the dam when it is filled with the dam, as shown in Figure 3.

4.5 Comparison and analysis of calculation results and monitoring data

According to the calculation, the maximum displacement of dam settlement on the section of riverbed centerline during the completion period is 1.2 m. Compared with the monitoring results, the location is similar, and the value is smaller than the monitoring value, with a difference of 0.14 m. At the same time, the three-dimensional calculation results show that due to the asymmetric “V” shape of the river valley, the dam settlement has obvious arch effect, and two large deformation and settlement areas are formed along the dam height, as shown in Figure 11. However, due to the limitation of the layout scope of monitoring instruments, this feature was not found in the monitoring results. Compared with the displacement and deformation in the horizontal direction of the dam, Figure 12 shows that the range of the horizontal displacement in the vertical direction along the river of the upstream face of the dam is basically close to the monitoring results, and the range of the downstream displacement along the river greater than 0.42 m is relatively small, which is in the shape of a long strip close to the slope. Compared with the monitoring results, the calculated values at the same location are smaller. Due to the limitation of the layout of monitoring points, the monitoring values cannot reflect the overall horizontal displacement of the downstream dam.

Comparing the calculated and monitored horizontal displacement and deformation of the extrusion-sidewall along the river, it is found that the calculated value of 30 cm is less than the monitored value of 34.7 cm, and the range of calculated displacement of more than 30 cm is also less than the monitored value of more than 30 cm. However, the results of calculation and monitoring are in good agreement with each other. The maximum horizontal displacement occurs slightly less than one-half of the dam height, and deformation towards the downstream of the river occurs at the top of the dam, as shown in Figure 13. Figure 14 shows that it reflects the calculated vertical displacement diagram of the extrusion-sidewall during the completion period of the dam. The maximum calculated value is 28 cm, which is 6.7 cm smaller than the monitored vertical displacement 34.7 of the side wall. However, the maximum vertical displacement is located at two-thirds of the dam height, which is similar to the monitoring data and has the same rule, and also conforms to the general rule of the deformation of the extrusion-sidewall.

Comparing the monitoring and calculation results, the deformation laws of the two are the same. The calculated data is less than the monitoring data, and the error is about 10%. It shows that

TABLE 1 The Nanshui model's parameters of the dam's material.

Dam zoning	ρ (g/cm ³)	φ_o (°)	$\Delta\varphi$ (°)	K	n	R_f	C_d	n_d	R_d
Cushion 2A	2.28	54.5	8.7	906	0.28	0.61	0.49	0.59	0.60
Transition layer 3A	2.28	54.1	9.2	1,043	0.24	0.63	0.51	0.61	0.62
Main rockfill 3B	2.25	53.7	9.4	1,014	0.23	0.67	0.51	0.67	0.62
Secondary rockfill 3C	2.24	50.3	9.1	616	0.27	0.65	0.77	0.58	0.64
Riverbed gravel 3C	2.29	52.5	8.2	1,301	0.28	0.70	0.26	0.72	0.64

Note: Extruded sidewall is considered as per linear elastic model, $\rho_d = 2.4$ g/cm³, $E = 9$ GPa, $\mu = 0.28$.

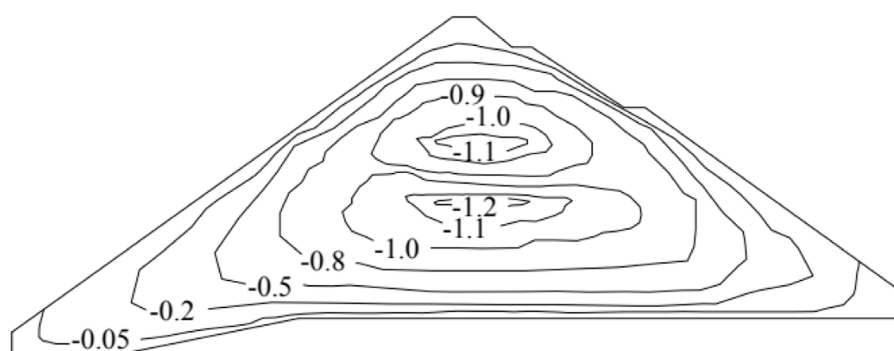


FIGURE 11
Settlement of the section of the river center line in Completion period (unit: m).

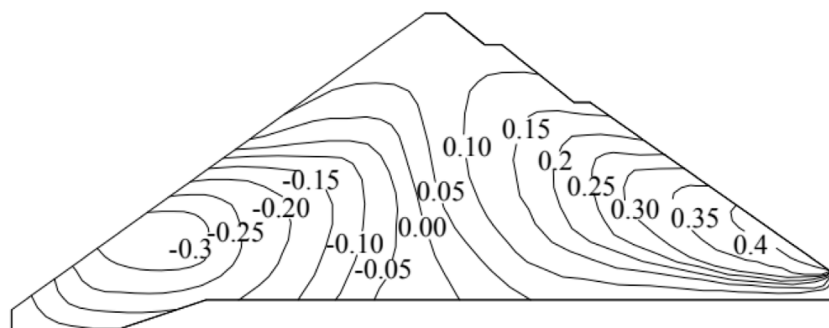


FIGURE 12
Horizontal deformation of the section of river center line in Completion period (unit: m).

the numerical calculation method is more scientific and reasonable, which can better reflect the deformation law of the dam and the extruded side wall.

It is appropriate to use the settlement characteristic value C_s of the dam, the upstream horizontal displacement characteristic value C_{Du} of the dam and the downstream horizontal displacement characteristic value C_{Dd} of the dam to evaluate the dam deformation behavior (Li 2011b).

$$C_s = \frac{S_{\max}}{H_{\max}^2}, C_{Du} = \frac{D_u}{H_{\max}}, C_{Dd} = \frac{D_d}{H_{\max}} \quad (1)$$

Where C_s , C_{Du} and C_{Dd} are respectively the characteristic value of dam settlement, the characteristic value of dam upstream horizontal

displacement and dam downstream horizontal displacement, and S_{\max} , D_u and D_d are respectively the maximum settlement of the dam at the dam axis, the horizontal displacement of the dam upstream and the dam downstream, and H_{\max} are the maximum dam height at the dam axis. Table 2 shows that the test results and finite element calculation results.

The C_s value of 200 m high concrete faced rockfill dams (Shuibuya, Sanbanxi and Hongjiadu) built in the 21st century are mostly in the range of 0.2×10^{-4} – 0.5×10^{-4} , and the characteristic values of horizontal displacements are in the range of 3×10^{-4} – 18×10^{-4} (Li 2011b). When the characteristic values of settlement and horizontal displacement are within this

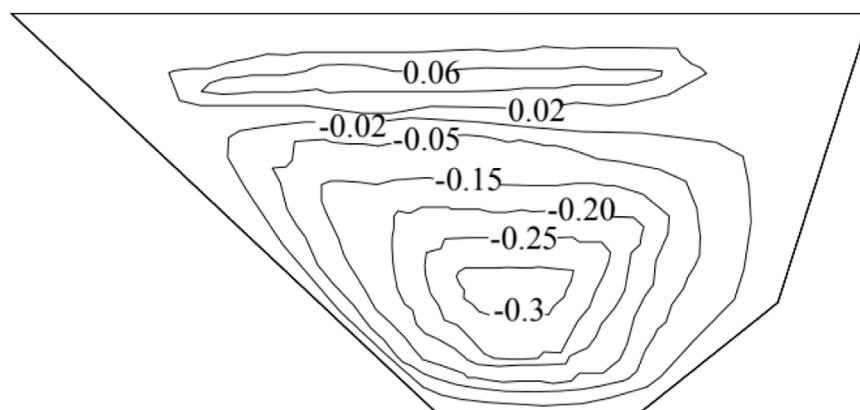


FIGURE 13
Horizontal deformation of the extruding side-wall in Completion period (unit: m).

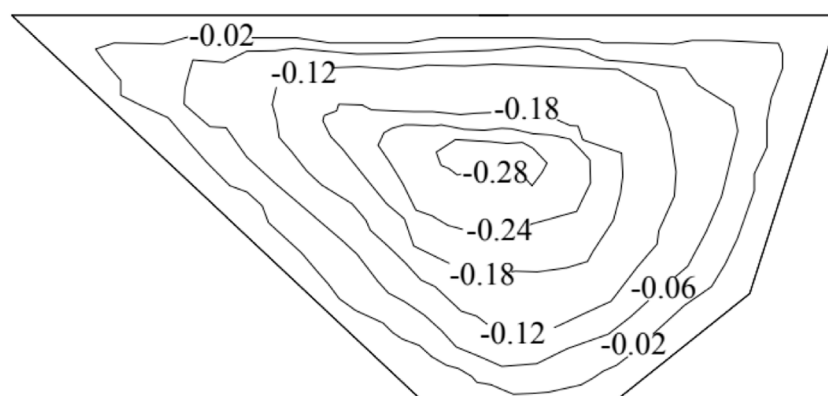


FIGURE 14
Vertical deformation of the extruding side-wall in Completion period (unit: m).

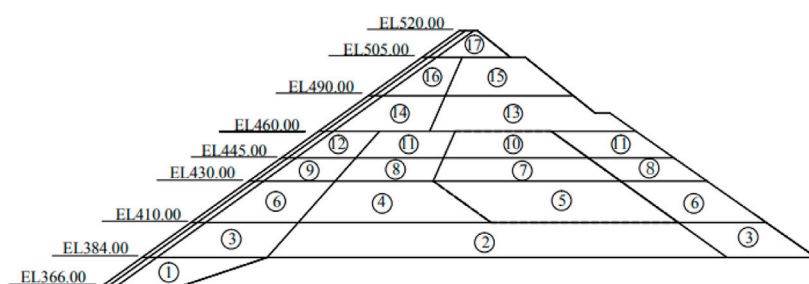


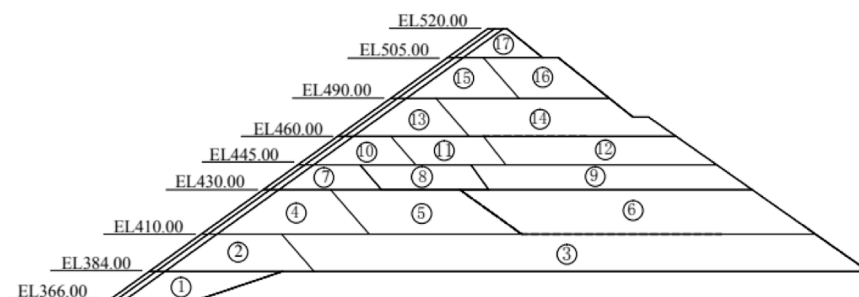
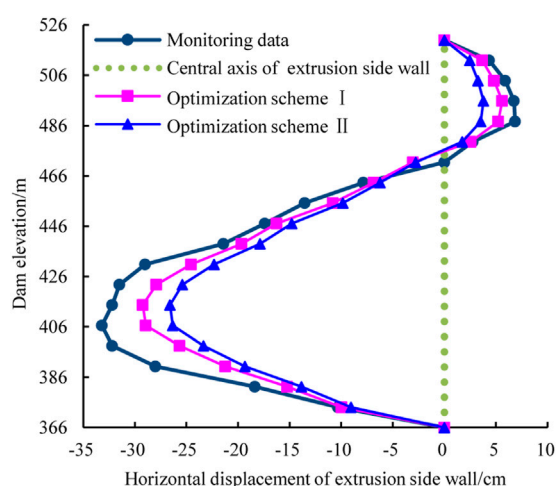
FIGURE 15
Plan I of optimize the filling sequence.

range, the cracks in cushion area, the voids and cracks in the panel and the extrusion failure of the panel concrete are rarely found in the general dam. The monitoring and calculation values of the dam

are close to this range, and some are within this range, which conforms to the principle of deformation coordination in the design of high concrete faced rockfill dam.

TABLE 2 Settlement and horizontal displacement's characteristic value of numerical calculation and monitoring.

Characteristic value of dam	Monitoring value results	Finite element calculation results
Characteristic value of dam settlement C_s (1/m)	0.38×10^{-4}	0.58×10^{-5}
Characteristic value of upstream horizontal displacement of dam C_{Du}	18×10^{-4}	16.7×10^{-4}
Characteristic value of downstream horizontal displacement of dam C_{Dd}	—	22×10^{-4}

**FIGURE 16**
Plan II of optimize the filling sequence.**FIGURE 17**
Displacement of Squeezing sidewall along the elevation along the river.

5 Influence of filling sequence on deformation of extrusion-sidewall and dam

5.1 Optimization of dam filling sequence

The extrusion-sidewall is generally trapezoidal, the upper thickness is generally 10 cm, and the lower thickness is about 70 cm. After the completion of dam filling, the extrusion-sidewall may have some slope loss or surplus. In order to lay the panel to reach the design coordinates, the method of partial slope cutting or filling

after excavating the extrusion-sidewall is generally adopted. The other method is to predict the possible settlement and horizontal displacement of the extrusion-sidewall at a certain elevation of the dam surface through certain calculation and analysis, leaving a certain space for compensation during the dam filling process. On the basis of verifying the correctness of the numerical simulation method, this paper optimizes and selects two kinds of dam filling sequence schemes are shown in Figures 15, 16. In order to minimize the upstream deformation of dam, influence of the filling sequence on the horizontal displacement and settlement deformation of the extrusion-sidewall is studied. The correlation between the horizontal displacement of the extrusion side wall and the settlement deformation of the dam is compared and analyzed, and the dam filling sequence to reduce the deformation of the extrusion side wall is analyzed.

5.2 Analysis of calculation results of optimization scheme

The deformation of the dam is mainly caused by the weight of the rockfill. When filling by stages, the deformation sequence of the upstream and downstream sections of the dam is different. Analyzing the upstream displacement along the river of the extrusion-sidewall after changing the filling sequence of the dam, it is found that the downstream first small block filling in the optimized scheme reduces the horizontal displacement along the river to the upstream compared with the original actual large block filling, and the maximum value decreases by 4.2 cm. The position where the maximum value occurs rises slightly, the area decreases, and the deformation is gentle. At the same time, the deformation from the dam top to the downstream also decreases. When the upstream is filled first and the downstream is filled later, the upstream section has been filled and tends to be stable, and the later filling has little impact on its deformation, while the newly filled dam has large deformation, so the optimization

TABLE 3 Compare results of different filling the order.

Statistical indicators	Extrusion-sidewall					Dam			
	Monitoring data of original filling scheme	Optimized scheme I	Optimized scheme II	Maximum change rate (%)	Original calculated value	Monitoring data of original filling scheme	Optimized scheme I	Optimized scheme II	Maximum change rate (%)
Upstream displacement along river/cm	33.4	29.2	26.6	−20.3	30.0	33.0	28.1	25.0	−22.0
Downstream displacement along river/cm	—	—	—	—	—	—	35.7	39.4	—
Maximum settlement/cm	34.7	31.2	29.8	−14.1	132.0	134.1	127.5	124.4	−7.0

scheme II of the upstream early filling is better. As the filling is divided into small blocks, the deformation of the extrusion-sidewall towards the upstream decreases by 6.8 cm compared with the actual filling, and the maximum deformation is −26.6 cm, as shown in Figure 17.

In order to compare the deformation of the side wall and dam under different filling schemes better and more intuitively, the calculation results are summarized as follows. From Table 3, it can be clearly seen that the maximum deformation of the side wall under the two filling schemes and the change rate between the monitoring value of the original filling scheme and the optimized scheme II.

It is reflected that when the optimum scheme II is used for stage filling, the upstream section is filled first, then the downstream section in Table 3. The downstream section filling causes a small increment of settlement and horizontal displacement of the filled part of the dam. The final settlement and horizontal displacement of the dam are mainly affected by the upstream section filling body and the lower filling body. In scheme II, the displacement of the extrusion-sidewall along the river to the upstream is reduced by 20.3%, the maximum settlement is reduced by 14.1%, the displacement of the dam to the upstream is reduced by 22%, and the maximum settlement is reduced by 7%. It also reflects that the filling sequence has more influence on the horizontal displacement of dam and extrusion-sidewall than the settlement deformation.

6 Conclusion

According to the monitoring data of concrete faced rockfill dams of some hydro-electric station in Hubei Province, the three-dimensional finite element analysis method is used to simulate the original filling sequence process of the concrete face rockfill dam. The conclusions are as follows.

- (1) According to the deformation monitoring results of the extrusion side wall and the dam, the displacement of the extrusion side wall along the river to the upstream occurs at 1/4 of the dam height at the lower part of the dam body, and the maximum settlement occurs at 2/3 of the dam height at the middle of the side wall. The maximum horizontal displacement and vertical displacement occur in different locations, and the upper part of the side wall produces a smaller area of downstream shrinkage deformation.

- (2) Comparing the monitoring and three-dimensional calculation results of the dam and the extrusion side wall, the deformation laws of the two are the same. The calculated data is less than the monitoring data, and the error is about 10%. It shows that the finite element calculation method is more scientific and reasonable, which can better reflect the deformation law of the dam and the extruded side wall. It is found that the eigenvalue of the dam is close to that of general concrete face rockfill dam.
- (3) Through the optimization of the original filling sequence of the dam, it is found that the scientific and reasonable zoning filling sequence can reduce the horizontal displacement along the river of the extrusion-sidewall, especially the displacement and deformation towards the upstream of the dam. But its influence on vertical displacement is less obvious than that on horizontal displacement.

Data availability statement

The original contributions presented in the study are included in the article/Supplementary Material, further inquiries can be directed to the corresponding author.

Author contributions

LH provided overall guidance on the article as well as wrote this paper. YM and LJ modified the article language.

Funding

This work was supported by Loess Soil Mechanics and Engineering Key Laboratory of Shaanxi Province Foundation (13JS073), Natural Science Foundation of Shaanxi Province (2017JM5059).

Conflict of interest

The authors declare that the research was conducted in the absence of any commercial or financial relationships that could be construed as a potential conflict of interest.

Publisher's note

All claims expressed in this article are solely those of the authors and do not necessarily represent those of their affiliated

organizations, or those of the publisher, the editors and the reviewers. Any product that may be evaluated in this article, or claim that may be made by its manufacturer, is not guaranteed or endorsed by the publisher.

References

- Cheng, S., Zhang, G., and Zhang, J.-M. (2011). The analysis and amendatory measures of temperature stress of face slab of a concrete-faced rockfill dam with extrusion wall. *Chin. J. Eng. Mech.* 28 (4), 76–81.
- Deng, G., Wang, X., and Wen, Y. (2015). Study on conceptualization method of deformation pattern and horizontal breakage of face slab of concrete faced rockfill dam. *J. Hydraulic Eng.* 46 (4), 396–404.
- Deng, G., Xu, Z., and Lu, S. (2008). Analysis on long term stress and deformation of high concrete face rockfill dam in narrow valley. *J. Hydraulic Eng.* 39 (6), 639–646.
- Galvao, D., Materon, B., and Resende, F. (1999). Itá update: A new technology for CFRDs. *Int. Water Power & Dam Constr.* 51 (3), 28–31.
- Hou, W., Zhang, G., and Zhang, J. (2008). Behavior of interface between extrusion-sidewall and slab face of CFRD. *Chin. J. Geotechnical Eng.* 30 (9), 1356–1360.
- Hu, Z., Lan, G., and Miao, Y. (2016). Deformation law of upstream slope during construction of high concrete-faced rock-fill dam. *Chin. J. Geotechnical Eng.* 38 (2), 293–298.
- Jiang, G. (1997). *China's concrete rock-fill dam for 20 years*. Beijing: China Water Power Press.
- Li, N. (2011b). Performance of high concrete face rockfill dams in China and its inspiration. *Chin. J. Geotechnical Eng.* 33 (2), 165–173.
- Li, N. (2011). Performance of high concrete face rockfill dams in China and its inspiration. *Chin. J. Geotechnical Eng.* 13 (3), 12–18+28.
- Li, N., and Yang, Z. (2012). Technical advances in concrete face rockfill dams in China. *Chin. J. Geotechnical Eng.* 34 (8), 1361–1368.
- Liu, M., Gao, Y., and Liu, H. (2010). Finite element analysis of long-term stress-deformation behavior for concrete-faced rockfill dam. *Rock Soil Mech.* 31 (1), 412–418.
- Liu, N., Li, L., Wang, S., Li, G., and Song, Z. (2023). A fully coupled thermo-hydro-mechanical model for fractured rock masses in cold regions. *Cold Regions Sci. Technol.* 205, 103707. doi:10.1016/j.coldregions.2022.103707
- Liu, S., and Liu, X. (2013). Stress and deformation analysis of extruded side wall concrete faced gravel dam. *J. Water Resour. Water Eng.* 24 (02), 192–195.
- Luo, Q., and Xiu-run, G. (2008). *Stress-strain method study of concrete face rockfill dam*. Beijing: Water Resources and Electric Power Press.
- Luo, X., Wu, X., and Tong, F. (2005). Research on the stress-strain of ShuiBuYa concrete face rockfill dam based on the concrete crushing-type side wall technology. *Chin. J. Rock Mech. Eng.* 24 (13), 2342–2349.
- Pan, F., Wang, R., and Zhang, Z. (2014). Research on staged filling section optimization of high concrete-faced rock-fill dams. *J. Hydroelectr. Eng.* 33 (4), 227–234.
- Peng, C., Guo, D., and Wang, Q. (2008). Application of extrusion-sidewall technology to the project of rock fill dam with face slab. *Rock Soil Mech.* 29 (1), 201–203.
- Popp, A., Gitterle, M., Gee, M. W., and Wall, W. A. (2010). A dual mortar approach for 3D finite deformation contact with consistent linearization. *Int. J. Numer. Meth. Engng.* 83 (11), 1428–1465. doi:10.1002/nme.2866
- Sun, T., Gao, X.-Z., and Yang, J. (2006). Stress-strain analysis of Zipingpu concrete faced rockfill dam. *Rock Soil Mech.* 27 (2), 247–251.
- Yang, J., Guoying, L., and Shen, T. (2014). Stress-deformation properties of super-high CFRDs under complex terrain conditions. *Chin. J. Geotechnical Eng.* 36 (4), 775–781.
- Zhang, J., Zhang, G., and Liu, F. (2005). A simplified equivalent numerical model of extrusion-sidewall for CFRD and its application. *Chin. J. Geotechnical Eng.* 27 (3), 249–253.
- Zhang, Y., Song, Z., and Weng, X. (2022). A constitutive model for loess considering the characteristics of structurality and anisotropy. *Soil Mech. Found. Eng.* 59 (1), 32–43DOI. doi:10.1007/s11204-022-09781-z
- Zhou, M., Zhang, B., and Zhang, Z. (2015). Mechanisms and simulation methods for extrusion damage of concrete faces of high concrete-faced rockfill dams. *Chin. J. Geotechnical Eng.* 37 (8), 1426–1432.
- Zhou, W., Hua, J., Chang, X., and Yanhui, C. (2008). Cause analysis of cracking of concrete slab for high CFRD based on concrete crushing-type side wall technology. *Rock Soil Mech.* 29 (8), 2037–2042.
- Zou, D., You, H., and Kong, X. (2009). Research on joint simplified model and defects of joint parameters on panel stress and joint displacements of faced rockfill dam. *Chin. J. Rock Mech. Eng.* 28 (1), 2357–2363.



OPEN ACCESS

EDITED BY
Naifei Liu,
Xi'an University of Architecture and
Technology, China

REVIEWED BY
Zhong Han,
Wuhan University, China
Shunchao Qi,
Sichuan University, China

*CORRESPONDENCE
Zhang Hongri,
✉ 253541461@qq.com

SPECIALTY SECTION
This article was submitted to
Environmental Informatics and Remote
Sensing,
a section of the journal
Frontiers in Earth Science

RECEIVED 02 December 2022

ACCEPTED 28 December 2022

PUBLISHED 02 February 2023

CITATION

Youjun L, Hongri Z, Liming H, Sulian L,
Hongming L and Xuexiao W (2023),
Reaction and deformation mechanism of a
slipping-stretching landslide: Example of
the Liangtianao ancient landslide, Guangxi
Province, China.
Front. Earth Sci. 10:1114292.
doi: 10.3389/feart.2022.1114292

COPYRIGHT

© 2023 Youjun, Hongri, Liming, Sulian,
Hongming and Xuexiao. This is an open-
access article distributed under the terms
of the [Creative Commons Attribution
License \(CC BY\)](#). The use, distribution or
reproduction in other forums is permitted,
provided the original author(s) and the
copyright owner(s) are credited and that
the original publication in this journal is
cited, in accordance with accepted
academic practice. No use, distribution or
reproduction is permitted which does not
comply with these terms.

Reaction and deformation mechanism of a slipping-stretching landslide: Example of the Liangtianao ancient landslide, Guangxi Province, China

Li Youjun¹, Zhang Hongri^{1,2*}, Huang Liming¹, Lan Sulian³,
Li Hongming¹ and Wu Xuexiao¹

¹Guangxi Transportation Science and Technology Group Co., Ltd., Nanning, Guangxi, China, ²School of Naval Architecture, Ocean & Civil Engineering, Shanghai Jiaotong University, Shanghai, China, ³Guangxi Transport Vocational and Technical College, Nanning, Guangxi, China

Slipping-stretching landslides have long been recognized as a common type of landslide case, but such reactions have rarely been reported. There was a slipping-stretching landslide reaction at Liangtianao, Guangxi Province, China, and the geological background and deformation characteristics of the case were identified by detailed geological survey and long-term monitoring. A FEM model of the case was built using GEO5 to analyze the mechanism of reaction and deformation. The results are as follows. 1) The Liangtianao landslide is a bedding rock ancient landslide, which remained in a creeping state after the landslide occurred in geological history. 2) The new sliding surface in the Liangtianao landslide is basically consistent with the weak interlayers formed by ancient landslides, and the fault-type is a slipping-stretching type with the following deformation process: strain at leading edge by road excavation→ leading edge instability→ middle part shear and creep→ back edge tensile. 3) Micro-geomorphology, rock mass bedding, and weak interlayers are internal causes of the Liangtianao landslide reaction, while excavation unloading and rainfall are the external causes. The inclinometer indicates that the Liangtianao landslide is still highly sensitive to rainfall after the landslide reaction, which may trigger a secondary landslide reaction. 4) The numerical analysis results indicate that the maintenance of a passive state in the anti-sliding section is highly beneficial to maintaining basic stability after the landslide reaction; unloading only 1/20 of the sliding section makes the landslide stable in the long term.

KEYWORDS

landslide reaction mechanism, deformation mechanism, slipping-stretching landslide, unloading effect, rainfall touch-slip effect, deformation characteristics, secondary reaction

1 Introduction

As the frequency of human engineering activities and extreme weather increase, reaction cases of ancient landslides are increasing. Landslides in British Columbia have moved to the Thompson River Valley, posing a threat to the Canadian Pacific Railway and the Canadian National Railway (Macciotta et al., 2016). The OSO landslide in Washington, D.C. has been studied for decades, but its reaction had still not stopped in 2014 (Wartman et al., 2016). The retreat of the Barry Glacier has exposed many ancient landslides in southern Alaska, which pose potentially disastrous consequences if these landslides enter the fjord in reaction, raising

questions about its stability and potential cascade hazards (Wolken et al., 2021). Therefore, it is especially important to study the reaction mechanism of ancient landslides.

Slipping-stretching landslides activate a bedding sliding section in their middle-upper part and a passive compression section in their lower part. Under the action of gravity, the middle-upper part slides along the weak interlayer zone, and the lower part produces passive extrusion. When the interlayer weak zone in the lower part cannot sufficiently maintain passive extrusion, the sliding surface penetrates and slides. The presence of rock strata and the properties of the interlayer zone are the main controlling factors for such landslides, and are considered a common type of landslide (Broadbent and Ko, 1971; Lo et al., 1978). Huang (2009) summarized the main characteristics of such landslides, and proposed that they are mainly induced by rainfall and weak interlayers. Li M et al. (2008) proposed that bedrock bedding landslides have a weak slide face at the interlaminar shear band stage, and are prone to forming new disasters. Li X et al. (2008) proposed that the range of monoclinic bedrock ancient landslides obtained from geomorphological analysis had multiple causes. Zhang (2016) researched the process of slipping-stretching landslides; because the pull-cracks located at landslide trailing were directly connected to the slip surface, the influence of rainfall on landslide stability required special attention. Burda et al. (2013) proposed that continuous underground mining and rainfall had induced the secondary reaction of the Eisenberg ancient landslide in northern Bohemia. Deng et al. (2017) indicated that the unloading effect caused by river down-cutting had gradually penetrated the formation process of ancient landslides, complex landslides, and multi-level landslides. Song et al. (2012), Huang et al. (2013), Zou et al. (2012), Chen et al. (2014), Xue et al. (2015), Qu et al. (2016), Wu et al. (2018), Wei et al. (2018), Huang et al. (2020), Zhang X et al. (2021), Zhong et al. (2021), and Zhang et al. (2022) have proposed that bottom unloading and heavy rainfall cause weight gain and shear-strength weakening, which promote ancient landslide reaction. Wei et al. (2018) and Sangirardi et al. (2020) observed that unloading at the slope foot is a common inducement for ancient landslide reactions. Liu et al. (2023) concluded that rock fractures cracked significantly at low temperatures. Cail et al. (2021) concluded that the Diexi earthquake in 1933 triggered tension cracks in the Xinmo landslide and that long-term rainfall caused landslide reaction. Deng et al. (2017) conducted the Brazilian splitting test on slate under different bedding angles θ , and observed that the slipping-stretching landslide mode appeared when $30^\circ < \theta < 45^\circ$. Zhang C et al. (2021) concluded, based on the centrifuge physical model test and numerical simulation, that a dominant infiltration channel formed by cracks was necessary for aggravating geotechnical mixed ancient landslide reactions. Pradhan et al. (2022) concluded that road cuttings increased landslides during rainfall and decreased minimum starting rainfall. Zhang C et al. (2021) found that the hydraulic gradient was the most important factor for the Taping landslide. Liu et al. (2022) concluded that rock degradation was caused by freeze-thaw cycles, and that this degradation or loss of strength could cause damage when the rock was thawed. According to all this research, unloading, loading, rainfall, earthquake, and bad lithology are the main factors for ancient landslide reaction. As the slipping-stretching landslides are regularly reported, exploring such landslides' deformation characteristics and reaction mechanisms is beneficial for reducing the loss they cause.

There was a slipping-stretching landslide reaction in Liangtianao, Guangxi Province, China. The deformation characteristics, evolution

process, cause analysis, and reaction characteristics were evaluated by geological drilling, geotechnical testing, long-term deep displacement monitoring, and numerical analysis. The reaction and deformation mechanisms of the landslide were analyzed by daily rainfall, monitoring data, and numerical modeling. The principles of this landslide are discussed in this study to provide an analogy and prevention reference for similar ancient landslides.

2 Geological background of landslide area

This case is located at Tian'e country in Guangxi Province, China. The geomorphic type of the case area is mainly erosion dissolution low mountain valley landform (Figure 1). Its elevation is 800 m–1,450 m, and the valley bottom is a relatively open “V” shape with gradients of between 40 and 90°. Overall, the peak bridge fluctuates in waves, and the valley is shallow and wide in strips. The study area is in the Nandan fault zone of the Guixi sag, Youjiang regeneration geosyncline, Nanhua platform. Affected by the regional structure of the Tian'e anticline, the Bala-Longfeng normal fault (NW60°) developed along the left flank of the anticline; it has a steep wall of soft Middle Triassic rock, a the lower wall comprising rigid Middle Permian rock. The groundwater type of the case area is a poor amount of bedrock fissure water. Its climate is subtropical humid monsoon. Annual rainfall precipitation (1,370 mm) occurs in the wet season (May–October), and accounts for 85% of the rainfall throughout the year (Zhang et al., 2021b).

The case was in Liangtian'ao village (Figure 2). The G243 national way designed sections of K16 + 300 to K18 + 500 near this village. As the height difference between front and rear is 120 m, double-S turning curves were taken to overcome the longitudinal slope, with total excavation of these sections of 43,898 m³. All excavation was completed in July 2018 and formed platforms 11 m–20 m wide at 757.0, 790.0, 818.0, and 833.0 m. Nearly 22 concrete-brick houses with 100 villagers are scattered on the top of the slope.

The main composition of the lithology is as follows. The surface layer is yellowish-brown quaternary residual silty clay, with a gravel content of 5%–10%, and an exposed thickness varying 0.5–6.0 m. The lower part is thin to medium thickness layered argillaceous siltstone, with an argillaceous silt structure and developed joints and fissures, exposed 5.0 m–45.0 m-thick. The rock mass occurrence is 260°∠26°.

3 Landslide features

3.1 Development of the landslide

The tongue-shaped landslide occurred suddenly on August 13, 2018, and its failure characteristics were as follows. a) At 870 m, the soil was separated from the steep rock wall behind it and slinked about 30 cm; at 860 m, three houses' load-bearing columns were cracked by 0.5 cm–1.0 cm. b) At 831 m–873 m, the shallow soil was stretched by 10 cm to 30 cm-thick, and the new retaining wall was staggered 10 cm–25 cm. c) At 790 m–818 m, the old road sustained goose-sharped shear dislocations, and the old retraining walls cracked diagonally 1–2 cm wide. d) At 750 m–790 m, there was only slope slump outside the boundary on both sides, and the sliding surface was not exposed. In order to determine the spatial characteristics of this

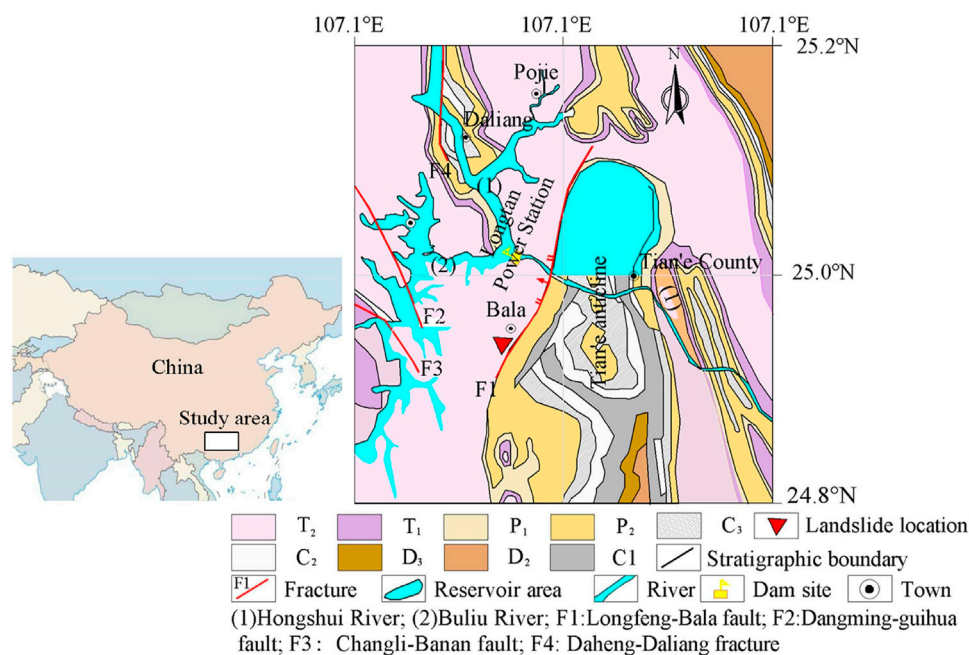


FIGURE 1

Geographical location map of landslide area.

landslide, three geological profiles were laid along the main direction, and deep displacement monitoring was set up. The specific layout positions and sliding surfaces are shown in Figures 2 and 3.

The plane of the landslide was tongue-shaped, with a narrow upper and a wider lower. The trailing edge was bounded by steep-standing soft Middle Triassic rock, with boundaries both sides of the U-shaped groove. The main shaft length was 220 m. The elevations of the front and rear edges were 760 and 880 m respectively, which is in the direction of the vertical main axis—the width varied 69 m–110 m. The average thickness of the sliding body was about 20 m, and landslide volume was about $250 \times 10^3 \text{ m}^3$. The Liangtianao landslide was thus a medium-sized dipping thick bedrock landslide.

3.2 Relationship between landslides and rainfall

Pre-landslide rainfall was characterized by prolonged, high intensity (Figure 4). The cumulative rainfall from March 2018 to the landslide reached 2,137.0 mm, accounting for 70.3% of the whole year (3,040.0 mm). The average daily rainfall was up to 12.64 mm/d. Furthermore, the rain continued from 30 March 2018 to 12 August 2018 (11 days) before the landslide, with a large day rainfall of 72.6 mm on 11 August 2018. As all on-site works had stopped before the landslide occurred, it can be qualitatively judged that the rainfall contributed to the landslide.

After the landslide occurred, on-site construction was stopped until March 2019. However, the daily rainfall and deep cumulative displacement curve showed a continuous deformation trend, which was closely related to rainfall.

1) The slip gradually stabilized from the leading to the rear edge. After the landslide, the cumulative rainfall between 1 August 2018 and

19 September 2019 (39 days) was 634.6 mm, of which the average daily rainfall from 17 September 2019 to 19 September 2019 was 61.0 mm/d. Consequently, shallow soil at the trailing edge slipped 219° , causing the village road to dislocate (Figure 5). The dry season had been from 19 August 2018 to 31 March 2019, with cumulative rainfall down to 502.8 mm (2.60 mm/d). By comparison, the average daily evaporation in the region was 3.40 mm, so the rainfall effect on the landslide was weak. However, the middle sliding body was still slipping. The subsidence gap of the retaining wall near ZK2-6 cracked in October 2018 (Figure 6). Moreover, as deep displacement monitoring was completed on 21 November 2019, the average displacement rate of all sliding surfaces during the dry season was 0.08 mm/d, 0.15 mm/d, 0.12 mm/d, and 0.42 mm/d. This reveals that, 152 d after the landslide reaction, landslide had entered a gradual stabilized stage from its rear to upper edge.

2) Rainfall can cause landslides to re-deform. On 1 March 2019, there was no change in the deep displacement monitoring data after the deep drainage holes were completed. However, with the average daily rainfall reaching 5.48 mm/d (26 March 2019 to 30 April 2019), the cumulative displacement of the sliding surface at ZK2-3 suddenly increased from 18.7 mm to 34.85 mm (+16.15 mm). In contrast, the ZK2-6 cumulative displacement did not change.

3.2.1 Landslide deformation and rainfall distribution

There was good correspondence between landslide deformation and rainfall distribution. Continuous high-intensity rainfall can trigger a secondary landslide reaction.

3) Deformation failure feature. The ZK2-6 borehole at the front edge exposed two broken layers (Figure 3). The upper layer is

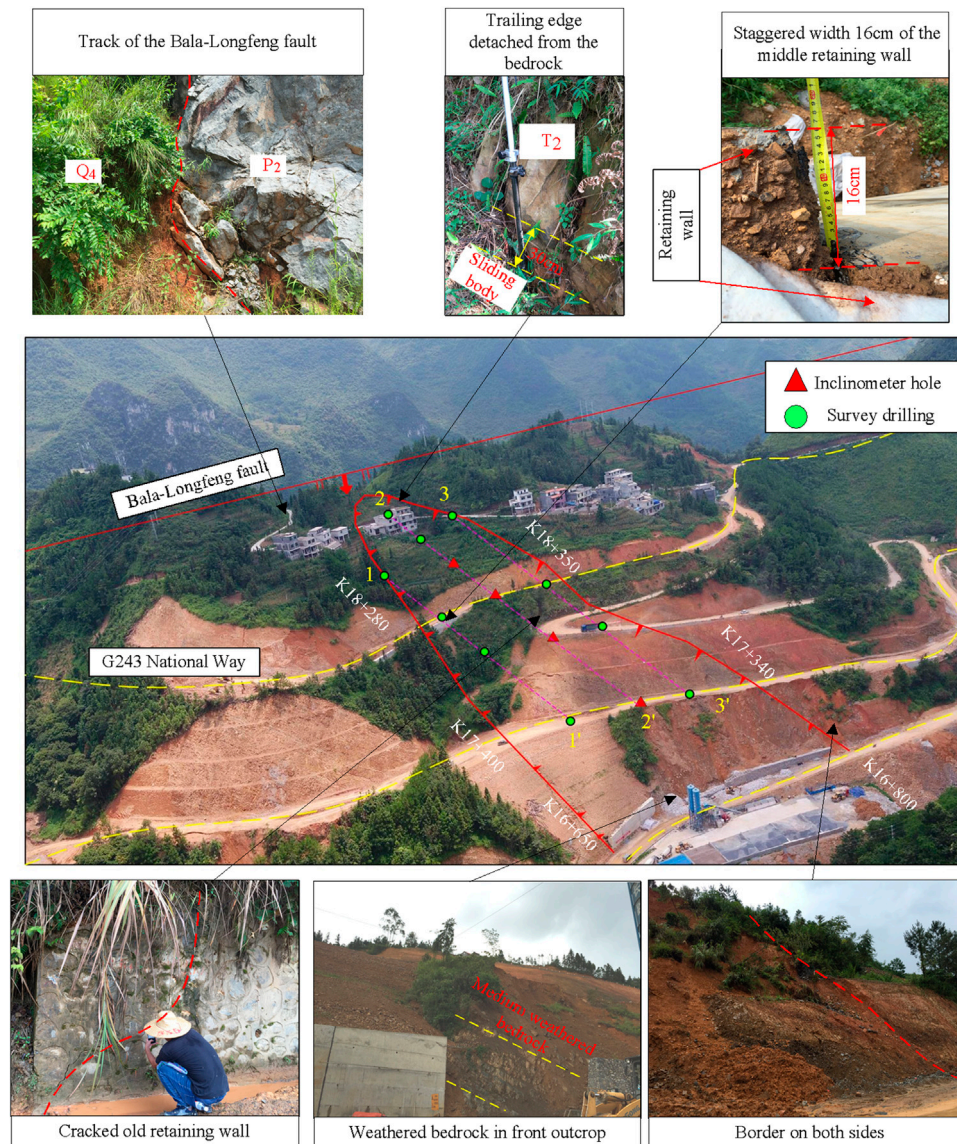


FIGURE 2
Landslide plan and typical damage photos (SE139°, August 2018).

composed of gravel-like yellow argillaceous siltstone, sub-angular and sub-circular, with a particle size of 3 ~ 5 cm. It contained 0.2–2.0 cm of loose sandy breccia—evidence of interlayer dislocation caused by ancient landsliding.

3.3 Identification of ancient landslide characteristics

The identification of ancient landslide characteristics in this case is mainly based on surface morphology, stratum lithology, deformation, and failure characteristics.

- 1) Geomorphic features of the study area. The original landform formed a gentle platform at 815 m to 818 m, each section having angles of 40°, 26°, and 50°. From top to bottom, the landform was steep–gentle–steep, with obvious grading, forming a typical chair-

shaped landform. A 5 m-high steep rock wall appeared outside the boundary at the trailing edge of the landslide, which was formed when the rear part of the ancient landslide slipped.

- 2) Stratigraphic lithology. Longitudinally, rock formation is $260^{\circ}\angle 26^{\circ}$ in the upper part and $260^{\circ}\angle 0^{\circ}$ in the lower part, forming a gently dipping-out layered slope. At 100 m from the left of the landslide, the rock formation changed from $260^{\circ}\angle 26^{\circ}$ to $180^{\circ}\angle 25^{\circ}$, and an obvious interlayer fracture zone with a thickness of 0.2–0.3 m was seen in the excavation face (Figure 7).
- 3) Deformation failure feature. The ZK2-6 borehole had exposed two broken layers (Figure 3). The upper layer was composed of soft argillaceous siltstone, sub-angular and sub-circular, with particle sizes 3 cm–5 cm and contained 0.2 cm–2.0 cm thickness of loose sandy breccia, which belonged to the basis of the interlayer dislocation caused by ancient landslides in geological history.

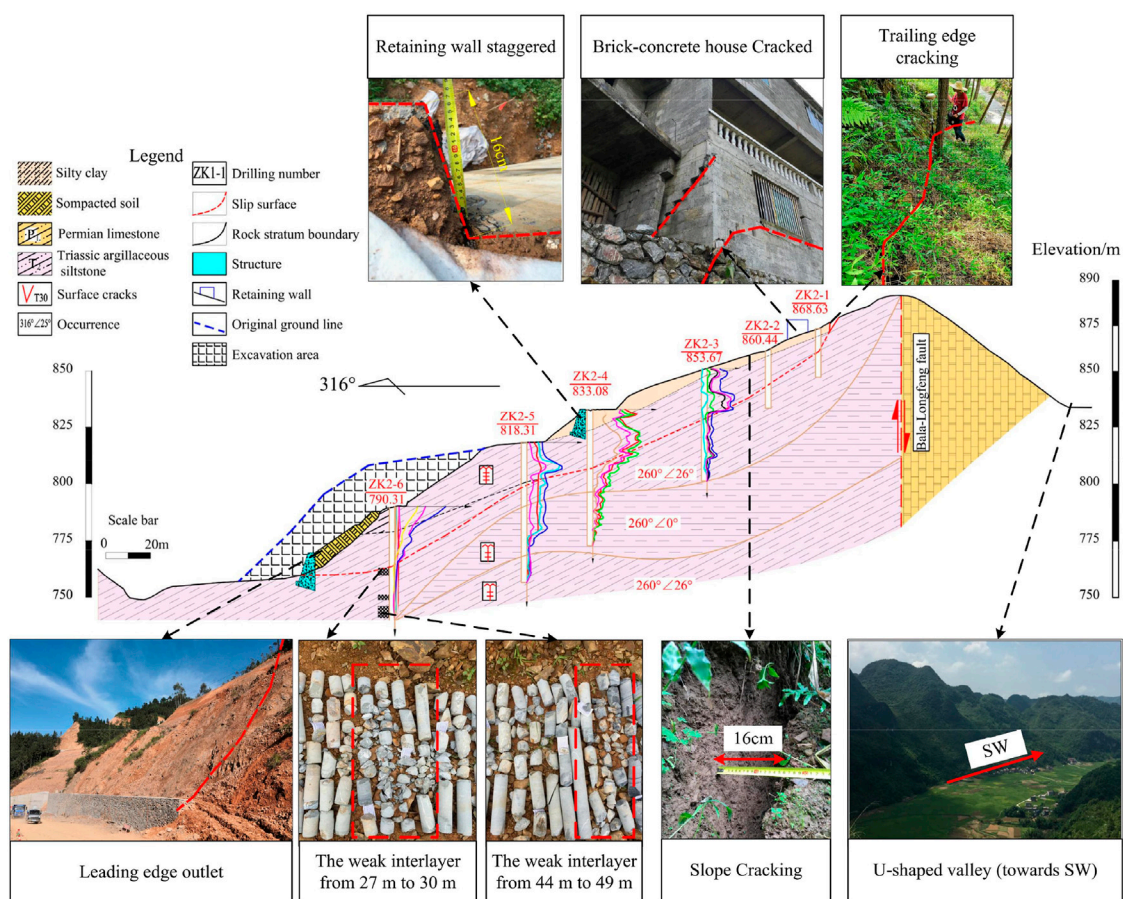


FIGURE 3
Geological profile of the main axis of a typical landslide.

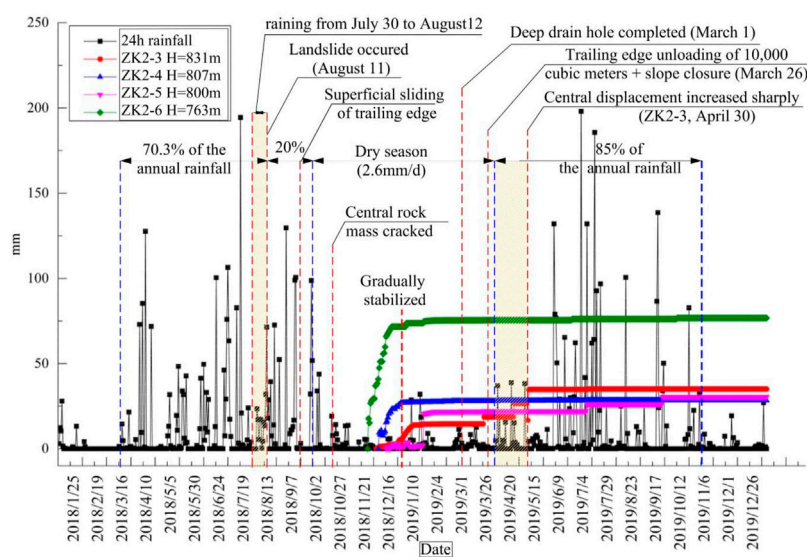


FIGURE 4
Daily rainfall and deep displacement data in the study area.



FIGURE 5
Deformation signs in the middle part entering the dry season.



FIGURE 6
Creep remaining after landslide reaction.

In general, the above characteristics show that the landslide is a slipping-stretching ancient landslide formed in geological history.

3.4 Preliminary discussion on the landslide mechanism

Rainfall leads the landslide body to gain weight and decreases the sliding surface shear strength. When the sliding surface shear force is

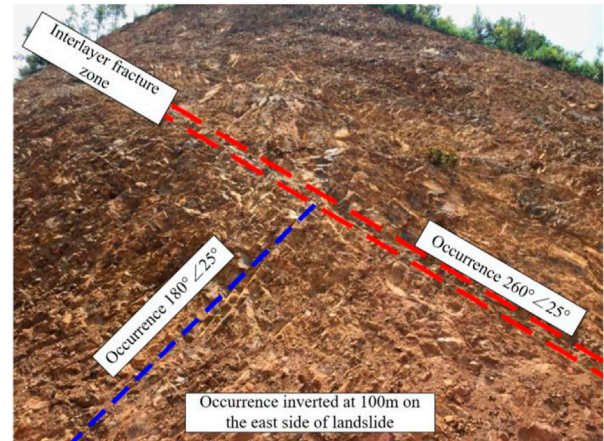


FIGURE 7
Occurrence and interlayer fracture zone on the east side of the landslide area.

less than the sliding force, a bottom-up deformation occurs: leading edge slips → newly formed retaining walls in the middle are dragged to the wrong platform → shallow soil at trailing edge is pulled and cracked by traction. In addition, the slope body is still active in the rainy season after the treatment is completed, indicating that the ancient landslide still inherited its sensitivity to rainfall after the landslide reaction. Therefore, there is good correspondence between landslide reaction development and rainfall. Rainfall is thus the external force in slipping-stretching ancient landslide reaction.

4 Analysis of mechanism of slipping-stretching ancient landslide caused by unloading

The Liangtian'ao ancient landslide remained stable for decades, so its original stability coefficient F_s is taken as 1.18. In order to analyze the unloading effect on an ancient landslide reaction, a FEM model was established based on the existing results to analyze the strain characteristics of landslide during the excavation process.

4.1 Numerical model and its parameters

- 1) Determination for the position of the sliding surface. ZK2-6 has an interlayer broken zone 27 m (760 m) – 30 m (763 m), and a deep displacement monitoring curve change at 763 m. Thus, the sliding surface of the leading edge is located at an elevation of 760 m–763 m. The distribution of the sliding surface is shown in Figure 8.
- 2) Selection of physical and mechanical parameters. A comprehensive method that combines test evaluation, empirical assessment, and back calculation was used to evaluate the physical and mechanical parameters of the rock and soil. For the underlying bedrock, these parameters have little effect on the results of slope simulation analysis, which can be evaluated directly based on field investigation data. For

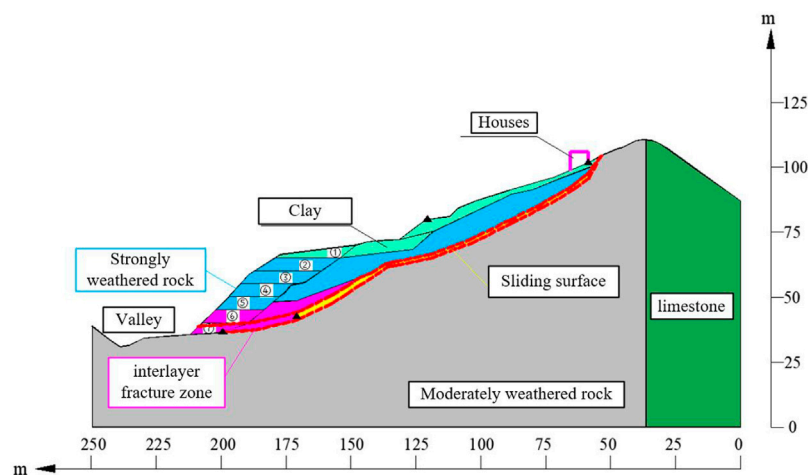


FIGURE 8

Numerical simulation model of the study case.

TABLE 1 Physical and mechanical parameters.

Material	E/MPa	ν	$\gamma/\text{kN}\cdot\text{m}^{-3}$	C/kPa	$\Phi/^\circ$
Clay	80	.35	18.7	11.0	16.0
Strongly weathered rock	120	.25	23.0	45.0	28.0
Moderately weathered rock	20,000	.25	26.5	150	45.0
Sliding surface	100	.3	21.0	25.0	15.8
Limestone	30,000	.20	26.5	200	55.0
Interlayer fracture zone	100	.35	23.0	20.0	25.0

residual soil—interlayer zone and sliding surface—key parameters such as modulus and strength are calculated by a back analysis method according to the parameter interval provided by laboratory tests. According to the consistency requirements of landslide failure characteristics, stability coefficient in each excavation stage of landslide simulation analysis, and actual working conditions, the rock and soil conforms to the Mohr-Coulomb model, with the parameters under saturated conditions shown in Table 1. The displacement of the left and right model boundary is fixed in the X-direction, and the bottom constrains the displacement in the XY-direction. GEO5 software was used for this calculation.

- 3) Simulation results. In vertical view, the equivalent plastic strain zone gradually expands from top to bottom with the excavation process, and the leading rock blocks the expansion while the excavation is completed. Taking half of the unloading height as a boundary, the expansion is not obvious when it is less than this value. In contrast, when it exceeds half, the expansion rapidly accelerates to the front edge of the landslide. During the excavation process, the slope deformation proceeds from back to front. When the unloading height of the leading edge reaches half, the middle sliding

surface is completely formed. When the unloading height of the leading edge reaches 25 m, the rock mass at the leading edge is deformed, and the influence range spreads 27–30 m below the surface. At the same time, F_s decreases 1.18–0.998 with the excavation time step. Overall, the deformation characteristics of the landslide extend from bottom to top.

4.2 Reaction mechanism of slipping-stretching ancient landslide reaction

As shown in Figure 9. The slipping-stretching ancient landslide remains stable before excavation, and the original sliding surface produces strain with the unloading process acting on the leading edge; at the same time, the stability of the ancient landslide gradually decreases. As gradual cutting at the leading edge support and slope stress is adjusted, the original sliding surface strain cumulates to a qualitative change, leading to a sudden ancient landslide reaction. The reaction is manifested as a chair-shaped crack on the back edge and a subsidence gap cracked onto retaining wall. The weathered rock mass in the front edge blocks the whole from sliding, leading to fewer signs of on-site deformation—consistent with on-site observations. The slipping-stretching landslide is still sensitive to rainfall; with a heavy rainfall season, even a secondary landslide will deform.

Based on these results, the geological background is the internal cause for the formation of slipping-stretching ancient landslides. Landslide reaction is caused by external causes like excavation, with rainfall as the internal cause.

4.3 Principles of treatment for slipping-stretching ancient landslide reactions

The reaction in this study case is mainly related to the unloading effect and rainfall touch-slip effect. The integrity and shear strength

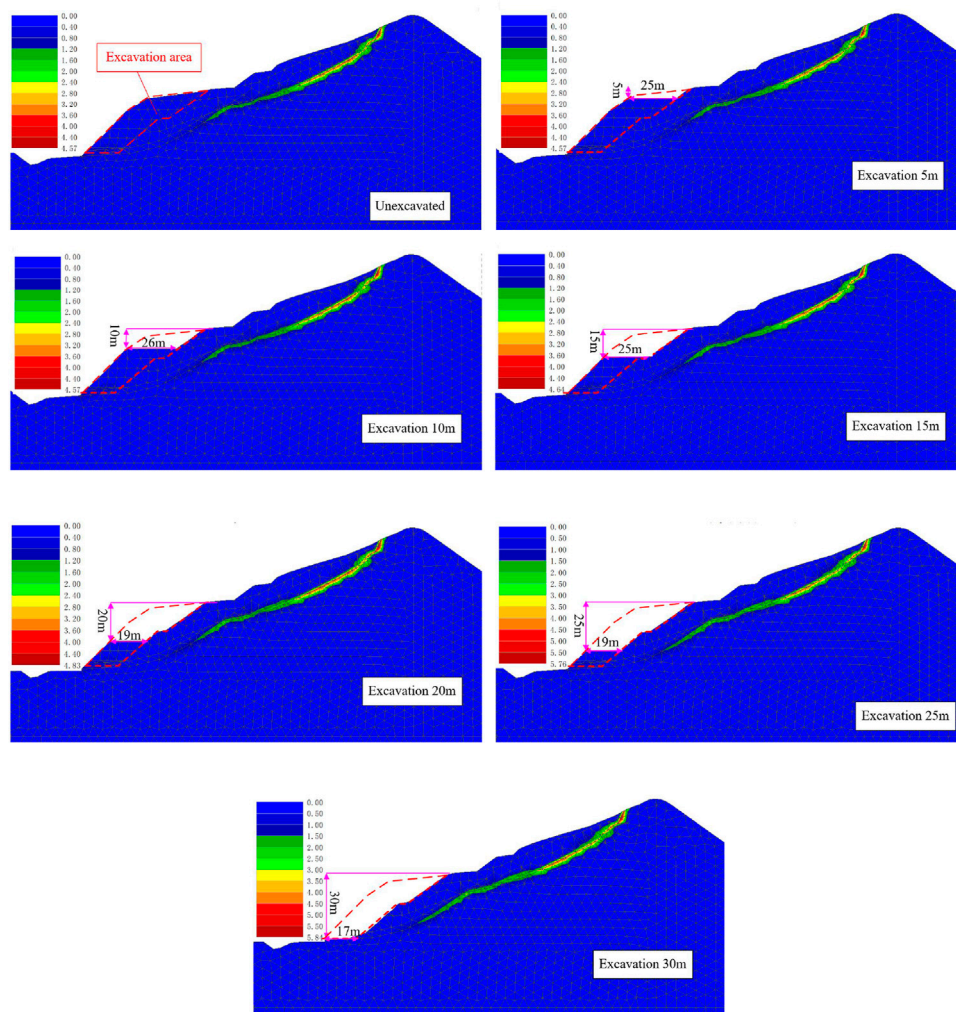


FIGURE 9
Equivalent plastic strain distribution map during excavation.

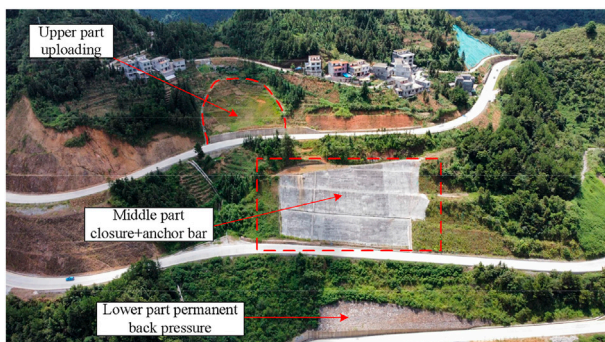


FIGURE 10
Aerial photograph of landslide after treatment (October 2021).

of the leading-edge anti-slip segment affects whether deformation and damage continue to develop. Moreover, rainfall has great significance. The principles governing such landslides can thus be derived.

- 1) The primary requirements that ensure the stability of the whole slope are control of the thickness of the passively compressed rock mass at its leading edge, and the distance between the excavation surface and the leading edge. As the base support for the slope is cut off, the shear strength of the original sliding surface cannot provide sufficient resistance to sliding.
- 2) Once a slipping-stretching ancient landslide is revived, it is extremely important to maintain the stability of the passively compressed section at leading edge to control the overall deformation, thereby effectively controlling the downward trend.
- 3) The different parts of slipping-stretching ancient landslides have various deformed states, and the best time for treatment occurs at the stage of gradual stabilization. For example, the Liangtian'ao landslide unloaded 10,000 m³ (1/20 of the sliding volume) to stop the landslide downtrend completely.
- 4) Rainfall is unfavorable to the stability of slipping-stretching ancient landslides, and this type of landslide still inherits the above characteristics after its reaction. In the treatment plan, the rainfall should be cut off as much as possible, and the groundwater should be drained. For example, after the Liangtianao landslide, groundwater was drained and slope

surface was closed so that the threat of re-sliding was avoided during the 2019–2021 rain season (Figure 10).

5 Conclusion

- 1) The geological background and deformation characteristics indicate that the failure-type of the Liangtian'ao ancient landslide is slipping-stretching, but the ancient macroscopic characteristics are not obvious, and attention should be paid to screening such a landslide in engineering construction.
- 2) Unloading is the factor that induces a slipping-stretching ancient landslide reaction, and heavy rainfall is the external factor. The slope deformation characteristics advance from bottom to top during the reaction process. Such a landslide still inherits sensitivity to rainfall after reactivation, and rainfall may trigger a secondary reaction.
- 3) The intact rock mass at the leading edge prevents an overall slide, so its minimum thickness should be controlled during excavation, with attention to the distance between the excavation surface and front rock mass.
- 4) In treating a slipping-stretching landslide reaction, disturbance to the intact rock mass at the leading edge should be avoided, and the downhill section should be properly unloaded. It is always beneficial to keep the landslide stable by preventing the unencumbered entry of rain into the slope.
- 5) Due to the restriction of site conditions, the variation law of the Liangtianao landslide in rainfall infiltration was not obtained, and much work is still needed to evaluate the rainfall touch-slip effect on the whole processes of slipping-stretching ancient landslide reactions.

References

- Broadbent, C. D., and Ko, K. C. (1971). In Proceedings of the 13th Symp on Rock Mechanics, Urbana, Illinois, September 1971, 537–572.
- Burda, J., Hartvich, F., Valenta, J., Smitka, V., and Rybář, J. (2013). Climate-induced landslide reactivation at the edge of the Most Basin (Czech Republic)—progress towards better landslide prediction. *Nat. Hazards Earth Syst. Sci.* 13 (2), 361–374. doi:10.5194/nhess-13-361-2013
- Cai, Y. J., Xu, F. X., Zhu, M., Li, Y. H., and Gao, J. H. (2021). Risk analysis of instability and blockage of the residual body of the Baige landslide on the Jinsha River. *Eng. Sci. Technol.* 53 (06), 33–42. (in Chinese).
- Chen, X. L., Hui, H. J., and Zhao, Y. H. (2014). The relationship between fault properties and landslide distribution: Taking the large-scale landslide in the Wenchuan earthquake as an example. *Seismol. Geol.* 36 (2), 358–367. (in Chinese).
- Deng, H., Wu, L. Z., Huang, R. Q., Guo, X. G., and He, Q. (2017). formation of the siwanli ancient landslide in the dadu river, China. *Landslides* 14 (1), 385–394. doi:10.1007/s10346-016-0756-9
- Huang, R. Q. (2009). Some catastrophic landslides since the twentieth century in the southwest of China. *Landslides* 6 (1), 69–81. doi:10.1007/s10346-009-0142-y
- Huang, X. H., Yi, W., Gong, C., Huang, H. F., and Yu, Q. (2020). Research on the deformation mechanism of ancient landslides caused by excavation. *Chin. J. Geotechnical Eng.* 42 (7), 1276–1285. (in Chinese).
- Huang, X., Yang, W. M., Zhang, C. S., Shen, J. F., and Liu, T. (2013). Deformation characteristics and formation mechanism of Xieliupo landslide in Zhouqu. *J. Geomechanics* 19 (2), 178–187.
- Li, M. H., Zheng, W. M., Shi, S. W., and Xie, Z. S. (2008). The revival mechanism and stability analysis to Jiayu landslide of Danba county in Sichuan province. *J. Mt. Sci.* 26 (5), 577–582. (in Chinese).
- Li X. X., Li, S. D., Chen, J., and Liao, Q. L. (2008). The internal and external dynamic coupling mechanism of geological disasters. *Chin. J. Rock Mech. Eng.* (9), 1792–1806. (in Chinese).
- Liu, N. F., Li, N., Li, G. F., and Song, Z. P. (2022). Method for evaluating the equivalent thermal conductivity of a freezing rock mass containing systematic fractures. *Rock Mech. Rock Eng.* doi:10.1007/s00603-022-03038-9
- Liu, N. F., Li, N., Wang, S. J., Li, G. F., and Song, Z. P. (2022). A fully coupled thermo-hydro-mechanical model for fractured rock masses in cold regions. *Cold Regions Sci. Technol.* 205, 103707. doi:10.1016/j.coldregions.2022.103707
- Lo, K. Y., Wai, R. S. C., Palmer, J. H. L., and Quigley, R. M. (1978). Time-dependent deformation of shaly rocks in southern Ontario. *Can. Geotechnical J.* 15 (4), 537–547. doi:10.1139/t78-057
- Macciotta, R., Hendry, M., and Martin, C. D. (2016). Developing an early warning system for a very slow landslide based on displacement monitoring. *Nat. Hazards* 81 (2), 887–907. doi:10.1007/s11069-015-2110-2
- Pradhan, S., Toll, D. G., Rosser, N. J., and Brain, M. J. (2022). An investigation of the combined effect of rainfall and road cut on landsliding. *Eng. Geol.* 307, 106787. doi:10.1016/j.enggeo.2022.106787
- Qu, S. J., Zhao, J. J., Ding, X. M., Xie, M. L., and Bu, F. (2016). Discrete element simulation of rainfall-induced gently dipping bedding landslide mechanism. *Hydrogeology Eng. Geol.* 43 (6), 120–126. (in Chinese).
- Sangirardi, M., Amorosi, A., and de Felice, G. (2020). A coupled structural and geotechnical assessment of the effects of a landslide on an ancient monastery in Central Italy. *Eng. Struct.* 225, 111249. doi:10.1016/j.engstruct.2020.111249
- Song, L., Zuo, S. S., Ding, J., Zhong, H. J., Zhang, H., et al. (2012). Analysis of the cause and mechanism of the resurrection of the hongmei village landslide in dujiangyan, sichuan. *Chin. J. Geol. Hazard Control* 23 (2), 34–37. (in Chinese).
- Wartman, J., Montgomery, D. R., Anderson, S. A., Keaton, J. R., Benoit, J., dela Chapelle, J., et al. (2016). The 22 March 2014 oso landslide, Washington, USA. *Geomorphology* 253, 275–288. doi:10.1016/j.geomorph.2015.10.022
- Wei, C. L., Zhang, Y., Feng, W. K., et al. (2018). Genesis and reactivation analysis of large-scale landslides in the meandering section of the upper minjiang river—taking yuanbazi ancient landslide in songpan county as an example. *Hydrogeology Eng. Geol.* 45 (6), 141–149. (in Chinese).
- Wolken, G. J., Liljedahl, A. K., Brubaker, M., Coe, J. A., Fiske, G., Christiansen, H. H., et al. (2021). *Arctic report card*. Glacier and permafrost hazards
- Wu, R. A., Zhang, Y. S., Guo, C. B., Yang, Z. H., Ren, S. S., and Chen, P. (2018). Study on the resurrection characteristics and risk prediction of the Shangyaogou ancient landslide in Songpan, Western Sichuan-Wu Ruian. *Chin. J. Geotechnical Eng.* 40 (9), 1659–1667. (in Chinese).
- Xue, D., Li, T., Wei, Y., and Gao, M. (2015). Mechanism of reactivated badu landslide in the badu mountain area, southwest China. *Environ. Earth Sci.* 73 (8), 4305–4312. doi:10.1007/s12665-014-3714-7

Data availability statement

The original contributions presented in the study are included in the article/Supplementary Material, and further inquiries can be directed to the corresponding author.

Author contributions

LY, drafting papers. ZH (corresponding author), work concept or design, make important revisions to the paper, approve the final paper to be published. LS, HL, LH, and WX, data collection.

Conflict of interest

LY, ZH, HL, LH, and WX were employed by Guangxi Transportation Science and Technology Group Co., Ltd.

The remaining author declares that the research was conducted in the absence of any commercial or financial relationships that could be construed as a potential conflict of interest.

Publisher's note

All claims expressed in this article are solely those of the authors and do not necessarily represent those of their affiliated organizations, or those of the publisher, the editors, and the reviewers. Any product that may be evaluated in this article, or claim that may be made by its manufacturer, is not guaranteed or endorsed by the publisher.

- Zhang C, C., Yin, Y., Yan, H., Li, H., Dai, Z., and Zhang, N. (2021). Reactivation characteristics and hydrological inducing factors of a massive ancient landslide in the three Gorges Reservoir, China. *Eng. Geol.* 292, 106273. doi:10.1016/j.enggeo.2021.106273
- Zhang, X., Zhou, H. L., Liu, F., Yu, F., and Xie, C. T. (2021). Research on the characteristics of temperature changes in Tian'e in the past 60 years. *Agric. Disaster Res.* 11 (8), 73–75+8. (in Chinese).
- Zhang, Y. W., Fan, S. Y., Yang, D. H., and Zhou, F. (2022b). Investigation about variation law of frost heave force of seasonal cold region tunnels: A case study. *Front. Earth Sci.* 9, 806843. doi:10.3389/feart.2021.806843
- Zhang, Y. W., Song, Z. P., and Weng, X. L. (2022a). A constitutive model for loess considering the characteristics of structurality and anisotropy. *Soil Mech. Found. Eng.* 59 (1), 32–43. doi:10.1007/s11204-022-09781-z
- Zhang, Z. Y. (2016). *The principle of engineering geological analysis*. 4th. Kolkata India: Geological Press. (in Chinese).
- Zhong, Y. J., Fan, X. M., Dai, L. X., Zhou, C. B., Zhang, F. Y., and Xu, Q. (2021). Research on the giant ancient landslide in Diexi on the minjiang river. *Prog. Geophys.* 36 (4), 1784–1796. (in Chinese).
- Zou, Z. X., Tang, H. M., Xiong, C. G., Wu, Y. P., Liu, X., and Liao, S. B. (2012). Progressive failure geomechanical model and stability analysis of large bedding rock landslides. *Chin. J. Rock Mech. Eng.* 31 (11), 2222–2231. (in Chinese).



OPEN ACCESS

EDITED BY

Yuwei Zhang,
Xi'an University of Architecture and
Technology, China

REVIEWED BY

Yanbo Cao,
Chang'an University, China
Bolong Liu,
Shaoxing University, China

*CORRESPONDENCE

Hong Zenglin,
✉ lhqhzl@163.com

SPECIALTY SECTION

This article was submitted to
Environmental Informatics
and Remote Sensing,
a section of the journal
Frontiers in Earth Science

RECEIVED 22 November 2022

ACCEPTED 24 January 2023

PUBLISHED 15 February 2023

CITATION

Wei S, Zenglin H, Min Y, Ning L and
Tianxiang T (2023), Impact of subway
shield tunnel construction on deformation
of existing utility tunnel.
Front. Earth Sci. 11:1104865.
doi: 10.3389/feart.2023.1104865

COPYRIGHT

© 2023 Wei, Zenglin, Min, Ning and
Tianxiang. This is an open-access article
distributed under the terms of the [Creative
Commons Attribution License \(CC BY\)](#).
The use, distribution or reproduction in
other forums is permitted, provided the
original author(s) and the copyright
owner(s) are credited and that the original
publication in this journal is cited, in
accordance with accepted academic
practice. No use, distribution or
reproduction is permitted which does not
comply with these terms.

Impact of subway shield tunnel construction on deformation of existing utility tunnel

Shi Wei¹, Hong Zenglin^{1*}, Yang Min², Li Ning² and Tan Tianxiang²

¹Shaanxi Engineering Technology Research Center for Urban Geology and Underground Space, Hydrogeology, Engineering Geology and Environment Geology Survey Center, Shaanxi, China, ²Department of Civil and Architecture Engineering, Xi'an University of Technology, Shaanxi, China

In recent years, the development of urban underground space in China, especially the construction and operation of subway tunnels, has greatly relieved the pressure of urban traffic. Due to the imperfect planning of urban facility, many subway tunnels have to be built under the existing utility tunnels (pipe galleries). Nevertheless, shield construction of subway tunnel has a great adverse impact on the deformation and safety of the existing pipe gallery. Therefore, this paper takes Xi'an Metro Line 2 as an example, and studies the safety depth for subway tunnel shield construction under different regional conditions in Xi'an through numerical simulation. The results show that the deformation of the existing pipe gallery and its influence range decrease with the rising buried depth of the double-line subway tunnel when the soil properties are good. For example, in the loess tableland area, when the buried depth of the subway tunnel is greater than 12 m, the settlement deformation of the pipe gallery basically meets the control standard. When the soil properties are poor or the soil properties vary greatly, the subway tunnel excavation has a great impact on the safety of the pipe gallery. For example, in the first-level alluvial fan area with sand layer, when the buried depth of the subway tunnel is less than 24 m and more than 12 m, the deformation standard cannot be satisfied. In addition, in the first-level alluvial fan area with sand layer, the lower soil layer should be treated or the construction parameters should be optimized before the excavation of subway tunnel. The research results can provide reference for similar engineering construction.

KEYWORDS

geological characteristics, shield tunnel, construction disturbance, utility tunnel, deformation

1 Introduction

In cities, utility tunnels are underground structures commonly used to transport water, sewage, oil, gas, etc. Utility tunnels have been constructed throughout the world since their first appearance in Paris in 1851. With the rapid expansion of underground space, the construction of underground structures will inevitably lead to the change of the surrounding stress field and displacement field, which will greatly affect the stability of the existing underground structures around them (Chen et al., 2011a; 2011b; Ma et al., 2017). How to reduce the mutual influence between tunnel lines is an urgent problem to be solved in the construction of underground buildings in the future.

Most of the previous studies focus on the seismic response of underground pipe galleries (Li et al., 2009; Shi et al., 2010; Tang et al., 2009; You, 2011; Luo, 2013; Ye, 2014; Shamsabadi et al., 2001; 2002; Dashti et al., 2016; Kimura et al., 2005; Qin et al., 2022; Li et al., 2023; Liu et al., 2022a). But with the rapid growth of underground pipe galleries in recent years, ground fracture, a special geological disaster, has brought great challenges to the construction of

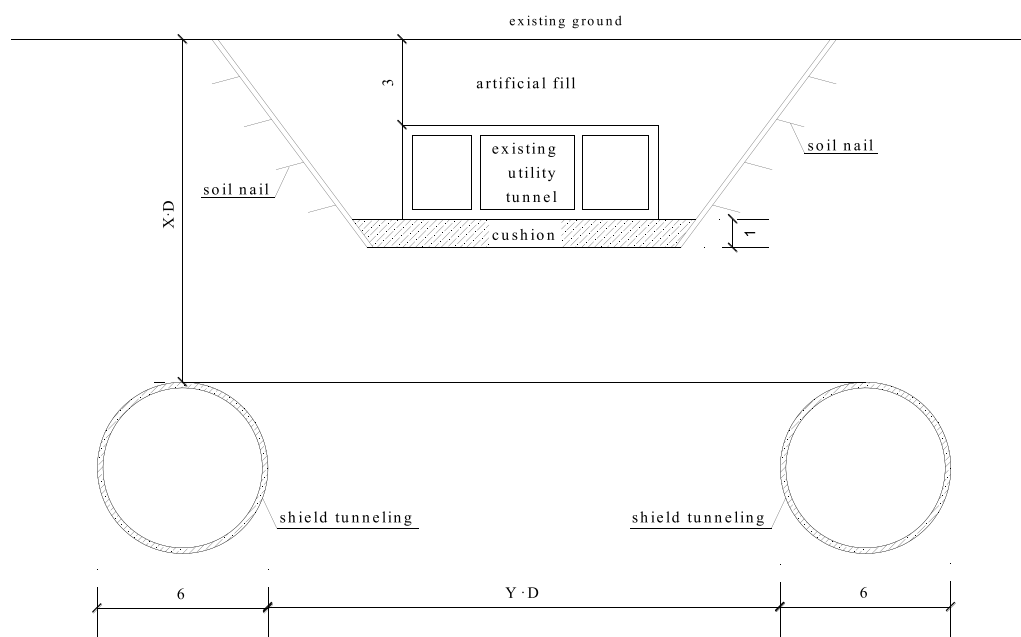


FIGURE 1
Relative position of tunnel and pipe gallery (unit: m).

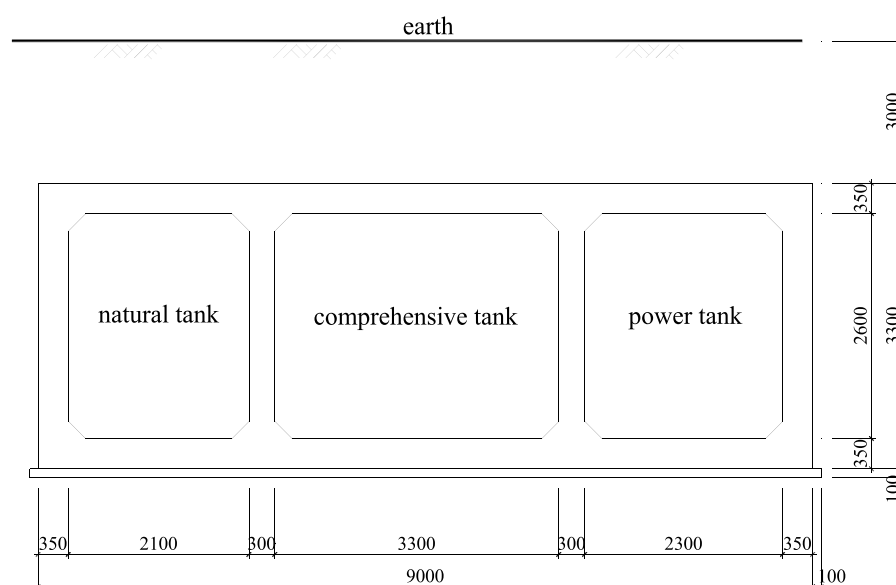


FIGURE 2
Dimensions of the underground pipe gallery (unit: mm).

underground pipe galleries. Therefore, many scholars have shifted their research focus to the impact of ground factors on underground pipe galleries (Zhu, 2018; Hu et al., 2019; Ma et al., 2019; Yang et al., 2019; Yan et al., 2018; Yan 2019). Some have also studied the mechanical characteristics of underground utility tunnel during its construction. For example, Hu and Xue (2010) studied the mechanical characteristics of prefabricated prestressed utility tunnel through

monotone static test. Duan et al. (2020), based on the actual monitoring data of post-construction settlement of a high loess filling site in Shaanxi province, investigated the stress deformation state of the underground utility tunnel at the combined position of excavation and filling through physical tests.

With the increase of the number of underground pipe galleries, various problems have emerged one after another, especially when

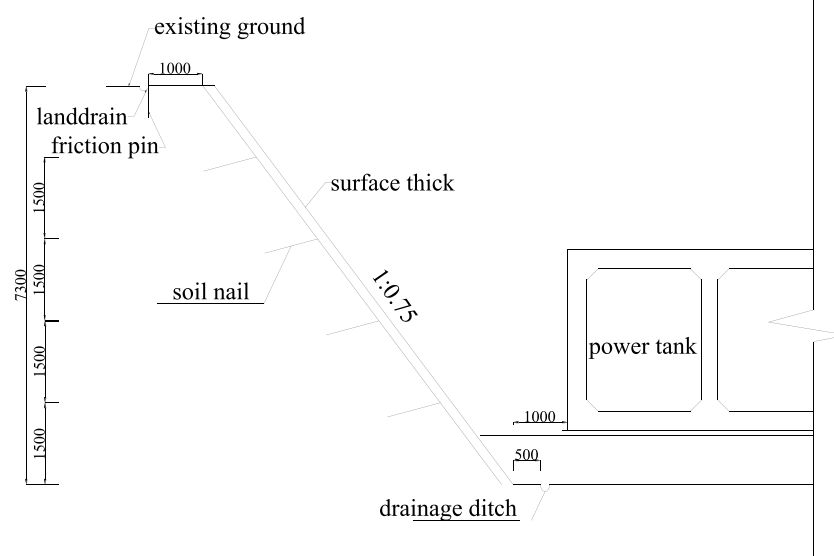


FIGURE 3
Schematic diagram of the left half of the pipe gallery (unit: mm).

TABLE 1 Calculation conditions.

Region	Buried depth of tunnel (m)
Loess tableland	12
First-level terrace of Weihe River	18
First-level alluvial fan area	24

they are close to or crossing under existing buildings (structures) (You 2017). Some achievements have been made in the research on the joint construction of underground utility tunnel and urban subway. For example, Zhao et al. (2018) conducted a numerical simulation analysis on the impact of the explosion in the natural gas compartment of the utility tunnel on the adjacent subway tunnel. Gao and Haifeng (2018) analyzed the tunneling conditions with and without reinforcement measures during the excavation of underground utility tunnel that crosses existing subway tunnel. Feng et al. (2018) simulated the open-cut construction process of underground utility tunnel of Metro Line 1 in Baotou through finite element software Midas-GTX, and analyzed the influence of the open-cut construction on the structure of nearby subways. Peng (2017) studied the technical feasibility of simultaneous construction of utility tunnel and subway. Wu (2017) used ABAQUS to conduct finite element modeling on the excavation process of the underground utility tunnel in Tongzhou, Beijing, and analyzed the impact of the excavation process on the tunnel structure and surrounding soil. Yang et al. (2019) studied the reinforcement measures that should be taken when the underground utility tunnel in the soft soil area of Kunming is close to the existing subway. Wang and Jiang (2019) took the project of an underground utility tunnel in Beijing as an example to analyze and optimize the construction scheme of comprehensive utility tunnel passing through the existing subway. Yang et al. (2020, 2021) studied the

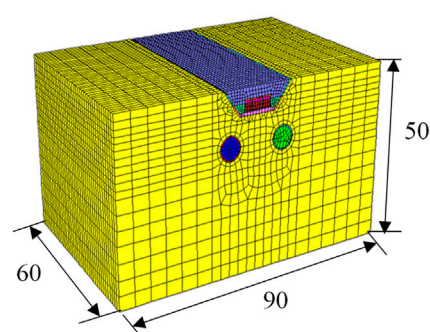


FIGURE 4
Diagram of model (unit: m).

interaction between subway and comprehensive tunnel in loess area. The existing research mainly focuses on the construction technology, the mechanical effect of underground utility tunnel, and the influence of utility tunnel construction on the existing subway, but there are few reports on the influence of subway construction on the deformation of the existing utility tunnel. More in-depth research and analysis should be carried out on the large-scale construction of underground pipe galleries and subways in the future. It is therefore of great practical significance to investigate the interaction between underground utility tunnel and existing subway under different regional conditions.

Based on a Metro shield tunnel project in Xi'an, this paper numerically simulates and analyzes the influence of three-dimensional dynamic construction of shield tunnel on the displacement of existing underground utility tunnel under different regional conditions and subway buried depths, so as to provide reference for similar projects.

TABLE 2 Soil properties of loess tableland.

Soil layer	Buried depth of top plate (m)	Soil thickness (m)	Natural bulk weight γ (kN/m ³)	Modulus of deformation E_0 (MPa)	Poisson's ratio ν	Cohesive force c (kPa)	Internal friction angle φ (°)
Loess	0.00	8.85	14.8	8.5	0.33	27.4	17.1
Paleosol	8.85	1.64	19.0	26.4	0.29	43.7	23.4
Loess	10.49	4.89	15.0	17.1	0.33	29.6	15.4
Paleosol	15.38	1.06	16.8	28.0	0.27	31.7	19.6
Loess	16.44	4.54	17.4	23.6	0.32	27.8	20.3
Paleosol	20.97	1.27	17.8	14.0	0.31	31.4	21.3
Loess	22.24	6.33	16.8	11.3	0.28	26.8	17.8
Paleosol	28.57	1.24	18.7	16.3	0.27	25.1	17.2
Loess	29.82	5.68	19.8	6.7	0.29	42.2	27.1
Paleosol	35.49	4.45	20.0	19.1	0.3	45	22
Loess	39.94	7.56	19.1	12.1	0.29	42	26
Paleosol	47.51	1.26	19.8	7.2	0.31	45	20
Loess	48.77	10.18	20.0	9.2	0.3	42	26
Paleosol	58.95	0.76	12.2	15.8	0.32	45	20

TABLE 3 Soil properties of first-level terrace of Weihe River.

Soil layer	Buried depth of top plate (m)	Soil thickness (m)	Natural bulk weight γ (kN/m ³)	Modulus of deformation E_0 (MPa)	Poisson's ratio ν	Cohesive force c (kPa)	Internal friction angle φ (°)
Plain fill	0.00	2.17	17.4	5.1	0.33	32	24.9
Loess-like soil	2.17	1.77	17.9	35.6	0.29	40	16
Medium sand	3.94	7.58	20.0	24	0.2	0	33
Silty clay	11.52	3.70	20.2	8.3	0.32	37	25.2
Medium sand	15.22	5.20	18.6	24	0.2	0	33
Silty clay	20.42	8.63	21.4	12.4	0.31	37.4	24.5
Medium sand	29.05	4.20	20.0	24	0.2	0	33
Silty clay	33.25	4.40	20.1	8.3	0.29	28	26.5
Medium sand	37.65	12.43	19.5	24	0.12	0	32
Silty clay	50.08	4.45	19.1	21.2	0.3	35	24
Medium sand	54.53	10.98	19.5	24	0.12	0	32

2 Project profile

2.1 Geological condition

According to the hydrogeological survey data, Xi'an is mainly divided into seven regions: the first-level alluvial fan, the second-level alluvial fan, the third-level alluvial fan, the first-level terrace of Weihe

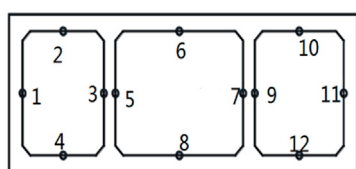
River, the second-level terrace of Weihe River, the third-level terrace of Weihe River, and the loess tableland. These regions have different soil layer distribution as well as soil parameters. According to regional soil characteristics, this paper selects the loess tableland, first-level terrace of Weihe River, and first-level alluvial fan as the research objects. Because the soil layer distribution in each area is quite different, three typical areas are selected for numerical simulation in this paper.

TABLE 4 Soil properties of the first-level alluvial fan.

Soil layer	Buried depth of top plate (m)	Soil thickness (m)	Natural bulk weight γ (kN/m ³)	Modulus of deformation E_0 (MPa)	Poisson's ratio ν	Cohesive force c (kPa)	Internal friction angle φ (°)
Plain fill	0.00	2.0	16.6	2.9	0.33	32	24.9
Loess-like soil	2.0	1.2	17.9	35.6	0.29	40	16
Medium sand	3.2	4.1	20.0	24	0.2	0	33
Silty clay	7.3	2.1	20.2	8.3	0.32	37	25.2
Coarse sand	9.4	2.1	18.6	24	0.2	0	33
Silty clay	11.5	4.9	18.8	7.7	0.31	57	24.5
Coarse sand	16.4	7.6	20.0	24	0.2	0	33
Silty clay	24	17.8	20.1	10.4	0.29	28	26.5
Coarse sand	41.8	2.2	19.5	24	0.25	0	32
Silty clay	43.9	9.1	20.2	13.7	0.3	35	24
Medium sand	53	2.6	19.5	24	0.25	0	32

TABLE 5 Structural parameters of subway tunnel and pipe gallery.

Subject	Bulk weight (kN/m ³)	Modulus of elasticity E (MPa)	Poisson's ratio ν
Pipe	25	2.84E+04	0.20
Equivalent layer (early stage)	23	0.9	0.30
Equivalent layer (late stage)	23	400	0.20
Soil nail wall	22	2.18E+04	0.30
Soil nail	78.5	2.00E+05	0.20
Cushion	23	2.60E+04	0.20
Pipe gallery	25	3.15E+04	0.20

FIGURE 5
Layout of monitoring points.

The soil layer in the loess tableland area is mainly loess alternating with paleosol, and the soil quality is relatively stable. In the first-level terrace of Weihe River, the overburden layer is plain fill and loess-like soil, and the bottom layer is alternately medium sand and silty clay, and the soil property parameters are poor. The soil layer of the first-

level alluvial fan is composed of plain fill and loess in the upper part, and silty clay and coarse sand in the lower part.

2.2 Overview of shield tunnel and utility tunnel (pipe gallery)

The subway shield tunnel of Xi'an Metro Line 2 is the research object of this paper. It is a double-line tunnel with parallel right and left lines and circular cross section. The panel-meter earth pressure balance shield machine is adopted for tunneling. Prefabricated C50 reinforced concrete pipes are used for supporting, and they are connected by bending bolts. The outer diameter of pipes is 6.0 m, the ring width is 1.5 m, and the thickness is generally 300 mm.

The subway tunnel will be built under an existing utility tunnel (to distinct it from subway tunnel, it will be referred to as pipe gallery hereinafter) in Xi'an. The axes of the subway tunnel and the pipe

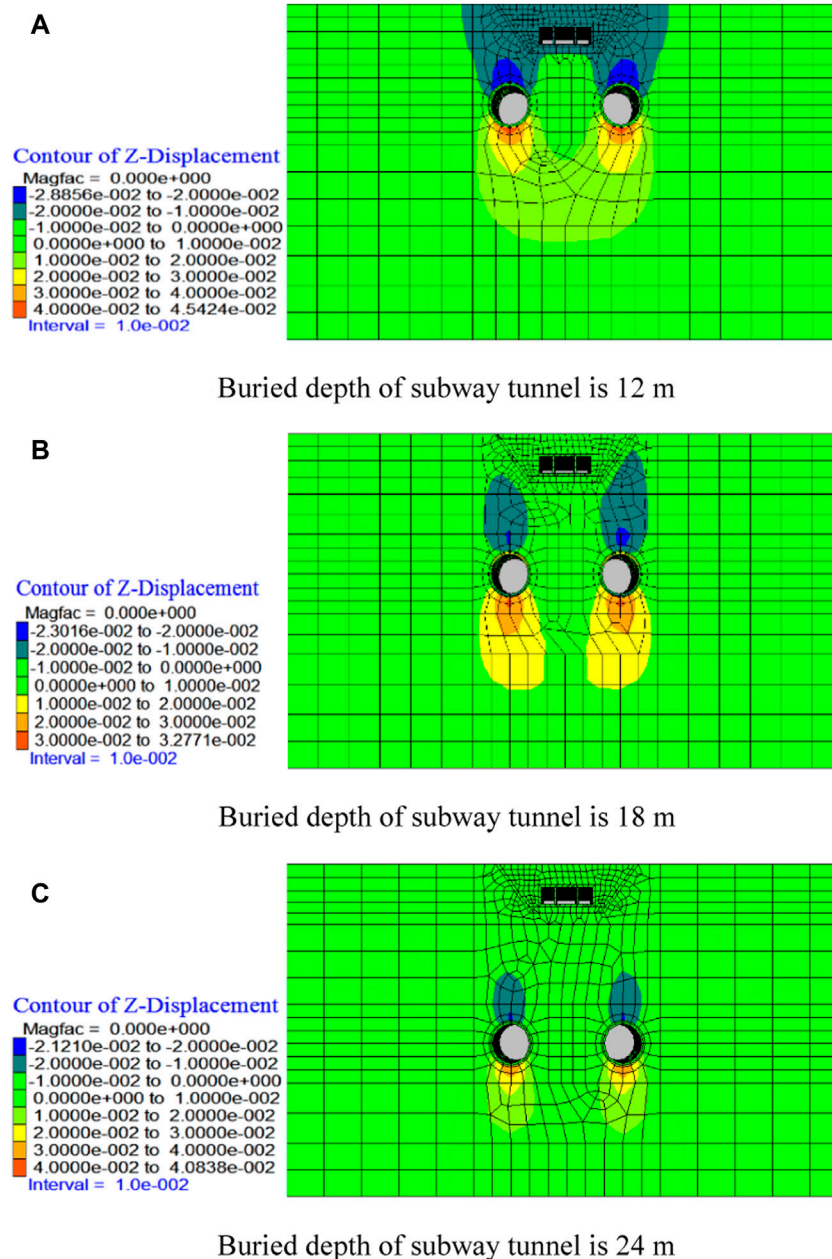


FIGURE 6
 Vertical displacement diagram under different tunnel burial depths (unit: m).

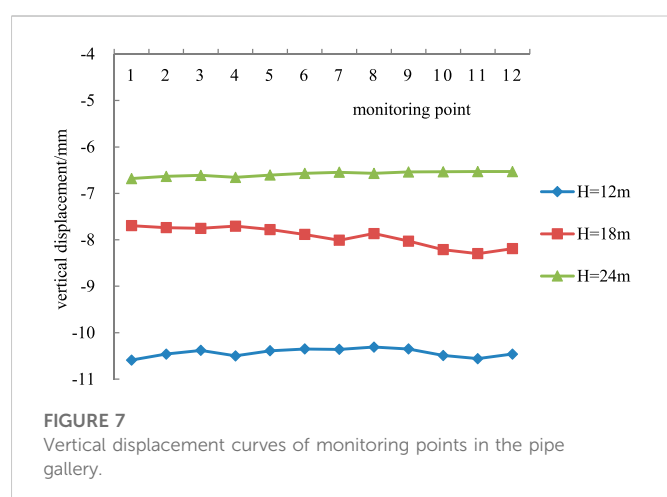
gallery are on the same vertical line. The relative position relationship between a tunnel section and the underground pipe gallery is shown in Figure 1. The pipe gallery is a typical asymmetric three-cabin project consisting of a natural gas cabin, an integrated cabin and a power cabin from left to right. Their specific dimensions are shown in Figure 2.

The underground pipe gallery adopts the economical open-cut method, and its buried depth is 3 m. The pipe gallery structure is cast with C35 concrete. After the excavation, the reinforcement method of sloping and soil nailing was adopted. The slope was 1:0.75. After the soil nails was applied, wire mesh was fixed on the slope surface, which was then sprayed with C20 concrete. The soil nails are HRB400 steel bars with a diameter of 14 mm, and their vertical spacing and longitudinal spacing are 1.5 m and 1.0 m respectively. The

thickness of the shotcrete support is 60 mm. After the foundation pit is excavated to the bottom, the cushion with a thickness of 1.0 m is poured with C15 concrete in time. The left and right sides of the pipe gallery foundation pit are the same, so only the schematic diagram of the left half of the foundation pit is shown in Figure 3.

3 Establishment of numerical model and parameter selection

With strong pre-processing ability, the finite element software ANSYS can provide a variety of subdivision methods according to user requirements, and can control the mesh size. The finite difference



software FLAC^{3D} can provide constitutive models of 11 kinds of materials, which are divided into three groups: cavitation, elasticity and plasticity. Each model represents the physical model of constitutive relations of some specific rock and soil. Therefore, this paper uses ANSYS to establish the numerical model, and then inputs it into FLAC^{3D} for numerical simulation calculation.

3.1 Simulation scheme

In order to investigate the influence of soil properties and subway tunnel burial depth on the deformation of the existing pipe gallery, this paper designs the following calculation conditions, as shown in Table 1.

3.2 Establishment of calculation model

The construction footage of the shield tunnel simulated in this paper is 1.5 m, that is, the tunneling distance of each excavation is the ring width of one pipe pieces, and the simplified treatment is as follows.

- (1) The longitudinal length of the model is 60 m, that is, the length of 40 pipe pieces. Herein, the shell of the shield machine and the pipe are discretionally divided according to the ring width. In order to better simulate the size of the shield machine, the total length of the shield machine is set to 9.0 m, that is, the length of 6 pipe pieces.
- (2) The tunnel structure and pipe gallery structure both adopt linear elastic constitutive relationship.
- (3) The pipe pieces are regarded as a whole, regardless of the pipe connection.

Given that the influence range of tunnel excavation is about 2–3 times the hole diameter, the model size is set to $90 \times 60 \times 50$ m, as shown in Figure 4. Solid elements are used for soil layer, backfill soil, cushion and pipes, among which, soil layer adopts Moore Coulomb model, and cushion and pipes adopts elastic model. The shell of shield machine is simulated by shell element, while the grouting layer, soil nail wall layer and main structure of pipe gallery are calculated by solid element and elastic model. The soil nail is embedded into the soil and surface layer with cable structural unit. Displacement boundary conditions of the model: horizontal constraints are

imposed on the vertical boundary, free constraints on the top, and vertical and horizontal constraints on the bottom. A vertical downward force of gravity is applied to the entire model.

The open-cut method is used to excavate the utility tunnel. The excavation depth of the foundation pit is divided into two excavations. The first excavation is 4 m and the second excavation depth is 3.3 m. In addition, the slope of the foundation pit will be sprayed and soil nailed immediately after excavation in the project. Pit bottom immediately after the cushion construction to prevent excessive exposure of the pit bottom soil.

The simulation process is divided into three stages: (1) the geostress equilibrium of the model under the action of gravity only, (2) excavation of the existing underground pipe gallery, that is, simulation of the deformation and settlement caused by open excavation and casting of the pipe gallery tunnel, and (3) excavation of a double-line subway tunnel beneath the existing pipe gallery. This paper mainly studies the calculation results of the third stage, so after the calculation of the first and second stages, the displacement of soil and structure is reset to zero. Thus, the deformation of the existing pipe gallery is essentially the displacement increment of the pipe gallery caused by the excavation of the new double-line subway tunnel.

3.3 Calculation parameters

In this paper, the physical and mechanical parameters of the soil layers in the three study areas are from the survey data provided by Shaanxi Hydrogeology, Engineering Geology and Environment Geology Survey Center, and the experimental values of the mechanical parameters of loess (Zhu et al., 2010a; Zhang et al., 2022a; 2022b; Liu et al., 2022b). Table 2~ Table 4 present the soil properties of the soil layers in the three regions and the thickness of each layer determined according to the survey data.

The pipes of shield tunnel are made of C50 reinforced concrete. Considering the influence of the stiffness reduction of the spliced pipes, the elastic modulus of the pipe is reduced by 20%, and the elastic modulus of the grouting slurry is determined according to the initial strength and late strength (Zhu et al., 2010b; 2011). During excavation of shield tunnel, the surrounding rock and soil cannot directly contact the pipes (lining), so the gap is filled with grout. To simplify the calculation in the simulation analysis, the mixture of the grouting slurry and the surrounding rock and soil is simplified into a homogeneous equivalent layer, with a thickness of 30 cm. The early and late stages in Table 4 are the early and late stages after grouting between the pipe and the surrounding rock. The weighting method is used to determine the modulus of the soil nail wall of the pipe gallery, and the corresponding structures are simplified into elastic models. The parameters are determined according to Ministry of Housing and Urban-Development of the People's Republic of China (2011) and Ministry of Housing and Urban-Development of the People's Republic of China (2015), as shown in Table 5.

3.5 Arrangement of monitoring points

The monitoring time is the time when the right and left tunnel lines are excavated to the middle of the pipe gallery. Monitoring points are arranged at the midpoint of each chamber in the longitudinal central section of the pipe gallery, as shown in Figure 5.

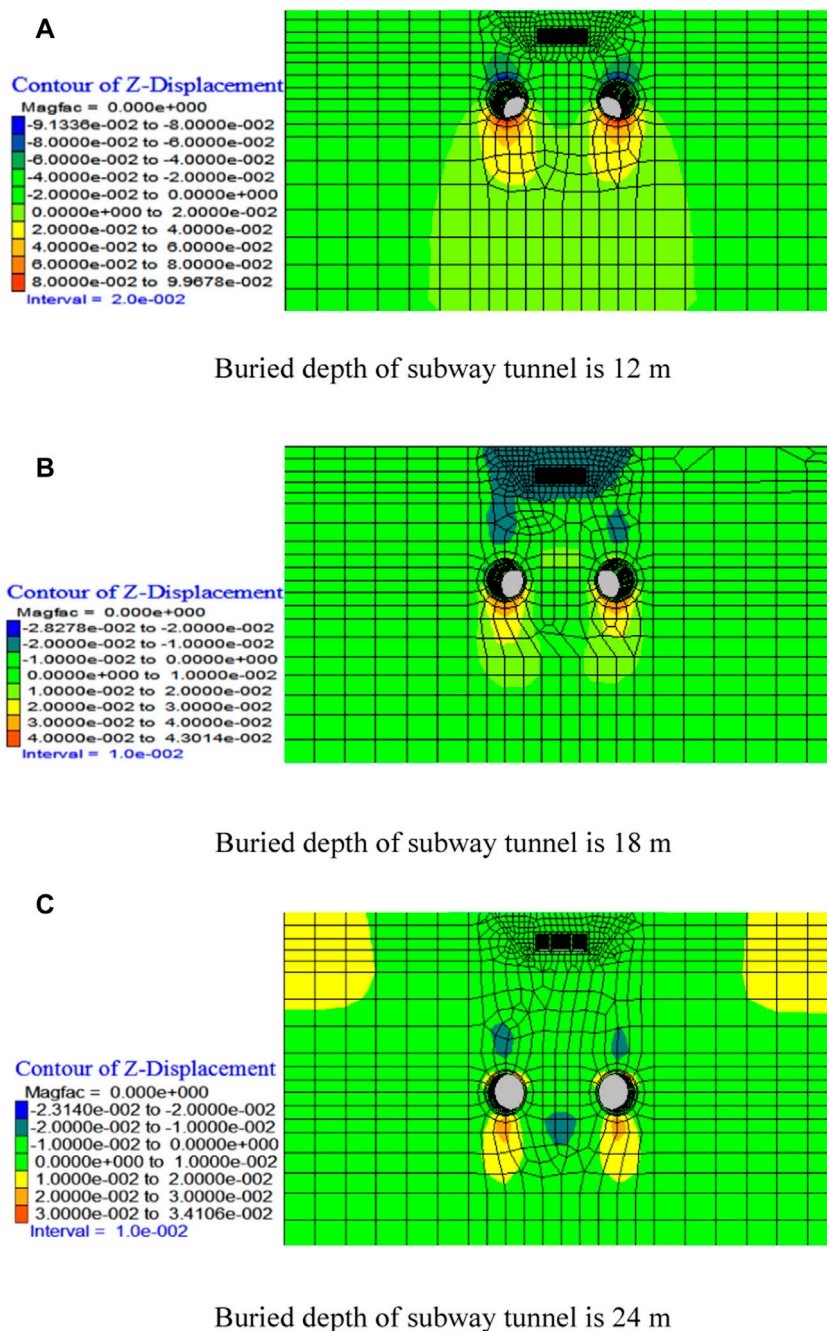


FIGURE 8

Vertical displacement diagram under different tunnel burial depths (unit: m).

4 Analysis of numerical simulation results

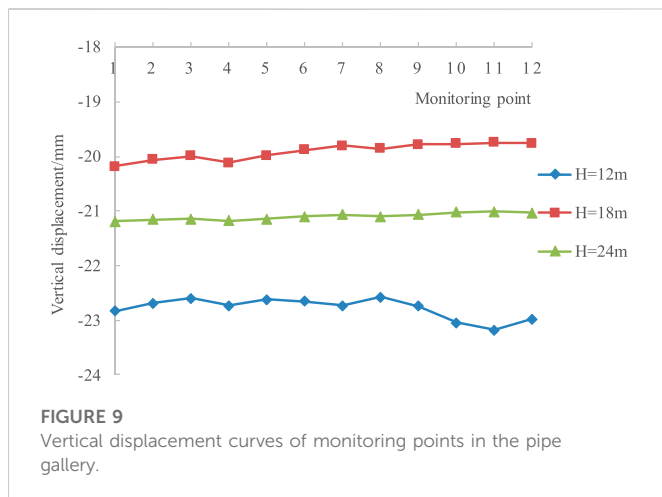
The utility tunnel is a gallery for carrying multiple pipelines, and its deformation control standard is stricter than the general pipeline control standard. However, due to the imperfect regulations on the pipe gallery, according to specification (Ministry of Housing and Urban-Rural Development of the People's Republic of China, 2013), the relevant deformation standard with importance level I is taken as the benchmark, that is, the maximum settlement is -10 mm. In addition, the maximum uplift herein is set to 5 mm according to the control standard

of subway. Since the maximum horizontal displacement of the existing pipe gallery caused by subway tunnel excavation is only 0.3 mm, the vertical deformation of the pipe gallery is mainly analyzed in this paper.

4.1 Impact of tunnel buried depth on existing pipe gallery

4.1.1 Loess tableland

According to the distribution of soil layers in the loess tableland, the corresponding mechanical parameters are assigned to the model.



After the excavation of shield tunnel is completed, the deformation at the monitoring point 30 m away from the portal of the pipe gallery is analyzed. The vertical displacement of pipe gallery and subway tunnel under different buried depths is illustrated in Figure 6, and the vertical displacement curves of the monitoring points are shown in Figure 7.

As shown in Figure 6, the excavation of the new tunnel causes the disturbance of the soil mass, which leads to the displacement of the surrounding rock and soil of the existing pipe gallery. It can be seen that the excavation of the tunnel mainly causes deformation of the soil beneath the pipe gallery—settlement of the soil towards the tunnel. With the increase of tunnel depth, that is, the spacing between the two increases, the influence of tunnel excavation on the stability of the existing pipe gallery decreases.

It can be seen from Figure 7 that as the tunnel buried depth rises, that is, the distance between the tunnel and the pipe gallery increases, the settlement and deformation of the existing pipe gallery decreases. In other words, the influence of soil disturbance on the pipe gallery is reduced, which is clearly shown in the displacement diagram. The maximum settlement of pipe gallery occurs when the tunnel depth is 12 m, and the maximum vertical displacement is 10.5 mm. When the tunnel depth is 24 m, the settlement deformation of pipe gallery reaches its minimum of 7 mm. The settlement curve is roughly a straight line, that is, the pipe gallery is disturbed and produces uniform settlement. This is because the double-line subway is excavated in the same direction at the same time. According to the standard for deformation control of utility tunnel (the allowable maximum settlement is -10 mm, and the maximum uplift is 5 mm), when the tunnel buried depth is greater than 12 m, the deformation criterion is met. Therefore, it is recommended to excavate the right and left lines of the shield tunnel in the same direction at the same time, which can not only ensure the safety of the existing pipe gallery, but also speed up the construction progress of the project.

4.1.2 First-level terrace of Weihe River

According to the distribution of soil layer in Weihe first-level terrace, the corresponding mechanical parameters of each soil layer are assigned to the model. The deformation at the monitoring points 30 m away from the front portal of pipe gallery is analyzed after tunnel excavation. The vertical displacement diagrams of pipe gallery and subway tunnel are shown in Figure 8, and the vertical displacement curves of monitoring points are shown in Figure 9.

As shown in Figure 8, the excavation of subway tunnel mainly causes the deformation of the soil below the pipe gallery, that is, the settlement of the soil towards the subway tunnel. When the tunnel depth is 12 m, the tunnel excavation has the greatest impact on the pipe gallery, while when the tunnel depth is 18 m, this impact is the smallest.

As shown in Figure 9, in the first-level terrace area of Weihe River, the vertical displacement of the pipe gallery does not decrease with the rising tunnel buried depth. When the tunnel depth is 12 m, the vertical displacement of the pipe gallery is the largest, and when the tunnel depth is 18 m, its vertical displacement is the smallest. This is because the strata of 20–30 m in the first class terrace area of Weihe River are alternately distributed with medium-fine sand and silty clay, and the soil condition is poor. Therefore, when the tunnel depth is 24 m, the disturbance to the pipe gallery is greater than that when the tunnel depth is 18 m. But such disturbance is smaller in the case of an 18 m buried depth than a 12 m buried depth due to the increasing spacing, which is clearly shown on the displacement diagram. The maximum settlement of pipe gallery occurs when the tunnel buried depth is 12 m, in which case the maximum vertical displacement is 22.7 mm. Under the same spacing, the deformation curve can be roughly seen as a straight line, that is, the pipe gallery has uniform settlement. This is caused by the excavation of the double-line subway tunnel in the same direction at the same time. According to the standard for deformation control of utility tunnel (i.e., the allowable maximum settlement is -10 mm, and the maximum uplift is 5 mm), when the tunnel buried depth is smaller than or equals 24 m, the deformation criterion cannot be satisfied. In that case, reinforcement measures should be taken for the existing pipe gallery.

4.1.3 First-level alluvial fan area

According to the distribution of the soil layer in the first-level alluvial fan area, the corresponding mechanical parameters are assigned to each soil layer of the model. Similarly, the deformation at the monitoring points 30 m away from the front portal of pipe gallery is analyzed after tunnel excavation. Figure 10 shows the vertical displacement diagram of the pipe gallery under different buried depths. Figure 11 shows the vertical displacement curves of different monitoring points.

It can be observed from Figure 10 that the excavation of subway tunnel mainly causes the deformation of the soil beneath the pipe gallery, i.e., the settlement of soil towards the subway tunnel. When the tunnel depth is 18 m, the excavation has the greatest influence on the pipe gallery, while when the tunnel depth is 24 m, this impact is the smallest.

As shown in Figure 11, in the first-level alluvial fan area, the vertical displacement of the pipe gallery does not decrease with the rising tunnel buried depth. The vertical displacement of the pipe gallery is the largest under an 18 m tunnel buried depth, but the smallest under a 24 m tunnel buried depth. The reason is that the lower soil layer of the first-level alluvial fan area is alternately distributed with coarse sand and silty clay. When the tunnel buried depth is 18 m, the corresponding stratum is composed of coarse sand, and the soil condition is poor, so the excavation has the greatest impact on the upper area. Therefore, the disturbance to the pipe gallery under an 18 m buried depth is larger than that under a 12 m buried depth, in which case the settlement of the pipe gallery is larger, as shown in the displacement diagram. The maximum settlement of pipe gallery occurs when the tunnel buried depth is 18 m, and the maximum

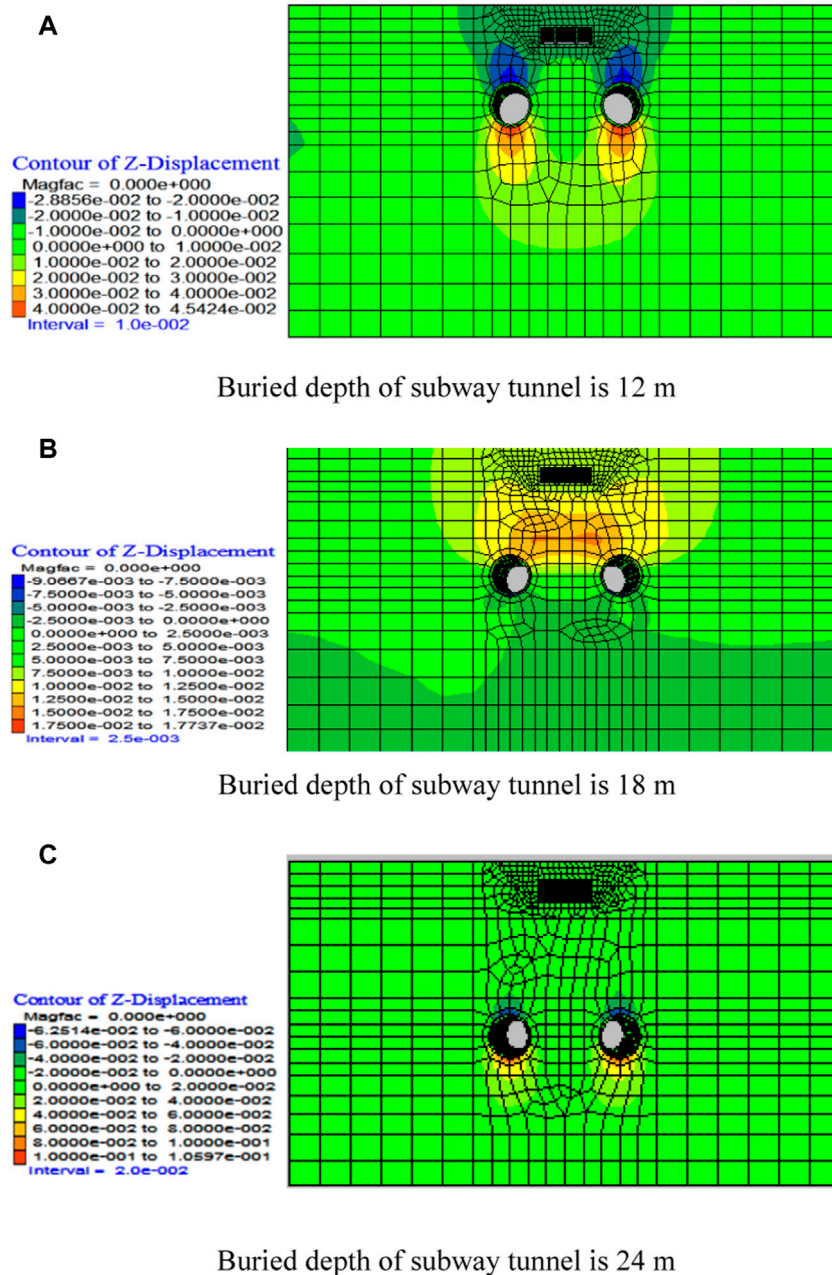


FIGURE 10

Vertical displacement diagram under different tunnel burial depths (unit: m).

vertical displacement is 18 mm. In addition, under the same buried depth, the deformation curve can be roughly seen as a straight line. That indicates that the existing pipe gallery is disturbed and produces uniform settlement, which is caused by the excavation of double-line subway tunnel in the same direction at the same time. When the tunnel depth is 24 m, the settlement deformation of the pipe gallery is the minimum, with a value of 6.2 mm. According to the standard for deformation control of utility tunnel (i.e., the allowable maximum settlement is -10 mm, and the maximum uplift is 5 mm), when the tunnel buried depth is 12 m and 24 m, the deformation criterion can be satisfied. Therefore, it is suggested to excavate the two lines of the shield tunnel in the same direction at the same time, which not only

ensures the safety of the existing pipe gallery, but also speeds up the construction progress of the project. By contrast, when the tunnel buried depth is 18 m, the deformation criterion cannot be met. In this case, it is necessary to take measures to reinforce the existing pipe gallery.

4.2 Impact of soil quality on existing pipe gallery

The subsection compares the influence of tunnel excavation on the stability of existing pipe gallery under different soil properties when

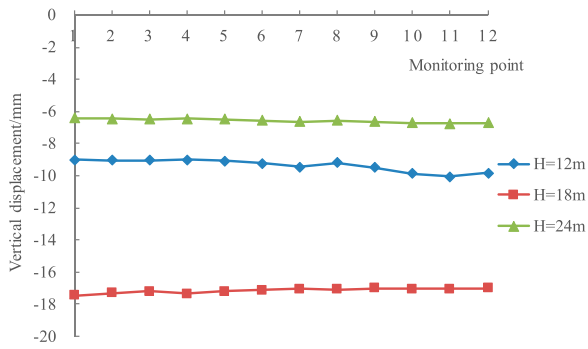


FIGURE 11
Vertical displacement curves of monitoring points in the pipe gallery.

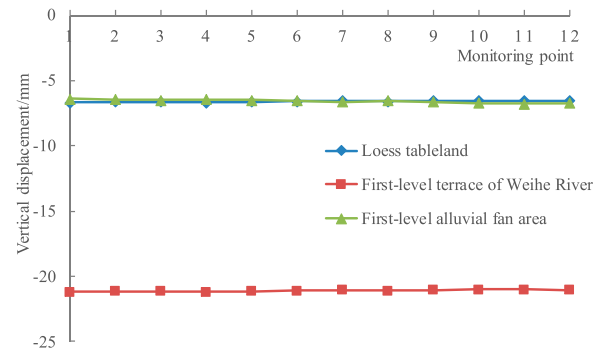


FIGURE 14
Vertical displacement curves under a 24 m tunnel buried depth.

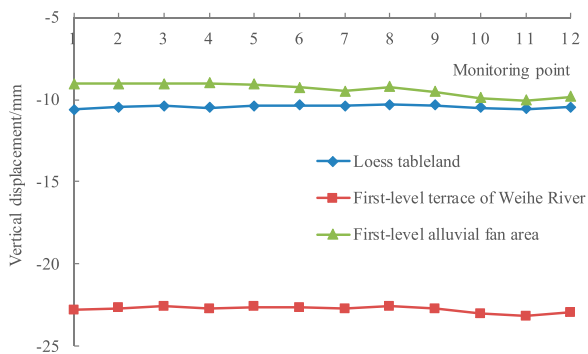


FIGURE 12
Vertical displacement curves under a 12 m tunnel buried depth.

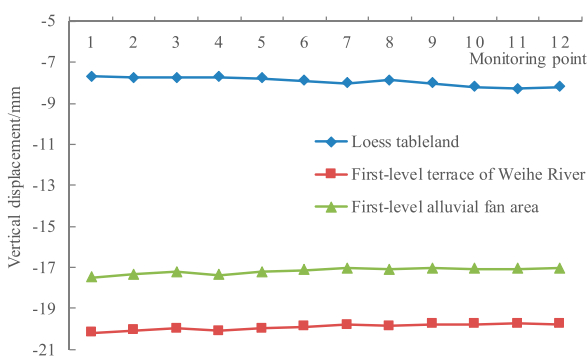


FIGURE 13
Vertical displacement curves under an 18 m tunnel buried depth.

the tunnel depth is constant. Figure 12 and Figure 14 show that the vertical displacement curves of monitoring points in the existing pipe gallery under different tunnel buried depths.

It can be seen from Figure 12 that the excavation of subway tunnel in the first-level alluvium fan area has the smallest impact on the existing pipe gallery, with a vertical displacement of pipe gallery of about 9.5 mm, followed by that in the loess tableland, with a vertical

displacement of about 10.5 mm. According to the standard for deformation control of utility tunnel, the stability of pipe gallery in these two areas can satisfy the deformation criterion. The excavation of the subway tunnel on the first-level terrace of Weihe River has the greatest impact on the pipe gallery, and the maximum vertical displacement of pipe gallery is 23 mm. According to the standard for deformation control of utility tunnel, the pipe gallery stability in this case cannot meet the deformation criterion. This is because the soil in the lower part of the Weihe first-level terrace is alternately distributed with silty clay and medium sand, and the tunnel is basically in the medium sand layer with poor soil conditions. Thus, the excavation has the greatest impact on the structure above.

As shown in Figure 13, the excavation of subway tunnel in the Loess tableland area has the smallest impact on the existing pipe gallery, and the vertical displacement of pipe gallery is basically 8 mm. According to the standard for deformation control of utility tunnel, the stability of the pipe gallery can roughly satisfy the deformation criterion. The subway tunnel excavation in the first-level alluvial fan area has the second smallest impact on the pipe gallery stability, with a vertical displacement of 17 mm. In this case, the stability of the pipe gallery cannot meet the deformation criterion. This is because when the buried depth is 18 m, the tunnel is in the layer consisting of silty clay and coarse sand, and the soil property is poor. As a result, the excavation has a great impact on the structure above. The excavation of the subway tunnel in the first-level terrace of Weihe River has the greatest impact on the existing pipe gallery, and the maximum vertical displacement of pipe gallery is 20.1 mm. According to the standard for deformation control of utility tunnel, the stability of the pipe gallery cannot satisfy the deformation criterion. This is because the lower soil layer of the first-level terrace of Weihe River is alternately distributed with silty clay and medium sand, and the tunnel is basically located in the silty clay layer. Additionally, the overall soil property of the first-level terrace of Weihe River is poor, and the upper and lower layers are medium sand, so the excavation has the greatest impact on the structure above.

It can be seen from Figure 14 that the excavation of subway tunnel in the loess tableland and the first-level alluvial fan area has almost the same impact on the existing pipe gallery, with a vertical displacement of pipe gallery of about 6.5 mm. According to the standard for deformation control of utility tunnel, the stability of the pipe gallery in these two areas can satisfy the deformation criterion. The lower soil layer in the first-level alluvial fan area is alternately

distributed with silty clay and coarse sand, but the subway tunnel is in the thick layer of silty clay. Thus, tunnel excavation has a small influence on the existing pipe gallery. The tunnel excavation in the first-level terrace of Weihe River has the greatest impact on the pipe gallery, and the maximum vertical displacement of pipe gallery is 21 mm. The pipe gallery stability in this case does not meet the deformation criterion. This is because the lower soil layer of the Weihe first-level terrace is alternatively distributed with silty clay and medium sand, and the tunnel is located between the two soil layers of silty clay and medium sand. Moreover, the overall soil quality of the Weihe first-level terrace is poor, so the excavation has the greatest impact on the structure above.

5 Conclusion

According to the simulation analysis in different regions of Xi'an, the supporting measures such as cushion and bolt play a crucial role in reinforcing the existing pipe gallery when it is subjected to the influence of the excavation of subway tunnel beneath it. For this reason, the lateral displacement of the pipe gallery is quite small, and thus can be ignored. And the pipe gallery is mainly affected by settlement deformation. The major conclusions of this paper are as follows.

- (1) When the regional soil quality is relatively stable and the difference of soil parameters is small, the settlement of pipe gallery declines with the rising spacing (buried depth of subway tunnel), such as the loess tableland. When the regional soil quality is unstable and the soil parameters differ significantly, the settlement of pipe gallery is greatly affected by the soil layer where the tunnel is located, such as the first-level terrace of Weihe River and the first-level alluvial fan area.
 - (2) In the loess tableland area, when the buried depth of subway tunnel is greater than 12 m, the settlement deformation of the existing pipe gallery does not exceed the allowable limit of 10 mm, which meets the deformation criterion. In the first-level terrace of Weihe River, when the tunnel depth is less than or equal to 24 m, the deformation criterion is not met. In the first-level alluvial fan area, when the tunnel burial depth is 12 m and 24 m, the deformation criterion is met; whereas when the tunnel burial depth is 18 m, the settlement deformation of the existing pipe gallery exceeds the allowable limit of 10 mm, so the deformation criterion is not met.
- Therefore, to reduce the disturbance of tunnel excavation to the existing pipe gallery, the influence of soil parameters and the

spacing between the tunnel and the pipe gallery should be considered first. In addition, various supporting methods such as soil layer grouting (to improve the soil properties) and cushion can also be considered.

Data availability statement

The original contributions presented in the study are included in the article/Supplementary Material, further inquiries can be directed to the corresponding author.

Author contributions

SW: Project administration, methodology, modeling, formal analysis, visualization, writing - original draft; HZ: Project administration, methodology, formal analysis, writing—review and Editing; YM: Methodology, formal analysis, writing—original draft; LN: Methodology, formal analysis, writing—original draft; TT: Modeling, visualization, writing—original draft.

Funding

This work was supported by Shaanxi Provincial Key Research and Development Project (2021SF2-02), the Public Welfare Geology Special Project of Shaanxi Province (202109, 20180303).

Conflict of interest

The authors declare that the research was conducted in the absence of any commercial or financial relationships that could be construed as a potential conflict of interest.

Publisher's note

All claims expressed in this article are solely those of the authors and do not necessarily represent those of their affiliated organizations, or those of the publisher, the editors and the reviewers. Any product that may be evaluated in this article, or claim that may be made by its manufacturer, is not guaranteed or endorsed by the publisher.

References

- Chen, R. P., Tang, L. J., Ling, D. S., and Chen, Y. M. (2011b). Face stability analysis of shallow shield tunnels in dry sandy ground using the discrete element method. *Geotech.* 38 (2), 187–195. doi:10.1016/j.compgeo.2010.11.003
- Chen, R. P., Zhu, J., Liu, W., and Tang, X. W. (2011a). Ground movement induced by parallel epb tunnels in silty soils. *Tunn. Undergr. Space Technol.* 1 (26), 163–171. doi:10.1016/j.tust.2010.09.004
- Dashti, S., Hashash, Y., Gillis, K., Musgrove, M., and Walker, M. (2016). Development of dynamic centrifuge models of underground structures near tall buildings. *Soil Dyn. Earthq. Eng.* 86, 89–105. doi:10.1016/j.soildyn.2016.04.014
- Duan, Xu, Dong, Qi, Ye, Wanjun, Men, Yuming, and Zhang, Chang yi (2020). Study on utility tunnel's strained condition crossing the transition zone of loess high embankment. *Chin. J. Undergr. Space Eng.* (5): 1529–1537 + 1579.
- Feng, Tianwei, Lü, Baowei, Li, Jingmei, and Li, Dechang (2018). Study on the influence of open-cut construction of utility tunnels on adjacent subway tunnel. *Mod. Tunn. Technol.* 55 (S2), 1116–1121. doi:10.13807/j.cnki.mtt.2018.S2.143
- Gao, Kai, and Haifeng, S. I. (2018). The impact of utility pipe tunnel on the overhead existing subway tunnel. *Cuangzhou Archit.* (4), 32–36.
- Hu, Xiang, and Xue, Weichen (2010). Experimental study on mechanical performance of prefabricated prestressed composite pipe rack. *J. Civ. Eng.* 43 (5), 29–37. doi:10.15951/j.tmgxb.2010.05.017
- Hu, Ziping, Zhang, Dan, and Zhang, Yaguo (2019). Test study on deformation and failure mechanisms of utility tunnels obliquely crossing ground fissures. *Chin. J. Rock Mech. Eng.* 38 (12), 2550–2560. doi:10.13722/j.cnki.jrme.2019.0308

- Kimura, H., Itoh, T., Iwata, M., and Fujimoto, K. (2005). Application of new urban tunneling method in baikoh tunnel excavation. *Tunneling Undergr. Space Technol.* 20 (20), 151–158. doi:10.1016/j.tust.2003.11.007
- Li, Jie, Yue, Qingxia, and Chen, Juan (2009). Research on shaking-table test and finite element numerical simulation of utility tunnel. *Earthq. Eng. Eng. Dyn.* 29 (4), 41–45. doi:10.13197/j.eeev.2009.04.016
- Li, Z. Q., Lai, J. X., Ren, Z. D., Shi, Y., and Kong, X. (2023). Failure mechanical behaviors and prevention methods of shaft lining in China. *Eng. Fail. Anal.* Vol. 143, 106904. Article ID 106904. doi:10.1016/j.engfailanal.2022.106904
- Liu, Naifei, Ning, Li, Li, Guofeng, Song, Zhanping, and Wang, Shuangjie (2022a). Method for evaluating the equivalent thermal conductivity of a freezing rock mass containing systematic fractures. *Rock Mech. Rock Eng.* 2022, 7333. doi:10.1007/s00603-022-03038-9
- Liu, Naifei, Ning, Li, Wang, Shuangjie, Li, Guofeng, and Song, Zhanping (2022b2023). A fully coupled thermo-hydro-mechanical model for fractured rock masses in cold regions. *Cold Regions Sci. Technol.* 205, 103707. doi:10.1016/j.coldregions.2022.103707
- Luo, Tao (2013). *Rayleigh wave research based on wavelet transform and response of the utility tunnel*. Shandong: Jianzhu University.
- Ma, Huiyong, Zhang, Liang, Zhang, Yutong, Mei, Yuan, and Zhao, Jiabing (2019). Ground cracking impact on utility tunnel stress properties under multiple working conditions. *J. Munic. Technol.* 37 (05), 206–209.
- Ma, S., Shao, Y., Liu, Y., Jiang, J., and Fan, X. L. (2017). Responses of pipeline to side-by-side twin tunnelling at different depths: 3d centrifuge tests and numerical modelling. *Tunn. Undergr. Space Technol.* 66, 157–173. doi:10.1016/j.tust.2017.04.006
- Ministry of Housing and Urban-Rural Development of the People's Republic of China (2011). *GB50007-2011 Code for design of building foundation*. Beijing: China Architecture and Building Press.
- Ministry of Housing and Urban-Rural Development of the People's Republic of China (2015). *GB50010-2010 Code for design of concrete structures*. Beijing: China Architecture and Building Press.
- Ministry of Housing and Urban-Rural Development of the People's Republic of China (2013). *GB50911-2013 Urban rail transit engineering monitoring technical specification*. Beijing: China Architecture and Building Press.
- Peng, Shixing. (2017). Consideration on the technical feasibility of the simultaneous construction of the utility tunnel and subway. *Fujian Archit. Constr.* (7), 164–166.
- Qin, Y. W., Lai, J. X., Yang, T., Zan, W. B., Feng, Z. H., Liu, T., et al. (2022). Failure analysis and countermeasures of a tunnel constructed in loose granular stratum by shallow tunnelling method. *Eng. Fail. Anal.* 141, 106667. doi:10.1016/j.engfailanal.2022.106667
- Shamsabadi, A., Law, H., and Amini, M. (2002). "Seismic rock-tunnel-structure interaction analysis," in Elsevier Science Ltd:12th European Conference on Earthquake Engineering, Oxford, 9-13 September 2002 (Oxford: Elsevier), 1–8.
- Shamsabadi, A., Sedarat, H., and Kozak, A. (2001). *Seismic soil tunnel structure interaction analysis of the posey webster street tunnels*. Oxford: Ustapan Soil-Structure-Interaction Workshop, 1–21.
- Shi, Xiaojun, Chen, Juan, and Li, Jie (2010). Shaking table test on utility tunnel under non-uniform seismic excitations(I): Experimental setup. *Earthq. Eng. Eng. Dyn.* 30 (1), 45–52.
- Tang, Aiping, Li, Zhiqiang, Feng, Ruicheng, and Zhou, Xiyuan (2009). Model experiment and analysis on seismic response of utility tunnel systems using a shaking table. *J. Harbin Inst. Technol.* (6), 1–5.
- Wang, Li, and Jiang, Shichao (2019). Research on the construction scheme of utility tunnel above-crossing existing subway. *Chin. J. Undergr. Space Eng.* 15 (S2), 717–723.
- Wu, Yuhai (2017). Numerical simulation of influence of the underground construction of the utility tunnel to underneath shield tunnel. *Constr. Technol.* (17), 105–109. doi:10.7672/sjgs2017170105
- Yang, Min, Li, Hongru, Ning, Li, and Yang, Shun (2020). Effect of subway excavation with different support pressures on existing utility tunnel in xi'an loess. *Adv. Civ. Eng.* 2020, 1–14. doi:10.1155/2020/8818949
- Yang, Min, Li, Hongru, Ning, Li, and Yang, Shun (2021). Influence of utility tunnel on the lower part of the existing double-track shield tunnel in loess soil. *Adv. Mater. Sci. Eng.* 2021, 1–13. doi:10.1155/2021/9927245
- Yang, Youbin, Li, Huapei, and Tong, Lin (2019). Study on the influence of adjacent construction of integrated pipe gallery foundation pits on existing subway tunnels. *Chin. J. Undergr. Space Eng.* 15 (S1), 188–194.
- Ye, Fei. (2014). *Seismic response analysis of pipe-utility tunnel structural system*. China: Institute of Engineering Mechanics.
- You, Haoyu. (2011). *Seismic isolation analysis on pipeline in utility tunnel*. China: Harbin Institute of Technology.
- You, Xinhua. (2017). Present status and future development trend of urban utility tunnel construction. *Urban Archit. Space* 24 (3), 6–9.
- Zhang, Yuwei, Fan, Shengyuan, Yang, Donghui, and Zhou, Fei (2022b). Investigation about variation law of frost heave force of seasonal cold region tunnels: A case study. *Front. Earth Sci.* 9, 806843. doi:10.3389/feart.2021.806843
- Zhang, Yuwei, Song, Zhanping, and Weng, Xiaolin (2022a). A constitutive model for loess considering the characteristics of structurality and anisotropy. *Soil Mech. Found. Eng.* 59 (1), 32. doi:10.1007/s11204-022-09781-z
- Zhao, Yongjian, Gong, Yi, Ding, Yong, and Dong, Xuehua (2018). Effect of explosion in a gas pipeline compartment of a utility tunnel on neighboring Metro tunnels. *Mod. Tunn. Technol.* 55 (06), 139–143. doi:10.13807/j.cnki.mtt.2018.06.019
- Zhu, Caihui, Li, Ning, Liu, Houxiang, and Zhang, Zhiqiang (2011). Analysis of ground settlement induced by workmanship of shield tunnelling. *Rock Soil Mech.* 32 (01), 158–164. doi:10.16285/j.rsm.2011.01.019
- Zhu, Caihui, Ning, Li, and Zhang, Zhiqiang (2010a). Analysis and prediction of land subsidence induced by shield construction in loess strata in Xi'an. *Chin. J. Geotechnical Eng.* 32 (07), 1087–1095.
- Zhu, Caihui, Ning, Li, and Zhang, Zhiqiang (2010b). Analysis and prediction of land subsidence induced by shield construction in loess strata in Xi'an. *Chin. J. Geotechnical Eng.* 32 (07), 1087–1095.
- Zhu, Lin. (2018). *Study on the harm of ground fissures on integrated pipe gallery in loess area*. China: Xi'an University of Technology.

Frontiers in Earth Science

Investigates the processes operating within the major spheres of our planet

Advances our understanding across the earth sciences, providing a theoretical background for better use of our planet's resources and equipping us to face major environmental challenges.

Discover the latest Research Topics

[See more →](#)

Frontiers

Avenue du Tribunal-Fédéral 34
1005 Lausanne, Switzerland
frontiersin.org

Contact us

+41 (0)21 510 17 00
frontiersin.org/about/contact

